INNER EAR BIOLOGY: DEVELOPMENT, PHYSIOPATHOLOGY, REPAIR AND RECOVERY

EDITED BY: Berta Alsina, Stefan Heller and Isabel Varela-Nieto
PUBLISHED IN: Frontiers in Cell and Developmental Biology

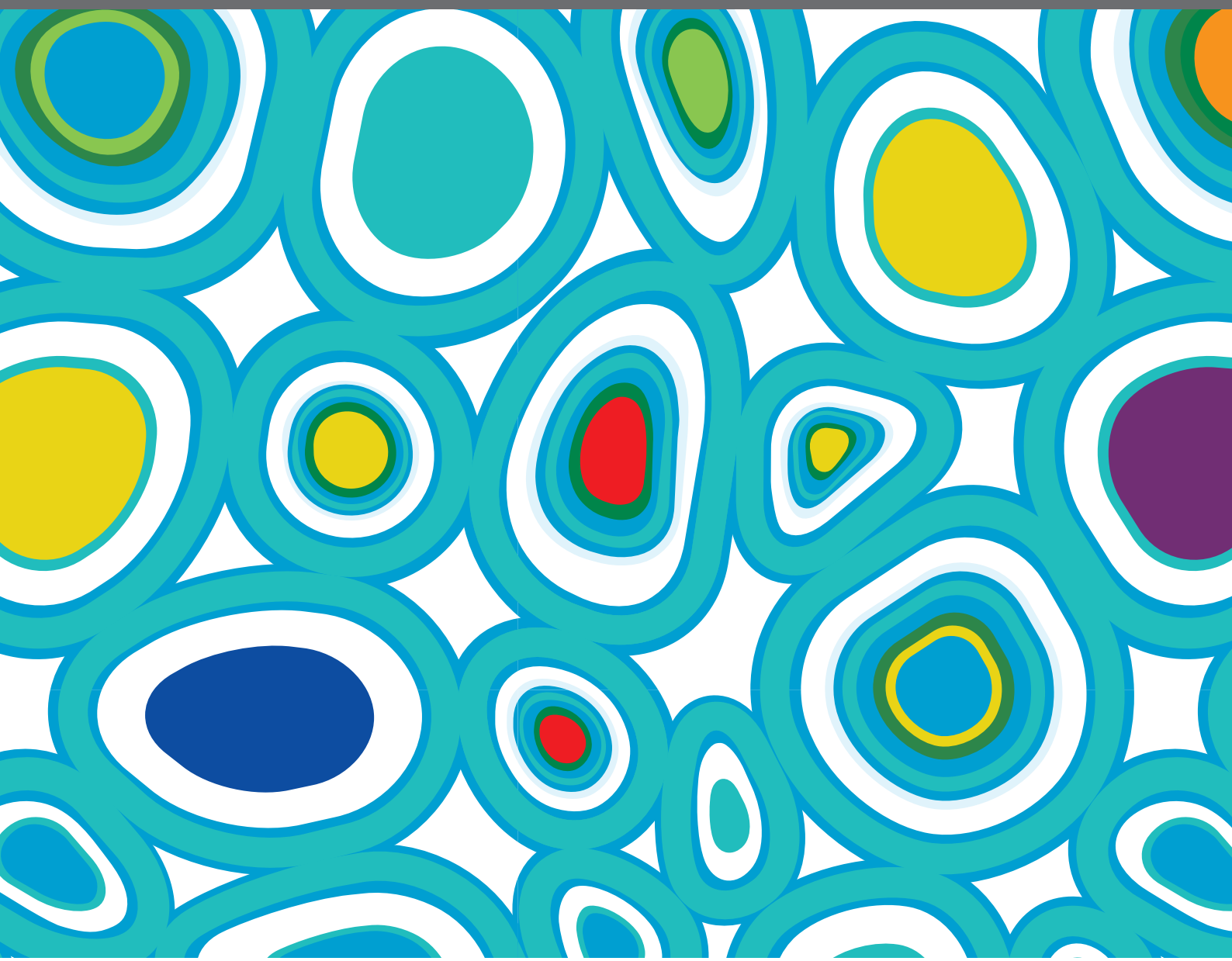

frontiers Research Topics

frontiers

ISSN 1664-8714
ISBN 978-2-83250-621-9
DOI 10.3389/978-2-83250-621-9

About Frontiers

Frontiers is more than just an open-access publisher of scholarly articles: it is a pioneering approach to the world of academia, radically improving the way scholarly research is managed. The grand vision of Frontiers is a world where all people have an equal opportunity to seek, share and generate knowledge. Frontiers provides immediate and permanent online open access to all its publications, but this alone is not enough to realize our grand goals.

Frontiers Journal Series

The Frontiers Journal Series is a multi-tier and interdisciplinary set of open-access, online journals, promising a paradigm shift from the current review, selection and dissemination processes in academic publishing. All Frontiers journals are driven by researchers for researchers; therefore, they constitute a service to the scholarly community. At the same time, the Frontiers Journal Series operates on a revolutionary invention, the tiered publishing system, initially addressing specific communities of scholars, and gradually climbing up to broader public understanding, thus serving the interests of the lay society, too.

Dedication to Quality

Each Frontiers article is a landmark of the highest quality, thanks to genuinely collaborative interactions between authors and review editors, who include some of the world's best academicians. Research must be certified by peers before entering a stream of knowledge that may eventually reach the public - and shape society; therefore, Frontiers only applies the most rigorous and unbiased reviews.
Frontiers revolutionizes research publishing by freely delivering the most outstanding research, evaluated with no bias from both the academic and social point of view. By applying the most advanced information technologies, Frontiers is catapulting scholarly publishing into a new generation.

What are Frontiers Research Topics?

Frontiers Research Topics are very popular trademarks of the Frontiers Journals Series: they are collections of at least ten articles, all centered on a particular subject. With their unique mix of varied contributions from Original Research to Review Articles, Frontiers Research Topics unify the most influential researchers, the latest key findings and historical advances in a hot research area! Find out more on how to host your own Frontiers Research Topic or contribute to one as an author by contacting the Frontiers Editorial Office: frontiersin.org/about/contact

INNER EAR BIOLOGY: DEVELOPMENT, PHYSIOPATHOLOGY, REPAIR AND RECOVERY

Topic Editors:
Berta Alsina, Pompeu Fabra University, Spain
Stefan Heller, Stanford University, United States
Isabel Varela-Nieto, Spanish National Research Council (CSIC), Spain

Citation: Alsina, B., Heller, S., Varela-Nieto, I., eds. (2022). Inner Ear Biology: Development, Physiopathology, Repair and Recovery. Lausanne: Frontiers Media SA. doi: 10.3389/978-2-83250-621-9

Table of Contents

frontiers | Frontiers in Cell and Developmental Biology

TYPE Editorial
PUBLISHED 13 October 2022
DOI 10.3389/fcell.2022.1049463

OPEN ACCESS

EDITED AND REVIEWED BY
Hong-Bo Zhao,
Yale University, United States

*CORRESPONDENCE
Berta Alsina,
berta.alsina@upf.edu
Stefan Heller,
hellers@stanford.edu
Isabel Varela-Nieto,
ivarela@iib.uam.es

SPECIALTY SECTION
This article was submitted to Molecular and Cellular Pathology, a section of the journal Frontiers in Cell and Developmental Biology

RECEIVED 20 September 2022
ACCEPTED 27 September 2022
PUBLISHED 13 October 2022

CITATION
Alsina B, Heller S and Varela-Nieto I (2022), Editorial: Inner ear biology: Development, physiopathology, repair and recovery.
Front. Cell Dev. Biol. 10:1049463.
doi: 10.3389/fcell.2022.1049463

Editorial: Inner ear biology: Development, physiopathology, repair and recovery

Berta Alsina[1]*, Stefan Heller[2,3]* and Isabel Varela-Nieto[4,5,6]*

[1]Department of Medicine and Life Sciences, Universitat Pompeu Fabra, Parc de recerca Biomèdica de Barcelona, Barcelona, Spain, [2]Department of Otolaryngology, Head and Neck Surgery, Stanford University School of Medicine, Stanford, CA, United States, [3]Institute for Stem Cell Biology and Regenerative Medicine, Stanford University School of Medicine, Stanford, CA, United States, [4]Institute for Biomedical Research "Alberto Sols" (IIBm), Spanish National Research Council-Autonomous University of Madrid (CSIC-UAM), Madrid, Spain, [5]Rare Diseases Networking Biomedical Research Centre (CIBERER), CIBER, Carlos III Institute of Health, Madrid, Spain, [6]La Paz Hospital Institute for Health Research (IdiPAZ), Madrid, Spain

KEYWORDS

inner ear development, regeneration, hearing loss, cochlea, morphogenesis, neural activity

Editorial on the Research Topic
Inner ear biology: Development,physiopathology,repair and recovery

Inner Ear biology is broad and multidisciplinary, ranging from studies on cell and tissue organization mechanisms during development, the causes of hearing loss, and novel treatment therapies for repair. These questions are tackled using state-of-the-art methodologies and different animal model systems, some being highlighted in this Research Topic.

During embryogenesis, the inner ear acquires a highly complex 3D structure, with very apparent dorsal semicircular canals and the ventral coiled cochlea. In this Research Topic, several papers investigate the tissue rearrangements that help acquiring the adult shape of the inner ear. In Jones et al., the power of zebrafish genetics and live imaging are combined to uncover the requirement of sulfate proteoglycans for projection outgrowth necessary for semicircular development. The zebrafish mutant exostosin (ext2) that impairs heparan sulphate synthesis has defects in the formation of the semicircular canals, together with deficiencies in cartilage, bone, and teeth development. This paper highlights the relevance of ECM in inner ear morphogenesis. During cochlear maturation, a dynamic interplay between cell death and epithelial remodeling is revealed by Borse et al., who show that the appearance of macrophages in the cochlea correlates with the time of greater epithelial ridge (GER) cell death. How macrophages are attracted to the GER is an open question since experiments indicate that they need another attractant than the CX3CL1 chemokine. Despite the link between macrophage invasion and GER remodeling, macrophages are indispensable for GER regression.

Most cochlear cells derive from otic precursor cells, but intermediate cells of the stria vascularis derive from neural crest cells that ingress into the developing cochlea. Genetic linage

tracing reveals the migratory path of neural crest cells and shown in Renauld et al. In the developing cochlea, melanocytic cells of neural crest origin extend protrusions, ingress, and migrate on top of the marginal cells. These melanocytes have a dual origin; on the one hand, they derive from migratory neural crest cells, and on the other, from Schwann cell precursors located at the cochlea-vestibular ganglion. It would be interesting to perform live imaging to explore in detail these cell movements.

Recent advancements in understanding cochlear development have been made by improving the culturing conditions of cochleae *in vitro*. Together with imaging, a better understanding of the heterogeneity of cells and molecular networks operating during cell specification is currently achieved thanks to novel single-cell sequencing technologies. As discussed in the review by Kelley, different methods of scRNA-seq are available, each with particular advantages depending on the type of data sought. Methods sequencing full-length cDNA allow the discovery of novel splicing variants, while bar-coding approaches allow sequencing a greater number of cells and can improve the description of cellular diversity within a tissue. The author suggest that the difficulty of isolating cells of the inner ear at late postembryonic stages makes isolation of single nuclei the preferred option. In these cell dissociation experiments, unfortunately, spatial information is lost. New techniques of scRNA-seq on top of frozen sections, although still expensive, are the future for capturing the transcriptome while maintaining the knowledge of the position of each cell.

One of the master regulators of inner ear neuronal lineage specification is the proneural factor NeuroD. In Filova et al., the effects of early NeuroD elimination are analyzed in mice using Foxg1 cre that is expressed in the otic placode but not the brainstem. As expected, the auditory ganglion is severely reduced in the NeuroD KO, but interestingly the cochlea and vestibular sensory patches are also severely developmentally affected. In particular, the cochlea is shorter, with ectopic and disorganized hair cells within and outside the sensory epithelium. Further work should elucidate the underlying mechanisms of the different phenotypes.

The zebrafish is a well-established model for studying tissue regeneration, and, in contrast to mammals, hair cells regenerate. However, whether inner ear sensory neurons can regenerate upon damage is unknown. Schwarzer et al. establish a lesion paradigm to investigate whether the cochlea-vestibular ganglion regenerates after cell death upon damage. While NeuroD-positive cells are proliferative during development, they become postmitotic later on. NeuroD cells reenter the cell cycle after lesion and new neurons are generated. It will be interesting to analyze the cell identities of newly generated cochleo-vestibular neurons, perhaps with scRNA-seq, and to determine whether the neurons are functional. The zebrafish lateral line is an excellent system to image hair cell and neuronal activity *in vivo* with light sheet fluorescent microscopy (LSFM). Zhang et al. reveal that spontaneous activity of hair cells happens in two distinct domains, at the bundle and the presynaptic compartment, where it drives the synapse activity. This work highlights the detection of spontaneous activity in several cells, such as supporting cells and efferent nerves, being uncoupled with the spontaneous activity of hair cells. In another set of experiments, Le Prell et al., explore whether Calcitonin-gene-related-peptide (CGRP) modulates sound-evoked auditory nerve (AN) activity or affects the AN spontaneous activity. Infusion of CGRP into the pig cochlea and measurements in the round window suggest that can do both. The work provides new information of the role of olivocochlear efferent neurotransmitters in modulating auditory nerve activity.

This topic also presents advances in research to understand the genetic and molecular bases of hearing and deafness to study new possible targets for the prevention and treatment of hearing loss.

The stria vascularis, an important tissue for maintaining the adult endocochlear potential is becoming more and more interesting for its roles in cochlear metabolic homeostasis, ageing, and its roles in response to insults including noise and ototoxic drugs. Thulasiram et al. review how the different cell types that compose the stria vascularis contribute to maintaining adult hearing with a focus on how its alterations contribute to cochlear degeneration and, finally, hearing loss.

The control of redox balance is key to the survival of hair cells and, therefore, of the rest of cochlear cell types and for hearing. This control also regulated from the stria vascularis, although not only, has been the subject of numerous studies whose ultimate goal is the design of otoprotective treatments. On this topic, the original article by Rousset et al. addresses the study of the deficiency in NOX3, one of the enzymes involved in controlling the redox response. After studying a mouse deficient in *Nox3*, the authors propose that inhibition of this mechanism protects against cochlear insult caused by excessive exposure to noise. This finding confirms that during the response to noise, the over-activation of NOX3 increases the release of reactive oxygen species (ROS), ultimately resulting in cell damage and death. It would be interesting to know if temporary inhibition of NOX3 in the acute phase of injury has similar otoprotective effects since NOX3 activity is necessary for cellular functioning.

Draf et al. show how by using a collection of small molecules designed for the study of autophagy, they were able to dissect the participation of the proteasome in the cochlear response to the insult caused by toxic drugs. Specifically, they study the deterioration and loss of hair cells caused by treatment with broad-spectrum aminoglycoside antibiotics. This study provides relevant data on the proteasome's role in maintaining the delicate cochlear homeostasis. It opens new perspectives for the development of new strategies in the prevention of ototoxicity.

Finally, Blanc et al. establish a novel delivery route for adeno-associated virus delivery to both inner ears of mice. This relevant study shows that a single virus injection into the cisterna magna, a cerebrospinal fluid-filled opening close to the brain, is sufficient

for efficient binaural transduction of inner hair cells and, to a lesser extent, spiral ganglion neurons. Reaching both inner ears with a single and straightforward delivery strategy is innovative but likely requires the development of specific viruses for their respective inner ear target cell types.

We hope that the reader will find in this Research Topic a flavor of the emerging questions in the exciting field of inner ear biology and hearing loss.

Author contributions

All authors listed have made a substantial, direct, and intellectual contribution to the work and approved it for publication.

Conflict of interest

The authors declare that the research was conducted in the absence of any commercial or financial relationships that could be construed as a potential conflict of interest.

Publisher's note

frontiers in Cell and Developmental Biology

ORIGINAL RESEARCH
published: 26 October 2021
doi: 10.3389/fcell.2021.762751

A Screen of Autophagy Compounds Implicates the Proteasome in Mammalian Aminoglycoside-Induced Hair Cell Damage

Clara Draf[1,2], Taylor Wyrick[3], Eduardo Chavez[1], Kwang Pak[1], Arwa Kurabi[1], Anke Leichtle[4], Stefan Dazert[2] and Allen F. Ryan[1,5,6]*

[1] Department of Surgery/Otolaryngology, University of California, San Diego, San Diego, CA, United States, [2] Department of Otolaryngology, St. Elisabeth-Hospital, Ruhr University Bochum, Bochum, Germany, [3] Department of Biology, University of California, San Diego, San Diego, CA, United States, [4] Department of Otolaryngology, University Medical Center Schleswig-Holstein, Lübeck, Germany, [5] Department of Neurosciences, University of California, San Diego, San Diego, CA, United States, [6] VA San Diego Healthcare System, San Diego, CA, United States

OPEN ACCESS

Edited by:
Isabel Varela-Nieto, Consejo Superior de Investigaciones Científicas (CSIC), Spain

Reviewed by:
Laura Astolfi, University of Padua, Italy
Nesrine Benkafadar, Stanford University, United States
Federico Kalinec, University of California, Los Angeles, United States

***Correspondence:**
Clara Draf
claradraf@gmail.com

Specialty section:
This article was submitted to Molecular and Cellular Pathology, a section of the journal Frontiers in Cell and Developmental Biology

Received: *22 August 2021*
Accepted: *05 October 2021*
Published: *26 October 2021*

Citation:
Draf C, Wyrick T, Chavez E, Pak K, Kurabi A, Leichtle A, Dazert S and Ryan AF (2021) A Screen of Autophagy Compounds Implicates the Proteasome in Mammalian Aminoglycoside-Induced Hair Cell Damage. Front. Cell Dev. Biol. 9:762751. doi: 10.3389/fcell.2021.762751

Introduction: Autophagy is a degradative pathway to safely break down and recycle dysfunctional cellular components. There is prior evidence of autophagy participation during hair cell (HC) damage. Our goal was to screen compounds targeting different aspects of autophagy for their effects on HC loss due to an ototoxic aminoglycoside, gentamicin (GM).

Methods: The SELLECKChem autophagy compound library, consisting of 154 compounds with defined autophagy inducing or inhibitory activity, was used for targeted screening *in vitro* model of ototoxicity. Organ of Corti from postnatal days 3–5 pou4f3/GFP transgenic mice (HCs express green fluorescent protein) were utilized. The organs were micro-dissected, and basal and middle turns divided into micro-explants individually placed into the single wells of a 96-well plate. Samples were treated with 200 μM of GM plus three dosages of tested compound and cultured for 72 h. Negative controls were treated with media only; positive ototoxicity controls were treated with GM only.

Results: The majority of the library compounds had no effect on GM-induced HC loss. However, 18 compounds exhibited a significant, protective effect, two compounds were protective at low dosage but showed enhanced GM toxicity at higher doses and one compound was toxic to HCs in the absence of GM.

Conclusions: This study evaluated many autophagy compounds that have not been tested previously on HCs. The disparate results obtained underscore the complexity of autophagy events that can influence HC responses to aminoglycosides, but also implicate the proteosome as an important damage mechanism. The screening results can serve as basis for further studies with protective compounds as potential drug targets.

Keywords: autophagy, hair cell, aminoglycoside–ototoxicity, *in vitro* screen, inner ear

INTRODUCTION

Ototoxicity is a significant side effect of some valuable medications that are used to treat life-threatening diseases. Ototoxic drugs can cause irreversible damage to the inner ear, leading to loss of hearing and balance function. A major class of ototoxic drugs are the aminoglycoside antibiotics. Aminoglycoside-induced ototoxicity occurs in as many as 50% of patients with multi-drug resistance tuberculosis and in up to 20% of children treated for cystic fibrosis (Al-Malky et al., 2015; Sagwa et al., 2015).

The aminoglycoside antibiotic, gentamicin (GM) was discovered in 1963 as an extract of *Micromonospora purpurea*. It is recommended as an effective, safe and essential medicine (Abou-Zeid et al., 1978; Obregon et al., 1994), widely used to treat endocarditis, meningitis, pelvic inflammatory disease, urinary tract infections, bone infections, pneumonia and other bacterial infections, including sepsis (Hamilton, 2001). Although GM is an extremely effective antimicrobial, ototoxicity is its major side effect (Kim et al., 2017; Sapizhak et al., 2017). The sensory hair cells (HCs) of the inner ear are major targets of GM toxicity. As terminally differentiated cells, HCs are unable to regenerate. Loss of HCs due to ototoxicity causes permanently reduced hearing sensitivity, with complete deafness in severe cases (Xing et al., 2017).

Oxidative stress and apoptosis are major drivers of GM induced ototoxicity, which implies that autophagy is also involved (He et al., 2018). Autophagy is an intracellular, lysosomal-mediated process in which dysfunctional cell material is broken down and recycled (Mizushima, 2011; He et al., 2018). This results in a dynamic relationship between autophagy, oxidative stress, damage to organelles and proteins, and apoptosis (Lee et al., 2012; Benkafadar et al., 2019). Autophagy is an important component of apoptosis, packaging damaged cellular constituents prior to cell dissolution. Autophagy can also play a role in the survival of cells in stress conditions, such as starvation and oxidative stress, by preventing the intracellular and extracellular spread of damage (Mizushima et al., 2008; Esclatine et al., 2009; Rabinowitz and White, 2010). Autophagy participates in regulating other physiological processes in non-stress situations, such as cell proliferation and differentiation, where cellular constituents must be destroyed or recycled (Esclatine et al., 2009; Oh et al., 2012; Magarinos et al., 2017). However, when autophagy is over-enhanced, cellular components essential for cell survival can be degraded, leading to cell death (Chen et al., 2010). Given its multifunctional nature, it is not surprising that autophagy dysfunction has been suggested to be involved in several pathological changes, such as cancer, inflammation, neurodegenerative disease, and metabolic disorders (Levine and Kroemer, 2008; Arroyo et al., 2014; Ryter et al., 2014).

Autophagy (**Figure 1**) is initiated by the formation of double membrane cytosolic vesicles, called the phagophore or isolation membrane, that contains damaged cellular constituents (Mizushima and Komatsu, 2011). The phagophore matures into a closed double-membrane-bound structure and then fuses with lysosomes, called the autophagosome, for disposal of its contents (Ohsumi, 2001). Autophagy involves the coordinated, and sequential activation of specific sets of autophagy-related genes (Ohsumi, 2001).

In the inner ear, autophagy has been shown to be an essential catabolic mechanism which is necessary for normal embryonic development (Taylor and Kirkegaard, 2008). The mechanism also responds to otic injury in the adult mouse, for autophagic recycling of intracellular components and elimination of deleterious molecules and organelles (Taylor and Kirkegaard, 2008). Inhibition of the autophagic pathway has been shown to provoke HC degeneration, the damage of neurogenesis and the aberrant axonal outgrowth, leading to hearing loss (Aburto et al., 2012). Conversely, activation of autophagy in HCs and oC-derived cell lines reduces ROS levels and also promotes cell survival (He et al., 2018). With respect to aminoglycoside ototoxicity, a relatively small number of autophagy studies have been performed. However, inhibition of autophagy has been shown to enhance Neomycin damage to HCs (He et al., 2018), and impaired autophagy has been proposed as a mechanism of delayed HC death in GM ototoxicity (Kim et al., 2017).

Given the complexity of the autophagy process and its diverse roles in cellular function and damage, the objective of this study was to screen compounds targeting different aspects of autophagy for their effects on HC loss due to GM. The goal was to enhance understanding of the role of autophagy in ototoxicity, and to identify and compare potentially protective compounds.

MATERIALS AND METHODS

Animals

Transgenic neonatal mice (3–5 days) in which eGFP was selectively expressed in HCs under the control of a *pou4f3* promoter construct (Masuda et al., 2011) were used. All experiments were performed to National Institutes of Health guidelines and approved by the Institutional Animal Care and Use Committee of the VA San Diego Medical Center.

Microdissection

The organ of Corti (oC) was dissected from the cochlea of 3–5 postnatal day *pou4f3*/eGFP mouse neonates. The apical region of each epithelium, which is relatively insensitive to aminoglycoside toxicity, was discarded. The basal and middle regions of the epithelium were divided using a diamond scalpel into micro-explants consisting of approximately 20 inner HCs and the 60 associated outer HCs. Micro-explants were individually plated in each well of a flat-bottom 96 well plate in media consisting of DMEM F-12(Gibco) plus 30 U/ml Penicillin and 5% FBS, and maintained in a humidified tissue culture incubator (37°C, 5% CO_2). Methods workflow is depicted in **Figure 2**. Mature hair cells at later times are more difficult to micro-dissect and also do not survive well in culture.

Screening

Targeted screening was performed using the SelleckChem Autophagy Compound Library (Z167594, Selleck Chem,

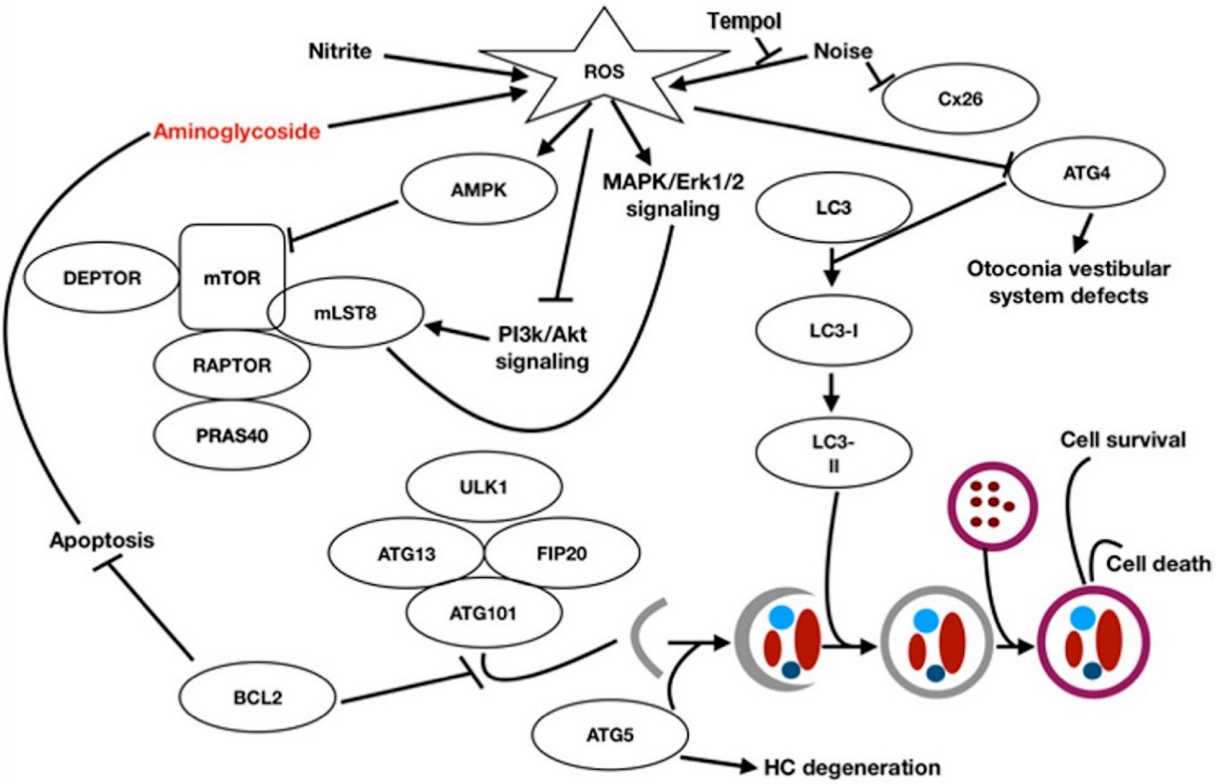

FIGURE 1 | Autophagy signal pathway and relationship with the auditory system [Figure modified after He et al. (2018)] Macroautophagy: A part of the endoplasmic reticulum encloses the structures to be degraded and isolates them with a double membrane (autophagosome). The autophagosome binds to a lysosome under hydrofusion. This results in the degradation of the autophagosomal components.

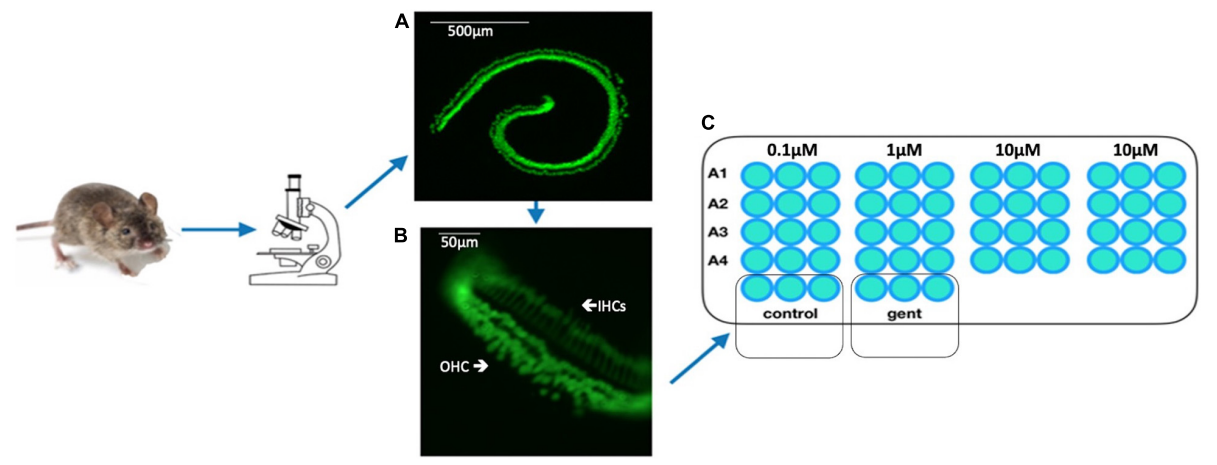

FIGURE 2 | Schematic of workflow from the organ of Corti **(A)** of the pou4f3/GFP transgenic mouse to microexplants **(B)** into the 96-well plate which contained nutrient medium, autophagy compound (A1–A4) and GM **(C)**. The microexplant **(B)** at the beginning of the treatment. The typical structure of one row of IHCs and 3 rows of OHCs is visible.

Houston, TX, United States), consisting of 154 autophagy-related compounds targeting the: PI3K/Akt/mTOR (15%), DNA damage and sirtuin (15%), cell cycle (15%), proteasome and ubiquitin (10%), transmembrane transporters (10%), apoptosis (5%), cytoskeletal signaling (5%), GPCR and G-protein (5%) among other (20%) pathways. The library represents a variety of classes of compounds, including a number of autophagy inducing and autophagy inhibiting compounds which at present had not previously been applied to HC damage. Test compounds were initially dissolved in DMSO and diluted in

culture media with the total amount of DMSO adjusted to a final concentration of 0.1%. Each experimental oC micro-explant was pretreated for 24 h with one of the library compounds at concentration of 0.1, 1, or 10 μM, performed in triplicate wells. On the following day media containing 200 μM gentamicin as well as the test autophagy compound with the appropriate concentration was added, and the micro-explants were cultured for 72 h. Untreated (negative) controls were maintained in media alone and positive controls were treated with 200 μM GM alone (**Figure 3**). Compound controls were treated with the highest concentration of the compound (10 μM) alone. Media for all control groups contained 0.1% DMSO, to match the experimental groups. Compounds were screened in duplicated 96-well plates with 5–7 autophagy compounds per plate, plus controls. Green fluorescent protein-positive HCs were imaged by fluorescence microcopy on each day of treatment, and survival curves were generated for each compound and condition. HC counts, including both inner and outer HCs, were evaluated in ImageJ with the Macro "ITCN" or "Cell Counter," and normalized as percentages to the number of HCs present on D1, prior to the start of GM treatment. Any micro-explants that did not attach and flatten in the well by D1 were excluded, because HC counts could not be accurately quantified at that time. There were sufficient wells on each plate that three micro-explants per condition could almost always be accommodated even with some unattached samples. Autophagy compounds that showed a significant protective effect, as compared to the control, in the initial screen were repeated for a second round at the three different concentrations. A compound was scored as "protective" if there was an overall significance for six wells of any concentration. A dose-dependent protection was attributed if there was a statistical significance at all three concentrations (18 wells).

Statistical analysis was performed using GraphPad Prism6, StatView5, using the Kruskal–Wallis non-parametric ANOVA to detect treatment effects. Individual condition comparisons were performed using the Mann–Whitney *U* test, with correction for multiple comparisons. For purposes of the figures, standard deviations were calculated from the non-normalized HC counts. Validation Redox compound "hits" were identified in the initial round of screening as deviating significantly from the controls. Following this initial screen, repeat plates were prepared in an identical manner for all hits, for a total N of six micro-explants. Statistical analysis was then repeated. Compounds that demonstrated a significant effect when the following round was included were considered to be confirmed.

RESULTS

Control Micro-Explants and Gentamicin Cytotoxicity

Each 96 well plate had its own negative and positive control. HC counts from negative and positive control micro-explants were converted to percent survival relative to Day 1 (D1, just prior to GM exposure), and averaged across all plates. Imaging of GFP-positive HCs in control wells typically showed HC survival similar to that illustrated in **Figure 3**. Untreated (negative control) micro-explants maintained only in culture media showed near-complete HC survival from D1-D3 ranging from 94% on D2 to 91% on D3. On Day 4, HC survival was reduced to a range of 80–68%. In contrast, HCs treated with 200 μM GM

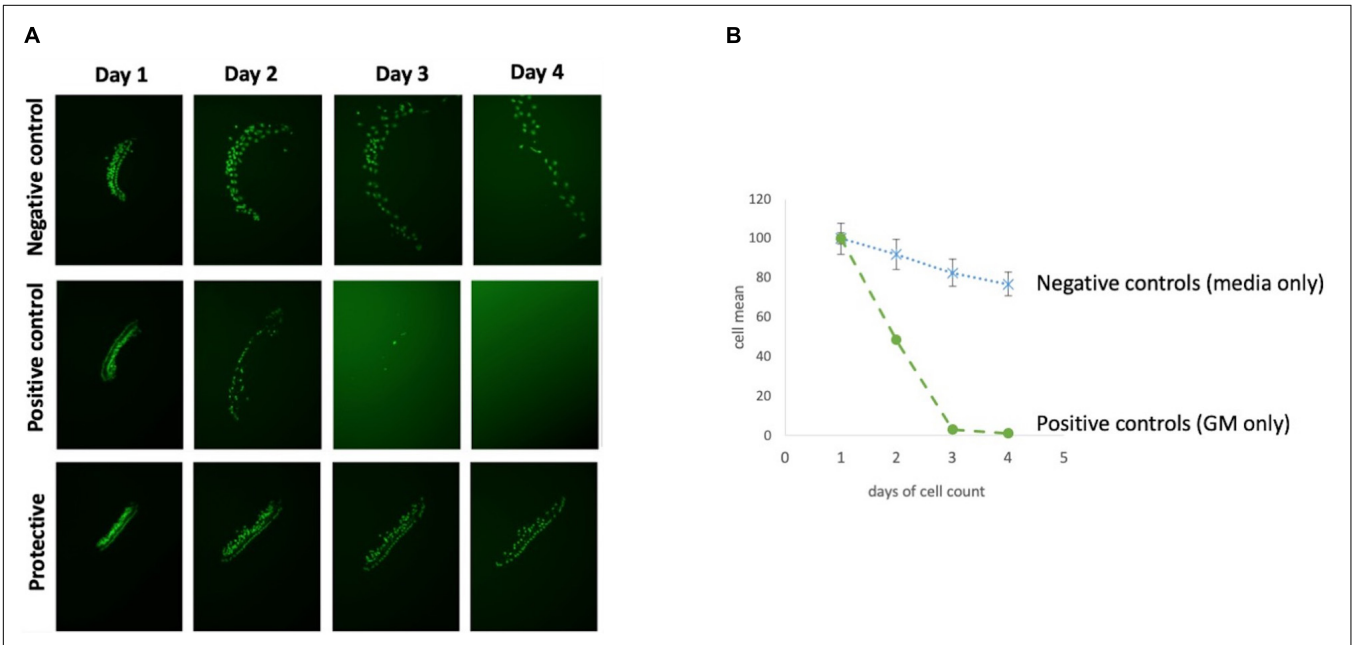

FIGURE 3 | Overview of HC decrease over 72 h. **(A)** Micro-explant pictures showing the fluorescent HCs over the experimental time course and **(B)** Illustration survival curves of positive and negative control of an autophagy compound.

(positive control) showed significant losses by D2 with an average HC survival of 52%, D3 HC survival was 13%, while D4 showed continued losses to 8% survival. As expected, Kruskal–Wallis and Mann–Whitney analysis showed a significant difference between negative and positive controls from D2–D4. No differences were observed between explants from the basal or middle regions of the cochlea, consistent with the high dosage of GM. Nevertheless, there were plates in which some variation occurred in the positive and/or negative controls. Therefore the results for each compound were compared statistically to positive controls from the same plate, generated with the same batches of media and GM. Additionally, each compound that was statistically different from the control was repeated for validation.

Library Results

The effects of the 154 compounds could be divided into three groups, autophagy compounds which exhibited:

I. No effect.
II. Protective effect.
III. Toxic effect.

Group I: No Effect

The majority of the 154 autophagy- inducing and/or -inhibiting compounds had no significant effect on HCs after GM treatment. An example is illustrated in **Figure 4**. When the highest concentration (10 μM) of autophagy compound was added to the micro-explant HC numbers were similar to that seen for negative control micro-explants cultures in media alone. Adding three different concentrations of autophagy compound plus 200 μM GM produced HC survival rates comparable to those observed with GM alone.

Group II: Protective

Eighteen autophagy compounds showed statistically significant protection of HCs in micro-explants treated with both the compound and gentamicin (**Table 1**). Within the group of protective compounds the observed protective effect could be divided into strong, medium and slight protection (**Table 2**). Strong protective compounds exhibited significant HC survival on all 3 days, varying in concentration (**Figure 5A**). Medium protective compounds showed improved HC survival on 2 days with one or two concentrations (**Figure 5B**), while slightly/mildly protective compounds reduced HC loss on D1 and only for 10 μM concentration (**Figure 5C**). There were two test substances that exhibited a bimodal trait i.e., significant protection at low concentrations, but enhancing GM damage at the highest concentration. Bortezomib and Brefeldin A exhibited significant protective traits at 0.1 μM, Brefeldin A also with 1 μM on Day 2, they both demonstrated significantly enhanced early HC loss due to gentamicin at 10 μM (**Figure 6**). We observed this "push-pull" effect with tyrosine kinase inhibitors in previous studies (Ryals et al., 2017).

Group III: Toxic

One autophagy compound BGT 226 showed HC decrease when treated with 10 μM of the compound alone (even in the absence of gentamicin). This was significant at 48 and 72 h (**Figure 7**).

DISCUSSION

Summary

Using an assay based on micro-explants of the neonatal mouse organ of Corti, a variety of autophagy compounds were screened for their ability to alter aminoglycoside damage to mammalian cochlear HCs *in vitro*. All statistically significant "hits" were confirmed by re-screening. Of a total of 154 compounds tested, 18 exhibited protective effects against GM toxicity, two of these compounds: Bortezomib, a protein homeostasis inhibitor and Brefeldin A, a cell cycle regulator were protective at low dosage but showed enhanced GM toxicity at high dosage. One compound, BGT 226 an Inhibitor of the PI3K/AKT/mTOR pathway was toxic to HCs in the absence of GM.

HC Protective Autophagy Compounds

Among the 154 compounds tested, 18 proved to be protective to HCs. To our knowledge, none of the autophagy compounds identified in the screen have been previously identified as influencing HC damage *in vitro* or *in vivo*. While all exhibited statistically significant effects, the range of protection varied from slight to strong. The protective autophagy compounds had a broad spectrum of activities ranging from protein homeostasis inhibitors, cell cycle and receptor kinase inhibitors to calcium channel and calcium uptake blockers. However, unlike our prior screens of kinase inhibitors (Ryals et al., 2017) and antioxidants (Noack et al., 2017), many of the compounds in the autophagy library are not highly specific to autophagy. The protective autophagy compounds found in this screen can be divided into the following categories, listed in order of the number of protective library compounds per category.

Inhibitors of Protein Homeostasis

Proteasomes are protein complexes that degrade unneeded, misfolded or damaged proteins by proteolysis. Misfolded proteins trafficked from the Golgi to the ER are retained in the ER and retro-translocated to the cytosol in vesicles (Omari et al., 2018). Along with damaged proteins, they are tagged for proteasome proteolysis by ubiquitins (Taxis et al., 2002). Autophagy is thought to co-operate with the ubiquitin-proteasome system in responding to cell injury (Ji and Kwon, 2017). The proteasome is known to protect cells from degeneration by removing damaged proteins (Jones and Tepe, 2019), but an overactive proteasome can enhance tissue damage (Meller, 2009; Chen et al., 2010). Six compounds out of the 18 protective compounds were proteasome inhibitors.

a. LDN-57444: Reversible, competitive proteasome inhibitor for Uch-L1.
b. MG-132: Cell permeable proteasome and calpain inhibitor, in low dosage protective, in high dosage toxic.
c. Bortezomib: Proteasome inhibitor.
d. Omeprazole: Proton pump inhibitor. Proton pump inhibition reduces the expression of proteasome subunits, leading to proteasome inhibition (Cao et al., 2020).
e. PYR-41: Ubiquitin Proteasome inhibitor. Reduces ubiquitination, required for proteasome degradation of

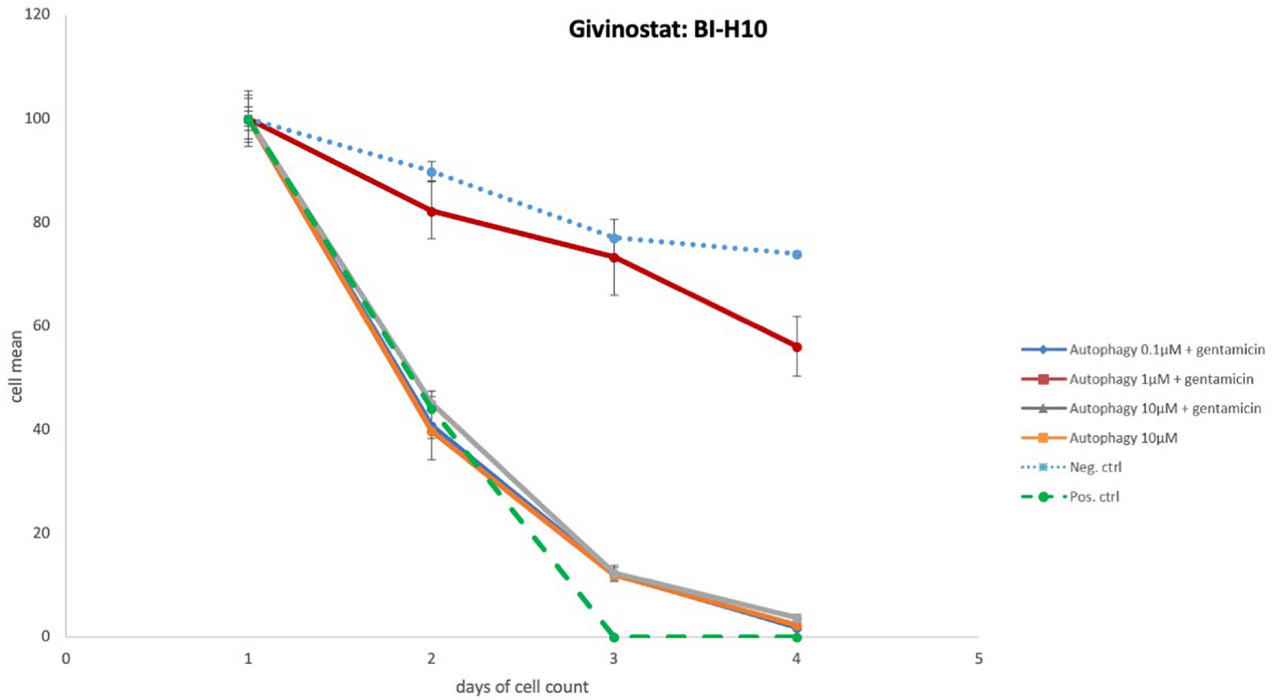

FIGURE 4 | Autophagy compound without protective effects. Illustration of Survival curves of representative compound that had no effect on GM-treated oC explants. Treatment with the highest concentration (10 μM) of autophagy compound resulted in HC numbers similar to that seen for negative control micro-explants cultures in media alone. Treatment with compound plus GM was not significantly different from gentamicin alone.

proteins, but also inhibits NFkB depending on its half-maximal inhibitory concentrations (IC50) which has been identified between 10–25 μM in cells (Yang et al., 2007).

f. Brefeldin A. An inhibitor of macro-autophagy, reduces the release of proteins from the ER.

The library had twelve inhibitory compounds targeting the proteasome pathway and of which six were identified protective in our screen. These results strongly suggest that the proteasome overactivity contributes to HC damage. Cheng et al. (2016) identified that Atoh1 (Atonal BHLH Transcription Factor 1) was regulated by the ubiquitin-proteasome system and hence ubiquitin proteasome pathway appears necessary for hair cell fate determination and survival. Also, we recently reported that multiple proteins of the ubiquitin-proteasome system are up-regulated in the cochlea following noise damage (Jongkamonwiwat et al., 2020), suggesting the possibility of a similar involvement in noise-induced HC damage associated with protein abundance and protein misfolding.

TABLE 1 | Overview of the results of the SELLECKChem autophagy compound library.

Compounds tested	No effect	Toxic effect	Protective effect
N = 154 = 100%	135 = 87.7%	1 = 0.6%	18 = 11.7%

Microtubule Interfering Agents

In autophagy, mature autophagosomes are transported to lysosomes along microtubules with force generated by the actin cytoskeleton. Microtubules are also involved in the transport of other cellular constituents, cell structure and cell migration. The library had twelve compounds associated with autophagy, microtubules and actin of which four inhibitors of were protective.

a. Nocodazole: Reversible inhibitor of Abl and microtubule polymerization:
b. Vincristine: binds tubulin protein and counteracts the formation of microtubules.
c. Y- 27632: Inhibitor of ROCK-1, which promotes contractile force generation in the actin cytoskeleton and movement along microtubules.
d. Fasudil: ROCK inhibitor.

Inhibitors of Calcium Regulation

Calcium regulates autophagy at several different points in the process (Bootman et al., 2018). Increases in intracellular calcium, from calcium channels, calcium uptake or release from mitochondria, can induce autophagy. Conversely, calcium release leading to entry into mitochondria increases ATP production, which inhibits mitochondria (Kondratskyi et al., 2013). However, calcium also plays multiple additional roles in cells. Loss of calcium homeostasis is a major factor in cell injury and death through multiple mechanisms include

TABLE 2 | Overview of the protective autophagy compounds identified in the *in vitro* screening assay.

Strong = day 2 + 3 + 4		Medium = day 2 + 3		Weak = day 2	
Compound	**Function**	**Compound**	**Function**	**Compound**	**Function**
MG-132 (AMG-IIB2)	Protein homeostasis inhibitor	Fasudil (AMG-IG8)	Microtubule interfering agents	Rotundine (AMG-IIA1)	Calcium regulation
Omeprazole (AMG-IB7)	Protein homeostasis inhibitor	GDC-0349: (AMG-IIA9)	Inhibitors of the PI3K/AKT/mTOR pathway	BAY 11-7082 (AMG-IIB5)	Inflammation and immunity inhibitor
Bortezomib: (AMG-IC1)	Protein homeostasis inhibitor			AMG-900: (AMG-IIB3)	Cell cycle regulator
LDN-57444: (AMG-IIA7)	Protein homeostasis inhibitor			PI-103 (AMG-IE1)	Inhibitors of the PI3K/AKT/mTOR pathway
Vincristine: (AMG-ID6)	Microtubule interfering agents			MK-5108: (AMG-IIB4)	Cell cycle regulator
Nocodazole: (AMG-IIC4)	Microtubule interfering agents				
Y-27632:(AMG-IC2)	Microtubule interfering agents				
Manidipine HCL (AMG-IIG1)	Calcium regulation				
Nimodipine: (AMG-ID9)	Calcium regulation				
Brefeldin A: (AMG-IIB6)	Cell cycle regulator				
Ranolazine (AMG-IE7)	Potassium channel blocker				

apoptosis and necrosis (Dong et al., 2006). Intracellular calcium is tightly regulated in part to prevent the accumulation of excessive levels. HCs in particular contain high levels of calcium buffering proteins and express multiple calcium channels and transporters. Calcium subserves multiple normal functions of HCs (Heller et al., 2002). A number of studies have highlighted the role of calcium in HC damage, including release of calcium from the endoplasmic reticulum and mitochondria. It has been suggested that differences in HC vulnerability to damage along the length of the cochlea are related to variation in the ability to handle calcium load (Fettiplace and Nam, 2019). It has been suggested that calcium channel blockers should be investigated as therapeutic agents for acquired hearing loss (Naples, 2017). In this screen, the library had fourteen compounds that influence intracellular calcium levels and four were found to be protective.

a. Manidipine: Calcium channel blocker (L and T gated channels).
b. Nimodipine: Calcium channel blocker (L gated channels).
c. Ranolazine: Calcium uptake inhibitor.
d. Rotundine: Rotundine is a natural plant alkaloid with complex effects. It has been reported to block L-type calcium channels, but also dopamine receptors, and to activates potassium channels. It has been shown to be neuroprotective e.g., in alpha synuclein accumulating diseases such as Parkinson (Ghanem et al., 2021).

The expected results of these inhibitors would be to reduce intracellular calcium. While this strongly supports a critical role for calcium in HC damage, it cannot be attributed with any certainty to the regulation of autophagy.

Inhibitors of the PI3K/AKT/mTOR Pathway

The PI3K/AKT/mTOR is an evolutionally conserved cascade that integrates signals from multiple pathways, including nutrients (e.g., amino acids and glucose), growth factors (e.g., EGF, PDGF, IGF-1), hormones (e.g., leptin), and stresses (e.g., starvation, hypoxia, and DNA damage) to regulate a wide variety of eukaryotic cellular functions, such as autophagy, translation, transcription, protein turnover, metabolism, energy balance, and stress response, as well as cell proliferation, growth, differentiation and survival. mTOR can also be activated independently of PI3K and AKT. The library contains 25 compounds related to PI3K/mTOR and three inhibitors were protective.

a. PI-103: PI3K/mTOR inhibitor.
b. BGT 226: PI3K/mTOR inhibitor.
c. GDC-0349: Selective ATP-competitive inhibitor of mTOR.

Because of the diverse rolls of the PI3K/AKT/mTOR pathway, the mechanism by which these inhibitors protect HCs is not clear. mTOR reduces autophagy by negatively regulating several key molecules (Kim and Guan, 2015), so the promotion of autophagy is one possibility. However, in our prior screen of kinase inhibitors (Ryals et al., 2017), one EGFR inhibitor, two PDGF receptor and two AKT inhibitors were found to be protective. This result is consistent with a damaging role for the PI3K/AKT/mTOR pathway, which is activated by growth factors. However, one of the autophagy compounds, BGT 226, showed a "push pull" relationship with a toxic effect in the highest concentration leading to HC death. Deletion of either AKT1 or AKT2 has been shown to enhance HC death due

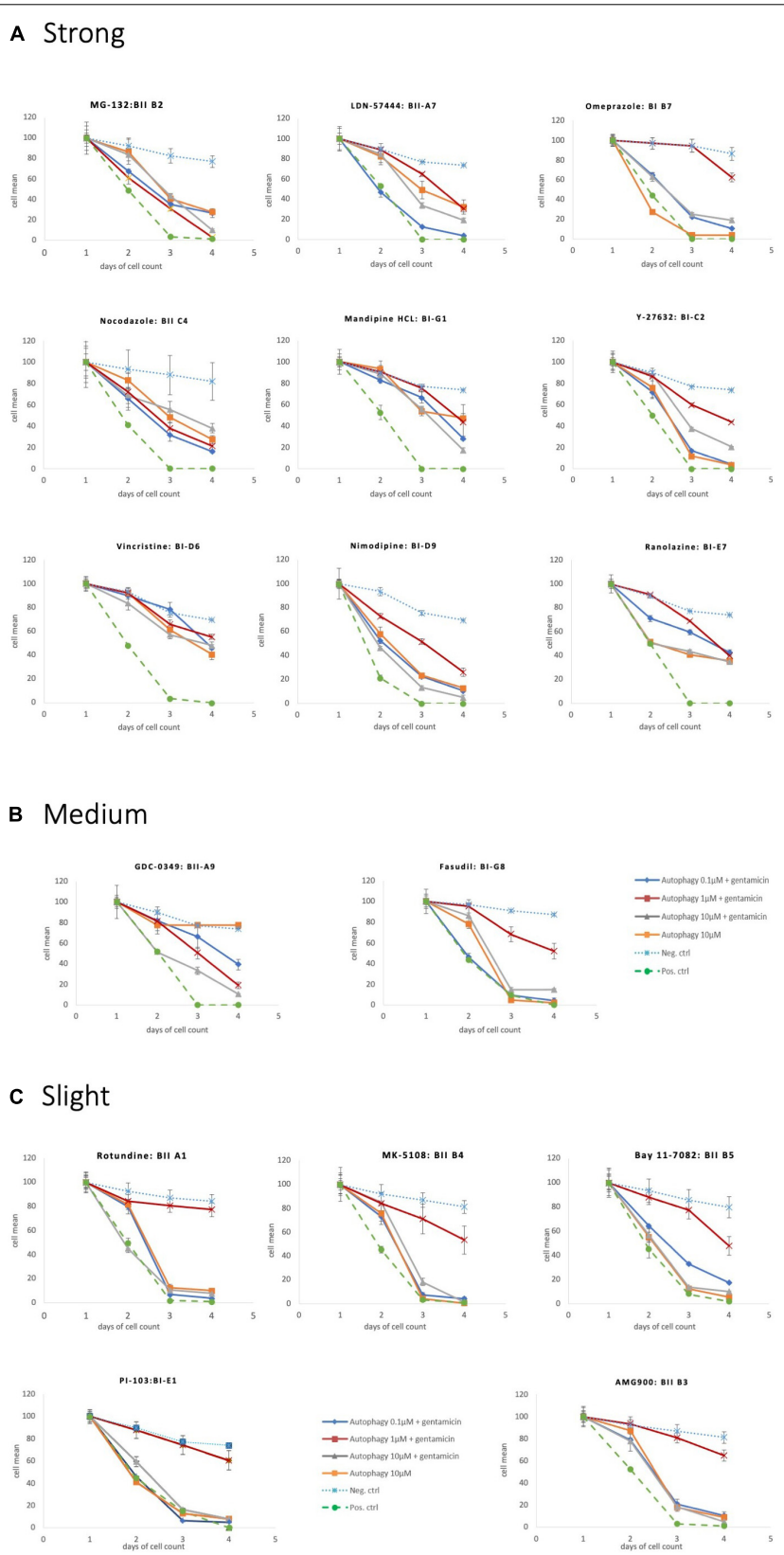

FIGURE 5 | Protective autophagy compounds Survival plots showing the autophagy compounds classified as **(A)** Strong, **(B)** medium and **(C)** slight depending on the HCs survival curves.

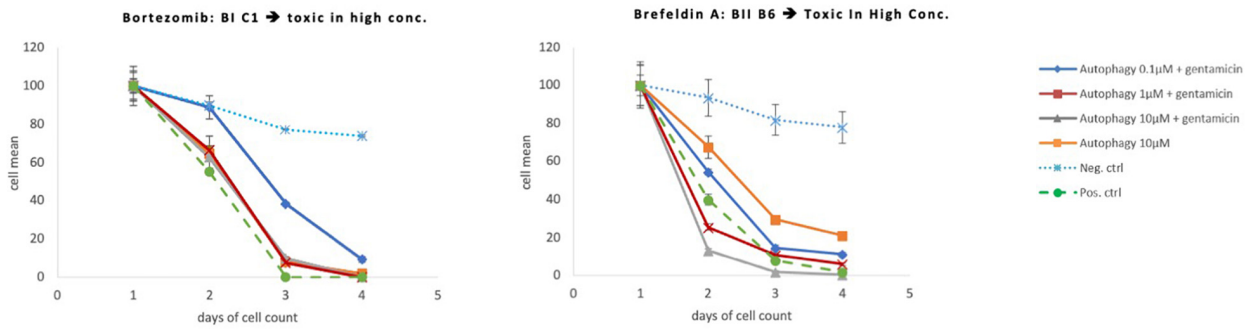

FIGURE 6 | Protective and toxic autophagy compounds. These compounds had a strong protective effects at low doses but were toxic at the highest concentration dose tested (10 μM).

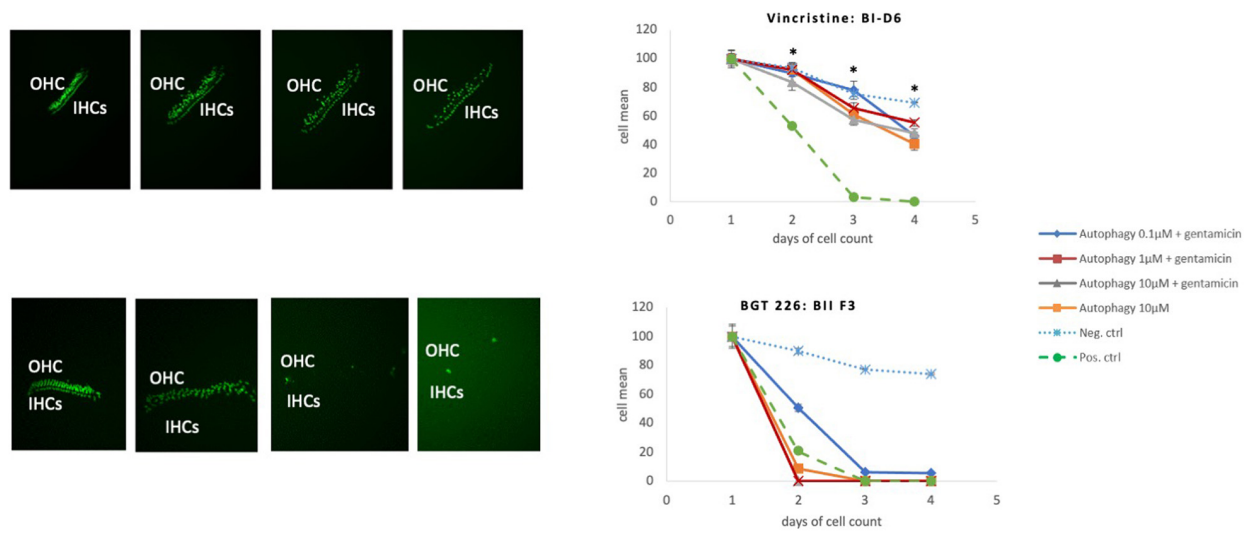

FIGURE 7 | Toxic autophagy compounds. Comparison of an autophagy compounds with a protective effect (Vincristine) with an autophagy compound with a toxic effect (BGT 226). Protective Effect: Vincristine has a significant protective effect in all three dosages *($p < 0.05$). Toxic effect of BGT 226 (AMG-IIF3), Inhibitor of the PI3K/AKT/mTOR pathway, exhibiting HC loss even in the absence of GM.

to aminoglycosides (Brand et al., 2015). It is possible that the three PI3K/mTOR inhibitors preferentially target PI3K/mTOR mediation of stress responses. Alternatively, they may target one of the several mTOR responses that are independent of AKT.

Inhibitors of the Cell Cycle

Aurora kinase A is critical to the process of mitotic spindle formation and separation, and thus of cell division. Inhibition of Aurora kinase A blocks cell proliferation and can induce autophagy (Zou et al., 2012). In our screening assay two inhibitors of Aurora kinase inhibitors showed a protective effect:

a. AMG900: Selective pan-Aurora kinase inhibitor.
b. MK-5108: Selective Aurora kinase A inhibitor.

Overall the library had 20 compounds related to the Aurora kinase pathway and only two compounds were protective. This is consistent with the finding that maintaining the fully differentiated state is critical for HC survival and that forced cell cycle re-entry in differentiated, post-mitotic cells in response to stress can lead to mitotic catastrophe and cell death (Weber et al., 2008; Sharma et al., 2017). This provides strong evidence that one aspect of gentamicin-induced HC damage may be induction of the cell cycle.

Inhibitor of Inflammation and Immunity

NFkB Inhibitor: BAY 11-7082. The role of immune responses and inflammation in HC damage is increasingly recognized (Frye et al., 2019). Damage to HCs results in the release of inflammatory mediators such as the inflammatory cytokine TNFα (Tan et al., 2016). Damaged cells can also release cellular constituents that serve as damage-associated molecular patterns (DAMPs). Damps in turn can activate innate immune receptors such as the Toll-like receptors (TLRs), leading to the production of inflammatory cytokines such as IL1β and TNFα, as well chemokines that attract immune cells including macrophages. Many inflammatory responses are mediated by the transcription

factor NFkB, which can also stimulate autophagy. An inhibitor of this factor was protective in the screen. This result supports a role for inflammation in ototoxic HC damage.

Protein Trafficking

An inhibitor of protein trafficking was protective, Brefeldin A. Brefeldin A is an inhibitor of protein trafficking between the endoplasmic reticulum and the Golgi apparatus (Chardin and McCormick, 1999). These results suggest that the movement of intracellular elements, possibly including autophagosomes, contribute to ototoxic HC damage.

The majority of the compounds that proved to be protective to HCs against gentamicin damage would be expected to reduce autophagy. While several of these compounds have complex effects, the fact that multiple autophagy inhibitors reduced HC loss argues for an autophagy role in promoting HC damage due to GM. Levano and Bodmer found that mutation of the *Stat1* gene protected HCs from ototoxic damage in part by modulating autophagy genes so as to reduce autophagy (Levano and Bodmer, 2015).

Autophagy is often considered to be protective of cells under stress, but it has been shown that excessive activation of autophagy can lead to autophagic cell death, or autosis (Liu and Levine, 2015). The high dosage of GM used in this study may have induced excessive autophagy. Apoptosis, necrosis and necroptosis have been shown to participate in HC death (Ruhl et al., 2019). However, autosis has not previously been linked to HC damage. Autosis is characterized by nuclear shrinkage with focal concavities and ballooning of the perinuclear space. These characteristics are visible in some published electron micrographs of aminoglycoside-damaged HCs (Lang and Liu, 1997).

While most autophagy inhibiting compounds were protective, we also observed protection with compounds that would be expected to enhance autophagy. Again, while these compounds have complex effects, the results support the concept that autophagy can be protective against aminoglycoside damage. It seems likely that autophagy plays a complex role in ototoxic HC damage, such that manipulation of different aspects of the process can have differing effects. The interactions of identified compounds with the autophagy machinery warrants further mechanistic studies because these candidate leads may employ one or more of several mechanisms. Therefore, differences in their effectiveness may vary with differences in the cellular processes involved and aminoglycoside impact. Given the complexity, it would not be expected that all compounds in a category would have equivalent effects on cell damage and survival.

Mammalian Organ of Corti Micro-Explant Assay

There are multiple screening assays available today. The assay presented here, like many preclinical assays, has both advantages and disadvantages. A major advantage is that organ of Corti micro-explant screening employs mammalian cochlear HCs. Cochlear HCs in mammals include inner and outer HCs, as in humans, while the HCs of other classes of non-mammalian animals are quite different from human HCs. This is important, since outer HCs are more sensitive to damage than other HC types. They are also highly specialized, with structural and functional features that are very distinct. The damage process in these highly specialized cells may not be adequately modeled by that in other HC types, or by those in immortalized cell lines derived from the organ of Corti. These cell lines are de-differentiated, and express genes of both early developing HCs and supporting cells.

In general, a larger number of compounds can be tested in an *in vitro* oC assay than can be achieved using *in vivo* models, which are the only alternatives that allows testing of mammalian cochlear HCs. For this assay, the use of oC micro-explants enables an even larger number of compounds evaluations. Several micro-explants can be generated from each murine organ of Corti. Moreover, because the HCs of *pou4f3*/GFP mice are selectively fluorescent, they do not need to be stained and can be quantified throughout the period of culture in a single micro-explant. Thus multiple groups of explants are not necessary to determine the kinetics of compound effects. Because of these features, screening of a few hundred compounds is readily achieved. The ototoxin chosen for the assay, GM, is commonly prescribed for life-threatening infections and is thus relevant to human therapy.

Disadvantages include the fact that the assay is based on neonatal HCs, which have known differences from adult HCs (Hur et al., 2018). Mature adult HC do not survive in culture and many studies have demonstrated that cell cycle reactivation in mammalian cochlear HCs results in cell death *in vitro* and *in vivo* (Laine et al., 2007; Sulg et al., 2010). Moreover, like in other screening techniques, the micro-explant screening assay identified candidates must be confirmed by post-screen characterization of hits and testing in *in vivo*. Finally, when compared to immortalized cell line or zebrafish lateral line screens, the assay is only medium-throughput. Very large compound libraries cannot be screened, and the number of compound and ototoxin dosages tested must be limited.

CONCLUSION

The preponderance of the results from our screen of an autophagy library suggest that autophagy contributes to ototoxic HC damage in a complex manner. However, the compounds tested have many potential alternative effects. For this reason we cannot conclude with confidence that changes in autophagy were the primary reason for HC protection. Additional studies will need to be performed to further validate the results of our screen and to determine the relationship between autophagy and HC damage *in vivo*. However, the data strongly implicate the proteasome and proteolysis as contributors to HC damage.

DATA AVAILABILITY STATEMENT

The original contributions presented in the study are included in the article/**Supplementary Material**, further inquiries can be directed to the corresponding author/s.

ETHICS STATEMENT

The animal study was reviewed and approved by VA IACUC.

AUTHOR CONTRIBUTIONS

CD, TW, EC, and KP performed the laboratory experiments and screening assay. CD, AK, and AL analyzed the data. CD, SD, and AR conceived the study and designed the experiments. CD wrote the initial manuscript and generated figures. All authors reviewed and approved the manuscript.

FUNDING

The research for this study was supported by the German Research Foundation (Deutsche Forschungsgemeinschaft DFG) and by grant BX001205 from the Veterans Health Administration.

SUPPLEMENTARY MATERIAL

The Supplementary Material for this article can be found online at: https://www.frontiersin.org/articles/10.3389/fcell.2021.762751/full#supplementary-material

REFERENCES

Abou-Zeid, A. A., Eissa, A. I., and Salem, H. M. (1978). Mode of action of gentamicin antibiotics produced by *Micromonospora purpurea*. *Zentralbl. Bakteriol. Naturwiss.* 133, 362–368. doi: 10.1016/S0323-6056(78)80054-8

Aburto, M. R., Sanchez-Calderon, H., Hurle, J. M., Varela-Nieto, I., and Magarinos, M. (2012). Early otic development depends on autophagy for apoptotic cell clearance and neural differentiation. *Cell Death Dis.* 3:e394. doi: 10.1038/cddis.2012.132

Al-Malky, G., Dawson, S. J., Sirimanna, T., Bagkeris, E., and Suri, R. (2015). High-frequency audiometry reveals high prevalence of aminoglycoside ototoxicity in children with cystic fibrosis. *J. Cyst. Fibros.* 14, 248–254. doi: 10.1016/j.jcf.2014.07.009

Arroyo, D. S., Gaviglio, E. A., Peralta Ramos, J. M., Bussi, C., Rodriguez-Galan, M. C., and Iribarren, P. (2014). Autophagy in inflammation, infection, neurodegeneration and cancer. *Int. Immunopharmacol.* 18, 55–65. doi: 10.1016/j.intimp.2013.11.001

Benkafadar, N., François, F., Affortit, C., Casas, F., Ceccato, J. C., Menardo, J., et al. (2019). ROS-Induced activation of DNA damage responses drives senescence-like state in postmitotic cochlear cells: implication for hearing preservation. *Mol. Neurobiol.* 56, 5950–5969. doi: 10.1007/s12035-019-1493-6

Bootman, M. D., Chehab, T., Bultynck, G., Parys, J. B., and Rietdorf, K. (2018). The regulation of autophagy by calcium signals: do we have a consensus? *Cell Calcium* 70, 32–46. doi: 10.1016/j.ceca.2017.08.005

Brand, Y., Levano, S., Radojevic, V., Naldi, A. M., Setz, C., Ryan, A. F., et al. (2015). All Akt isoforms (Akt1, Akt2, Akt3) are involved in normal hearing, but only Akt2 and Akt3 are involved in auditory hair cell survival in the mammalian inner ear. *PLoS One* 10:e0121599. doi: 10.1371/journal.pone.0121599

Cao, Y., Zhu, H., He, R., Kong, L., Shao, J., Zhuang, R., et al. (2020). Proteasome, a promising therapeutic target for multiple diseases beyond cancer. *Drug Des. Devel. Ther.* 14, 4327–4342. doi: 10.2147/DDDT.S265793

Chardin, P., and McCormick, F. (1999). Brefeldin A: the advantage of being uncompetitive. *Cell* 97, 153–155. doi: 10.1016/S0092-8674(00)80724-2

Chen, Y., Azad, M. B., and Gibson, S. B. (2010). Methods for detecting autophagy and determining autophagy-induced cell death. *Can. J. Physiol. Pharmacol.* 88, 285–295. doi: 10.1139/Y10-010

Cheng, Y. F., Tong, M., and Edge, A. S. (2016). Destabilization of Atoh1 by E3 ubiquitin ligase Huwe1 and casein kinase 1 is essential for normal sensory hair cell development. *J. Biol. Chem.* 291, 21096–21109. doi: 10.1074/jbc.M116.722124

Dong, Z., Saikumar, P., Weinberg, J. M., and Venkatachalam, M. A. (2006). Calcium in cell injury and death. *Annu. Rev. Pathol.* 1, 405–434. doi: 10.1146/annurev.pathol.1.110304.100218

Esclatine, A., Chaumorcel, M., and Codogno, P. (2009). Macroautophagy signaling and regulation. *Curr. Top. Microbiol. Immunol.* 335, 33–70. doi: 10.1007/978-3-642-00302-8_2

Fettiplace, R., and Nam, J. H. (2019). Tonotopy in calcium homeostasis and vulnerability of cochlear hair cells. *Hear. Res.* 376, 11–21. doi: 10.1016/j.heares.2018.11.002

Frye, M. D., Ryan, A. F., and Kurabi, A. (2019). Inflammation associated with noise-induced hearing loss. *J. Acoust. Soc. Am.* 146, 4020. doi: 10.1121/1.5132545

Ghanem, S. S., Fayed, H. S., Zhu, Q., Lu, J. H., Vaikath, N. N., Ponraj, J., et al. (2021). Natural alkaloid compounds as inhibitors for alpha-synuclein seeded fibril formation and toxicity. *Molecules* 26:3736. doi: 10.3390/molecules26123736

Hamilton, J. W. (2001). Gentamicin in pharmacogenetic approach to treatment of cystic fibrosis. *Lancet* 358, 2014–2016. doi: 10.1016/S0140-6736(01)07138-0

He, L., Zhang, J., Zhao, J., Ma, N., Kim, S. W., Qiao, S., et al. (2018). Autophagy: the last defense against cellular nutritional stress. *Adv. Nutr.* 9, 493–504. doi: 10.1093/advances/nmy011

Heller, S., Bell, A. M., Denis, C. S., Choe, Y., and Hudspeth, A. J. (2002). Parvalbumin 3 is an abundant Ca2+ buffer in hair cells. *J. Assoc. Res. Otolaryngol.* 3, 488–498. doi: 10.1007/s10162-002-2050-x

Hur, D. G., Kurabi, A., and Ryan, A. F. (2018). Screening antioxidants for the protection of cochlear sensory cells. *Neural Regen. Res.* 13, 62–64. doi: 10.4103/1673-5374.224371

Ji, C. H., and Kwon, Y. T. (2017). Crosstalk and interplay between the ubiquitin-proteasome system and autophagy. *Mol. Cells* 40, 441–449.

Jones, C. L., and Tepe, J. J. (2019). Proteasome activation to combat proteotoxicity. *Molecules* 24:2841. doi: 10.3390/molecules24152841

Jongkamonwiwat, N., Ramirez, M. A., Edassery, S., Wong, A. C. Y., Yu, J., Abbott, T., et al. (2020). Noise exposures causing hearing loss generate proteotoxic stress and activate the proteostasis network. *Cell Rep.* 33:108431. doi: 10.1016/j.celrep.2020.108431

Kim, Y. C., and Guan, K. L. (2015). mTOR: a pharmacologic target for autophagy regulation. *J. Clin. Invest.* 125, 25–32. doi: 10.1172/JCI73939

Kim, Y. J., Tian, C., Kim, J., Shin, B., Choo, O. S., Kim, Y. S., et al. (2017). Autophagic flux, a possible mechanism for delayed gentamicin-induced ototoxicity. *Sci. Rep.* 7:41356. doi: 10.1038/srep41356

Kondratskyi, A., Yassine, M., Kondratska, K., Skryma, R., Slomianny, C., and Prevarskaya, N. (2013). Calcium-permeable ion channels in control of autophagy and cancer. *Front. Physiol.* 4:272. doi: 10.3389/fphys.2013.00272

Laine, H., Doetzlhofer, A., Mantela, J., Ylikoski, J., Laiho, M., Roussel, M. F., et al. (2007). p19(Ink4d) and p21(Cip1) collaborate to maintain the postmitotic state of auditory hair cells, their codeletion leading to DNA damage and p53-mediated apoptosis. *J. Neurosci.* 27, 1434–1444. doi: 10.1523/JNEUROSCI.4956-06.2007

Lang, H., and Liu, C. (1997). Apoptosis and hair cell degeneration in the vestibular sensory epithelia of the guinea pig following a gentamicin insult. *Hear. Res.* 111, 177–184. doi: 10.1016/S0378-5955(97)00098-1

Lee, J., Giordano, S., and Zhang, J. (2012). Autophagy, mitochondria and oxidative stress: cross-talk and redox signalling. *Biochem. J.* 441, 523–540. doi: 10.1042/BJ20111451

Levano, S., and Bodmer, D. (2015). Loss of STAT1 protects hair cells from ototoxicity through modulation of STAT3, c-Jun, Akt, and autophagy factors. *Cell Death Dis.* 6:e2019. doi: 10.1038/cddis.2015.362

Levine, B., and Kroemer, G. (2008). Autophagy in the pathogenesis of disease. *Cell* 132, 27–42. doi: 10.1016/j.cell.2007.12.018

Liu, Y., and Levine, B. (2015). Autosis and autophagic cell death: the dark side of autophagy. *Cell Death Differ.* 22, 367–376. doi: 10.1038/cdd.2014.143

Magarinos, M., Pulido, S., Aburto, M. R., de Iriarte Rodriguez, R., and Varela-Nieto, I. (2017). Autophagy in the vertebrate inner ear. *Front. Cell Dev. Biol.* 5:56. doi: 10.3389/fcell.2017.00056

Masuda, M., Dulon, D., Pak, K., Mullen, L. M., Li, Y., Erkman, L., et al. (2011). "Regulation of POU4F3 gene expression in hair cells by 5' DNA in mice. *Neuroscience* 197, 48–64. doi: 10.1016/j.neuroscience.2011.09.033

Meller, R. (2009). The role of the ubiquitin proteasome system in ischemia and ischemic tolerance. *Neuroscientist* 15, 243–260. doi: 10.1177/1073858408327809

Mizushima, N. (2011). Autophagy in protein and organelle turnover. *Cold Spring Harb. Symp. Quant. Biol.* 76, 397–402. doi: 10.1101/sqb.2011.76.011023

Mizushima, N., and Komatsu, M. (2011). Autophagy: renovation of cells and tissues. *Cell* 147, 728–741. doi: 10.1016/j.cell.2011.10.026

Mizushima, N., Levine, B., Cuervo, A. M., and Klionsky, D. J. (2008). Autophagy fights disease through cellular self-digestion. *Nature* 451, 1069–1075. doi: 10.1038/nature06639

Naples, J. G. (2017). Calcium-channel blockers as therapeutic agents for acquired sensorineural hearing loss. *Med. Hypotheses* 104, 121–125. doi: 10.1016/j.mehy.2017.05.036

Noack, V., Pak, K., Jalota, R., Kurabi, A., and Ryan, A. F. (2017). An antioxidant screen identifies candidates for protection of cochlear hair cells from gentamicin toxicity. *Front. Cell. Neurosci.* 11:242. doi: 10.3389/fncel.2017.00242

Obregon, A. M., Escalante, L., Gonzalez, R., Rodriguez, R., and Sanchez, S. (1994). Physiological studies on gentamicin: phosphate repression of antibiotic formation. *J. Antibiot. (Tokyo)* 47, 1442–1446. doi: 10.7164/antibiotics.47.1442

Oh, J. M., Choi, E. K., Carp, R. I., and Kim, Y. S. (2012). Oxidative stress impairs autophagic flux in prion protein-deficient hippocampal cells. *Autophagy* 8, 1448–1461. doi: 10.4161/auto.21164

Ohsumi, Y. (2001). Molecular dissection of autophagy: two ubiquitin-like systems. *Nat. Rev. Mol. Cell Biol.* 2, 211–216. doi: 10.1038/35056522

Omari, S., Makareeva, E., Roberts-Pilgrim, A., Mirigian, L., Jarnik, M., Ott, C., et al. (2018). Noncanonical autophagy at ER exit sites regulates procollagen turnover. *Proc. Natl. Acad. Sci. U.S.A.* 115, E10099–E10108. doi: 10.1073/pnas.1814552115

Rabinowitz, J. D., and White, E. (2010). Autophagy and metabolism. *Science* 330, 1344–1348. doi: 10.1126/science.1193497

Ruhl, D., Du, T. T., Wagner, E. L., Choi, J. H., Li, S., Reed, R., et al. (2019). Necroptosis and apoptosis contribute to cisplatin and aminoglycoside ototoxicity. *J. Neurosci.* 39, 2951–2964. doi: 10.1523/JNEUROSCI.1384-18.2019

Ryals, M., Pak, K., Jalota, R., Kurabi, A., and Ryan, A. F. (2017). A kinase inhibitor library screen identifies novel enzymes involved in ototoxic damage to the murine organ of Corti. *PLoS One* 12:e0186001. doi: 10.1371/journal.pone.0186001

Ryter, S. W., Koo, J. K., and Choi, A. M. (2014). Molecular regulation of autophagy and its implications for metabolic diseases. *Curr. Opin. Clin. Nutr. Metab. Care* 17, 329–337. doi: 10.1097/MCO.0000000000000068

Sagwa, E. L., Ruswa, N., Mavhunga, F., Rennie, T., Leufkens, H. G., and Mantel-Teeuwisse, A. K. (2015). Comparing amikacin and kanamycin-induced hearing loss in multidrug-resistant tuberculosis treatment under programmatic conditions in a Namibian retrospective cohort. *BMC Pharmacol. Toxicol.* 16:36. doi: 10.1186/s40360-015-0036-7

Sapizhak, I., Timen, H., Semenova, V., and Staino, L. (2017). The neuronal stem cells effect on inner ear structure in experimental gentamicin ototoxicity. *Ukr. Neurosurg. J.* 4, 55–59. doi: 10.25305/unj.115236

Sharma, P., Haycocks, J. R. J., Middlemiss, A. D., Kettles, R. A., Sellars, L. E., Ricci, V., et al. (2017). The multiple antibiotic resistance operon of enteric bacteria controls DNA repair and outer membrane integrity. *Nat. Commun.* 8:1444. doi: 10.1038/s41467-017-01405-7

Sulg, M., Kirjavainen, A., Pajusola, K., Bueler, H., Ylikoski, J., Laiho, M., et al. (2010). Differential sensitivity of the inner ear sensory cell populations to forced cell cycle re-entry and p53 induction. *J. Neurochem.* 112, 1513–1526. doi: 10.1111/j.1471-4159.2009.06563.x

Tan, W. J., Thorne, P. R., and Vlajkovic, S. M. (2016). Characterisation of cochlear inflammation in mice following acute and chronic noise exposure. *Histochem. Cell Biol.* 146, 219–230. doi: 10.1007/s00418-016-1436-5

Taxis, C., Vogel, F., and Wolf, D. H. (2002). ER-golgi traffic is a prerequisite for efficient ER degradation. *Mol. Biol. Cell* 13, 1806–1818. doi: 10.1091/mbc.01-08-0399

Taylor, M. P., and Kirkegaard, K. (2008). Potential subversion of autophagosomal pathway by picornaviruses. *Autophagy* 4, 286–289. doi: 10.4161/auto.5377

Weber, T., Corbett, M. K., Chow, L. M., Valentine, M. B., Baker, S. J., and Zuo, J. (2008). Rapid cell-cycle reentry and cell death after acute inactivation of the retinoblastoma gene product in postnatal cochlear hair cells. *Proc. Natl. Acad. Sci. U.S.A.* 105, 781–785. doi: 10.1073/pnas.0708061105

Xing, Y., Ji, Q., Li, X., Ming, J., Zhang, N., Zha, D., et al. (2017). Asiaticoside protects cochlear hair cells from high glucose-induced oxidative stress via suppressing AGEs/RAGE/NF-kappaB pathway. *Biomed. Pharmacother.* 86, 531–536. doi: 10.1016/j.biopha.2016.12.025

Yang, Y., Kitagaki, J., Dai, R. M., Tsai, Y. C., Lorick, K. L., Ludwig, R. L., et al. (2007). Inhibitors of ubiquitin-activating enzyme (E1), a new class of potential cancer therapeutics. *Cancer Res.* 67, 9472–9481. doi: 10.1158/0008-5472.CAN-07-0568

Zou, Z., Yuan, Z., Zhang, Q., Long, Z., Chen, J., Tang, Z., et al. (2012). Aurora kinase A inhibition-induced autophagy triggers drug resistance in breast cancer cells. *Autophagy* 8, 1798–1810. doi: 10.4161/auto.22110

Conflict of Interest: AR is a co-founder, shareholder, and consultant of Otonomy Inc., which develops slow-release drug compounds for the treatment of middle and inner ear diseases. The UCSD Committee on Conflict of Interest has approved this relationship. Otonomy Inc., played no part in the research reported here.

The remaining authors declare that the research was conducted in the absence of any commercial or financial relationships that could be construed as a potential conflict of interest.

Publisher's Note: All claims expressed in this article are solely those of the authors and do not necessarily represent those of their affiliated organizations, or those of the publisher, the editors and the reviewers. Any product that may be evaluated in this article, or claim that may be made by its manufacturer, is not guaranteed or endorsed by the publisher.

frontiers in Cell and Developmental Biology

ORIGINAL RESEARCH
published: 12 November 2021
doi: 10.3389/fcell.2021.752963

Effects of Calcitonin-Gene-Related-Peptide on Auditory Nerve Activity

Colleen G. Le Prell[1,2]*, *Larry F. Hughes*[3], *David F. Dolan*[1] and *Sanford C. Bledsoe Jr*[1]

[1]Department of Otolaryngology, University of Michigan, Ann Arbor, MI, United States, [2]Department of Speech, Language, and Hearing, University of Texas at Dallas, Richardson, TX, United States, [3]Department of Surgery, Southern Illinois University School of Medicine, Springfield, IL, United States

Calcitonin-gene-related peptide (CGRP) is a lateral olivocochlear (LOC) efferent neurotransmitter. Depression of sound-driven auditory brainstem response amplitude in CGRP-null mice suggests the potential for endogenous CGRP release to upregulate spontaneous and/or sound-driven auditory nerve (AN) activity. We chronically infused CGRP into the guinea pig cochlea and evaluated changes in AN activity as well as outer hair cell (OHC) function. The amplitude of both round window noise (a measure of ensemble spontaneous activity) and the synchronous whole-nerve response to sound (compound action potential, CAP) were enhanced. Lack of change in both onset adaptation and steady state amplitude of sound-evoked distortion product otoacoustic emission (DPOAE) responses indicated CGRP had no effect on OHCs, suggesting the origin of the observed changes was neural. Combined with results from the CGRP-null mice, these results appear to confirm that endogenous CGRP enhances auditory nerve activity when released by the LOC neurons. However, infusion of the CGRP receptor antagonist CGRP (8–37) did not reliably influence spontaneous or sound-driven AN activity, or OHC function, results that contrast with the decreased ABR amplitude measured in CGRP-null mice.

Keywords: cochlea, CGRP, auditory nerve, auditory brainstem response, lateral olivocochlear efferent

OPEN ACCESS

Edited by:
Isabel Varela-Nieto, Consejo Superior de Investigaciones Científicas (CSIC), Spain

Reviewed by:
Anne E. Luebke, University of Rochester, United States
Rudolf Glueckert, Innsbruck Medical University, Austria

***Correspondence:**
Colleen G. Le Prell
colleen.leprell@utdallas.edu

Specialty section:
This article was submitted to Molecular and Cellular Pathology, a section of the journal Frontiers in Cell and Developmental Biology

Received: *04 August 2021*
Accepted: *20 October 2021*
Published: *12 November 2021*

Citation:
Le Prell CG, Hughes LF, Dolan DF and Bledsoe SC (2021) Effects of Calcitonin-Gene-Related-Peptide on Auditory Nerve Activity. Front. Cell Dev. Biol. 9:752963. doi: 10.3389/fcell.2021.752963

INTRODUCTION

A variety of evidence suggests a role for Calcitonin-gene-related-peptide (CGRP) in auditory function, with CGRP released by the lateral olivocochlear (LOC) efferent neurons mediating the neural response to sound. The guinea pig is a common model for studies of the LOC system. LOC efferents have been immunolabeled with antibodies to CGRP in the cochlea in guinea pigs (Takeda et al., 1987; Sliwinska-Kowalska et al., 1989; Ylikoski et al., 1989; Ohno et al., 1993; Cabanillas and Luebke, 2002). Other studies of the LOC system document CGRP-like immunoreactivity in additional species including mice (Maison et al., 2003a; Wu et al., 2018), rats (Kitajiri et al., 1985; Takeda et al., 1986; Lu et al., 1987; Tohyama et al., 1989; Ylikoski et al., 1989; Kuriyama et al., 1990; Merchan-Perez et al., 1990), hamsters (Simmons et al., 1996), cats (Lu et al., 1987), and humans (Kong et al., 2002).

Immunolabeling of the human cochlea revealed CGRP-like immunoreactivity in the inner spiral bundle and tunnel spiral bundle suggesting expression of CGRP in both the LOC and medial olivococlear (MOC) efferent neurons with no notable differences from base to apex (Schrott-Fischer et al., 2007). CGRP immunoreactive terminals are distributed under the inner hair cells (IHCs) in

approximately equal numbers throughout the length of the cochlea in rats (Vetter et al., 1991) and mice (Maison et al., 2003a) although some mouse strains may have a gradient with less robust CGRP presence in the apex (Wu et al., 2018). There are some reports that CGRP-positive labeling of the LOC system is robust across the length of the guinea pig cochlea (Sliwinska-Kowalska et al., 1989; Ylikoski et al., 1989) although there are also reports that CGRP-positive cells are less abundant in the apex and upper third turn of the guinea pig cochlea (Safieddine and Eybalin, 1992). Sliwinska-Kowalska et al. (1989) investigated CGRP distribution in pigmented female guinea pigs weighing 150–300 g, Ylikoski et al. (1989) used 200–350 G guinea pigs but did not specify sex or strain, and Safieddine and Eybalin (1992) used pigmented guinea pigs weighing 200–250 g with sex not specified, thus it is not known if there are sex or strain (pigmented/albino) differences in CGRP distribution. In the only study assessing potential sex differences in the effects of CGRP within the LOC system, Allen and Luebke (2017) reported no functional differences between male and female CGRP-null mice. The lack of sex differences in that mouse study contrasts with sex differences in CGRP immunoreactivity observed in other tissues from rat and from human (Valdemarsson et al., 1990; Herbison and Spratt, 1995; Ji et al., 2019), with sex differences in humans potentially explaining sex differences in the efficacy of antimigraine medications that target CGRP receptors (Barbanti et al., 2021; de Vries Lentsch et al., 2021).

The mature CGRP receptor is a G-protein coupled receptor (GPCR) composed of three proteins, including calcitonin-like receptor (CLR), receptor activity-modifying protein (RAMP1), and CGRP-receptor component protein (RCP) (for additional detail, see Dickerson et al., 2016). Post-natal maturation of the CGRP receptor has been documented in the mouse (Dickerson et al., 2016). In mice, the CGRP receptor complex within the cochlea shows developmental maturation over the first 3-months (Dickerson et al., 2016). The guinea pig is precocial, whereas the mouse is altricial, and receptor development may follow different timelines in guinea pig and mouse. Post-natal receptor maturation of the CGRP receptor has not been studied in the guinea pig. Interestingly, observations of CGRP expression in the Type II SGNs have also been reported, although release of CGRP from type II afferent terminals in the cochlear nucleus has not been established and functional actions are not yet determined (Wu et al., 2018; Vyas et al., 2019).

The lateral superior olive (LSO) is the site of origin for the descending LOC efferent neurons. CGRP-like immunolabeling of the LSO is also well described in multiple species (Lu et al., 1987; Vetter et al., 1991; Simmons and Raji-Kubba, 1993; Safieddine et al., 1997; Simmons et al., 1997; Moore et al., 1999; Reuss et al., 1999). Co-localization of CGRP and other LOC transmitters has been described by several groups, and species differences have emerged with respect to colocalization as well as overall distribution. For example, in the human LSO, Moore et al. (1999) describe CGRP-positive terminals that are also positive for antibodies to choline acetyltransferase (ChAT); these cells were distinct from a second population which immunostained for ChAT but not CGRP. In the rat LSO and cochlea, Vetter et al. (1991) describe CGRP-positive terminals that are also positive for antibodies to ChAT; these cells were distinct from a second population which immunostained with antibodies to glutamic acid decarboxylase (GAD, the enzyme that decarboxylates glutamate to make GABA). In contrast, in the mouse, GABA and CGRP were extensively co-localized with ACh in LOC terminals (Maison et al., 2003a), whereas dopaminergic (DA) neurons were a separate subpopulation (Darrow et al., 2006). In studies evaluating CGRP co-localization with other LOC transmitters in guinea pigs, LSO cell bodies have been found to co-localize CGRP and encephalin (enk) (Tohyama et al., 1990), or CGRP, enk, and ACh (Safieddine and Eybalin, 1992). Finally, extensive colocalization has been observed with double and triple immunolabeling for ChAT and either CGRP, enk, GAD, or tyrosine hydroxylase (TH, the enzyme responsible for catalyzing the conversion of L-tyrosine to the DA precursor dihydroxyphenylalanine) (Safieddine et al., 1997).

That CGRP is present in the LSO and the LOC terminals in a variety of species suggests the potential for a functional role of CGRP in modulating the ascending auditory signal. This possibility has been explored, and supported, by data from a small number of studies. Depressed amplitude of auditory brainstem response (ABR) wave I in αCGRP-null mice (Maison et al., 2003b) has been shown, an effect that is consistent with excitatory modulation of sound-evoked auditory nerve (AN) activity by CGRP. One interpretation is that sound stimulation drives release of CGRP by LOC efferents during acoustic stimulation of the LOC reflex loop, and in the absence of CGRP release (in the αCGRP-null mice), sound-evoked responses are depressed. Alternatively, if CGRP is tonically released, the observed effects might also be explained by changes in AN spontaneous response properties. In mammals, AN fibers with higher spontaneous firing rates have lower (better) thresholds, are less sharply tuned, and adapt to sound more rapidly than other fibers with lower spontaneous firing rates (see Sachs and Abbas, 1974; Liberman, 1978; Rhode and Smith, 1985; Winter et al., 1990; Muller and Robertson, 1991; Yates, 1991). Consistent with the hypothesis that CGRP can increase spontaneous neural activity, application of CGRP produced an increase in spontaneous neural activity in the *Xenopus* lateral line organ (Adams et al., 1987; Sewell and Starr, 1991; Bailey and Swell, 2000a; Bailey and Swell, 2000b).

In the study by Maison et al. (2003b), which revealed that ABR amplitude was depressed in αCGRP-null mice, there were no corresponding changes in ABR threshold, distortion product otoacoustic emission (DPOAE) threshold and amplitude, or the strength of the MOC reflex. Allen and Luebke (2017) similarly report intact DPOAE responses in αCGRP-null mice. The lack of change in DPOAE outcomes [reflecting no change in outer hair cell (OHC) function] and the MOC metric are perhaps somewhat surprising. Earlier literature described CGRP-containing nerve endings on OHCs in rodents (Cabanillas and Luebke, 2002; Maison et al., 2003a) and humans (Kong et al., 2002; Schrott-Fischer et al., 2007), suggesting CGRP may function as an MOC transmitter as well as an LOC transmitter (see also Vyas et al., 2019). The limited DPOAE changes detected in the knock-out mice might provide an incomplete description of the role of CGRP in auditory physiology, however, if there is central nervous system

compensation during development (as suggested by May et al., 2002, who evaluated auditory sensitivity in mice lacking alpha-9 receptors). In another recent investigation, mature CGRP-null mice (3 months of age) not only had reduced cochlear nerve activity, they were also observed to have increased thresholds both in quiet and in broadband noise background (with thresholds measured using pre-pulse inhibition of the acoustic startle reflex) (Allen and Luebke, 2017). Development of deficits from 1 to 3 months of age was consistent with the timing of CGRP receptor maturation in mice shown by Dickerson et al. (2016).

In contrast to earlier research using CGRP-null mice, the current study evaluated the effects of infusing CGRP into the cochlea on auditory function, including assessments for both LOC and MOC-like functional effects. Effects of CGRP on sound-evoked response were evaluated using both CGRP and CGRP fragment 8–37, which acts as an antagonist at CGRP receptors. To evaluate the hypothesis that CGRP mediates changes in spontaneous AN activity as well as sound-driven AN activity, we measured electrical activity at the round window membrane, which provides a measure of ensemble spontaneous activity of the AN fiber population (Kiang et al., 1976; Dolan et al., 1990; Groff and Liberman, 2003). Changes in DPOAE amplitude and onset adaptation were used to assess effects of the study drugs on OHC responses. The use of experimental designs that combine both agonists and antagonists has allowed the effects of exogenous drug delivery and tonic endogenous release to be distinguished for the LOC transmitter DA (Garrett et al., 2011); the current data extend understanding of putative LOC transmitter substances to the peptide CGRP.

METHODS

Animal Model

Fourteen guinea pigs (Elm Hill Breeding Labs, Chelmsford, MA) were used in these experiments (5 female, 5 male, sex records not available for 4 animals). Two additional animals were excluded from the investigation based on permanent profound post-operative hearing loss. Animal weights were ~250–300 g on arrival (approximately 4 weeks old) and ~350–500 g (approximately 6 weeks old) at study entry. All animals were maintained with free access to food (Guinea Pig Chow, PMI Nutrition International Inc., Brentwood, MO) and water. The animal care program was AALAC accredited. Husbandry met or exceeded all applicable standards, including the Guide for the Use and Care of Laboratory Animals, prepared by the National Research Council (1996). The University Committee on Use and Care of Animals at the University of Michigan approved all animal care and testing protocols.

Apparatus and Procedures

Surgical Procedure

The studies described here used a chronic unilateral left-ear drug-infusion paradigm. CGRP has a molecular weight of ~3,800; it is a large enough molecule that it is unlikely to readily diffuse across the round window membrane (as larger molecules less readily diffuse across this membrane, see Goycoolea and Lundman, 1997; Mikulec et al., 2008). Therefore, it was delivered directly into the cochlea using a surgically implanted cannula. The surgical implant procedures were closely modeled after those we have described previously (Le Prell et al., 2004). Animals were anesthetized (40 mg/kg ketamine, 10 mg/kg xylazine), then a cannula filled with an artificial perilymph (AP) solution (145 mM NaCl, 2.7 mM KCl, 2.0 mM $MgSO_4$, 1.2 mM $CaCl_2$, 5.0 mM HEPES; pH = 7.40, osmolality = 280–285 mOsm) was inserted through the wall of the left cochlea via a small fenestra slightly lateral to the round window. The site of insertion was at a place with a best frequency of approximately 22.4 kHz (based on surgically-induced threshold deficits described in Le Prell et al., 2004). A silastic ball located 0.5 mm away from the end of the cannula prevented over-insertion of the cannula and prevented leaking of fluids from the cochlea. The other end of the cannula was connected to an osmotic mini-pump (model 2002, 0.5 µl/h x 14 days; Durect corporation, Cupertino, CA), also filled with the AP solution.

After inserting the cannula, a ball electrode (0.25 mm diameter, constructed of teflon-coated platinum-iridium wire) was carefully placed on the left round window membrane following procedures we have described previously (Le Prell et al., 2006). A ground wire was inserted into the middle ear via the defect in the bulla, and carboxylate cement (Durelon, ESPE, Germany) was used to seal the bulla defect and permanently fix both the cannula and the electrodes in place. The opposing ends of the electrodes were soldered to a two-pin connector (HSS-132-G2, Samtec Inc., IN) prior to the onset of the surgical procedure. Methyl methacrylate cement (Jet Repair Acrylic, Lang Dental Manufacturing, IL) was used to fix the cannula and the connector for the electrodes to the skull, and to seal the tissue edges surrounding the head-mounted connector. The post-auricular incision was then sutured and the incision cleaned.

AP was infused unilaterally for 12–14 days during which a variety of post-operative baseline data were collected. Guinea pigs then underwent a brief surgical procedure during which a small incision exposed the depleted osmotic pump, the depleted pump was extruded, the cannula clamped and cut, and a new osmotic-pump attached. The new pump was filled with either 200 µM CGRP (CGRP rat, Sigma Chemical C0292, CAS No. 96827-03-1; dissolved in AP) (n = 5; four female, sex not recorded for one animal) or 250 µM CGRP fragment 8–37 (synthetic human CGRP fragment 8–37, Sigma Chemical C2806, CAS No. 119911-68-1; dissolved in AP) (n = 7; four male, one female, sex not recorded for two animals).

Electrophysiology

Animals were anesthetized (20 mg/kg ketamine, 5 mg/kg xylazine), and placed on a warm heating pad to maintain body temperature. Acoustic stimuli were brief pure-tone stimuli (4, 8, 16, or 22.4 kHz) presented at levels ranging from 0 to 100-dB SPL in 5-dB increments (5-msec duration, 0.5-msec rise-fall; 10/sec). Acoustic stimuli were generated using Tucker-Davis Technology (TDT; Alachua, FL) System II/System III hardware and SigGen32 software. Signals were converted to

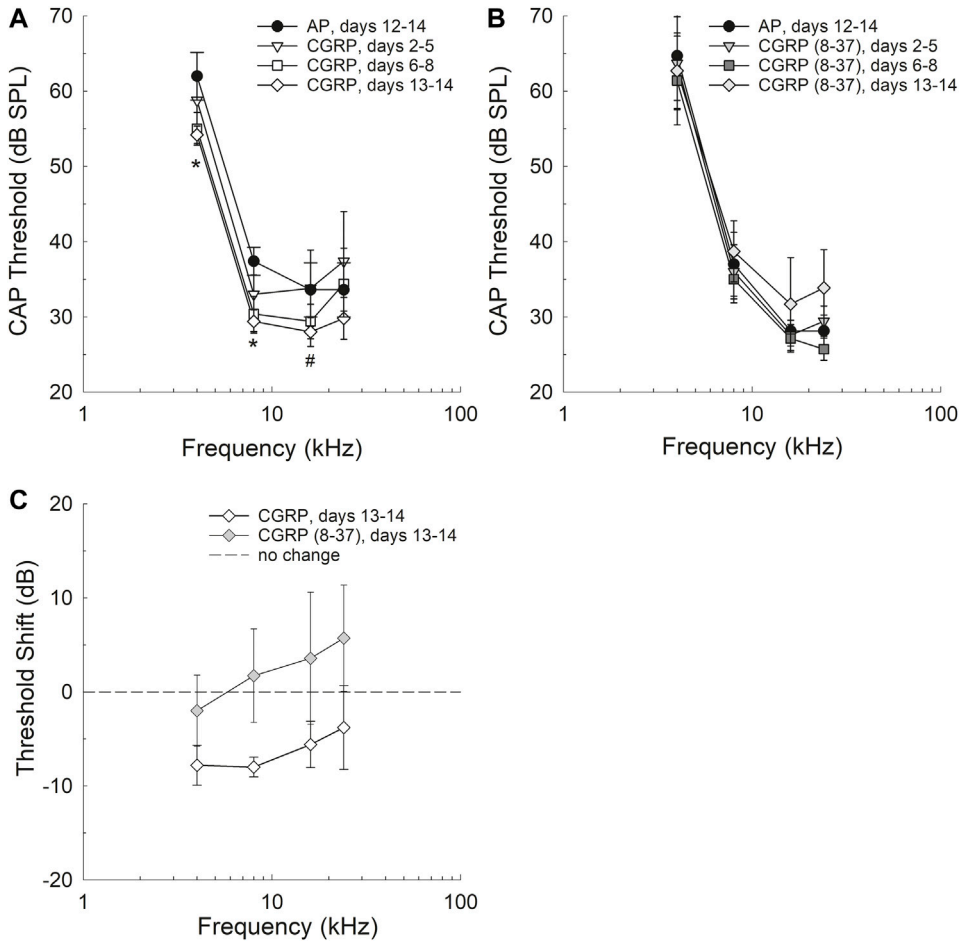

FIGURE 1 | Threshold sensitivity was improved after 13–14 days of CGRP agonist infusion, but not at earlier infusion times including days 2–5 and 6–8 **(A)**. Differences between AP and CGRP thresholds were statistically significant at 4 and 8 kHz (see asterisks) and approached statistical significance at 16 kHz ($p = 0.0853$). Threshold sensitivity after 13–14 days of CGRP antagonist [CGRP (8–37)] infusion was not reliably different from AP control **(B)** and no pair-wise comparisons were completed. The change in thresholds as a function of drug was significantly different when threshold shift as a function of drug assignment was compared **(C)**.

analog (DA1), filtered (FT6-2, F_c = 40 kHz), attenuated (PA5), and presented using a 200-Ohm transducer (Beyer Dynamic, Farmingdale, NY) coupled to the animals' ear canal *via* vinyl tubing. Cochlear potentials were filtered (300–3,000 Hz) and amplified (1,000x) using a Grass P55 amplifier. BioSig32 (TDT) was used to average 25 evoked responses for each frequency/level combination. Threshold to evoke a compound action potential (CAP) response of the auditory nerve was defined as the sound level that produced a 10-μV response; threshold estimates were determined using linear interpolation. CAP responses were measured using the implanted electrode; thus, testing was unilateral. CAP testing was repeated at 2–3 day intervals to monitor stability of post-surgical responses during AP infusion (the control condition), with additional testing at 2–3 day intervals during CGRP or CGRP (8–37) infusion (the experimental conditions) to monitor progressive changes as the experimental substances increased in concentration in the cochlea with continued infusion.

Round Window Noise

Baseline tests were conducted once during the second week of unilateral AP infusion (between days 9–11); repeat testing during drug infusion was conducted on the 11th day of either CGRP (n = 4; one animal not tested) or CGRP (8–37) (n = 7) infusion. RWN recordings were performed in anesthetized animals (20 mg/kg ketamine, 5 mg/kg xylazine) maintained on a warm heating pad. RWN was measured using the round window recording electrode. Using a digital oscilloscope, fast Fourier transformation of ensemble activity was conducted as in Dolan et al. (1990). The broad spectral peak (0.8–1.0 kHz) that is typical of round-window noise was measured. RWN was measured using the implanted electrode; thus, testing was unilateral.

DPOAE

Baseline DPOAE tests were conducted once during the second week of unilateral AP infusion (days 9–11); repeat testing during

CGRP infusion was conducted on the 9th day of CGRP (n = 4; one animal not tested) or CGRP (8–37) (n = 5; two animals not tested). Animals were anesthetized (58.8 mg/kg ketamine, 2.4 mg/kg xylazine, and 1.2 mg/kg acepromazine), and placed on a warm heating pad to maintain body temperature, then time-dependent amplitude of the cubic DPOAE ($2F_2$-F_1) was assessed using procedures we have described in detail previously (Halsey et al., 2005; Le Prell et al., 2005). In brief, the DPOAE tests were conducted using TDT system II/III equipment in combination with an Etymotic Research microphone-earphone assembly (ER-10B + Low Noise Microphone) coupled to the subject's ear by a short segment of flexible vinyl tubing, minimally smaller than the guinea pig ear canal and which sealed the ear canal to provide a closed field test condition. Testing was unilateral and limited to the experimental ear.

Onset adaptation of the DPOAE is a measure of the strength of the MOC reflex (see Liberman et al., 1996; Maison and Liberman, 2000; Kujawa and Liberman, 2001). Onset adaptation of the cubic distortion product was measured as described previously (Halsey et al., 2005; Le Prell et al., 2005); primary tone frequencies (F_1, F_2) were fixed at 8 kHz (F_1) and 9.6 kHz (F_2) and the cubic distortion product ($2F_1$-F_2) was 6.4 kHz. F_1 and F_2 levels (L_1, L_2) were initially set to approximately 92-dB SPL; L_2 was then systematically decreased over a 12-dB range in 1-dB steps. This procedure was repeated for at least six levels of F_1, with F_1 decreasing in 1-dB steps, until the levels producing maximum DPOAE adaptation were determined for both positive and negative deflections. Additional tests were then conducted with L_1 and L_2 level increments changing in 0.4-dB increments over at least six levels of F_1, with twelve F_2 levels presented for each level of F_1. A MatLab program was used to control stimulus generation (TDT hardware) and presentation (Beyer sound drivers), as well as data collection.

Primary tones were 1 s in duration, with a 1.5 s pause between presentations. Sound levels for F_1, F_2, and the DPOAE were determined during each level series using Fourier transform of the microphone input. For each level combination, responses to four stimulus presentations were collected and averaged. DPOAE amplitude was sampled at 50-msec intervals during the 1-s primary tone duration. If standard deviations exceeded 2-dB at any time point, the data were excluded and the level combination was repeated. Adaptation of the DPOAE response was defined as the difference between DPOAE amplitude at the onset of the primary tones and the steady-state amplitude of the DPOAE (defined as the average DPOAE amplitude during the final four time points).

Statistical Analysis

All data values in the text and figures are mean ± S.E.M.; all statistical comparisons were performed using SPSS 13.0. Statistical reliability of group differences was via ANOVA. Adjustment for violation of sphericity was accomplished using the Greenhouse-Geisser correction. Bonferroni corrections were applied for multiple comparisons.

CAP data collected during unilateral AP infusion were evaluated as a function of time post-implant (AP1: days 3–8; AP2: days 12–14) to assess possible post-operative changes in function. Functional data collected during unilateral CGRP infusion were evaluated as a function of the duration of drug delivery (CGRP1: days 2–5; CGRP2: days 6–8; CGRP3: days 13–14) to account for increasing intra-cochlear CGRP concentration during the 14-day infusion period.

RESULTS

Changes in Evoked Potentials During AP Infusion

Threshold changes during AP were minimal, consistent with Brown et al. (1993) and Le Prell et al. (2004). Whereas Brown et al. (1993) monitored ABR threshold measures in saline-infused animals as a surgical control during the development of this surgical procedure, Le Prell et al. (2004) measured both ABR thresholds and behavioral thresholds during 14–56 days of AP infusion prior to drug manipulation (Le Prell et al., 2004). With respect to CAP amplitude, there was a statistically significant Frequency x Replication (AP1, AP2) effect (p = 0.042) of time post-implant on CAP amplitude. Pair-wise comparisons revealed that differences between AP1 and AP2 measurements were limited to a small but statistically reliable decrease in CAP amplitude at 4 (p = 0.037) and 8 (p = 0.045) kHz, with no time-related changes in CAP amplitude at 16 or 24 kHz (p's > 0.05). Larger decreases in amplitude were evident in the surgical controls included by Sly et al. (2012). They reported small but largely reversible post-surgical reductions in DPOAE amplitude and slowly progressive decreases in ABR wave III amplitude over 4-week of infusion of Ringer's solution which they attributed to surgical trauma to the cochlea. Effects of CGRP were measured relative to the AP2 baseline collected during days 12–14 of AP infusion.

Intra-Cochlear CGRP Improved Threshold Sensitivity

Threshold sensitivity during AP, CGRP, and CGRP (8–37) antagonist infusion are shown in **Figures 1A,B**; because each subject contributed both baseline (AP) and either CGRP or CGRP (8–37) data points, the within-subject change in threshold is also shown (**Figure 1C**). CAP threshold was lower (better) during CGRP infusion when compared to within-subject pre-drug (AP) baseline (p = 0.043); after Bonferroni correction, the only pair-wise comparison that approached statistical reliability was AP versus the latter CGRP time point (days 13–14, see **Figure 1A**) ($F_{1,4}$ = 6.998, p = 0.057). To determine which frequencies had reliable differences between AP and CGRP days 13–14 thresholds, two-tailed paired t-tests were completed at each frequency. Differences were statistically significant at 4 kHz (t_4 = 3.661, p = 0.0216) and 8 kHz (t_4 = 7.682, p = 0.00159), and approached statistical significance at 16 kHz (t_4 = 2.275p = 0.0853), but not at 24 kHz (t_4 = 0.851, p = 0.443). CAP threshold measured during infusion of the CGRP receptor antagonist, CGRP (8–37), was not different from baseline (1B) ($F_{1,6}$ = 0.187, p = 0.681) and no additional pair-wise comparisons were completed within test frequencies. When change in threshold (on day 13–14 of infusion) was compared as a function

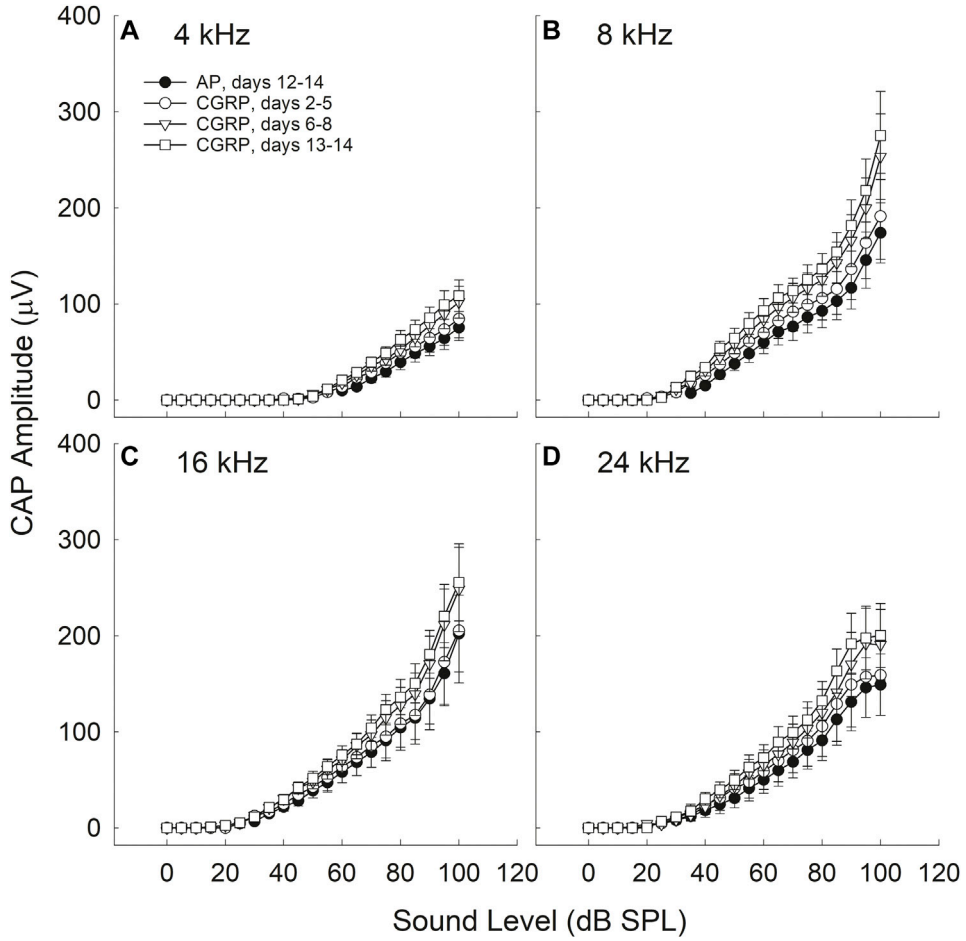

FIGURE 2 | CAP amplitude increased during CGRP infusion; all comparisons are relative to control measurements on the 12th-14th day of artificial perilymph (AP) infusion, immediately prior to the pump change surgery during which the AP pump was replaced with a pump containing CGRP. Increases in CAP amplitude (30–35%) were statistically reliable at 4 **(A)**, 8 **(B)**, 16 **(C)**, and 24 **(D)** kHz for the CGRP (days 13–14) comparisons with the AP data set (all p's < 0.005). CGRP-induced changes are shown as a function of duration of infusion; tests were conducted at least once from days 2–5, on days 6, 7, or 8, and on days 13 or 14.

of the treatment agent [CGRP vs. CGRP (8–37)] using a two-way ANOVA with treatment and frequency as factors, there was a statistically significant difference between the treatment groups ($F_{1,47}$ = 6.003, p = 0.019) with no effect of frequency ($F_{3,47}$ = 0.532, p = 0.663) and no drug × frequency interaction ($F_{3,47}$ = 0.0700, p = 0.976).

Intra-Cochlear CGRP Enhanced CAP Amplitude

CGRP-induced increases in CAP amplitude were time-, frequency-, and intensity-dependent (see **Figure 2**).

Time-Dependence

There were no reliable CGRP-induced changes in CAP amplitude during the earliest infusion days (days 2–4). When CAP amplitude was assessed on days 6–8 of infusion, the increase in CAP amplitude (20–30%) approached statistical reliability (4 kHz, p = 0.055; 8 kHz, p = 0.071; 16 kHz; p = 0.136; 24 kHz, p = 0.053). The most robust increases in CAP amplitude (30–35%) were observed at the 13–14 days time point, and these amplitude increases were statistically reliable (4 kHz, p = 0.016; 8 kHz, p = 0.026; 16 kHz, p = 0.052; 24 kHz, p = 0.027). Time-dependent changes are likely a consequence of the slow infusion rate of the osmotic mini-pump, with significant drug accumulations building slowly over multiple days or weeks (for discussion see Le Prell et al., 2004).

Frequency-Dependence

For the data set collected on the 13th and 14th days of infusion, a time at which the effects of CGRP on CAP amplitude were highly reliable, there was a statistically significant Condition × Frequency interaction (p = 0.022). The difference between AP and CGRP was smaller at 4 kHz than at the other (higher) test frequencies. Smaller effects at the lowest frequencies, furthest from the site of infusion, are not surprising as drug diffusion depends on the slow cochlear fluid gradient (approximately 1.6 nl/min, see Ohyama et al., 1988; for discussion

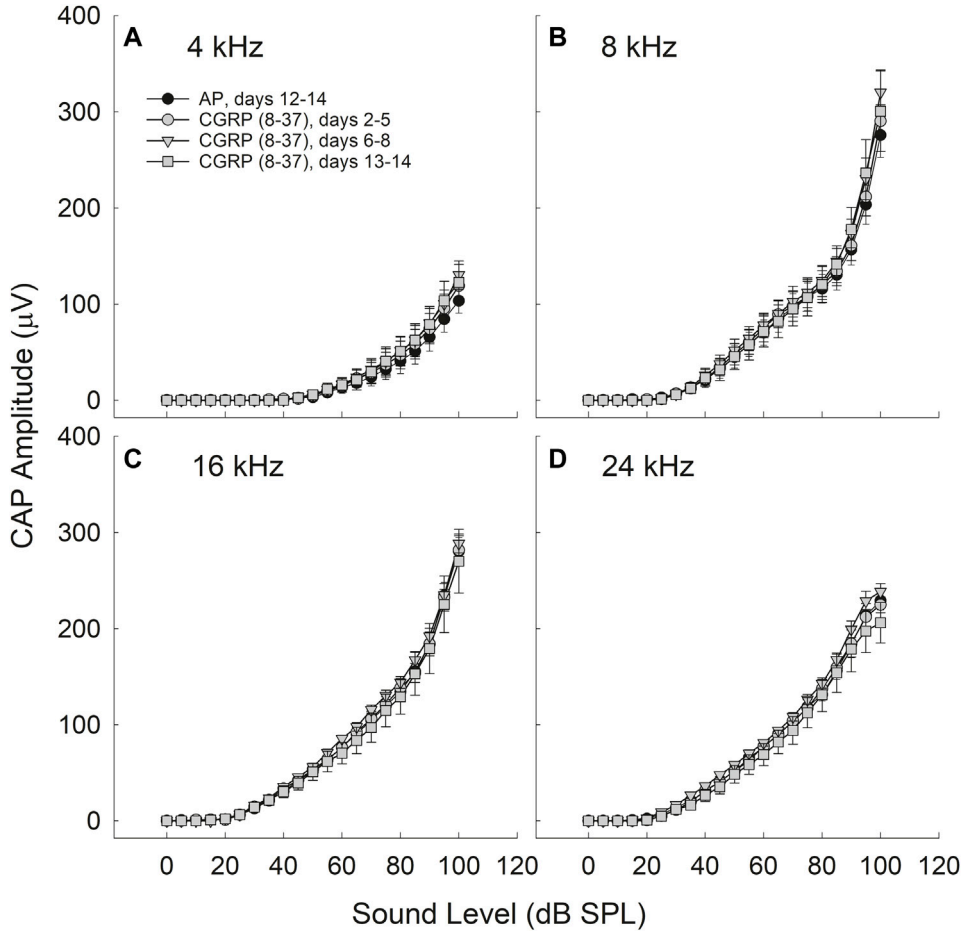

FIGURE 3 | CAP amplitude did not change as a function of CGRP (8–37) infusion at 4 **(A)**, 8 **(B)**, 16 **(C)**, and 24 **(D)** kHz. CAP tests were conducted at least once from days 2–5, on days 6, 7, or 8, and on days 13 or 14 for CGRP (8–37). All comparisons are relative to control measurements on the 12th–14th day of artificial perilymph (AP) infusion, immediately prior to the pump change surgery during which the AP pump was replaced with a pump containing CGRP (8–37).

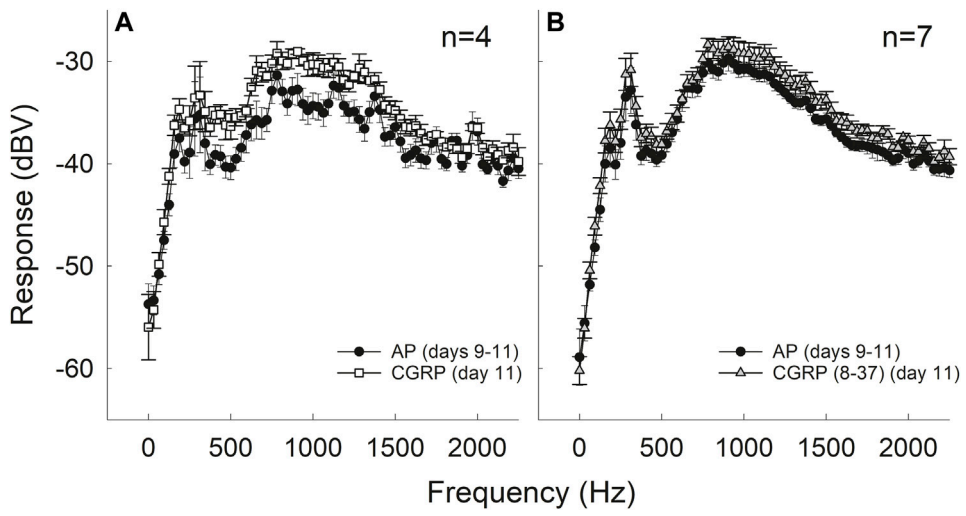

FIGURE 4 | Intra-cochlear infusion of CGRP enhanced round window noise from approximately 500–1,200 Hz; the frequency range associated with spontaneous firing of the auditory nerve **(A)**. There were no changes in round window noise during infusion of CGRP (8–37) **(B)**.

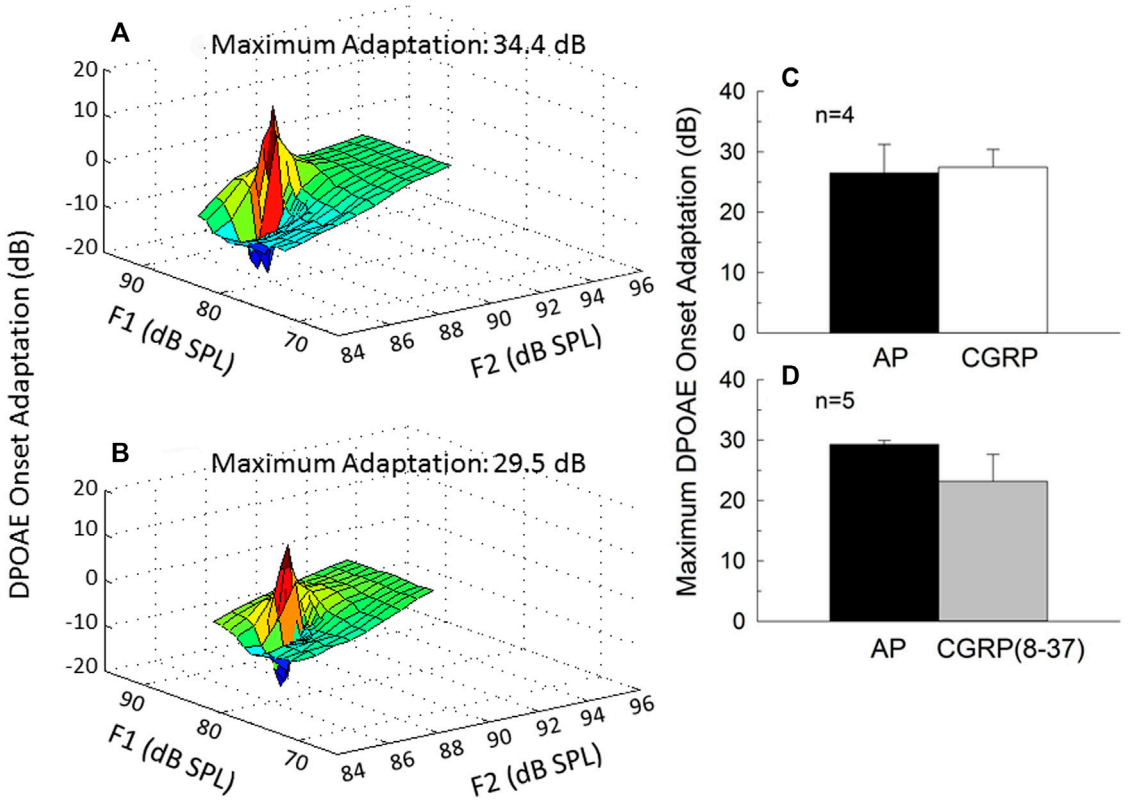

FIGURE 5 | Onset adaptation of the outer hair cell distortion product otoacoustic emission (DPOAE) shows a rapid level-dependent adaptation shortly after signal onset when the medial olivocochlear pathway is intact. DPOAE adaptation is depicted on day 9 of artificial perilymph **(A)** and CGRP **(B)** infusion for one representative animal. The maximum adaptation was extracted from the fine-structure plots shown in **(A,B)**. Onset adaptation was not reliably affected by either CGRP **(C)** or CGRP (8–37) **(D)** (all p's > 0.25).

see Le Prell et al., 2004). LOC innervation has been sparser in the apex than in the base in some (Safieddine and Eybalin, 1992) but not all (Sliwinska-Kowalska et al., 1989; Ylikoski et al., 1989) reports thus frequency effects could be related not only to drug distribution but also to CGRP receptor distribution.

Intensity-dependence

The difference in CAP amplitude during AP and CGRP increased with increasing intensity (4 kHz: $p = 0.028$; 8 kHz: $p = 0.077$; 16 kHz: $p = 0.069$; 24 kHz: $p = 0.019$). In contrast to the statistically significant time, frequency, and intensity dependent effects of CGRP infusion, there were no statistically significant treatment effects for CGRP (8–37) ($F_{1,6} = 0.004$, $p = 0.984$) (**Figure 3**).

Intra-Cochlear CGRP Increased Spontaneous Neural Activity

Electrical activity at the round window increased during CGRP infusion in the 800–1,200 Hz region ($F_{1,3} = 13.025$, $p = 0.037$); this "hump" region reflects spontaneous firing of multiple auditory nerve fibers (**Figure 4A**) (for discussion of 'hump' region, see Kiang et al., 1976; Dolan et al., 1990; Groff and Liberman, 2003). In contrast, comparisons between AP and the antagonist, CGRP (8–37), revealed no significant differences in electrical activity ($F_{1,6} = 3.229$, $p = 0.122$) (**Figure 4B**). Baseline measures in the group of guinea pigs that later received CGRP systematically differed from the baseline measures in the group that later received CGRP (8–37) ($F_{1,9} = 4.830$, $p = 0.056$ when all frequencies were used and $F_{1,9} = 5.625$, $p = 0.042$ when only frequencies less than 1,100 Hz were used).

Intra-Cochlear CGRP Does not Affect MOC Reflex Strength

The strength of the MOC reflex, measured using onset adaptation of the DPOAE, was essentially the same during AP, CGRP infusion, and CGRP (8–37). DPOAE adaptation is illustrated for one representative animal in **Figure 5** (5A: AP; 5B: CGRP). Adaptation was clearly robust (>20 dB) in both conditions; mean adaptation data for all animals is illustrated in **Figure 5** [5C: CGRP; 5D: CGRP (8–37)]. Although adaptation magnitude was seemingly reduced during infusion of the CGRP receptor antagonist, these differences were not statistically reliable (all p's > 0.25). In contrast to the lack of effect shown here, manipulations known to disrupt the MOC system, including intra-venous strychnine and OCB transection, cause a profound depression of DPOAE adaptation (approximately 20-dB, see Le Prell et al., 2005).

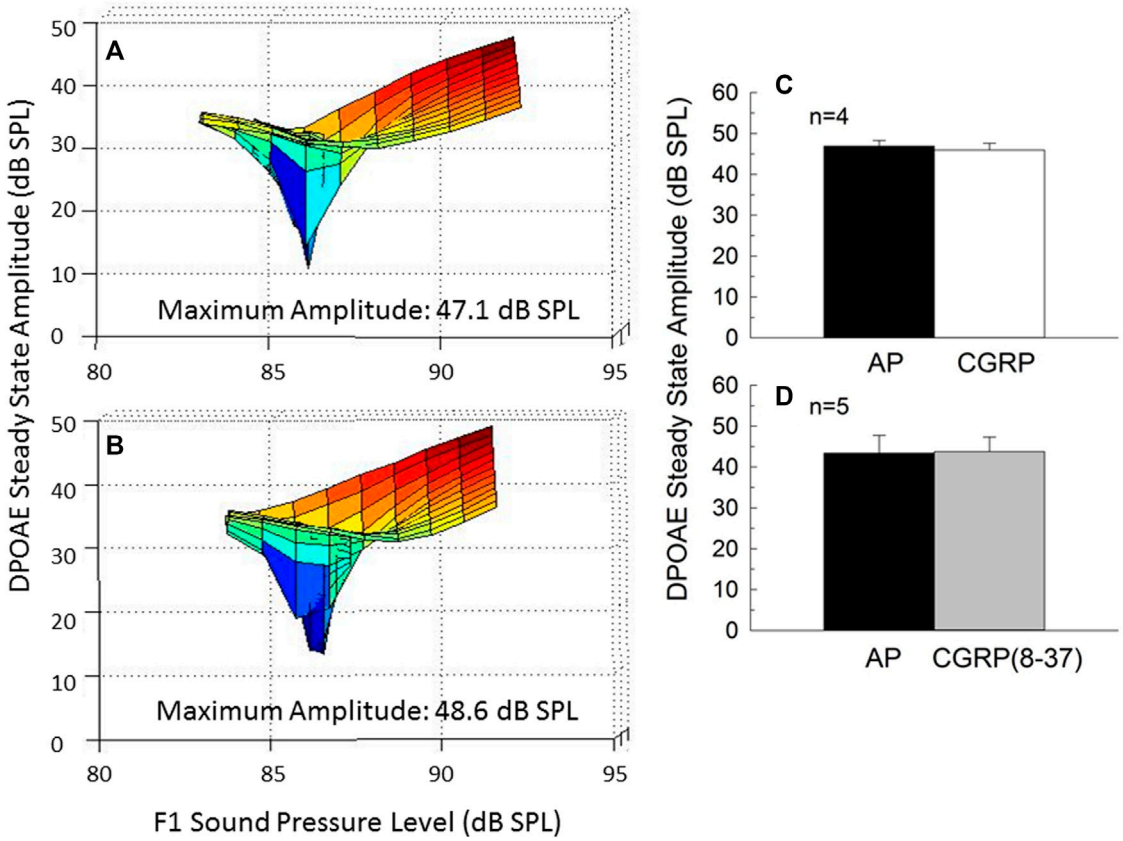

FIGURE 6 | Steady-state amplitude of the outer hair cell distortion product otoacoustic emission (DPOAE) varies with F1 and F2 sound level, and provides as a measure of the integrity of the outer hair cell population. DPOAE amplitude is depicted on day 9 of artificial perilymph **(A)** and CGRP **(B)** infusion for one representative animal. The steady state amplitude was extracted from the fine-structure plots shown in **(A,B)**. The level-dependent steady-state DPOAE amplitude was unchanged by either CGRP **(C)** or CGRP (8–37) **(D)** infusion (all p's > 0.05).

Intra-Cochlear CGRP Does not Affect Outer Hair Cell Function

DPOAE amplitude, a measure of the functional integrity of the OHC population, is illustrated for one representative animal in **Figure 6** (6A: AP; 6B: CGRP). Mean steady-state amplitude data for all animals is illustrated in **Figure 6** [6C: CGRP; 6D: CGRP (8–37)]. The lack of effect of CGRP and CGRP (8–37) on DPOAE amplitude indicates that OHC function was not influenced by intra-cochlear infusion of CGRP ligands, at least within the range of levels tested here. Lack of effect of CGRP and CGRP (8–37) contrasts with profound depression of DPOAE steady-state amplitude following intra-cochlear neomycin (Le Prell et al., 2004) or euthanasia with an overdose of sodium pentobarbital (Le Prell et al., 2005).

DISCUSSION

The primary outcome reported here is an increase in CAP amplitude accompanied by small improvements in CAP threshold during CGRP infusion into the cochlea. These results are consistent with the decreases in ABR Wave I amplitude reported by Maison et al. (2003b), who observed a decrease in sound-driven auditory nerve activity in the absence of endogenous αCGRP. Although no changes in thresholds were detected in the 16-week old mutant mice described by Maison et al. (2003b), changes in thresholds were detected in the 3-month old mutant mice described by Allen and Luebke (2017), with CGRP-null mice having poorer hearing in both quiet and in noise. The current results in guinea pigs are consistent with Allen and Luebke (2017) in that thresholds were better when exogenous CGRP was infused; however, threshold deficits did not emerge when CGRP (8–37) was infused. In addition to sound-evoked neural response, the current study evaluated spontaneous neural activity using round window noise. The increased round window noise described here during CGRP infusion suggests that CGRP induced an increase in spontaneous AN firing. The observed effects are consistent not only with data from CGRP-null mice, but also with the increase in spontaneous activity observed after bath application of CGRP to *Xenopus* lateral line organ (Adams et al., 1987; Sewell and Starr, 1991; Bailey and Swell, 2000a; Bailey and Swell, 2000b). Having demonstrated excitatory effects of CGRP in the current study, additional studies are warranted to determine a dose-response curve. A preliminary test with a single subject infused with a lower dose (125 μM) showed no effects of

CGRP on CAP threshold or amplitude at any of the test times over the 14-day infusion, but the lowest effective dose is not known, and the effects of increasing either the concentration of CGRP or the duration of CGRP infusion are not known.

In their description of the effects of CGRP-null mutations, Maison et al. (2003b) reported they did not observe any changes in DPOAE threshold or amplitude, or the strength of the MOC reflex. Allen and Luebke (2017) similarly reported DPOAE responses to be intact in CGRP-null mice. The lack of effect of CGRP-null mutations on measures of OHC function is perhaps surprising given robust CGRP-positive immunolabeling of the MOC efferents that innervate the OHCs (Cabanillas and Luebke, 2002; Kong et al., 2002; Maison et al., 2003a). However, the data collected here using both CGRP and the CGRP (8–37) fragment, a receptor antagonist, were consistent with the reports by Maison et al. (2003b) and Allen and Luebke (2017). Just as CGRP-null mice did not have any changes with respect to DPOAE metrics, no changes were observed here in guinea pigs that underwent chemical manipulation of the cochlea fluids with CGRP ligands. Taken together, the data show CGRP effects on the AN but not the OHCs, although we cannot exclude the possibility for as-yet unknown effects of CGRP on the OHCs. Future studies should continue to include detailed input-output functions for DPOAE responses across a wide range of sound levels to assure that OHC function is well characterized.

The earlier data from Maison et al. (2003b) and Allen and Luebke (2017) reflect the loss of CGRP-mediated modulation of AN activity that is present in the wild-type controls. In mutant CGRP-null mice there is a loss of excitation; here, with CGRP infusion, there is evidence of increased spontaneous and sound driven AN activity. While we interpret these data to reflect direct effects of CGRP on the AN, the possibility that CGRP-mediated changes in blood flow could also contribute to the observed results must be considered. The spiral modiolar artery, a primary supplier of blood to the cochlea, contains CGRP-positive terminals (Ylikoski et al., 1989; Carlisle et al., 1990; Lyon and Payman, 2000; Qiu et al., 2001; Herzog et al., 2002) as well as CLR mRNA (Herzog et al., 2002). Micro-infusion of CGRP directly into the arterial network of the cochlea increases cochlear blood flow (Quirk et al., 1994), as does intra-venous CGRP infusion (Hillerdal and Andersson, 1991). However, when drugs that influence cochlear blood flow have been delivered directly into the cochlear fluids via round window application in the rat, instead of being delivered directly into the bloodstream, the otherwise vasoactive drugs failed to reduce cochlear blood flow (Laurikainen et al., 1993). Because the CGRP ligands were administered into the cochlear fluids in this study, the data from Laurikainen et al. (1993) suggest the current infusions to be unlikely to influence cochlear blood flow. However, even if the CGRP ligands did move into the blood supply, intra-arterial CGRP has no effect on CAP (Quirk et al., 1994), and other blood-flow promoting drugs have also failed to affect CAP amplitude after intra-venous drug delivery (Lamm and Arnold, 2000).

Changes in CAP have accompanied cochlear blood flow alterations only if the drug treatment resulted in arterial blockade, ischemia, and excitotoxic AN swelling, in which case CAP decreases (e.g., Asai et al., 1996; Kong et al., 1996; Scheibe et al., 1997; Tabuchi et al., 1998). Thus, even if intra-cochlear CGRP did influence cochlear blood flow, the observed increases in CAP amplitude are not readily explained by changes in cochlear blood flow. It is possible that inflammation affecting the cochlear vascular system could occur after cochlear surgery, and inflammation has the potential to influence cochlear blood flow (Sharaf et al., 2016). However, normal post-operative hearing thresholds suggest inflammation not to be a major concern as inflammation is increasingly understood to be associated with hearing loss (Frye et al., 2019; Zhang et al., 2021). Here, thresholds were not only normal, they showed statistically significant decreases (improvements) during CGRP infusion, which would not be expected in the presence of surgical trauma and significant inflammation. Taken together, the overall pattern of results is more consistent with direct effects on the AN than with indirect effects on the AN mediated via changes in cochlear blood flow.

Previous studies have showed that cutting the olivocochlear bundle (OCB), which eliminates both MOC and LOC innervation, depressed spontaneous (Liberman, 1990; Walsh et al., 1998; Zheng et al., 1999) and sound-driven (Zheng et al., 1999) AN activity. When the LSO is lesioned in the guinea pig brainstem using melittin (Le Prell et al., 2003b) or the LOC system is lesioned in the guinea pig cochlea using MPTP (Le Prell et al., 2005), sound-driven AN activity is decreased. When the guinea pig LOC system is lesioned using MPTP, spontaneous AN firing is also decreased (Le Prell et al., 2014a). We have long speculated that the decreases in spontaneous and sound driven AN firing after OCB transection, LSO lesion, or LOC lesion could be the result of compromised CGRP release when the LOC system is disrupted (Le Prell et al., 2003b; Le Prell et al., 2005; Le Prell, 2007; Le Prell et al., 2014a). The observation that CGRP infusion directly increased ensemble spontaneous and sound-driven AN activity in this study adds new support for the hypothesis that endogenous CGRP release by the LOC efferent neurons has an excitatory effect on the AN.

The chemical transmitters that might mediate the net-excitatory effect in the intact (undamaged) system are a question of significant interest (for review and discussion see Le Prell et al., 2003a; Le Prell et al., 2003b; Le Prell et al., 2005; Reijntjes and Pyott, 2016). In brief, most data suggest that DA is largely inhibitory with respect to AN activity (d'Aldin et al., 1995a; d'Aldin et al., 1995b; Oestreicher et al., 1997; Ruel et al., 2001), although new data using selective agonists and antagonists acting at D_2 receptors suggest tonic release of endogenous DA has an excitatory action at the D_2 receptor (Garrett et al., 2011). Similar, but more limited, documentation of inhibitory effects on AN activity have been reported for enk (Burki et al., 1993) and GABA (Felix and Ehrenberger, 1992; Arnold et al., 1998). Comprehensive discussion of these diverse pharmacological studies is available in Reijntjes and Pyott (2016). Recent data suggest differential release of ACh and DA in different sound conditions and a "fine-tuning" of the activity of the auditory nerve via the release of these two LOC neurotransmitters (Wu et al., 2020).

Overall understanding of the LOC system will require improved understanding of other LOC transmitters that are co-localized with CGRP in the LOC terminals, including, for example, ACh and dyn. The effects of ACh on the OHCs have been carefully characterized, although the potential effects of ACh on the AN remain less well understood (for detailed reviews, see Puel, 1995; Le Prell et al., 2001; Reijntjes and Pyott, 2016; Fuchs and Lauer, 2019). Some studies have used cochlear perfusion, and others have used microiontophoresis to restrict ACh delivery to the vicinity of the AN dendrites; chemical antagonists and genetic manipulations have also been employed. Release of ACh from the MOC efferents onto the OHCs inhibits OHC electromotile action. This body of work suggests that the α9/α10 nicotinic receptors may provide a novel pharmacotherapeutic target (Elgoyhen et al., 2009). Early data collected with ACh delivered via intracochlear perfusion indicated that 250 μM ACh had no effect on the cochlear microphonic (CM) or CAP; however, 250 μM ACh delivered in combination with 10 μM eserine (which blocks the metabolism of ACh) augmented CM amplitude and depressed CAP amplitude, suggesting neural effects may be secondary to changes in OHC response to sound (Bobbin and Konishi, 1971). In contrast to the decreases in CAP with cochlear perfusion, when 0.5 M ACh was applied in the vicinity of the AN dendrites using microiontophoresis, increased subsynaptic spiking and enhanced glutamate-induced AN activity were observed, suggesting direct excitatory effects of ACh on the AN (Felix and Ehrenberger, 1992). Other recent data also suggest direct excitatory effects of ACh on the AN; specifically, selective deletion of several muscarinic receptor (M_1 and/or M_4) subtypes decreased neural response amplitude without effecting DPOAEs (Maison et al., 2010). Taken together, this data suggests the potential that ACh may also serve as an excitatory transmitter when released from the LOC efferent neurons.

The effects of dynorphin (dyn) have been less clear, with data from Sahley and colleagues, who assessed supra-physiological doses, suggesting excitatory (Sahley et al., 1991; Sahley and Nodar, 1994), or biphasic (Sahley et al., 2008) effects. In contrast, data collected using biologically plausible drug concentrations instead suggested that dyn inhibits sound-evoked AN activity (Le Prell et al., 2014b). More recently, Sahley et al. (2019) suggested that release of dyn by the LOC neurons may in part drive well-observed cascades including glutamate-induced swelling, inflammation, excitotoxicity, and hearing loss as dyn has been linked to such responses (immune, inflammatory, and excitotoxic) in other neural systems. Taken together, the transmitter data collected using DA, GABA, enk, and dyn have largely failed to explain the net excitatory effects of LOC innervation on the AN that are suggested by the net-inhibitory effects of LOC lesions, as well as observation that electrical current applied at some locations within the LSO enhances CAP amplitude (Groff and Liberman, 2003). The data from Maison et al. (2003b) and Allen and Luebke (2017) using CGRP-null mice suggest CGRP as a candidate transmitter substance, and the current data using chemical manipulations confirm CGRP has the potential to upregulate AN activity, with ACh also remaining a potentially excitatory neurotransmitter substance within the LOC system.

The extent to which endogenous CGRP is released from the LOC efferents in either a tonic state or stimulus-driven (sound) condition is not currently known; thus, important questions remain. In an effort to identify endogenous release, we assessed the effects of a CGRP receptor antagonist, CGRP (8–37). The finding that CGRP (8–37) did not influence AN or OHC outcomes may suggest there is no appreciable tonic or sound-driven release of CGRP by the LOC or MOC efferents, at least under these test conditions. Caution is required with respect to this interpretation however, as the extent to which CGRP (8–37) is an effective antagonist in the guinea pig inner ear remains an open question. It would be worthwhile to include combinations of agents in future studies to directly assess whether the antagonist selected for use competitively blocks the effects attributed to agonist infusion, and we strongly encourage this approach in future investigations to reduce questions about the potential effectiveness of the antagonist selected for investigation. Another approach that might be used to more precisely localize the observed drug effects to the LOC system would be repeating the drug studies in guinea pigs with efferent lesions, although LOC lesions are often incomplete which would make data from such studies difficult to interpret. LSO lesions induced in the brainstem using melittin do not completely eliminate the LOC innervation in the cochlea (Le Prell et al., 2003b), and LOC lesions induced in the cochlea using MPTP are also incomplete (Le Prell et al., 2005).

We selected CGRP (8–37) as competitive blockade of CGRP1 receptors has been shown in guinea pig basilar artery using CGRP (8–37) (Jansen-Olesen et al., 2001). In addition, CGRP (8–37) has been an effective antagonist when delivered in equimolar concentrations with CGRP (Buffelli et al., 2001). From a practical perspective, CGRP (8–37) was the only antagonist readily available through common commercial sources. However, CGRP (8–37) is widely regarded to not be very potent as an antagonist (Doods et al., 2000), and there have been significant efforts to develop more potent antagonists. The novel CGRP receptor antagonist BIBN4096BS (olcegepant) has been an effective antagonist when applied to brainstem slices from the mouse (Zheng et al., 2021), resulted in decreased bone volume when administered systematically in the mouse (Köhli et al., 2021), and decreased CGRP-induced light aversion when olcegepant was co-administered in the mouse (Russo et al., 2009). In contrast, neither olcegepant nor CGRP (8–37) affected uptake of CGRP in rat dura mater preparations (Gupta et al., 2010). Olcegepant has not been well studied in guinea pigs and thus it is not clear if olcegepant would be more effective than CGRP (8–37) when small drug volumes are infused into guinea pig cochlea. However, olcegepant binding in rat, rabbit, dog, and guinea pig models has been reported to be is as much as 100 times less than that observed in primate models (rhesus macaque, marmoset) (Doods et al., 2000; Hershey et al., 2005).

Given better binding in non-human primates and in humans, multiple drugs that antagonize CGRP release or the CGRP receptor are either in clinical trials or approved for use for antimigraine purposes (Mohanty and Lippmann, 2020). Despite the availability of drugs that are potent in non-human primates and humans, there continues to be a need for antagonists that are effective in rodent models for use in basic (pre-clinical) investigation. In addition to binding issues, stability of the antagonists must be considered for chronic infusion paradigms such as this one. The stability of CGRP (8–37) *in vivo* has been

questioned (Miranda et al., 2013). However, CGRP (8–37) was biologically effective when delivered via osmotic mini-pump for 7-days *in vivo* in rats (Reinshagen et al., 1998; Buffelli et al., 2001; Yin et al., 2004). Our infusions extended over a longer period, to 14 days. However, even if CGRP (8–37) were inactivated at later test times, we did not observe any functional changes within the first 6–8 days (see **Figure 3**), times at which the data from rats suggest the CGRP (8–37) fragment to be stable via osmotic mini-pump delivery.

In summary, this is the first direct demonstration that CGRP infusion enhances spontaneous and sound-driven AN activity. Based on these results, we conclude that CGRP has the potential to play an excitatory role in the AN response, confirming and extending data from knock-out mice (see Maison et al., 2003b). These key data set the stage for psychophysical data to be collected during periods of chronic cochlear drug infusion using osmotic mini-pumps (as in Le Prell et al., 2004) to confirm the possible role of CGRP in modulation of hearing in noise, following the decreased hearing-in-noise documented in CGRP-null mice by Allen and Luebke (2017). Studies in awake animals would have the added benefit of precluding the possibility that ketamine anesthesia may attenuate responses to CGRP. The effects of CGRP are commonly measured in ketamine-anesthetized animals (Radziszewski et al., 2003; Sakamoto et al., 2014; Sakamoto et al., 2017; Søndergaard et al., 2019). However, intra-venous ketamine attenuated CGRP-induced vasodilation of the dural artery in rats (Chan et al., 2010). Possible effects of ketamine on the excitatory effects of CGRP in the cochlea are speculative; however, if CGRP has less excitatory effect when measured under ketamine anesthesia, then the effect of CGRP on AN activity could be even more robust than was shown in this report. Taken together, the data provide direct confirmation of excitatory effects of CGRP on the AN, and support a potentially important role for CGRP in auditory function.

DATA AVAILABILITY STATEMENT

The raw data supporting the conclusion of this article will be made available by the authors, without undue reservation.

ETHICS STATEMENT

The animal study was reviewed and approved by the University Committee on Use and Care of Animals at the University of Michigan.

AUTHOR CONTRIBUTIONS

CL, DD, and SB designed the experiments; CL and DD collected data; LH performed statistical analyses; CL, DD, SB, and LH interpreted results; CL and LH wrote the manuscript; DD and SB reviewed and revised the manuscript.

FUNDING

Financial support was provided by the American Hearing Research Foundation (CL), the National Organization for Hearing Research (CL), and NIH-NIDCD grants R03-DC007342 (CL) and P30-DC05188 (DD).

ACKNOWLEDGMENTS

The authors thank Chris Ellinger, Kärin Halsey, Beth Hand, Lisa Kabara, Diane Prieskorn, and Sarah Weisbuch, for their invaluable technical assistance.

REFERENCES

Adams, J. C., Mroz, E. A., and Sewell, W. F. (1987). A Possible Neurotransmitter Role for CGRP in a Hair-Cell Sensory Organ. *Brain Res.* 419, 347–351. doi:10.1016/0006-8993(87)90606-8

Allen, P. D., and Luebke, A. E. (2017). Reflex Modification Audiometry Reveals Dual Roles for Olivocochlear Neurotransmission. *Front. Cel. Neurosci.* 11, 361. doi:10.3389/fncel.2017.00361

Arnold, T., Oestreicher, E., Ehrenberger, K., and Felix, D. (1998). GABAA Receptor Modulates the Activity of Inner Hair Cell Afferents in Guinea Pig Cochlea. *Hear. Res.* 125, 147–153. doi:10.1016/s0378-5955(98)00144-0

Asai, Y., Umemura, K., and Nakashima, M. (1996). Reversibility of Compound Action Potential during the Acute Phase after Transitory Local Ischemia. *Ann. Otol. Rhinol. Laryngol.* 105, 472–475. doi:10.1177/000348949610500610

Bailey, G. P., and Sewell, W. F. (2000b). Calcitonin Gene-Related Peptide Suppresses Hair Cell Responses to Mechanical Stimulation in the Xenopus Lateral Line Organ. *J. Neurosci.* 20, 5163–5169. doi:10.1523/JNEUROSCI.20-13-05163.2000

Bailey, G. P., and Sewell, W. F. (2000a). Pharmacological Characterization of the CGRP Receptor in the Lateral Line Organ of *Xenopus laevis*. *J. Assoc. Res. Otolaryngol.* 1, 82–88. doi:10.1007/s101620010007

Barbanti, P., Aurilia, C., Cevoli, S., Egeo, G., Fofi, L., Messina, R., et al. (2021). Long-term (48 Weeks) Effectiveness, Safety, and Tolerability of Erenumab in the Prevention of High-frequency Episodic and Chronic Migraine in a Real World: Results of the EARLY 2 Study. *Headache* 61 (9), 1351–1363. doi:10.1111/head.14194

Bobbin, R. P., and Konishi, T. (1971). Acetylcholine Mimics Crossed Olivocochlear Bundle Stimulation. *Nat. New Biol.* 231, 222–223. doi:10.1038/newbio231222a0

Brown, J. N., Miller, J. M., Altschuler, R. A., and Nuttall, A. L. (1993). Osmotic Pump Implant for Chronic Infusion of Drugs into the Inner Ear. *Hear. Res.* 70, 167–172. doi:10.1016/0378-5955(93)90155-t

Buffelli, M., Pasino, E., and Cangiano, A. (2001). *In Vivo* Acetylcholine Receptor Expression Induced by Calcitonin Gene-Related Peptide in Rat Soleus Muscle. *Neuroscience* 104, 561–567. doi:10.1016/s0306-4522(01)00090-2

Bürki, C., Felix, D., and Ehrenberger, K. (1993). Enkephalin Suppresses Afferent Cochlear Neurotransmission. *ORL* 55, 3–6. doi:10.1159/000276344

Cabanillas, L. A., and Luebke, A. E. (2002). CGRP- and Cholinergic-Containing Fibers Project to Guinea Pig Outer Hair Cells. *Hear. Res.* 172, 14–17. doi:10.1016/s0378-5955(02)00305-2

Carlisle, L., Aberdeen, J., Forge, A., and Burnstock, G. (1990). Neural Basis for Regulation of Cochlear Blood Flow: Peptidergic and Adrenergic Innervation of the Spiral Modiolar Artery of the Guinea Pig. *Hear. Res.* 43, 107–113. doi:10.1016/0378-5955(90)90219-f

Chan, K., Gupta, S., de Vries, R., Danser, A., Villalón, C., Muñoz-Islas, E., et al. (2010). Effects of Ionotropic Glutamate Receptor Antagonists on Rat Dural Artery Diameter in an Intravital Microscopy Model. *Br. J. Pharmacol.* 160, 1316–1325. doi:10.1111/j.1476-5381.2010.00733.x

d'Aldin, C., Eybalin, M., Puel, J.-L., Charachon, G., Ladrech, S., Renard, N., et al. (1995a). Synaptic Connections and Putative Functions of the Dopaminergic

Innervation of the Guinea Pig Cochlea. *Eur. Arch. Otorhinolaryngol.* 252, 270–274. doi:10.1007/BF00185388

d'Aldin, C., Puel, J.-L., Leducq, R., Crambes, O., Eybalin, M., and Pujol, R. (1995b). Effects of a Dopaminergic Agonist in the Guinea Pig Cochlea. *Hear. Res.* 90, 202–211. doi:10.1016/0378-5955(95)00167-5

Darrow, K. N., Simons, E. J., Dodds, L., and Liberman, M. C. (2006). Dopaminergic Innervation of the Mouse Inner Ear: Evidence for a Separate Cytochemical Group of Cochlear Efferent Fibers. *J. Comp. Neurol.* 498, 403–414. doi:10.1002/cne.21050

de Vries Lentsch, S., Rubio-Beltrán, E., and MaassenVanDenBrink, A. (2021). Changing Levels of Sex Hormones and Calcitonin Gene-Related Peptide (CGRP) during a Woman's Life: Implications for the Efficacy and Safety of Novel Antimigraine Medications. *Maturitas* 145, 73–77. doi:10.1016/j.maturitas.2020.12.012

Dickerson, I. M., Bussey-Gaborski, R., Holt, J. C., Jordan, P. M., and Luebke, A. E. (2016). Maturation of Suprathreshold Auditory Nerve Activity Involves Cochlear CGRP-Receptor Complex Formation. *Physiol. Rep.* 4, e12869. doi:10.14814/phy2.12869

Dolan, D. F., Nuttall, A. L., and Avinash, G. (1990). Asynchronous Neural Activity Recorded from the Round Window. *J. Acoust. Soc. Am.* 87, 2621–2627. doi:10.1121/1.399054

Doods, H., Hallermayer, G., Wu, D., Entzeroth, M., Rudolf, K., Engel, W., et al. (2000). Pharmacological Profile of BIBN4096BS, the First Selective Small Molecule CGRP Antagonist. *Br. J. Pharmacol.* 129, 420–423. doi:10.1038/sj.bjp.0703110

Elgoyhen, A. B., Katz, E., and Fuchs, P. A. (2009). The Nicotinic Receptor of Cochlear Hair Cells: A Possible Pharmacotherapeutic Target? *Biochem. Pharmacol.* 78, 712–719. doi:10.1016/j.bcp.2009.05.023

Felix, D., and Ehrenberger, K. (1992). The Efferent Modulation of Mammalian Inner Hair Cell Afferents. *Hear. Res.* 64, 1–5. doi:10.1016/0378-5955(92)90163-h

Frye, M. D., Ryan, A. F., and Kurabi, A. (2019). Inflammation Associated with Noise-Induced Hearing Loss. *J. Acoust. Soc. Am.* 146, 4020–4032. doi:10.1121/1.5132545

Fuchs, P. A., and Lauer, A. M. (2019). Efferent Inhibition of the Cochlea. *Cold Spring Harb. Perspect. Med.* 9, a033530. doi:10.1101/cshperspect.a033530

Garrett, A. R., Robertson, D., Sellick, P. M., and Mulders, W. H. A. M. (2011). The Actions of Dopamine Receptors in the Guinea Pig Cochlea. *Audiol. Neurotol.* 16, 145–157. doi:10.1159/000316674

Goycoolea, M. V., and Lundman, L. (1997). Round Window Membrane. Structure Function and Permeability: A Review. *Microsc. Res. Tech.* 36, 201–211. doi:10.1002/(sici)1097-0029(19970201)36:3<201:aid-jemt8>3.0.co;2-r

Groff, J. A., and Liberman, M. C. (2003). Modulation of Cochlear Afferent Response by the Lateral Olivocochlear System: Activation via Electrical Stimulation of the Inferior Colliculus. *J. Neurophysiol.* 90, 3178–3200. doi:10.1152/jn.00537.2003

Gupta, S., Amrutkar, D. V., Mataji, A., Salmasi, H., Hay-Schmidt, A., Sheykhzade, M., et al. (2010). Evidence for CGRP Re-uptake in Rat Dura Mater Encephali. *Br. J. Pharmacol.* 161, 1885–1898. doi:10.1111/j.1476-5381.2010.01012.x

Halsey, K., Skjönsberg, A., Ulfendahl, M., and Dolan, D. F. (2005). Efferent-mediated Adaptation of the DPOAE as a Predictor of Aminoglycoside Toxicity. *Hear. Res.* 201, 99–108. doi:10.1016/j.heares.2004.09.010

Herbison, A. E., and Spratt, D. P. (1995). Sexually Dimorphic Expression of Calcitonin Gene-Related Peptide (CGRP) mRNA in Rat Medial Preoptic Nucleus. *Mol. Brain Res.* 34, 143–148. doi:10.1016/0169-328x(95)00144-h

Hershey, J. C., Corcoran, H. A., Baskin, E. P., Salvatore, C. A., Mosser, S., Williams, T. M., et al. (2005). Investigation of the Species Selectivity of a Nonpeptide CGRP Receptor Antagonist Using a Novel Pharmacodynamic Assay. *Regul. Peptides* 127, 71–77. doi:10.1016/j.regpep.2004.10.010

Herzog, M., Scherer, E. Q., Albrecht, B., Rorabaugh, B., Scofield, M. A., and Wangemann, P. (2002). CGRP Receptors in the Gerbil Spiral Modiolar Artery Mediate a Sustained Vasodilation via a Transient cAMP-Mediated Ca2+-Decrease. *J. Membr. Biol.* 189, 225–236. doi:10.1007/s00232-002-1017-5

Hillerdal, M., and Andersson, S. E. (1991). The Effects of Calcitonin Gene-Related Peptide (CGRP) on Cochlear and Mucosal Blood Flow in the Albino Rabbit. *Hear. Res.* 52, 321–328. doi:10.1016/0378-5955(91)90022-2

Jansen-Olesen, I., Kaarill, L., and Edvinsson, L. (2001). Characterization of CGRP1 Receptors in the Guinea Pig Basilar Artery. *Eur. J. Pharmacol.* 414, 249–258. doi:10.1016/s0014-2999(01)00760-9

Ji, Y., Rizk, A., Voulalas, P., Aljohani, H., Akerman, S., Dussor, G., et al. (2019). Sex Differences in the Expression of Calcitonin Gene-Related Peptide Receptor Components in the Spinal Trigeminal Nucleus. *Neurobiol. Pain* 6, 100031. doi:10.1016/j.ynpai.2019.100031

Kiang, N. Y. S., Moxon, E. C., and Kahn, A. R. (1976). "The Relationship of Gross Potentials Recorded from the Cochlea to Single Unit Activity in the Auditory Nerve," in *Electrocochleography*. Editors R. J. Ruben, C. Elberling, and G. Solomon (Baltimore: University Park), 95–115.

Kitajiri, M., Yamashita, T., Tohyama, Y., Kumazawa, T., Takeda, N., Kawasaki, Y., et al. (1985). Localization of Calcitonin Gene-Related Peptide in the Organ of Corti of the Rat: An Immunohistochemical Study. *Brain Res.* 358, 394–397. doi:10.1016/0006-8993(85)90992-8

Köhli, P., Appelt, J., Otto, E., Jahn, D., Baranowsky, A., Bahn, A., et al. (2021). Effects of CGRP Receptor Antagonism on Glucose and Bone Metabolism in Mice with Diet-Induced Obesity. *Bone* 143, 115646. doi:10.1016/j.bone.2020.115646

Kong, W.-J., Ren, T., and Nuttall, A. L. (1996). Electrophysiological and Morphological Evaluation of the Acute Ototoxicity of Sodium Nitroprusside. *Hear. Res.* 99, 22–30. doi:10.1016/s0378-5955(96)00076-7

Kong, W.-J., Scholtz, A. W., Kammen-Jolly, K., Glückert, R., Hussl, B., von Cauvenberg, P. B., et al. (2002). Ultrastructural Evaluation of Calcitonin Gene-Related Peptide Immunoreactivity in the Human Cochlea and Vestibular Endorgans. *Eur. J. Neurosci.* 15, 487–497. doi:10.1046/j.0953-816x.2001.01880.x

Kujawa, S. G., and Liberman, M. C. (2001). Effects of Olivocochlear Feedback on Distortion Product Otoacoustic Emissions in Guinea Pig. *J. Assoc. Res. Otolaryngol.* 2, 268–278. doi:10.1007/s101620010047

Kuriyama, H., Shiosaka, S., Sekitani, M., Tohyama, Y., Kitajiri, M., Yamashita, T., et al. (1990). Electron Microscopic Observation of Calcitonin Gene-Related Peptide-like Immunoreactivity in the Organ of Corti of the Rat. *Brain Res.* 517, 76–80. doi:10.1016/0006-8993(90)91010-e

Lamm, K., and Arnold, W. (2000). The Effect of Blood Flow Promoting Drugs on Cochlear Blood Flow, Perilymphatic pO2 and Auditory Function in the Normal and Noise-Damaged Hypoxic and Ischemic Guinea Pig Inner Ear. *Hear. Res.* 141, 199–219. doi:10.1016/s0378-5955(00)00005-8

Laurikainen, E. A., Miller, J. M., Quirk, W. S., Kallinen, J., Ren, T., Nuttall, A. L., et al. (1993). Betahistine-induced Vascular Effects in the Rat Cochlea. *Am. J. Otol.* 14, 24–30.

Le Prell, C. G., Dolan, D. F., Schacht, J., Miller, J. M., Lomax, M. I., and Altschuler, R. A. (2003a). Pathways for Protection from Noise Induced Hearing Loss. *Noise Health* 5, 1–17.

Le Prell, C. G., Bledsoe, S. C., Jr., Bobbin, R. P., and Puel, J. L. (2001). "Neurotransmission in the Inner Ear: Functional and Molecular Analyses," in *Physiology of the Ear*. Editors A. F. Jahn and J. Santos-Sacchi. Second ed (New York: Singular Publishing), 575–611.

Le Prell, C. G., Dolan, D. F., Hughes, L. F., Altschuler, R. A., Shore, S. E., and Bledsoe, S. C., Jr. (2014a). Disruption of Lateral Olivocochlear Neurons with a Dopaminergic Neurotoxin Depresses Spontaneous Auditory Nerve Activity. *Neurosci. Lett.* 582, 54–58. doi:10.1016/j.neulet.2014.08.040

Le Prell, C. G., Halsey, K., Hughes, L. F., Dolan, D. F., and Bledsoe, S. C., Jr. (2005). Disruption of Lateral Olivocochlear Neurons via a Dopaminergic Neurotoxin Depresses Sound-Evoked Auditory Nerve Activity. *J. Assoc. Res. Otolaryngol.* 6, 48–62. doi:10.1007/s10162-004-5009-2

Le Prell, C. G., Hughes, L. F., and Bledsoe, S. C. (2014b). Dynorphin Release by the Lateral Olivocochlear Efferents May Inhibit Auditory Nerve Activity: A Cochlear Drug Delivery Study. *Neurosci. Lett.* 571, 17–22. doi:10.1016/j.neulet.2014.04.024

Le Prell, C. G., Kawamoto, K., Raphael, Y., and Dolan, D. F. (2006). Electromotile Hearing: Acoustic Tones Mask Psychophysical Response to High-Frequency Electrical Stimulation of Intact Guinea Pig Cochlea. *J. Acoust. Soc. Am.* 120, 3889–3900. doi:10.1121/1.2359238

Le Prell, C. G. (2007). Role for the Lateral Olivocochlear Neurons in Auditory Function. Focus on "Selective Removal of Lateral Olivocochlear Efferents Increases Vulnerability to Acute Acoustic Injury". *J. Neurophysiol.* 97, 963–965. doi:10.1152/jn.01223.2006

Le Prell, C. G., Shore, S. E., Hughes, L. F., and Bledsoe, S. C., Jr. (2003b). Disruption of Lateral Efferent Pathways: Functional Changes in Auditory Evoked Responses. *J. Assoc. Res. Otolaryngol.* 4, 276–290. doi:10.1007/s10162-002-3018-6

Le Prell, C. G., Yagi, M., Kawamoto, K., Beyer, L. A., Atkin, G., Raphael, Y., et al. (2004). Chronic Excitotoxicity in the Guinea Pig Cochlea Induces Temporary Functional Deficits without Disrupting Otoacoustic Emissions. *J. Acoust. Soc. Am.* 116, 1044–1056. doi:10.1121/1.1772395

Liberman, M. C. (1978). Auditory-nerve Response from Cats Raised in a Low-noise Chamber. *J. Acoust. Soc. Am.* 63, 442–455. doi:10.1121/1.381736

Liberman, M. C. (1990). Effects of Chronic Cochlear De-efferentation on Auditory-Nerve Response. *Hear. Res.* 49, 209–223. doi:10.1016/0378-5955(90)90105-x

Liberman, M. C., Puria, S., and Guinan, J. J., Jr. (1996). The Ipsilaterally Evoked Olivocochlear Reflex Causes Rapid Adaptation of the 2 F1–f2 Distortion Product Otoacoustic Emission. *J. Acoust. Soc. Am.* 99, 3572–3584. doi:10.1121/1.414956

Lu, S. M., Schweitzer, L., Cant, N. B., and Dawbarn, D. (1987). Immunoreactivity to Calcitonin Gene-Related Peptide in the Superior Olivary Complex and Cochlea of Cat and Rat. *Hear. Res.* 31, 137–146. doi:10.1016/0378-5955(87)90119-5

Lyon, M. J., and Payman, R. N. (2000). Comparison of the Vascular Innervation of the Rat Cochlea and Vestibular System. *Hear. Res.* 141, 189–198. doi:10.1016/s0378-5955(00)00004-6

Maison, S. F., Emeson, R. B., Adams, J. C., Luebke, A. E., and Liberman, M. C. (2003b). Loss of αCGRP Reduces Sound-Evoked Activity in the Cochlear Nerve. *J. Neurophysiol.* 90, 2941–2949. doi:10.1152/jn.00596.2003

Maison, S. F., and Liberman, M. C. (2000). Predicting Vulnerability to Acoustic Injury with a Noninvasive Assay of Olivocochlear Reflex Strength. *J. Neurosci.* 20, 4701–4707. doi:10.1523/JNEUROSCI.20-12-04701.2000

Maison, S. F., Liu, X. P., Vetter, D. E., Eatock, R. A., Nathanson, N. M., Wess, J., et al. (2010). Muscarinic Signaling in the Cochlea: Presynaptic and Postsynaptic Effects on Efferent Feedback and Afferent Excitability. *J. Neurosci.* 30, 6751–6762. doi:10.1523/JNEUROSCI.5080-09.2010

Maison, S. p. F., Adams, J. C., and Liberman, M. C. (2003a). Olivocochlear Innervation in the Mouse: Immunocytochemical Maps, Crossed versus Uncrossed Contributions, and Transmitter Colocalization. *J. Comp. Neurol.* 455, 406–416. doi:10.1002/cne.10490

May, B. J., Prosen, C. A., Weiss, D., and Vetter, D. (2002). Behavioral Investigation of Some Possible Effects of the Central Olivocochlear Pathways in Transgenic Mice. *Hear. Res.* 171, 142–157. doi:10.1016/s0378-5955(02)00495-1

Merchan-Perez, A., Gil-Loyzaga, P., and Eybalin, M. (1990). Immunocytochemical Detection of Calcitonin Gene-Related Peptide in the Postnatal Developing Rat Cochlea. *Int. J. Develop. Neurosci.* 8, 603–612. doi:10.1016/0736-5748(90)90052-4

Mikulec, A. A., Hartsock, J. J., and Salt, A. N. (2008). Permeability of the Round Window Membrane is Influenced by the Composition of Applied Drug Solutions and by Common Surgical Procedures. *Otol. Neurotol.* 29, 1020–1026. doi:10.1097/MAO.0b013e31818658ea

Miranda, L. P., Shi, L., Holder, J. R., Wright, M., Gegg, C. V., Johnson, E., et al. (2013). Peptide Antagonists of the Calcitonin Gene-Related Peptide (CGRP) Receptor with Improved Pharmacokinetics and Pharmacodynamics. *Biopolymers* 100, 422–430. doi:10.1002/bip.22270

Mohanty, D., and Lippmann, S. (2020). CGRP Inhibitors for Migraine. *Innov. Clin. Neurosci.* 17, 39–40.

Moore, J. K., Simmons, D. D., and Guan, Y.-L. (1999). The Human Olivocochlear System: Organization and Development. *Audiol. Neurotol.* 4, 311–325. doi:10.1159/000013855

Müller, M., and Robertson, D. (1991). Relationship between Tone Burst Discharge Pattern and Spontaneous Firing Rate of Auditory Nerve Fibres in the Guinea Pig. *Hear. Res.* 57, 63–70. doi:10.1016/0378-5955(91)90075-k

National Research Council (1996). *Guide for the Care and Use of Laboratory Animals*. Washington D.C.: National Academy Press.

Oestreicher, E., Arnold, W., Ehrenberger, K., and Felix, D. (1997). Dopamine Regulates the Glutamatergic Inner Hair Cell Activity in Guinea Pigs. *Hear. Res.* 107, 46–52. doi:10.1016/s0378-5955(97)00023-3

Ohno, K., Takeda, N., Tanaka-Tsuji, M., and Matsunaga, T. (1993). Calcitonin Gene-Related Peptide in the Efferent System of the Inner Ear: A Review. *Acta Otolaryngol.* 113, 16–20. doi:10.3109/00016489309126206

Ohyama, K., Salt, A. N., and Thalmann, R. (1988). Volume Flow Rate of Perilymph in the Guinea-pig Cochlea. *Hear. Res.* 35, 119–129. doi:10.1016/0378-5955(88)90111-6

Puel, J.-L. (1995). Chemical Synaptic Transmission in the Cochlea. *Prog. Neurobiol.* 47, 449–476. doi:10.1016/0301-0082(95)00028-3

Qiu, J.-H., Steyger, P. S., Trune, D. R., and Nuttall, A. L. (2001). Co-existence of Tyrosine Hydroxylase and Calcitonin Gene-Related Peptide in Cochlear Spiral Modiolar Artery of Guinea Pigs. *Hear. Res.* 155, 152–160. doi:10.1016/s0378-5955(01)00231-3

Quirk, W. S., Seidman, M. D., Laurikainen, E. A., Nuttall, A. L., and Miller, J. M. (1994). Influence of Calcitonin-Gene Related Peptide on Cochlear Blood Flow and Electrophysiology. *Am. J. Otol.* 15, 56–60.

Radziszewski, P., Soller, W., and Mattiasson, A. (2003). Calcitonin Gene-Related Peptide and Substance P Induce Pronounced Motor Effects in the Female Rat Urethra *In Vivo*. *Scand. J. Urol. Nephrol.* 37, 275–280. doi:10.1080/00365590310004761

Reijntjes, D. O. J., and Pyott, S. J. (2016). The Afferent Signaling Complex: Regulation of Type I Spiral Ganglion Neuron Responses in the Auditory Periphery. *Hear. Res.* 336, 1–16. doi:10.1016/j.heares.2016.03.011

Reinshagen, M., Flämig, G., Ernst, S., Geerling, I., Wong, H., Walsh, J. H., et al. (1998). Calcitonin Gene-Related Peptide Mediates the Protective Effect of Sensory Nerves in a Model of Colonic Injury. *J. Pharmacol. Exp. Ther.* 286, 657–661.

Reuss, S., Disque-Kaiser, U., De Liz, S., Ruffer, M., and Riemann, R. (1999). Immunfluorescence Study of Neuropeptides in Identified Neurons of the Rat Auditory Superior Olivary Complex. *Cel Tissue Res.* 297, 13–21. doi:10.1007/s004410051329

Rhode, W. S., and Smith, P. H. (1985). Characteristics of Tone-Pip Response Patterns in Relationship to Spontaneous Rate in Cat Auditory Nerve Fibers. *Hear. Res.* 18, 159–168. doi:10.1016/0378-5955(85)90008-5

Ruel, J., Nouvian, R., D'Aldin, C. G., Pujol, R., Eybalin, M., and Puel, J.-L. (2001). Dopamine Inhibition of Auditory Nerve Activity in the Adult Mammalian Cochlea. *Eur. J. Neurosci.* 14, 977–986. doi:10.1046/j.0953-816x.2001.01721.x

Russo, A. F., Kuburas, A., Kaiser, E. A., Raddant, A. C., and Recober, A. (2009). A Potential Preclinical Migraine Model: CGRP-Sensitized Mice. *Mol. Cel. Pharmacol.* 1, 264–270.

Sachs, M. B., and Abbas, P. J. (1974). Rate versus Level Functions for Auditory-nerve Fibers in Cats: Tone-burst Stimuli. *J. Acoust. Soc. Am.* 56, 1835–1847. doi:10.1121/1.1903521

Safieddine, S., and Eybalin, M. (1992). Triple Immunofluorescence Evidence for the Coexistence of Acetylcholine, Enkephalins and Calcitonin Gene-Related Peptide within Efferent (Olivocochlear) Neurons of Rats and Guinea-pigs. *Eur. J. Neurosci.* 4, 981–992. doi:10.1111/j.1460-9568.1992.tb00124.x

Safieddine, S., Prior, A. M. S., and Eybalin, M. (1997). Choline Acetyltransferase, Glutamate Decarboxylase, Tyrosine Hydroxylase, Calcitonin Gene-Related Peptide and Opioid Peptides Coexist in Lateral Efferent Neurons of Rat and Guinea-pig. *Eur. J. Neurosci.* 9, 356–367. doi:10.1111/j.1460-9568.1997.tb01405.x

Sahley, T. L., Anderson, D. J., and Chernicky, C. L. (2008). Bi-phasic Intensity-dependent Opioid-Mediated Neural Amplitude Changes in the Chinchilla Cochlea: Partial Blockade by an N-Methyl-D-Aspartate (NMDA)-receptor Antagonist. *Eur. J. Pharmacol.* 580, 100–115. doi:10.1016/j.ejphar.2007.10.038

Sahley, T. L., Anderson, D. J., Hammonds, M. D., Chandu, K., and Musiek, F. E. (2019). Evidence for a Dynorphin-Mediated Inner Ear Immune/inflammatory Response and Glutamate-Induced Neural Excitotoxicity: An Updated Analysis. *J. Neurophysiol.* 122, 1421–1460. doi:10.1152/jn.00595.2018

Sahley, T. L., Kalish, R. B., Musiek, F. E., and Hoffman, D. W. (1991). Effects of Opioid Be Drugs on Auditory Evoked Potentials Suggest a Role of Lateral Olivocochlear Dynorphins in Auditory Function. *Hear. Res.* 55, 133–142. doi:10.1016/0378-5955(91)90099-u

Sahley, T. L., and Nodar, R. H. (1994). Improvement in Auditory Function Following Pentazocine Suggests a Role for Dynorphins in Auditory Sensitivity. *Ear Hear.* 15, 422–431. doi:10.1097/00003446-199412000-00003

Sakamoto, K., Kuroki, T., Okuno, Y., Sekiya, H., Watanabe, A., Sagawa, T., et al. (2014). Activation of the TRPV1 Channel Attenuates N-Methyl-D-Aspartic Acid-Induced Neuronal Injury in the Rat Retina. *Eur. J. Pharmacol.* 733, 13–22. doi:10.1016/j.ejphar.2014.03.035

Sakamoto, K., Kuroki, T., Sagawa, T., Ito, H., Mori, A., Nakahara, T., et al. (2017). Opioid Receptor Activation is Involved in Neuroprotection Induced by TRPV1 Channel Activation against Excitotoxicity in the Rat Retina. *Eur. J. Pharmacol.* 812, 57–63. doi:10.1016/j.ejphar.2017.07.002

Scheibe, F., Haupt, H., and Baumgärtl, H. (1997). Effects of Experimental Cochlear Thrombosis on Oxygenation and Auditory Function of the Inner Ear. *Eur. Arch. Otorhinolaryngol.* 254, 91–94. doi:10.1007/BF01526187

Schrott-Fischer, A., Kammen-Jolly, K., Scholtz, A., Rask-Andersen, H., Glueckert, R., and Eybalin, M. (2007). Efferent Neurotransmitters in the Human Cochlea and Vestibule. *Acta Otolaryngol.* 127, 13–19. doi:10.1080/00016480600652123

Sewell, W. F., and Starr, P. A. (1991). Effects of Calcitonin Gene-Related Peptide and Efferent Nerve Stimulation on Afferent Transmission in the Lateral Line Organ. *J. Neurophysiol.* 65, 1158–1169. doi:10.1152/jn.1991.65.5.1158

Sharaf, K., Ihler, F., Bertlich, M., Reichel, C. A., Berghaus, A., and Canis, M. (2016). Tumor Necrosis Factor-Induced Decrease of Cochlear Blood Flow can be Reversed by Etanercept or JTE-013. *Otol. Neurotol.* 37, e203–e208. doi:10.1097/mao.0000000000001095

Simmons, D. D., Moulding, H. D., and Zee, D. (1996). Olivocochlear Innervation of Inner and Outer Hair Cells during Postnatal Maturation: An Immunocytochemical Study. *Develop. Brain Res.* 95, 213–226. doi:10.1016/0165-3806(96)00084-3

Simmons, D. D., Raji-Kubba, J., Popper, P., and Micevych, P. E. (1997). Developmentally Regulated Expression of Calcitonin Gene-Related Peptide in the Superior Olive. *J. Comp. Neurol.* 377, 207–216. doi:10.1002/(sici)1096-9861(19970113)377:2<207:aid-cne4>3.0.co;2-7

Simmons, D. D., and Raji-Kubba, J. (1993). Postnatal Calcitonin Gene-Related Peptide in the Superior Olivary Complex. *J. Chem. Neuroanat.* 6, 407–418. doi:10.1016/0891-0618(93)90015-v

Sliwinska-Kowalska, M., Parakkal, M., Schneider, M. E., and Fex, J. (1989). CGRP-like Immunoreactivity in the Guinea Pig Organ of Corti: A Light and Electron Microscopy Study. *Hear. Res.* 42, 83–95. doi:10.1016/0378-5955(89)90119-6

Sly, D. J., Hampson, A. J., Minter, R. L., Heffer, L. F., Li, J., Millard, R. E., et al. (2012). Brain-derived Neurotrophic Factor Modulates Auditory Function in the Hearing Cochlea. *J. Assoc. Res. Otolaryngol.* 13, 1–16. doi:10.1007/s10162-011-0297-9

Søndergaard, A. M., Overgaard, C. B., Mazur, A., Postnov, D. D., Matchkov, V. V., and Aalkjaer, C. (2019). Rat Mesenteric Small Artery Neurogenic Dilatation is Predominantly Mediated by β 1 -adrenoceptors *In Vivo*. *J. Physiol.* 597, 1819–1831. doi:10.1113/jp277368

Tabuchi, K., Ito, Z., Wada, T., Hara, A., and Kusakari, J. (1998). The Effect of Mannitol upon Cochlear Dysfunction Induced by Transient Local Anoxia. *Hear. Res.* 126, 28–36. doi:10.1016/s0378-5955(98)00142-7

Takeda, N., Doi, K., Mori, N., Yamazaki, H., Tohyama, M., and Matsunaga, T. (1987). Localization and Fine Structure of Calcitonin Gene-Related Peptide (CGRP)-like Immunoreactive Nerve Fibres in the Organ of Corti of Guinea Pigs by Immunohistochemistry. *Acta Otolaryngol.* 103, 567–571.

Takeda, N., Kitajiri, M., Girgis, S., Hillyard, C. J., MacIntyre, I., Emson, P. C., et al. (1986). The Presence of a Calcitonin Gene-Related Peptide in the Olivocochlear Bundle in Rat. *Exp. Brain Res.* 61, 575–578. doi:10.1007/BF00237583

Tohyama, Y., Kiyama, H., Kitajiri, M., Yamashita, T., Kumazawa, T., and Tohyama, M. (1989). Ontogeny of Calcitonin Gene-Related Peptide in the Organ of Cortl of the Rat. *Develop. Brain Res.* 45, 309–312. doi:10.1016/0165-3806(89)90050-3

Tohyama, Y., Senba, E., Yamashita, T., Kitajiri, M., Kuriyama, H., Kumazawa, T., et al. (1990). Coexistence of Calcitonin Gene-Related Peptide and Enkephalin in Single Neurons of the Lateral Superior Olivary Nucleus of the Guinea Pig that Project to the Cochlea as Lateral Olivocochlear System. *Brain Res.* 515, 312–314. doi:10.1016/0006-8993(90)90613-g

Valdemarsson, S., Edvinsson, L., Hedner, P., and Ekman, R. (1990). Hormonal Influence on Calcitonin Gene-Related Peptide in Man: Effects of Sex Difference and Contraceptive Pills. *Scand. J. Clin. Lab. Invest.* 50, 385–388. doi:10.3109/00365519009091595

Vetter, D. E., Adams, J. C., and Mugnaini, E. (1991). Chemically Distinct Rat Olivocochlear Neurons. *Synapse* 7, 21–43. doi:10.1002/syn.890070104

Vyas, P., Wu, J. S., Jimenez, A., Glowatzki, E., and Fuchs, P. A. (2019). Characterization of Transgenic Mouse Lines for Labeling Type I and Type II Afferent Neurons in the Cochlea. *Sci. Rep.* 9, 5549. doi:10.1038/s41598-019-41770-5

Walsh, E. J., McGee, J., McFadden, S. L., and Liberman, M. C. (1998). Long-term Effects of Sectioning the Olivocochlear Bundle in Neonatal Cats. *J. Neurosci.* 18, 3859–3869. doi:10.1523/JNEUROSCI.18-10-03859.1998

Winter, I. M., Robertson, D., and Yates, G. K. (1990). Diversity of Characteristic Frequency Rate-Intensity Functions in Guinea Pig Auditory Nerve Fibres. *Hear. Res.* 45, 191–202. doi:10.1016/0378-5955(90)90120-e

Wu, J. S., Vyas, P., Glowatzki, E., and Fuchs, P. A. (2018). Opposing Expression Gradients of Calcitonin-Related Polypeptide Alpha (Calca/Cgrp α) and Tyrosine Hydroxylase (Th) in Type II Afferent Neurons of the Mouse Cochlea. *J. Comp. Neurol.* 526, 425–438. doi:10.1002/cne.24341

Wu, J. S., Yi, E., Manca, M., Javaid, H., Lauer, A. M., and Glowatzki, E. (2020). Sound Exposure Dynamically Induces Dopamine Synthesis in Cholinergic LOC Efferents for Feedback to Auditory Nerve Fibers. *Elife* 9, e52419. doi:10.7554/eLife.52419

Yang Zheng, X., Henderson, D., McFadden, S. L., Ding, D. L., and Salvi, R. J. (1999). Auditory Nerve Fiber Responses Following Chronic Cochlear De-efferentation. *J. Comp. Neurol.* 406, 72–86. doi:10.1002/(sici)1096-9861(19990329)406:1<72:aid-cne5>3.3.co;2-1

Yates, G. K. (1991). Auditory-nerve Spontaneous Rates Vary Predictably with Threshold. *Hear. Res.* 57, 57–62. doi:10.1016/0378-5955(91)90074-j

Yin, H., Chao, L., and Chao, J. (2004). Adrenomedullin Protects against Myocardial Apoptosis after Ischemia/reperfusion through Activation of Akt-GSK Signaling. *Hypertension* 43, 109–116. doi:10.1161/01.hyp.0000103696.60047.55

Ylikoski, J., Pirvola, U., Häppölä, O., Panula, P., and Virtanen, I. (1989). Immunohistochemical Demonstration of Neuroactive Substances in the Inner Ear of Rat and Guinea Pig. *Acta Otolaryngol.* 107, 417–423. doi:10.3109/00016488909127533

Zhang, Y., Li, Y., Fu, X., Wang, P., Wang, Q., Meng, W., et al. (2021). The Detrimental and Beneficial Functions of Macrophages after Cochlear Injury. *Front. Cell Dev. Biol.* 9, 631904. doi:10.3389/fcell.2021.631904

Zheng, F., Nixdorf-Bergweiler, B. E., van Brederode, J., Alzheimer, C., and Messlinger, K. (2021). Excitatory Effects of Calcitonin Gene-Related Peptide (CGRP) on Superficial Sp5C Neurons in Mouse Medullary Slices. *Int. J. Mol. Sci.* 22, 3794. doi:10.3390/ijms22073794

Conflict of Interest: The authors declare that the research was conducted in the absence of any commercial or financial relationships that could be construed as a potential conflict of interest.

Publisher's Note: All claims expressed in this article are solely those of the authors and do not necessarily represent those of their affiliated organizations, or those of the publisher, the editors and the reviewers. Any product that may be evaluated in this article, or claim that may be made by its manufacturer, is not guaranteed or endorsed by the publisher.

frontiers in Cell and Developmental Biology

ORIGINAL RESEARCH
published: 09 December 2021
doi: 10.3389/fcell.2021.777836

Programmed Cell Death Recruits Macrophages Into the Developing Mouse Cochlea

Vikrant Borse[1], Tejbeer Kaur[2], Ashley Hinton[1], Kevin Ohlemiller[1] and Mark E. Warchol[1]**

[1]Department of Otolaryngology, Washington University School of Medicine, St. Louis, MO, United States, [2]Department of Biomedical Sciences, School of Medicine, Creighton University, Omaha, NE, United States

Programmed cell death (PCD) plays a critical role in the development and maturation of the cochlea. Significant remodeling occurs among cells of the greater epithelial ridge (GER) of Kölliker's organ, leading to tissue regression and formation of the inner sulcus. In mice, this event normally occurs between postnatal days 5–15 (P5-15) and is regulated by thyroid hormone (T3). During this developmental time period, the cochlea also contains a large population of macrophages. Macrophages are frequently involved in the phagocytic clearance of dead cells, both during development and after injury, but the role of macrophages in the developing cochlea is unknown. This study examined the link between developmental cell death in the GER and the recruitment of macrophages into this region. Cell death in the basal GER begins at P5 and enhanced numbers of macrophages were observed at P7. This pattern of macrophage recruitment was unchanged in mice that were genetically deficient for CX3CR1, the receptor for fractalkine (a known macrophage chemoattractant). We found that injection of T3 at P0 and P1 caused GER cell death to begin at P3, and this premature PCD was accompanied by earlier recruitment of macrophages. We further found that depletion of macrophages from the developing cochlea (using $CX3CR1^{DTR/+}$ mice and treatment with the CSF1R antagonist BLZ945) had no effect on the pattern of GER regression. Together, these findings suggest that macrophages are recruited into the GER region after initiation of developmental PCD, but that they are not essential for GER regression during cochlear remodeling.

Keywords: cochlea, development, GER, cell death, macrophage, thyroid hormone

OPEN ACCESS

Edited by:
Stefan Heller,
Stanford University, United States

Reviewed by:
Marta Roccio,
University Hospital Zürich, Switzerland
Jonathan E. Gale,
University College London, United Kingdom

****Correspondence:***
Vikrant Borse
borsevikrant@wustl.edu
Mark E. Warchol
mwarchol@wustl.edu

Specialty section:
This article was submitted to Molecular and Cellular Pathology, a section of the journal Frontiers in Cell and Developmental Biology

Received: *15 September 2021*
Accepted: *19 November 2021*
Published: *09 December 2021*

Citation:
Borse V, Kaur T, Hinton A, Ohlemiller K and Warchol ME (2021) Programmed Cell Death Recruits Macrophages Into the Developing Mouse Cochlea. Front. Cell Dev. Biol. 9:777836. doi: 10.3389/fcell.2021.777836

INTRODUCTION

The cochlea of the inner ear detects sound vibrations and transmits information to the auditory brainstem. Cochlear development is a complex process, and any defects in developmental patterning can lead to congenital hearing loss (Anniko 1983; Rueda et al., 1987; Kamilya et al., 2001; Korver et al., 2017). The developing cochlea also undergoes considerable cellular remodeling, in which certain cell populations die and are removed from surrounding tissues. In mice, such remodeling occurs during the first two postnatal weeks (Ruben 1967; Anniko 1983; Rueda et al., 1987; Sohmer and Freeman 1995; Kamilya et al., 2001; Dayaratne et al., 2014). Among the most critical remodeling events is the regression of a columnar epithelial structure known as the greater epithelial ridge (GER, also known as Kölliker's organ). This event occurs via programmed cell death (PCD) (Ruben 1967; Anniko 1983; Rueda et al., 1987; Kamilya et al., 2001; Dayaratne et al., 2014), and creates a large

cavity known as the inner spiral sulcus. This process is vital for the normal onset of hearing (Ruben 1967; Sohmer and Freeman 1995; Lukashkin et al., 2010; Dayaratne et al., 2014), and genetic deficits that prevent PCD result in profound hearing loss (Kuida et al.,1996; Morishita et al., 2001; Takahashi et al., 2001; Makishima et al., 2011). However, the signals that initiate PCD in the developing cochlea have not been completely identified.

Thyroid hormone signaling is critical for normal cochlear development (Kelley and Forrest 2001; Ng et al., 2013). Hypothyroidism and mutations in the thyroid hormone receptor β gene (THRB) have been linked to hearing loss (Kelley and Forrest 2001; Christ et al., 2004; Johnson et al., 2007; Mustapha et al., 2009; Sundaresan et al., 2016). Notably, thyroid hormone has been shown to initiate regression of the GER during cochlear development (Kelley and Forrest 2001; Peeters et al., 2015). Mutations in THRB lead to delayed GER remodeling (Kelley and Forrest 2001), while ectopic treatment with T3 (3,5-triiodo-L-thyronine) at P0 and P1 induces premature GER remodeling (Peeters et al., 2015).

Programmed cell death also requires the clearance of dying cells. In many developing tissues, the removal of cellular debris is mediated by macrophages, which recognize apoptotic cells *via* pattern recognition molecules and phagocytic receptors (Henson and Hume 2006; Erwig and Henson, 2008; Davies et al., 2013; Wynn et al., 2013; Varol et al., 2015; Gordon and Plüddemann 2018). Resident macrophages are present in the developing and mature cochlea (Hirose et al., 2005; Brown et al., 2017; Hirose et al., 2017; Warchol 2019), and deletion of macrophages results in hearing loss caused by excessive glial cells, abnormal myelin formation and edema in stria vascularis. Macrophage number transiently increases during cochlear development and declines as the cochlea matures (Brown et al., 2017; Dong et al., 2018), but the role of macrophages in cellular remodeling of the developing cochlea is not known. In this study, we examined the involvement of macrophages in the clearance of dying cells during GER remodeling. We found that macrophages were recruited into the GER after the initiation of cell death, and that those macrophages were engaged in the removal of cellular debris. In addition, we observed that early induction of PCD by ectopic injection of T3 hormone leads to earlier recruitment of macrophages in the GER region. Finally, we found that macrophage depletion did not affect GER regression in the developing mouse cochlea. Together, these findings suggest that developmental cell death leads to macrophage recruitment into the cochlea. Although such macrophages are actively involved in the clearance of cellular debris, they are not essential for GER regression.

MATERIALS AND METHODS

Animals: Studies used CX3CR1-GFP and CX3CR1-DTR mice (Diehl et al., 2013), of both sexes, on a C57BL/6 (B6) background. Samples were obtained at post-natal (P) day 1, P3, P5 P7, P10, P13, P21 and P30, in order to study the role of macrophages in cochlear development and function. Each experimental group consisted of 3-6 animals, taken from multiple litters. CX3CR1-GFP mice express enhanced green fluorescent protein (EGFP) under control of the endogenous *CX3CR1* promoter (Jung et al., 2000). We generated $CX3CR1^{GFP/+}$ mice by breeding CX3CR1-null ($CX3CR1^{GFP/GFP}$) mice with wild type C57BL/6 mice. Similarly, we generated $CX3CR1^{DTR/+}$ mice by breeding CX3CR1-null ($CX3CR1^{DTR/DTR}$) mice with wild type C57BL/6 mice. All mice were housed in the animal facilities at Washington University, School of Medicine, and were maintained on a 12-h/day-night light cycle with open access to food and water. All experimental protocols involving animals were approved by the Animal Studies Committee of the Washington University School of Medicine, in Saint Louis, MO.

Treatment: At P0 and P1, mouse pups were subcutaneously injected with 1.5 µg of T3 (catalog# T6397, Sigma) (10 µL) or saline (control), in order to induce premature apoptosis and GER remodeling (Peeters et al., 2015). Saline injected animals were used as controls. Temporal bones from these mice were collected between P3 to P30. Also, some mice received subcutaneous injections of Diphtheria toxin (DT, Sigma), or the colony stimulating factor receptor 1 (CSF1R) inhibitor BLZ945 (MW: 398.48, MedChem Express HY-12768/CS-3971), to eliminate macrophages (Diehl et al., 2013; Milinkeviciute et al., 2019). In these studies, a single dose of 5 ng/gm DT was injected at P0, P2, P4, P6, P8, P10 and P12 in CX3CR1-DTR mice. Other mice received a single dose of 200 mg/kg BLZ945 at P2, P4, P6, P8, P10 and P12. Control mice received either saline or DMSO. Mice were euthanized and temporal bones were collected between P3 to P13.

Genotyping: Genotyping of CX3CR1-GFP mice (GFP heterozygous and GFP homozygous) and CX3CR1-DTR mice (DTR heterozygous) was performed by Transnetyx (Cordova, Memphis, TN), following previously described methods (Jung et al., 2000; Diehl et al., 2013).

Histological Methods

Animals were euthanized either by quick decapitation or deep anesthesia (Fatal Plus, 50 mg/kg). Temporal bones were isolated and fixed overnight with 4% paraformaldehyde (in PBS) at 4°C. After fixation, cochleae were isolated and washed 3x for 5 min each in PBS, pH 7.4 at room temperature. All specimens, except those collected at P5, were then incubated for ~24 h in 10% EDTA in PBS, pH 7.4 at room temperature. Specimens were thoroughly washed 3x for 5 min each in PBS, pH 7.4 at room temperature and were then dissected into whole mount samples. Other samples were prepared as frozen mid-modiolar sections (30 µm thickness). Those cochleae were incubated in 10% EDTA in PBS, pH 7.4 at room temperature for 3–5 days and then washed 3x for 5 min each in PBS, pH 7.4 at room temperature. Cochlear whole mounts and mid-modiolar sections were immunolabel for GFP-expressing macrophages (rabbit anti-GFP antibody, catalog #A11122, Invitrogen, 1:500 or chicken anti-GFP antibody, catalog #1010, Aves, 1:500), neurons were labeled with mouse monoclonal anti-β-III tubulin (catalog #MMS-435P, Covance, 1:500), combined with mouse anti-Neurofilament (Catalog #2H3, Developmental Studies Hybridoma Bank, 1:100) antibodies, and apoptotic cells were labeled using rabbit anti-cleaved caspase-3 antibody

(catalog # 9,661, Cell signaling, 1:100). To avoid non-specific binding of the antibodies, samples were preincubated in a blocking solution consisting of 5% normal horse serum/0.2% Triton X-100 in PBS for 1 h at room temperature. Samples were then incubated overnight with primary antibodies prepared in PBS with 2% normal horse serum and 0.2% Triton X-100 at room temperature. Samples were washed 3x for 5 min each in PBS, pH 7.4 at room temperature and then labeled with secondary antibodies, conjugated with Alexa-488, Alexa-568 or 555, and Alexa 647, (Life Technologies, 1:500). Secondaries were prepared in PBS with 2% normal horse serum and 0.2% Triton X-100. Samples were incubated in secondaries for 2–3 h at room temperature. The secondary solution also contained DAPI, in order to counterstain cell nuclei (catalog #D9542, Sigma- Aldrich, 1 µg/ml). All samples were washed 3x for 5 min each in PBS, pH 7.4 at room temperature, mounted on glass slides in glycerol: PBS (9:1), and coverslipped.

Cellular imaging and analyses: Fluorescence images were obtained using an LSM 700 confocal microscope (Zeiss). For cochlear whole mounts and mid modiolar sections, Z-series images were obtained using the following objective lenses: ×5 (~40-micron z-step-size), 20x (1 or 2 -micron z-step-size), or 63x (0.5 or 1.0-micron z-step-size). Images were processed and analyzed using Volocity 3D image analysis software (version 6.3, PerkinElmer) and Fiji (ImageJ2.0) (National Institutes of Health) and Adobe illustrator CS5.1.

Auditory brainstem responses (*ABR*)*:* The hearing of 1-month old CX3CR1-GFP mice (T3-treated or saline controls) was assessed by quantifying thresholds for auditory brainstem responses (ABR). Prior studies have shown that $CX3CR1^{GFP/GFP}$ mice have normal ABR thresholds (Kaur et al., 2019). Mice were anesthetized using intraperitoneal injections of ketamine (100 mg/kg) and xylazine (20 mg/kg). Responses were recorded from subcutaneous electrodes placed at the vertex (active electrode), and behind the right ear (reference electrode). A ground electrode was placed on the back. ABR thresholds were measured in response to tone pips at 5.6, 8, 11.2, 16, 22.6, 32, 45.2, and 64 kHz, using 5 ms tone pips (including 0.5 ms $cosine^2$ rise/fall) at a repetition rate of 20 per second. The responses were amplified 100,00x, filtered (100 Hz–3 kHz), and averaged using BioSig software (System 3; Tucker-Davis Technologies). Stimuli were presented in 5 dB steps from 5 to 100 dB SPL, in decreasing order, to the right ear. At each level, up to 1,000 responses were averaged. The lowest sound level at which a recognizable and reproducible wave 1 and 2 complex was noted, and considered threshold. If hearing threshold was not present at 100 dB SPL (the typical maximum sound level in our system), the threshold value was assigned as 100 dB for graphing and statistical purposes.

Macrophage, pyknotic nuclei and hair cell counts: Quantification was performed from 20X images, using Fiji software (ImageJ2.0) (National Institutes of Health). For counts of macrophages, hair cells and pyknotic nuclei, 2-3 areas from the apical and basal GER regions were selected. The Cell Counter plug-in was used for all counts. Macrophages were identified by strong GFP and CD45 labeling. Pyknotic nuclei were identified by small size and intense DAPI nuclear labeling, and apoptosis was verified by immunolabeling for cleaved caspase-3. All macrophages, pyknotic nuclei and hair cells counts were obtained manually, within the designed area of complete z-stack using Fiji software.

Statistical analysis: All data analysis and statistical tests were carried out using GraphPad Prism version 6.0d. Data are presented as mean ± SD. Student's t-tests or analyses of variance (ANOVA), followed by post hoc tests, were applied as appropriate. Results were considered statistically significant when $p < 0.05$.

RESULTS

Recruitment of Macrophages Into the GER Region of the Developing Mouse Cochlea

The mouse cochlea undergoes considerable structural changes during the first two postnatal weeks (Ruben 1967; Anniko 1983; Rueda et al., 1987; Kamilya et al., 2001; Dayaratne et al., 2014). One critical event is the death of columnar epithelial cells of the GER, leading to the opening of the inner sulcus. This process progresses along the tonotopic gradient of the cochlea, starting at the base (high frequency region) and then moving towards the apex (low frequency region) (Ruben 1967; Anniko 1983; Rueda et al., 1987; Kamilya et al., 2001; Dayaratne et al., 2014). Numerous macrophages are also present in the developing cochlea (Dong et al., 2018), but the role of macrophages in cellular remodeling is unknown. To resolve this issue, we first characterized the patterns of programmed cell death and the corresponding recruitment of macrophages in the GER of developing cochlea, using $CX3CR1^{GFP/+}$ mice, which express GFP in macrophages, microglia, monocytes and related cells (Diehl et al., 2013; Kaur et al., 2015a). Specimens were fixed at various developmental timepoints and prepared as whole mounts or mid-modiolar frozen sections. Immunolabeling was used to enhance GFP fluorescence in macrophages, and to identify apoptotic cells (cleaved caspase-3), and neurons (TUJ1+NF). DAPI staining facilitated the identification of pyknotic nuclei (a hallmark of apoptosis). Increased numbers of dying cells with pyknotic nuclei and/or immunolabeled for activated caspase-3 were observed in the basal GER region between P5-10, with the number peaking at P7 (**Figures 1B–E′,G**). Over the next 2–3 days, the appearance of pyknotic nuclei progressed from the base toward the apex, and the number of pyknotic nuclei in the apical GER peaked at P10 (**Figures 1D,G**). Macrophages were also observed in the GER between P7-13. Large numbers of macrophages initially appeared in the basal GER and then spread toward the apex. The numbers of macrophages in the basal and apical GER regions peaked at P10 and P13, respectively (**Figures 1B–E′,H**). The spatial distribution of macrophages followed a similar base-to-apex pattern that was observed for developmental cell death, with a temporal delay of ~3 days (**Figure 1B'**). By P13, very few apoptotic cells were present within the GER region (**Figures 1E,E'**), but macrophage numbers in the GER remained elevated after cell death had terminated (**Figure 1H**). We also observed cleaved-caspase 3-labeled (i.e., apoptotic) cells being engulfed by macrophages

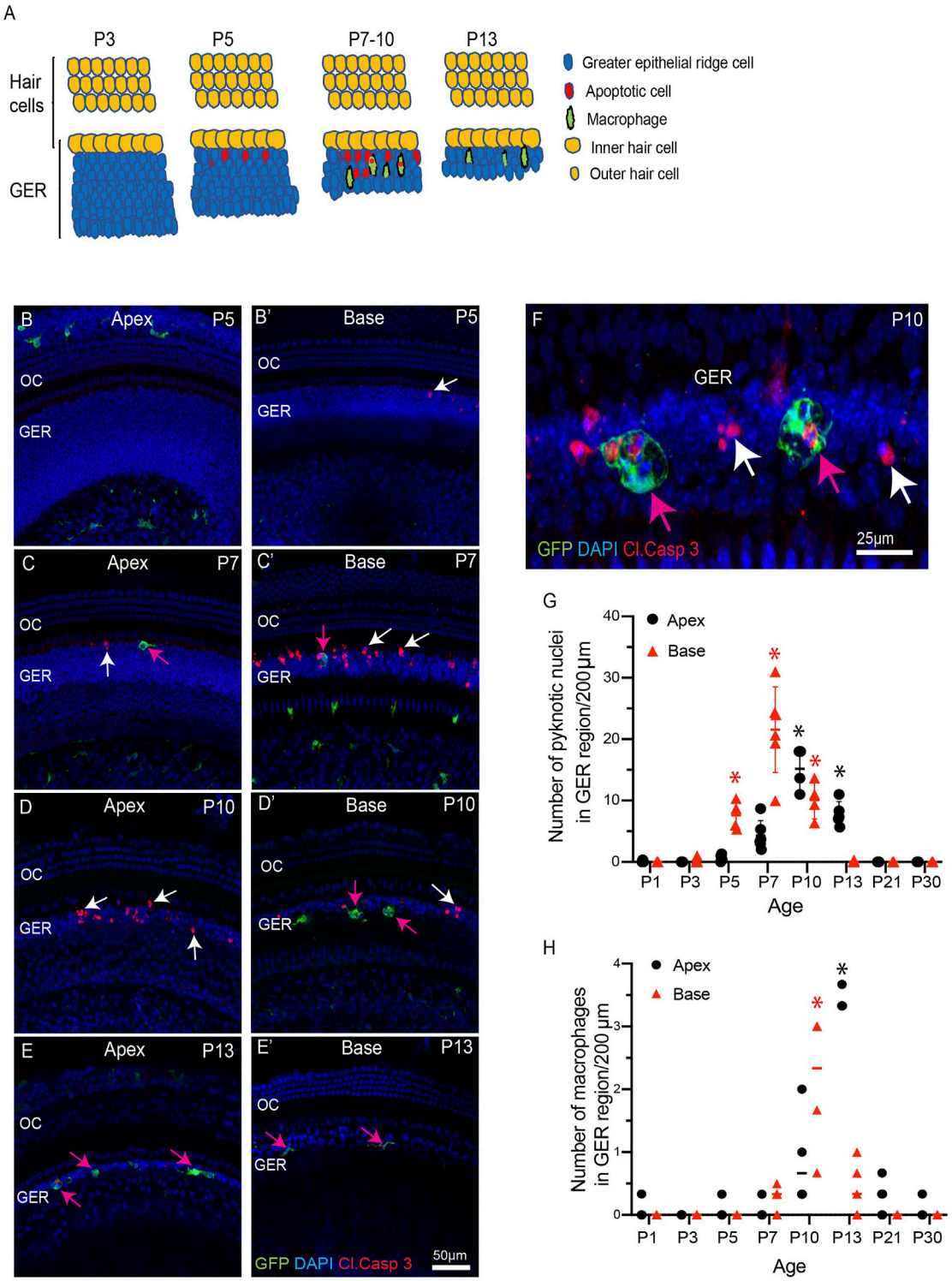

FIGURE 1 | Progression of apoptosis and macrophage recruitment in the developing cochlea of CX3CR1$^{GFP/+}$ mice. **(A)** Schematic representation of the patterns of apoptosis and macrophage recruitment in the GER region. **(B–E′)** Sensory epithelium of the developing cochlea. Apoptotic cells were first observed in the basal region at P5 [white arrow, **(B′)**] and the apex at P7 [white arrow, **(C)**]. Cell death continued at later time points [white arrows, **(C)**, **(D)**, **(C′)**, **(D′)**] and was accompanied by the recruitment of macrophages (magenta arrows). **(F)** A representative image of GFP-labeled macrophages engulfing pyknotic nuclei and activated caspase-3-labeled cells in the GER region at P10. **(G)** Number of pyknotic nuclei (a hallmark of apoptotic cells) in the GER region, as a function of developmental time. Cell death in the basal region peaked at P7, and in the apical region at P10. **(H)** Number of macrophages in the GER region, as a function of developmental time. The number of macrophages in both the basal and apical regions peaked at ~3 days after the time of maximal cell death. Images in **(B-E′)** were taken using a ×20 objective lens and the image in **(F)** was taken using a ×63 objective lens. Labels: Red-cleaved caspase 3, Green-GFP + macrophages, Blue-DAPI. White arrows: cleaved caspase-3-labeled (apoptotic) cells, magenta arrows: GFP + macrophages. Abbreviations: OC: organ of Corti, GER: Greater Epithelial Ridge, *p: $p < 0.05$, relative to P1. (N = 3–6).

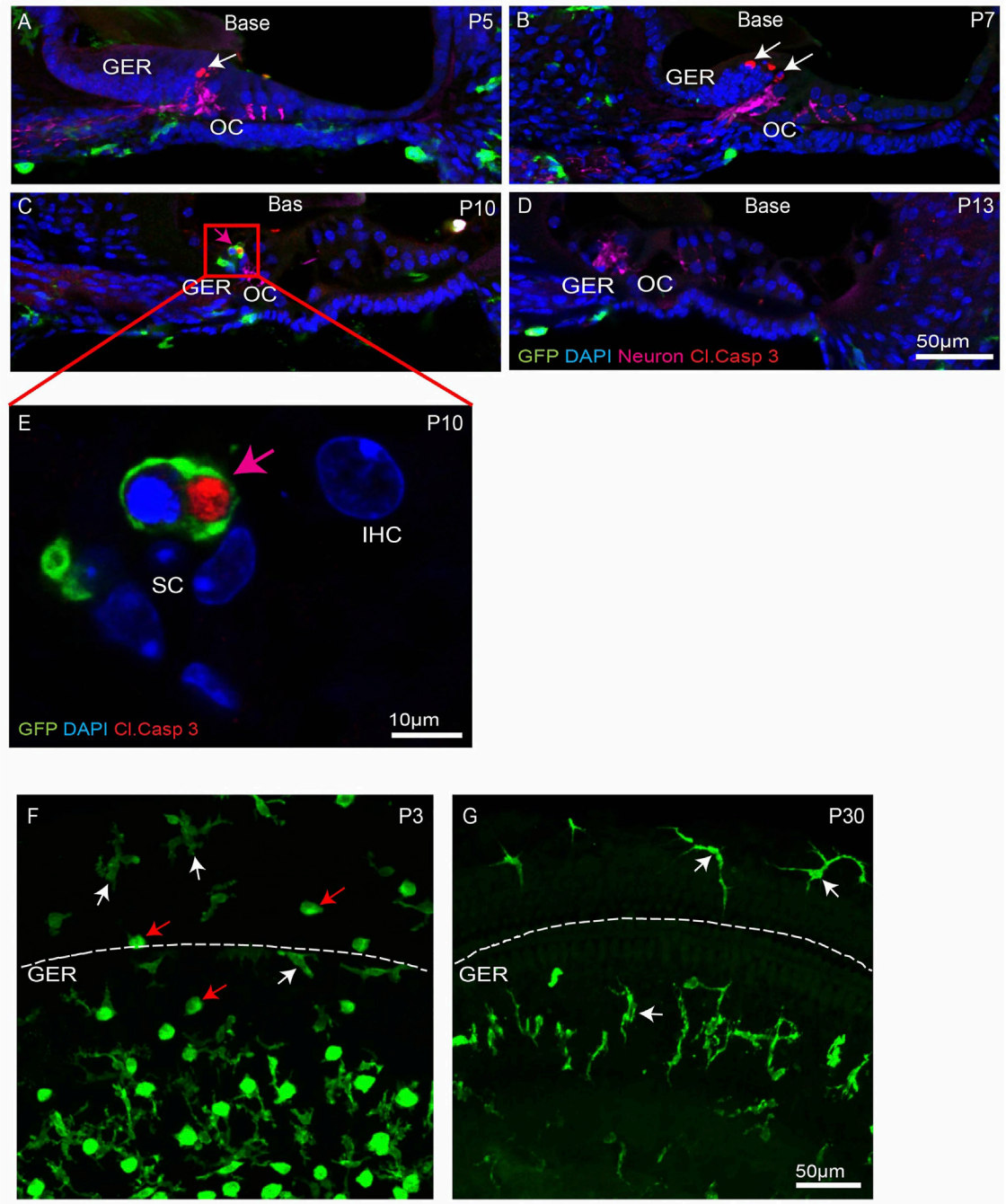

FIGURE 2 | Progression of apoptosis and macrophage infiltration in the basal region of the developing cochlea. **(A–D)** Mid-modiolar sections of the developing cochlea. Apoptotic cells (white arrows, cleaved caspase-3, red) were observed at P5-10. Such cells were often engulfed by macrophages (magenta arrow, GFP, green) **(E)** High magnification image taken from organ of Corti (red box shown in C) showing GFP-labeled macrophage engulfing pyknotic nuclei at P10. **(F–G)** Presence of ameboid (red arrow) and ramified (white arrow) macrophages in cochlear whole mounts. Note: GER region is present just below the dotted white line. Images in **(A–D)**, **(F–G)** were taken using a ×20 objective lens and the image in **(E)** was taken using a ×63 objective lens. Labels: Red-cleaved caspase- 3, Green-GFP + macrophages, Blue-DAPI. Abbreviations: OC: organ of Corti, GER: Greater Epithelial Ridge, IHC: Inner Hair Cell, SC: Supporting Cell (N = 3–6).

(**Figure 1D**). Similar patterns of cell death and macrophage recruitment were observed in mid-modiolar sections of the developing cochlea (**Figures 2A–E**). Macrophages in the neonatal cochlea possessed both ameboid and ramified morphologies, while those in the mature cochlea were predominantly ramified (**Figures 2F,G**). The neonatal cochlea also contained larger numbers of macrophages than were present in mature cochleae. Taken together, these observations indicate

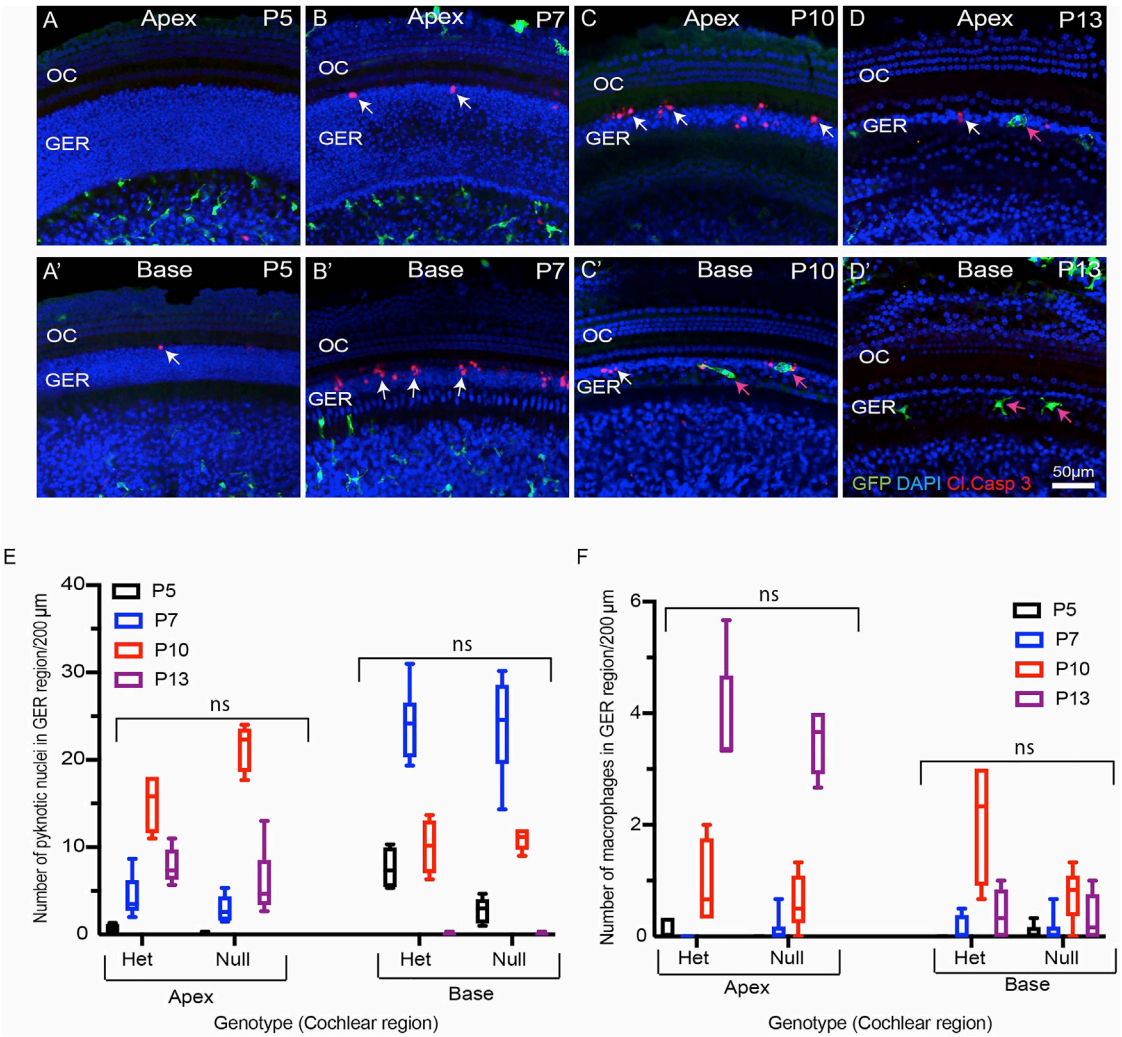

FIGURE 3 | Progression of developmental apoptosis and macrophage recruitment is not affected by genetic deletion of CX3CR1. **(A–D′)** Sensory epithelium of the developing cochlea of CX3CR1-null mice. The patterns of cell death (white arrows, cleaved caspase-3) and macrophage recruitment (magenta arrows, GFP) are similar to those observed in CX3CR1$^{GFP/+}$ mice (e.g., **Figure 1**). **(E)** Total number of pyknotic nuclei in the GER region of CX3CR1-null mice vs CX3CR1$^{GFP/+}$ mice. **(F)** Number of macrophages in the GER region of the developing cochlea of CX3CR1-null mice vs. CX3CR1$^{GFP/+}$ mice. Images in **(A–D)**, **(F–G)** were taken using a ×20 objective lens. Labels **(A–D′)** Red-cleaved caspase 3, Green-GFP + macrophages, Blue-DAPI. White arrow-cleaved caspase-3-labeled cells, and magenta arrows-GFP + macrophages. Abbreviations: OC: organ of Corti, GER: Greater Epithelial Ridge, ns: not significant. (N = 3–6).

that macrophages are recruited into the cochlea in response to developmental cell death and are actively involved in clearing dying cells from the GER region.

Fractalkine Signaling Is Not Required for Macrophage Recruitment Into the Developing Cochlea

Apoptotic cells secrete a number of signaling molecules that are chemoattractants for phagocytes (Diehl et al., 2013; Sokolowski et al., 2014; Hirose et al., 2017; Park and Kim 2017). Examples of such 'find-me' signals include lysophosphatidylcholine (LPC), sphingosine-1-phosphate (S1P), nucleotides (ATP and UTP) and the CX_3C motif chemokine ligand 1 (CX3CL1, also called as fractalkine) (Park and Kim 2017). CX3CL1 is the sole ligand for the CX3CR1 receptor, which is expressed by macrophages, microglia, monocytes and related cells. One function of fractalkine signaling is to meditate chemoattraction between dying cells and macrophages (Sokolowski et al., 2014; Park and Kim 2017). To investigate the role of fractalkine signaling in macrophage recruitment and GER apoptosis, we compared macrophage numbers and cell death in the developing cochleae of CX3CR1$^{GFP/+}$ mice (which possess one allele of *CX3CR1* and retain sensitivity to fractalkine) and CX3CR1$^{GFP/GFP}$ mice (in which both copies of *CX3CR1* had been replaced with the gene for GFP). Cochleae were collected from mice of both genotypes at P5, P7, P10 and P13 and processed as whole mounts. Samples were immunolabeled for GFP (to enhance the fluorescent signal in

macrophages), cleaved caspase-3 (to identify apoptotic cells), and stained with DAPI. These specimens displayed similar patterns of cell death and macrophage recruitment to those described above (**Figure 3**). Apoptotic cells were first detected in the basal region of the GER at P5 (**Figure 3A'**), and progressed towards the apex between P7-P10. By P13, few apoptotic cells were detected in the apical region and no apoptotic cells were found in the basal GER (**Figures 3A–D′,E**). Macrophages were first apparent in the basal GER at P7 and their numbers moved apically at later ages (**Figure 3F**). Macrophages remained present at P13, after cell death in the basal GER region had ended. The spatial and temporal patterns of macrophage recruitment were similar in both $CX3CR1^{GFP/+}$ and $CX3CR1^{GFP/GFP}$ (**Figure 1** and **Figure 3**), and there was no statistically significant difference between the number of recruited macrophages and pyknotic nuclei in the GER region of $CX3CR1^{GFP/+}$ vs. $CX3CR1^{GFP/GFP}$ mice (**Figures 3E,F**). These results indicate that fractalkine signaling is not essential for apoptosis or for recruitment of macrophages in the developing GER.

Thyroid Hormone (T3) Promotes Premature Cell Death and Early Recruitment of Macrophages

Thyroid hormone plays an important role in cochlear development and in the onset of hearing function (Kelley and Forrest 2001; Ng et al., 2013). Both hypothyroidism and mutation of the thyroid hormone receptor β (*THRB*) gene delay the onset of GER remodeling and result in subsequent hearing loss (Kelley and Forrest 2001; Christ et al., 2004; Johnson et al., 2007; Mustapha et al., 2009; Sundaresan et al., 2016). It has also been shown that treating early neonatal mice with T3 hormone induces premature GER remodeling and accompanying hearing loss (Peeters et al., 2015). We investigated whether treatment with thyroid hormone (T3) also leads to earlier macrophage recruitment. Early apoptosis was induced in $CX3CR1^{GFP/+}$ mice by injecting T3 at P0 and P1 (1.5 μg/pup, s. c.). We collected cochleae from both T3-treated and saline-injected (control) mice at various developmental time points. Whole mount specimens were labeled with anti-GFP (to enhance GFP signal in macrophages, cleaved caspase-3 (apoptotic marker), and DAPI. Both T3-and saline-treated cochleae showed a base-to-apex pattern of GER remodeling. However, treatment with T3 resulted in a significant increase in cell death at P3, which was followed by early recruitment of macrophages into the GER region at P5 (**Figure 4A**). In contrast, cell death in saline treated samples began at P5 and was followed by recruitment of macrophages at P7 (**Figures 4A–E**). Similarly, cell death in T3-treated cochleae terminated earlier than in control specimens (**Figures 4A–E**). We also quantified hearing function in both T3-and saline-treated animals, using ABRs. Consistent with previous studies (Peeters et al., 2015), we observed significantly elevated hearing thresholds in the T3-treated animals, when compared with saline-treated animals (**Figure 4F**). Together, these data suggest that systemic injection of T3 hormone at P0 and P1 promotes premature apoptosis in the GER, which is followed by early recruitment of macrophages. This outcome is consistent with a positive correlation between developmental cell death and macrophage recruitment.

Deletion of Macrophages Does Not Affect GER Remodeling

We investigated whether deletion of macrophages delays or impairs GER remodeling during cochlear development. We treated $CX3CR1^{DTR/+}$ mice and wild type control mice with diphtheria toxin (Diehl et al., 2013) at P0, P2, P4, P6, P8, P10 and P12. Multiple doses of DT were delivered to prevent macrophage repopulation during the experimental period. Cochleae were fixed at P5, P7, P10 and P13 and processed as whole mounts (**Figure 6A**). Samples were immunolabeled for CD45 (to identify macrophages) and cleaved caspase-3 (to identify apoptotic cells). Cell nuclei were also stained with DAPI. As depicted in **Figures 5B–D′**, DT treatment led to nearly-complete deletion of macrophages from the developing cochlea of $CX3CR1^{DTR/+}$ mice. Macrophage infiltration in the GER region of control animals was normal, but no macrophages were observed in the GER region of $CX3CR1^{DTR/+}$ mice (**Figures 5E–L′**). However, we observed normal patterns of apoptosis and GER regression in the developing cochlea of the $CX3CR1^{DTR/+}$ and control mice (**Figures 5E–L'**). Except in the apical region of P13 cochleae, we observed no significant increase in number of apoptotic cells in $CX3CR1^{DTR/+}$ mice, in comparison with controls. These data suggest that depletion of macrophages may cause a slight delay in the clearance of cellular debris in the apex, but does not otherwise affect GER regression (**Figures 5M,N**). Interestingly, we also noted that the DT treatment leads to loss of OHCs (**Figures 6A,B**). We observed missing OHC nuclei and labeling for cleaved caspase-3 in both $CX3CR1^{DTR/+}$ and WT control mice that were treated with DT at P10. No missing nuclei or apoptotic OHCs were observed in mice that did not receive DT.

In addition to the $CX3CR1^{DTR/+}$ mouse model, we also used a pharmacological approach to eliminate macrophages from the developing cochlea. $CX3CR1^{GFP/+}$ mice were given s. c. injections of the CSF1R antagonist BLZ945 (Milinkeviciute et al., 2019) at P2, P4, P6, P8, P10 and P12. (Multiple doses of BLZ945 were delivered, in order to avoid macrophage repopulation.) Cochleae were fixed at P5, P7, P10 and P13, and processed as whole mounts (**Figure 7A**). Treatment with BLZ945 eliminated nearly all macrophages from the developing cochlea (**Figures 7B–D′**), including the GER region (**Figures 7E–L'**). Notably, we observed normal patterns of apoptosis and GER regression in the developing cochleae of both the BLZ945-treated and control animals (**Figure 7M**). Macrophage depletion led to no significant difference in the numbers of pyknotic nuclei in the GER, when compared to controls (**Figures 7M,N**). Collectively, these findings suggest that macrophage depletion has no substantial effect on GER remodeling during development.

DISCUSSION

This study was undertaken to examine the role of macrophages in cochlear development. We found that the spatial and temporal

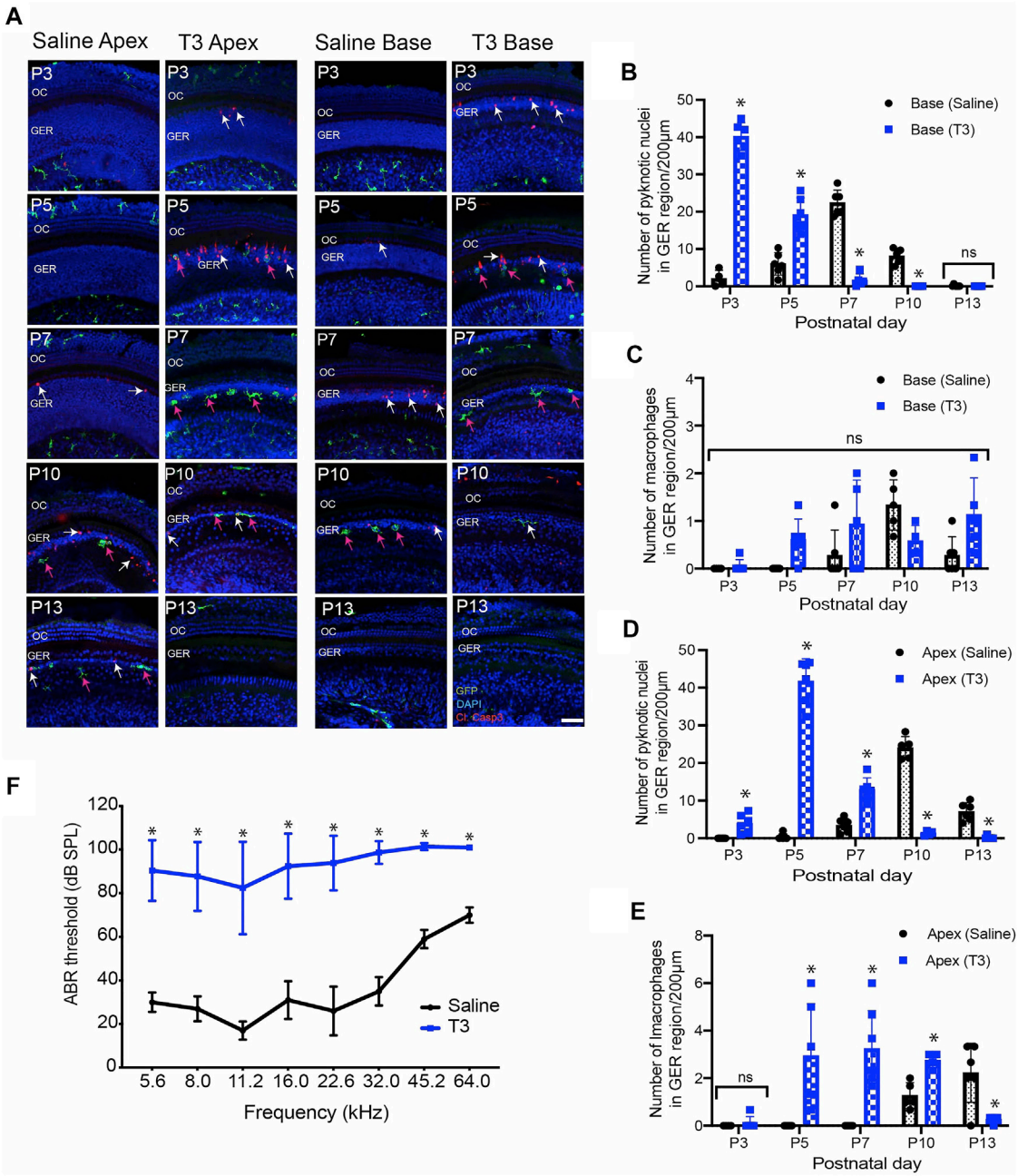

FIGURE 4 | Thyroid hormone (T3) induces early apoptosis and macrophage infiltration in the GER region of the developing cochlea. **(A)** Sensory epithelia of developing cochleae in saline-treated (control) and T3-treated CX3CR1$^{GFP/+}$ mice. Note that dying cells (white arrows) and macrophages (magenta arrows) are present ~2 days earlier in mice that received T3. **(B–D)** Number of pyknotic nuclei in the GER region of the developing cochlea of T3 treated and control (saline) mice. **(C–E)** Number of macrophages in the GER region of the developing cochlea of T3-treated and control mice. **(F)** ABR thresholds in T3-treated and saline treated control adult mice. ABR's were assessed at P30. Treatment with T3 at P0-1 led to a ~60 dB elevation in ABR thresholds across the entire frequency range. Images in **(A)** were taken using ×20 objective lens. Labels: Red-cleaved caspase-3, Green-GFP + macrophages, Blue-DAPI. Abbreviations: OC: organ of Corti, GER: Greater Epithelial Ridge, *p: $p < 0.05$, relative to saline treated, ns-not significant. (N = 3–6).

patterns of macrophage recruitment into the GER region of the developing cochlea is correlated with the pattern of programmed cell death in that region, i.e. starting from high frequency basal region and then moving towards low frequency apical region. We first observed apoptosis and macrophage recruitment in the GER region at P5 and P7, respectively (**Figure 1**). In previous studies of cochlear development, apoptosis was first reported to occur at P7 (Kamiya et al., 2001; Peeters et al., 2015). This difference in timing may be due to differences in technique and mouse strain. We also observed macrophages engulfing apoptotic cells and pyknotic

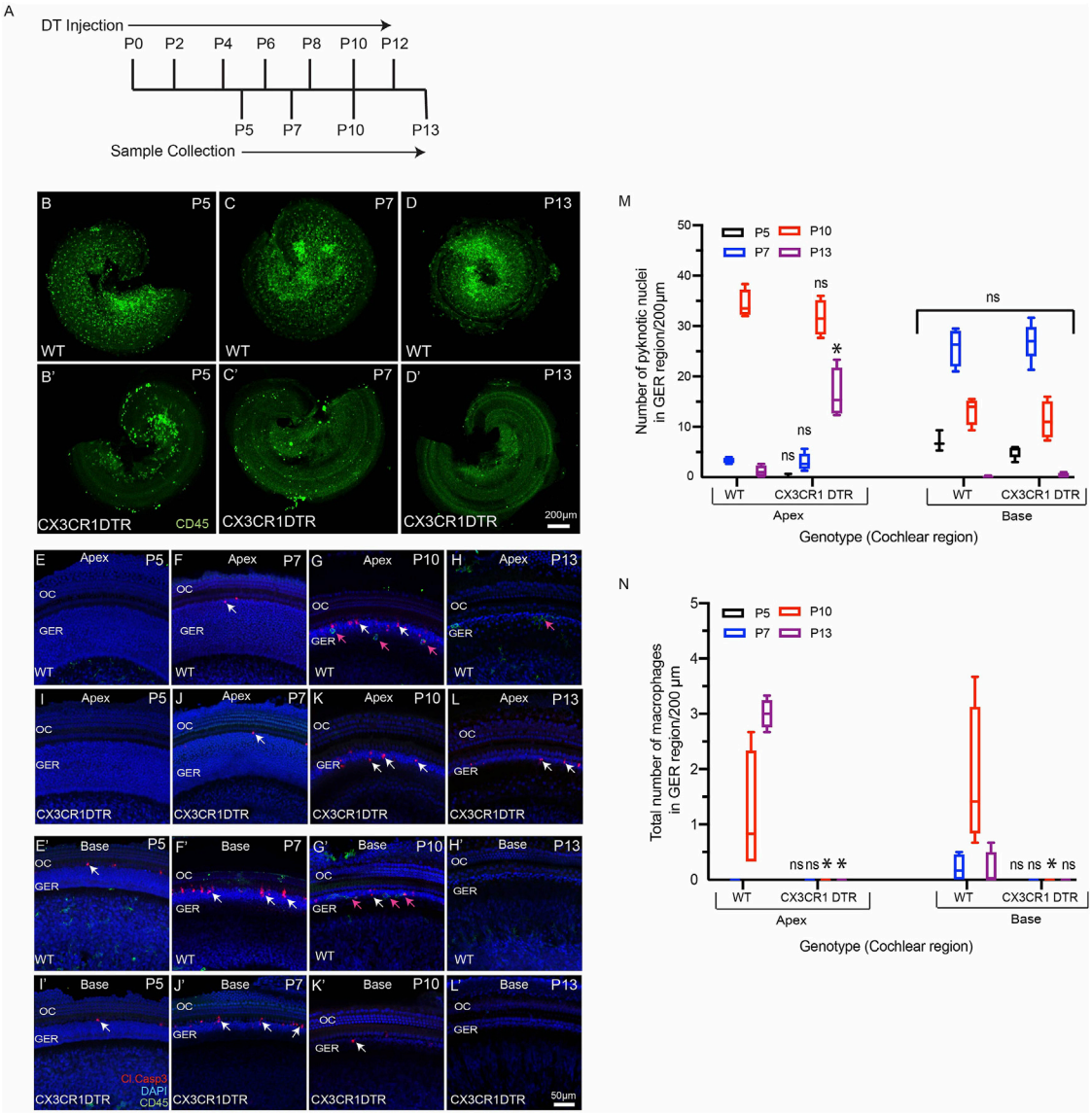

FIGURE 5 | Depletion of macrophages in the cochlea of neonatal CX3CR-DTR mice. **(A)** Treatment and sample collection timeline. **(B–D′)** Cochlear whole mounts showing depletion of macrophages (Green: CD45) following DT treatment. **(E–L′)** Sensory epithelium of developing cochleae showing occurrence of cell death (red, cleaved caspase-3, white arrows) in normal and DT-treated cochleae. Although DT treatment eliminated macrophages in the cochleae of CX3CR-DTR mice, normal patterns of cell death were observed. **(M)** Number of pyknotic nuclei (blue: DAPI) in the GER region of developing cochleae. **(N)** Quantification of macrophages in the GER region of developing cochleae. Treatment with DT led to a large reduction in macrophage numbers. Images in **(B–D′)** were taken using ×5 objective lens and images in **(E–L′)** were taken using ×20 objective lens. Abbreviations: OC: Organ of Corti, GER: Greater Epithelial Ridge (*p: *p* value <0.05, relative to WT, ns: not significant. (N = 3–6).

nuclei in the GER region and some macrophages that remained in the GER region after the wave of apoptosis had terminated. Our findings demonstrate that macrophages are recruited into the GER region about 2 days after apoptosis has begun. During development, the resident macrophages of the cochlea originate from precursors in the yolk sac and fetal liver, and reach the inner ear *via* systemic circulation (Kishimoto et al., 2019). The specific source of macrophages recruited into the GER region during cochlear remodeling is not known, but they may originate from circulation, or from other regions of the developing ear and/or surrounding mesenchymal tissue. We also observed two morphologically-distinct populations of macrophages in the developing cochlea (ameboid and ramified), but only ramified macrophages were present in the mature cochlea. The significance of these morphological types is not clear. Microglia (the resident macrophages of CNS) also possess similar morphologies. Microglia with a ramified morphology are thought to be in a 'resting' or 'quiescent' state, while ameboid microglia are associated with tissue injury (Savage et al., 2019). However, the possible differential roles of

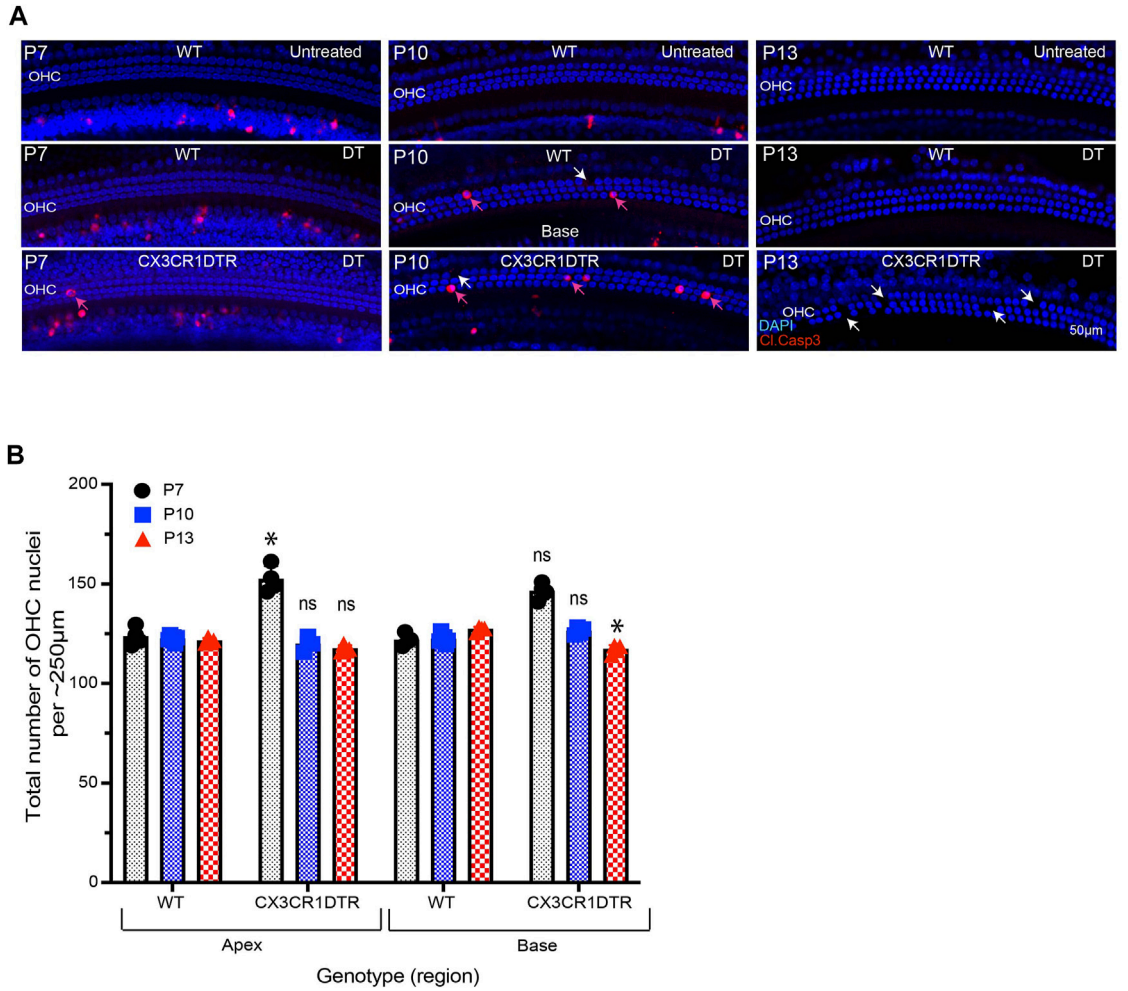

FIGURE 6 | Treatment with DT leads to loss of OHCs from the developing cochlea. **(A)** Apoptotic cells (red, cleaved caspase-3) in the base of the sensory epithelium of the developing cochlea. Treatment with DT caused the death of a small number of OHCs, which was evident at P7-13. **(B)** Total number of OHCs in the cochlea of CX3CR-DTR and control mice. Images in A were taken using a ×20 objective lens. Abbreviations: OHC: Outer hair cell, DT: Diphtheria toxin. *p: $p < 0.05$, relative to WT), ns: not significant. (N = 3–6).

ameboid vs. ramified macrophages during cochlear development are not understood.

Apoptotic cells release signaling molecules, known as 'find-me' signals, to promote the chemotaxis of macrophages to sites of cell death (Park and Kim 2017). A number of such signaling molecules have been identified. Fractalkine (CX3CL1) is a chemokine that can recruit macrophages to dying cells by activating the CX3CR1 receptor on macrophages (Sokolowski et al., 2014; Park and Kim 2017). Previously, our lab has shown that disruption of fractalkine (CX3CL1/CX3CR1) signaling leads to reduced macrophage recruitment into the sensory region and spiral ganglion of the cochlea after selective hair cell ablation (Kaur et al., 2015a). However, it was not known whether fractalkine also influences macrophage behavior during cochlear development. We investigated the role of fractalkine signaling by quantifying macrophage recruitment into the developing cochleae of CX3CR1-null ($CX3CR1^{GFP/GFP}$) mice. We observed similar patterns of apoptosis and macrophage recruitment in both $CX3CR1^{GFP/GFP}$ and $CX3CR1^{GFP/+}$ (control) mice (**Figure 1** and **Figure 3**), suggesting that fractalkine signaling is not required for normal macrophage recruitment into the developing cochlea. This finding suggests that other 'find-me' signals, such as LPC, S1P and/or nucleotides (ATP and UTP) might recruit macrophages into the neonatal cochlea. It is notable that spontaneous release of ATP occurs during cochlear development (Dayaratne et al., 2014; Wang et al., 2015; Park and Kim 2017), and this may be one signal that recruits macrophages into the GER.

In order to determine the relationship between GER cell death and macrophage recruitment, we studied whether early induction of apoptosis by T3 hormone affected the recruitment of macrophages into the GER. Similar to Peeters et al. (2015), we observed robust early apoptosis in the GER region of T3 treated animals. In addition, we noted that induction of premature apoptosis by T3 injection led to early recruitment of macrophages. Treatment with T3 caused cell death in the GER

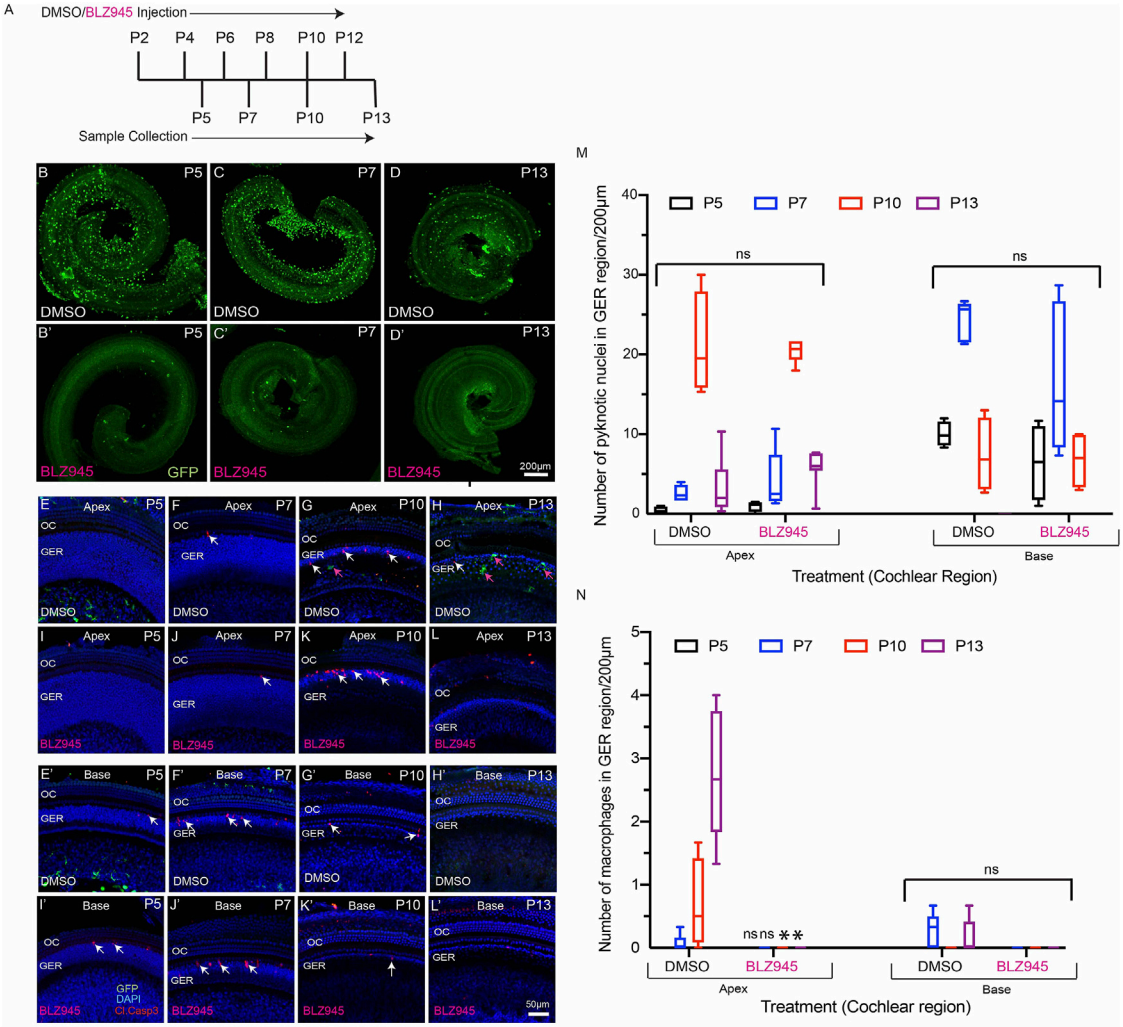

FIGURE 7 | BLZ945 treatment eliminates macrophages in the developing cochlea. **(A)** Treatment and sample collection timeline. **(B–D′)** Cochlear whole mounts showing depletion of macrophages following treatment with the CSF1R antagonist BLZ945 (Green-GFP + macrophages). **(E–L′)** Sensory epithelium of the developing cochlea showing apoptotic cells (red-cleaved caspase-3) and macrophages (green-GFP). Normal patterns of dying cells (white arrows) were observed in BLZ945-treated cochleae. **(M)** Number of macrophages in the GER region of the developing cochlea. Note that BLZ945 sharply reduced the number of macrophages in the GER. **(N)** Number of pyknotic nuclei in the GER region of the developing cochlea. Images in B-**(D′)** were taken using a ×5 objective lens and images in **(E-L')** were taken using ×20 objective lens. Abbreviations: OC: Organ of Corti, GER: Greater Epithelial Ridge, P: Postnatal Day. (*p: $p < 0.05$, relative to controls (DMSO), ns: not significant. (N = 3–6).

to begin approximately 4–5 days earlier than in normal cochleae and, in accordance with earlier studies, led to profound hearing loss (Peeters et al., 2015). We further found that T3 treatment led to correspondingly earlier macrophage recruitment into the GER, but that the delay between the onset of cell death and the appearance of macrophages was ~2 days in both normal and T3-treated cochleae. These observations suggest a relationship between cell death and macrophage recruitment, whereby dying cells release a chemoattractant that causes macrophages to migrate into the GER within ~2 days. We acknowledge, however, that the present data do not prove that these two events are causally related.

A prior study reported that short-term depletion of macrophages during cochlear development leads to hearing impairment, which was attributed to the presence of excessive glial cells, abnormal myelin formation, and defects in the stria vascularis (Brown et al., 2017). The present study employed two methods for depletion of macrophages: treating CX3CR1$^{DTR/+}$ mice with DT (Diehl et al., 2013), and treating CX3CR1$^{GFP/+}$ mice with the CSF1R antagonist BLZ945 (Milinkeviciute et al., 2019). Similar to earlier studies, we observed that multiple doses of DT and BLZ945 resulted in sustained near-complete depletion of macrophages from the developing cochlea (Diehl et al., 2013; Milinkeviciute et al., 2019). We further found that eliminating macrophages did not disrupt the normal pattern of apoptosis in the GER region of the developing cochlea. These results suggest that the cells in the GER region may engage in self-clearance by autophagy and/or by phagocytosis (Monzack

et al., 2015; Hou et al., 2019). Similarly, in the mature ear, both macrophages and supporting cells have been shown to contribute to the phagocytic clearance of dead hair cells (Kaur et al., 2015b; Monzack et al., 2015). Recruited macrophages may assist GER cells in rapid clearance of dead cells, but they do not appear to be essential for GER regression during normal cochlear development.

In conclusion, the results of this study demonstrate that programmed cell death recruits macrophages in the GER of the developing cochlea and that macrophages engage in the phagocytic clearance of dead cells. However, elimination of macrophages does not affect the patterns of cell death and remodeling in the GER. Thus, although the developing cochlea contains a higher density of macrophages than are present in the mature cochlea, macrophages may not play an essential role in the development of the organ of Corti.

DATA AVAILABILITY STATEMENT

The original contributions presented in the study are included in the article/Supplementary Material, further inquiries can be directed to the corresponding authors.

ETHICS STATEMENT

All experimental protocols involving animals were reviewed and approved by the Animal Studies Committee of the Washington University School of Medicine, in Saint Louis, MO.

AUTHOR CONTRIBUTIONS

VB and MW wrote the main manuscript text, prepared figures, designed and performed experiments, TK, AH, and KO designed and performed experiments.

FUNDING

Supported by grant R01DC015790 from the NIH (MW).

ACKNOWLEDGMENTS

We thank Dr. Keiko Hirose (Washington University) for providing CX3CR1^{DTR} mouse line.

REFERENCES

Anniko, M. (1983). Postnatal Maturation of Cochlear Sensory Hairs in the Mouse. *Anat. Embryol.* 166 (3), 355–368. doi:10.1007/bf00305923

Brown, L. N., Xing, Y., Noble, K. V., Barth, J. L., Panganiban, C. H., Smythe, N. M., et al. (2017). Macrophage-Mediated Glial Cell Elimination in the Postnatal Mouse Cochlea. *Front. Mol. Neurosci.* 10, 407. doi:10.3389/fnmol.2017.00407

Christ, S., Biebel, U. W., Hoidis, S., Friedrichsen, S., Bauer, K., and Smolders, J. W. T. (2004). Hearing Loss in Athyroid Pax8 Knockout Mice and Effects of Thyroxine Substitution. *Audiol. Neurotol* 9 (2), 88–106. doi:10.1159/000076000

Davies, L. C., Jenkins, S. J., Allen, J. E., and Taylor, P. R. (2013). Tissue-resident Macrophages. *Nat. Immunol.* 14 (10), 986–995. doi:10.1038/ni.2705

Dayaratne, M. W. N., Vlajkovic, S. M., Lipski, J., and Thorne, P. R. (2014). Kölliker's Organ and the Development of Spontaneous Activity in the Auditory System: Implications for Hearing Dysfunction. *Biomed. Res. Int.* 2014, 1–8. doi:10.1155/2014/367939

Diehl, G. E., Longman, R. S., Zhang, J.-X., Breart, B., Galan, C., Cuesta, A., et al. (2013). Microbiota Restricts Trafficking of Bacteria to Mesenteric Lymph Nodes by CX3CR1hi Cells. *Nature* 494 (7435), 116–120. doi:10.1038/nature11809

Dong, Y., Zhang, C., Frye, M., Yang, W., Ding, D., Sharma, A., et al. (2018). Differential Fates of Tissue Macrophages in the Cochlea during Postnatal Development. *Hearing Res.* 365, 110–126. doi:10.1016/j.heares.2018.05.010

Erwig, L.-P., and Henson, P. M. (2008). Clearance of Apoptotic Cells by Phagocytes. *Cell Death Differ* 15 (2), 243–250. doi:10.1038/sj.cdd.4402184

Gordon, S., and Plüddemann, A. (2018). Macrophage Clearance of Apoptotic Cells: A Critical Assessment. *Front. Immunol.* 9, 127. doi:10.3389/fimmu.2018.00127

Henson, P. M., and Hume, D. A. (2006). Apoptotic Cell Removal in Development and Tissue Homeostasis. *Trends Immunol.* 27 (5), 244–250. doi:10.1016/j.it.2006.03.005

Hirose, K., Discolo, C. M., Keasler, J. R., and Ransohoff, R. (2005). Mononuclear Phagocytes Migrate into the Murine Cochlea after Acoustic Trauma. *J. Comp. Neurol.* 489 (2), 180–194. doi:10.1002/cne.20619

Hirose, K., Rutherford, M. A., and Warchol, M. E. (2017). Two Cell Populations Participate in Clearance of Damaged Hair Cells from the Sensory Epithelia of the Inner Ear. *Hearing Res.* 352, 70–81. doi:10.1016/j.heares.2017.04.006

Hou, S., Chen, J., and Yang, J. (2019). Autophagy Precedes Apoptosis during Degeneration of the Kölliker's Organ in the Development of Rat Cochlea. *Eur. J. Histochem.* 63 (2), 3025. doi:10.4081/ejh.2019.3025

Johnson, K. R., Marden, C. C., Ward-Bailey, P., Gagnon, L. H., Bronson, R. T., and Donahue, L. R. (2007). Congenital Hypothyroidism, Dwarfism, and Hearing Impairment Caused by a Missense Mutation in the Mouse Dual Oxidase 2 Gene, Duox2. *Duox2. Duox2. Mol. Endocrinol.* 21 (7), 1593–1602. doi:10.1210/me.2007-0085

Jung, S., Aliberti, J., Graemmel, P., Sunshine, M. J., Kreutzberg, G. W., Sher, A., et al. (2000). Analysis of Fractalkine Receptor CX3CR1 Function by Targeted Deletion and Green Fluorescent Protein Reporter Gene Insertion. *Mol. Cel Biol* 20 (11), 4106–4114. doi:10.1128/MCB.20.11.4106-4114.2000

Kamiya, K., Takahashi, K., Kitamura, K., Momoi, T., and Yoshikawa, Y. (2001). Mitosis and Apoptosis in Postnatal Auditory System of the C3H/He Strain. *Brain Res.* 901 (1-2), 296–302. doi:10.1016/s0006-8993(01)02300-9

Kaur, T., Clayman, A. C., Nash, A. J., Schrader, A. D., Warchol, M. E., and Ohlemiller, K. K. (2019). Lack of Fractalkine Receptor on Macrophages Impairs Spontaneous Recovery of Ribbon Synapses after Moderate Noise Trauma in C57BL/6 Mice. *Front. Neurosci.* 13, 620. doi:10.3389/fnins.2019.00620

Kaur, T., Hirose, K., Rubel, E. W., and Warchol, M. E. (2015b). Macrophage Recruitment and Epithelial Repair Following Hair Cell Injury in the Mouse Utricle. *Front. Cel. Neurosci.* 9, 150. doi:10.3389/fncel.2015.00150

Kaur, T., Zamani, D., Tong, L., Rubel, E. W., Ohlemiller, K. K., Hirose, K., et al. (2015a). Fractalkine Signaling Regulates Macrophage Recruitment into the Cochlea and Promotes the Survival of Spiral Ganglion Neurons after Selective Hair Cell Lesion. *J. Neurosci.* 35 (45), 15050–15061. doi:10.1523/JNEUROSCI.2325-15.2015

Kishimoto, I., Okano, T., Nishimura, K., Motohashi, T., and Omori, K. (2019). Early Development of Resident Macrophages in the Mouse Cochlea Depends on Yolk Sac Hematopoiesis. *Front. Neurol.* 10, 1115. doi:10.3389/fneur.2019.01115

Korver, A. M. H., Smith, R. J. H., Van Camp, G., Schleiss, M. R., Bitner-Glindzicz, M. A. K., Lustig, L. R., et al. (2017). Congenital Hearing Loss. *Nat. Rev. Dis. Primers* 3, 16094. doi:10.1038/nrdp.2016.94

Kuida, K., Zheng, T. S., Na, S., Kuan, C.-Y., Yang, D., Karasuyama, H., et al. (1996). Decreased Apoptosis in the Brain and Premature Lethality in CPP32-Deficient Mice. *Nature* 384 (6607), 368–372. doi:10.1038/384368a0

Lukashkin, A. N., Richardson, G. P., and Russell, I. J. (2010). Multiple Roles for the Tectorial Membrane in the Active Cochlea. *Hearing Res.* 266 (1-2), 26–35. doi:10.1016/j.heares.2009.10.005

Makishima, T., Hochman, L., Armstrong, P., Rosenberger, E., Ridley, R., Woo, M., et al. (2011). Inner Ear Dysfunction in Caspase-3 Deficient Mice. *BMC Neurosci.* 12, 102. doi:10.1186/1471-2202-12-102

Milinkeviciute, G., Henningfield, C. M., Muniak, M. A., Chokr, S. M., Green, K. N., and Cramer, K. S. (2019). Microglia Regulate Pruning of Specialized Synapses in the Auditory Brainstem. *Front. Neural Circuits* 13, 55. doi:10.3389/fncir.2019.00055

Monzack, E. L., May, L. A., Roy, S., Gale, J. E., and Cunningham, L. L. (2015). Live Imaging the Phagocytic Activity of Inner Ear Supporting Cells in Response to Hair Cell Death. *Cel Death Differ* 22 (12), 1995–2005. doi:10.1038/cdd.2015.48

Morishita, H., Makishima, T., Kaneko, C., Lee, Y.-S., Segil, N., Takahashi, K., et al. (2001). Deafness Due to Degeneration of Cochlear Neurons in Caspase-3-Deficient Mice. *Biochem. Biophysical Res. Commun.* 284 (1), 142–149. doi:10.1006/bbrc.2001.4939

Mustapha, M., Fang, Q., Gong, T.-W., Dolan, D. F., Raphael, Y., Camper, S. A., et al. (2009). Deafness and Permanently Reduced Potassium Channel Gene Expression and Function in Hypothyroid Pit1dw Mutants. *J. Neurosci.* 29 (4), 1212–1223. doi:10.1523/JNEUROSCI.4957-08.2009

Ng, L., Kelley, M. W., and Forrest, D. (2013). Making Sense with Thyroid Hormone-The Role of T3 in Auditory Development. *Nat. Rev. Endocrinol.* 9 (5), 296–307. doi:10.1038/nrendo.2013.58

Park, S. Y., and Kim, I. S. (2017). Engulfment Signals and the Phagocytic Machinery for Apoptotic Cell Clearance. *Exp. Mol. Med.* 49 (5), e331. doi:10.1038/emm.2017.52

Peeters, R. P., Ng, L., Ma, M., and Forrest, D. (2015). The Timecourse of Apoptotic Cell Death during Postnatal Remodeling of the Mouse Cochlea and its Premature Onset by Triiodothyronine (T3). *Mol. Cell Endocrinol.* 407, 1–8. doi:10.1016/j.mce.2015.02.025

Ruben, R. J. (1967). Development of the Inner Ear of the Mouse: a Radioautographic Study of Terminal Mitoses. *Acta Otolaryngol.* Suppl 220, 1–44.

Rueda, J., de la Sen, C., Juiz, J. M., and Merchan, J. A. (1987). Neuronal Loss in the Spiral Ganglion of Young Rats. *Acta Oto-Laryngologica* 104 (5-6), 417–421. doi:10.3109/00016488709128269

Rüsch, A., Ng, L., Goodyear, R., Oliver, D., Lisoukov, I., Vennström, B., et al. (2001). Retardation of Cochlear Maturation and Impaired Hair Cell Function Caused by Deletion of All Known Thyroid Hormone Receptors. *J. Neurosci.* 21 (24), 9792–9800. doi:10.1523/JNEUROSCI.21-24-09792.2001

Savage, J. C., Carrier, M., and Tremblay, M.-È. (2019). Morphology of Microglia across Contexts of Health and Disease. *Methods Mol. Biol.* 2034, 13–26. doi:10.1007/978-1-4939-9658-2_2

Sohmer, H., and Freeman, S. (1995). Functional Development of Auditory Sensitivity in the Fetus and Neonate. *J. Basic Clin. Physiol. Pharmacol.* 6 (2), 95–108. doi:10.1515/jbcpp.1995.6.2.95

Sokolowski, J. D., Chabanon-Hicks, C. N., Han, C. Z., Heffron, D. S., and Mandell, J. W. (2014). Fractalkine Is a "Find-Me" Signal Released by Neurons Undergoing Ethanol-Induced Apoptosis. *Front. Cel. Neurosci.* 8, 360. doi:10.3389/fncel.2014.00360

Sundaresan, S., Kong, J.-H., Fang, Q., Salles, F. T., Wangsawihardja, F., Ricci, A. J., et al. (2016). Thyroid Hormone Is Required for Pruning, Functioning and Long-Term Maintenance of Afferent Inner Hair Cell Synapses. *Eur. J. Neurosci.* 43 (2), 148–161. doi:10.1111/ejn.13081

Takahashi, K., Kamiya, K., Urase, K., Suga, M., Takizawa, T., Mori, H., et al. (2001). Caspase-3-deficiency Induces Hyperplasia of Supporting Cells and Degeneration of Sensory Cells Resulting in the Hearing Loss. *Brain Res.* 894 (2), 359–367. doi:10.1016/s0006-8993(01)02123-0

Varol, C., Mildner, A., and Jung, S. (2015). Macrophages: Development and Tissue Specialization. *Annu. Rev. Immunol.* 33, 643–675. doi:10.1146/annurev-immunol-032414-112220

Wang, H. C., Lin, C.-C., Cheung, R., Zhang-Hooks, Y., Agarwal, A., Ellis-Davies, G., et al. (2015). Spontaneous Activity of Cochlear Hair Cells Triggered by Fluid Secretion Mechanism in Adjacent Support Cells. *Cell* 163 (6), 1348–1359. doi:10.1016/j.cell.2015.10.070

Warchol, M. E. (2019). Interactions between Macrophages and the Sensory Cells of the Inner Ear. *Cold Spring Harb Perspect. Med.* 9 (6), a033555. doi:10.1101/cshperspect.a033555

Wynn, T. A., Chawla, A., and Pollard, J. W. (2013). Macrophage Biology in Development, Homeostasis and Disease. *Nature* 496 (7446), 445–455. doi:10.1038/nature12034

Conflict of Interest: The authors declare that the research was conducted in the absence of any commercial or financial relationships that could be construed as a potential conflict of interest.

Publisher's Note: All claims expressed in this article are solely those of the authors and do not necessarily represent those of their affiliated organizations, or those of the publisher, the editors and the reviewers. Any product that may be evaluated in this article, or claim that may be made by its manufacturer, is not guaranteed or endorsed by the publisher.

frontiers in Cell and Developmental Biology

ORIGINAL RESEARCH
published: 11 January 2022
doi: 10.3389/fcell.2021.783504

A Single Cisterna Magna Injection of AAV Leads to Binaural Transduction in Mice

Fabian Blanc[1,2], Alexis-Pierre Bemelmans[3,4], Corentin Affortit[1], Charlène Joséphine[3,4], Jean-Luc Puel[1†], Michel Mondain[1,2†] and Jing Wang[1,2]**

[1]Institute for Neurosciences of Montpellier (INM), University Montpellier, INSERM, Montpellier, France, [2]CHRU Montpellier—Centre Hospitalier Régional Universitaire, Montpellier, France, [3]Molecular Imaging Research Center, Institut de Biologie François Jacob, Direction de la Recherche Fondamentale, CEA, Fontenay-aux-Roses, France, [4]Université Paris-Saclay, CEA, CNRS, Laboratoire des Maladies Neurodégénératives, mécanismes, thérapies, imagerie, Fontenay-aux-Roses, France

Viral-mediated gene augmentation, silencing, or editing offers tremendous promise for the treatment of inherited and acquired deafness. Inner-ear gene therapies often require a safe, clinically useable and effective route of administration to target both ears, while avoiding damage to the delicate structures of the inner ear. Here, we examined the possibility of using a cisterna magna injection as a new cochlear local route for initiating binaural transduction by different serotypes of the adeno-associated virus (AAV2/8, AAV2/9, AAV2/Anc80L65). The results were compared with those following canalostomy injection, one of the existing standard inner ear local delivery routes. Our results demonstrated that a single injection of AAVs enables high-efficiency binaural transduction of almost all inner hair cells with a basal-apical pattern and of large numbers of spiral ganglion neurons of the basal portion of the cochlea, without affecting auditory function and cochlear structures. Taken together, these results reveal the potential for using a cisterna magna injection as a local route for binaural gene therapy applications, but extensive testing will be required before translation beyond mouse models.

Keywords: cisterna magna injection, AAV, cochlea, binaural gene transduction, hearing

OPEN ACCESS

Edited by:
Stefan Heller,
Stanford University, United States

Reviewed by:
Renjie Chai,
Southeast University, China
Yilai Shu,
Fudan University, China

****Correspondence:***
Fabian Blanc
fabian-blanc@chu-montpellier.fr
Jing Wang
jing.wang@inserm.fr

†These authors have contributed equally to this work

Specialty section:
This article was submitted to Molecular and Cellular Pathology, a section of the journal Frontiers in Cell and Developmental Biology

Received: *26 September 2021*
Accepted: *13 December 2021*
Published: *11 January 2022*

Citation:
Blanc F, Bemelmans A-P, Affortit C, Joséphine C, Puel J-L, Mondain M and Wang J (2022) A Single Cisterna Magna Injection of AAV Leads to Binaural Transduction in Mice. Front. Cell Dev. Biol. 9:783504. doi: 10.3389/fcell.2021.783504

INTRODUCTION

Hearing loss is currently the most frequent human sensory deficit and will affect almost one billion people worldwide in 2050 (World Health Organization, 2021). An underlying genetic cause is estimated to be responsible for deafness in 50–60% of affected persons (Angeli et al., 2012). To date, no curative treatment is available for sensorineural hearing loss. The only existing options are sound amplification by hearing aids, and electrical stimulation of auditory nerves *via* cochlear implants. However, the quality of the sound perceived via these two devices still cannot match that of the normal ear (Kronenberger et al., 2014; Illg et al., 2017; Jiam et al., 2017).

During the past decade, promising results have been obtained in cochlear gene therapy of mouse models of genetic deafness (Askew et al., 2015; Isgrig et al., 2017; Pan et al., 2017; Akil et al., 2019; Wu et al., 2021). Recombinant adeno-associated virus (AAV) is the preferred viral vector for gene therapy, due to its non-pathogenicity, low immunogenicity, and long-lasting expression in non-dividing cells (Naso et al., 2017). A major challenge for the delivery of genetic therapeutic materials into the cochlea comes from the inner ear's anatomical isolation; it is a small, complex structure

encased within the densest portion of the temporal bone (Salt and Hirose, 2018). To date, several local routes have been tested to introduce viral vectors into the cochlea (see for review: (Blanc et al., 2020)); one of them is by round-window injection (Chien et al., 2015). After opening the middle ear compartment through the round window membrane, the viral vectors are injected directly in the cochlear perilymph. Recently, Yoshimura and others (Yoshimura et al., 2018) proposed a combined approach that enhances the efficacy of transduction and reduces cochlear damage induced by the puncture of the round window. Indeed, they made an "exit hole" in the posterior semicircular canal (PSCC) before injecting the viral vectors through the round window membrane. This method showed a preferential perfusion flow pattern from the base to the apex in scala tympani without impacting auditory thresholds. Another route is injection into the posterior semicircular canal (PSCC) of the vestibule (Kawamoto et al., 2001), or into the utricle (Lee et al., 2020). These routes allow a high efficiency of transduction of the cochlear and vestibular epithelium (Suzuki et al., 2017; Guo et al., 2018; Tao et al., 2018). Instead of local injections, AAV can also be injected intravenously and reach the inner ear sensory cells efficiently. A recent study (Shibata et al., 2017) showed that intravenous injection of an AAV2/9 carrying the enhanced green fluorescent protein (eGFP) reporter gene resulted in binaural transduction of IHCs, SGNs and vestibular hair cells. However, this systemic route of foreign gene administration requires the intravenous injection of a larger volume of the viral solution, thus increasing the potential of systemic toxicity.

In all the local injections strategies, however, one unilateral injection leads to viral gene transduction only in the injected ear. In addition, opening of the bony labyrinth and the perilymphatic space, and - for round window injection - opening of the middle ear, is mandatory. Disturbance of middle ear sound transduction (Zhu et al., 2016) and of the ionic composition of the perilymph (Mynatt et al., 2006), as well as excessive pressure induced by the injection (Yoshimura et al., 2018) may occur. Taken together, the success of gene therapy still needs a significant and lasting effort to develop safe and clinically useable gene-delivery routes.

The cochlear aqueduct has recently been described as a natural shunt of perilymph away from the cochlea, following perilymphatic injections (Talaei et al., 2019). The cochlear aqueduct is a natural opening in the bony labyrinth, and allows communications between the cochlear perilymph and the cerebrospinal fluid (CSF) (Schuknecht and Seifi, 1963; Salt et al., 2003). It may serve as a pressure-release valve, draining any excess perilymph into the cranial cavity. The Cisterna magna (CM), or posterior cerebellomedullary cistern, collects the CSF produced in the cerebral ventricles. It is located between the cerebellum and the dorsal surface of the medulla oblongata, in proximity to the opening of the cochlear aqueduct. The membrane of the CM can be perforated for CSF collection (Xavier et al., 2018; Manouchehrian et al., 2021). CM injection is a validated technique for CSF-injection of gene transfer vectors in mice (Liu and Duff, 2008; Xavier et al., 2018; Manouchehrian et al., 2021).

In this study to explore the possibility of using CM injection as a new cochlear local delivery route for binaural viral gene transfer, we used AAV2/8, AAV2/9, and AAV2/Anc80L65-expressing eGFP driven by a ubiquitous chicken β-actin (CBA) promoter. Vectors were delivered into adult mice *via* the CM. The efficiency and safety of AAV-mediated gene transfer were evaluated functionally and morphologically, and compared with those from PSCC canalostomy injection. Our results demonstrate for the first time the successful use of CM injection as a novel delivery route for binaural therapeutic gene transfer.

METHODS

Animals

Male C57BL/6J mice aged 1 month were purchased from Janvier Laboratories (Le Genest Saint Isle) and housed in facilities accredited by the French Ministry of Agriculture and Forestry (C-34-172-36; December 19, 2014). Experiments were carried out in accordance with French Ethical Committee stipulations regarding the care and use of animals for experimental procedures (agreements C75-05-18 and 01476.02, license #6711).

AAV Production

The AAV-CBA-eGFP construct has been described elsewhere (d'Orange et al., 2018). Recombinant viral particles were generated by transient co-transfection of HEK 293T cells with a three-plasmid system (Berger et al., 2015) with either AAV8, AAV9, or AAVAnc80L65 packaging plasmids. Briefly, 3 days following transfection, viral particles were extracted from cell supernatant and cell lysate, concentrated by PEG precipitation, purified by ultracentrifugation on an iodixaniol step-gradient, and desalted by tangential ultrafiltration. The resulting AAV vector batches were stored at 4°C until further use. AAV concentration was estimated by qPCR using a plasmid of known concentration for the standard curve (Aurnhammer et al., 2012), and is expressed as vector genome per ml (vg/ml).

Animal Surgery

Mice were anaesthetized with intra-peritoneal injection of zolazepam (40 mg/kg) and xylazine (5 mg/kg). During surgery, their body temperature was maintained at 37.5°C using a heated blanket. After the injection, the animals were closely monitored daily, and no neurological symptoms were observed in the following days. All animals were operated by the same surgeon.

PSCC canalostomy injections were performed as previously described (Guo et al., 2018; Tao et al., 2018). After ensuring that the animal exhibited no reflex to painful stimulation, a left post-auricular incision was made under sterile conditions. Blunt dissection of the sterno-cleïdo-mastoïd muscle exposed the posterior part of the temporal bone and made visible the square angle formed by the lateral and the posterior semicircular canals. Canalostomy of the posterior canal was performed with a 26G bevelled needle and the tip of a polyimitube (microlumen) was inserted toward the crus commune. A small piece of muscle and tissue adhesive (3 M Vetbond, St. Paul, MN) sealed the tube to the temporal bone,

avoiding leakage. The polyimide tube was connected to a polyethylene tube, and this to a 30G Hamilton syringe. Injection of 1.5 µL of viral vector (0.5 µL/min) was driven by a micro-pump (Harvard Apparatus), and left in place for 5 min. After removing the tube, the canal was carefully closed by a plug of muscle and tissue adhesive. The skin was closed by 4/0 resorbable sutures. Terramycine (0.04 ml) and Carprofene (0.2 mg/kg) were then administered. The total duration of the procedure was about 20 min. The titer used for AAV2/8, AAV2/9, and AAV2/Anc80L65 was 3.16×10^{14} vg/ml, 9.1×10^{13} vg/ml and 3.1×10^{13} vg/ml, respectively. The chosen titers were based on our pilot study to ensure high level of transduction without compromising hearing functions.

Cisterna magna injection was performed following the same technique as for central nervous system delivery of gene transfer vectors (Liu and Duff, 2008; Xavier et al., 2018; Manouchehrian et al., 2021). Under an operating microscope, an incision was made on the scalp. Median dissection of the muscles of the neck exposed the atlanto-occipital membrane covering the Cisterna Magna. Using a 30G Hamilton syringe, within 30 s, 5 µL of viral vector, or 5 µL of physiological saline, was injected into the Cisterna Magna of AAV-injected or saline-injected mice, respectively. The syringe was left in place for 5 min, and then removed. To avoid leakage, the atlanto-occipital membrane was immediately covered by tissue adhesive. The skin was closed by 4/0 resorbable sutures. Terramycine (0.04 ml) and Carprofene (0.2 mg/kg) were then administered. The total duration of the surgery was about 15 min. For each surgical approach (CM or PSCC canalostomy), for each AAV-serotype and control-saline injected group, three to five mice were used.

Functional Hearing Assessment

To assess the effect of AAV transduction on hearing function, we recorded the auditory brainstem responses (ABRs) and distortion-product otoacoustic emissions (DPOAEs) before, and 2 weeks after, AAV-injections through both CM and PSCC routes. In addition, five animals of the PSCC group were followed up to 3 months after injection, their hearing function was evaluated once per month by ABR recording (**Supplementary Figure S1**). All functional evaluations were performed under anesthesia, in a Faraday-shielded, anechoic, sound-proof cage. Body temperature was measured using a thermistor rectal probe, and maintained at 37.5°C ± 1 using a heated blanket.

Auditory Brainstem Response

ABR recordings were conducted on anaesthetized mice, and electrodes were placed subcutaneously on the vertex, beneath the ear, and in the back. Tone bursts of 10 ms duration with a 1 ms rise-and-fall time were delivered at a rate of 3/s at 4, 8, 16, and 32 kHz. Sound was delivered by a Tucker-Davis loudspeaker in a calibrated closed-field condition. Amplification of cochlear potentials (20,000) was achieved *via* a Grass P511 differential amplifier, and averaged 1,000 times (Dell Dimensions). Level-amplitude functions of the ABRs were obtained at each frequency (4, 8, 16, and 32 kHz) by varying the level of the tone bursts from 0 to 80 dB sound pressure levels (SPL), in 5 dB incremental steps. ABR threshold was defined as the lowest sound level at which a reproducible waveform could be observed.

Distortion-Product Otoacoustic Emissions

DPOAEs were recorded in the external auditory canal using an ER-10C S/N 2528 probe (Etymotic research Inc. Elk Grove Village, IL, United States). The two primary tones of frequency f1 and f2 were generated with a constant f2/f1 ratio of 1.2, and the distortion product 2f1-f2 processed by a Cubdis system HID 40133DP (Mimosa Acoustics Inc., Champaign, IL, United States). The probe was self-calibrated for the two stimulating tones before each recording. f1 and f2 were presented simultaneously, sweeping f2 from 20 to 2 kHz in quarter-octave steps. For each f2 frequency, the distortion product 2f1-f2 and the neighbouring noise amplitude levels were measured and expressed as a function of f2.

Immunochemistry

Following the last functional hearing assessments 2 weeks after surgery, the mice were sacrificed and their cochleae quickly removed and fixed for 45 min in 4% paraformaldehyde. Immunocytochemistry was performed in cochlear whole-mount preparations. The samples were immunostained with anti-Vglut3 (1/500, Synapic Systems, #135204, RRID: AB_2619825) to label the inner hair cells, and neurofilament (NF 200, 1/500, Sigma Aldrich, AB_477257) to identify the spiral ganglion neurones. Rhodamine-conjugated phalloidin (1:1,000, Thermos Fisher, AB_2572408) was used to label actin. All secondary antibodies were used at a dilution of 1:1,000. These included donkey anti-mouse, anti-rabbit, and anti-guinea pig IgG conjugated to Alexa 488, Alexa 568, or Alexa 664 (Molecular Probes, RRID: AB_141607, RRID: AB_2535792, RRID: AB_2735091). DNA was stained using Hoechst 33,342 (0.002% wt: vol, Sigma). Fluorescent tags were visualized using a confocal microscope (Zeiss 880 Airysc). Direct fluorescence was used to asses for GFP expression, i.e. we did not use any anti-GFP antibodies in our experiments. For IHC cell quantification, control ears were the right - uninjected - ears of the PSCC canalostomy group. No eGFP fluorescence was observed in these cochleae. Images were processed using ImageJ (Wayne Rasband).

Statistics

Data are expressed as the mean ± SEM. Significant differences between groups were assessed with one-way ANOVA; once the significance of the group differences ($p \leq 0.05$) was established, Dunn's tests were used for post-hoc comparisons between pairs of groups. p values are indicated in the legends of each figure.

RESULTS

A Single CM Injection of Fast Green Led to Green Coloration of Both Cochleae

To ensure the injected solution *via* the CM route could enter into both left and right cochleae, we firstly compared the coloration of both cochleae following a single CM injection of fast green dye

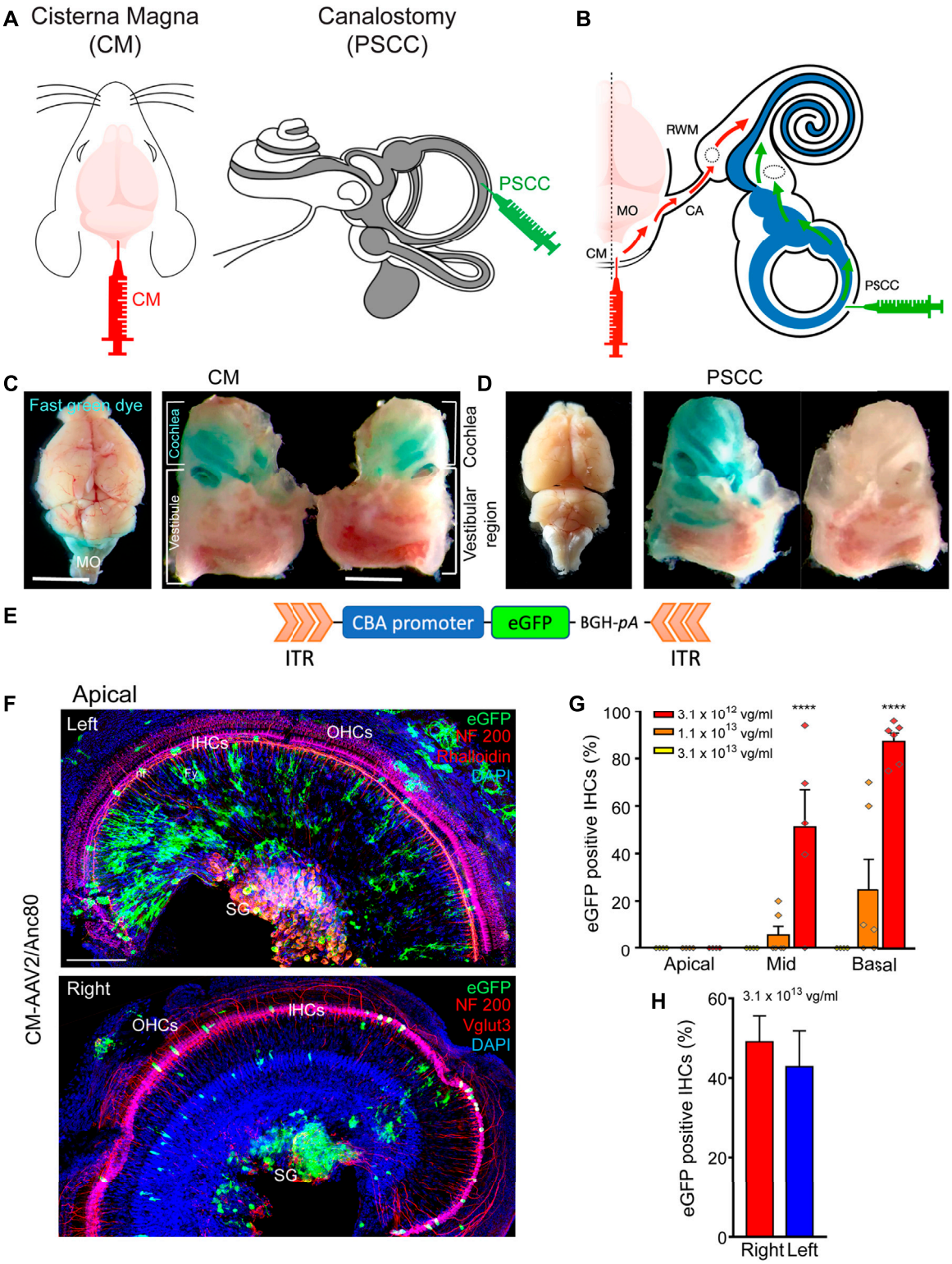

FIGURE 1 | CM injection and cochlear targeting efficiencies. **(A,B)**: Schematics of the surgical approaches for Cisterna Magna (CM) and posterior semicircular canal (PSCC) canalostomy injection **(A)** and diffusion of viral vectors from the CM to the cochlea through the cochlear aqueduct (red arrows) and from the PSCC to the cochlea (green arrows) **(B)**. The grey and white colors in **(A)** indicate the endolymphatic and perilymphatic spaces in the inner ear, respectively. **(C,D)**: Stereomicroscope images of the dissected brain and cochleae following CM injection **(C)** and left PSCC injection **(D)** of green dye. Note the coloration of both cochleae and medulla oblongata (MO in **C**) after CM injection. Note the coloration of the injected cochlea and the vestibule after PSCC injection. **(E)**: Schematic representation of the AAV

(*Continued*)

FIGURE 1 | recombinant genome for AAV2/8, AAV2/9, and AAV2/Anc80L65-CBA-eGFP. CBA: chicken β-actin promoter; eGFP: enhanced Green Fluorescent Protein; BGH-pA: Bovine growth hormone polyadenylation signal. ITR: Inverted terminal repeat. **(F)**: Representative confocal images showing eGFP positive cells in flat-mounted preparations of the apical portion of the left and right cochleae 15 days after CM injection with AAV2/Anc80L65. eGFP positive cells are in green, NF200 immunolabelled auditory nerve fibres (nf, top and bottom images) and spiral ganglion neurons (SG, top and bottom images), Vglut three labelled inner hair cells (bottom image) and Phalloidin-labelled inner and outer hair cells (IHCs and OHCs respectively, top image) are in red. DAPI-labelled nuclei are in blue. Fy: fibrocytes. Scale bar: 50 μm. **(G)**: Transduction efficiency (eGFP positive IHCs) as a function of concentration, at the apical, mid-, and basal regions of the cochlea, 2 weeks after CM injection with AAV2/Anc80L65 (n = 3 animals, six cochleae, for each concentration). **(H)**: Average eGFP positive IHCs along the length of the cochlea from the left and right ears following a single CM injection with AAV2/Anc80L65 (n = 3 cochleae in each group). Data are expressed as mean ± SEM. One-way ANOVA test was followed by Dunn's test: $^{***}p \leq 0.0001$, the highest concentration vs. the lowest concentration.

(5 μL of 5% fast green dye in 1X PBS, **Figures 1A,B**). Our results showed a strong green coloration of the medulla oblongata and the mid- and basal parts of both cochleae (**Figure 1C**), without green staining of the extreme apical part of the cochleae or the vestibules (**Figure 1C**). The baso-apical gradient of coloration following CM injection confirmed that the diffusion of the dye in the cochlea was mostly *via* the cochlear aqueduct (**Figure 1B**). PSCC canalostomy injection (1.5 μL, **Figures 1A,B**) led to a green coloration only of the cochlea and vestibule of the injected ear, but not of the brain or the contralateral ear (**Figure 1D**). These results clearly demonstrated the feasibility of two-ear incubation *via* a single CM injection.

CM Delivery of AAV Allowed Similar Binaural Titer-Dependent IHC Transduction

To assess the cochlear cell-targeting properties, and to define the most efficient viral titer for cochlear gene transfer *via* CM injection, we injected the AAV2/Anc80L65-CBA-eGFP at three different titers: 3.1×10^{13} vg/ml, 1.1×10^{13} vg/ml, and 3.1×10^{12} vg/ml (respectively 1.6×10^{11}, 5.5×10^{10}, and 1.6×10^{10} genome copies) (**Figures 1E–G**). We found a viral titer–dependent IHC transduction. The percentage of eGFP-positive IHCs was notably lower with the titer of 1.1×10^{13} vg/ml (cochlear base: 24.7 ± 12.9%, middle: 5.7 ± 3.7%, apex: 0.0 ± 0.0%) and was null for the lower titer (3.1×10^{12} vg/ml). By contrast, in the basal cochlear region, almost all IHCs were eGFP positive with the higher titer of 3.1×10^{13} vg/ml (87.4 ± 3.6%, **Figure 1G**). Therefore, we chose this concentration for the remaining experiments. The efficiency of the IHC transduction displayed a base-to-apex gradient (3.1×10^{13} vg/ml: base: 87.4 ± 3.6, middle: 51.2 ± 15.7%, apex: 0.0 ± 0.0%, **Figures 1F,G**). More importantly, one CM injection led to a similar transduction of IHCs in both cochleae: 49.0% ± 6.5 and 42.8% ± 9.0 of eGFP positive IHCs along the entire length of the cochlea for the right and left cochleae, respectively (**Figures 1F,H**).

In addition to IHC transduction, CM injection of AAV2/Anc80L65-CBA-eGFP also efficiently transduced spiral ganglion neurones (SGNs), some auditory nerve-fibre terminals, and fibrocytes in the spiral limbus (**Figure 1F**).

Vector- and Route-Dependent Inner Hair-Cell Transduction

Determining the cochlear cell targeted by different AAV serotypes can identify therapeutically relevant AAV capsids for gene delivery to treat hearing disorders *via* CM injection. Here, we assessed the distribution of AAV vector-mediated eGFP expression throughout the cochlea following CM (**Figures 2A,C,E**) or PSCC injection (**Figures 2B,D,F**) of three AAV serotypes (AAV2/8, AAV2/9, and AAV2/Anc80L65), all driven by the ubiquitous CBA promoter. We found that the IHCs showed clear evidence of eGFP expression from all of the AAV serotypes, and *via* both routes of injection (**Figures 2A–F**). We did not find evidence of transduction of the outer hair cells (OHCs) for any serotype or either delivery route (**Figures 2A–F**).

Quantitative analysis of IHC transduction revealed that the more efficient serotypes following CM injection (**Figure 2G**) were the AAV2/Anc80L65 (cochlear base: 87.4 ± 3.6%, middle: 51.2 ± 15.7%, apex: 0.0 ± 0.0%) and AAV2/8 (base: 78.5 ± 4.7%, middle: 18.2 ± 18.2%, apex: 16.0 ± 2.0%). AAV2/9 was less efficient (base 41.0 ± 13.6%, middle 15.8 ± 15.8%, apex 4.0 ± 3.1%). This result clearly demonstrated that when injected into the CM, all three AAVs efficiently transduced cochlear IHCs with a baso-apical gradient *in vivo* in adult mice. In the case of the PSCC canalostomy injection, a significantly higher level of the transduction of the IHCs was obtained using AAV2/8 (base: 80.4 ± 7.1%, middle: 73.3 ± 3.2%, apex 81.0 ± 4.1%, $p < 0.05$, AAV2/8 *vs.* using AAV2/Anc80L65 or vs. AAV2/9), and there was no baso-apical gradient for any of the three AAV vectors (**Figure 2H**). The eGFP expression was only observed in the injected ears but not the uninjected contralateral ears in PSCC injection group. These results are consistent with previous reports (Kawamoto et al., 2001; Tao et al., 2018).

Altogether, these results indicate that one single CM injection of AAV leads to binaural IHC transduction, while one canalostomy injection results in single-ear IHC transduction.

CM Delivery of AAV Allowed the Transduction of the Binaural Spiral-Ganglion Neurones and of the Nerve Fibre Terminals

In the cochlea, each IHC is contacted by multiple type-1 SGN axons, each of which follows a radial trajectory terminating at the IHCs and can be specifically labelled by anti-NF200 antibody. OHCs are innervated by type-2 SGNs, whose axons pass the IHC row and take a spiral trajectory, contacting multiple OHCs in the same row. Interestingly, following CM injection, some type-1 and type-2 auditory nerve fibers in the apical and basal cochlear regions were transduced by AAV2/Anc80L65 (**Figures 3A–D,G,H**). CM delivery of AAV2/Anc80L65 also transduced

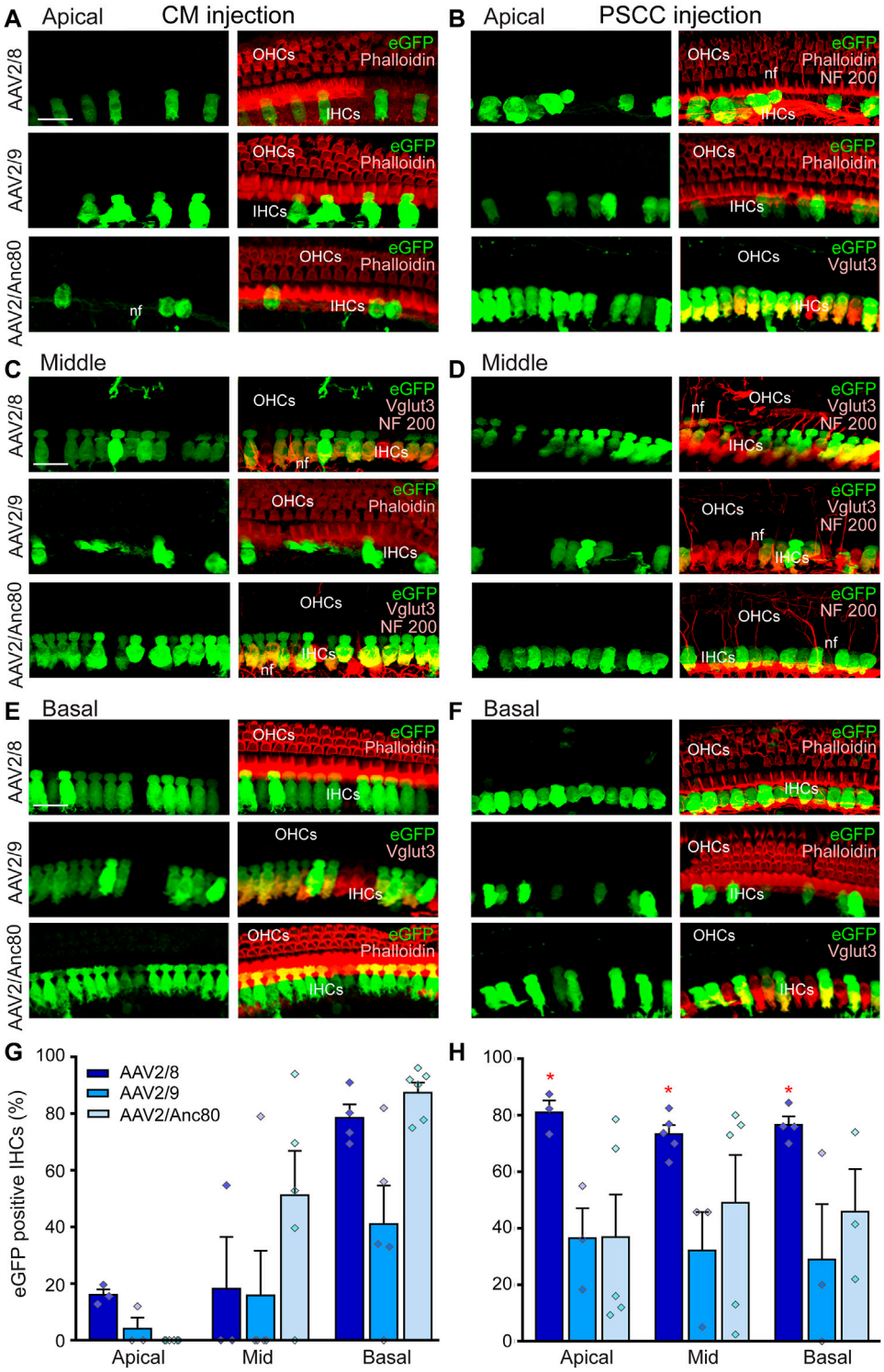

FIGURE 2 | Effects of AAV serotypes on cochlear IHC transduction efficiencies. **(A–F)**: Representative confocal images showing eGFP-positive IHCs in flat-mounted preparations of the organ of Corti of the apical **(A,B)**, middle **(C, D)** and basal **(E,F)** regions of the cochleae 15 days after CM **(A,C,E)** or canalostomy **(B,D,F)** injection with AAV2/8, AAV2/9, or AAV2/Anc80L65. eGFP positive cells are in green, NF200 immunolabelled auditory nerve fibers (nf), Phalloidin-labelled IHCs and OHCs and Vglut3 immunolabelled IHCs are in red. Scale bar: 15 µm. **(G,H)**: Transduction efficiency (eGFP positive IHCs) of the AAV2/8, AAV2/9, and AAV2/Anc80L65 at the apical, mid-, and basal regions of the cochlea, 2 weeks after CM **(G)** or canalostomy **(H)** injection ($n = 3$ to six cochleae for each group). Data are expressed as mean ± SEM. One-way ANOVA test was followed by Dunn's test: $^*p \leq 0.05$, AAV2/8 vs. AAV2/9 or AAV2/Anc80L65.

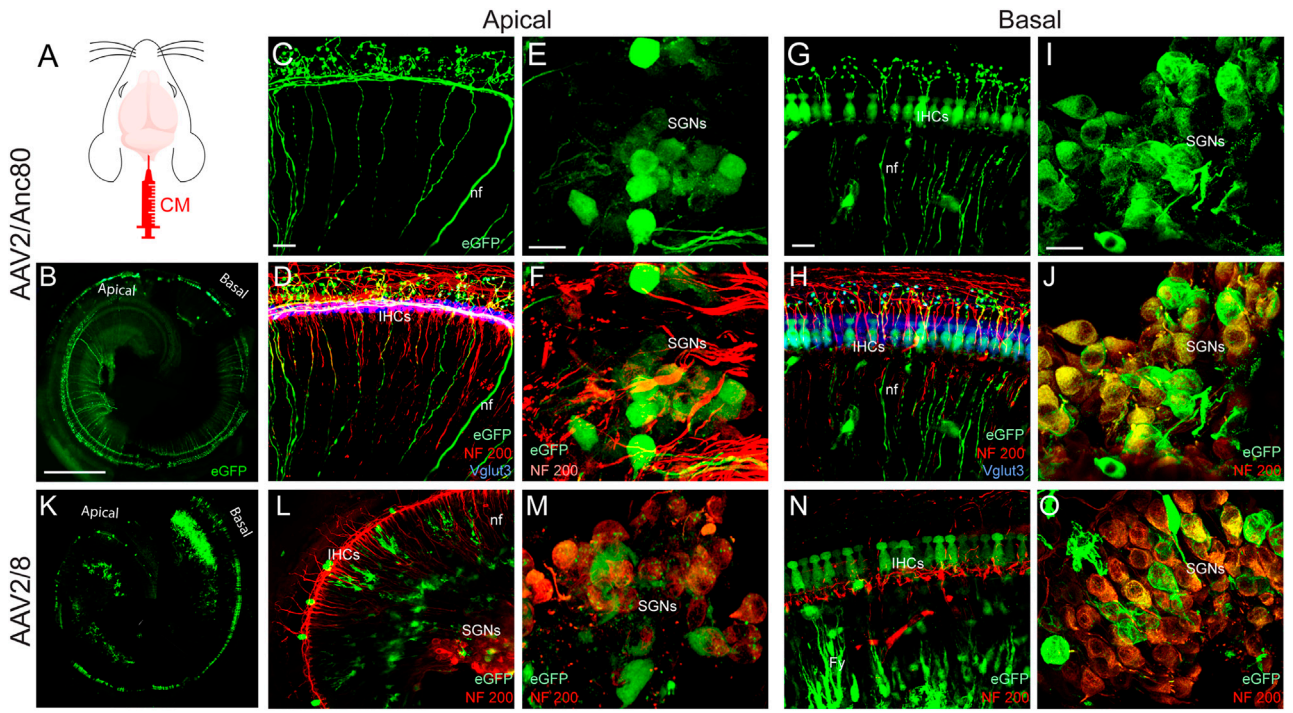

FIGURE 3 | Effects of CM injection of AAV on cochlear neural structure transduction efficiencies. **(A)**: schematization of the CM injection technique. **(B,K)**: Representative mosaic confocal images showing eGFP-positive cochlear structures in whole-mount preparations of cochleae 15 days after CM injection with AAV2/Anc80L65 **(B)** and AAV2/8 **(K)**. Scale bar: 400 µm. **(C,D,G,H,L,N)**: Representative magnification of organs of Corti from the apical **(C,D,L)** and basal regions **(G,H,N)** and the spiral ganglions from the apical **(E,F,M)** and basal regions **(I,J,O)** of the cochleae 15 days after CM injection of AAV2/Anc80L65 **(C–J)** and AAV2/8 (**L–O**). **(C,E,G,I)**: eGFP (green)-positive auditory-nerve fibre terminals (nf, **C,G**), inner hair cells (IHCs, **G**), and spiral ganglion neurons (SGNs, **E, I**). **(D,F,H,J, L–O)**: Merged images. NF200 immunolabelled auditory-nerve fibers and somata of the SGNs are in red. Vglut3 immunolabelled IHCs are in blue. Fy: fibrocytes. Scale bars: 20 µm.

the SGNs in the apical and basal regions but more importantly in the basal region (**Figures 3E,F,I–J**). CM injection of AAV2/8 transduced the auditory nerve fibre terminals with less efficiency (**Figures 3K–L,N**). By contrast, a large number of the SGNs were efficiently transduced with AAV2/8 through CM injection in the apical and basal regions (**Figures 3M,O**). However, no obvious transduction of the SGNs was observed with AAV2/9 (Data not shown).

CM Injection did not Affect Hearing or Cochlear Cell Survival

To investigate the potential impact on hearing function of AAV delivery *via* CM injection, we recorded the auditory brainstem responses (ABR), which reflect the synchronous activation of auditory neurones from the cochlea up to the colliculi in response to sound before and 2 weeks after injection. In addition, the distortion-product otoacoustic emissions (DPOAE), reflecting the function of OHCs, were measured at the same times. Our results showed that AAV or control saline injection *via* CM did not affect ABR thresholds or DPOAE amplitude (**Figures 3A,B**). Similar results were obtained with canalostomy injection (**Figures 3C,D**). In addition, we did not find any ABR threshold degradation 2 and 3 months after canalostomy injection (**Supplementary Figure S1A**), which argues in favor of the absence of long-term adverse effects following viral transduction.

Consistent with these functional results, surface preparations of uninjected and injected cochleae revealed that losses of OHCs were rarely observed in any conditions. A very slight increase of IHC loss was observed in all injected cochleae. Counting of IHC loss was performed on surface preparations of the organ of Corti (**Figure 4E**) in which the IHCs were immuno-labelled with anti-Vglut3, and the OHC and IHC from the apical, mid and basal regions were stained with rhodamine-phalloidin conjugate (**Supplementary Figure S1B**). Our results revealed a negligible and non-significant increase in IHC loss both in CM injected (Basal: 1.4 ± 0.3 IHC loss/400 µm) and in PSCC canalostomy injected (Basal: 0.9 ± 0.3 IHC loss/400 µm) cochleae compared with control, non-injected cochleae (Basal: 0.4 ± 0.7, **Figure 4F**).

CM Injection did not Alter Neurological or Vestibular Functions

To avoid the most common reported complication of CM injection in mice (Liu and Duff, 2008), caused by direct damage to the medulla oblongata, we inserted only 1.5 mm of

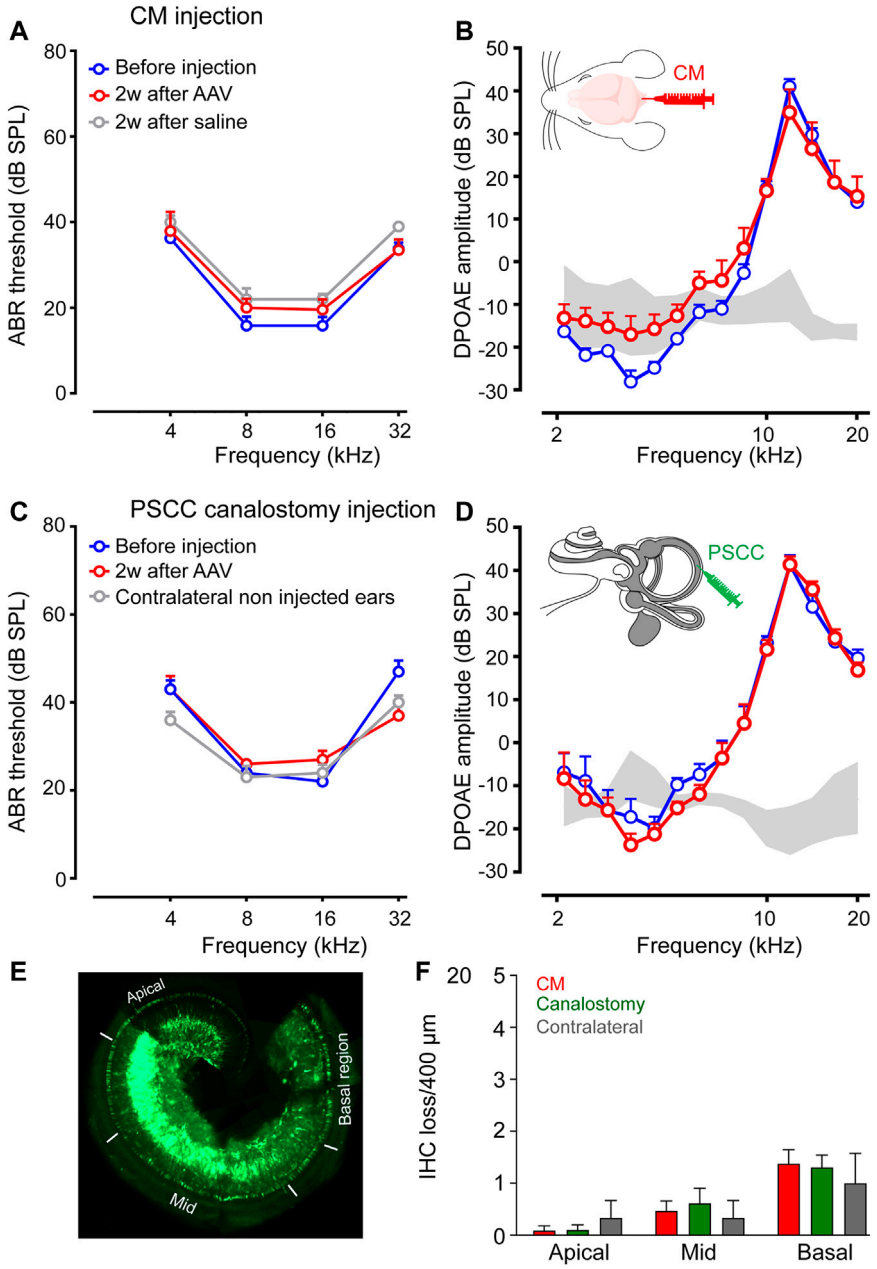

FIGURE 4 | CM and PSCC injection did not alter hearing or cochlear cell morphology. **(A–D)**: Auditory brainstem response (ABR) **(A,C)** and distortion-product otoacoustic emission (DPOAE) amplitudes **(B,D)** recorded before (blue plots) and 2 weeks after AAV injection (red plots), or saline injection (grey plot) *via* Cisterna Magna (CM, **A,B**) or PSCC canalostomy **(C,D)** routes. In the PSCC group, contralateral non-injected ears served as the control (n = 5–9 cochleae per group). **(E)**: Representative image showing a whole-mount cochlea 15 days after PSCC injection of AAV2/8. The white lines indicate the apical, mid-, and basal regions in which the counting of the IHC losses were performed. **(F)**: The number of missing cells in the apical, mid-, and basal regions of the cochleae 15 days after CM or PSCC injections or the contralateral non-injected cochleae. Data are expressed as mean ± SEM. One-way ANOVA test.

the tip of the needle into the CM. The injected mice were carefully monitored for 2 weeks following surgery. Consistent with a previous report of the central nervous system (Xavier et al., 2018), our results showed that CM injection did not cause any neurological disorders (e.g., disturbance of consciousness, inability to walk, weight loss, wound infection . . .) during the 2-week post-operative period.

In addition, we did not observe any specific signs of alterations in vestibular function, such as circling behavior, head tilting, or side-preferences for all injected mice in both CM and PSCC canalostomy groups. In addition, the general behavior of the animals such as their walking and body height was not affected by the surgery, except moderate pain for 2 days. Altogether, both the CM and canalostomy routes seem to be well tolerated by animals.

This observation was important in our mind for the future users of CM route for delivering drugs or genes into the inner ear.

DISCUSSION

CM Injection and Cochlear Targeting Efficiencies

Due to the anatomical location of the delicate sensory cells surrounded by the dense bony labyrinth, cochlear gene transfer is technically challenging. Intra-cochlear or intra-vestibular injections have been demonstrated as efficient methods of cochlear gene delivery (Askew et al., 2015; Tao et al., 2018). However, there are several shortcomings, including disturbance of the middle ear (Zhu et al., 2016), of cochlear function (Chien et al., 2015; Zhu et al., 2016), and excessive pressure (Salt and DeMott, 1998; Yoshimura et al., 2018), or lack of specificity of the targeted cells (Lee et al., 2020; Wu et al., 2021). In this study, we investigated the diffusion of the three most efficient and commonly used AAV vectors for cochlear gene transfer (AAV2/8, AAV2/9, and AAV2/Anc80L65) following CM or PSCC delivery. The CSF in the CM communicates with the perilymph of the inner ear *via* the cochlear aqueduct in mammals (Salt and Hirose, 2018). Physiologically, a small volume of CSF (30 nL/min) enters the basal portion of the cochlea in guinea pigs (Salt et al., 2015). A recent study of dye tracking following round-window membrane injection and PSCC canalostomy injection in mice showed that the cochlear aqueduct dictates dye diffusion in the inner ear, by ensuring a pressure shunt to the cranial cavity (Talaei et al., 2019). In our study, we demonstrated the proof of concept that this shunt can be used in reverse (i.e. from the cranial cavity to the cochlea) to transduce the cochlear sensory IHC and SGN.

Consistent with previous studies (Kawamoto et al., 2001; Suzuki et al., 2017; Guo et al., 2018; Tao et al., 2018), we showed that PSCC canalostomy injection resulted in efficient transduction of IHCs without a baso-apical gradient, and to a lesser extent, of some SGNs in the injected ear. Interestingly, a single CM injection of all three AAVs resulted in a bilateral transduction of IHCs, with a base-to-apex gradient. This gradient of transduction is consistent with a diffusion of viral vectors from the cochlear aqueduct to the apex *via* the scala tympani. The baso-apical gradient was also found by Chien et al. (2015) after round-window membrane injection of AAV2/8, and probably resulted from the direction of the injection of AAV into the base of the cochlea. In our study, CM injection led to a significant gradient of transduction from basal to apical IHC. This pattern could be highly relevant for treating high-frequency hearing disorders involving dysfunction of basal hair cells, such as DFNA2 (Kharkovets et al., 2006; Carignano et al., 2019), DFNA3 (Smith and Ranum, 1993), DFNA5 (Laer et al., 1998), DFNA9 (Robertson et al., 1998), and DFNA17 (Lalwani et al., 2000).

In addition to IHC transduction, CM injection targeted a large number of spiral ganglion neurons and auditory nerve fibers along the cochlea, with both AAV2/Anc80L65 and AAV2/8. The efficient transduction of SGN by CM injection could, in part, be driven by diffusion along the cochlear nerve in the modiolus, independent of diffusion along the scala tympani. Anatomically, from its emergence from the brainstem to the most distal part of the modiolus, the cochlear nerve is surrounded by CSF (Salt and Hirose, 2018), and is thus in direct contact with viral vectors injected into the CM. Future dye-tracking studies would be interesting, to investigate how, and in which proportion, the modiolus facilitates the passage of viral vectors to the SGN in CM injection.

Consistent with other studies (Shu et al., 2016; Landegger et al., 2017; Tao et al., 2018), we did not observe transduction of OHC in adult mice with the three AAV capsids that we tested, *via* either CM and PSCC canalostomy injection. Suzuki et al. (Suzuki et al., 2017) showed that AAV2/Anc80L65 induced a strong transduction of OHC in adult cochleae after PSCC canalostomy injection, whereas we did not find transduction of OHCs with this serotype. One of the explanations of this contradicting finding could be the different promotors used in their study and ours. Although both vectors were derived from the AAV2 genome and contain a Woodchuck Hepatitis Virus Regulatory Element (WPRE) to boost transgene expression, Suzuki et al. (Suzuki et al., 2017) used a CMV promoter, whereas our construct contained a CBA promoter.

Effects of AAV Serotypes on Cochlear Cell-Transduction Efficiencies

In this study, to probe the possibility of using CM injection as a new cochlear local route for binaural transduction we tested AAV2/8, AAV2/9, and AAV2/Anc80L65. The transduction profile of the first two is already well defined in the cochlea (Isgrig et al., 2017; Landegger et al., 2017; Tao et al., 2018). The last one, a synthetic serotype (Zinn et al., 2015), displays better transduction properties in several neuro-sensory tissues and the central nervous system than any previously identified AAV (Wang et al., 2017; Carvalho et al., 2018; Hudry et al., 2018). In line with these previous studies, our results attest that AAV2/Anc80L65 is the most efficient vector for IHC transduction *via* CM injection. In addition, among the three tested capsids, Anc80L65 induced strong transduction in the SGNs and the nerve fibre terminals following CM injection.

Binaural Cochlear Gene Delivery Without Imperilling Hearing, Vestibular, or Neurological Functions

Distanced gene delivery into the cochlea through the utricle or PSCC canalostomy injection (Kawamoto et al., 2001; Lee et al., 2020) seems to be a promising option for cochlear gene transfer to avoid injection-related trauma by removing the injection site from the cochlea. In addition, these more distant delivery routes may still drive a high-efficiency transduction of the cochlear and vestibular sensory hair cells (Suzuki et al., 2017; György et al., 2019), their supporting cells (Wang et al., 2014; Isgrig et al., 2019), and SGN (Suzuki et al., 2017).

Here, following CM and PSCC injection, we did not observe any neurological disorders (e.g., disturbance of consciousness, inability to walk, weight loss, wound infection . . .) or vestibular

disorders (circling behavior, head tilting, or side-preferences). In addition, the hearing function assessments showed that AAV injection *via* both routes did not affected ABR thresholds or DPOAE amplitudes. These functional results were then confirmed by hair-cell counts. Our results reveal the potential for using CM injection as a safe local route for binaural AAV-mediated gene therapy applications in mice. Compared with all existing local routes, the advantages of the CM injection route are: 1) no opening of inner-ear liquid compartments is needed, thus preventing inner-ear anatomical and functional disorders; 2) it results in binaural gene transduction with a single injection. Our results demonstrated that AAV vectors injected into the CSF cross the cochlear aqueduct to reach the cochleae of both ears. This delivery route may also be of interest for delivering other therapeutic materials such as non-viral particles, drugs, and/or ototoxic molecules into the two ears.

Potential Future Human Application and Challenges

In humans, the CM is an established route used for CSF collection and drug injection into the central nervous system (CNS) (Ayer, 1920; Lutters and Koehler, 2020). Recently, it has been proposed as an efficient route for CNS gene therapy in non-human primates (Hinderer et al., 2014). More importantly, a recent pioneering study in two Tay-Sachs patients showed the safety and feasibility of AAV9 gene transfer to the CNS through CM infusion (Taghian et al., 2020). In this study, the AAV vector was successfully delivered to the CM through adaptation of an intravascular microcatheter without any complications.

For translational cochlear gene transfer following viral vector infusion into the CM, the issue of opening of the cochlear aqueduct must be raised. The role of the cochlear aqueduct is unclear, but it may serve as a pressure regulator of the inner ear (Carlborg et al., 1982). Indeed, while the cochlear aqueduct is constantly open in small mammals (e.g., guinea pig (Salt et al., 2012) and mouse (Talaei et al., 2019)), it seems only to be open in 34% of patients. Instead, it is partially filled with connective tissue in 59%, and totally obstructed in 7%, as attested by a post-mortem study of 101 temporal bones (Gopen et al., 1997). High-resolution Magnetic Resonance Imaging (MRI) is a precise tool to explore diffusion of Gadolinium in the inner ear fluid compartments. Nakashima et al. (Nakashima et al., 2012) showed that Gadolinium injected into the inner ear moves into the CSF *via* the internal auditory meatus. However, pathological situations inform us of the possibility of passage for viral and bacterial pathogens, and even erythrocytes, between the inner ear and CSF (Holden and Schuknecht, 1968; Marsot-Dupuch et al., 2001). Such passage is much more common in infants, possibly because of the shorter length of the cochlear aqueduct (Palva, 1970). More precise data based on MRI, taking into account the size of AAV particles, could be relevant in the future. Moreover, strategies to improve viral passage through a cochlear aqueduct filled with connective tissue, such as by transiently loosening the extracellular matrix (Dalkara et al., 2009), could be explored, with careful monitoring of potential neurotoxicity.

Local injections, and much more distant-site injections, expose patients to the risk of off-target side effects. Communications between the cochlear perilymph and the systemic circulation include: the cochlear aqueduct, the cochlear vascularization, the bone marrow surrounding the bony labyrinth, the round and oval windows, and the modiolus (for review see Salt and Hirose (Salt and Hirose, 2018)). Since we chose to focus on inner-ear genetic transduction, we did not look for eGFP expression in the brain. However, a similar study using CM injection of AAV9 described strong transduction of meninges, cerebellum, cerebral cortex, and medulla oblongata in non-human primates (Hinderer et al., 2014). Infusion into the CSF conventionally led to transduction in the brain in mice and rats (Chatterjee et al., 2021; DeRosa et al., 2021; Francis et al., 2021). To transfer these surgical approaches of the inner ear into clinical practice, progress will have to be made to set up molecular strategies to avoid off-target side effects. Ubiquitous promoters, such as CBA, PGK, or CMV open the risk of the unwanted transduction of structures surrounding the cochlea, in particular those in the central nervous system. Defining a cochlear-specific AAV serotype or promoter could limit the effect of a transgene specifically to the targeted cochlear cells.

DATA AVAILABILITY STATEMENT

The raw data supporting the conclusion of this article will be made available by the authors, without undue reservation.

ETHICS STATEMENT

The animal study was reviewed and approved by the French Ethical Committee stipulations regarding the care and use of animals for experimental procedures (agreements C75-05-18 and 01476.02, license #6711).

AUTHOR CONTRIBUTIONS

JW and FB designed the experiments. FB performed all AAV injections in mice as well as vestibular, neurological, and hearing function monitoring. CA and FB realised morphological assessments. A-PB and CJ produced all AAV vectors. JW, FB, and A-PB wrote the manuscript. JW, FB, J-LP, MM, and CA reviewed the manuscript. All authors read and approved the final manuscript.

FUNDING

This work was supported by the French ministry of Health, the Labex EpiGenMed, an « Investissements d'avenir » program (ANR-10-LABX-12-01), the Fondation de l'Avenir (Et2-675) and the Fondation Gueules Cassées (77-2017).

ACKNOWLEDGMENTS

Confocal microscope acquisitions were performed at the Montpellier RIO Imaging-INM core facility. English-language services were provided by stels-ol. de.

SUPPLEMENTARY MATERIAL

The Supplementary Material for this article can be found online at: https://www.frontiersin.org/articles/10.3389/fcell.2021.783504/full#supplementary-material

REFERENCES

Akil, O., Dyka, F., Calvet, C., Emptoz, A., Lahlou, G., Nouaille, S., et al. (2019). Dual AAV-Mediated Gene Therapy Restores Hearing in a DFNB9 Mouse Model. *Proc. Natl. Acad. Sci. USA* 116, 4496–4501. doi:10.1073/pnas.1817537116

Angeli, S., Lin, X., and Liu, X. Z. (2012). Genetics of Hearing and Deafness. *Anat. Rec.* 295, 1812–1829. doi:10.1002/ar.22579

Askew, C., Rochat, C., Pan, B., Asai, Y., Ahmed, H., Child, E., et al. (2015). Tmc Gene Therapy Restores Auditory Function in Deaf Mice. *Sci. Transl. Med.* 7, 295ra108. doi:10.1126/scitranslmed.aab1996

Aurnhammer, C., Haase, M., Muether, N., Hausl, M., Rauschhuber, C., Huber, I., et al. (2012). Universal Real-Time PCR for the Detection and Quantification of Adeno-Associated Virus Serotype 2-Derived Inverted Terminal Repeat Sequences. *Hum. Gene Ther. Methods* 23, 18–28. doi:10.1089/hgtb.2011.034

Ayer, J. B. (1920). Puncture of the Cisterna magna. *Arch. Neurpsych* 4, 529–541. doi:10.1001/archneurpsyc.1920.02180230052005

Berger, A., Lorain, S., Joséphine, C., Desrosiers, M., Peccate, C., Voit, T., et al. (2015). Repair of Rhodopsin mRNA by Spliceosome-Mediated RNA Trans -Splicing: A New Approach for Autosomal Dominant Retinitis Pigmentosa. *Mol. Ther.* 23, 918–930. doi:10.1038/mt.2015.11

Blanc, F., Mondain, M., Bemelmans, A.-P., Affortit, C., Puel, J.-L., and Wang, J. (2020). rAAV-Mediated Cochlear Gene Therapy: Prospects and Challenges for Clinical Application. *Jcm* 9, 589. doi:10.3390/jcm9020589

Carignano, C., Barila, E. P., Rías, E. I., Dionisio, L., Aztiria, E., and Spitzmaul, G. (2019). Inner Hair Cell and Neuron Degeneration Contribute to Hearing Loss in a DFNA2-like Mouse Model. *Neuroscience* 410, 202–216. doi:10.1016/j.neuroscience.2019.05.012

Carlborg, B., Densert, B., and Densert, O. (1982). Functional Patency of the Cochlear Aqueduct. *Ann. Otol. Rhinol. Laryngol.* 91, 209–215. doi:10.1177/000348948209100219

Carvalho, L. S., Xiao, R., Wassmer, S. J., Langsdorf, A., Zinn, E., Pacouret, S., et al. (2018). Synthetic Adeno-Associated Viral Vector Efficiently Targets Mouse and Nonhuman Primate Retina *In Vivo*. *Hum. Gene Ther.* 29, 771–784. doi:10.1089/hum.2017.154

Chatterjee, D., Marmion, D. J., McBride, J. L., Manfredsson, F. P., Butler, D., Messer, A., et al. (2021). Enhanced CNS Transduction from AAV.PHP.eB Infusion into the Cisterna magna of Older Adult Rats Compared to AAV9. *Gene Ther.*. doi:10.1038/s41434-021-00244-y

Chien, W. W., McDougald, D. S., Roy, S., Fitzgerald, T. S., and Cunningham, L. L. (2015). Cochlear Gene Transfer Mediated by Adeno-Associated Virus: Comparison of Two Surgical Approaches. *The Laryngoscope* 125, 2557–2564. doi:10.1002/lary.25317

Dalkara, D., Kolstad, K. D., Caporale, N., Visel, M., Klimczak, R. R., Schaffer, D. V., et al. (2009). Inner Limiting Membrane Barriers to AAV-Mediated Retinal Transduction from the Vitreous. *Mol. Ther.* 17, 2096–2102. doi:10.1038/mt.2009.181

DeRosa, S., Salani, M., Smith, S., Sangster, M., Miller-Browne, V., Wassmer, S., et al. (2021). *MCOLN1* Gene Therapy Corrects Neurologic Dysfunction in the Mouse Model of Mucolipidosis IV. *Hum. Mol. Genet.* 30, 908–922. doi:10.1093/hmg/ddab093

d'Orange, M., Aurégan, G., Cheramy, D., Gaudin-Guérif, M., Lieger, S., Guillermier, M., et al. (2018). Potentiating Tangle Formation Reduces Acute Toxicity of Soluble Tau Species in the Rat. *Brain* 141, 535–549. doi:10.1093/brain/awx342

Francis, J. S., Markov, V., Wojtas, I. D., Gray, S., McCown, T., Samulski, R. J., et al. (2021). Preclinical Biodistribution, Tropism, and Efficacy of Oligotropic AAV/Olig001 in a Mouse Model of Congenital white Matter Disease. *Mol. Ther. - Methods Clin. Dev.* 20, 520–534. doi:10.1016/j.omtm.2021.01.009

Gopen, Q., Rosowski, J. J., and Merchant, S. N. (1997). Anatomy of the normal Human Cochlear Aqueduct with Functional Implications. *Hearing Res.* 107, 9–22. doi:10.1016/s0378-5955(97)00017-8

Guo, J.-Y., He, L., Qu, T.-F., Liu, Y.-Y., Liu, K., Wang, G.-P., et al. (2018). Canalostomy as a Surgical Approach to Local Drug Delivery into the Inner Ears of Adult and Neonatal Mice. *JoVE* e57351. doi:10.3791/57351

György, B., Meijer, E. J., Ivanchenko, M. V., Tenneson, K., Emond, F., Hanlon, K. S., et al. (2019). Gene Transfer with AAV9-PHP.B Rescues Hearing in a Mouse Model of Usher Syndrome 3A and Transduces Hair Cells in a Non-human Primate. *Mol. Ther. - Methods Clin. Dev.* 13, 1–13. doi:10.1016/j.omtm.2018.11.003

Hinderer, C., Bell, P., Vite, C. H., Louboutin, J.-P., Grant, R., Bote, E., et al. (2014). Widespread Gene Transfer in the central Nervous System of Cynomolgus Macaques Following Delivery of AAV9 into the Cisterna magna. *Mol. Ther. - Methods Clin. Dev.* 1, 14051. doi:10.1038/mtm.2014.51

Holden, H. B., and Schuknecht, H. F. (1968). Distribution Pattern of Blood in the Inner Ear Following Spontaneous Subarachnoid Haemorrhage. *J. Laryngol. Otol.* 82, 321–329. doi:10.1017/s0022215100068833

Hudry, E., Andres-Mateos, E., Lerner, E. P., Volak, A., Cohen, O., Hyman, B. T., et al. (2018). Efficient Gene Transfer to the Central Nervous System by Single-Stranded Anc80L65. *Mol. Ther. - Methods Clin. Dev.* 10, 197–209. doi:10.1016/j.omtm.2018.07.006

Illg, A., Haack, M., Lesinski-Schiedat, A., Büchner, A., and Lenarz, T. (2017). Long-Term Outcomes, Education, and Occupational Level in Cochlear Implant Recipients Who Were Implanted in Childhood. *Ear Hear* 38, 577–587. doi:10.1097/AUD.0000000000000423

Isgrig, K., McDougald, D. S., Zhu, J., Wang, H. J., Bennett, J., and Chien, W. W. (2019). AAV2.7m8 Is a Powerful Viral Vector for Inner Ear Gene Therapy. *Nat. Commun.* 10, 427. doi:10.1038/s41467-018-08243-1

Isgrig, K., Shteamer, J. W., Belyantseva, I. A., Drummond, M. C., Fitzgerald, T. S., Vijayakumar, S., et al. (2017). Gene Therapy Restores Balance and Auditory Functions in a Mouse Model of Usher Syndrome. *Mol. Ther.* 25, 780–791. doi:10.1016/j.ymthe.2017.01.007

Jiam, N. T., Caldwell, M. T., and Limb, C. J. (2017). What Does Music Sound like for a Cochlear Implant User? *Otol. Neurotol.* 38, e240–e247. doi:10.1097/MAO.0000000000001448

Kawamoto, K., Oh, S.-H., Kanzaki, S., Brown, N., and Raphael, Y. (2001). The Functional and Structural Outcome of Inner Ear Gene Transfer via the Vestibular and Cochlear Fluids in Mice. *Mol. Ther.* 4, 575–585. doi:10.1006/mthe.2001.0490

Kharkovets, T., Dedek, K., Maier, H., Schweizer, M., Khimich, D., Nouvian, R., et al. (2006). Mice with Altered KCNQ4 K+ Channels Implicate Sensory Outer Hair Cells in Human Progressive Deafness. *EMBO J.* 25, 642–652. doi:10.1038/sj.emboj.7600951

Kronenberger, W. G., Beer, J., Castellanos, I., Pisoni, D. B., and Miyamoto, R. T. (2014). Neurocognitive Risk in Children with Cochlear Implants. *JAMA Otolaryngol. Head Neck Surg.* 140, 608. doi:10.1001/jamaoto.2014.757

Laer, L. V., Huizing, E. H., Verstreken, M., Zuijlen, D. v., Wauters, J. G., Bossuyt, P. J., et al. (1998). Nonsyndromic Hearing Impairment Is Associated with a Mutation in DFNA5. *Nat. Genet.* 20, 194–197. doi:10.1038/2503

Lalwani, A. K., Goldstein, J. A., Kelley, M. J., Luxford, W., Castelein, C. M., and Mhatre, A. N. (2000). Human Nonsyndromic Hereditary Deafness DFNA17 Is Due to a Mutation in Nonmuscle Myosin MYH9. *Am. J. Hum. Genet.* 67, 1121–1128. doi:10.1016/S0002-9297(07)62942-5

Landegger, L. D., Pan, B., Askew, C., Wassmer, S. J., Gluck, S. D., Galvin, A., et al. (2017). A Synthetic AAV Vector Enables Safe and Efficient Gene Transfer to the Mammalian Inner Ear. *Nat. Biotechnol.* 35, 280–284. doi:10.1038/nbt.3781

Lee, J., Nist-Lund, C., Solanes, P., Goldberg, H., Wu, J., Pan, B., et al. (2020). Efficient Viral Transduction in Mouse Inner Ear Hair Cells with Utricle

Injection and AAV9-PHP.B. *Hearing Res.* 394, 107882. doi:10.1016/j.heares.2020.107882

Liu, L., and Duff, K. (2008). A Technique for Serial Collection of Cerebrospinal Fluid from the Cisterna Magna in Mouse. *JoVE*, 960. doi:10.3791/960

Lutters, B., and Koehler, P. J. (2020). A Road Less Travelled: the Centenary of Cisterna magna Puncture. *Brain* 143, 2858–2862. doi:10.1093/brain/awaa254

Manouchehrian, O., Ramos, M., Bachiller, S., Lundgaard, I., and Deierborg, T. (2021). Acute Systemic LPS-Exposure Impairs Perivascular CSF Distribution in Mice. *J. Neuroinflammation* 18, 34. doi:10.1186/s12974-021-02082-6

Marsot-Dupuch, K., Djouhri, H., Meyer, B., Pharaboz, C., and Tran Ba Huy, P. (2001). Inner Ear and Subarachnoid Spaces: Relations and Diseases. *Ann. Otolaryngol. Chir Cervicofac* 118, 171–180.

Mynatt, R., Hale, S. A., Gill, R. M., Plontke, S. K., and Salt, A. N. (2006). Demonstration of a Longitudinal Concentration Gradient along Scala Tympani by Sequential Sampling of Perilymph from the Cochlear apex. *Jaro* 7, 182–193. doi:10.1007/s10162-006-0034-y

Nakashima, T., Sone, M., Teranishi, M., Yoshida, T., Terasaki, H., Kondo, M., et al. (2012). A Perspective from Magnetic Resonance Imaging Findings of the Inner Ear: Relationships Among Cerebrospinal, Ocular and Inner Ear Fluids. *Auris. Nasus. Larynx* 39, 345–355. doi:10.1016/j.anl.2011.05.005

Naso, M. F., Tomkowicz, B., Perry, W. L., and Strohl, W. R. (2017). Adeno-Associated Virus (AAV) as a Vector for Gene Therapy. *BioDrugs* 31, 317–334. doi:10.1007/s40259-017-0234-5

Palva, T. (1970). Cochlear Aqueduct in Infants. *Acta Oto-Laryngologica* 70, 83–94. doi:10.3109/00016487009181863

Pan, B., Askew, C., Galvin, A., Heman-Ackah, S., Asai, Y., Indzhykulian, A. A., et al. (2017). Gene Therapy Restores Auditory and Vestibular Function in a Mouse Model of Usher Syndrome Type 1c. *Nat. Biotechnol.* 35, 264–272. doi:10.1038/nbt.3801

Robertson, N. G., Lu, L., Heller, S., Merchant, S. N., Eavey, R. D., McKenna, M., et al. (1998). Mutations in a Novel Cochlear Gene Cause DFNA9, a Human Nonsyndromic Deafness with Vestibular Dysfunction. *Nat. Genet.* 20, 299–303. doi:10.1038/3118

Salt, A. N., and DeMott, J. E. (1998). Longitudinal Endolymph Movements Induced by Perilymphatic Injections. *Hearing Res.* 123, 137–147. doi:10.1016/s0378-5955(98)00106-3

Salt, A. N., Gill, R. M., and Hartsock, J. J. (2015). Perilymph Kinetics of FITC-Dextran Reveals Homeostasis Dominated by the Cochlear Aqueduct and Cerebrospinal Fluid. *Jaro* 16, 357–371. doi:10.1007/s10162-015-0512-1

Salt, A. N., Hartsock, J. J., Gill, R. M., Piu, F., and Plontke, S. K. (2012). Perilymph Pharmacokinetics of Markers and Dexamethasone Applied and Sampled at the Lateral Semi-circular Canal. *Jaro* 13, 771–783. doi:10.1007/s10162-012-0347-y

Salt, A. N., and Hirose, K. (2018). Communication Pathways to and from the Inner Ear and Their Contributions to Drug Delivery. *Hearing Res.* 362, 25–37. doi:10.1016/j.heares.2017.12.010

Salt, A. N., Kellner, C., and Hale, S. (2003). Contamination of Perilymph Sampled from the Basal Cochlear Turn with Cerebrospinal Fluid. *Hearing Res.* 182, 24–33. doi:10.1016/s0378-5955(03)00137-0

Schuknecht, H. F., and Seifi, A. E. (1963). LII Experimental Observations on the Fluid Physiology of the Inner Ear. *Ann. Otol. Rhinol. Laryngol.* 72, 687–712. doi:10.1177/000348946307200308

Shibata, S. B., Yoshimura, H., Ranum, P. T., Goodwin, A. T., and Smith, R. J. H. (2017). Intravenous rAAV2/9 Injection for Murine Cochlear Gene Delivery. *Sci. Rep.* 7, 9609. doi:10.1038/s41598-017-09805-x

Shu, Y., Tao, Y., Wang, Z., Tang, Y., Li, H., Dai, P., et al. (2016). Identification of Adeno-Associated Viral Vectors that Target Neonatal and Adult Mammalian Inner Ear Cell Subtypes. *Hum. Gene Ther.* 27, 687–699. doi:10.1089/hum.2016.053

Smith, R. J., and Ranum, P. T. (1993). "Nonsyndromic Hearing Loss and Deafness, DFNA3," in *GeneReviews®*. M. P. Adam, H. H. Ardinger, R. A. Pagon, S. E. Wallace, L. J. Bean, G. Mirzaa, et al. (Seattle: University of Washington).

Suzuki, J., Hashimoto, K., Xiao, R., Vandenberghe, L. H., and Liberman, M. C. (2017). Cochlear Gene Therapy with Ancestral AAV in Adult Mice: Complete Transduction of Inner Hair Cells without Cochlear Dysfunction. *Sci. Rep.* 7, 45524. doi:10.1038/srep45524

Taghian, T., Marosfoi, M. G., Puri, A. S., Cataltepe, O. I., King, R. M., Diffie, E. B., et al. (2020). A Safe and Reliable Technique for CNS Delivery of AAV Vectors in the Cisterna Magna. *Mol. Ther.* 28, 411–421. doi:10.1016/j.ymthe.2019.11.012

Talaei, S., Schnee, M. E., Aaron, K. A., and Ricci, A. J. (2019). Dye Tracking Following Posterior Semicircular Canal or Round Window Membrane Injections Suggests a Role for the Cochlea Aqueduct in Modulating Distribution. *Front. Cell. Neurosci.* 13, 471. doi:10.3389/fncel.2019.00471

Tao, Y., Huang, M., Shu, Y., Ruprecht, A., Wang, H., Tang, Y., et al. (2018). Delivery of Adeno-Associated Virus Vectors in Adult Mammalian Inner-Ear Cell Subtypes without Auditory Dysfunction. *Hum. Gene Ther.* 29, 492–506. doi:10.1089/hum.2017.120

Wang, G.-P., Guo, J.-Y., Peng, Z., Liu, Y.-Y., Xie, J., and Gong, S.-S. (2014). Adeno-associated Virus-Mediated Gene Transfer Targeting normal and Traumatized Mouse Utricle. *Gene Ther.* 21, 958–966. doi:10.1038/gt.2014.73

Wang, L., Xiao, R., Andres-Mateos, E., and Vandenberghe, L. H. (2017). Single Stranded Adeno-Associated Virus Achieves Efficient Gene Transfer to Anterior Segment in the Mouse Eye. *PLOS ONE* 12, e0182473. doi:10.1371/journal.pone.0182473

World Health Organization (2021). Deafness and Hearing Loss. Available at: https://www.who.int/news-room/fact-sheets/detail/deafness-and-hearing-loss (Accessed September 5, 2019).

Wu, J., Solanes, P., Nist-Lund, C., Spataro, S., Shubina-Oleinik, O., Marcovich, I., et al. (2021). Single and Dual Vector Gene Therapy with AAV9-PHP.B Rescues Hearing in Tmc1 Mutant Mice. *Mol. Ther.* 29, 973–988. doi:10.1016/j.ymthe.2020.11.016

Xavier, A. L. R., Hauglund, N. L., von Holstein-Rathlou, S., Li, Q., Sanggaard, S., Lou, N., et al. (2018). Cannula Implantation into the Cisterna Magna of Rodents. *JoVE*, 57378. doi:10.3791/57378

Yoshimura, H., Shibata, S. B., Ranum, P. T., and Smith, R. J. H. (2018). Enhanced Viral-Mediated Cochlear Gene Delivery in Adult Mice by Combining Canal Fenestration with Round Window Membrane Inoculation. *Sci. Rep.* 8, 2980. doi:10.1038/s41598-018-21233-z

Zhu, B. Z., Saleh, J., Isgrig, K. T., Cunningham, L. L., and Chien, W. W. (2016). Hearing Loss after Round Window Surgery in Mice Is Due to Middle Ear Effusion. *Audiol. Neurotol* 21, 356–364. doi:10.1159/000449239

Zinn, E., Pacouret, S., Khaychuk, V., Turunen, H. T., Carvalho, L. S., Andres-Mateos, E., et al. (2015). In Silico Reconstruction of the Viral Evolutionary Lineage Yields a Potent Gene Therapy Vector. *Cell Rep.* 12, 1056–1068. doi:10.1016/j.celrep.2015.07.019

Conflict of Interest: The authors declare that the research was conducted in the absence of any commercial or financial relationships that could be construed as a potential conflict of interest.

Publisher's Note: All claims expressed in this article are solely those of the authors and do not necessarily represent those of their affiliated organizations, or those of the publisher, the editors and the reviewers. Any product that may be evaluated in this article, or claim that may be made by its manufacturer, is not guaranteed or endorsed by the publisher.

frontiers in Cell and Developmental Biology

ORIGINAL RESEARCH
published: 17 February 2022
doi: 10.3389/fcell.2022.845461

Early Deletion of *Neurod1* Alters Neuronal Lineage Potential and Diminishes Neurogenesis in the Inner Ear

Iva Filova[1], *Romana Bohuslavova*[1], *Mitra Tavakoli*[1], *Ebenezer N. Yamoah*[2], *Bernd Fritzsch*[3] *and Gabriela Pavlinkova*[1]*

[1]Laboratory of Molecular Pathogenesis, Institute of Biotechnology CAS, Vestec, Czechia, [2]Department of Physiology and Cell Biology, Institute for Neuroscience, University of Nevada, Reno, NV, United States, [3]Department of Biology, University of Iowa, Iowa City, IA, United States

Neuronal development in the inner ear is initiated by expression of the proneural basic Helix-Loop-Helix (bHLH) transcription factor *Neurogenin1* that specifies neuronal precursors in the otocyst. The initial specification of the neuroblasts within the otic epithelium is followed by the expression of an additional bHLH factor, *Neurod1.* Although NEUROD1 is essential for inner ear neuronal development, the different aspects of the temporal and spatial requirements of NEUROD1 for the inner ear and, mainly, for auditory neuron development are not fully understood. In this study, using Foxg1^{Cre} for the early elimination of *Neurod1* in the mouse otocyst, we showed that *Neurod1* deletion results in a massive reduction of differentiating neurons in the otic ganglion at E10.5, and in the diminished vestibular and rudimental spiral ganglia at E13.5. Attenuated neuronal development was associated with reduced and disorganized sensory epithelia, formation of ectopic hair cells, and the shortened cochlea in the inner ear. Central projections of inner ear neurons with conditional *Neurod1* deletion are reduced, unsegregated, disorganized, and interconnecting the vestibular and auditory systems. In line with decreased afferent input from auditory neurons, the volume of cochlear nuclei was reduced by 60% in *Neurod1* mutant mice. Finally, our data demonstrate that early elimination of *Neurod1* affects the neuronal lineage potential and alters the generation of inner ear neurons and cochlear afferents with a profound effect on the first auditory nuclei, the cochlear nuclei.

Keywords: Foxg1, cochlear nuclei, Neurod1, vestibular system, auditory system, neurons, hair cells, projections

OPEN ACCESS

Edited by:
Isabel Varela-Nieto, Spanish National Research Council (CSIC), Spain

Reviewed by:
Nicolas Daudet, University College London, United Kingdom
Tanya T. Whitfield, The University of Sheffield, United Kingdom

***Correspondence:**
Gabriela Pavlinkova
gpavlinkova@ibt.cas.cz

Specialty section:
This article was submitted to Molecular and Cellular Pathology, a section of the journal Frontiers in Cell and Developmental Biology

Received: *29 December 2021*
Accepted: *25 January 2022*
Published: *17 February 2022*

Citation:
Filova I, Bohuslavova R, Tavakoli M, Yamoah EN, Fritzsch B and Pavlinkova G (2022) Early Deletion of Neurod1 Alters Neuronal Lineage Potential and Diminishes Neurogenesis in the Inner Ear. Front. Cell Dev. Biol. 10:845461. doi: 10.3389/fcell.2022.845461

INTRODUCTION

The inner ear is a highly organized structure of interlinked channels and chambers built to encode sound, space orientation, and motion (Goodrich, 2016; Elliott et al., 2021). The sensory organs are represented by five vestibular epithelia (the maculae of utricle and saccule, and the cristae of the three semicircular canal ampullae), and, in mammals, by the auditory sensory organ of the cochlea, the organ of Corti (Rubel and Fritzsch, 2002; Fritzsch et al., 2013). The sensory receptors for hearing and balance are mechanotransducing hair cells (Elliott et al., 2018). Apart from sensory hair cells, the sensory epithelium consists of non-sensory supporting cells necessary for hair cells' development,

function, and maintenance. The sensory epithelia are innervated by neurons of the inner ear of two different ganglia, the vestibular and spiral ganglia. The vestibular ganglion is located in the lateral portion of the internal auditory meatus, with the superior division innervating the utricle, the superior semi-circular canal, and the lateral semi-circular canal, while the inferior region of the vestibular ganglion innervates the saccule and the posterior semi-circular canal (Khan and Chang, 2013). The auditory spiral ganglion twists along the length of the cochlear duct with peripheral neuronal processes innervating hair cells within the auditory sensory epithelium and central axons merging into the cochlear nerve (Pavlinkova, 2020). These inner ear neurons transmit received information from the sensory cells to the central nervous system.

All sensory organs of the inner ear and its associated sensory ganglia derive from a single embryonic source, the otic placode. Neurons seem to be the first differentiated cells in the developing inner ear in all species examined (Fritzsch and Straka, 2014). The initial specification of the neuroblasts within the otic epithelium is followed by the delamination of neuroblasts as early as embryonic day nine (E9) in the mouse embryo. The neuronal cells form the inner ear ganglion, later separating into the vestibular and spiral ganglia between E9.5 and E14.5 (Ma et al., 2000). Cells fated to develop as sensory hair cells and supporting cells of the sensory epithelia arise from the prosensory domain of the otocyst (Wu and Kelley, 2012). Deciphering the developmental mechanisms of these specialized neurosensory cells of the inner ear is a central focus of cell-based therapy strategies.

The development of sensory hair cells, neurons, and non-sensory cells in the inner ear is regulated by a network of signaling pathways and transcription factors. Proneural atonal-related basic helix-loop-helix (bHLH) transcription factors, ATOH1, NEUROGENIN1 (NEUROG1), and NEUROD1, are critical players in inner ear development. ATOH1 is essential for sensory cell differentiation (Bermingham et al., 1999). NEUROG1, the first bHLH factor upregulated in the otocyst, initiates the specification and differentiation of inner ear neurons (Ma et al., 2000). *Neurog1* null mice lack inner ear neurons and have a massive loss of sensory epithelia through the alteration of *Atoh1* expression (Ma et al., 2000; Matei et al., 2005; Kim et al., 2001).

Additionally, NEUROG1 activates the expression of the downstream bHLH gene, *Neurod1*, which is essential for neuronal differentiation (Kim et al., 2001). *Neurod1* null mice exhibit severely impaired differentiation of auditory and vestibular neurons (Liu et al., 2000a; Kim et al., 2001) but they also suffer from other neuronal developmental defects (Miyata et al., 1999; Liu et al., 2000b) and a severe diabetic phenotype (Kim et al., 2001). Therefore, conditional *Neurod1* deletion mutants were generated to investigate more specifically its role in inner ear neuronal development and hearing function. Conditional $Pax2^{Cre}$; $Neurod1^{f/f}$ deletion mice showed abnormalities in the formation of inner ear ganglia, disorganized cochlear innervation, and unsegregated vestibular and spiral ganglion afferents (Jahan et al., 2010a). Unfortunately, $Pax2^{Cre}$; $Neurod1^{f/f}$ mice have *Neurod1* deletion in the ear and the central auditory nuclei, limiting the evaluation of spiral ganglion neuronal viability and central projections and hampering physiological assessment of the wiring defects. Furthermore, $Pax2^{Cre}$ activity decreases with age, starting at E10.5 and producing uneven deletion effects (Duncan and Fritzsch, 2013). A delayed conditional *Neurod1* deletion using $Isl1^{Cre}$ eliminates *Neurod1* from differentiating inner ear neurons and retains *Neurod1* expression in the auditory nuclei and midbrain (Macova et al., 2019). The $Isl1^{Cre}$; $Neurod1^{f/f}$ mutants form the unsegregated and disorganized peripheral projection map of spiral ganglion neurons with altered sensory information processing in the central auditory pathway (Macova et al., 2019; Filova et al., 2020). However, detailed insights into the effects of an early absence of *Neurod1* in otic neuroblasts are lacking.

To go beyond existing data and reveal the dependency of early neuronal development on the otocyst-expressed NEUROD1 protein, we chose the $Foxg1^{Cre}$ transgene to eliminate *Neurod1*. $Foxg1^{Cre}$ has been demonstrated to lead to earlier and more profound recombination than other Cre drivers expressed in the ear placode and the developing ear (Duncan and Fritzsch, 2013; Dvorakova et al., 2020). $Foxg1^{Cre}$ is not expressed in the auditory and vestibular nuclei to possibly affect neuronal viability in the inner ear (Hébert and McConnell, 2000; Bérubé et al., 2005; Kasberg et al., 2013; Abrams and Reiter, 2021). In this study, we revisited the embryonic phenotype of *Neurod1* deletion mice to determine NEUROD1 requirements for the generation and survival of neuroblasts and, overall, for early inner ear development.

MATERIAL AND METHODS

Experimental Animals

All experiments with mice were approved by the Animal Care and Use Committee of the Institute of Molecular Genetics, Czech Academy of Sciences. Animals were housed in a controlled environment with 12-h light/dark cycles and free access to water and food. For obtaining the mouse model with conditional deletion of *Neurod1*, we crossbred $Foxg1^{Cre/+}$ knock-in/knock-out mice ($129(Cg)\text{-}Foxg1^{tm1(cre)Skm}/J$; #004337 The Jackson Laboratory) with mice carrying the *Neurod1* gene flanked by loxP sites ($Neurod1^{loxP/loxP}$ (Goebbels et al., 2005)). Mice were genotyped using DNA isolated from the tail. The following PCR primers were used: Cre Forward 5′-GCC TGC ATT ACC GGT CGA TGC AAC GA-3′ and Cre Reverse 5′-GTG GCA GAT GGC GCG GCA ACA CCA TT-3′ with a 700 bp product; Neurod1 Forward 5′-ACC ATG CAC TCT GTA CGC ATT-3′ and Neurod1 Reverse 5′-GAG AAC TGA GAC ACT CAT CTG-3′ with a 400 bp product for the WT allele or 600 bp for the allele containing loxP sites. The noon of the day the vaginal plug was found was defined as embryonic day 0.5 (E0.5). Mice of both sexes were used for experiments.

Morphological Evaluation of the Inner Ear, Cochlear Nucleus, and Inferior Colliculus

Pregnant mice were sacrificed at noon, and embryos or dissected embryonic tissues were then fixed in 4% paraformaldehyde (PFA) in phosphate-buffered saline (PBS). Neonates were transcardially perfused with PBS followed by 4% PFA. Brains and inner ear were dissected from the skull and fixed in 4% PFA. For longtime

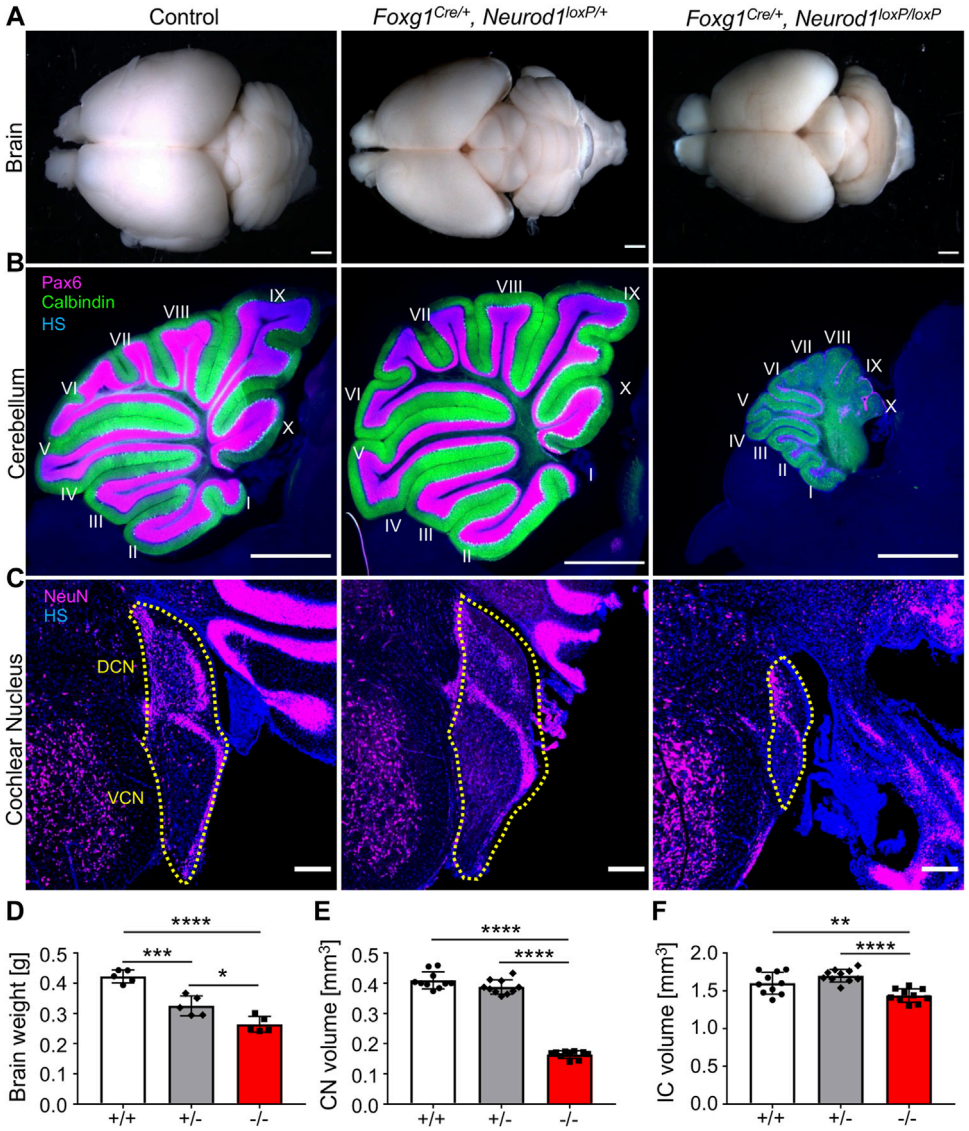

FIGURE 1 | Brain abnormalities are detected in *Neurod1CKO* mutants. **(A,D)** Adult brain size was reduced in *Foxg1*$^{Cre/+}$, *Neurod1*$^{loxP/+}$ heterozygotes (+/–) and *Foxg1*$^{Cre/+}$, *Neurod1*$^{loxP/loxP}$ homozygous (–/–) mutants compared to controls. **(B)** The *Neurod1CKO* cerebellum was smaller with many Purkinje cells (Calbindin^{+}) but with fewer granule cells (Pax6^{+}). **(C,E,F)** The cochlear nucleus's size and inferior colliculus were significantly reduced in *Neurod1CKO* mutants compared to controls and heterozygotes. The dotted line indicates the boundaries of the cochlear nucleus. The values represent means ± SD, one-way ANOVA, $^{*}p \leq 0.05$, $^{**}p \leq 0.01$, $^{***}p \leq 0.001$, $^{****}p \leq 0.0001$. Scale bars: 1,000 µm **(A,B)**; 200 µm **(C)**. CN, cochlear nucleus; DCN, dorsal cochlear nucleus; HS, Hoechst nuclear staining; IC, inferior colliculus; VCN, ventral cochlear nucleus.

storage, tissues were kept in methanol at −20°C. Embryos or tissues were stained as whole mounts or 80-µm vibratome sections (Leica VT1000 S). Samples were blocked in a blocking solution consisting of 2.5% donkey or goat serum, 0.5% Tween20, and 0.1% Triton X-100 for at least 1 h at room temperature. Next, samples were incubated with primary antibodies (**Supplementary Table S1**) diluted in blocking solution for 72 h at 4°C. After several washes with PBS, samples were incubated with secondary antibodies (**Supplementary Table S1**) for 24 h at 4°C. Finally, cell nuclei were labeled with Hoechst 33258 (Merck 861405; always showed as blue staining) diluted 1:2000 in PBS. After staining, samples were mounted in Aqua-Poly/Mount (Polysciences 18606) or prepared an anti-fade medium. Images were taken on Zeiss LSM 880 NLO inverted confocal microscope and Nikon CSU-W1 spinning disk confocal microscope. NIS-Elements, ImageJ, and ZEN software were used for image processing.

The area of the inner ear ganglion at E10.5 was determined as ISL1^{+} area in 80-µm vibratome transverse sections of the embryo (dotted area). For quantification, sections with the two largest areas containing the inner ear ganglion were picked for each embryo, and outliers were excluded (n = 10 embryos/genotype; 16

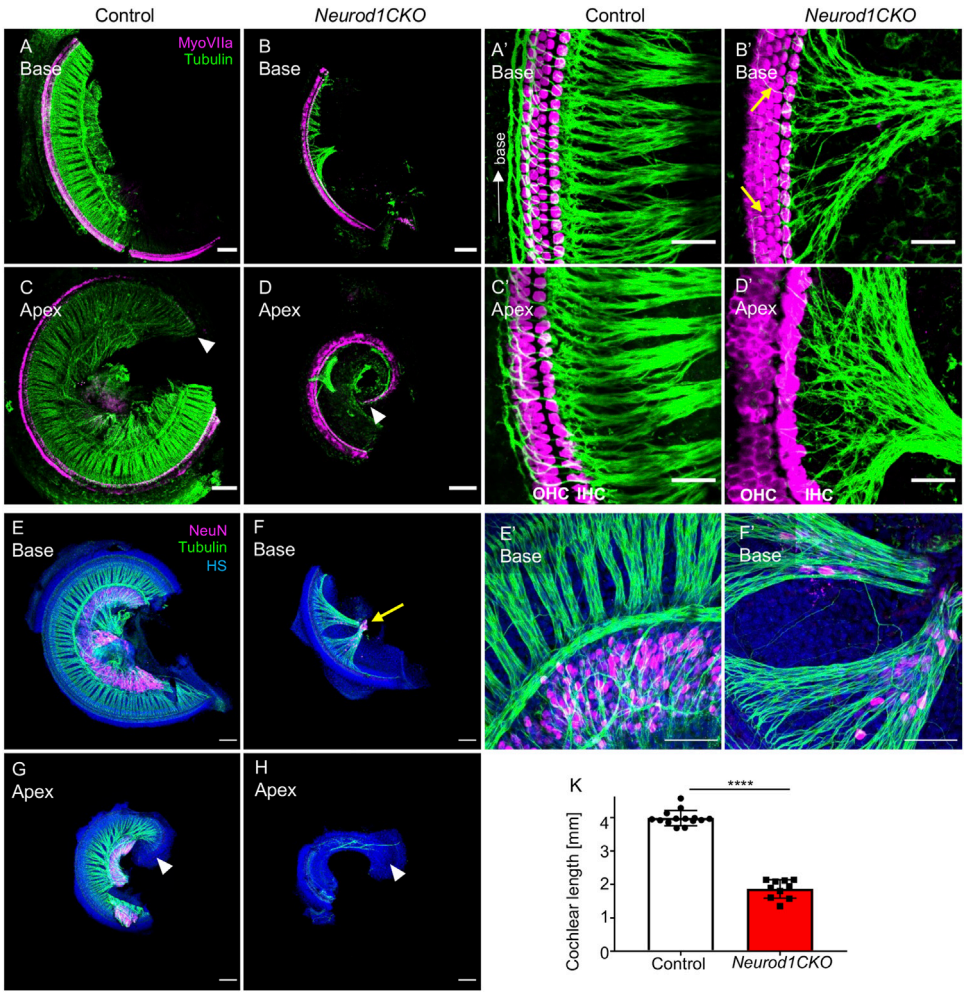

FIGURE 2 | The elimination of *Neurod1* results in the rudimental spiral ganglion, disorganized sensory epithelium, and the shortened cochlea. **(A–D)** Representative images of whole-mount immunolabeling of the cochlear base and apex with anti-MyosinVIIa (MyoVIIa, a marker of hair cells) and anti-α-tubulin (nerve fibers) at E18.5. Arrowheads indicate the apical end. **(A'–D')** Higher-magnification images show a dense network of radial fibers, three rows of outer hair cells (OHC), and one row of inner hair cells (IHC), forming the organ of Corti in the control cochlea. Note the formation of parallel outer spiral bundles turned toward the base in the control cochlea (arrow in **A'**). In *Neurod1CKO*, radial fibers are severely reduced and disorganized, turning randomly towards the base or apex (arrows in **B'**). The increased number of OHC rows in the apex indicates the disorganized sensory epithelium of the *Neurod1CKO* cochlea (**D'**). **(E–H)** The cochlea's whole-mounted basal and apical half immunolabeled with anti-NeuN (a nuclear marker of differentiated neurons) and anti-tubulin (nerve fibers) shows $NeuN^+$ neurons forming spiral ganglion in control at P0. In contrast, only a small cluster of $NeuN^+$ neurons is found in the *Neurod1CKO* cochlea (arrow in **F**). Note the reduced size of the cochlea and massive reduction of innervation. **(E', F')** Higher-magnification images of the base show the aberrant distribution of $NeuN^+$ neurons entangled with radial fibers in *Neurod1CKO* compared to the spiral ganglion neurons restricted to the Rosenthal's canal in the control cochlea. **(K)** The length of the organ of Corti is significantly shorter in *Neurod1CKO* compared to control littermates. Error bars represent mean ± SD; unpaired *t*-test, $^{****}p \leq 0.0001$ ($n \geq 5$/genotype). Scale bars: 100 μm **(A–H)**, 25 μm **(A'–D')**, 50 μm **(E',F')**. HS, Hoechst nuclear staining.

sections/genotype). In the area of inner ear ganglion, $ISL1^+$ cells were counted in the same sections using the Cell Counter ImageJ plugin. For quantifying proliferation and apoptosis, anti-Phospho-Histone H3 and Cleaved Caspase3 antibodies were used, respectively. Phospho-Histone H3 or Cleaved Caspase3 positive cells were counted in the $ISL1^+$ ganglion area in vibratome sections at E10.5. For each genotype two sections per embryo were selected (n = 5 embryos/genotype). We compared the size of E18.5 auditory and vestibular organs between controls and mutants. Inner ear whole mounts were stained with an antibody against hair cell marker, MyosinVIIa. The cochlear length was established as a line between inner and outer hair cells from the apical tip to the base. The length of the organ of Corti was measured using the "Measure line" ImageJ plugin. The size of the vestibular organ epithelium was measured using immunolabeling of the $MyosinVIIa^+$ area using "Polygon selection," and "Measure" functions of ImageJ. Volumes of the cochlear nucleus (CN) and inferior colliculus (IC) were determined by using 80-μm coronal brain sections (n = 5 brains/genotype). The areas of the left and right CNs and ICs were measured in all sections, and the total volume of the brain structures was calculated. $Parvalbumin^+$ bushy cells were counted

in 80-μm vibratome sections (image view 134.95 × 134.95 μm) of adult VCN (two sections/one animal and four animals/genotype). Number of parvalbumin$^+$ bushy cells per measured area of VCN was determined. To quantify endbulbs of Held, we used vibratome sections of the adult VCN. Three cells with the visually largest VGLUT1$^+$ area were selected and measured in each section (two sections/one animal and four animals/genotype). The VGLUT1$^+$ area of the synapse was determined per the bushy cell area.

Lipophilic Dye Tracing

Heads of P0 pups were fixed in 4% PFA in 0.1 M phosphate buffer with 300 mM sucrose (to minimize neuronal swelling) for 48 h at 4°C and processed for dye tracing. To trace projections of the ear to the brain, we used NeuroVue dyes (NV Jade, NVJ; NV Red, NVR) as previously described (Fritzsch et al., 2016; Schmidt and Fritzsch, 2019). Lipophilic dyes were applied using dye-soaked filter strips, which provide a more precise and reliable dye application than crystals or dye-injections (Schmidt and Fritzsch, 2019). For tracing inner ear central projections to the brain, the dye was placed into the inner ear to label the spiral ganglion, organ of Corti, and vestibular neurons. The dye was allowed to diffuse for 24–72 h, depending on the embryonic age and dye. Mutant and control samples were always processed in parallel, with an identical dye placement and dye diffusion time. Brains and ears were subsequently microdissected, mounted in glycerol, and imaged using a Leica SP8 confocal microscope. After imaging, some brains and ears were post-fixed in 4% PFA and either processed for immunohistochemistry (*see* above) or sectioned at 100-μm, mounted in glycerol, and imaged to reveal the distribution of projections in sections.

Scanning Electron Microscopy

Inner ears devoid of cartilage were fixed in 2.5% glutaraldehyde and 2% formaldehyde in 1×PHEM buffer at °C overnight. After that, tissues were washed with 1×PHEM buffer a few times, dehydrated in graded ethanol series, and finally transferred into 100% acetone and dried to a critical point in Leica CPD300 with CO_2. The dried samples were mounted on regular SEM stubs using conductive carbon and coated with 7 nm of platinum in Leica ACE600. The images were taken using a dual-beam system FEI Helios NanoLab 660 G3 UC scanning electron microscope at 2 kV and 0.2 nA with an Everhart-Thornley secondary electron detector.

Experimental Design and Statistical Analysis

All comparisons were made between animals with the same genetic background, typically littermates, and we used male and female mice. The number of samples (*n*) for each comparison can be found in the individual method descriptions and in the corresponding figures. Phenotyping and data analysis was performed blind to the genotype of the mice. All values are presented either as the mean ± standard deviation (SD) or standard error of the mean (SEM). For statistical analysis, GraphPad Prism software was used. The differences in the mean were compared using unpaired two-tailed *t*-test or one-way ANOVA tests for statistical evaluation. Significance was determined as $p < 0.05$ (*), $p < 0.01$ (**), $p < 0.001$ (***) or $p < 0.0001$ (****). Complete results of the statistical analyses are included in the figure legends.

RESULTS

Neurod1 Mutants Have Reduced Body Size and Vestibular Dysfunction

Neurod1 was eliminated by crossing *Neurod1*$^{loxP/loxP}$ mice (Goebbels et al., 2005) with *Foxg1*$^{Cre/+}$ line (Hébert and McConnell, 2000), which has efficient Cre activity during early ear development, starting in the otic placode (Dvorakova et al., 2020). We confirmed *Foxg1*^{Cre} expression in sensory cells and neurons in the inner ear using *tdTomatoAi14* reporter mice (**Supplementary Figures S1A,B**). Foxg1^{Cre} activity was undetectable in the cochlear nucleus, showing no tdTomato expression in neurons of the cochlear nucleus (**Supplementary Figures S1C,D**). Homozygous mutant embryos (*Neurod1CKO*; genotype *Foxg1*$^{Cre/+}$, *Neurod1*$^{loxP/loxP}$) were recovered at the expected Mendelian ratios at all embryonic days examined *in utero* (**Supplementary Figure S2A**), suggesting no effect of *Neurod1* elimination on embryonic survival. However, postnatal development of homozygous *Neurod1CKO* and heterozygous (*Foxg1*$^{Cre/+}$, *Neurod1*$^{loxP/+}$) mutants was reduced (**Supplementary Figure S2B**), with fewer mice identified at the time of genotyping (3 weeks of age) compared to control mice (without Cre allele, genotypes: *Foxg1*$^{+/+}$, *Neurod1*$^{loxP/+}$ or *Foxg1*$^{+/+}$, *Neurod1*$^{loxP/loxP}$). *Neurod1CKO* mice were born significantly smaller than their littermates (**Supplementary Figure S2C**), indicating abnormalities during embryonic development. *Neurod1CKO* failed to thrive from birth to weaning with significant deficits in body size and body weight compared to controls at postnatal day P21. *Neurod1CKO* mice suffered from severe ataxia (**Supplementary Movie**), and due to rapid deterioration, had to be sacrificed 3–4 weeks after birth. Surprisingly, the decreased gene dose of *Neurod1* in heterozygous mutant mice negatively affected their postnatal development. Although these mice did not present any signs of ataxia, they were significantly smaller than controls.

To investigate the reduced postnatal survival of homozygous and heterozygous *Neurod1* mutants, we first evaluated changes in the brain since *Foxg1*^{Cre} is highly expressed in the forebrain. Correspondingly, the size of the forebrain was visibly more petite, and the weight of the brain was significantly reduced in both homozygous and heterozygous *Neurod1* mutants compared to controls (**Figures 1A,D**). The size and morphology of the cerebellum and the size of the cochlear nucleus were exclusively affected only in *Neurod1CKO* mutants (**Figures 1B,C,E,F**). Analysis of the gross external morphology of born pups showed no abnormalities in an eye formation, in a shape of the forehead or the snout (**Supplementary Figure S2D**). *Foxg1*^{Cre} is expressed in the olfactory system and eye (Dvorakova et al., 2020), but the aspects of the olfactory epithelium and retina of the visual system were comparable between control and *Neurod1CKO* (**Supplementary Figure S3**). Our results confirmed the previous study's conclusions that NEUROD1 is

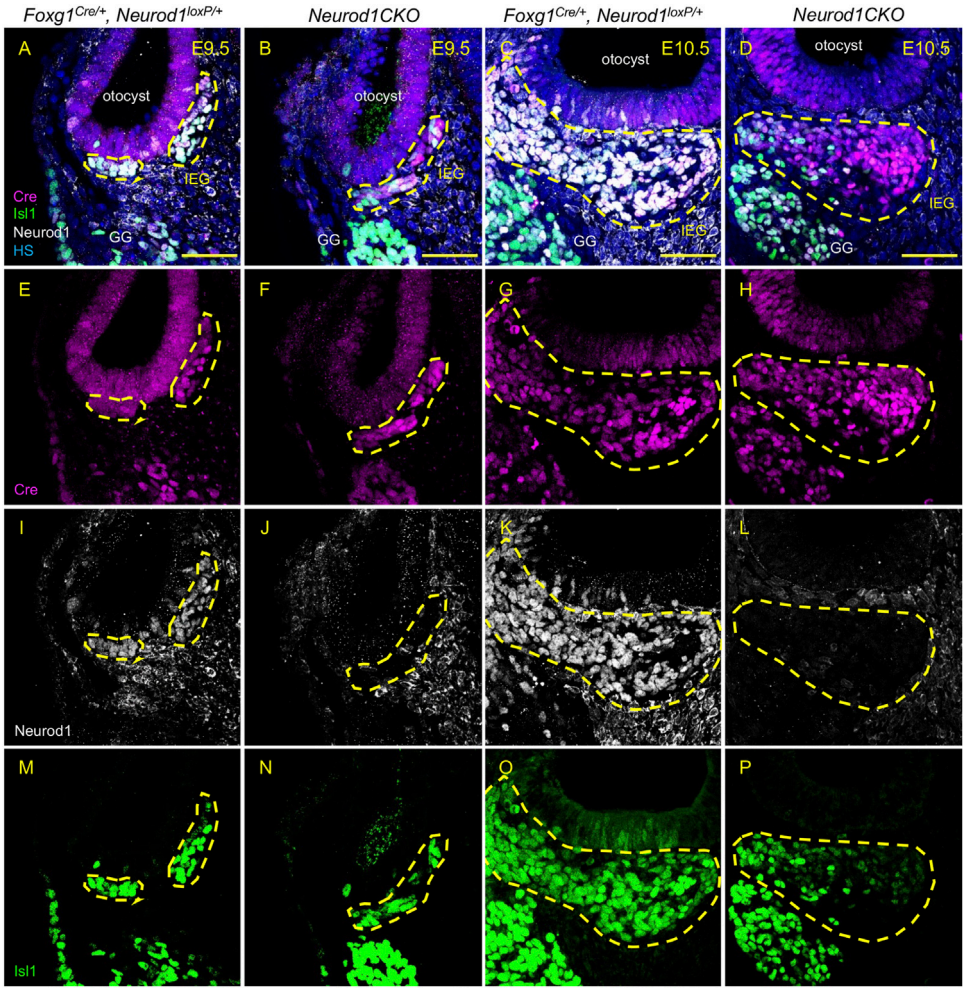

FIGURE 3 | Efficient elimination of *Neurod1* by Foxg1-Cre is shown in delaminating neuroblasts and the inner ear ganglion. Cre recombinase (red) was detected as early as E9.5 in mouse *Foxg1*$^{Cre/+}$ otocyst **(A**,**B**,**E**,**F)**. Neurod1 (white) is eliminated using Foxg1^{Cre} in mutants at E9.5 **(J)** as well as at E10.5 **(L)**, while in controls, NEUROD1 is expressed in delaminating neurons **(I**,**K)** that are co-labeled by Isl1 antibody (green; **M**–**P**). The area of the inner ear ganglion is delineated by the dotted line. Scale bars: 50 μm. GG, geniculate ganglion; HS, Hoechst nuclear staining; IEG, inner ear/otic ganglion.

not required for eye (Pennesi et al., 2003) and olfactory embryonic development (Packard et al., 2011).

Reduced Sensory Epithelia and a Severe Loss of Spiral Ganglion Neurons are Found in the *Neurod1CKO* Inner Ear

Next, we evaluated the inner ear morphology of heterozygous and homozygous *Neurod1* mutants. Radial fibers, spiral ganglion, and the organ of Corti of heterozygous *Foxg1*$^{Cre/+}$, *Neurod1*$^{loxP/+}$ mice were comparable to the morphology of the control cochlea (**Supplementary Figure S4**). The formation and size of sensory epithelia of the vestibular-end organs and innervation of Foxg1$^{Cre/+}$, *Neurod1*$^{loxP/+}$ were also similar to control mice. Thus, the normal inner ear morphology and the normal vestibular behavior indicate that eliminating one *Neurod1* allele did not affect the inner ear development of the heterozygous *Neurod1* mutant. In contrast, the cochlea of *Neurod1CKO* was severely shortened, with the length of the organ of Corti reaching only 47% of the littermate control at E18.5 (**Figures 2A–D,K**). Besides the length of the cochlea, the most noticeable deficiency in *Neurod1CKO* was a reduction of radial fibers. Higher-magnification images showed substantially decreased and disorganized innervation of the sensory epithelium with a few fibers of outer spiral bundles turning randomly toward the base or apex (**Figure 2B'**) compared to dense parallel outer spiral bundles directed toward the base in the control cochlea (**Figure 2A'**). Additionally, abnormalities in the apical epithelium of *Neurod1CKO* with multiple hair cell rows were noticeable compared to the control cochlea (**Figures 2C,D**). Correspondingly, all sensory epithelia of the vestibular end-organs of *Neurod1CKO* were significantly reduced compared to controls (**Supplementary Figure S5**).

In line with severe reduction of innervation in the *Neurod1CKO* cochlea, we found only a rudiment of the spiral

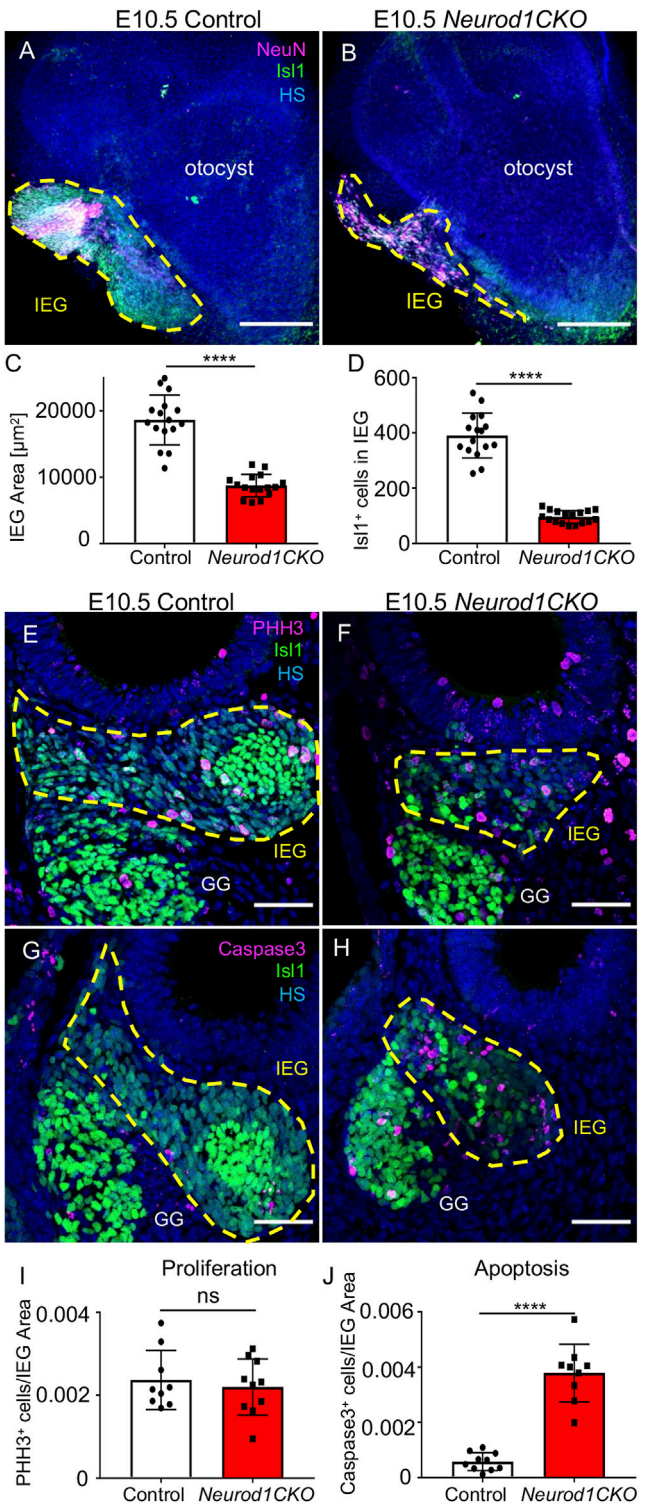

FIGURE 4 | Diminished inner ear ganglion and massive apoptosis are detected in *Neurod1CKO* at E10.5. **(A,B)** Representative whole-mount immunolabeling of the otocyst shows the size of otic ganglia (dotted line area) with anti-Isl1 and anti-NeuN (a nuclear marker of neurons). **(C,D)** Quantification of the ganglion size and number of ISL1$^+$ neurons in the inner ear ganglion. The values represent mean ± SD, *t*-test, ****$p \leq 0.0001$ ($n = 10$ embryos/genotype, 16 vibratome sections/embryo). **(E,F)** Immunohistochemistry for Phosphohistone H3 (PHH3) and ISL1 shows proliferating neurons in the otic ganglion (dotted line area) in the vibratome sections of *Neurod1CKO* and control embryos. **(G,H)** Anti-Cleaved Caspase3-labeled apoptotic cells are shown in the ISL1$^+$ ganglion area (delineated by the dotted line) at E10.5. **(I)** A number of proliferating neurons and **(J)** apoptotic neurons per the ganglion area were counted in the vibratome sections of *Neurod1CKO* and control embryos. The values represent means ± SD, *t*-test; ns, not significant; ****$p \leq 0.0001$ ($n = 5$ embryos/genotype). Scale bars: 200 µm **(A,B)**; 50 µm **(E–H)**. GG, geniculate ganglion; HS, Hoechst nuclear staining; IEG, inner ear/otic ganglion.

ganglion at P0, represented by a clump of NeuN$^+$ neurons (**Figures 2F,H**), compared to the spiral ganglion neurons located in the Rosenthal's spiral canal in controls (**Figures 2E,G**). In contrast to controls, some NeuN$^+$ neurons were entangled with fibers in the *Neurod1CKO* cochlea (**Figures 2E',F'**). Some of these fibers were type Ia neuron afferents, as shown by anti-calretinin labeling of the cochlea in adult mice (**Supplementary Figure S6**). Thus, these results indicate a significant loss of neurons, severe abnormalities in the formation of the spiral ganglion and innervation.

Early Inner Ear Neuronal Development Is Altered in *Neurod1CKO*

Having recognized a severe loss of neurons of *Neurod1CKO*, we wanted to determine the effects of *Neurod1* elimination on early inner ear development. First, we determined the efficiency and relative onset of *Neurod1* deletion in the otocyst of *Neurod1CKO*. We could not detect any NEUROD1 expressing cells in the ear epithelium or any NEUROD1$^+$ delaminating neuroblasts in *Neurod1CKO* at E9.5 and E10.5 (**Figure 3**). The elimination of NEUROD1 protein was consistent with the regional expression of Cre recombinase under *Foxg1*. ISL1 expressing neurons were detected in the otic ganglion of *Neurod1CKO*. However, the number of ISL1$^+$ cells was noticeably reduced as early as E9.5, indicating a negative effect of *Neurod1* elimination on early neurogenesis in the inner ear. Note the decreased ISL1$^+$ neuroblasts in the epithelium of the *Neurod1CKO* otocyst compared to the control. Second, we measured the size of the inner ear ganglion. The *Neurod1CKO* ganglion was reduced by 53% compared to control embryos at E10.5 (**Figures 4A–D**). The number of neurons expressing ISL1 in *Neurod1CKO* was decreased on average by about 80% (96 ± 5, $n = 10$ embryos) compared to controls (390 ± 20, $n = 10$ embryos). Interestingly, the number of proliferating cells in the ganglion was similar between the control and *Neurod1CKO* inner ear (**Figures 4E,F,I**). However, we detected massive apoptosis in neurons of the *Neurod1CKO* ganglion. The number of apoptotic cells was six times higher in the mutant than in the control otic ganglion (**Figures 4G,H,J**). These results indicate that NEUROD1 is important for neurogenesis and neuronal survival in the early stages of inner ear neuronal development.

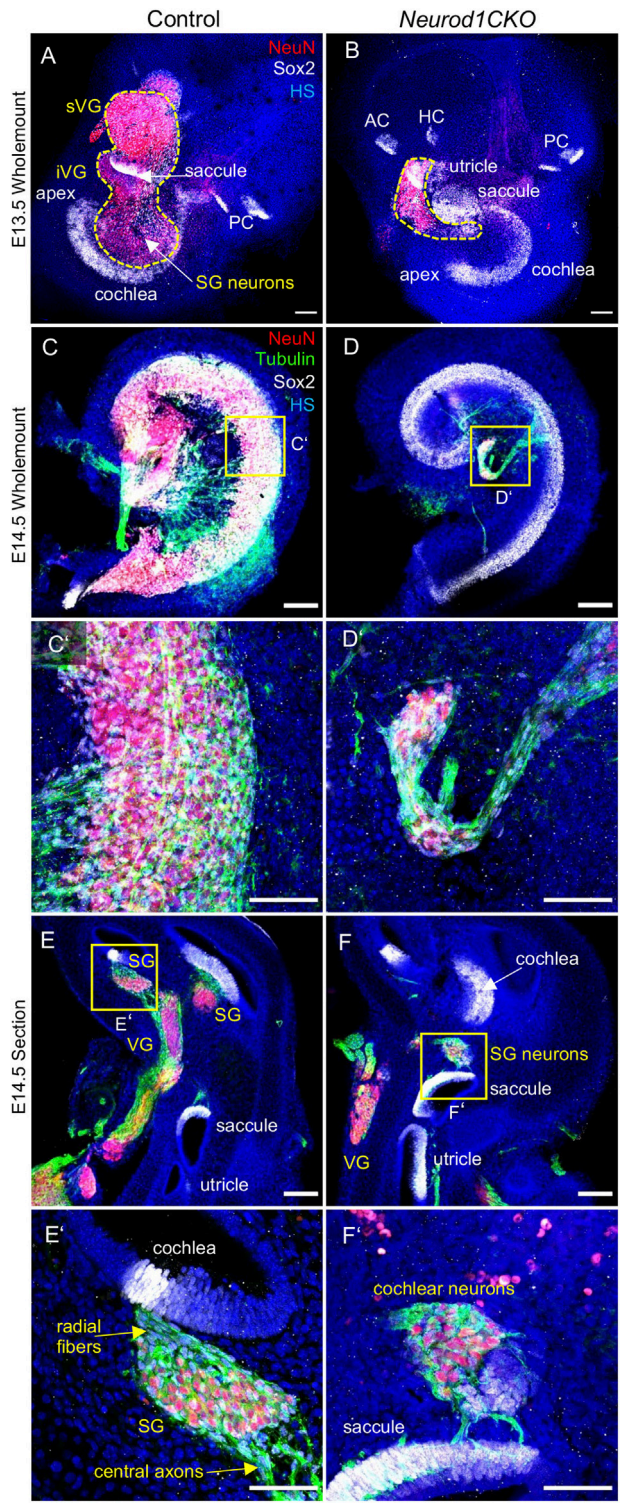

FIGURE 5 | The ganglion formation in the *Neurod1CKO* cochlea is severely disrupted. **(A,B)** Representative images of whole-mounted inner ear labeled by anti-NeuN (a marker of differentiated neurons) and SOX2 (a marker of sensory epithelial and glial cells). The dashed line delineates the VG and SG areas containing neurons. **(C,D,C',D')** At E14.5, cochlear neurons form the SG along with the sensory cells of the organ of Corti in the control (*Continued*)

FIGURE 5 | cochlea. In contrast, neurons in the *Neurod1CKO* cochlea form a rudimental ganglion located far off the organ of Corti and project unusual long fibers to the sensory epithelium. **(E,F)** The section of the inner ear show distribution of neurons in the VG and SG and the location of sensory epithelia. **(E',F')** Higher-magnification images show SG neurons projecting radial fibers towards the sensory epithelium and central axons in the control inner ear. In *Neurod1CKO,* cochlear neurons project aberrant fibers toward the sensory epithelium of the saccule. Scale bars: 100 μm **(A–F)**, 50 μm **(C'–F')**. AC, anterior crista; HC, horizontal crista; HS, Hoechst nuclear staining; PC, posterior crista; SG, spiral ganglion; VG, vestibular ganglion; iVG, inferior vestibular ganglion; sVG, superior vestibular ganglion.

Depleted Inner Ear Neurons of *Neurod1CKO* Form an Aberrant Cochlear and Vestibular Ganglia

After a period of proliferation, all inner ear neurons undergo terminal mitosis, begin to differentiate and extend their processes to the peripheral and central targets (Pavlinkova, 2020). By E13.5, sensory neurons cease to proliferate as the last spiral ganglion neurons exit the cell cycle in the apex, and thus, the final number of neurons of the mouse inner ear is established (Matei et al., 2005). The superior and inferior vestibular ganglia in the control inner ear were segregated, and the cochlear neurons formed a spiral along the sensory epithelia at E13.5 (**Figure 5A**). In contrast, the number of neurons in *Neurod1CKO* was severely reduced, forming a diminished vestibular ganglion and a rudiment of the cochlear ganglion near the saccule and cochlear base (**Figure 5B**). The abnormalities in neuronal development were even more apparent in the *Neurod1CKO* cochlea at E14.5. The spiral ganglion neurons were in the Rosenthal's canal, extending projections, and located near the $SOX2^+$ sensory epithelium in the control cochlea (**Figures 5C,C'**). In the *Neurod1CKO*, $SOX2^+$ sensory cells formed the spiral, whereas a few residual cochlear neurons were in the modiolus away from the epithelium (**Figures 5D,D'**). These misplaced neurons formed projections towards the cochlea's sensory epithelium and the saccule (**Figures 5F,F'**). No such projections were distinguished in the control inner ear (**Figures 5E,E'**). Unusual connections of these residual neurons were further explored by dye tracing analyses with dyes applied to the vestibular end-organ, the utricle, and to the cochlear apex (**Figure 6**). Double-labeling shows unique bundles of overlapping projections in *Neurod1CKO* (white fibers) labeled in the apex and utricle that reach the middle organ of Corti with a few branches extending to the base and the saccule (**Figures 6C,D**). An aberrant *Neurod1CKO* ganglion positioned next to the saccule contained double-labeled neurons projecting to the cochlear apex and the utricle. Vestibular and cochlear neurons can be identified based on their characteristic soma size. At P0, most neurons in the vestibular ganglion have an average size ~90 μm^2 with many of these neurons larger than 200 μm^2, in contrast, most spiral ganglion neurons are ~25 μm^2 (Huang et al., 2001). A remnant of vestibular ganglion ("spiro-vestibular" ganglion) contained double-labeled neurons and a mixture of vestibular neurons (larger size soma) and cochlear neurons with noticeable

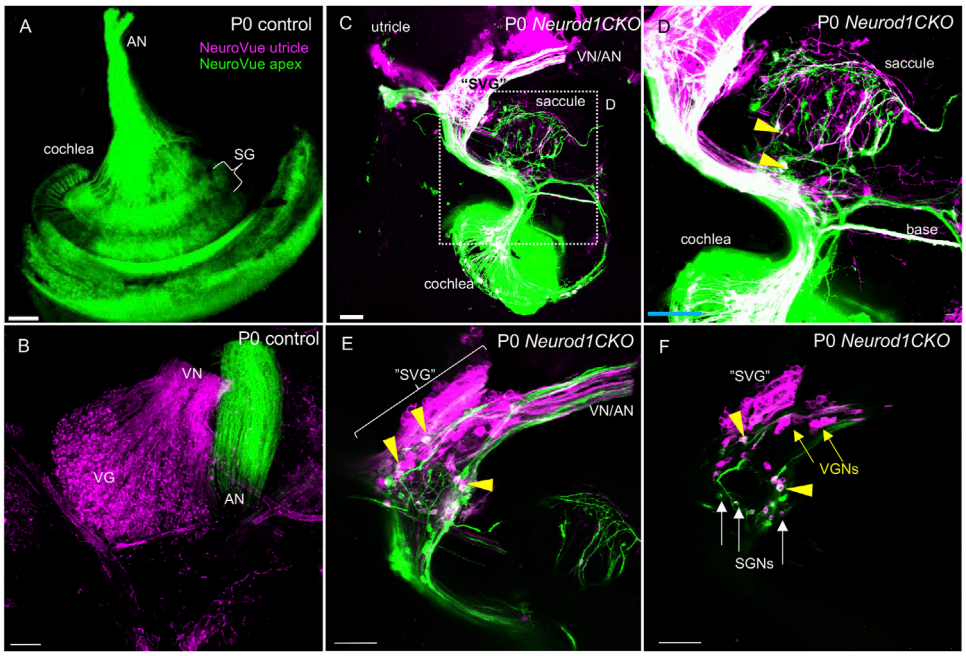

FIGURE 6 | Unsegregated inner ear neurons interconnect sensory epithelia of the auditory and vestibular peripheral organs in *Neurod1CKO*. **(A,B)** A NeuroVue dye labeling from the utricle (magenta) and apex (green) shows restricted labeling in the cochlea, auditory nerve (AN), and vestibular ganglion neurons in the vestibular ganglion of control mice. **(C,D)** A similar dye application shows a unique pattern of double-labeled bilateral projections to reach saccule, base, and apex in *Neurod1CKO*. Note double-labeled neurons (arrowheads). **(E)** A larger magnification image shows the aberrant "spiro-vestibular" ganglion ("SVG") containing a mix of neurons labeled by dyes applied to the apex and utricle in *Neurod1CKO*. Arrowheads indicate double labeled neurons with projections reaching the utricle and cochlear apex. Note unsegregated axons of vestibular and auditory neurons. **(F)** A representative one z-stack image of "SVG" shows a clutter of larger-size vestibular ganglion neurons (VGNs, arrows) with smaller-size cochlear neurons (SGNs, arrows), and double-labeled neurons (arrowheads). Scale bars: 100 μm. SG, spiral ganglion; SGNs, spiral ganglion neurons; VG, vestibular ganglion; VN, vestibular nerve.

smaller size soma in *Neurod1CKO* (**Figures 6E,F**) in contrast to the vestibular ganglion of control mice with neurons exclusively labeled by utricle-dye applications (**Figure 6B**).

Elimination of *Neurod1* Affects Central Projections of Inner Ear Neurons

The cochlear nucleus is the first auditory nucleus in the brain, where the auditory nerve fibers project. Although *Foxg1*^{Cre} is not expressed in the cochlear nucleus (**Supplementary Figure S1**), a substantial size reduction of the cochlear nucleus in *Neurod1CKO* indicates a secondary effect of reduced afferent input from the cochlea (**Figure 1E**). In line with reduced auditory afferents, we found significantly attenuated clusters of auditory-nerve endbulbs of Held that wrap the somas of spherical bushy cells in the *Neurod1CKO* cochlear nucleus (**Figure 7**). A critical step in inner ear neurogenesis is the segregation of auditory and vestibular neurons into a spiral ganglion and vestibular ganglion and the segregation of the central projections (Dvorakova et al., 2020). Dye tracing analyses demonstrated disorganized and reduced central projections in the cochlear nucleus of *Neurod1CKO* compared to the segregated basal and apical projections in control mice (**Figures 8A,B**). Note the unusual projections from the apex near the cochlear nucleus entry area. Coronal sections of control mice showed clear segregation of the base and apex with minimal overlap (**Figure 8C**) in contrast to primarily overlapping and diminished basal and apical projections in the *Neurod1CKO* AVCN (**Figures 8D,D'**). Lipophilic NeuroVue dyes applied to the vestibular end-organs showed projections to the vestibular nuclei in the control brain (**Figure 8E**). Using single dye tracing, we showed that fibers labeled by dye application in the utricle reach both the cochlear nucleus (AVCN) and vestibular nuclei (LVN, SVN, MVN) in *Neurod1CKO* mice (**Figure 8F**), indicating an interconnection between the vestibular and auditory system.

Ectopic Hair Cells Are Formed in the *Neurod1CKO* Inner Ear

The development of sensory cells was disrupted by the elimination of *Neurod1,* indicated by significantly smaller vestibular end-organ sensory epithelia and a shorter organ of Corti in the cochlea (**Figure 2** and **Supplementary Figure S5**). Additionally, the cochlear sensory epithelium was disorganized. Immunolabeling with the inner hair cell (IHC) marker calretinin and prestin, a marker of outer hair cells (OHC), showed multiple OHC rows, transdifferentiated (ectopic) IHCs among OHCs, and two rows of IHCs in the adult apex of *Neurod1CKO* compared to three rows of OHCs and a single row of IHCs in control (**Figures 9C,D**). Missing OHCs were found in the *Neurod1CKO* base (**Figures 9A,B**). Scanning electron microscopy images demonstrated cellular abnormalities in the sensory epithelium

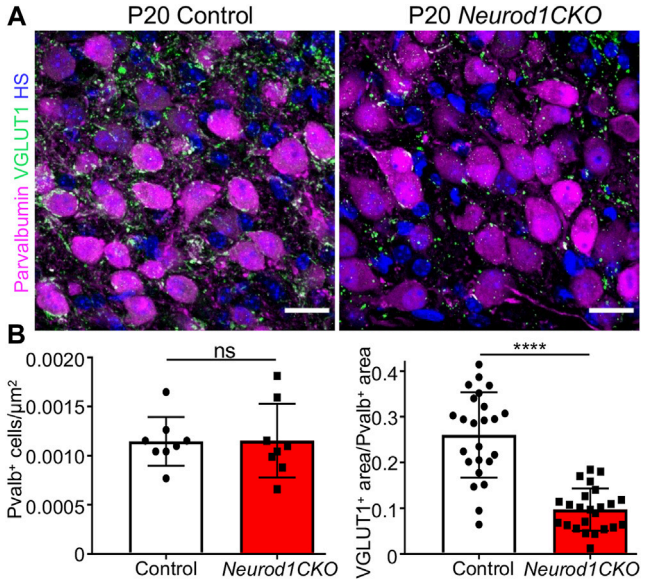

FIGURE 7 | Auditory afferent synapses are reduced in the anteroventral cochlear nucleus of *Neurod1CKO* adult mice. **(A)** Representative confocal images of anti-parvalbumin labeled spherical bushy cells and anti-VGLUT1 labeled auditory-nerve endings, endbulbs of Held, show a loss of auditory afferent synapses in *Neurod1CKO* that wrap the soma of bushy cells. **(B)** Quantification of spherical bushy cells (n = 4 mice/two sections/genotype) and VGLUT1$^+$ synapses per the parvalbumin$^+$ area (n = 4 mice/two sections/three cells per section/genotype). The values represent means ± SD, t-test; ns, not significant; ****$p \leq 0.0001$. Scale bars: 20 µm. HS, Hoechst nuclear staining.

of *Neurod1CKO*, indicating disrupted planar cell polarity (**Figures 9E,F**). An additional effect associated with *Neurod1* deficiency was a noticeable presence of ectopic hair cells located outside of sensory epithelia. Besides regular sensory epithelia containing MyosinVIIa expressing hair cells in the saccule, and IHCs and OHCs in the organ of Corti *Neurod1CKO* cochlea, extra ectopic MyosinVIIa positive cells were found near the saccule (**Figure 10A** and **Supplementary Figure S5B**) and in the cochlea, near the rudimental spiral ganglion (**Figures 10A,B**). Detailed images showed the distribution of ectopic hair cells intermingled with neuronal fibers, and some cells were double labeled by tubulin and MyosinVIIa (**Figures 10A',B'**). These topologically inappropriate "trans-fated" ectopic hair cells form a unique organization in the area of the two neuronal aggregations of vestibular and cochlear neurons, independent of known inner ear structures.

DISCUSSION

The focus of this study was to determine the requirements for NEUROD1 in the early neuronal development of the inner ear and processes that are affected by *Neurod1* elimination (**Figure 11**). NEUROD1, a bHLH transcription factor, is an essential factor for the lineage commitment and differentiation in various developmental systems, including gastrointestinal cells (Cherry et al., 2011), pancreas (Romer et al., 2019; Bohuslavova et al., 2021), brain (Miyata et al., 1999; Liu et al., 2000b; Hevner et al., 2006), and neurosensory organs (Liu et al., 2000a; Cherry et al., 2011). The main function of NEUROD1 in neurogenesis and the promotion of neuronal fate is supported by its ability to reprogram other somatic cells into neurons. For example, forced expression of *Neurod1* enhances neuronal conversion from human fibroblasts (Pang et al., 2011), and exogenous *Neurod1* expression converts mouse astrocytes to neurons (Guo et al., 2014). In the inner ear, neuronal development is initiated by the upregulation of *Neurog1* in the anteroventral quadrant of the otocyst. *Neurog1* is followed by the upregulation of *Neurod1* in the proneural domain of the otocyst, resulting in the delamination and migration of primary neuroblasts to the forming otic ganglion. Delaminating neuronal progenitors proliferate and differentiate to produce vestibular and auditory neurons between E9.5 to E13.5 (Matei et al., 2005).

In contrast to the *Neurog1* deletion mutant with no neurons found in the E10.5 otic ganglion (Ma et al., 1998) or any later stages of inner ear development (Liberman, 1991), some inner ear neurons differentiate and form peripheral and central projections in *Neurod1* null mice (Liu et al., 2000a; Kim et al., 2001). Previously, we generated a delayed *Neurod1* conditional deletion using *Isl1*^{Cre} that spares many cochlear and vestibular neurons, resulting in the near-normal vestibular behavior and partially preserved auditory system function (Macova et al., 2019). Similarly, *Pax2*^{Cre} is delayed and leaves many more neurons in conditional *Neurod1* deletion mice (Jahan et al., 2010a) relative to *Foxg1*^{Cre}, used in this study. Consequently, these phenotypes indicate a temporal effect of *Neurod1* elimination for the neuronal loss in the developing inner ear. However, mechanisms of neuronal loss due to the *Neurod1* elimination are not fully understood. Different mechanisms have been implicated in determining neuron quantities, including neuronal delamination, migration, proliferation, and survival. Our study revisited the major events of early neuronal development of the inner ear to address different regulatory functions and temporal requirements for NEUROD1.

Foxg1^{Cre} recombination occurs efficiently and invariably in the ear placode, forebrain, olfactory and pre-lens placodes, anterior optic vesicle, pharyngeal endoderm, and mid-hindbrain junction, matching the normal pattern of *Foxg1* expression (Dvorakova et al., 2020; Hébert and McConnell, 2000; Dastidar et al., 2011; Duggan et al., 2008; Shen et al., 2018; Panaliappan et al., 2018). A caveat must be considered in using *Foxg1*^{Cre} line. First, haploinsufficiency of the *Foxg1* gene due to a partial replacement of *Foxg1* coding sequences with the cre gene (Hébert and McConnell, 2000) is associated with impaired development of the telencephalon and microcephaly in heterozygous *Foxg1*$^{Cre/+}$ transgenic mice similar to the phenotype of heterozygous *Foxg1*$^{-/+}$ null mice (Shen et al., 2018; Frullanti et al., 2016; Eagleson et al., 2007; Kawaguchi et al., 2016). Correspondingly, a similar neurodevelopmental phenotype of a reduced size of the forebrain was found in our heterozygous *Foxg1*$^{Cre/+}$, *Neurod1*$^{loxP/+}$ mutants (**Figure 1**). Second, ectopic low levels of Cre activity have been reported due to genetic background effects (Hébert and McConnell, 2000;

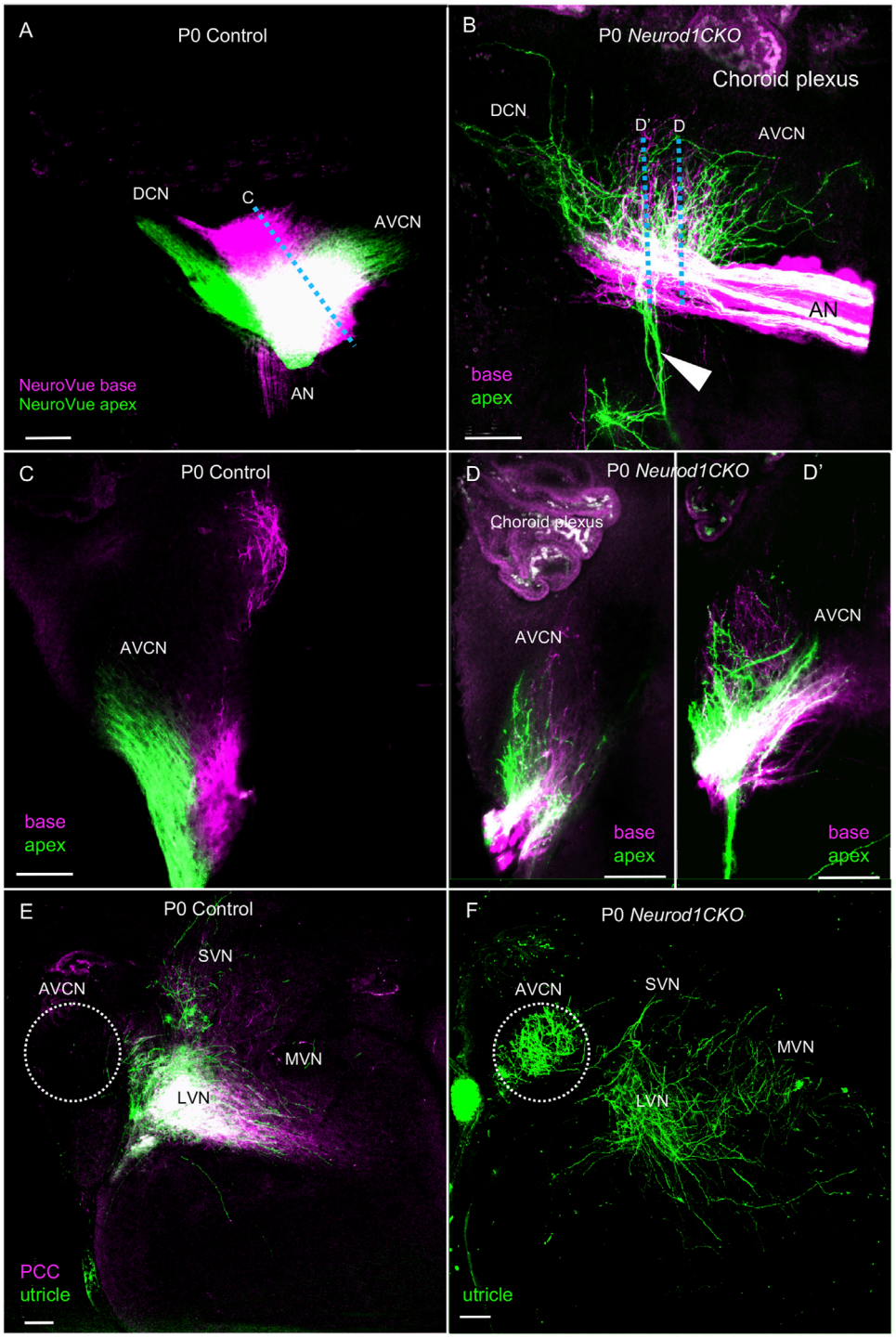

FIGURE 8 | Disorganized central projections of *Neurod1CKO* inner ear neurons show aberrant interconnections between the auditory and vestibular systems. **(A**,**B)** Lipophilic differently colored NeuroVue dyes were applied to the apex and base to label cochlear afferents. In the lateral view of the cochlear nucleus of the control, dye tracing shows the normal segregated basal and apical cochlear afferents of the auditory nerve and segregated projections to the AVCN and DCN. In contrast, reduced, disorganized, and overlapping central projections are shown in the cochlear nucleus of *Neurod1CKO* mice. Note unusual fibers from the apex projecting away from the cochlear nucleus and auditory nerve (arrowhead). **(C)** Coronal sections of control show the segregation of basal and apical afferents. **(D**,**D')** Sections of *Neurod1CKO* show an overlap of disorganized fibers from the apex and base. Dotted lines in corresponding figures indicate the section planes in **(A**,**B)**. **(E**,**F)** Dye tracing from the utricle and the posterior canal crista (PCC) shows vestibular afferents innervating the lateral, medial, and superior vestibular nuclei that are immediately adjacent to the AVCN in the control mice. A single dye tracing from the utricle shows vestibular afferents reach vestibular nuclei and form a profound projection to the AVCN in *Neurod1CKO* mice. The area of the AVCN is indicated by dotted circle. Scale bars: 100 μm. AN, auditory nerve; AVCN, anteroventral cochlear nucleus; DCN, dorsal cochlear nucleus; LVN, MVN, SVN, lateral, medial, and superior vestibular nuclei; VN, vestibular nerve.

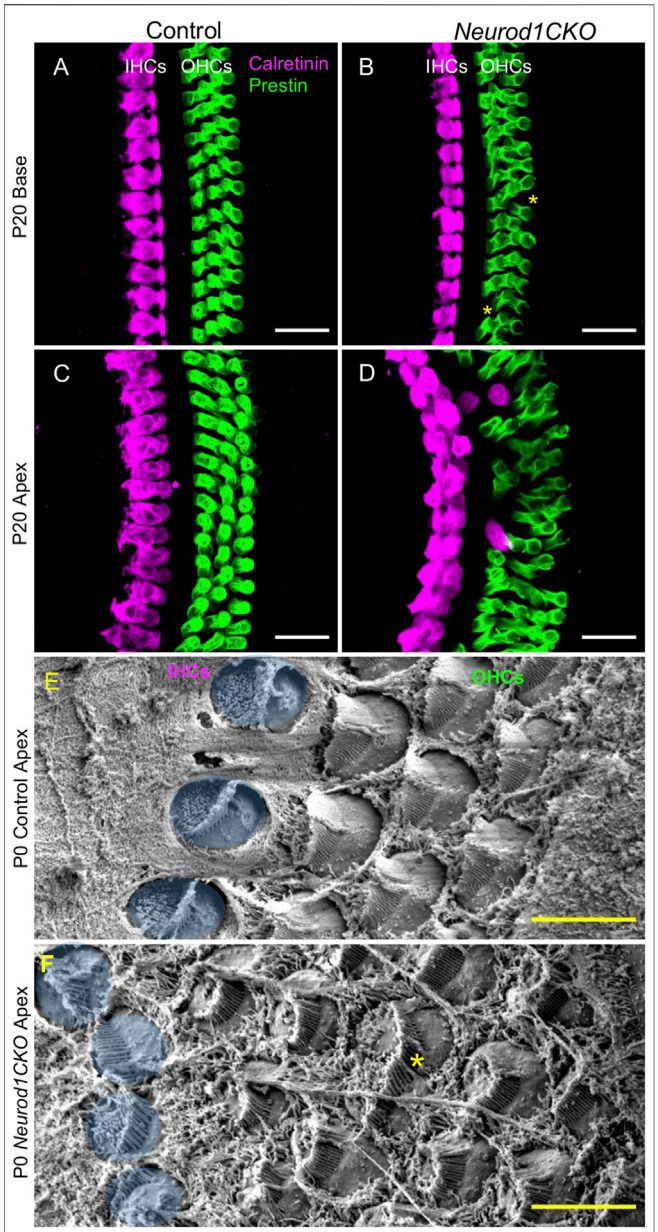

FIGURE 9 | The sensory epithelium of the cochlea is disorganized in *Neurod1CKO*. **(A–D)** In contrast to adult controls, the sensory epithelium in the base of *Neurod1CKO* has missing cells (asterisks), as shown by confocal images of immunolabeling with inner hair cell (IHC) marker calretinin and with prestin, a marker of outer hair cells (OHCs). Ectopic (transdifferentiated) IHCs located among OHCs, two IHC rows, and multiple OHC rows are found in the *Neurod1CKO* apex compared to the single row of IHCs and three rows of OHCs in control cochlea. **(E,F)** Scanning electron microscopy revealed abnormalities in the cellular characteristics and hair cell stereocilia organization in *Neurod1CKO*. Compared to the control epithelium, HCs in the *Neurod1CKO* cochlea differed in their size (asterisk marks a fused cell), the orientation of cells, and stereocilia. IHCs are pseudocoloured blue. Scale bars: 20 μm **(A–D)**; 5 μm **(E,F)**.

Ma et al., 2002). To confirm the scope of Cre activity in our model, we crossed *Foxg1*^{Cre} mice to a *tdTomatoAi14* reporter mouse strain. We verified Foxg1^{Cre}-mediated loxP recombination in the organ of Corti, spiral ganglion neurons, and the cerebellum of adult progeny recapitulating endogenous *Foxg1* expression (**Supplementary Figure S1**). We did not detect any Foxg1^{Cre} activity in the cochlear nucleus, showing no tdTomato expression in neurons of the cochlear nucleus. Because *Foxg1*^{Cre} is not expressed in the cochlear nucleus, the reduced size of the *Neurod1CKO* cochlear nucleus is exclusively an effect of diminished afferent input from spiral ganglion type I neurons, similar to cochlear ablation studies (Mostafapour et al., 2000).

We showed that early elimination of *Neurod1* affected delaminating and migrating ISL1^{+} neurons in the E9.5 and E10.5, resulting in a significantly smaller inner ear ganglion at E10.5 (**Figure 4**). One mechanism contributing to the diminished number of inner ear neurons in *Neurod1CKO* was massive apoptosis at E10.5, confirming that *Neurod1* is required for early neuronal survival (Liu et al., 2000a). In contrast, neuroblasts lacking *Neurod1* proliferate at a similar rate as neuronal precursors in control embryos, suggesting that NEUROD1 is not needed for the proliferation of neurons, at least in the E10.5 inner ear. Intriguingly, our data confirmed the initial finding in the global *Neurod1* deletion mutant (Liu et al., 2000a) that some inner ear neurons survive without *Neurod1*. One could speculate that the neurogenic fate commitment is predefined early in some Neurog1^{+} specified neuronal precursors ensuring terminal differentiation of these *Neurod1* null neurons. Alternatively, residual neurons might survive by compensatory activation of different transcription factor(s), such as GATA3 (Duncan and Fritzsch, 2013) or NHLH1/NHLH2 bHLH factors (Krüger et al., 2006).

Despite diminished neurogenesis, these *Neurod1* lacking neurons form inner ear ganglia, grow neuritic processes, establish bipolar connections to their targets, and persist up to the adulthood of *Neurod1CKO* mice. The formation of inner ear ganglia was considerably disrupted when the last sensory neurons undergo terminal mitosis, at E13.5 (Matei et al., 2005). The vestibular ganglion was diminished, and the spiral ganglion was represented by a small clump of neurons near the saccule in the *Neurod1CKO* inner ear (**Figure 5**). In addition to a significant loss of neurons, the rudiment of the spiral ganglion was misplaced away from the sensory epithelium in the *Neurod1CKO* cochlea, indicating migration defects. Cochlear neurons found in the aberrant vestibular ganglion ("spiro-vestibular" ganlion) of *Neurod1CKO* further corroborate abnormalities in inner ear neurons' migration (**Figure 6**). The remaining neurons projected disorganized peripheral fibers, with some neurons forming unusual peripheral projections connecting the cochlea and the vestibular end-organs. The central projections of our *Neurod1CKO* mutant are primarily identical to central projection abnormalities in various *Neurod1* deletion mutants (Kim et al., 2001; Jahan et al., 2010a; Macova et al., 2019; Filova et al., 2020). Mainly, central projections of cochlear and vestibular neurons are reduced, unsegregated, and disorganized. Using our *Neurod1* mutant, we showed, for the first time, central projections from vestibular neurons reached the cochlear nucleus, the first processing station in the central auditory system (**Figure 8**). Consistently with the aberrant migration and disorganized innervation phenotypes of *Neurod1* mutants, NEUROD1

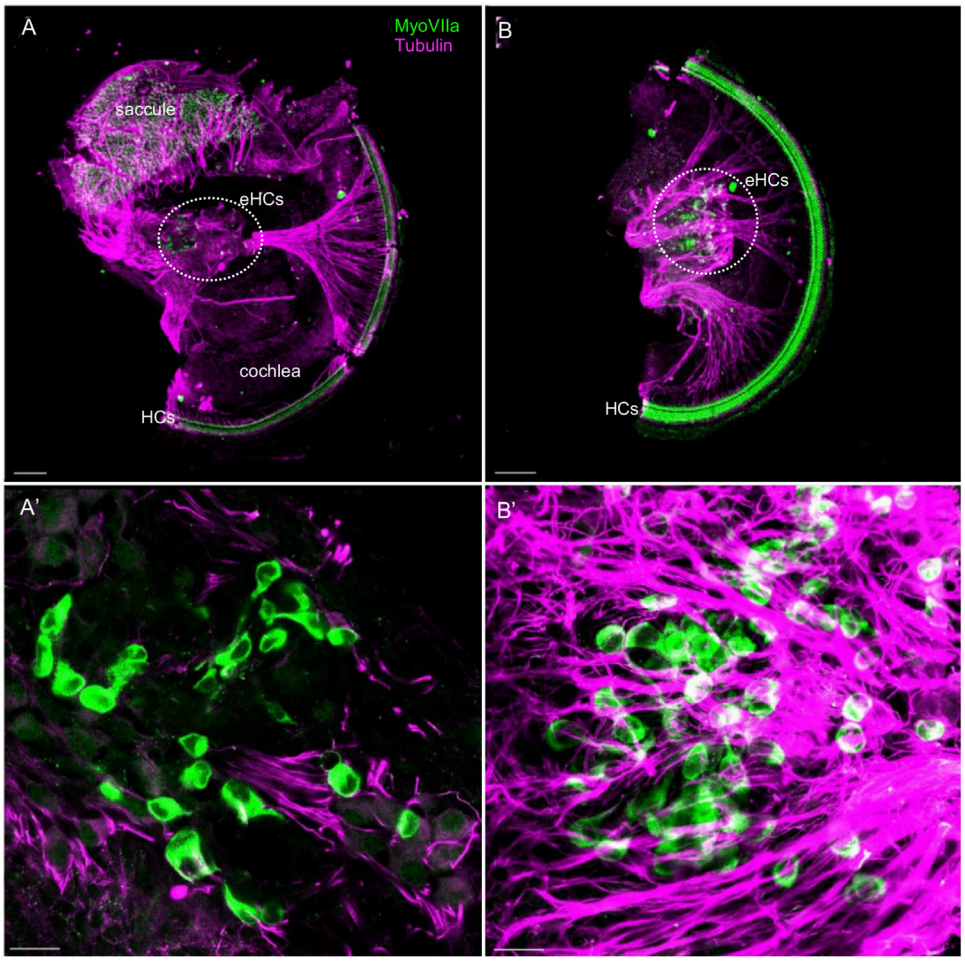

FIGURE 10 | Ectopic hair cells differentiate outside the sensory epithelia in the *Neurod1CKO* inner ear. Representative images of whole mount immunolabeling with MyosinVIIa (MyoVII, a marker of hair cells) and tubulin (neuronal fibers) show hair cells in the saccule and rows of hair cells forming the organ of Corti in the *Neurod1CKO* cochlea. Ectopic MyoVIIa positive cells (eHCs) are found near the saccule and the aberrant cochlear ganglion (a dotted line delineates the area). Larger magnification images show eHCs entangled with neuronal fibers, and some cells are double-labeled for tubulin and MyoVIIa. Scale bars: 100 μm **(A,B)**; 20 μm **(A',B')**.

orchestrates transcriptional networks regulating axon guidance, neurite growth, cell migration, and adhesion in post-mitotic inner ear neurons (Filova et al., 2020).

In addition to neuronal phenotypes, *Neurod1* deletion affects the development of inner ear sensory organs (Kim et al., 2001; Macova et al., 2019; Filova et al., 2020; Jahan et al., 2010b). Like other *Neurod1* deletion mutants, due to $Foxg1^{Cre}$ activity in the sensory precursors, we were unable to uncouple secondary effects of *Neurod1* deletion in inner ear neurons on sensory cell development. The elimination of *Neurod1* affects the size of inner ear sensory epithelia and the differentiation and organization of apical epithelium in the cochlea. Nevertheless, some effects are more pronounced in our *Neurod1CKO* than in delayed *Neurod1* mutants suggesting a temporal dependency of *Neurod1* elimination. Particularly, the truncated cochlea of *Neurod1CKO* reached 47% length of the control cochlea compared to 60% of the cochlea of mice with delayed *Neurod1* mutation (Macova et al., 2019). We also found a more profound formation of ectopic myosin VIIa positive hair cells near the two remaining neuronal aggregations of vestibular and cochlear sensory neurons (**Figure 10**) compared to the *Neurod1* conditional mutation generated by $Pax2^{Cre}$ (Jahan et al., 2010b). Previous work identified a set of upregulated genes in the absence of *Neurod1*, particularly *Atoh1*, *Fgf8,* and *Nhlh2* (Jahan et al., 2010b), suggesting that some neuronal precursors adopt a hair cell fate and differentiate as hair cells (Fritzsch and Elliott, 2017; Elliott et al., 2021). Taken together, NEUROD1 mediates a neuronal program and promotes neuronal fate by the upregulation of downstream targets and through suppression of other bHLH genes such as *Atoh1*. Another possible role of NEUROD1 in neurogenesis and neurogenic competence may be reprograming of the epigenome in the developing inner ear (Matsuda et al., 2019). Further experiments will be necessary to investigate how NEUROD1 mediates transcriptional and possibly epigenetic networks during neuronal development in the inner ear. By understanding the interplay of NEUROD1 regulatory

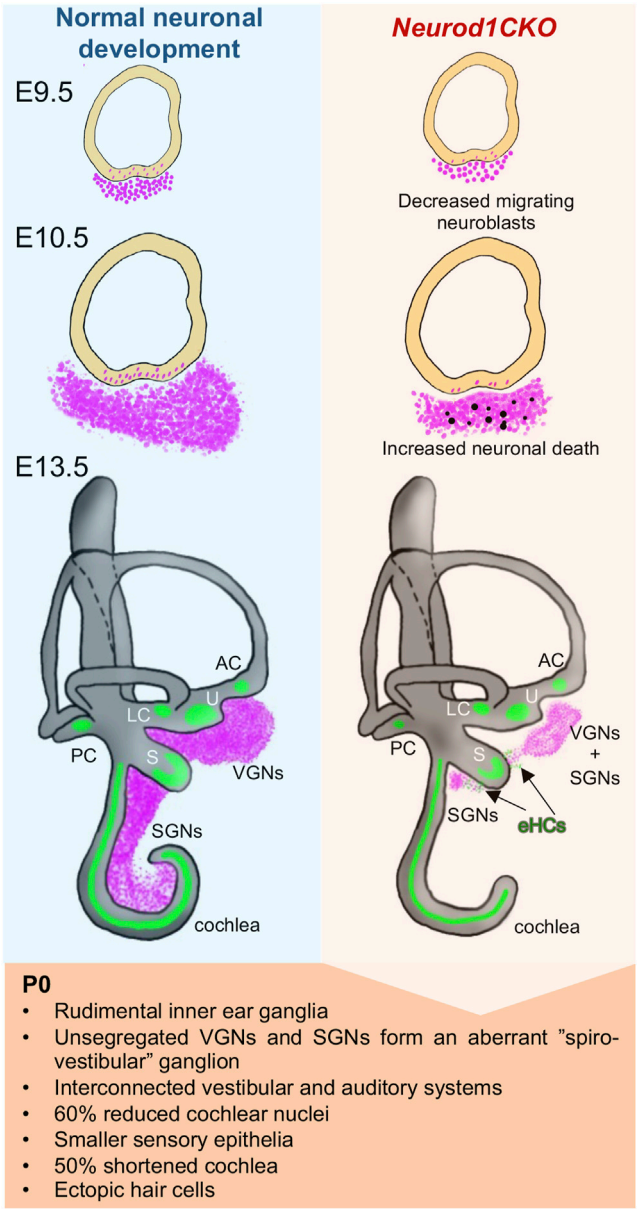

FIGURE 11 | Schematics of changes induced by the elimination of *Neurod1* in the inner ear. Absence of *Neurod1* results in reduced delamination and increased apoptosis of neuroblasts at E10.5. Remaining post-mitotic neurons form a misplaced rudimental spiral ganglion and diminished vestibular ganglion ("spiro-vestibular" ganglion), containing unsegregated vestibular and cochlear neurons that extend unsegregated peripheral and central projections, resulting in circuits interconnecting peripheral sensory organs and brain nuclei of both the auditory and vestibular systems. The reduced afferent input from the cochlea affects the size of the cochlear nucleus of the brain stem in *Neurod1CKO* mice. Additionally, *Neurod1* elimination results in smaller sensory epithelia, a loss of more than the half size of the cochlea, disorganization of sensory cells, multiple rows of inner and outer hair cells, trans-differentiation of outer hair cells in the apex, and generation of ectopic hair cells (eHCs) in the areas of inner ear ganglia.

networks capable of initiating cell-fate changes, we hope to develop efficient therapeutic strategies to restore and regenerate neurons for clinical applications.

A crucial role of NEUROD1 in neurogenesis and neuronal differentiation in the inner ear is conserved across vertebrates, as shown by studies in chicken (Evsen et al., 2013), *Xenopus laevis* (Schlosser and Northcutt, 2000), and zebrafish (Schwarzer et al., 2020). These studies also provide significant insights into the role of NEUROD1 as a neurogenic programing factor. For example, ectopic expression of *Neurod1* is sufficient to mediate neurogenesis in the chicken developing inner ear (Evsen et al., 2013). In zebrafish, the expression of *Neurod1* is maintained in progenitor cells in a neurogenic niche that are expected to contribute to neuronal regeneration in the adult zebrafish statoacoustic ganglion (Schwarzer et al., 2020). Understanding a role of NEUROD1 in neurogenesis of species that can produced neurons throughout life and regenerate damaged neurons can provide significant insights into the rekindling of regeneration in the mammalian inner ear. An importance of NEUROD1 as a neurogenic reprograming factor is supported by *in vivo* studies utilizing *Neurod1* to produce functional neurons by reprograming astrocytes (Guo et al., 2014; Brulet et al., 2017). A reprogramming cells within the auditory system is considered a promising way to cure hearing loss (Meas et al., 2018).

CONCLUDING REMARKS

Our findings provide insights into the temporal requirements for NEUROD1 during inner ear development. In early neuronal development, we demonstrated that NEUROD1 is necessary for the generation and survival of neuronal precursors, as the absence of *Neurod1* results in massive apoptosis of E10.5 neuroblasts. In later neuronal development of post-mitotic neurons, *Neurod1* is critical for segregating neurons of the vestibular and auditory systems, migration, and formation of peripheral and central projections of these neurons. Understanding how neuronal fate is promoted within the nervous system and how neural circuit assemblies are organized has essential implications for cell-based therapy.

DATA AVAILABILITY STATEMENT

The original contributions presented in the study are included in the article/**Supplementary Material**, further inquiries can be directed to the corresponding author.

ETHICS STATEMENT

The animal study was reviewed and approved by the Animal Care and Use Committee of the Institute of Molecular Genetics, Czech Academy of Sciences.

AUTHOR CONTRIBUTIONS

GP and BF designed and supervised the experiments. IF, RB, MT, EY, and BF performed experiments and analyzed the data. IF prepared the first draft of the manuscript. GP, EY, and BF

reviewed the manuscript. All authors read and approved the final manuscript.

FUNDING

This research was supported by the Czech Science Foundation (20-06927S to GP), by PPLZ, the Czech Academy of Sciences (L200972052 to IF); by the institutional support of the Czech Academy of Sciences (RVO: 86652036 to GP), and NIH/NIA (R01 AG060504, DC016099, AG051443 to BF and EY).

ACKNOWLEDGMENTS

We acknowledge the Animal facility Czech Centre for Phenogenomics at the Institute of Molecular Genetics supported by the Czech Academy of Sciences RVO 68378050 and by the project LM2018126 by the MEYS CR; and Imaging Methods Core Facility at BIOCEV supported by the MEYS CR (Large RI Project LM2018129 Czech-BioImaging) and ERDF (project No. CZ.02.1.01/0.0/0.0/18_046/0016045) for its support with obtaining imaging data presented in this paper. Thank M. Anderova, Institute of Experimental Medicine CAS, for the reporter mouse line *Ai14* and A. Pavlinek (King's College London) for editing the MS.

SUPPLEMENTARY MATERIAL

The Supplementary Material for this article can be found online at: https://www.frontiersin.org/articles/10.3389/fcell.2022.845461/full#supplementary-material

REFERENCES

Abrams, S. R., and Reiter, J. F. (2021). Ciliary Hedgehog Signaling Regulates Cell Survival to Build the Facial Midline. *Elife* 10, e68558. doi:10.7554/elife.68558

Bermingham, N. A., Hassan, B. A., Price, S. D., Vollrath, M. A., Ben-Arie, N., Eatock, R. A., et al. (1999). Math1 : An Essential Gene for the Generation of Inner Ear Hair Cells. *Science* 284, 1837–1841. doi:10.1126/science.284.5421.1837

Bérubé, N. G., Mangelsdorf, M., Jagla, M., Vanderluit, J., Garrick, D., Gibbons, R. J., et al. (2005). The Chromatin-Remodeling Protein ATRX Is Critical for Neuronal Survival During Corticogenesis. *J. Clin. Invest.* 115, 258–267. doi:10.1172/jci200522329

Bohuslavova, R., Smolik, O., Malfatti, J., Berkova, Z., Novakova, Z., Saudek, F., et al. (2021). NEUROD1 Is Required for the Early Alpha and Beta Endocrine Differentiation in the Pancreas. *Int. J. Mol. Sci.* 22, 6713. doi:10.3390/ijms22136713

Brulet, R., Matsuda, T., Zhang, L., Miranda, C., Giacca, M., Kaspar, B. K., et al. (2017). NEUROD1 Instructs Neuronal Conversion in Non-reactive Astrocytes. *Stem Cel Rep.* 8, 1506–1515. doi:10.1016/j.stemcr.2017.04.013

Cherry, T. J., Wang, S., Bormuth, I., Schwab, M., Olson, J., and Cepko, C. L. (2011). NeuroD Factors Regulate Cell Fate and Neurite Stratification in the Developing Retina. *J. Neurosci.* 31, 7365–7379. doi:10.1523/jneurosci.2555-10.2011

Dastidar, S. G., Landrieu, P. M. Z., and D'Mello, S. R. (2011). FoxG1 Promotes the Survival of Postmitotic Neurons. *J. Neurosci.* 31, 402–413. doi:10.1523/jneurosci.2897-10.2011

Duggan, C. D., DeMaria, S., Baudhuin, A., Stafford, D., and Ngai, J. (2008). Foxg1 Is Required for Development of the Vertebrate Olfactory System. *J. Neurosci.* 28, 5229–5239. doi:10.1523/jneurosci.1134-08.2008

Duncan, J. S., and Fritzsch, B. (2013). Continued Expression of GATA3 Is Necessary for Cochlear Neurosensory Development. *PLoS One* 8, e62046. doi:10.1371/journal.pone.0062046

Dvorakova, M., Macova, I., Bohuslavova, R., Anderova, M., Fritzsch, B., and Pavlinkova, G. (2020). Early Ear Neuronal Development, but Not Olfactory or Lens Development, Can Proceed Without SOX2. *Dev. Biol.* 457, 43–56. doi:10.1016/j.ydbio.2019.09.003

Eagleson, K. L., Schlueter McFadyen-Ketchum, L. J., Ahrens, E. T., Mills, P. H., Does, M. D., Nickols, J., et al. (2007). Disruption of Foxg1 Expression by Knock-In of Cre Recombinase: Effects on the Development of the Mouse Telencephalon. *Neuroscience* 148, 385–399. doi:10.1016/j.neuroscience.2007.06.012

Elliott, K. L., Fritzsch, B., and Duncan, J. S. (2018). Evolutionary and Developmental Biology Provide Insights into the Regeneration of Organ of Corti Hair Cells. *Front Cel Neurosci* 12, 252. doi:10.3389/fncel.2018.00252

Elliott, K. L., Pavlínková, G., Chizhikov, V. V., Yamoah, E. N., and Fritzsch, B. (2021). Development in the Mammalian Auditory System Depends on Transcription Factors. *Ijms* 22, 4189. doi:10.3390/ijms22084189

Evsen, L., Sugahara, S., Uchikawa, M., Kondoh, H., and Wu, D. K. (2013). Progression of Neurogenesis in the Inner Ear Requires Inhibition of Sox2 Transcription by Neurogenin1 and Neurod1. *J. Neurosci.* 33, 3879–3890. doi:10.1523/jneurosci.4030-12.2013

Filova, I., Dvorakova, M., Bohuslavova, R., Pavlinek, A., Elliott, K. L., Vochyanova, S., et al. (2020). Combined Atoh1 and Neurod1 Deletion Reveals Autonomous Growth of Auditory Nerve Fibers. *Mol. Neurobiol.* 57, 5307–5323. doi:10.1007/s12035-020-02092-0

Fritzsch, B., Duncan, J. S., Kersigo, J., Gray, B., and Elliott, K. L. (2016). Neuroanatomical Tracing Techniques in the Ear: History, State of the Art, and Future Developments. *Springer*, 243–262. doi:10.1007/978-1-4939-3615-1_14

Fritzsch, B., and Elliott, K. L. (2017). Gene, Cell, and Organ Multiplication Drives Inner Ear Evolution. *Dev. Biol.* 431, 3–15. doi:10.1016/j.ydbio.2017.08.034

Fritzsch, B., Pan, N., Jahan, I., Duncan, J. S., Kopecky, B. J., Elliott, K. L., et al. (2013). Evolution and Development of the Tetrapod Auditory System: An Organ of Corti-Centric Perspective. *Evol. Dev.* 15, 63–79. doi:10.1111/ede.12015

Fritzsch, B., and Straka, H. (2014). Evolution of Vertebrate Mechanosensory Hair Cells and Inner Ears: Toward Identifying Stimuli that Select Mutation Driven Altered Morphologies. *J. Comp. Physiol. A.* 200, 5–18. doi:10.1007/s00359-013-0865-z

Frullanti, E., Amabile, S., Lolli, M. G., Bartolini, A., Livide, G., Landucci, E., et al. (2016). Altered Expression of Neuropeptides in FoxG1-Null Heterozygous Mutant Mice. *Eur. J. Hum. Genet.* 24, 252–257. doi:10.1038/ejhg.2015.79

Goebbels, S., Bode, U., Pieper, A., Funfschilling, U., Schwab, M. H., and Nave, K.-A. (2005). Cre/loxP-mediated Inactivation of the bHLH Transcription Factor Gene NeuroD/BETA2. *Genesis* 42, 247–252. doi:10.1002/gene.20138

Goodrich, L. V. (2016). Early Development of the Spiral Ganglion, the Primary Auditory Neurons of the Mammalian Cochlea. *Springer* 1, 11–48. doi:10.1007/978-1-4939-3031-9_2

Guo, Z., Zhang, L., Wu, Z., Chen, Y., Wang, F., and Chen, G. (2014). In Vivo Direct Reprogramming of Reactive Glial Cells into Functional Neurons After Brain Injury and in an Alzheimer's Disease Model. *Cell Stem Cell* 14, 188–202. doi:10.1016/j.stem.2013.12.001

Hébert, J. M., and McConnell, S. K. (2000). Targeting of Cre to the Foxg1 (BF-1) Locus Mediates loxP Recombination in the Telencephalon and Other Developing Head Structures. *Dev. Biol.* 222, 296–306. doi:10.1006/dbio.2000.9732

Hevner, R. F., Hodge, R. D., Daza, R. A. M., and Englund, C. (2006). Transcription Factors in Glutamatergic Neurogenesis: Conserved Programs in Neocortex, Cerebellum, and Adult hippocampus. *Neurosci. Res.* 55, 223–233. doi:10.1016/j.neures.2006.03.004

Huang, E. J., Liu, W., Fritzsch, B., Bianchi, L. M., Reichardt, L. F., and Xiang, M. (2001). Brn3a Is a Transcriptional Regulator of Soma Size, Target Field Innervation and Axon Pathfinding of Inner Ear Sensory Neurons. *Development* 128, 2421–2432. doi:10.1242/dev.128.13.2421

Jahan, I., Kersigo, J., Pan, N., and Fritzsch, B. (2010). Neurod1 Regulates Survival and Formation of Connections in Mouse Ear and Brain. *Cell Tissue Res* 341, 95–110. doi:10.1007/s00441-010-0984-6

Jahan, I., Pan, N., Kersigo, J., and Fritzsch, B. (2010). Neurod1 Suppresses Hair Cell Differentiation in Ear Ganglia and Regulates Hair Cell Subtype Development in the Cochlea. *PLoS One* 5, e11661. doi:10.1371/journal.pone.0011661

Kasberg, A. D., Brunskill, E. W., and Steven Potter, S. (2013). SP8 Regulates Signaling Centers During Craniofacial Development. *Dev. Biol.* 381, 312–323. doi:10.1016/j.ydbio.2013.07.007

Kawaguchi, D., Sahara, S., Zembrzycki, A., and O'Leary, D. D. M. (2016). Generation and Analysis of an Improved Foxg1-IRES-Cre Driver Mouse Line. *Dev. Biol.* 412, 139–147. doi:10.1016/j.ydbio.2016.02.011

Khan, S., and Chang, R. (2013). Anatomy of the Vestibular System: A Review. *Nre* 32, 437–443. doi:10.3233/nre-130866

Kim, W. Y., Fritzsch, B., Serls, A., Bakel, L. A., Huang, E. J., Reichardt, L. F., et al. (2001). NeuroD-null Mice Are Deaf Due to a Severe Loss of the Inner Ear Sensory Neurons During Development. *Development* 128, 417–426. doi:10.1242/dev.128.3.417

Krüger, M., Schmid, T., Krüger, S., Bober, E., and Braun, T. (2006). Functional Redundancy of NSCL-1 and NeuroD during Development of the Petrosal and Vestibulocochlear Ganglia. *Eur. J. Neurosci.* 24, 1581–1590. doi:10.1111/j.1460-9568.2006.05051.x

Liberman, M. C. (1991). The Olivocochlear Efferent Bundle and Susceptibility of the Inner Ear to Acoustic Injury. *J. Neurophysiol.* 65, 123–132. doi:10.1152/jn.1991.65.1.123

Liu, M., Pereira, F. A., Price, S. D., Chu, M.-j., Shope, C., Himes, D., et al. (2000). Essential Role of BETA2/NeuroD1 in Development of the Vestibular and Auditory Systems. *Genes Dev.* 14, 2839–2854. doi:10.1101/gad.840500

Liu, M., Pleasure, S. J., Collins, A. E., Noebels, J. L., Naya, F. J., Tsai, M.-J., et al. (2000). Loss of BETA2/NeuroD Leads to Malformation of the Dentate Gyrus and Epilepsy. *Proc. Natl. Acad. Sci.* 97, 865–870. doi:10.1073/pnas.97.2.865

Ma, L., Harada, T., Harada, C., Romero, M., Hebert, J. M., McConnell, S. K., et al. (2002). Neurotrophin-3 Is Required for Appropriate Establishment of Thalamocortical Connections. *Neuron* 36, 623–634. doi:10.1016/s0896-6273(02)01021-8

Ma, Q., Anderson, D. J., and Fritzsch, B. (2000). Neurogenin 1 Null Mutant Ears Develop Fewer, Morphologically Normal Hair Cells in Smaller Sensory Epithelia Devoid of Innervation. *Jaro* 1, 129–143. doi:10.1007/s101620010017

Ma, Q., Chen, Z., Barrantes, I. d. B., Luis de la Pompa, J., and Anderson, D. J. (1998). neurogenin1 Is Essential for the Determination of Neuronal Precursors for Proximal Cranial Sensory Ganglia. *Neuron* 20, 469–482. doi:10.1016/s0896-6273(00)80988-5

Macova, I., Pysanenko, K., Chumak, T., Dvorakova, M., Bohuslavova, R., Syka, J., et al. (2019). Neurod1 Is Essential for the Primary Tonotopic Organization and Related Auditory Information Processing in the Midbrain. *J. Neurosci.* 39, 984–1004. doi:10.1523/jneurosci.2557-18.2018

Matei, V., Pauley, S., Kaing, S., Rowitch, D., Beisel, K. W., Morris, K., et al. (2005). Smaller Inner Ear Sensory Epithelia in Neurog1 Null Mice Are Related to Earlier Hair Cell Cycle Exit. *Dev. Dyn.* 234, 633–650. doi:10.1002/dvdy.20551

Matsuda, T., Irie, T., Katsurabayashi, S., Hayashi, Y., Nagai, T., Hamazaki, N., et al. (2019). Pioneer Factor NeuroD1 Rearranges Transcriptional and Epigenetic Profiles to Execute Microglia-Neuron Conversion. *Neuron* 101, 472–485. doi:10.1016/j.neuron.2018.12.010

Meas, S. J., Zhang, C.-L., and Dabdoub, A. (2018). Reprogramming Glia into Neurons in the Peripheral Auditory System as a Solution for Sensorineural Hearing Loss: Lessons from the Central Nervous System. *Front. Mol. Neurosci.* 11, 77. doi:10.3389/fnmol.2018.00077

Miyata, T., Maeda, T., and Lee, J. E. (1999). NeuroD Is Required for Differentiation of the Granule Cells in the Cerebellum and hippocampus. *Genes Dev.* 13, 1647–1652. doi:10.1101/gad.13.13.1647

Mostafapour, S. P., Cochran, S. L., Del Puerto, N. M., and Rubel, E. W. (2000). Patterns of Cell Death in Mouse Anteroventral Cochlear Nucleus Neurons after Unilateral Cochlea Removal. *J. Comp. Neurol.* 426, 561–571. doi:10.1002/1096-9861(20001030)426::4<561aid-cne5>3.0.co;2-g

Packard, A., Giel-Moloney, M., Leiter, A., and Schwob, J. E. (2011). Progenitor Cell Capacity of NeuroD1-Expressing Globose Basal Cells in the Mouse Olfactory Epithelium. *J. Comp. Neurol.* 519, 3580–3596. doi:10.1002/cne.22726

Panaliappan, T. K., Wittmann, W., Jidigam, V. K., Mercurio, S., Bertolini, J. A., Sghari, S., et al. (2018). Sox2 Is Required for Olfactory Pit Formation and Olfactory Neurogenesis through BMP Restriction and Hes5 Upregulation. *Development* 145, dev153791. doi:10.1242/dev.153791

Pang, Z. P., Yang, N., Vierbuchen, T., Ostermeier, A., Fuentes, D. R., Yang, T. Q., et al. (2011). Induction of Human Neuronal Cells by Defined Transcription Factors. *Nature* 476, 220–223. doi:10.1038/nature10202

Pavlinkova, G. (2020). Molecular Aspects of the Development and Function of Auditory Neurons. *Int. J. Mol. Sci.* 22, 131. doi:10.3390/ijms22010131

Pennesi, M. E., Cho, J.-H., Yang, Z., Wu, S. H., Zhang, J., Wu, S. M., et al. (2003). BETA2/NeuroD1 Null Mice: A New Model for Transcription Factor-dependent Photoreceptor Degeneration. *J. Neurosci.* 23, 453–461. doi:10.1523/jneurosci.23-02-00453.2003

Romer, A. I., Singer, R. A., Sui, L., Egli, D., and Sussel, L. (2019). Murine Perinatal β-Cell Proliferation and the Differentiation of Human Stem Cell-Derived Insulin-Expressing Cells Require NEUROD1. *Diabetes* 68, 2259–2271. doi:10.2337/db19-0117

Rubel, E. W., and Fritzsch, B. (2002). Auditory System Development: Primary Auditory Neurons and Their Targets. *Annu. Rev. Neurosci.* 25, 51–101. doi:10.1146/annurev.neuro.25.112701.142849

Schlosser, G., and Northcutt, R. G. (2000). Development of Neurogenic Placodes inXenopus Laevis. *J. Comp. Neurol.* 418, 121–146. doi:10.1002/(sici)1096-9861(20000306)418::2<121aid-cne1>3.0.co;2-m

Schmidt, H., and Fritzsch, B. (2019). Npr2 Null Mutants Show Initial Overshooting Followed by Reduction of Spiral Ganglion Axon Projections Combined with Near-normal Cochleotopic Projection. *Cel Tissue Res* 378, 15–32. doi:10.1007/s00441-019-03050-6

Schwarzer, S., Asokan, N., Bludau, O., Chae, J., Kuscha, V., Kaslin, J., et al. (2020). Correction: Neurogenesis in the Inner Ear: the Zebrafish Statoacoustic Ganglion Provides New Neurons from a Neurod/Nestin-Positive Progenitor Pool Well into Adulthood. *Development* 147, 7. doi:10.1242/dev.191775

Shen, W., Ba, R., Su, Y., Ni, Y., Chen, D., Xie, W., et al. (2018). Foxg1 Regulates the Postnatal Development of Cortical Interneurons. *Cereb. Cortex* 29(4):1547. doi:10.1093/cercor/bhy051

Wu, D. K., and Kelley, M. W. (2012). Molecular Mechanisms of Inner Ear Development. *Cold Spring Harbor Perspect. Biol.* 4, a008409. doi:10.1101/cshperspect.a008409

Conflict of Interest: The authors declare that the research was conducted in the absence of any commercial or financial relationships that could be construed as a potential conflict of interest.

Publisher's Note: All claims expressed in this article are solely those of the authors and do not necessarily represent those of their affiliated organizations, or those of the publisher, the editors and the reviewers. Any product that may be evaluated in this article, or claim that may be made by its manufacturer, is not guaranteed or endorsed by the publisher.

frontiers in Cell and Developmental Biology

ORIGINAL RESEARCH
published: 22 February 2022
doi: 10.3389/fcell.2022.832314

NADPH Oxidase 3 Deficiency Protects From Noise-Induced Sensorineural Hearing Loss

Francis Rousset[1], German Nacher-Soler[1], Vivianne Beatrix Christina Kokje[1,2], Stéphanie Sgroi[1], Marta Coelho[1], Karl-Heinz Krause[3†] and Pascal Senn[1,2†]*

[1]The Inner Ear and Olfaction Lab, Department of Pathology and Immunology, Faculty of Medicine, University of Geneva, Geneva, Switzerland, [2]Department of Clinical Neurosciences, Service of ORL and Head and Neck Surgery, University Hospital of Geneva, Geneva, Switzerland, [3]Department of Pathology and Immunology, Faculty of Medicine, University of Geneva, Geneva, Switzerland

OPEN ACCESS

Edited by:
Isabel Varela-Nieto,
Spanish National Research Council (CSIC), Spain

Reviewed by:
Fabiola Paciello,
Catholic University of the Sacred Heart, Italy
Xia Gao,
Nanjing Drum Tower Hospital, China

***Correspondence:**
Francis Rousset
Francis.Rousset@unige.ch

†These authors have contributed equally to this work and share last authorship

Specialty section:
This article was submitted to Molecular and Cellular Pathology, a section of the journal Frontiers in Cell and Developmental Biology

Received: 09 December 2021
Accepted: 24 January 2022
Published: 22 February 2022

Citation:
Rousset F, Nacher-Soler G, Kokje VBC, Sgroi S, Coelho M, Krause K-H and Senn P (2022) NADPH Oxidase 3 Deficiency Protects From Noise-Induced Sensorineural Hearing Loss. Front. Cell Dev. Biol. 10:832314. doi: 10.3389/fcell.2022.832314

The reactive oxygen species (ROS)-generating NADPH oxidase NOX3 isoform is highly and specifically expressed in the inner ear. NOX3 is needed for normal vestibular development but NOX-derived ROS have also been implicated in the pathophysiology of sensorineural hearing loss. The role of NOX-derived ROS in noise-induced hearing loss, however, remains unclear and was addressed with the present study. Two different mouse strains, deficient in NOX3 or its critical subunit $p22^{phox}$, were subjected to a single noise exposure of 2 h using an 8–16 kHz band noise at an intensity of 116–120 decibel sound pressure level. In the hours following noise exposure, there was a significant increase in cochlear mRNA expression of NOX3 in wild type animals. By using RNAscope *in situ* hybridization, NOX3 expression was primarily found in the Rosenthal canal area, colocalizing with auditory neurons. One day after the noise trauma, we observed a high frequency hearing loss in both knock-out mice, as well as their wild type littermates. At day seven after noise trauma however, NOX3 and $p22^{phox}$ knockout mice showed a significantly improved hearing recovery and a marked preservation of neurosensory cochlear structures compared to their wild type littermates. Based on these findings, an active role of NOX3 in the pathophysiology of noise-induced hearing loss can be demonstrated, in line with recent evidence obtained in other forms of acquired hearing loss. The present data demonstrates that the absence of functional NOX3 enhances the hearing recovery phase following noise trauma. This opens an interesting clinical window for pharmacological or molecular intervention aiming at post prevention of noise-induced hearing loss.

Keywords: NADPH oxidase, NOX3, cochlea, noise-induced hearing loss, auditory neurons, neuroprotection

Abbreviations: NIHL, Noise-Induced Hearing Loss; NOX, NADPH oxidase; OC, Organ of Corti; ROS, Reactive Oxygen Species; SGN, Spiral Ganglion Neurons; SV, Stria Vascularis.

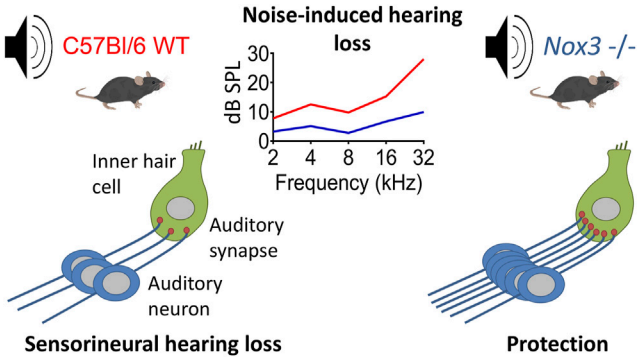

GRAPHICAL ABSTRACT |

INTRODUCTION

Hearing loss is the most common neurosensory deficit in humans and the third most prevalent chronic disability over 65 years old, affecting over 460 million people world-wide (World Health Organization, 2022). Noise exposure is reported to account for ~30% of hearing loss cases (Le et al., 2017) and the prevalence of noise-induced hearing loss in industrial populations ranges from 37–60%. Sound pressure vibrations travel to the cochlea and activate inner hair cells at frequency specific locations, leading to glutamate release in the auditory synapses and generation of electrical stimuli traveling from the auditory neurons to the central nervous system, where they are perceived as sound (Wang and Puel, 2018). A variety of insults can damage the peripheral auditory system and lead to transient or permanent hearing loss. Recent evidence suggests that the auditory neurons and their synaptic connections to the hair cells are the most vulnerable elements in the peripheral auditory system, at least for noise-induced hearing loss and presbyacusis (Liberman and Kujawa, 2017; Wu et al., 2019; Rousset et al., 2020; Peineau et al., 2021). Even moderate sound pressure levels over prolonged time periods can cause degeneration of spiral ganglion neurons and their synaptic connections (Kujawa and Liberman, 2006; Kaur et al., 2019). This so-called cochlear synapthopathy can even occur in cochleae with intact hair cell populations and normal audiograms, leading to a situation referred to as hidden hearing loss (Kujawa and Liberman, 2009; Wu et al., 2019). Sensorineural hearing loss persisting beyond few days after any insult, including neuronal apoptosis, is irreversible in humans (Rousset F et al., 2020).

Over the past decades it became clear that oxidative stress is a common denominator of many forms of acquired sensorineural hearing loss (Henderson et al., 2006; Rousset et al., 2015; Fetoni et al., 2019; Ramkumar et al., 2021). Noise-induced oxidative damages, including hair cell membrane lipid peroxidation or DNA oxidation, appear as early as a few hours following the insult (Maulucci et al., 2014). In addition to oxidative stress, specific redox signaling was proposed to lead to excitotoxic degeneration of afferent auditory neurons, as recently demonstrated in a mouse model of age-related hearing loss (Rousset et al., 2020).

Growing evidence suggests that the reactive oxygen species (ROS) generating NADPH oxidase enzyme NOX3 is an important mediator of oxidative damages and a possible common mediator in several forms of sensorineural hearing loss (Mukherjea et al., 2010; Rousset et al., 2015; Rousset et al., 2020; Mohri et al., 2021). NADPH oxidases (NOX) are a family of seven isoenzymes expressed in mammals dedicated to the production of ROS. NOX are virtually expressed in all tissues of the body and have essential physiological functions, including bacteria killing, thyroid hormone synthesis, otoconia formation and redox cellular signaling (Egea et al., 2018). The NOX3 isoform is highly and specifically expressed in the inner ear and needed for normal vestibular development. The physiological role of NOX3 has been demonstrated in NOX3 mutant mice (also referred to as head-tilt mice) where it plays a key role in the formation of otoconia: small bio-crystals essential for the perception of linear accelerations and gravity (Paffenholz et al., 2004). Mice with a loss of function mutation in the common NOX1, NOX2, NOX3, and NOX4 subunit $p22^{phox}$, have a similar vestibular phenotype, comparable to the head-tilt phenotype of NOX3 mutant mice (Nakano et al., 2008). Although NOX3 expression is also found at significant levels in the cochlear part of the inner ear, a clear physiological role in cochlear development or maintenance has not been demonstrated (Bánfi et al., 2004; Rousset et al., 2020) and NOX3 deficient mice exhibit comparable hearing thresholds to wild-type (WT) mice (Nakano et al., 2008; Lavinsky et al., 2015). However, in a pathogenic context such as ageing or cisplatin exposure, the NOX3-derived ROS contribute significantly to morphological and functional consequences with destruction of the neurosensory cells in the cochlea and hearing loss (Rousset et al., 2015). In these two forms of acquired sensorineural hearing loss, NOX3 deficiency was shown to be protective (Mukherjea et al., 2010; Rousset et al., 2020). Noise induced hearing loss is thought to involve similar ROS-induced pathways (Henderson et al., 2006; Maulucci et al., 2014; Dhukhwa et al., 2019; Mohri et al., 2021). Counter-intuitively however, one recent report suggests a protective role of NOX3 in noise-induced hearing loss (Lavinsky et al., 2015). Therefore, clarification of the role of NOX3 in noise-induced hearing loss is needed and our study aims at filling this gap.

In the present study we addressed the role of NOX3 in noise-induced hearing loss by subjecting two different NOX3 deficient mouse strains and their wild type littermates to white noise exposure. One mouse strain carries a loss of function mutation in

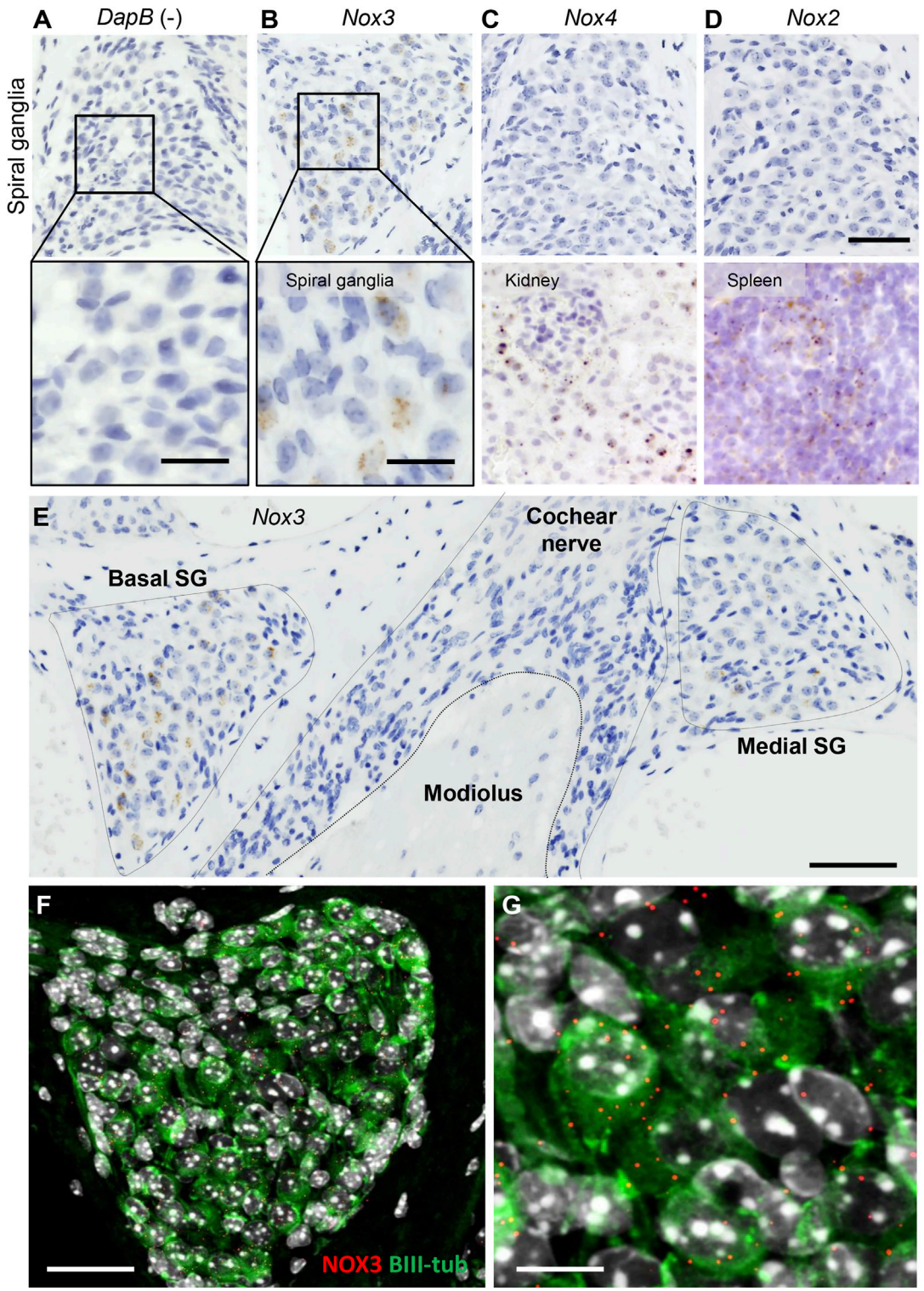

FIGURE 1 | Localization of NOX isoform in the mouse cochlea. RNAscope *in situ* hybridization of *Nox3* **(B)**, *Nox4* (**C**, upper panel) and *Nox2* (**D**, upper panel) in mouse spiral ganglion. Dihydrodipicolinate reductase (*Dapb*) expressed in the bacteria *E. Coli* was used as negative control **(A)**. Scale bar 50 µm (upper panel). **(A, B)** Lower panel show higher magnification of mouse spiral ganglion. Scale bar = 20 µm. **(C)** Kidney and **(D)** spleen slices were respectively used as positive control for *Nox4* and *Nox2*. **(E)** Mid-modiolar view of *Nox3* expression as detected by RNAscope *in situ hybridization* in a mouse cochlea: Nox3 is predominantly observed in the Rosenthal canal but not the central part of the cochlear nerve. scale bar = 100 µm. **(F, G)** Mid modiolar view of the mouse Rosenthal canal immunostained with BIII-tubulin (green) and Nox3 RNAscope fluorescent probe (red dots). Samples were counterstained with DAPI (grey). Scale bars = 50 and 20 µm respectively. Pictures are representative from 6 independent experiments (n = 6 WT mice).

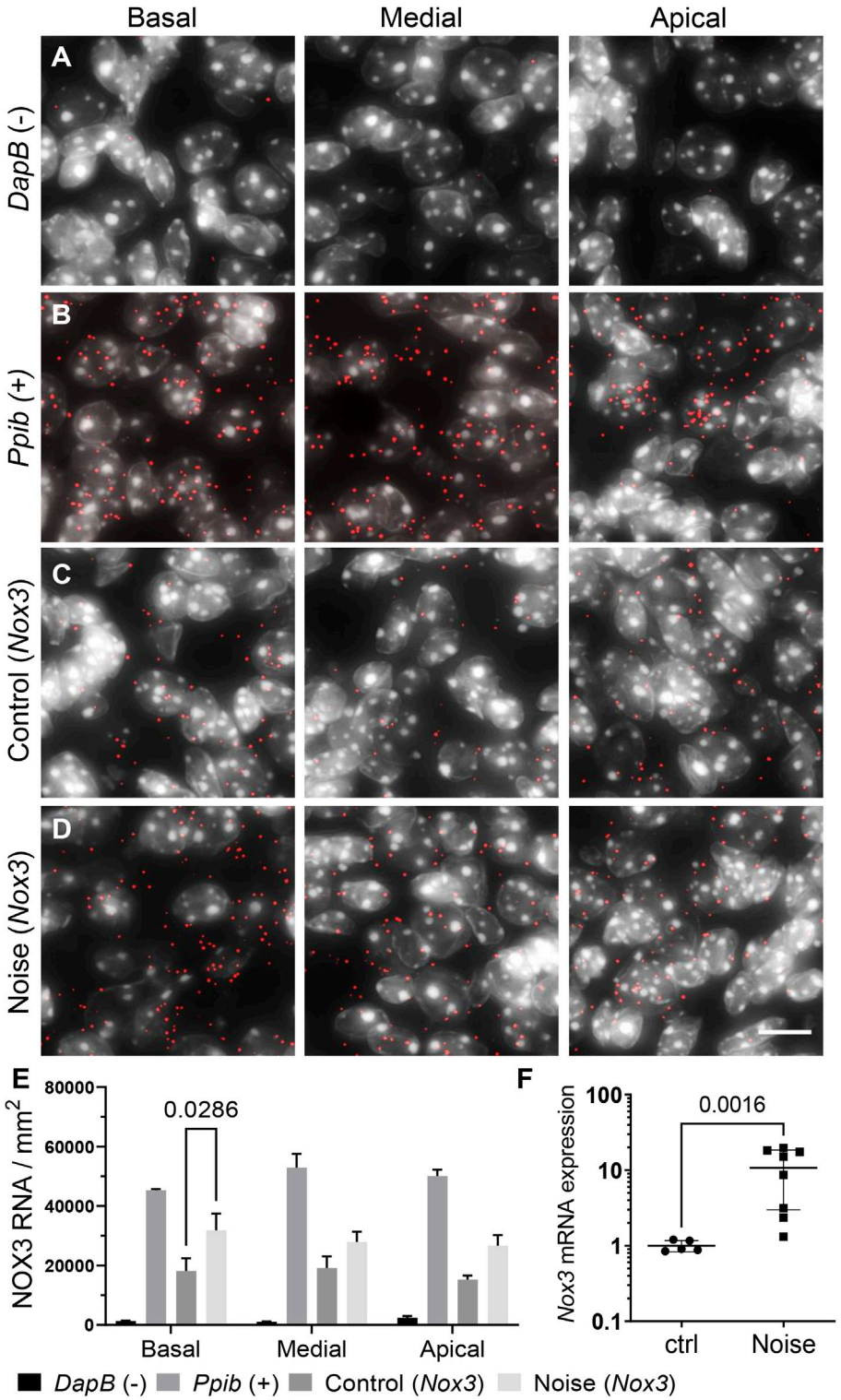

FIGURE 2 | Effect of noise exposure on cochlear expression of NOX3. C57Bl6/J mice were exposed to an 8–16 kHz 116dB SPL noise band for 2 h. 24 h following the noise exposure, cochleae were harvested for *Nox3* RNAscope *in situ* hybridization and Real time qPCR. **(A–D)** RNAscope *in situ* hybridization of dihydrodipicolinate reductase (*Dapb*) expressed in the bacteria *E. Coli* (negative control) **(A)**, Peptidyl-Prolyl Cis-Trans Isomerase B (*Ppib* gene) (positive control) **(B)** and *Nox3* in the mouse Rosenthal canal **(C, D)**. RNAscope signal is visualized with the red dots; all slices were counter stained with DAPI (grey). **(C)** Representative *Nox3* mRNA fluorescent staining in the 3 cochlear turns of non-exposed animals (control). **(D)** Representative *Nox3* mRNA fluorescent staining in the 3 cochlear turns of noise-exposed animals (Noise). Scale bar = 10 µm. Note that lower magnified pictures are available in **Supplementary Figure S2**. **(E)** Bar graph shows relative mRNA expression level of *Nox3* as quantified from *Nox3* RNAscope signal in the Rosenthal canal before and following noise exposure. $n = 3$ animals/group. $p = 0.0286$ with two-way ANOVA. **(F)** Real time qPCR of *Nox3* mRNA in the whole mouse cochlea. Post noise exposure level of *Nox3* ($n = 8$) was compared to *Nox3* expression in the cochlea of 5 non-exposed animals. $p = 0.0016$ with Mann-Whitney non-parametric test.

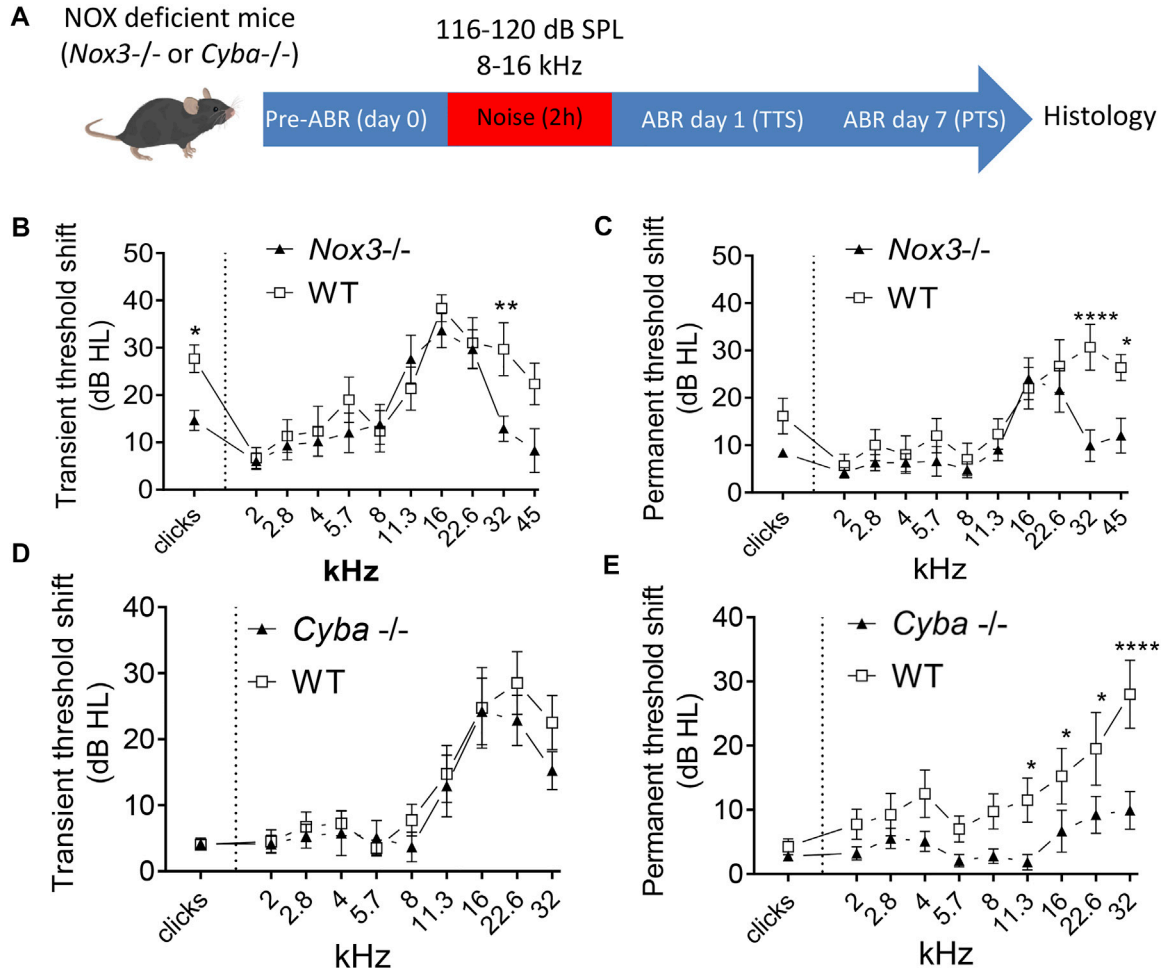

FIGURE 3 | Audiogram of NOX3 deficient mice upon noise exposure. **(A)** Six weeks old NOX3 mutant and p22^{phox} knockout mice and their respective WT and heterozygous littermates were subjected to a first ABR measurement (pre-ABR; Day 0) followed by 8–16 kHz noise band exposure of 2 h duration at 116 dB SPL (for NOX3) or 120 dB SPL (for p22^{phox}). Transient threshold shift (TTS) and permanent threshold shifts (PTS) were respectively calculated by substraction of the reference hearing threshold values (preABR; D0) to the D1 and D7 hearing threshold values. **(B, D)** TTS as recorded at day 1 following noise exposure in NOX3 mutant mice **(B)** and p22^{phox} ko mice **(D)** with their respective WT littermates. **(C, E)** PTS as recorded at day 7 following noise exposure in NOX3 mutant mice **(C)** and p22^{phox} ko mice **(E)** with their respective WT littermates. **(B, C)** $n = 9$ *Nox3*$^{+/+}$; 10 *Nox3*$^{-/-}$; **(D, E)** $n = 12$ *Cyba*+/+; 13 *Cyba* –/–. To facilitate comparison between WT and NOX3-deficient animals, hearing threshold shifts from heterozygous animals are not shown here but are available in **Supplementary Figure S5**.

NOX3 (C57BL/6J-*Nox3*$^{het–4J}$/J) (Flaherty et al., 2011) and the second strain has a constitutive p22^{phox} knockout (C57BL/N *Cyba* knockout) (Pircalabioru et al., 2016). The p22^{phox} knockout strain is devoid of NOX1, NOX2, NOX3 and NOX4 activity (Nakano et al., 2007; Prior et al., 2016). Our results demonstrate that NOX3 is predominantly expressed in the auditory neurons area and is upregulated upon noise exposure. Both NOX3 deficient mouse strains were partially, but significantly protected against noise-induced high frequency hearing loss, concurring with the tonotopic pattern of NOX3 expression in the auditory neurons. Histologically, NOX3 deficient strains showed a significant preservation of cellular structures in the sensory epithelium, the auditory synapses and the spiral ganglion in comparison to their wild type littermates. Based on these findings, an active role of the ROS generating enzyme NOX3 in the pathophysiology of noise-induced hearing loss can be demonstrated, in line with NOX3 implication in other forms of acquired hearing loss such as age-related hearing loss and cisplatin-induced hearing loss. The exclusive and specific expression of NOX3 in the inner ear opens interesting opportunities for pharmacological (Augsburger et al., 2019) or molecular (Rousset et al., 2019) interventions aiming at prevention of several acquired forms of hearing loss including noise-induced hearing loss.

RESULTS

NOX3 is Specifically Expressed in Spiral Ganglion Neurons

NOX-derived reactive oxygen species are prospective contributors of noise-induced damage to the inner ear. Several

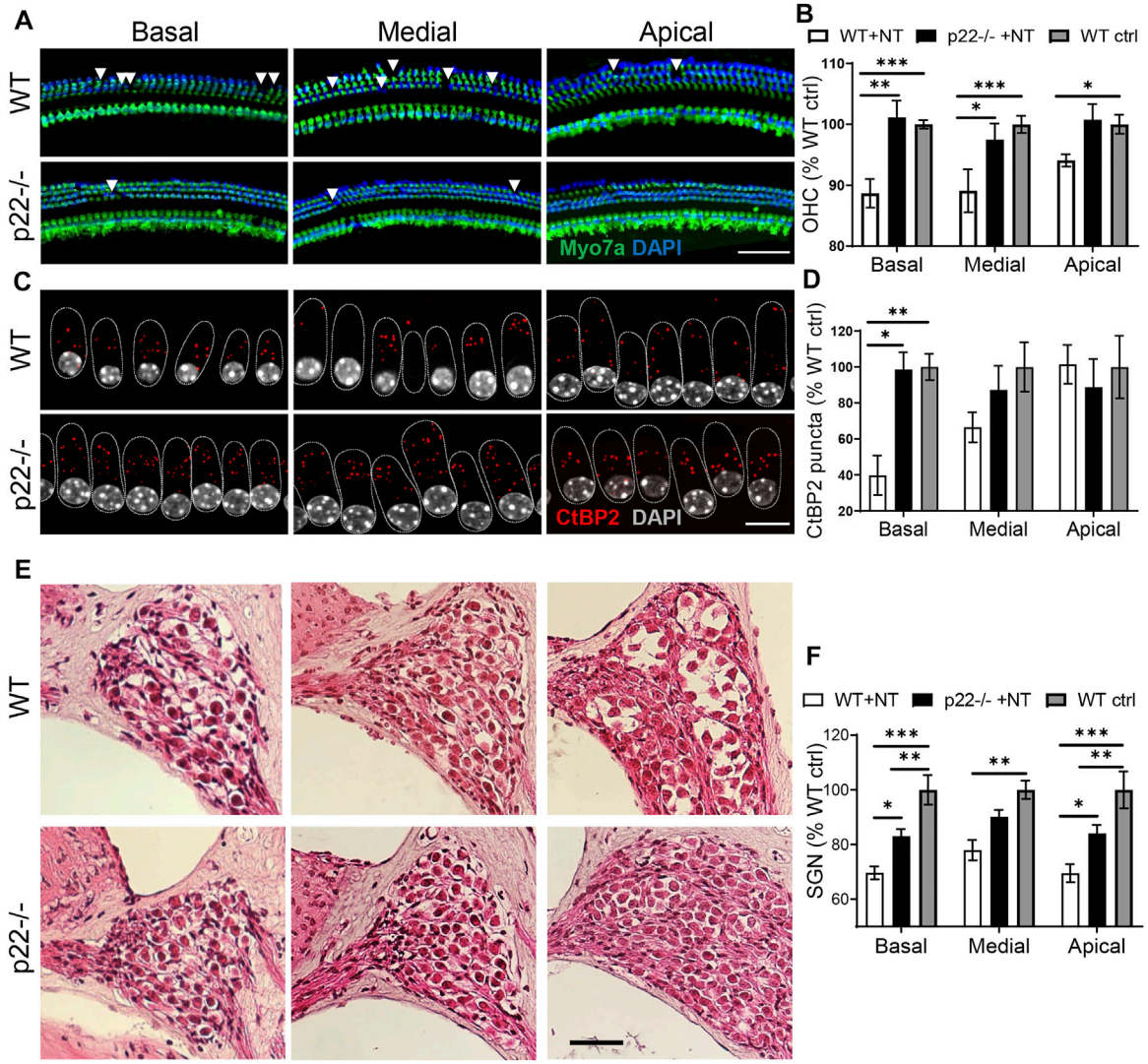

FIGURE 4 | Cochlear histology of p22^{phox} knockout mice upon noise exposure. Seven days following the noise exposure, after the last audiogram determination, mice were sacrificed for cochlear histology. **(A)** Cytocochleogram showing the sensory epithelium in the three cochlear turns in WT (upper picture) and p22^{phox}–/– littermates (lower picture). In green, the hair cell marker Myo7a and in blue, DAPI. Scale bar 20 µm. **(B)** Bar graph showing the outer hair cells number in the three cochlear turns of noise exposed WT and p22^{phox}–/– littermates expressed relatively to WT non-exposed controls. *n* = 8 WT noise exposed (WT + NT); *n* = 7 p22^{phox}–/– noise exposed (p22 + NT); *n* = 8 WT non-exposed controls (WT ctrl). **(C)** On the same samples, the number of synaptic ribbons between inner hair cells and spiral ganglion neurons was determined using CtBP2 immunostaining (red); upper panel WT and lower panel p22^{phox}–/–. Scale bar: 10 µm. **(D)** Bar graph showing the number of ribbons/inner hair cell (IHC) in the 3 cochlear turns of WT and p22^{phox}–/– littermates. The data are expressed relatively to non-exposed WT controls. **(E)** Representative mid modiolar hematoxylin and eosin staining showing the three cochlear turns of noise exposed WT (upper panel) and p22^{phox}–/– (lower panel) littermates. **(F)** Bar graph showing the density of spiral ganglion neurons in the different parts of the cochlea of noise exposed WT and p22^{phox}–/– littermates expressed relatively to WT controls. Scale bar 50 µm. *n* = 5 WT noise exposed (WT ctrl); *n* = 6 p22^{phox}–/– noise exposed (p22 + NT); *n* = 6 WT controls (WT ctrl).

NOX isoforms, including NOX2, NOX3 and NOX4 were found to be expressed in the mouse and human cochlea (Rousset et al., 2020). Addressing more specifically the localization of NOX in the sub-compartments of the cochlea, we performed a RNAscope *in situ* hybridization (**Figure 1**; **Supplementary Figure S1**). As expected, the bacterial gene *DapB*, used as negative control, did not result in any signal (**Figure 1A**). However, we observed a strong expression of *Nox3* in the spiral ganglion (**Figure 1B**). Conversely, *Nox2* and *Nox4*, respectively well expressed in kidney and spleen slices, used as positive controls, could not be detected in the spiral ganglion (**Figures 1C,D**). In the stria vascularis, little Nox3 and Nox4 expression could be found; however, no significant NOX expression was detected in the organ of Corti (**Supplementary Figure S1**). Interestingly, Nox3 expression was specific from the Rosenthal canal area but no expression could be detected in the central part of the auditory nerve (**Figure 1E**). By using fluorescent Nox3 probes and BIII tubulin staining (**Figures 1F,G**), we could observe an important Nox3 expression in the peripheral auditory neurons.

NOX3 Expression is Induced Upon Noise Exposure

Noise over-exposure is known to increase the level of ROS within the cochlea (Maulucci et al., 2014; Haryuna et al., 2016). Therefore, we assessed the expression level of the underlying ROS generating NOX enzymes (**Figure 2**; **Supplementary Figure S2, S3**). To compare the expression of NOX3 before and after noise exposure, we used both RNAscope *in situ* hybridization and RT-qPCR (**Figure 2**). As already shown (**Figure 1**), *Nox3* mRNA was broadly expressed in the Rosenthal canal (**Figure 2C**). *Dapb* and *Ppib* genes were respectively used as negative and positive controls (**Figures 2A,B**; **Supplementary Figure S2**). Noise exposure resulted in an increase in the number of *Nox3* related punctate dots, each revealing a pool of *Nox3* mRNA (**Figures 2D,E**; **Supplementary Figure S2**). The increase in *Nox3* expression was statistically significant in the basal turn of the Rosenthal canal, with a similar trend observed in the medial and apical cochlear turns. The noise-induced upregulation of *Nox3* mRNA was also detected using RT-qPCR from whole cochlear samples (**Figure 2F**). Note that *Nox3* mRNA expression was neither induced in stria vascularis nor in the organ of Corti, where it remained at low level (**Supplementary Figure S1**; not shown). Similarly, the expression level of other Nox isoforms, including NOX2, NOX4 and pan-NOX subunit $p22^{phox}$ (*Cyba*) where not significantly affected by the noise stimulus (**Supplementary Figure S3**). Taken together, these findings demonstrate that NOX3 is the main isoform expressed in auditory neurons and is induced upon ototoxic noise exposure.

NOX3-Deficient Mice are Partially but Significantly Protected from Noise Induced Hearing Loss

To address whether NOX3 could contribute to noise-induced damages, we assessed the hearing of constitutive NOX3 deficient mice - namely NOX3 and $p22^{phox}$ knockout - following noise exposure (**Figure 3**, **Supplementary Figure S4, S5**). At 6 weeks of age, audiograms of NOX3 mutant or $p22^{phox}$ knockout mice were not significantly different from their respective heterozygous and WT littermates (**Figures 3B,C**, **Supplementary Figure S5**). Note that NOX3 and $p22^{phox}$ mouse lines were respectively generated in C57Bl6/J and C57Bl6/N genetic backgrounds. Interestingly, mice from the C57Bl6N background were more resistant to noise induced hearing loss (**Supplementary Figure S4**) and the protocol of noise exposure needed to be adapted for comparable deafening (116dB SPL for C57Bl6/J and 120dB SPL for C57Bl6/N). In both $p22^{phox}$ and NOX3 mouse strains, noise exposure led to a significant elevation of hearing thresholds within 24 h (**Figures 3B,D**; **Supplementary Figure S5**). The degree of hearing loss was comparable across mutants and wild-type animals and arose mostly at high frequencies, with about 20–40 dB SPL hearing loss between the frequencies of 16 and 32 kHz. Only in one frequency, at 32 kHz and only in the NOX3 mutant mice (**Figure 3B**), a statistically significant protection was observed compared to wild-type littermates at this time point. To address the more permanent threshold shift, ABR measurements were obtained 7 days following noise exposure (**Figures 3C,E**). At this time point, both mouse strains, $p22^{phox}$ and NOX3, showed a partial but statistically significant recovery of hearing, in contrast to wild type littermates, where no signs of recovery were observed (**Supplementary Figure S5**).

NOX3 Deficiency Prevents Noise-Induced Damage to the Neurosensory Cellular Structures in Cochlea

Animals were sacrificed for cochlear histology seven days after the noise over-exposure. In non-exposed control animals, consistent with the functional outcome (**Supplementary Figure S5**), comparable cochlear histology was obtained between genotypes (**Supplementary Figure S6**). However, the impact of noise trauma on the sensory epithelium was milder in both $p22^{phox}$ (**Figure 4**) and NOX3 (data not shown) mouse strains, showing a statistically smaller loss of outer hair cells when compared to wild type animals (**Figure 4B**). In WT mice, noise exposure led to dramatic decrease in the number of auditory synapses, predominantly in the basal cochlear turn (**Figures 4C,D**). This was accompanied by a decrease in auditory neuron density in all cochlear turns (**Figures 4E,F**). Remarkably, $p22^{phox}$ knockout and NOX3 mutant mice were both protected against noise induced auditory synaptopathy and auditory neuropathy, with markedly conserved auditory synapses and neuron integrity (**Figures 4E,F**). NOX3-mediated damages were predominantly observed in the basal and, to lesser extent, medial turn of the cochlea.

DISCUSSION

Oxidative stress is an underlying feature of several forms of acquired sensorineural hearing loss, including noise trauma (Henderson et al., 2006; Maulucci et al., 2014; Rousset et al., 2015). In the present study, we investigated the possible contribution of the ROS generating NADPH oxidase NOX3 in noise-induced sensorineural hearing loss using two different mice strains: the NOX3 mutant C57BL/6J-*NOX3*$^{het-4J}$/J and a constitutive $p22^{phox}$ knockout (C57BL/N *Cyba* knockout), both deficient in NOX3 activity. Our results demonstrate a partial, but statistically significant protection against noise-induced hearing loss along with preserved cochlear cellular structures in both mouse strains. These findings are in line with previous studies on two other forms of acquired hearing loss, namely the drug-induced and age-associated hearing loss (Mukherjea et al., 2010; Kaur et al., 2016; Dhukhwa et al., 2019; Rousset et al., 2020; Mohri et al., 2021).

To the best of our knowledge, two previous studies investigated the effect of NOX on noise-induced hearing loss (Mohri et al., 2021; Lavinsky et al., 2015). The first study reported a small protective effect of NOX3 against noise-induced hearing loss but solely at a very specific frequency (8 kHz) (Lavinsky et al., 2015). In contrast, the study by Mohri et al. showed significant protection of NOX3-deficient mice (Mohri et al., 2021). We were not able to identify major differences in experimental protocols

that could explain the discrepancies. Therefore, the role of NOX3 in the context of noise induced hearing loss remained to be clarified. Our study showed a significant protection of hearing at high frequencies in NOX3-deficient mice, however no frequency-specific protection at 8 kHz. In addition, the high frequency thresholds protection was validated in the second mouse strain with a loss of function mutation in the NOX3 subunit $p22^{phox}$. Note also that the similarities of the protective effect of NOX3 deficiency and $p22^{phox}$ deficiency suggest that there is not a major role of other $p22^{phox}$-dependent NOX isoforms (i.e. NOX1, NOX2, and NOX4) in the pathophysiology of noise induced hearing loss. Furthermore, *Nox1* was not detectable in cochlear samples by real-time qPCR and neither *Nox2* nor *Nox4* were found at significant level in cochlear structures important for hearing, such as auditory neurons, organ of Corti, or stria vascularis, at least by using the RNAscope method (**Figure 1**; **Supplementary Figure S1**). Finally, noise overexposure primarily affects the high frequencies reflecting increased damage susceptibility of the basal cochlear turn. Interestingly, the tonotopic pattern of noise induced damages in the cochlea correlates with *Nox3* induction of expression [**Figure 2**, and reference (Son et al., 2012)] and is significantly mitigated upon Nox3 or $p22^{phox}$ deletion.

To palliate the lack of specific antibodies against Nox3 (Diebold et al., 2019), Mohri et al. recently developed a mouse model with a reporter gene expressed upon Nox3 promoter (Mohri et al., 2021). *In situ* hybridization is another sensitive and reliable method to detect NOX mRNA (Moll et al., 2018; Rousset et al., 2020). Our data show important enrichment of *Nox3* mRNA in the Rosenthal canal area, whereas, the study by Mohri et al. shows rather scarce number of Nox3 positive auditory neurons. This apparent discrepancy could be explained by differences in sensitivity to detect *Nox3* at low levels. It is also possible that, since reporter gene knock-in with the *Nox3* reporter mouse leads to *Nox3* allele inactivation, putative Nox3 self-regulation loops are affected. Nevertheless, both the Nox3 reporter mouse and *in situ* hybridization methods were able to detect the increased transcription of *Nox3* following Noise exposure and upon ageing (Rousset et al., 2020).

In response to excessive noise, the kinetics of oxidative damage includes a rapid NADPH oxidation followed by lipid peroxidation, affecting membrane properties of cochlear hair cells and preceding metabolic impairment and cellular degeneration (Maulucci et al., 2014). In this context, the increase of NOX3 expression upon noise exposure is particularly interesting. Consistent with a previous report (Dhukhwa et al., 2019), we observed an increase in NOX3 expression within 24 h following the noise exposure, suggesting a possible time correlation with the increase of NADPH oxidation and lipid peroxidation. Whether NOX3 is directly responsible for NADPH oxidation as a result of its catalytic activity requires further experimental demonstration, as NADPH is also a major electron donor for antioxidant systems (Agledal et al., 2010). Furthermore, as suggested in our previous study on presbycusis, NOX-derived ROS may not only damage the neurosensory cells of the cochlea through oxidative stress but rather through indirect consequences of specific redox signaling (Rousset et al., 2020). The precise kinetics of NOX3 expression and its histological correlates remain therefore to be fully understood in the context of noise-induced hearing loss.

It is noteworthy to mention the difference in noise susceptibility between C57Bl6/J and C57Bl6/N genetic backgrounds (**Supplementary Figure S4**). As previously reported (Kendall and Schacht, 2014), C57Bl6/N mice were more resistant to noise insult than C57Bl6/J mice. In fact, C57Bl6/J mice present a deletion in the NNT (Nicotinamide Nucleotide transhydrogenase) gene resulting in a significantly decreased enzyme activity. Interestingly, this gene encodes an enzyme that uses energy from the mitochondrial proton gradient to produce high concentrations of NADPH, used for instance for free radical detoxification. It appears therefore likely that C57Bl6/J mice are more susceptible to oxidative damage, as induced by noise exposure *via* NOX3 activity.

NOX3-derived oxidants are essential for normal vestibular development (Paffenholz et al., 2004; Kiss et al., 2006; Nakano et al., 2008; Jones et al., 2010). However, its physiological relevance for the development and normal functioning of the cochlea remains unclear. We observed no difference in hearing thresholds and cochlear histology between NOX3-deficient mice and their wild-type littermates, corroborating the fact that NOX3 is not needed for a normal cochlear development and function, at least to a relevant extent. In a recent study, we have demonstrated that NOX3 is regulating the expression of genes involved in the auditory neuron excitatory pathway (Rousset et al., 2020). One could therefore propose NOX3 as a regulator of auditory neuron excitability in the auditory system, possibly tuning firing thresholds of auditory neurons, consistent with a previous proposed role for redox signaling in cortical neurons (Bothwell and Gillette, 2018). Further electrophysiological characterization of NOX3-deficient auditory neurons is needed to validate this hypothesis. In pathological conditions, including ageing (Rousset et al., 2020) cisplatin (Mukherjea et al., 2010) or noise overexposure, NOX3 may lead to neuron overactivation and excitotoxicity (Morton-Jones et al., 2008).

From a therapeutic perspective the observed temporal functional changes after noise trauma offer interesting opportunities: the inactivation of NOX3 seems to be functionally more relevant in the context of recovery from the insult at 7 days after the noise exposure compared to the immediate aftermath at day one. In a clinical context, patients with acute noise trauma (i.e. explosions and various other accidents) could be offered NOX3 inhibiting treatment in the hours following the insult and expect a better recovery. Whether the commonly used glucocorticoids for these situations today work through inhibition of NOX3, or whether a more specific NOX3 inhibition through pharmacological or molecular intervention is more effective remains to be investigated in the future. In absence of a bona fide NOX3 inhibitor, a nucleotide-based approach seems to be more promising (Rousset et al., 2019), at least based on the situation today.

In conclusion, our data demonstrates that NOX3 contributes significantly to noise-induced cochlear damage as previously demonstrated for two other forms of acquired forms of

sensorineural hearing loss, namely age-related and cisplatin-induced hearing loss. NOX3 activity therefore seems to be a common molecular trigger influencing redox regulated neuronal activity, pathologically altered in different forms of acquired sensorineural hearing loss (Bothwell and Gillette, 2018; Wang and Puel, 2018; Rousset et al., 2020; Mohri et al., 2021). This corroborates the strong rationale to target NOX3 activity for prevention or treatment of noise-induced and other forms of acquired sensorineural hearing loss.

METHODS

Animal Procedures

C57Bl6/J and C57Bl6/N mice sub-strains were employed during this study. *Nox3* mutant mice (C57BL/6J-Nox3^{het-4J}/J, stock 005014) were purchased from Jackson laboratory, while p22^{phox} knockout (C57BL/N *Cyba* knockout) were generated in Prof. Ulla Knaus laboratory (Pircalabioru et al., 2016). Both mouse lines are constitutively deficient in functional NOX3 complex. In addition to NOX3 deficiency, p22^{phox} knockout mice are also devoid of functional NOX1, NOX2 and NOX4. Colonies were maintained at the animal facility of the University of Geneva through heterozygous x heterozygous breading, ensuring equal proportion of WT and NOX3 or p22^{phox} deficient littermates. All animal procedures inducing animal discomfort were performed under intraperitoneal (IP) ketamine (10%) and xylazine (5%) anesthesia (dose 10 µL/g). If necessary 10% ketamine solution was injected intramuscularly (dose 5 µL/g) to elongate the anesthesia. For the noise trauma, 6 weeks old mice were subjected to an 8–16 kHz noise band for 2 h at 116–120 dB SPL (**Figure 3A**), under anesthesia. At the end of the experiment (day 7), animals were sacrificed by cervical dislocation followed by decapitation. Cochlear samples were collected for histology evaluation or mRNA extraction.

Auditory Brainstem Response

Hearing thresholds were tested by Auditory Brainstem Response (ABR) before noise exposure (pre-ABR), 24 h (D1) and 7 days (D7) after noise trauma. ABR recordings were performed conform previously described protocols (Rousset et al., 2020). Briefly, anesthetized animals were placed in a sound proof chamber (IAC Acoustics, Illinois IL, United States) upon a heating pad to maintain body temperature. Depth of anesthesia was tested every 30 min by the pedal withdrawal reflex. For the recordings, platinum electrodes were placed subcutaneously on the mouse forehead (+), on the mastoid of the recorded ear (−) and a reference electrode on the back. ABRs were recorded, following stimulation with 100 µs clicks or 3 m tone pipes (2.0–45.2 kHz at a resolution of 2 steps per octave). For all frequencies, they were recorded from 0 to 90 dB SPL in 3 dB steps. Electrical responses were averaged over 256 repetitions of stimulus pairs with alternating phase. Hearing thresholds were defined as the last sound pressure level with a conserved response pattern, identified by visual inspection of the averaged signal. For stimulus generation and recording of responses, a multi-function IO-Card (National Instruments, Austin TX, United States) and an IBM compatible computer were used. An integrated software package for stimulus generation and recording (Audiology_lab; Otoconsult, Frankfurt, Germany) was used. The sound pressure level was controlled with an attenuator and amplifier (Otoconsult, Frankfurt, Germany). Stimuli were delivered to the ear in a calibrated open system by a loudspeaker (AS04004PR-R, PUI Audio, Inc., Dayton, United States) placed 3 cm lateral to the animals' pinna. The sound pressure was calibrated on-line prior to each measurement with a microphone probe system (Bruel and Kjaer 4191) placed near the animals' ear. Recorded signals were amplified and bandpass filtered (80 dB; 0.2–3.0 kHz) using a filter/amplifier unit (Otoconsult, Frankfurt, Germany).

Cochlea Histology

Following D7 ABR, anaesthetized mice were sacrificed. Temporal bones were isolated from the mice skull, in order to further dissect the auditory bulla. Dissected cochleae were placed in 4% paraformaldehyde overnight at room temperature. Cochleae were decalcified using USEDECALC solution (Medite commercial solution) under sonication for 48 h (Medite, Cat. No. 03-3300-00). After decalcification, both cochlea from the same animal were arranged for different protocols. While one cochlea was embedded in paraffin for cochlear morphology assessment (Hematoxilin-Eosin staining or RNAscope), the contralateral cochlea was micro-dissected to evaluate the sensory epithelium (cytocochleograms) as previously described (Rousset et al., 2020).

Immunohistochemistry and Confocal Microscopy (Cytocochleograms)

The decalcified cochleae were dissected with microsurgical forceps under a binocular microscope as previously described (Rousset et al., 2020). Briefly, the bony shell was removed to expose the Organ of Corti (OC), followed by the removal of the stria vascularis and separation of the sensory epithelium from the spiral ganglion. The basal, middle and apical turns of the OC were respectively separated and transferred into 400 uL PBS solution in a 48 well plate. Samples were then permeabilized (3% Triton-X 100 in PBS 1X) for 30 min at room temperature and immersed in a blocking buffer, containing 2% bovine serum albumin (BSA) and 0.01% Triton-X 100 in PBS, for 30 min at room temperature. Explants were incubated overnight at 4°C with the primary antibodies anti-MyoVIIa (1:200, rabbit; Proteus, United States) and anti-Ctbp2 (1:200, monoclonal mouse, BD Bioscience) prepared in blocking buffer. On the following day, tissues were rinsed three times with PBS and incubated, for 2 h at room temperature, with the secondary antibodies anti-rabbit Alexa Fluor 488 (1:500; Invitrogen, United States) and goat anti-mouse Alexa 555 (1:500; Life Technologies) diluted in blocking buffer. Explants were washed 3 times with PBS and mounted on a glass slide with Fluoroshield containing DAPI (Sigmaaldrich, United States). The labelled cells were visualized with a confocal laser-scanning microscope (Zeiss LSM700) equipped with a CCD camera (Leica Microsystems) employing the Plan-Neofluar 20X/0.50 and Plan-Apochromat 63X/1.4 (oil)

objectives. Hair cell and ribbons quantification was performed using ImageJ software.

Mid Modiolar Preparations

Following standardized protocols, decalcified cochleae were sequentially dehydrated and embedded in paraffin. Mid-modiolar cuts of 5 µm were processed and loaded onto gelatin-coated slides. Adjacent mid-modiolar cuts were employed on hematoxylin/eosin and RNAscope protocols (see sections below).

Hematoxylin Eosin Staining

Harris' hematoxylin/eosin staining was performed on 5 non-consecutive slides of each cochlea including all cochlear turns. Mid-modiolar paraffin slides were re-hydrated with successive xylene and alcohol baths, then exposed to Hematoxylin for 5 min, rinsed with H_2O and briefly submerged in an alcohol and HCl bath, and finally washed with alcohol 70%. Following Hematoxylin staining, slides were briefly (2–3 s) exposed to the eosin reagent. After staining the slides were dehydrated with alcohol and xylol in successive bath steps, and mounted with the commercial Eukitt mounting medium. Images were obtained with a Zeiss Axioskop 2 plus microscope. Spiral ganglia density was reported and assessed on the resulting images using ImageJ software.

Quantitative Analysis of Cochlea Morphology

Hematoxylin-eosin mid-modiolar cuts images were analyzed on the open source software ImageJ to determine the spiral ganglion neurons density. SGN nuclear quantification was performed and normalized to the Rosenthal's canal area (in mm^2) within all cochlear turns (apical, medial and basal). Five non-consecutive sections were evaluated for each turn and the densities were averaged. Similarly, cytocochleogram images were employed to determine the number of synapsis/inner hair cell and outer hair cell viability. For synaptic ribbons quantification, images were recorded with a 63X confocal objective, generating 10-15 um Z stack images (0.7 um steps). The resulting file was projected into a single plane to ensure accurate quantification of the ribbons distributed along the *Z* axis. For each cochlear turn, two different segments of 10–15 inner hair cells were assessed to obtain an average number of ribbon synapses. In the same way, the hair cell viability (cytocochleogram) was evaluated in two representative areas of 100 µm and the survival rate was averaged for each cochlear section (apical, medial and basal). Both Inner hair cells (IHC) and outer hair cells (OHC) were recorded with a 20X confocal objective. The open source ImageJ program was used for the image analysis.

Cochlea RNA Extraction

To avoid RNA degradation, cochleae were quickly dissected in cold PBS, removing remaining blood and surrounding tissues, immediately frozen in liquid nitrogen and kept at -80°C for further RNA extraction as previously described (Rousset et al., 2020). An adapted protocol was employed for the RNA extraction [adapted from (Vikhe Patil et al., 2015)], based on the Qiagen RNeasy Micro kit, replacing the lysis and homogenization steps. Samples were physically homogenized with clean steel beads and tissueLyser (Qiagen) for 30 s at 30 rpm. Trizol (750 uL) was added to the lysate, precipitating the sample DNA and RNA. After adding 150 ul chloroform, (shaking, resting and centrifuging step) the aqueous phase was collected and followed the purification protocol described on the commercial kit.

Real Time Quantitative Polymerase Chain Reaction

Following RNA purification and tritation, 500 ng of RNA were prepared for cDNA synthesis using the Takara PrimeScript RT reagent Kit, following manufacturer's instruction [see also (Rousset et al., 2020)]. Real-time PCR was performed using SYBR green assay on a 7900HT SDS system from ABI. The efficiency of each primer was verified with serial dilutions of cDNA. Relative expression levels were calculated by normalization to the geometric mean of the three house-keeping genes (*Eef1a*, *Tubb* and *Actb*). The highest normalized relative quantity was designated as a value of 1.0. Fold changes were calculated from the quotient of means of these RNA normalized quantities and reported as ±SEM. Sequences of the primers used are provided in **Supplementary Table S1**.

RNAscope® *in situ* Hybridization (ACDbio, Bio-Techne, Minneapolis, Minnesota, United States)

Mid-modiolar cuts (5 µm) obtained from decalcified cochleae (see section above - mid modiolar preparations) were loaded onto gelatin-coated slides and followed RNAscope probe hybridization. RNAscope 2.5 HD Assay–BROWN assay (Bio-techne, Cat. No. 322310) or Fluorescent multiplex assay (Bio-techne, Cat. No. 320850) was performed according to manufacturer's protocol. Selected paraffin sections were hybridized with the probes Mm-NOX3-C1 (Bio-techne, Cat. No. 481989), Mm-Cybb (Bio-techne, Cat. No. 403381), Mm-NOX4 (Bio-techne, Cat. No. 457261), Mm-Ppib-C1 (Bio-techne, Cat. No. 313911) as positive control and DapB-C1 (Bio-techne, Cat. No. 310043) as negative control at 40°C for 2 h and revealed with TSA Opal570 (Perkin Elmer, Cat. No. FP1488001KT). For BROWN assay, Mayer hematoxyline staining (30 s) was employed as counterstaining agent, whereas DAPI and β-III tubulin (1/1000, rabbit, Abcam, ab52623) immunostaining were used for Fluorescent multiplex assay. Finally, the slides were dehydrated, cleared and mounted with Tissue-Tek® Glas™ (Sakura, Cat. No. 1408). Samples were visualized with a confocal laser-scanning microscope (Zeiss LSM700) equipped with a CCD camera (Leica Microsystems) employing the Plan-Neofluar 20X/0.50 and Plan-Apochromat 63X/1.4 (Oil) objectives. Pictures were analyzed using the open source software ImageJ.

RNAscope® Signal Quantification

RNAscope samples were analyzed and quantified employing the open-source software FIJI. RNAscope signal quantification was

automatized employing FIJI's macro functionality together with Ilastik software as segmentation tool. Multi z-stack images were recorded employing a Axiocam Fluo microscope with a 40X EC Plan-Apochromat objective. Multiple tiles comprising the region of interest were acquired and merged employing Zeiss commercial software to generate a single image.

Employing FIJI macro software, the resulting z-stack images were projected into a single plane and divided into 2 channels. Blue channel (DAPI, nucleus) was processed accordingly to reduce background noise. The red channel (RNAscope signal) followed a Richardson-Lucy deconvolution (DeconvolutionLab2 plugin, 45 iterations) followed by proper processing (background subtraction). Appropriated PSF was provided during each image deconvolution, employing FIJI's plugin "PSF generator" (macro automatized). The deconvoluted red channel was then segmented following a previously trained Ilastik model, and transformed to a binary image with Huang's approach. Proper morphometric operators were applied and the RNAscope signal was quantified following FIJI's "Analyze particle" command (1.5-Infinity pixel).

The designed macro then normalized the number of dots quantified on the previous section (RNAscope signal, red channel) to the area of interest (except for the Organ of Corti, whose values are absolute). In order to proceed with the normalization, we manually determine the area of interest (Rosenthal canal or stria vascularis) following each image blue channel. The results were represented as RNAscope dots/mm2 (except for the Organ of Corti). RGB images were automatically generated during the macro processing, allowing the user to verify the absence of anomalies during the process.

Statistics

Real time qPCR data were analyzed using One-way ANOVA followed by Dunnett's multiple comparison test. Other datasets were analyzed using Two-way ANOVA followed by Bonferroni multiple comparison test. GraphPad Prism software (version 8.4.3) was used. Values with $p < 0.05$ was considered as statistically significant. $^{*}p < 0.05$, $^{**}p < 0.01$, $^{***}p < 0.005$, $^{****}p < 0.0005$.

Study Approval

All procedures were approved by the local veterinary office and the Commission for Animal experimentation of the Canton of Geneva, Switzerland, authorization number GE-28-18.

DATA AVAILABILITY STATEMENT

The raw data supporting the conclusion of this article will be made available by the authors, without undue reservation.

ETHICS STATEMENT

The animal study was reviewed and approved by Commission cantonale sur l'expérimentation animale de Genève.

AUTHOR CONTRIBUTIONS

FR, K-HK, and PS designed the study; FR, MC, GN-S, SS, and VK acquired the data; FR and GN-S analyzed the data; FR, VK, K-HK, and PS wrote the manuscript.

FUNDING

This work was supported by funding from the Fondation Louis Jeantet "recherche translationnelle" (to K-HK and PS), Swiss National Science Foundation (SNSF number 31003A-179478), Ligue Genevoise contre le cancer (grant no. 1500203), Foundations Gertrude Von Meissner, Bärgüf, Bodifée and Auris.

ACKNOWLEDGMENTS

The authors would like to thank Jessica Sordet from the Histology platform of the Ecole Polytechnique Fédérale de Lausanne (EPFL) for RNAscope® experiments and Prof. Ulla Knaus from University College Dublin for the kind gift of the *Cyba* knockout mouse strain.

SUPPLEMENTARY MATERIAL

The Supplementary Material for this article can be found online at: https://www.frontiersin.org/articles/10.3389/fcell.2022.832314/full#supplementary-material

REFERENCES

Agledal, L., Niere, M., and Ziegler, M. (2010). The Phosphate Makes a Difference: Cellular Functions of NADP. *Redox Rep.* 15, 2–10. doi:10.1179/174329210x12650506623122

Augsburger, F., Filippova, A., Rasti, D., Seredenina, T., Lam, M., Maghzal, G., et al. (2019). Pharmacological Characterization of the Seven Human NOX Isoforms and Their Inhibitors. *Redox Biol.* 26, 101272. doi:10.1016/j.redox.2019.101272

Bánfi, B., Malgrange, B., Knisz, J., Steger, K., Dubois-Dauphin, M., and Krause, K.-H. (2004). NOX3, a Superoxide-Generating NADPH Oxidase of the Inner Ear. *J. Biol. Chem.* 279, 46065–46072. doi:10.1074/jbc.m403046200

Bothwell, M. Y., and Gillette, M. U. (2018). Circadian Redox Rhythms in the Regulation of Neuronal Excitability. *Free Radic. Biol. Med.* 119, 45–55. doi:10.1016/j.freeradbiomed.2018.01.025

Dhukhwa, A., Bhatta, P., Sheth, S., Korrapati, K., Tieu, C., Mamillapalli, C., et al. (2019). Targeting Inflammatory Processes Mediated by TRPVI and TNF-α for Treating Noise-Induced Hearing Loss. *Front. Cel. Neurosci.* 13, 444. doi:10.3389/fncel.2019.00444

Diebold, B. A., Wilder, S. G., De Deken, X., Meitzler, J. L., Doroshow, J. H., McCoy, J. W., et al. (2019). Guidelines for the Detection of NADPH Oxidases by Immunoblot and RT-qPCR. *Methods Mol. Biol.* 1982, 191–229. doi:10.1007/978-1-4939-9424-3_12

Egea, J., Fabregat, I., Frapart, Y. M., Ghezzi, P., Görlach, A., Kietzmann, T., et al. (2018). European Contribution to the Study of ROS: A Summary of the Findings and Prospects for the Future from the COST Action BM1203 (EU-ROS). *Redox Biol.* 13, 694–696. doi:10.1016/j.redox.2017.05.007

Fetoni, A. R., Paciello, F., Rolesi, R., Paludetti, G., and Troiani, D. (2019). Targeting Dysregulation of Redox Homeostasis in Noise-Induced Hearing Loss: Oxidative Stress and ROS Signaling. *Free Radic. Biol. Med.* 135, 46–59. doi:10.1016/j.freeradbiomed.2019.02.022

Flaherty, J. P., Fairfield, H. E., Spruce, C. A., McCarty, C. M., and Bergstrom, D. E. (2011). Molecular Characterization of an Allelic Series of Mutations in the Mouse Nox3 Gene. *Mamm. Genome* 22, 156–169. doi:10.1007/s00335-010-9309-z

Haryuna, T. S. H., Riawan, W., Reza, M., Purnami, N., and Adnan, A. (2016). Curcumin Prevents Cochlear Oxidative Damage after Noise Exposure. *Int. J. Pharm. Pharm. Sci.* 8, 175–178. doi:10.1055/s-0036-1579742

Henderson, D., Bielefeld, E. C., Harris, K. C., and Hu, B. H. (2006). The Role of Oxidative Stress in Noise-Induced Hearing Loss. *Ear Hear* 27, 1–19. doi:10.1097/01.aud.0000191942.36672.f3

Jones, G. P., Lukashkina, V. A., Russell, I. J., and Lukashkin, A. N. (2010). The Vestibular System Mediates Sensation of Low-Frequency Sounds in Mice. *Jaro* 11, 725–732. doi:10.1007/s10162-010-0230-7

Kaur, T., Borse, V., Sheth, S., Sheehan, K., Ghosh, S., Tupal, S., et al. (2016). Adenosine A1 Receptor Protects against Cisplatin Ototoxicity by Suppressing the NOX3/STAT1 Inflammatory Pathway in the Cochlea. *J. Neurosci.* 36, 3962–3977. doi:10.1523/jneurosci.3111-15.2016

Kaur, T., Clayman, A. C., Nash, A. J., Schrader, A. D., Warchol, M. E., and Ohlemiller, K. K. (2019). Lack of Fractalkine Receptor on Macrophages Impairs Spontaneous Recovery of Ribbon Synapses after Moderate Noise Trauma in C57BL/6 Mice. *Front. Neurosci.* 13, 620. doi:10.3389/fnins.2019.00620

Kendall, A., and Schacht, J. (2014). Disparities in Auditory Physiology and Pathology between C57BL/6J and C57BL/6N Substrains. *Hearing Res.* 318, 18–22. doi:10.1016/j.heares.2014.10.005

Kiss, P. J., Knisz, J., Zhang, Y., Baltrusaitis, J., Sigmund, C. D., Thalmann, R., et al. (2006). Inactivation of NADPH Oxidase Organizer 1 Results in Severe Imbalance. *Curr. Biol.* 16, 208–213. doi:10.1016/j.cub.2005.12.025

Kujawa, S. G., and Liberman, M. C. (2006). Acceleration of Age-Related Hearing Loss by Early Noise Exposure: Evidence of a Misspent Youth. *J. Neurosci.* 26, 2115–2123. doi:10.1523/jneurosci.4985-05.2006

Kujawa, S. G., and Liberman, M. C. (2009). Adding Insult to Injury: Cochlear Nerve Degeneration after "temporary" Noise-Induced Hearing Loss. *J. Neurosci.* 29, 14077–14085. doi:10.1523/jneurosci.2845-09.2009

Lavinsky, J., Crow, A. L., Pan, C., Wang, J., Aaron, K. A., Ho, M. K., et al. (2015). Genome-wide Association Study Identifies Nox3 as a Critical Gene for Susceptibility to Noise-Induced Hearing Loss. *Plos Genet.* 11, e1005094. doi:10.1371/journal.pgen.1005094

Le, T. N., Straatman, L. V., Lea, J., and Westerberg, B. (2017). Current Insights in Noise-Induced Hearing Loss: a Literature Review of the Underlying Mechanism, Pathophysiology, Asymmetry, and Management Options. *J. Otolaryngol. - Head Neck Surg.* 46, 41. doi:10.1186/s40463-017-0219-x

Liberman, M. C., and Kujawa, S. G. (2017). Cochlear Synaptopathy in Acquired Sensorineural Hearing Loss: Manifestations and Mechanisms. *Hearing Res.* 349, 138–147. doi:10.1016/j.heares.2017.01.003

Maulucci, G., Troiani, D., Eramo, S. L. M., Paciello, F., Podda, M. V., Paludetti, G., et al. (2014). Time Evolution of Noise Induced Oxidation in Outer Hair Cells: Role of NAD(P)H and Plasma Membrane Fluidity. *Biochim. Biophys. Acta (Bba) - Gen. Subjects* 1840, 2192–2202. doi:10.1016/j.bbagen.2014.04.005

Mohri, H., Ninoyu, Y., Sakaguchi, H., Hirano, S., Saito, N., and Ueyama, T. (2021). Nox3-Derived Superoxide in Cochleae Induces Sensorineural Hearing Loss. *J. Neurosci.* 41, 4716–4731. doi:10.1523/jneurosci.2672-20.2021

Moll, F., Walter, M., Rezende, F., Helfinger, V., Vasconez, E., De Oliveira, T., et al. (2018). NoxO1 Controls Proliferation of Colon Epithelial Cells. *Front. Immunol.* 9, 973. doi:10.3389/fimmu.2018.00973

Morton-Jones, R. T., Cannell, M. B., and Housley, G. D. (2008). Ca2+ Entry via AMPA-type Glutamate Receptors Triggers Ca2+-Induced Ca2+ Release from Ryanodine Receptors in Rat Spiral Ganglion Neurons. *Cell Calcium* 43, 356–366. doi:10.1016/j.ceca.2007.07.003

Mukherjea, D., Jajoo, S., Kaur, T., Sheehan, K. E., Ramkumar, V., and Rybak, L. P. (2010). Transtympanic administration of short interfering (si)RNA for the NOX3 isoform of NADPH oxidase protects against cisplatin-induced hearing loss in the rat. *Antioxid. Redox Signaling* 13, 589–598. doi:10.1089/ars.2010.3110

Nakano, Y., Longo-Guess, C. M., Bergstrom, D. E., Nauseef, W. M., Jones, S. M., and Bánfi, B. (2008). Mutation of the Cyba Gene Encoding P22phox Causes Vestibular and Immune Defects in Mice. *J. Clin. Invest.* 118, 1176–1185. doi:10.1172/JCI33835

Nakano, Y., Banfi, B., Jesaitis, A. J., Dinauer, M. C., Allen, L.-A. H., and Nauseef, W. M. (2007). Critical Roles for P22phox in the Structural Maturation and Subcellular Targeting of Nox3. *Biochem. J.* 403, 97–108. doi:10.1042/bj20060819

Paffenholz, R., Bergstrom, R. A., Pasutto, F., Wabnitz, P., Munroe, R. J., Jagla, W., et al. (2004). Vestibular Defects in Head-Tilt Mice Result from Mutations in Nox3, Encoding an NADPH Oxidase. *Genes Dev.* 18, 486–491. doi:10.1101/gad.1172504

Peineau, T., Belleudy, S., Pietropaolo, S., Bouleau, Y., and Dulon, D. (2021). Synaptic Release Potentiation at Aging Auditory Ribbon Synapses. *Front. Aging Neurosci.* 13, 756449. doi:10.3389/fnagi.2021.756449

Pircalabioru, G., Aviello, G., Kubica, M., Zhdanov, A., Paclet, M.-H., Brennan, L., et al. (2016). Defensive Mutualism Rescues NADPH Oxidase Inactivation in Gut Infection. *Cell Host & Microbe* 19, 651–663. doi:10.1016/j.chom.2016.04.007

Prior, K.-K., Leisegang, M. S., Josipovic, I., Löwe, O., Shah, A. M., Weissmann, N., et al. (2016). CRISPR/Cas9-mediated Knockout of P22phox Leads to Loss of Nox1 and Nox4, but Not Nox5 Activity. *Redox Biol.* 9, 287–295. doi:10.1016/j.redox.2016.08.013

Ramkumar, V., Mukherjea, D., Dhukhwa, A., and Rybak, L. P. (2021). Oxidative Stress and Inflammation Caused by Cisplatin Ototoxicity. *Antioxidants (Basel)* 10, 1919. doi:10.3390/antiox10121919

Rousset F, K. V., Sipione, R., Schmidbauer, D., Nacher-Soler, G., Ilmjärv, S., Coelho, M., et al. (2020). Intrinsically Self-Renewing Neuroprogenitors from the A/J Mouse Spiral Ganglion as Virtually Unlimited Source of Mature Auditory Neurons. *Front. Cell Neurosci. press* 14, 395. doi:10.3389/fncel.2020.599152

Rousset, F., Salmon, P., Bredl, S., Cherpin, O., Coelho, M., Myburgh, R., et al. (2019). Optimizing Synthetic miRNA Minigene Architecture for Efficient miRNA Hairpin Concatenation and Multi-Target Gene Knockdown. *Mol. Ther. Nucleic Acids* 14, 351–363. doi:10.1016/j.omtn.2018.12.004

Rousset, F., Carnesecchi, S., Senn, P., and Krause, K.-H. (2015). Nox3-Targeted Therapies for Inner Ear Pathologies. *Cpd* 21, 5977–5987. doi:10.2174/1381612821666151029112421

Rousset, F., Nacher-Soler, G., Coelho, M., Ilmjarv, S., Kokje, V. B. C., Marteyn, A., et al. (2020). Redox Activation of Excitatory Pathways in Auditory Neurons as Mechanism of Age-Related Hearing Loss. *Redox Biol.* 30, 101434. doi:10.1016/j.redox.2020.101434

Son, E. J., Wu, L., Yoon, H., Kim, S., Choi, J. Y., and Bok, J. (2012). Developmental Gene Expression Profiling along the Tonotopic axis of the Mouse Cochlea. *PLoS One* 7, e40735. doi:10.1371/journal.pone.0040735

Vikhe Patil, K., Canlon, B., and Cederroth, C. R. (2015). High Quality RNA Extraction of the Mammalian Cochlea for qRT-PCR and Transcriptome Analyses. *Hearing Res.* 325, 42–48. doi:10.1016/j.heares.2015.03.008

Wang, J., and Puel, J.-L. (2018). Toward Cochlear Therapies. *Physiol. Rev.* 98, 2477–2522. doi:10.1152/physrev.00053.2017

World Health Organization (2022). Deafness and Hearing Loss. Available at: https://www.who.int/health-topics/hearing-loss#tab=tab_1.

Wu, P. Z., Liberman, L. D., Bennett, K., de Gruttola, V., O'Malley, J. T., and Liberman, M. C. (2019). Primary Neural Degeneration in the Human Cochlea: Evidence for Hidden Hearing Loss in the Aging Ear. *Neuroscience* 407, 8–20. doi:10.1016/j.neuroscience.2018.07.053

Conflict of Interest: The authors declare that the research was conducted in the absence of any commercial or financial relationships that could be construed as a potential conflict of interest.

Publisher's Note: All claims expressed in this article are solely those of the authors and do not necessarily represent those of their affiliated organizations, or those of the publisher, the editors and the reviewers. Any product that may be evaluated in this article, or claim that may be made by its manufacturer, is not guaranteed or endorsed by the publisher.

frontiers in Cell and Developmental Biology

REVIEW
published: 04 March 2022
doi: 10.3389/fcell.2022.841708

Hearing Function, Degeneration, and Disease: Spotlight on the Stria Vascularis

Matsya R Thulasiram[1]*, *Jacqueline M Ogier*[2] and *Alain Dabdoub*[1,2,3]*

[1]Department of Laboratory Medicine and Pathobiology, University of Toronto, Toronto, ON, Canada, [2]Biological Sciences, Sunnybrook Research Institute, Sunnybrook Health Sciences Centre, Toronto, ON, Canada, [3]Department of Otolaryngology–Head and Neck Surgery, University of Toronto, Toronto, ON, Canada

The stria vascularis (SV) is a highly vascularized tissue lining the lateral wall of the cochlea. The SV maintains cochlear fluid homeostasis, generating the endocochlear potential that is required for sound transduction. In addition, the SV acts as an important blood-labyrinth barrier, tightly regulating the passage of molecules from the blood into the cochlea. A healthy SV is therefore vital for hearing function. Degeneration of the SV is a leading cause of age-related hearing loss, and has been associated with several hearing disorders, including Norrie disease, Meniere's disease, Alport syndrome, Waardenburg syndrome, and Cytomegalovirus-induced hearing loss. Despite the SV's important role in hearing, there is still much that remains to be discovered, including cell-specific function within the SV, mechanisms of SV degeneration, and potential protective or regenerative therapies. In this review, we discuss recent discoveries elucidating the molecular regulatory networks of SV function, mechanisms underlying degeneration of the SV, and otoprotective strategies for preventing drug-induced SV damage. We also highlight recent clinical developments for treating SV-related hearing loss and discuss future research trajectories in the field.

Keywords: single-cell sequencing, regeneration, cochlear battery, blood-labyrinth barrier, cisplatin, virus, clinical trial

OPEN ACCESS

Edited by:
Stefan Heller,
Stanford University, United States

Reviewed by:
Hiroshi Hibino,
Osaka University, Japan
Guoqiang Wan,
Nanjing University, China

***Correspondence:**
Matsya R Thulasiram
matsya.thulasiram@mail.utoronto.ca
Alain Dabdoub
adabdoub@sri.utoronto.ca

Specialty section:
This article was submitted to Molecular and Cellular Pathology, a section of the journal Frontiers in Cell and Developmental Biology

Received: *22 December 2021*
Accepted: *20 January 2022*
Published: *04 March 2022*

Citation:
Thulasiram MR, Ogier JM and Dabdoub A (2022) Hearing Function, Degeneration, and Disease: Spotlight on the Stria Vascularis. Front. Cell Dev. Biol. 10:841708. doi: 10.3389/fcell.2022.841708

1 INTRODUCTION

The stria vascularis (SV) is a highly vascularized tissue located in the lateral wall of the cochlea that contributes to cochlear homeostasis in two ways (**Figure 1**). First, ion transport proteins in the SV perform active potassium ion (K^+) recycling between the endolymph of the scala media and the perilymph of the scala tympani. This maintains the endolymph at a high K^+ (~157 mM), low sodium (Na^+; ~1.3 mM) state, that contrasts with the low K^+ (~4.2–6.0 mM), high Na^+ (~141–148 mM) state of perilymph (Liu et al., 2017; reviewed in Wangemann 2002, Wangemann 2006). This contrasting ionic composition creates an electric potential difference of +80–100 mV between the cochlear fluids, known as the endocochlear potential (Nin et al., 2016). For this reason, the SV is often referred to as the cochlear battery (**Figure 2**).

The SV directly contributes to hearing function by maintaining the endocochlear potential, which is required for the process of hair cell transduction to occur. Hair cell transduction is the critical point of sensing sound, where the mechanical sound wave is converted by cochlear hair cells into an electrochemical signal for auditory perception. This detection process begins when sound waves stimulate mechanically gated K^+ channels in the hair cell stereocilia. Once open, these channels allow for the influx of K^+ and the depolarization of the hair cell (Zhang Q et al., 2021). Subsequently,

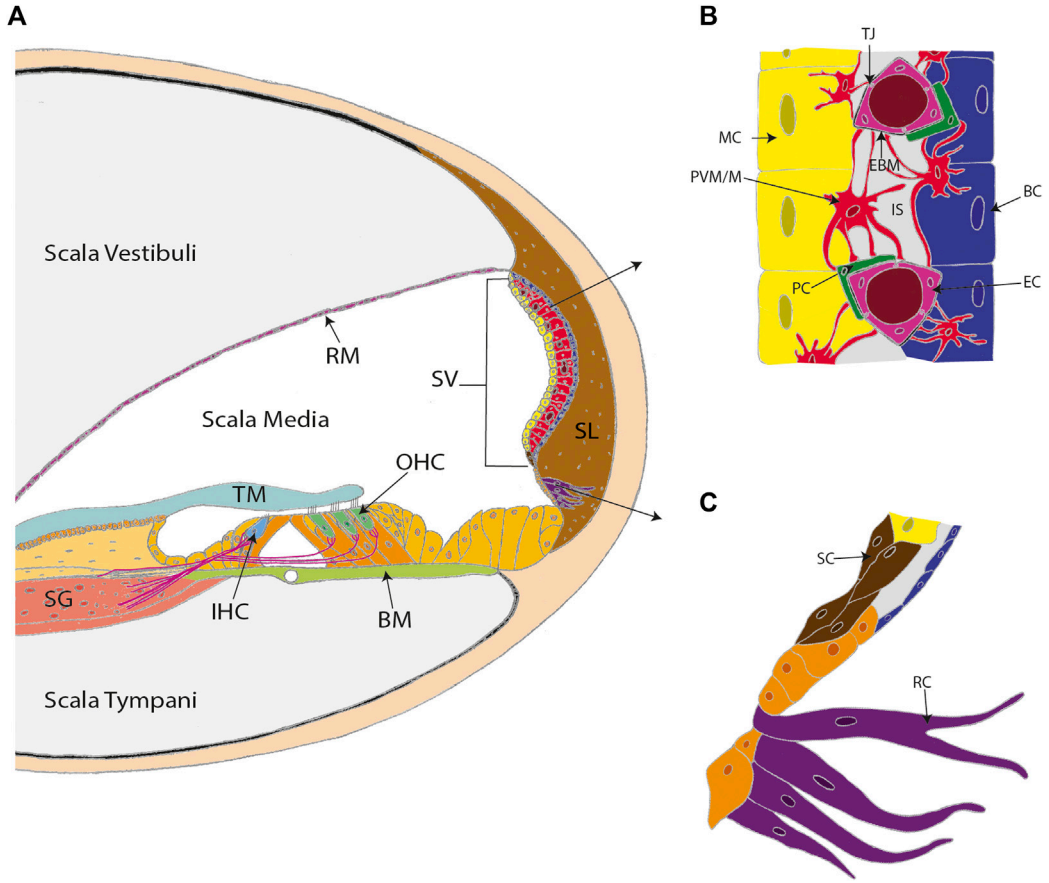

FIGURE 1 | The stria vascularis (SV) is a highly specialized and vascularized tissue lining the lateral wall of the cochlea. **(A)** A cross-section of the cochlea. **(B)** The three conventional cell layers of the SV include the marginal cell layer (MC), the intermediate cell layer, and the basal cell layer (BC). The marginal cell layer is exposed to the endolymph and the basal cell layer interacts with spiral ligament fibrocytes. The intermediate cell layer is composed of perivascular-resident macrophage-like melanocytes (PVM/M), pericytes (PC), and endothelial cells (EC). The cell layers are tightly interlocked by infoldings and projections between the basolateral membranes of marginal cells and the PVM/Ms, and the PVM/Ms and the basal cells. **(C)** Other cell types in the lateral wall that contribute to SV function include spindle cells (SC) and root cells (RC). Other labels: Reisner's membrane (RM); tectorial membrane (TM); spiral ganglion (SG); inner hair cell (IHC); outer hair cells (OHC); basilar membrane (BM); spiral ligament (SL); tight junctions (TJ); endothelial basement membrane (EBM) and intrastrial space (IS). **(C)** adapted from Gu et al. (2020).

voltage-dependent calcium ion (Ca^{2+}) channels are activated, allowing for the influx of Ca^{2+} and release of neurotransmitters, creating a signal that is sent to and processed by the brain (Gill and Salt 1997; Wangemann 2006). Once the hair cell is depolarized, K^+ exits the hair cell and is taken up by the fibrocytes of the spiral ligament (reviewed in Zdebik et al., 2009). Gap and tight junction proteins, such as connexin and claudin11, then transport K^+ into the SV, where ion transport channels, including the K^+ inwardly-rectifying channel Kir4.1, traffic K^+ through the SV layers, and back into the endolymph (Wangemann 2006). This active K^+ recycling ensures that the endocochlear potential is maintained for sound detection to occur (**Figure 2**).

In addition, the SV contains the cochlear blood-labyrinth barrier (BLB), that tightly controls the transfer of material from the SV capillary network into the endolymph (**Figure 1B**). The BLB is often compared to the blood-brain barrier (BBB), with both vascular networks creating a physical barrier that limits paracellular diffusion and prevents infiltration of pathogens into the cochlea or brain respectively (Inamura and Salt 1992). Paracellular diffusion across the BBB is limited to small lipophilic or gaseous molecules (molecular weight <400–500 Da), whereas BLB permeability appears to extend beyond 500 Da (Dulon et al., 1986). Notably, hydrophilic aminoglycosides are unable to cross the BBB, whereas aminoglycosides such as tobramycin (467.515 Da), amikacin (585.6 Da), and gentamicin (477.596 Da) are readily transported via the BLB into the cochlea (Nau et al., 2010). Other known differences between the BBB and BLB include the type of supporting cells present (astrocytes vs. perivascular resident macrophage-like melanocytes in the BBB and BLB respectively) and basement membrane composition (reviewed in Nyberg et al., 2019). Nevertheless, further research is required to define the specific cell types and diffusion properties of the BLB. The functional complexity of the SV, combined with its difficult to access location within the temporal bone, has hindered SV research. However, advances in sequencing technology and the investigation of SV-associated disease mechanisms are improving our understanding of the SV. This review

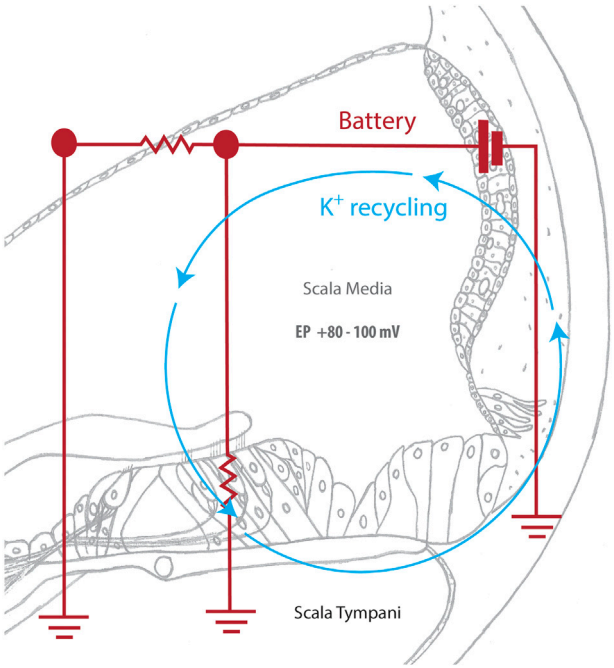

FIGURE 2 | The cochlear battery facilitates sound detection. Sound waves deflect hair cell stereocilia, mechanically opening K+ channels and allowing potassium ions (K+) from the scala media to enter the hair cell. The subsequent depolarization of the hair cell activates voltage-gated calcium channels, which triggers a calcium influx that causes neurotransmitter to be released at the base of the hair cell. Neurotransmitter then diffuses into the nerve terminal and causes an action potential to be created in the spiral ganglion. This signal is then transmitted to the brain for auditory processing. The SV actively returns potassium ions that were used during this process to the scala media, maintaining the endocochlear potential and allowing for continuous sound detection.

summarizes notable discoveries regarding SV function and novel opportunities that have been identified for developing SV-associated hearing loss treatments.

2 PHYSIOLOGY OF THE STRIA VASCULARIS

The SV has three cellular layers, with each layer performing a specific function (**Figure 1B**). The marginal cell layer is exposed to the endolymph, transporting K^+ from the SV into the scala media (Wangemann 2002). The intermediate cell layer includes the BLB and abundantly expresses the Kir4.1 ion channels that facilitate K^+ transport. The basal cell layer associates with the spiral ligament fibrocytes via junction proteins to control ion flow into the SV and prevent ion leakage between the cochlear chambers (Liu et al., 2017). During development, the layers of the SV originate from different cell lineages. The marginal cells arise from the otic epithelium, whereas the specialized intermediate cells known as perivascular-resident macrophage-like melanocytes (PVM/Ms) are derived from migratory neural crest cells (Kiernan et al., 2002). Basal cells are formed from the otic mesenchyme after the marginal and intermediate cell layers are established (Kiernan et al., 2002; Locher et al., 2015).

While knowledge of the SV layers remains limited, recent RNA sequencing and bioinformatic analysis have been used to further elucidate cell-specific gene expression in the SV. For instance, single-cell RNA sequencing of the adult CBA/J mouse SV identified previously unknown gene expression in the SV (Korrapati et al., 2019). Newly identified genes include the lipid transporter gene, ATP binding cassette G1 (*Abcg1*), and the Notch signaling pathway effector gene, Hes-related family BHLH transcription factor with YRPW motif (*Heyl*), expressed in marginal cells; the K^+ inwardly-rectifying channel J13 (*Kcnj13*) and a VEGF receptor gene, neuropilin 2 (*Nrp2*), expressed in intermediate cells; and the SRY-Box transcription factor 8 (*Sox8*), and the steroid/thyroid hormone receptor gene, nuclear receptor 2F2 (*Nr2f2*), expressed in basal cells. Further evaluation of these genes will likely provide important insight into cell-specific roles within the SV. In addition, Korrapati et al. used the Pharos database (https://pharos.nih.gov/) to demonstrate that 26 of the newly identified SV genes can be targeted by 93 FDA approved drugs, opening immediate avenues for SV-specific therapeutics.

Beyond the three conventional layers of the SV, single-nucleus RNA sequencing has also been used to identify distinct transcriptional profiles for rare spindle and root cells (**Figure 1C**). Spindle cells express annexin 1 (*Anxa1*) and dipeptidyl peptidase like 10 (*Dpp10*), which are target genes for the bric-a-brac (BTB) domain and cap'n'collar (CNC) homolog 2 (*Bach2*) transcription factor—a potent immune regulator (Gu et al., 2020). Therefore, spindle cells may contribute to immune regulation in the SV. In contrast, the expression of ion channel genes, such as the chloride/bicarbonate exchanger, solute carrier 26A4 (*Slc26A4*), and the K^+ inwardly-rectifying channel J10 (*Kcnj10*) in root cells suggests a role in maintaining the endocochlear potential (Gu et al., 2020). Notably, this finding supports previous electrophysiological observations made by Jagger et al. demonstrating that root cells display weak, rectifying whole-cell currents indicative of K^+ channel activity (Jagger et al., 2010). Furthermore, immunohistochemistry indicates colocalization of Kir4.1 (the protein encoded by *Kcnj10*) within root cells, providing further evidence that root cells contribute to K^+ recycling in the cochlea (Jagger et al., 2010). Significant research efforts are now required to correlate transcriptional findings with cell-specific function *in vivo*. However, these findings highlight the advantage of sequencing technology for identifying regulatory networks and SV cell-specific markers. Indeed, the characterization of previously unknown gene expression patterns in the SV has already provided novel targets for SV therapies and will likely increase our understanding of how complex biological functions are performed within the SV.

2.1 Characterizing the Stria Vascularis Blood-Labyrinth-Barrier

As discussed above, the SV provides a physical protective barrier that regulates which molecules enter the cochlea. Currently, the BLB is poorly understood, which has hindered the development and delivery of therapeutics to the cochlea. However, research focusing on pericytes and macrophage-like-melanocytes in the

SV has provided further information regarding the structure and function of the BLB.

2.1.1 The Role of Pericytes in the Blood-Labyrinth Barrier

Pericytes are specialized cells present along the abluminal surface of capillaries throughout the body. Within the cochlea, pericytes contribute to angiogenesis (the formation of new blood vessels), vascular integrity, and blood flow control (Reviewed in Caporarello et al., 2019). Pericyte depletion (in a Cre-mediated diphtheria toxin inducible mouse model) causes reduced vascular density, variable vessel size, vascular leakage, and hearing loss (Zhang J et al., 2021). Notably, RTqPCR and immunohistochemical analysis indicated that vascular endothelial growth factor isoform A165 (VEGFA165) is particularly important for pericyte function. Subsequently, Zhang et al. used an adeno-associated viral vector to deliver *Vegfa165* to pericyte-depleted mice, which promoted vascular growth and pericyte proliferation, ultimately restoring the endocochlear potential and hearing. These findings are consistent with previous observations made by Wang et al. who also demonstrated that VEGFA165 stimulates new vessel formation in adult C57BL/6 mouse SV explant cultures (Wang et al., 2019). Combined, these studies provide evidence that pericytes have a critical role for maintaining SV integrity, and that VEGFA165 might be a therapeutic target for preventing hearing loss associated with SV degradation. Other potential targets include zona occludens-1 (ZO-1) and VE-cadherin, which are tight junction proteins expressed by SV pericytes and associated with BLB endothelial cell integrity (Neng et al., 2013).

2.1.2 Perivascular Resident Macrophage-Like Melanocytes Have a Regulatory and Protective Role in the Stria Vascularis

PVM/Ms are a hybridized cell type in the lateral wall, expressing both macrophage and melanocyte markers, such as EGF-like module-containing mucin-like hormone receptor-like 1 (F4/80), CD68 molecule (CD68), integrin alpha M (CD11b), macrophage/monocyte antibody (MOMA2), glutathione S-transferase alpha 4 (GSTα4), glutathione S-transferase (GST), and Kir4.1 (Shi 2010; Zhang et al., 2012). PVM/M's regulate tight junctions, interact with endothelial cells of the SV capillary network, and contribute to the maintenance of cochlear homeostasis (Zhang et al., 2012). Interestingly, immunofluorescent labelling of PVM/Ms using ionized calcium binding adaptor molecule 1 (Iba1) identified that PVM/M morphology differs according to age in cochlear cross-sections from human donors (Noble et al., 2019). Specifically, PVM/Ms have a higher number of processes and lower nuclear cytoplasmic volume in samples from younger individuals (age 20–65) when compared to samples from older individuals (age 68–89+). Such structural differences may have important functional outcomes, particularly regarding the cochlear immune response, which might contribute to age-related hearing loss. In addition, Noble et al. observed that PVM/M morphology differs between the lateral wall and the auditory nerve regions. PVM/Ms in the SV have multiple thin projections of processes, whereas PVM/Ms in the auditory nerve appear to be bipolar and filopodia-like (Noble et al., 2019). This may indicate that lateral wall PVM/Ms have a surveillance function, whereas PVM/Ms of the auditory nerve are more motile and active in an injury response.

Overall, the macrophage activity of PVM/Ms is well-accepted. However, unanswered questions remain regarding PVM/M melanocyte activity in the SV. PVM/Ms are melanin-producing cells and interesting connections have been made regarding SV melanin content and hearing protection. Melanin is thought to preserve the endocochlear potential through melanin-Ca^{2+} interactions (Bush and Simon 2007; Gill and Salt 1997; Liu and Simon 2005). As mentioned previously, neurotransmission is dependent on Ca^{2+} influx into the hair cell following depolarization. Therefore, Ca^{2+} homeostasis is crucial for hearing transduction, and it is hypothesized that melanin acts as a Ca^{2+} chelator to modulate endolymphatic Ca^{2+} concentrations. Notably, a comparison of hearing ability (based on ABR measurements) in transgenic NMRI mice that were either pigmented and expressing melanin (YRT2 mice), non-pigmented but expressing the melanin precursor L-DOPA (TyrTH mice), or albino non-transgenic NMRI littermates (NMRI), demonstrated that aging YRT2 and TyrTH mice exhibit significantly less hearing loss after noise exposure than NMRI littermates (Murillo-Cuesta et al., 2010). Interestingly, hearing thresholds between YRT2 mice and TyrTH mice did not significantly differ, suggesting that the presence of melanin precursor is sufficient to protect hearing. Furthermore, YRT2 and TyrTH mice had better hearing recovery following noise insult when compared to non-transgenic littermates. Similarly, pigmentation appears to have a protective role for hearing in humans. Using the Fitzpatrick skin colour scale and audiometry, Lin et al. showed that individuals with darker skin have better hearing than those with lighter skin (Lin et al., 2012). Skin pigmentation appears to correlate with melanin content in the SV, and Andresen et al. demonstrated that SV melanin is indeed higher in African Americans when compared to Caucasians (Andresen et al., 2021).

Overall, melanocytes appear to have a particularly important role for supporting hearing function. However, the mechanism of protection is not clear. Melanocytes could be protecting the ear by providing immune surveillance in the SV, regulating cochlear Ca^{2+} levels, controlling vascular permeability, or any combination thereof. Furthermore, melanocyte-secreted melanin is a free radical scavenger that can prevent damaging redox stress in the ear (Sichel et al., 1991; Wu et al., 2001). Therefore, clarifying the role of melanin in the ear is worthwhile, as it may be possible to protect the cochlea in damaging situations using melanin supplementation. However, an important observation is that melanin does not protect against age-related SV degeneration. In fact, melanin content increases in

TABLE 1 | Summary of SV disorders and associated clinical trials.

Disorder	Prevalence	Identified Causative Genes	Phenotype	Intervention/Clinical trial identification	References
Norrie disease	400 cases worldwide	*Ndp*	Vascular degeneration	N.A.	Berger et al. (1996) Rehm et al. (2002) Sowden et al. (2020)
Meniere's disease	200–500 in 100,000	*Esrrb*	SNHL	NCT00802529	Gu et al. (2021)
		Atp1b2	Tinnitus	NCT03664674	Gürkov et al. (2016)
		Ednrb			
		Tmem176A		NCT04677972	Kil et al. (2022)
		Slc44a2		NCT03325790	Lambert et al. (2016)
		Col1a2			Patel et al. (2016)
Alport syndrome	1 in 5,000	*Col4a3*	Basement membrane dysfunction	NCT04947813	Dufek et al. (2020)
		Col4a4			
		Col4a5			Gratton et al. (2005)
Waardenburg Syndrome	2–3 in 100,000	*Mitf*	Loss of pigmentation	N.A.	Chen L. et al. (2016)
		Pax3			Chen L. et al. (2020)
		Sox10			Chen T. et al. (2018)
		Ednrb			Flesher et al. (2020)
		Edn3			Saleem, (2019)
		Snai2			Song et al. (2016)

the aging ear of mice and humans despite the prevalence of age-related hearing loss (Kobrina et al., 2020; Andresen et al., 2021).

3 STRIA VASCULARIS DYSFUNCTION AND HEARING LOSS

The SV protects the cochlea and preserves cochlear homeostasis, directly contributing to auditory detection. Therefore, dysfunction of the SV can have severe consequences for hearing. In this section, we discuss how SV dysfunction underlies age-related hearing loss, hearing loss induced by ototoxic medicines, several forms of heritable hearing loss (**Table 1**), and viral infection-mediated hearing loss.

3.1 Age Related Degeneration of the Stria Vascularis

Age-related hearing loss, known as presbycusis, affects over 25% of individuals above 60 years of age (World Health Organization 2021). Presbycusis has repeatedly been associated with the death of hair cells in the cochlea, and a widely recognized hypothesis suggests that degeneration of the SV, specifically the BLB and impaired SV blood flow, is the primary contributing factor (**Figure 3A**) (Schuknecht et al., 1974; Pauler et al., 1988; Gratton et al., 1996; McFadden et al., 1999; Gates and Mills 2005; Zhang et al., 2013; Carraro and Harrison 2016; Wang and Puel 2020). As previously discussed, tight regulation of ion channel function in the SV is an important aspect of endocochlear potential maintenance (reviewed in Peixoto Pinheiro et al., 2021). RTqPCR and immunohistochemical analysis of two essential players in the SV (Na+/K + ATPase and Kir4.1) in young (1.5–3-week-old) and aged (1.5–2.5-year-old) CBA/CaJ mice has demonstrated reduced ion channel expression in the SV of aged animals. Notably, reduced ion channel expression corresponded with dysregulation of the endocochlear potential and hearing loss (Ding et al., 2018; Liu T. et al., 2019). Similarly, in a guinea pig model of accelerated aging (induced by D-galactose), RTqPCR indicated reduced expression of the Ca^{2+}-activated chloride channel, transmembrane protein 16A (*TMEM16A*) in the SV of aged guinea pigs (1-year-old) when compared to young guinea pigs (2-week-old). The reduced *TMEM16A* expression corresponded with increased hearing thresholds (Zhou et al., 2019). Combined, these studies demonstrate that the aging SV can no longer support the endocochlear potential due to the loss of important ion channels, and that this directly causes age-related hearing loss. Interestingly, this hypothesis was challenged by Wu et al. who analysed 120 human inner ears (obtained during autopsy) and concluded that hair cell death preceded SV atrophy (Wu et al., 2020). However, this study relied solely on histopathological evidence, which cannot detect critical changes in ion recycling or the endocochlear potential changes that likely cause the death of sensory hair cells. Moreover, a similar histopathological study by Kurata et al. identified increased vascular thickness, reduced vessel counts, and decreased total SV area in the SV of individuals with presbycusis when compared to age-matched controls, contradicting the results obtained by Wu et al. (Kurata et al., 2016). However, cochlear fluid evaluation is required to truly answer the question of whether SV degeneration drives age-related hearing loss. Unfortunately, sampling from the living cochlea is not possible, as it is invasive and risks inducing hearing loss. Therefore, mouse models have been utilized to further understand age-related degeneration of the SV. For example, Carraro and Harrison developed a partial corrosion-cast technique using C57BL/6 mice, to capture the full structural integrity of the cochlear vasculature using polymer perfusion (**Figure 3B**) (Carraro and Harrison 2016). Using this technique in conjunction with SEM, Carraro and Harrison showed that 6-month-old mice have significantly narrower vasculature within the basal turn of the SV when

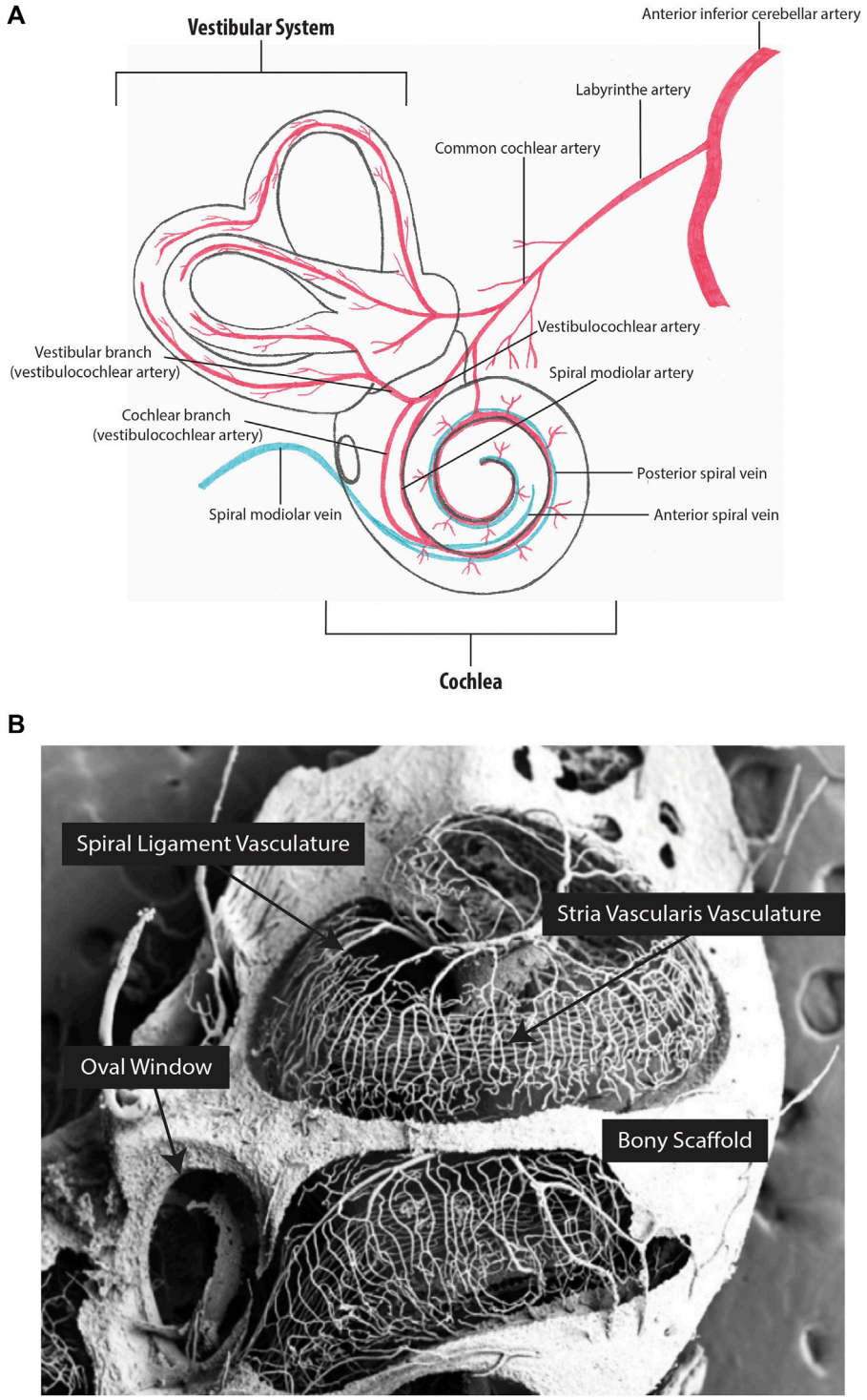

FIGURE 3 | Inner ear vascular network. **(A)** Arterial blood supply and venous drainage of the cochlear and vestibular systems. **(B)** Partial corrosion casts of the mouse cochlea. The capillaries of the stria vascularis run parallel along the length of the cochlea. **Figure 3B** image provided by M. Carraro and R.V. Harrison.

compared to 1-month-old mice, and that these changes correspond with increased high frequency ABR hearing thresholds. Immunohistochemical analysis of the BLB also identified a loss of pericytes and PVM/Ms in aged C57BL/6 mice which has been previously shown to cause vascular leakage (Neng et al., 2015). However, C57BL/6 mice carry the cadherin

23 mutation, which is a well-established cause of age-related hearing loss (Sotomayor et al., 2010). Accordingly, Kobrina et al. used CBA/CaJ mice (which have more robust hearing) to assess hearing and cochlear histopathology during the aging process (Kobrina et al., 2020). Aged mice demonstrated decreased behavioural sound detection, increased ABR hearing thresholds, decreased hair cell survival, reduced SV thickness, and increased SV melanin when compared to young mice. Taken together, findings from mice and humans indicate that age-related changes in the SV microvasculature impact circulation and perfusion within the cochlea, contributing to functional changes in hearing. However, further mechanistic investigations are required to confirm these observations. Using the data obtained from single cell sequencing, new conditional knockout mouse models can be created to study the role of specific genes in the SV. These will provide insights into the mechanisms by which the SV develops, degenerates with age, and possible means of prevention and regeneration.

3.2 Ototoxicity and the Stria Vascularis

Ototoxicity is the result of a substance damaging any part of the cochlea, vestibular system, or auditory nerve. While ototoxic medicines are generally avoided in the clinic, their use is often required as part of a life-saving medical intervention. Three ototoxic drug classes are particularly problematic. First are the aminoglycoside antibiotics, used to manage chronic or multi-drug resistant infection. Aminoglycoside ototoxicity typically damages hair cells directly after being trafficked through the BLB into the endolymph (Imamura and Adams 2003; Li and Steyger 2011; Wang and Steyger 2009). Secondly, loop diuretics, which are used to treat hypertension and edema, directly target the SV. Loop diuretics, such as ethacrynic acid, cause a transient reduction of the endocochlear potential due to disrupted SV blood flow and inhibited Na^+/K^+ ATPase and $Na^+/K^+/Cl^-$ cotransporter (NKCC1) function (Ding et al., 2016). Lastly, the platinum-based chemotherapeutics, which are used to treat a range of metastatic and refractory tumours in adults and children, appear to affect both the SV and the hair cells through long-term accumulation within the cochlea (Breglio et al., 2017). Several ototoxic platinum-based chemotherapeutics are used, including carboplatin, oxaliplatin, and cisplatin (Gersten et al., 2020). However, of these chemotherapeutics, cisplatin is the most widely used and the most ototoxic (Watanabe et al., 2002; Thomas et al., 2006). Cisplatin causes significant damage to hair cells, spiral ganglion neurons, and the SV, resulting in permanent hearing loss in both pediatric and adult recipients (Bertolini et al., 2004; Frisina et al., 2016). Inductively coupled plasma mass spectrometry shows long-term retention of cisplatin in the SV (Breglio et al., 2017) and cisplatin treatment reduces the endocochlear potential (Tsukasaki et al., 2000; Breglio et al., 2017). Immunofluorescent microscopy indicates that cisplatin reduces SV expression of the tight junction protein, ZO-1, and gap junction proteins, Connexin26 and Connexin34 (Zhang N. et al., 2020). Furthermore, PVM/Ms are activated and damaged in response to cisplatin treatment. Overall, cisplatin broadly affects SV barrier integrity, impacting the endocochlear potential, and initiating an immune response that leads to long-term SV damage, resulting in hearing loss. Therefore, given the necessity of platinum-based therapeutics for life-saving cancer treatment, there is a significant need for otoprotective substances that can prevent SV damage.

3.2.1 Protecting the Ear From Ototoxicity

The vast majority of proposed otoprotective compounds target redox stress specifically within the hair cell. However, antioxidants may also reduce redox stress within the SV, providing further protection for the cochlea. For example, Cai et al. investigated apoptotic events in the SV driven by cisplatin treatment and examined the protective effect of allicin, a natural lipophilic small molecule antioxidant (Cai et al., 2019). Mice were pre-treated with allicin twice, receiving 18.2 mg/kg intraperitoneally 1 day before, and then 2 hours before starting cisplatin treatment. Intraperitoneal cisplatin was then administered once daily for seven consecutive days at 3 mg/kg. Cisplatin treatment caused pro-apoptotic factors such as Poly [ADP-ribose] Polymerase 1 (PARP-1) and apoptosis inducing factor (AIF) to be expressed in the SV. However, PARP-1 and AIF expression was significantly reduced in allicin pre-treated mice. This indicates that allicin might be an otoprotective compound. However, functional hearing assessments were not performed. Furthermore, there is a risk that antioxidant use can reduce chemotherapeutic efficacy (Lawenda et al., 2008). Therefore, significantly more research is required to ascertain whether allicin treatment is a strategy for reducing cisplatin-associated ototoxicity. Alternatively, statin medications have shown otoprotective promise against platinum-based drug and aminoglycoside-induced ototoxicity (Brand et al., 2011), as well as noise-induced hearing loss (Park et al., 2012; Richter et al., 2018). Statin medications are cholesterol-lowering drugs that inhibit 3-hydroxy-3-methylglutaryl-CoA (HMG-CoA) reductase, the rate-limiting enzyme in cholesterol biosynthesis. Fernandez et al. predicted that statin otoprotection was due to reduced cisplatin uptake and retention within the SV (Fernandez et al., 2020). However, when testing this hypothesis, lovastatin treatment did not prevent high accumulation of cisplatin in the mouse SV (Fernandez et al., 2020). Therefore, the mechanism by which statins are otoprotective remains elusive. Nevertheless, a recent clinical observational study found that individuals taking atorvastatin with concurrent cisplatin therapy had significantly better hearing following cisplatin treatment compared to non-statin treated individuals (Fernandez et al., 2021; NCT03225157). Overall, 277 individuals with head and neck squamous cell carcinoma participated in the study, with 113 participants already receiving statin medication. Baseline audiometric thresholds for all participants were compared with follow up audiometry collected within 90 days of cisplatin treatment. High frequency threshold shifts were approximately 10 dB greater in participants receiving cisplatin alone when compared to those taking atorvastatin, and the otoprotective effect of atorvastatin was independent of the atorvastatin dose. Therefore, statins should be further evaluated as an otoprotective strategy, particularly given that statins are already FDA approved.

3.3 Heritable Forms of Hearing Loss Lead to Stria Vascularis Degeneration

3.3.1 Norrie Disease

Norrie disease is a rare X-linked recessive disorder associated with mutations of the Norrie disease protein gene (*Ndp*, Xp 11.3; Berger et al., 1996). Only 400 cases of Norrie disease have been documented worldwide (Sowden et al., 2020), associated with more than 115 *Ndp* mutations (Yamada et al., 2001; Halpin et al., 2005; Allen et al., 2006; Parzefall et al., 2014; Andarva et al., 2018; Rodríguez-Muñoz et al., 2018). While each mutation causes a unique phenotype, severe vascular degeneration is a common feature of Norrie disease, contributing to sensory degradation and developmental deficits. Most individuals diagnosed with Norrie disease have congenital blindness, and while they may develop hearing loss at any time from childhood to late adulthood, the median age of onset is early adolescence (Halpin and Sims 2008). Norrie disease is often misdiagnosed due to the rarity of the condition and the complexity of symptoms. However, improved genetic testing is facilitating earlier diagnosis (Wu et al., 2017; Liu J. et al., 2019; Marakhonov et al., 2020). Nevertheless, even with an accurate diagnosis, it is not possible to predict when hearing loss may occur for individuals with Norrie disease.

The progression of Norrie disease-associated hearing loss has been investigated using *Ndp* knockout mice (Rehm et al., 2002). In this model, mice develop progressive hearing loss at 3 months of age, corresponding with enlargement of the SV microvasculature (Rehm et al., 2002). The three SV cell layers progressively degrade, leading to a collapse of the SV and total hearing loss by 15 months of age. The degeneration of SV blood vessels in *Ndp* knockout mice is also consistent with observations made in the vasculature of the brain (Wang et al., 2012) and the retina (Ye et al., 2009) of other *Ndp* loss-of-function mouse models. In addition, recent evidence from Hayashi et al. found that Ndp plays a role in cochlear hair cell survival and maturation (Hayashi et al., 2021). Functional assessment of hearing using distortion product otoacoustic emission (DPOAE) measurements revealed elevated thresholds indicative of hair cell dysfunction in Ndp knockout mice at 2 months of age. Further research is required to ascertain the molecular mechanisms driving degeneration in Norrie disease and how individual *Ndp* mutations might affect specific cell types. However, it appears that the canonical Wnt/ß-catenin signalling pathway is impacted by Norrie disease-associated mutations.

Canonical Wnt/ß-catenin signalling regulates cell-fate determination and angiogenesis during cochlear development (Geng et al., 2016). Wnt ligands bind to different frizzled (Fzd) receptors and low-density lipoprotein receptor-related protein (Lrp) co-receptors, allowing for the accumulation and subsequent translocation of intracellular ß-catenin to the nucleus to activate the T-cell factor/lymphoid enhancer factor (TCF/LEF) transcription factors (reviewed in Franco et al., 2009). Interestingly, Ndp is an atypical Wnt ligand which activates canonical Wnt/ß-catenin signalling by selectively binding to frizzled-4 (Fzd-4) at the same interaction site as typical Wnt ligands (Chang et al., 2015). In addition, Ndp-mediated Wnt/ß-catenin signalling requires the interaction of both low-density lipoprotein receptor-related protein 5/6 (Lrp5/6), and the transmembrane protein, tetraspanin 12 (Tspan12) to function (Lai et al., 2017). Currently, it is predicted that *Ndp* mutations result in tight junction loss and vascular barrier remodelling which may contribute to Norrie disease SV degradation due to impaired interactions between Ndp, Fzd-4, and Tspan12 (Xu et al., 2004; Lai et al., 2017). Recent observations made by Hayashi et al. indicate that *Ndp* loss-of-function also impacts hair cell development due to irregular ß-catenin signalling (Hayashi et al., 2021); however, the EP as a measure of SV function was not investigated. Characterization of this pathway in the inner ear may distinguish the importance of Ndp compared to Wnt in mediating Norrie disease-associated hearing loss and identify potential therapeutic targets.

3.3.2 Meniere's Disease

Meniere's disease is a prominent hearing disorder affecting approximately 200–500 people per 100,000 (Gürkov et al., 2016). Meniere's disease is characterized by chronic sensorineural hearing loss, vertigo, and tinnitus. Three-dimensional reconstruction and magnetic-resonance-imaging of the inner ear indicate that endolymphatic hydrops (EH), or the expansion of the endolymphatic space to occupy areas normally only containing perilymph, contribute to Meniere's hearing loss (Morita et al., 2009; Naganawa et al., 2010; Naganawa and Nakashima, 2014). It is speculated that this is due to SV dysfunction, particularly an increased permeability of the BLB (Zhang W. et al., 2020).

Currently, there is no cure for Meniere's disease and treatments to manage Meniere's symptoms are limited. For severe cases of vertigo, the ototoxic aminoglycoside antibiotic, gentamicin, is injected intratympanically. This approach provides relief by destroying vestibular hair cells, which subsequently removes dysfunctional balance sensation. However, vestibular hair cell death impairs normal balance and intratympanic gentamicin can also damage cochlear hair cells, causing permanent hearing loss. Therefore, the corticosteroids methylprednisolone (NCT00802529) and dexamethasone (NCT03664674) have been tested in human clinical trials as potential gentamicin replacements (Lambert et al., 2016; Patel et al., 2016; Patel 2017). Encouragingly, methylprednisolone reduced the number of vertigo attacks experienced by individuals with Meniere's disease and did not impact speech recognition to the same extent as gentamicin. Likewise, dexamethasone reduced the severity of vertigo, without causing hearing loss (Patel 2017). In addition, the FDA has recently approved a phase three clinical trial for *ebselen*, another potential Meniere's therapeutic (NCT04677972; reviewed in Kil et al., 2022). *Ebselen* can be taken orally, avoiding painful intratympanic injections, and, while *ebselen* may not improve vertigo, it significantly reduces tinnitus and hearing loss in individuals with Meniere's disease (as observed in phase two clinical trials: NCT03325790). While the mechanism of effect needs to be better defined, these therapeutic advances could significantly improve the outcomes experienced by individuals with Meniere's disease, especially when compared to gentamicin treatment. In addition, a recent study by Gu et al. used published RNA-sequencing data in adult mice and compared it to published

datasets regarding Meniere's disease in humans to localize known Meniere's disease genes within specific cells of the SV (Korrapati et al., 2019; Gu et al., 2021). Estrogen related receptor beta (*Esrrb*) and Na^+/K^+ transporting ATPase 1b2 (*Atp1b2*) expression was identified in marginal cells, endothelin receptor type B (*Ednrb*) and transmembrane protein 176A (*Tmem176A*) in intermediate cells, and solute carrier 44a2 (*Slc44a2*) and collagen type 11 a2 (*Col11a2*) in basal cells. Future research to determine the involvement of these genes in Meniere's disease and SV function may improve Meniere's disease models and identify novel therapies.

3.3.3 Alport Syndrome

Alport syndrome is a rare inherited type IV collagen disorder, affecting approximately 1 in 5,000 people (Gratton et al., 2005). Alport syndrome symptoms include kidney failure and late-onset progressive sensorineural hearing loss, caused by the progressive thickening of the SV capillary basement membrane and the dysregulation of extracellular matrix proteins (Thomopoulos et al., 1997; Gratton et al., 2005; Cosgrove et al., 2008; Meehan et al., 2016). Mutations in collagen type 4 alpha 3, (COL4A3), collagen type 4 alpha 4 (COL4A4), and collagen type 4 alpha 5 (COL4A5) have been associated with Alport syndrome.

Notably, the COL4A4-knockout mouse has been used to demonstrate that SV function is impaired in the Alport syndrome model (Cosgrove et al., 1996). Specifically, SV capillary permeability is reduced in 8.5-week-old COL4A4 knockout mice when compared to age matched wild-type mice (demonstrated using intracardially injected Rhodamine dye and fluorescence spectrometry) (Dufek et al., 2020). In addition, RNA sequencing showed higher expression of inflammatory genes, such as nuclear factor kappa B inhibitor alpha (*NFKBIA*), in the SV of COL4A4 knockout mice when compared to wildtype controls. This would suggest that the host's inflammatory response damages the SV in those with Alport syndrome (Dufek et al., 2020). It remains to be seen what is causing this inflammation in the Alport syndrome-affected SV. However, inflammation is certainly associated with increased vascular permeability, indicating that Alport syndrome-associated SV degeneration and subsequent BLB degradation causes Alport syndrome-associated hearing loss.

Very little data is available regarding SV function in humans with Alport syndrome. However, an observational clinical trial is evaluating Alport syndrome-associated symptoms in people with a history of renal hematuria, and next generation sequencing confirmed COL4A mutations over a period of 4 years (NCT04947813). This study will produce important human-based information, but more research is needed in both animal models and humans to identify SV pathology so that treatments may be developed.

3.3.4 Waardenburg Syndrome

Waardenburg syndrome is a rare auditory-pigmentary disorder affecting 2-3 individuals per 100,000 (Saleem 2019). There are four types of Waardenburg syndrome, classified by symptom and primarily caused by six genetic mutations: melanocyte inducing transcription factor (*Mitf*), paired box 3 (*Pax3*), SRY-box transcription factor 10 (*Sox10*), Ednrb, endothelin 3 (*Edn3*), and snail family transcription factor 2 (*Snai2*) (reviewed in Song et al., 2016). Individuals with Waardenburg syndrome can experience a loss of pigmentation in their hair, eyes, skin, and melanocytes of the SV. As previously discussed, the protective role of melanocytes in the SV is not yet clear. Notably, research regarding Waardenburg-associated gene function has identified important regulatory factors that may be used to further elucidate the function of melanin-producing cells in the SV. For example, *Mitf* interacts with melanogenesis-associated enzymes, including tyrosinase and dopachrome tautomerase (Chen et al., 2018; Flesher et al., 2020). A *de novo* mutation in the *Mitf* promoter isoform, *Mitf-M*, causes pigmentation loss and hearing damage in mouse and porcine models, indicating that a loss of *Mitf-M* might hinder melanogenesis in the SV (Chen et al., 2016). Furthermore, RNA sequencing of the SV collected from *Mitf-M* animals also indicates that ion transport genes such as transmembrane receptor cation channel M1 (*Trpm1*), *Kcnj13*, and solute carrier 45A2 (*Slc45a2*) are downregulated (Chen et al., 2020). These results suggest that melanin-producing cells in the SV likely contribute to the ionic regulation of the cochlear fluid, however, ionic measurements are required to confirm this hypothesis. Furthermore, investigation of the candidate genes identified by RNA sequencing in Waardenburg syndrome animal models should be pursued to evaluate potential drug targets for protecting the melanocytes of the SV.

Interestingly, the MITF protein is a downstream regulatory factor of the Wnt/ß-catenin signaling pathway that interacts with the LEF-1 transcription factor (Takeda et al., 2000; Saito et al., 2002; Yasumoto et al., 2002). Therefore, combined with the observation that Wnt/ß-catenin signaling is impacted by Norrie disease associated mutations, it appears that the Wnt pathway has a prominent role for SV development and function.

3.4 Cytomegalovirus-Induced Hearing Loss

Congenital Cytomegalovirus (CMV) infection is one of the most common causes of pediatric sensorineural hearing loss. 35% of infants with symptomatic CMV and 7–10% of infants with asymptomatic CMV will develop hearing loss (Manicklal et al., 2013). The mechanism of CMV-induced hearing loss is not clear. However, studies in mice and humans indicate that CMV infection causes SV degeneration, which subsequently causes hearing loss. For example, when newborn BALB/c mice are inoculated with murine CMV, increased BLB permeability can be observed using the evans blue tracer assay as early as 3 weeks post infection. Corrosion casts have also been used to identify severe structural damage to the vessels of the SV 8 weeks post CMV infection (Carraro et al., 2017) and mature mice have increased ABR thresholds when compared to uninfected controls (Li et al., 2014; Carraro et al., 2017). Carraro et al. hypothesized that CMV induced SV structural damage is caused by viral accumulation in the cochelar bone marrow, that may then impact PVM/M differentiation (Bradford et al., 2015; Carraro et al., 2017). As discussed above, PVM/Ms are bone marrow-derived cells (Shi 2010) critical for the regulation of SV vascular permeability and immune surveillance. Therefore, PVM/M loss likely disrupts blood flow, ion homeostasis, and the endocochlear potential in the CMV infected ear. Conversely, Bradford et al. speculated that CMV-induced SV degeneration might be caused by inflammation and tested whether murine CMV induced an inner ear inflammatory response in intraperitoneally infected newborn BALB/c mice

(Bradford et al., 2015). 11 days post-infection, Bradford et al. observed CD3 positive cells in the SV and the spiral ganglion neurons. CD3 (cluster of differentiation three) is a T-lymphocyte coreceptor involved in immunoregulation. Therefore, the presence of $CD3^+$ cells is indicative of an inflammatory response occurring in the SV in response to CMV infection. Likewise, $CD8^+$ T lymphocytes have been observed near the sites of viral inclusion in electively terminated human fetuses (21-weeks gestational age) with congenital CMV infection (Gabrielli et al., 2013). Notably, in these fetuses, CMV DNA was observed in the marginal cells of the SV and Reisner's membrane, indicating that CMV can infect and damage the SV, and subsequently enter the cochlea. In addition, CMV-induced hearing loss has been associated with oxidative stress. Pecha et al. used a superoxide-sensitive fluorescent probe to examine the presence of reactive oxygen species (ROS) 7 days post-CMV-infection in neonatal BALB/c mice (Pecha et al., 2020). Increased ROS production occured in the CMV-infected spiral ganglia, osseous spiral lamina, and SV when compared to uninfected controls.

There is no cure for CMV-induced hearing loss. However, valganciclovir, an FDA approved, orally administered, anti-viral medication prevented CMV induced hearing loss in a phase three clinical trial (NCT00466817; Kimberlin et al., 2015). During the trial, infants (≤30 days old) with symptomatic congenital CMV received oral valganciclovir treatment, with short- and long-term treatments evaluated. For short-term administration, 49 participants received valganciclovir for 6 weeks, followed by a placebo for 18 weeks. For long-term administration, 47 participants received valganciclovir treatment for 6 months. Hearing was assessed using brainstem evoked response measurements at baseline, 6, 12, and 24 months. Participants in both treatment groups showed similar hearing outcomes at 6 months when compared to baseline. However, a greater number of participants in the long-term treatment cohort had improved hearing at 12- and 24-months than those receiving short-term treatment. Overall, improved hearing outcomes were seen in 78 and 86% of participants at 12- and 24-months respectively in the long-term treatment cohort, compared to 63 and 71% of participants in the short-term treatment cohort. Notably, valganciclovir decreased the participants' viral load in both treatment groups. However, discontinuation of valganciclovir in the short-term treatment group resulted in a CMV resurgence. This likely accounts for the poorer hearing outcomes observed in the short-term treatment cohort and highlights the need for prolonged valganciclovir treatment. Similar positive outcomes were observed by Bilavsky et al. in infants born with CMV and hearing impairment that were subsequently treated with valganciclovir for 12 months. After 12 months of valganciclovir treatment, 65% of the impaired ears had improved, with 76% of the improved ears returning to normal hearing levels (Bilavsky et al., 2016). Therefore, valganciclovir should certainly be considered for routine CMV treatment. In addition, valganciclovir and other newly developed anti-viral drugs may prove beneficial for treating other infections that cause hearing loss. While this remains to be tested, given the prevalence of hearing loss-inducing viruses and their associated mortality rates (reviewed in Cohen et al., 2014) the development of anti-viral drugs is a lifesaving and life-changing discovery. Indeed, for the children in both the Kimberlin and Bilavsky studies, the prevention of CMV-induced hearing loss will significantly improve their quality of life.

4 CONCLUSION AND FUTURE DIRECTIONS

The SV has a vital role for hearing. It regulates the strict ionic composition of cochlear fluids and produces the endocochlear potential required for sound transduction, while also protecting the cochlea by providing immune surveillance and maintaining the BLB. However, the BLB remains one of the most under studied aspects of the ear, despite being one of the most important targets for delivering inner ear therapeutics. Nevertheless, single-cell sequencing technologies, combined with human focused histology and functional hearing assessments have significantly improved our understanding of the SV. Novel SV cell types have been identified and known cell types are proving to have more dynamic roles than previously thought. Direct avenues for clinical intervention have been identified, such as gene networks that can be targeted by FDA approved therapeutics. Follow up studies using knockout models to evaluate the importance of genes identified by single nucleus RNA sequencing will also provide greater detail regarding cell-specific roles in the SV. Furthermore, evaluation of these SV cell-specific genes might also identify biomarkers for diagnosing or monitoring SV health. To date, only a few inner ear biomarkers have been evaluated, but none are specific to the SV (Mahshid et al., 2021).

While several questions remain regarding SV development and function, significant groundwork has set the scene for burgeoning discovery. It is likely that this will subsequently facilitate the development of research tools such as organoids or organ-on-a-chip technologies, that have proven invaluable for high throughput drug screening and disease modelling in other fields. Overall, critical knowledge has been gained particularly elucidating the mechanisms of age-related SV degeneration, ototoxic outcomes, and SV-associated hearing disorders, providing exciting opportunities for preventing hearing loss in the future.

AUTHOR CONTRIBUTIONS

MT conducted the literature review, wrote the manuscript, and made the figures and tables. JO contributed to the writing, revision, and editorial process, and supervised manuscript progress. AD contributed to the editorial process and supervised manuscript progress.

FUNDING

This work was supported by a Raymond Ng Graduate Student Award (MRT) from the University of Toronto, and a Harry Barberian Research Fund (MRT) from the University of

Toronto. This work was also supported by a Krembil Foundation grant geared towards accelerating biomedical research. Our Hearing Regeneration Lab receives support from the Koerner Foundation.

ACKNOWLEDGMENTS

We thank Drs. RV. Harrison and M. Carraro for providing the image in **Figure 3B** and feedback on this manuscript.

REFERENCES

Allen, R. C., Russell, S. R., Streb, L. M., Alsheikheh, A., and Stone, E. M. (2006). Phenotypic Heterogeneity Associated with a Novel Mutation (Gly112Glu) in the Norrie Disease Protein. *Eye* 20, 234–241. doi:10.1038/sj.eye.6701840

Andarva, M., Jamshidi, J., Ghaedi, H., Daftarian, N., Emamalizadeh, B., Alehabib, E., et al. (2018). A Novel c.240_241insGG Mutation in *NDP* Gene in a Family with Norrie Disease. *Clin. Exp. Optom.* 101 (2), 255–259. doi:10.1111/cxo.12599

Andresen, N. S., Coreas, S., Villavisanis, D. F., and Lauer, A. M. (2021). Comparison of Age-Related Pigmentary Changes in the Auditory and Vestibular Systems within Mouse and Human Temporal Bones. *Front. Neurosci.* 15, 1–9. doi:10.3389/fnins.2021.680994

Berger, W., van de Pol, D., Bachner, D., Oerlemans, F., Winkens, H., Hameister, H., et al. (1996). An Animal Model for Norrie Disease (ND): Gene Targeting of the Mouse ND Gene. *Hum. Mol. Genet.* 5 (1), 51–59. doi:10.1093/hmg/5.1.51

Bertolini, P., Lassalle, M., Mercier, G., Raquin, M. A., Izzi, G., Corradini, N., et al. (2004). Platinum Compound-Related Ototoxicity in Children. *J. Pediatr. Hematology/Oncology* 26 (10), 649–655. doi:10.1097/01.mph.0000141348.62532.73

Bilavsky, E., Shahar-Nissan, K., Pardo, J., Attias, J., and Amir, J. (2016). Hearing Outcome of Infants with Congenital Cytomegalovirus and Hearing Impairment. *Arch. Dis. Child.* 101 (5), 433–438. doi:10.1136/archdischild-2015-309154

Bradford, R. D., Yoo, Y.-G., Golemac, M., Pugel, E. P., Jonjic, S., and Britt, W. J. (2015). Murine CMV-Induced Hearing Loss Is Associated with Inner Ear Inflammation and Loss of Spiral Ganglia Neurons. *Plos Pathog.* 11 (4), e1004774–21. doi:10.1371/journal.ppat.1004774

Brand, Y., Setz, C., Levano, S., Listyo, A., Chavez, E., Pak, K., et al. (2011). Simvastatin Protects Auditory Hair Cells from Gentamicin-Induced Toxicity and Activates Akt Signaling *In Vitro*. *BMC Neurosci.* 12, 1–10. doi:10.1186/1471-2202-12-114

Breglio, A. M., Rusheen, A. E., Shide, E. D., Fernandez, K. A., Spielbauer, K. K., McLachlin, K. M., et al. (2017). Cisplatin Is Retained in the Cochlea Indefinitely Following Chemotherapy. *Nat. Commun.* 8, 1–9. doi:10.1038/s41467-017-01837-1

Bush, W. D., and Simon, J. D. (2007). Quantification of Ca2+binding to Melanin Supports the Hypothesis that Melanosomes Serve a Functional Role in Regulating Calcium Homeostasis. *Pigment Cel Res* 20 (2), 134–139. doi:10.1111/j.1600-0749.2007.00362.x

Cai, J., Wu, X., Li, X., Ma, C., Xu, L., Guo, X., et al. (2019). Allicin Protects against Cisplatin-Induced Stria Vascularis Damage: Possible Relation to Inhibition of Caspase-3 and PARP-1-AIF-Mediated Apoptotic Pathways. *Orl* 81 (4), 202–214. doi:10.1159/000500557

Caporarello, N., D'Angeli, F., Cambria, M. T., Candido, S., Giallongo, C., Salmeri, M., et al. (2019). Pericytes in Microvessels: From "Mural" Function to Brain and Retina Regeneration. *Ijms* 20 (24), 6351–6420. doi:10.3390/ijms20246351

Carraro, M., Almishaal, A., Hillas, E., Firpo, M., Park, A., and Harrison, R. V. (2017). Cytomegalovirus (CMV) Infection Causes Degeneration of Cochlear Vasculature and Hearing Loss in a Mouse Model. *JARO* 18, 263–273. doi:10.1007/s10162-016-0606-4

Carraro, M., and Harrison, R. V. (2016). Degeneration of Stria Vascularis in Age-Related Hearing Loss; A Corrosion Cast Study in a Mouse Model. *Acta Oto-Laryngologica* 136 (4), 385–390. doi:10.3109/00016489.2015.1123291

Chang, T.-H., Hsieh, F.-L., Zebisch, M., Harlos, K., Elegheert, J., and Jones, E. Y. (2015). Structure and Functional Properties of Norrin Mimic Wnt for Signalling with Frizzled4, Lrp5/6, and Proteoglycan. *ELife* 4, 1–27. doi:10.7554/eLife.06554

Chen, L., Guo, W., Ren, L., Yang, M., Zhao, Y., Guo, Z., et al. (2016). A De Novo Silencer Causes Elimination of MITF-M Expression and Profound Hearing Loss in Pigs. *BMC Biol.* 14, 1–15. doi:10.1186/s12915-016-0273-2

Chen, L., Wang, L., Chen, L., Wang, F., Ji, F., Sun, W., et al. (2020). Transcript Profiles of Stria Vascularis in Models of Waardenburg Syndrome. *Neural Plasticity* 2020, 1–9. doi:10.1155/2020/2908182

Chen, T., Zhao, B., Liu, Y., Wang, R., Yang, Y., Yang, L., et al. (2018). MITF-M Regulates Melanogenesis in Mouse Melanocytes. *J. Dermatol. Sci.* 90 (3), 253–262. doi:10.1016/j.jdermsci.2018.02.008

Cohen, B. E., Durstenfeld, A., and Roehm, P. C. (2014). Viral Causes of Hearing Loss: A Review for Hearing Health Professionals. *Trends Hearing* 18, 233121651454136–17. doi:10.1177/2331216514541361

Cosgrove, D., Meehan, D. T., Delimont, D., Pozzi, A., Chen, X., Rodgers, K. D., et al. (2008). Integrin α1β1 Regulates Matrix Metalloproteinases via P38 Mitogen-Activated Protein Kinase in Mesangial Cells. *Am. J. Pathol.* 172 (3), 761–773. doi:10.2353/ajpath.2008.070473

Cosgrove, D., Meehan, D. T., Grunkemeyer, J. A., Kornak, J. M., Sayers, R., Hunter, W. J., et al. (1996). Collagen COL4A3 Knockout: A Mouse Model for Autosomal Alport Syndrome. *Genes Dev.* 10 (23), 2981–2992. doi:10.1101/gad.10.23.2981

Ding, B., Walton, J. P., Zhu, X., and Frisina, R. D. (2018). Age-related Changes in Na, K-ATPase Expression, Subunit Isoform Selection and Assembly in the Stria Vascularis Lateral wall of Mouse Cochlea. *Hearing Res.* 367, 59–73. doi:10.1016/j.heares.2018.07.006.Age-related

Ding, D., Liu, H., Qi, W., Jiang, H., Li, Y., Wu, X., et al. (2016). Ototoxic Effects and Mechanisms of Loop Diuretics. *J. Otology* 11 (4), 145–156. doi:10.1016/j.joto.2016.10.001

Dufek, B., Meehan, D. T., Delimont, D., Wilhelm, K., Samuelson, G., Coenen, R., et al. (2020). RNA-seq Analysis of Gene Expression Profiles in Isolated Stria Vascularis from Wild-type and Alport Mice Reveals Key Pathways Underling Alport Strial Pathogenesis. *PLoS ONE* 15 (8), e0237907–19. doi:10.1371/journal.pone.0237907

Dulon, D., Aran, J. M., Zajic, G., and Schacht, J. (1986). Comparative Uptake of Gentamicin, Netilmicin, and Amikacin in the guinea Pig Cochlea and Vestibule. *Antimicrob. Agents Chemother.* 30 (1), 96–100. doi:10.1128/AAC.30.1.96

Fernandez, K. A., Allen, P., Campbell, M., Page, B., Townes, T., Li, C.-M., et al. (2021). Atorvastatin Is Associated with Reduced Cisplatin-Induced Hearing Loss. *J. Clin. Invest.* 131 (1), 1–11. doi:10.1172/JCI142616

Fernandez, K., Spielbauer, K. K., Rusheen, A., Wang, L., Baker, T. G., Eyles, S., et al. (2020). Lovastatin Protects against Cisplatin-Induced Hearing Loss in Mice. *Hearing Res.* 389, 107905–9. doi:10.1016/j.heares.2020.107905

Flesher, J. L., Paterson-Coleman, E. K., Vasudeva, P., Ruiz-Vega, R., Marshall, M., Pearlman, E., et al. (2020). Delineating the Role of MITF Isoforms in Pigmentation and Tissue Homeostasis. *Pigment Cel Melanoma Res* 33 (2), 279–292. doi:10.1111/pcmr.12828

Franco, C. A., Liebner, S., and Gerhardt, H. (2009). Vascular Morphogenesis: A Wnt for Every Vessel? *Curr. Opin. Genet. Develop.* 19 (5), 476–483. doi:10.1016/j.gde.2009.09.004

Frisina, R. D., Wheeler, H. E., Fossa, S. D., Kerns, S. L., Fung, C., Sesso, H. D., et al. (2016). Comprehensive Audiometric Analysis of Hearing Impairment and Tinnitus after Cisplatin-Based Chemotherapy in Survivors of Adult-Onset Cancer. *Jco* 34 (23), 2712–2720. doi:10.1200/JCO.2016.66.8822

Gabrielli, L., Bonasoni, M. P., Santini, D., Piccirilli, G., Chiereghin, A., Guerra, B., et al. (2013). Human Fetal Inner Ear Involvement in Congenital Cytomegalovirus Infection. *Acta Neuropathol. Commun.* 1, 1–9. doi:10.1186/2051-5960-1-63

Gates, G. A., and Mills, J. H. (2005). Presbycusis. *The Lancet* 366 (9491), 1111–1120. doi:10.1016/S0140-6736(05)67423-5

Geng, R., Noda, T., Mulvaney, J. F., Lin, V. Y. W., Edge, A. S. B., and Dabdoub, A. (2016). Comprehensive Expression of Wnt Signaling Pathway Genes during Development and Maturation of the Mouse Cochlea. *PLoS ONE* 11 (2), e0148339–18. doi:10.1371/journal.pone.0148339

Gersten, B. K., Fitzgerald, T. S., Fernandez, K. A., and Cunningham, L. L. (2020). Ototoxicity and Platinum Uptake Following Cyclic Administration of

Platinum-Based Chemotherapeutic Agents. *JARO* 21, 303–321. doi:10.1007/s10162-020-00759-y

Gill, S. S., and Salt, A. N. (1997). Quantitative Differences in Endolymphatic Calcium and Endocochlear Potential between Pigmented and Albino guinea Pigs. *Hear. Res.* 113 (1–2), 191–7. doi:10.1016/S0378-5955(97)00141-X

Gratton, M. A., Schmiedt, R. A., and Schulte, B. A. (1996). Age-related Decreases in Endocochlear Potential Are Associated with Vascular Abnormalities in the Stria Vascularis. *Hear. Res.* 102 (1–2), 181–90. doi:10.1016/s0378-5955(96)90017-9

Gratton, M. A., Rao, V. H., Meehan, D. T., Askew, C., and Cosgrove, D. (2005). Matrix Metalloproteinase Dysregulation in the Stria Vascularis of Mice with Alport Syndrome. *Am. J. Pathol.* 166 (5), 1465–1474. doi:10.1016/S0002-9440(10)62363-2

Gu, S., Olszewski, R., Nelson, L., Gallego-Martinez, A., Lopez-Escamez, J. A., and Hoa, M. (2021). Identification of Potential Meniere's Disease Targets in the Adult Stria Vascularis. *Front. Neurol.* 12, 1–16. doi:10.3389/fneur.2021.630561

Gu, S., Olszewski, R., Taukulis, I., Wei, Z., Martin, D., Morell, R. J., et al. (2020). Characterization of Rare Spindle and Root Cell Transcriptional Profiles in the Stria Vascularis of the Adult Mouse Cochlea. *Sci. Rep.* 10, 1–15. doi:10.1038/s41598-020-75238-8

Gürkov, R., Pyykö, I., Zou, J., and Kentala, E. (2016). What Is Menière's Disease? A Contemporary Re-evaluation of Endolymphatic Hydrops. *J. Neurol.* 263, 71–81. doi:10.1007/s00415-015-7930-1

Halpin, C., Owen, G., Gutiérrez-Espeleta, G. A., Sims, K., and Rehm, H. L. (2005). Audiologic Features of Norrie Disease. *Ann. Otol Rhinol Laryngol.* 114 (7), 533–538. doi:10.1177/000348940511400707

Halpin, C., and Sims, K. (2008). Twenty Years of Audiology in a Patient with Norrie Disease. *Int. J. Pediatr. Otorhinolaryngol.* 72 (11), 1705–1710. doi:10.1016/j.ijporl.2008.08.007

Hayashi, Y., Chiang, H., Tian, C., Indzhykulian, A. A., and Edge, A. S. B. (2021). Norrie Disease Protein Is Essential for Cochlear Hair Cell Maturation. *Proc. Natl. Acad. Sci. USA* 118 (39), e2106369118–12. doi:10.1073/pnas.2106369118

Imamura, S.-i., and Adams, J. C. (2003). Distribution of Gentamicin in the guinea Pig Inner Ear after Local or Systemic Application. *JARO - J. Assoc. Res. Otolaryngol.* 4, 176–195. doi:10.1007/s10162-002-2036-8

Inamura, N., and Salt, A. N. (1992). Permeability Changes of the Blood-Labyrinth Barrier Measured *In Vivo* during Experimental Treatments. *Hear. Res.* 61 (1–2), 12–8. doi:10.1016/0378-5955(92)90030-Q

Jagger, D. J., Nevill, G., and Forge, A. (2010). The Membrane Properties of Cochlear Root Cells Are Consistent with Roles in Potassium Recirculation and Spatial Buffering. *JARO* 11, 435–448. doi:10.1007/s10162-010-0218-3

Kiernan, A. E., Steel, K. P., and Fekete, D. M. (2002). "Development of the Mouse Inner Ear," in *Mouse Development: Patterning, Morphogenesis, and Organogenesis*. Editors J. Rossant and P. P. L. Tam (San Diego: Academic Press), 539–566. doi:10.1016/B978-012597951-1/50026-3

Kil, J., Harruff, E. E., and Longenecker, R. J. (2022). Development of Ebselen for the Treatment of Sensorineural Hearing Loss and Tinnitus. *Hearing Res.* 413, 108209. doi:10.1016/j.heares.2021.108209

Kimberlin, D. W., Jester, P. M., Sánchez, P. J., Ahmed, A., Arav-Boger, R., Michaels, M. G., et al. (2015). Valganciclovir for Symptomatic Congenital Cytomegalovirus Disease. *N. Engl. J. Med.* 372 (10), 933–943. doi:10.1056/NEJMoa1404599.Valganciclovir

Kobrina, A., Schrode, K. M., Screven, L. A., Javaid, H., Weinberg, M. M., Brown, G., et al. (2020). Linking Anatomical and Physiological Markers of Auditory System Degeneration with Behavioral Hearing Assessments in a Mouse (*Mus musculus*) Model of Age-Related Hearing Loss. *Neurobiol. Aging* 96, 87–103. doi:10.1016/j.neurobiolaging.2020.08.012

Korrapati, S., Taukulis, I., Olszewski, R., Pyle, M., Gu, S., Singh, R., et al. (2019). Single Cell and Single Nucleus RNA-Seq Reveal Cellular Heterogeneity and Homeostatic Regulatory Networks in Adult Mouse Stria Vascularis. *Front. Mol. Neurosci.* 12, 1–25. doi:10.3389/fnmol.2019.00316

Kurata, N., Schachern, P. A., Paparella, M. M., and Cureoglu, S. (2016). Histopathologic Evaluation of Vascular Findings in the Cochlea in Patients with Presbycusis. *JAMA Otolaryngol. Head Neck Surg.* 142 (2), 173–178. doi:10.1001/jamaoto.2015.3163

Lai, M. B., Zhang, C., Shi, J., Johnson, V., Khandan, L., McVey, J., et al. (2017). TSPAN12 Is a Norrin Co-receptor that Amplifies Frizzled4 Ligand Selectivity and Signaling. *Cel Rep.* 19 (13), 2809–2822. doi:10.1016/j.celrep.2017.06.004

Lambert, P. R., Carey, J., Mikulec, A. A., and LeBel, C. (2016). Intratympanic Sustained-Exposure Dexamethasone Thermosensitive Gel for Symptoms of Ménière's Disease. *Otology and Neurotology* 37 (10), 1669–1676. doi:10.1097/MAO.0000000000001227

Lawenda, B. D., Kelly, K. M., Ladas, E. J., Sagar, S. M., Vickers, A., and Blumberg, J. B. (2008). Should Supplemental Antioxidant Administration Be Avoided during Chemotherapy and Radiation Therapy? *JNCI J. Natl. Cancer Inst.* 100 (11), 773–783. doi:10.1093/jnci/djn148

Li, H., and Steyger, P. S. (2011). Systemic Aminoglycosides Are Trafficked via Endolymph into Cochlear Hair Cells. *Sci. Rep.* 1, 1–5. doi:10.1038/srep00159

Li, X., Shi, X., Qiao, Y., Xu, K., Zeng, L., Wang, C., et al. (2014). Observation of Permeability of Blood-Labyrinth Barrier during Cytomegalovirus-Induced Hearing Loss. *Int. J. Pediatr. Otorhinolaryngol.* 78 (7), 995–999. doi:10.1016/j.ijporl.2014.03.013

Lin, F. R., Maas, P., Chien, W., Carey, J. P., Ferrucci, L., and Thorpe, R. (2012). Association of Skin Color, Race/ethnicity, and Hearing Loss Among Adults in the USA. *JARO* 13, 109–117. doi:10.1007/s10162-011-0298-8

Liu, J., Zhu, J., Yang, J., Zhang, X., Zhang, Q., and Zhao, P. (2019). Prenatal Diagnosis of Familial Exudative Vitreoretinopathy and Norrie Disease. *Mol. Genet. Genomic Med.* 7 (1), e00503. doi:10.1002/mgg3.503

Liu, T., Li, G., Noble, K. V., Li, Y., Barth, J. L., Schulte, B. A., et al. (2019). Age-dependent Alterations of Kir4.1 Expression in Neural Crest-Derived Cells of the Mouse and Human Cochlea. *Neurobiol. Aging* 80, 210–222. doi:10.1016/j.neurobiolaging.2019.04.009

Liu, W., Schrott-Fischer, A., Glueckert, R., Benav, H., and Rask-Andersen, H. (2017). The Human "Cochlear Battery" - Claudin-11 Barrier and Ion Transport Proteins in the Lateral Wall of the Cochlea. *Front. Mol. Neurosci.* 10, 1–16. doi:10.3389/fnmol.2017.00239

Liu, Y., and Simon, J. D. (2005). Metal-ion Interactions and the Structural Organization of *Sepia* Eumelanin. *Pigment Cel Res* 18 (1), 42–48. doi:10.1111/j.1600-0749.2004.00197.x

Locher, H., de Groot, J. C. M. J., van Iperen, L., Huisman, M. A., Frijns, J. H. M., and Chuva de Sousa Lopes, S. M. (2015). Development of the Stria Vascularis and Potassium Regulation in the Human Fetal Cochlea: Insights into Hereditary Sensorineural Hearing Loss. *Devel Neurobio* 75 (11), 1219–1240. doi:10.1002/dneu.22279

Mahshid, S. S., Higazi, A. M., Ogier, J. M., and Dabdoub, A. (2021). Extracellular Biomarkers of Inner Ear Disease and Their Potential for point-of-care Diagnostics. *Adv. Sci.* e2104033, 1–13. doi:10.1002/advs.202104033

Manicklal, S., Emery, V. C., Lazzarotto, T., Boppana, S. B., and Gupta, R. K. (2013). The "Silent" Global burden of Congenital Cytomegalovirus. *Clin. Microbiol. Rev.* 26 (1), 86–102. doi:10.1128/CMR.00062-12

Marakhonov, A. V., Mishina, I. A., Kadyshev, V. V., Repina, S. A., Shurygina, M. F., Shchagina, O. A., et al. (2020). Prenatal Diagnosis of Norrie Disease after Whole Exome Sequencing of an Affected Proband during an Ongoing Pregnancy: A Case Report. *BMC Med. Genet.* 21, 1–5. doi:10.1186/s12881-020-01093-z

McFadden, S. L., Ding, D., Reaume, A. G., Flood, D. G., and Salvi, R. J. (1999). Age-related Cochlear Hair Cell Loss Is Enhanced in Mice Lacking Copper/zinc Superoxide Dismutase. *Neurobiol. Aging* 20 (1), 1–8. doi:10.1016/S0197-4580(99)00018-4

Meehan, D. T., Delimont, D., Dufek, B., Zallocchi, M., Phillips, G., Gratton, M. A., et al. (2016). Endothelin-1 Mediated Induction of Extracellular Matrix Genes in Strial Marginal Cells Underlies Strial Pathology in Alport Mice. *Hearing Res.* 341, 100–108. doi:10.1016/j.heares.2016.08.003

Morita, N., Kariya, S., Farajzadeh Deroee, A., Cureoglu, S., Nomiya, S., Nomiya, R., et al. (2009). Membranous Labyrinth Volumes in normal Ears and Ménière Disease: A Three-Dimensional Reconstruction Study. *The Laryngoscope* 119 (11), 2216–2220. doi:10.1002/lary.20723

Murillo-Cuesta, S., Contreras, J., Zurita, E., Cediel, R., Cantero, M., Varela-Nieto, I., et al. (2010). Melanin Precursors Prevent Premature Age-Related and Noise-Induced Hearing Loss in Albino Mice. *Pigment Cel Melanoma Res.* 23 (1), 72–83. doi:10.1111/j.1755-148X.2009.00646.x

Naganawa, S., and Nakashima, T. (2014). Visualization of Endolymphatic Hydrops with MR Imaging in Patients with Ménière's Disease and Related Pathologies: Current Status of its Methods and Clinical Significance. *Jpn. J. Radiol.* 32, 191–204. doi:10.1007/s11604-014-0290-4

Naganawa, S., Yamazaki, M., Kawai, H., Bokura, K., Sone, M., and Nakashima, T. (2010). Visualization of Endolymphatic Hydrops in Ménière's Disease with

Single-Dose Intravenous Gadolinium-Based Contrast Media Using Heavily T2-Weighted 3D-FLAIR. *Magn. Reson. Med. Sci.* 9 (4), 237–242. doi:10.2463/mrms.9.237

Nau, R., Sörgel, F., and Eiffert, H. (2010). Penetration of Drugs through the Blood-Cerebrospinal Fluid/blood-Brain Barrier for Treatment of central Nervous System Infections. *Clin. Microbiol. Rev.* 23 (4), 858–883. doi:10.1128/CMR.00007-10

Neng, L., Zhang, F., Kachelmeier, A., and Shi, X. (2013). Endothelial Cell, Pericyte, and Perivascular Resident Macrophage-type Melanocyte Interactions Regulate Cochlear Intrastrial Fluid-Blood Barrier Permeability. *JARO* 14, 175–185. doi:10.1007/s10162-012-0365-9

Neng, L., Zhang, J., Yang, J., Zhang, F., Lopez, I. A., Dong, M., et al. (2015). Structural Changes in Thestrial Blood-Labyrinth Barrier of Aged C57BL/6 Mice. *Cell Tissue Res*, 361(3), 685–696. doi:10.1007/s00441-015-2147-2

Nin, F., Yoshida, T., Sawamura, S., Ogata, G., Ota, T., Higuchi, T., et al. (2016). The Unique Electrical Properties in an Extracellular Fluid of the Mammalian Cochlea; Their Functional Roles, Homeostatic Processes, and Pathological Significance. *Pflugers Arch. - Eur. J. Physiol.* 468 (10), 1637–1649. doi:10.1007/s00424-016-1871-0

Noble, K. V., Liu, T., Matthews, L. J., Schulte, B. A., and Lang, H. (2019). Age-related Changes in Immune Cells of the Human Cochlea. *Front. Neurol.* 10, 1–13. doi:10.3389/fneur.2019.00895

Nyberg, S., Abbott, N. J., Shi, X., Steyger, P. S., and Dabdoub, A. (2019). Delivery of Therapeutics to the Inner Ear: The challenge of the Blood-Labyrinth Barrier. *Sci. Transl. Med.* 11 (482), 1–11. doi:10.1126/scitranslmed.aao0935

Park, J. S., Kim, S. W., Park, K., Choung, Y. H., Jou, I., and Park, S. M. (2012). Pravastatin Attenuates Noise-Induced Cochlear Injury in Mice. *Neuroscience* 208, 123–132. doi:10.1016/j.neuroscience.2012.02.010

Parzefall, T., Lucas, T., Ritter, M., Ludwig, M., Ramsebner, R., Frohne, A., et al. (2014). A Novel Missense NDP Mutation [p.(Cys93Arg)] with a Manifesting Carrier in an Austrian Family with Norrie Disease. *Audiol. Neurotol* 19 (3), 203–209. doi:10.1159/000358866

Patel, M., Agarwal, K., Arshad, Q., Hariri, M., Rea, P., Seemungal, B. M., et al. (2016). Intratympanic Methylprednisolone versus Gentamicin in Patients with Unilateral Ménière's Disease: a Randomised, Double-Blind, Comparative Effectiveness Trial. *The Lancet* 388 (10061), 2753–2762. doi:10.1016/S0140-6736(16)31461-1

Patel, M. (2017). Intratympanic Corticosteroids in Ménière's Disease: A Mini-Review. *J. Otology* 12 (3), 117–124. doi:10.1016/j.joto.2017.06.002

Pauler, M., Schuknecht, H. F., and White, J. A. (1988). Atrophy of the Stria Vascularis as a Cause of Sensorineural Hearing Loss. *The Laryngoscope* 98 (7), 754–759. doi:10.1288/00005537-198807000-00014

Pecha, P. P., Almishaal, A. A., Mathur, P. D., Hillas, E., Johnson, T., Price, M. S., et al. (2020). Role of Free Radical Formation in Murine Cytomegalovirus-Induced Hearing Loss. *Otolaryngol. Head Neck Surg.* 162 (5), 709–717. doi:10.1177/0194599820901485

Peixoto Pinheiro, B., Vona, B., Löwenheim, H., Rüttiger, L., Knipper, M., and Adel, Y. (2021). Age-related Hearing Loss Pertaining to Potassium Ion Channels in the Cochlea and Auditory Pathway. *Pflugers Arch. - Eur. J. Physiol.* 473 (5), 823–840. doi:10.1007/s00424-020-02496-w

Rehm, H. L., Zhang, D.-S., Brown, M. C., Burgess, B., Halpin, C., Berger, W., et al. (2002). Vascular Defects and Sensorineural Deafness in a Mouse Model of Norrie Disease. *J. Neurosci.* 22 (11), 4286–4292. doi:10.1523/jneurosci.22-11-04286.2002

Richter, C.-P., Young, H., Richter, S. V., Smith-Bronstein, V., Stock, S. R., Xiao, X., et al. (2018). Fluvastatin Protects Cochleae from Damage by High-Level Noise. *Sci. Rep.* 8, 1–12. doi:10.1038/s41598-018-21336-7

Rodríguez-Muñoz, A., García-García, G., Menor, F., Millán, J. M., Tomás-Vila, M., and Jaijo, T. (2018). The Importance of Biochemical and Genetic Findings in the Diagnosis of Atypical Norrie Disease. *Clin. Chem. Lab. Med.* 56 (2), 229–235. doi:10.1515/cclm-2017-0226

Saito, H., Yasumoto, K.-i., Takeda, K., Takahashi, K., Fukuzaki, A., Orikasa, S., et al. (2002). Melanocyte-specific Microphthalmia-Associated Transcription Factor Isoform Activates its Own Gene Promoter through Physical Interaction with Lymphoid-Enhancing Factor 1. *J. Biol. Chem.* 277 (32), 28787–28794. doi:10.1074/jbc.M203719200

Saleem, M. D. (2019). Biology of Human Melanocyte Development, Piebaldism, and Waardenburg Syndrome. *Pediatr. Dermatol.* 36 (1), 72–84. doi:10.1111/pde.13713

Shi, X. (2010). Resident Macrophages in the Cochlear Blood-Labyrinth Barrier and Their Renewal via Migration of Bone-Marrow-Derived Cells. *Cel Tissue Res* 342, 21–30. doi:10.1007/s00441-010-1040-2

Shuknecht, H. F., Watanuki, K., Takahashi, T., Belal, A. A., Kimura, R. S., Jones, D. D., et al. (1974). Atrophy of the Stria Vascularis, a Common Cause for Hearing Loss. *The Laryngoscope* 84 (10), 1777–1821. doi:10.1288/00005537-197410000-00012

Sichel, G., Corsaro, C., Scalia, M., Di Bilio, A. J., and Bonomo, R. P. (1991). *In Vitro* scavenger Activity of Some Flavonoids and Melanins against O2−dot. *Free Radic. Biol. Med.* 11 (1), 1–8. doi:10.1016/0891-5849(91)90181

Song, J., Feng, Y., Acke, F. R., Coucke, P., Vleminckx, K., and Dhooge, I. J. (2016). Hearing Loss in Waardenburg Syndrome: A Systematic Review. *Clin. Genet.* 89 (4), 416–425. doi:10.1016/0891-5849(91)90181-2

Sotomayor, M., Weihofen, W. A., Gaudet, R., and Corey, D. P. (2010). Structural Determinants of Cadherin-23 Function in Hearing and Deafness. *Neuron* 66 (1), 85–100. doi:10.1016/j.neuron.2010.03.028

Sowden, J. C., Kros, C. J., Sirimanna, T., Pagarkar, W., Oluonye, N., and Henderson, R. H. (2020). Impact of Sight and Hearing Loss in Patients with Norrie Disease: Advantages of Dual Sensory Clinics in Patient Care. *bmjpo* 4 (1), e000781–8. doi:10.1136/bmjpo-2020-000781

Takeda, K., Yasumoto, K.-i., Takada, R., Takada, S., Watanabe, K.-i., Udono, T., et al. (2000). Induction of Melanocyte-specific Microphthalmia-Associated Transcription Factor by Wnt-3a. *J. Biol. Chem.* 275 (19), 14013–14016. doi:10.1074/jbc.C000113200

Thomas, J. P., Lautermann, J., Liedert, B., Seiler, F., and Thomale, J. (2006). High Accumulation of Platinum-DNA Adducts in Strial Marginal Cells of the Cochlea Is an Early Event in Cisplatin but Not Carboplatin Ototoxicity. *Mol. Pharmacol.* 70 (1), 23–29. doi:10.1124/mol.106.022244

Thomopoulos, G. N., Spicer, S. S., Gratton, M. A., and Schulte, B. A. (1997). Age-related Thickening of Basement Membrane in Stria Vascularis Capillaries. *Hear. Res.* 111 (1–2), 31–41. doi:10.1016/S0378-5955(97)00080-4

Tsukasaki, N., Whitworth, C. A., and Rybak, L. P. (2000). Acute Changes in Cochlear Potentials Due to Cisplatin. *Hear. Res.* 149 (1–2), 189–98. doi:10.1016/S0378-5955(00)00182-9

Wang, J., and Puel, J.-L. (2020). Presbycusis: An Update on Cochlear Mechanisms and Therapies. *Jcm* 9 (1), 218–22. doi:10.3390/jcm9010218

Wang, Q., and Steyger, P. S. (2009). Trafficking of Systemic Fluorescent Gentamicin into the Cochlea and Hair Cells. *JARO* 10, 205–219. doi:10.1007/s10162-009-0160-4

Wang, X., Zhang, J., Li, G., Sai, N., Han, J., Hou, Z., et al. (2019). Vascular Regeneration in Adult Mouse Cochlea Stimulated by VEGF-A165 and Driven by NG2-Derived Cells *Ex Vivo*. *Hearing Res.* 377, 179–188. doi:10.1016/j.heares.2019.03.010

Wang, Y., Rattner, A., Zhou, Y., Williams, J., Smallwood, P. M., and Nathans, J. (2012). Norrin/Frizzled4 Signaling in Retinal Vascular Development and Blood Brain Barrier Plasticity. *Cell* 151 (6), 1332–1344. doi:10.1016/j.cell.2012.10.042

Wangemann, P. (2002). K+ Cycling and the Endocochlear Potential. *Hear. Res.* 165 (1–2), 1–9. doi:10.1016/S0378-5955(02)00279-4

Wangemann, P. (2006). Supporting Sensory Transduction: Cochlear Fluid Homeostasis and the Endocochlear Potential. *J. Physiol.* 576 (1), 11–21. doi:10.1113/jphysiol.2006.112888

Watanabe, K.-i., Jinnouchi, K., Hess, A., Michel, O., Baba, S., and Yagi, T. (2002). Carboplatin Induces Less Apoptosis in the Cochlea of guinea Pigs Than Cisplatin. *Chemotherapy* 48 (2), 82–87. doi:10.1159/000057667

World Health Organization. 2021. Deafness and Hearing Loss. Avaolable at: https://www.who.int/news-room/fact-sheets/detail/deafness-and-hearing-loss. [Accessed Dec 19, 2021]

Wu, L. H., Chen, L.-H., Xie, H., and Xie, Y.-J. (2017). Prenatal Diagnosis of a Case of Norrie Disease with Late Development of Bilateral Ocular Malformation. *Fetal Pediatr. Pathol.* 36 (3), 240–245. doi:10.1080/15513815.2017.1307474

Wu, P.-z., O'Malley, J. T., de Gruttola, V., and Liberman, M. C. (2020). Age-related Hearing Loss Is Dominated by Damage to Inner Ear Sensory Cells, Not the Cellular Battery that powers Them. *J. Neurosci.* 40 (33), 6357–6366. doi:10.1523/JNEUROSCI.093720.202010.1523/jneurosci.0937-20.2020

Wu, W. J., Sha, S. H., Mclaren, J. D., Kawamoto, K., Raphael, Y., and Schacht, J. (2001). Aminoglycoside Ototoxicity in Adult CBA, C57BL and BALB Mice and the Sprague-Dawley Rat. *Hear. Res.* 158 (1-2), 165–78. doi:10.1016/S0378-5955(01)00303-3

Xu, Q., Wang, Y., Dabdoub, A., Smallwood, P. M., Williams, J., Woods, C., et al. (2004). Vascular Development in the Retina and Inner Ear. *Cell* 116 (6), 883–895. doi:10.1016/S0092-8674(04)00216-8

Yamada, K., Limprasert, P., Ratanasukon, M., Tengtrisorn, S., Yingchareonpukdee, J., Vasiknanonte, P., et al. (2001). Two Thai Families with Norrie Disease (ND): Association of Two Novel Missense Mutations with Severe ND Phenotype, Seizures, and a Manifesting Carrier. *Am. J. Med. Genet.* 100 (1), 52–55. doi:10.1002/1096-8628(20010415)100:1<52:AID-AJMG1214>3.0.CO;2-B

Yasumoto, K.-i., Takeda, K., Saito, H., Watanabe, K. -I., Takahashi, K., and Shibahara, S. (2002). Microphthalmia-associated Transcription Factor Interacts with LEF-1, a Mediator of Wnt Signaling. *EMBO* 21 (11), 2703–2714. doi:10.1093/emboj/21.11.2703

Ye, X., Wang, Y., Cahill, H., Yu, M., Badea, T. C., Smallwood, P. M., et al. (2009). Norrin, Frizzled-4, and Lrp5 Signaling in Endothelial Cells Controls a Genetic Program for Retinal Vascularization. *Cell* 139 (2), 285–298. doi:10.1016/j.cell.2009.07.047

Zdebik, A. A., Wangemann, P., and Jentsch, T. J. (2009). Potassium Ion Movement in the Inner Ear: Insights from Genetic Disease and Mouse Models. *Physiology* 24 (5), 307–316. doi:10.1152/physiol.00018.2009

Zhang J, J., Hou, Z., Wang, X., Jiang, H., Neng, L., Zhang, Y., et al. (2021). VEGFA165 Gene Therapy Ameliorates Blood-Labyrinth Barrier Breakdown and Hearing Loss. *JCI Insight* 6 (8). doi:10.1172/jci.insight.143285

Zhang, N., Cai, J., Xu, L., Wang, H., and Liu, W. (2020). Cisplatin-induced Stria Vascularis Damage Is Associated with Inflammation and Fibrosis. *Neural Plasticity* 2020, 1–13. doi:10.1155/2020/8851525

Zhang, Q., Liu, H., McGee, J., Walsh, E. J., Soukup, G. A., and He, D. Z. Z. (2013). Identifying microRNAs Involved in Degeneration of the Organ of Corti during Age-Related Hearing Loss. *PLoS ONE* 8 (4), e62786–12. doi:10.1371/journal.pone.0062786

Zhang, Q., Ota, T., Yoshida, T., Ino, D., Sato, M. P., Doi, K., et al. (2021). Electrochemical Properties of the Non-excitable Tissue Stria Vascularis of the Mammalian Cochlea Are Sensitive to Sounds. *J. Physiol.* 599 (19), 4497–4516. doi:10.1113/jp281981

Zhang, W., Dai, M., Fridberger, A., Hassan, A., DeGagne, J., Neng, L., et al. (2012). Perivascular-resident Macrophage-like Melanocytes in the Inner Ear Are Essential for the Integrity of the Intrastrial Fluid-Blood Barrier. *Proc. Natl. Acad. Sci.* 109 (26), 10388–10393. doi:10.1073/pnas.1205210109

Zhang, W., Xie, J., Hui, L., Li, S., and Zhang, B. (2020). The Correlation between Endolymphatic Hydrops and Blood-Labyrinth Barrier Permeability of Meniere Disease. *Ann. Otol Rhinol Laryngol.* 130 (6), 578–584. doi:10.1177/0003489420964823

Zhou, Y., Song, J., Wang, Y. P., Zhang, A. M., Tan, C. Y., Liu, Y. H., et al. (2019). Age-associated V-ariation in the E-xpression and F-unction of TMEM16A C-alcium-activated C-hloride C-hannels in the C-ochlear S-tria V-ascularis of guinea P-igs. *Mol. Med. Rep.* 20 (2), 1593–1604. doi:10.3892/mmr.2019.10423

Conflict of Interest: The authors declare that the research was conducted in the absence of any commercial or financial relationships that could be construed as a potential conflict of interest.

Publisher's Note: All claims expressed in this article are solely those of the authors and do not necessarily represent those of their affiliated organizations, or those of the publisher, the editors and the reviewers. Any product that may be evaluated in this article, or claim that may be made by its manufacturer, is not guaranteed or endorsed by the publisher.

frontiers in Cell and Developmental Biology

ORIGINAL RESEARCH
published: 08 March 2022
doi: 10.3389/fcell.2022.867153

Intermediate Cells of Dual Embryonic Origin Follow a Basal to Apical Gradient of Ingression Into the Lateral Wall of the Cochlea

Justine M. Renauld[1†], *Vibhuti Khan*[1†] *and Martín L. Basch*[1,2,3,4*]

[1]Department of Otolaryngology, Head and Neck Surgery, Case Western Reserve University School of Medicine, Cleveland, OH, United States, [2]Department of Genetics and Genome Sciences, Case Western Reserve School of Medicine, Cleveland, OH, United States, [3]Department of Biology, Case Western Reserve University, Cleveland, OH, United States, [4]Department of Otolaryngology, Head and Neck Surgery, University Hospitals, Cleveland, OH, United States

OPEN ACCESS

Edited by:
Isabel Varela-Nieto,
Spanish National Research Council (CSIC), Spain

Reviewed by:
Helge Rask-Andersen,
Uppsala University, Sweden
Andy Groves,
Baylor College of Medicine, United States
Bernd Fritzsch,
The University of Iowa, United States

***Correspondence:**
Martín L. Basch
mlb202@case.edu

[†]These authors have contributed equally to this work

Specialty section:
This article was submitted to Molecular and Cellular Pathology, a section of the journal Frontiers in Cell and Developmental Biology

Received: 31 January 2022
Accepted: 22 February 2022
Published: 08 March 2022

Citation:
Renauld JM, Khan V and Basch ML (2022) Intermediate Cells of Dual Embryonic Origin Follow a Basal to Apical Gradient of Ingression Into the Lateral Wall of the Cochlea. Front. Cell Dev. Biol. 10:867153. doi: 10.3389/fcell.2022.867153

Intermediate cells of the stria vascularis are neural crest derived melanocytes. They are essential for the establishment of the endocochlear potential in the inner ear, which allows mechanosensory hair cells to transduce sound into nerve impulses. Despite their importance for normal hearing, how these cells develop and migrate to their position in the lateral wall of the cochlea has not been studied. We find that as early as E10.5 some Schwann cell precursors in the VIIIth ganglion begin to express melanocyte specific markers while neural crest derived melanoblasts migrate into the otic vesicle. Intermediate cells of both melanoblast and Schwann cell precursor origin ingress into the lateral wall of the cochlea starting at around E15.5 following a basal to apical gradient during embryonic development, and continue to proliferate postnatally.

Keywords: intermediate cells, neural crest, stria vascularis, inner ear, cochlea, schwann cell precursor, melanoblast, inner ear development

INTRODUCTION

The stria vascularis is a specialized epithelium that actively pumps potassium into the scala media to generate the positive endocochlear potential essential for sensory hair cells to transduce sound vibrations into action potentials (Hudspeth, 1989; Steel and Barkway, 1989; Takeuchi et al., 2000; Hibino et al., 2010). This specialized epithelium located on the lateral wall of the cochlea is composed of three different cell types: marginal cells, intermediate cells, and basal cells, each with a distinct embryonic origin. Marginal cells are derived from the otic epithelium and line the lumen of the scala media (Sagara et al., 1995). Intermediate cells are melanocyte-like cells derived from the neural crest (Cable et al., 1992). Basal cells are adjacent to the spiral ligament and are derived from otic mesenchyme (Trowe et al., 2011). Mesodermally-derived blood vessels are interspersed throughout the stria vascularis in close association with intermediate cells. (Steel and Barkway, 1989). In the vestibular organs, except for the sacculus, the potassium transport is mediated by dark cells. These dark cells express the same channels as marginal cells of the stria vascularis and are in close associations with neural crest derived pigmented cells underneath that are thought to regulate calcium homeostasis (Ciuman, 2009).

The presence of intermediate cells in the inner ear has been shown to be essential for hearing and developmental defects affecting intermediate cells are responsible for several congenital deafness (Edery et al., 1996; Matsushima et al., 2002; Ni et al., 2013). Those developmental disorders are part

of a larger group of diseases called neurocristopathies and originate from defects in development, differentiation or survival of neural crest cells (Ritter and Martin, 2019). Like most pigmented cells of vertebrates, intermediate cells originate from neural crest cells.

The neural crest is a transient population of multipotent embryonic vertebrate cells. It gives rise to multiple derivatives including most of the pigmented cells in the body, the peripheral nervous system and most of the craniofacial skeleton [Reviewed in (Basch et al., 2004; Sauka-Spengler and Bronner-Fraser, 2008)]. In avian embryos, most neural crest derivatives are originated from an early ventral migrating population of neural crest cells, while melanocytes are originated from a later migrating subset of neural crest cells that migrate dorsolaterally between the dermomyotome and the skin (Erickson and Goins, 1995; Kuo and Erickson, 2010). Recent studies in mouse have shown that in addition to neural crest that take the dorsolateral pathway, a significant number of melanocytes are derived from the re-differentiation of nerve-associated Schwann cell precursors that came from ventromedial migrating neural crest cells (Adameyko et al., 2009; Adameyko et al., 2012; Yoshimura et al., 2013; Furlan and Adameyko, 2018).

Despite being essential for hearing, little is known about the development of the stria vascularis. In this paper, we focused on the development of the pigmented cells of the stria. We followed their development all the way until their differentiation as intermediate cells. We analyzed the timing of their formation, their incorporation into the lateral wall of the cochlea, their differentiation, and their proliferation state. We found that intermediate cells can originate directly from dorsolateral migrating melanoblasts or from the differentiation of Schwann cell precursors. They incorporate into the lateral wall of the cochlea starting at around E15.5 following a basal to apical gradient reminiscent of the differentiation of hair cells in the organ of Corti. Intermediate cells continue to proliferate from embryonic stages until maturity in the postnatal strial epithelium.

MATERIALS AND METHODS

Experimental Animals

For this study we used the following mice: Wnt1Cre2 (stock no. 022137), tamoxifen inducible Wnt1CreER (stock no. 008851), Ai3-YFP [stock no.007903: ROSA26 enhanced yellow fluorescent protein (EYFP) reporter], Ai9-TdTomato (stock no. 007909), and Plp1-EYFP (stock no. 033357). All mice were obtained from Jackson Laboratory and bred in the animal facility of Case Western Reserve University following the IACUC guidelines for the use and care of laboratory animals (protocol no. 2018-0034). We set timed matings between heterozygous Wnt1Cre, Wnt1creER males with homozygous Ai3-YFP or Ai9-TdTomato reporter females. The following morning, vaginal plug visualization was considered embryonic day 0.5 (E0.5) and the day mice were born was considered as postnatal day 0 (P0). We analyzed at least three littermates and two litters from each embryonic and postnatal stage studied.

Lineage Tracing and Tamoxifen Administration

To fate map the contribution of neural crest cells to the inner ear we crossed hemizygous Wnt1Cre males with homozygous Ai3-YFP or Ai9-TdTomato reporter females and harvested embryos from E8.5 to E17.5 and dissected cochleae from pups at postnatal days P0, P6 and P14. To dissect the temporal contributions of neural crest, we crossed tamoxifen inducible Wnt1CreERT2 hemizygous males to Ai3-YFP homozygous females. To induce the activity of the CRE recombinase we administered a single dose of 2 mg tamoxifen with 2 mg progesterone (20 mg/ml in peanut oil) via oral gavage to the pregnant females at E8.5, E9.5, E10.5 and E11.5 and collected embryos at P0. To count the number of intermediate cells in stria vascularis we have analyzed three pups from three different pregnant females for each stage. We counted nine sections of 12 μm thickness covering 108 μm of the cochlea length from each of the three pups for a total of 27 sections per stage. Statistical analysis was done by using a 2-tailed student t test. A p-value ≤0.05 was considered as statistically significant.

Genotyping

Genotyping of embryos and pups was determined by PCR and confirmed by the presence of EYFP fluorescence under a Mercury lamp. Primers used for CRE genotyping were CreF: GCCTGC ATTACCGGTCGATGCAACGA and CreR: GTGGCAGAT GGCGCGGCAACACCATT.

Edu (5-Ethynyl-2-deoxyuridine) Labeling and Cell Death

To analyze the cell proliferation in stria at embryonic day E16.5 and E18.5, a single dose of EdU (100 μL/10 g of body weight, C10339, Invitrogen) was administered to timed pregnant females. The cochleae of the neonatal pups were dissected at P0. For the postnatal cell proliferation analyses a single dose of EdU (250 μg/10 g of body weight) was administered subcutaneously to the pups at P0, P3, P6 and P14. These pups were euthanized 6 h after the administration of EdU and their cochleae were extracted. EdU detection was performed according to the manufacturer's instructions with a ClickiT EdU Alexa Fluor 594 Imaging kit (C10339, Invitrogen). In Edu proliferation assay we have administered Edu in two different pregnant females or two different litters for each stage. For each stage analyzed, we have used three pups (nine sections from each pup). A total of 27 sections each of thickness 12 μm (covering around 108 μm of the cochlea length in each sample) were analyzed. Statistical analysis was done by using a 2-tailed student t test. A p-value ≤0.05 was considered as statistically significant.

Histology

Pregnant females were euthanized in a CO2 chamber for at least 10 min and cervical dislocation was used as a secondary method, embryos between E8.5 and E17.5 were collected. P0, P3, P6 and P14 pups were placed in a CO_2 chamber for over 30 min and immediately afterwards decapitated. Inner ears from P3, P6 and P14 pups were dissected prior to fixation. Embryos at E8.5, E9.5

and E10.5 were fixed with 4% paraformaldehyde for 1 hour at room temperature. All other tissues were fixed in 4% paraformaldehyde overnight at 4°C. After fixation all the samples were washed three times for 10 min in PBS. Inner ears from pups older than P3 were transferred to a 0.5M EDTA solution at 4°C for the decalcification. EDTA was changed daily until decalcification was complete (determined by gently pushing on the tissue with forceps). Thereafter all the samples were transferred to 30% sucrose in PBS at 4°C until fully sink. The embryos and the dissected inner ears were embedded in plastic cryomolds filled with OCT or gelatin-sucrose (7.5–15%) in a proper orientation and frozen either in dry ice or liquid nitrogen (embryos; P0, P3, P6 and P14 respectively). The inner ears (P0, P3, P6 and P14) were cut in 12 μm thick sections for immunohistochemistry and EdU cell counting. E8.5-E105 embryos were cut in 10 μm thick sections in three different planes (coronal, transverse and sagittal) for immunohistochemistry. E11.5 to E17.5 embryos were cut in 12 μm thick sections in a transverse plane for immunohistochemistry.

Immunohistochemistry

The cryosections were defrosted and washed with 1 × PBS for 5 min. The tissue permeabilization was done washing in 1% Triton X-100 followed by three washing in PBS for 5 min. Prior to immunostaining antigen retrieval was done by boiling the sections for 10 min in antigen retrieval (H-3300, Vector Laboratories). Thereafter, sections were blocked for 30 min using 10% lamb serum in PBS/0.1% Triton × 100 or PGT [PBS-gelatin (0.25%)-triton (0.3%)]. Sections were incubated in the primary antibodies overnight at 4°C. The next day, sections were washed three times in PBS for 10 min and then incubated in the corresponding secondary antibody for 1 h at room temperature. Sections were washed three times with PBS for 10 min and then mounted using DAPI Fluoromount (Southern Biotech).

Primary antibodies used in this study were anti-GFP (Abcam 13,970, chicken, 1:1,000), Caspase 3 (Cell signaling technology 9,662, rabbit, 1:1,000), CD44(Thermo Fisher Scientific MA4405, rat, 1:250), connexin 26(Alonome labs ACC-212, rabbit, 1:100), DCT (Abcam 74,073, rabbit, 1:100), KCNQ1 (Santa Cruz sc-20816, rabbit, 1:250), MITF (R&D Systems AF5769, goat, 1:500), P75 (Advanced Targeting Systems AB-N01, rabbit, 1:500), Prox1 (rabbit, 1:750). Secondary antibodies used were Alexa Fluor 488 goat anti-chicken IgY (ThermoFisher Scientific A11039, 1:1,000), Alexa Fluor 568 goat anti-rabbit IgG (ThermoFisher Scientific A11036, 1:500), Alexa Fluor 633 goat anti-rabbit IgG (ThermoFisher Scientific A21070, 1:500), anti-goat 594 (Jackson Immunoresearch, 705-005-003, 1:300).

RESULTS

Neural Crest Migration Into the Inner Ear

To understand the precise development of intermediate cells in the cochlea, we took advantage of genetic lineage tracing using a Wnt1-Cre2 crossed to Ai3-YFP mouse reporter line to label neural crest cells just before they undergo their epithelial-to-mesenchymal transition and follow their development in the inner ear (**Figure 1**). This combination of mouse lines has been commonly used to label neural crest cell derivatives in mice (Danielian et al., 1998; Chai et al., 2000; Freyer et al., 2011). In the mouse, neural crest cells begin to migrate around the time of neural tube closure at around E8.5 (Serbedzija et al., 1992; Trainor, 2005).

As early as E10.5, we can detect MITF positive cells, one of the earliest melanoblast markers, both in the delaminating ganglion and migrating into the otic vesicle from the dorsal neural tube (**Supplementary Figure S1**). E11.5 we continue to see MITF positive cells in the periphery of the VIIIth ganglion and in the proximity of the inner ear (**Figure 4**, left panel).

By E12.5, neural crest cells that form glial cells are surrounding the ganglion. In addition, we observe neural crest cells migrating and lining up just outside the roof of the cochlear duct (arrowheads, **Figure 1**). In the vestibular organs, neural crest cells are migrating to and surrounding the utricle and the saccule and are already lining the ampullae of the semicircular canals where they'll form close associations with the dark cells (arrows, **Figure 1**). As the cochlea elongates we observe more neural crest cells lining outside the cochlear duct at the site of the future lateral wall, up until E14.5. In the vestibular organs, cells have reached their final positions in the utricle and they begin to localize under the crista of the ampullae in the semicircular canals (arrows, **Figure 1**). Interestingly, we observed Wnt1Cre2-YFP positive cells scattered throughout the epithelium of the cochlea (see discussion). We also quantified the proportion of hair cells and supporting cells carrying the YFP expression at P0 (**Supplementary Figure S2B**).

Ingression of Intermediate Cells in the Developing Stria Vascularis Follows a Base-to-Apical Gradient and Precedes Morphological Maturation

Around E15.5 cells that were lining the roof of the basal turn of the cochlea begin to extend protrusions into the single cell epithelium that forms the roof of the cochlea at this stage. This partial invasion continues until birth and follows a basal to apical gradient reminiscent of the gradient of differentiation in the organ of Corti. At E16.5, the different steps of development can be all seen at the different positions in the same cochlea section as shown in **Figure 2A**. CD44, a cell surface adhesion receptor which labels intermediate cells (Morris et al., 2006; Rohacek et al., 2017), is shown in red to visualize the cell membrane of melanocytic cells during the ingression process (**Figure 2A**, right panel). At this stage, we can see the future intermediate cells migrating above the marginal cells layer at the apex, characterized by an elongated shape (arrows, **Figure 2A**–1). At the mid-apex level, the future intermediate cells present a round shape as they cease to migrate and begin to attach to the marginal cells layer (**Figure 2A**–2). The stage is followed by an increase in protrusions toward the marginal cell layer as seen in the mid-base level (arrowheads, **Figure 2A**–3). At the base, almost all intermediate cells started to partially invade the marginal cell layer (Arrowhead, **Figure 2A**–4). The ingression

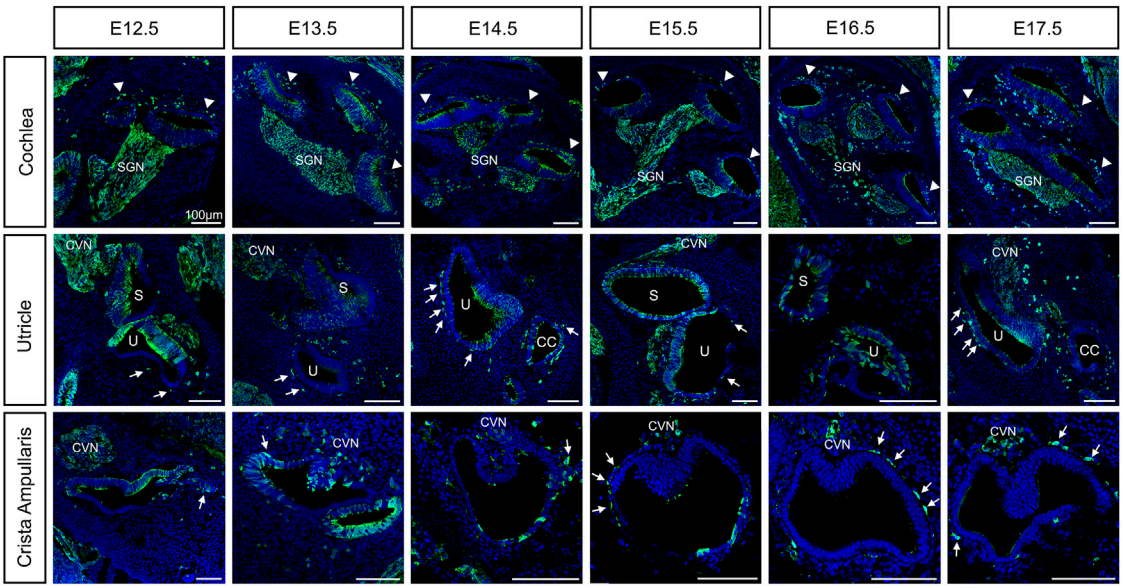

FIGURE 1 | Neural crest contributions to the inner ear during embryonic development from E12.5 to E17.5. Lineage tracing of neural crest cells using Wnt1-Cre2 mice crossed to an EYFP reporter line was visualized by staining with the anti-GFP antibody in green and DAPI for nucleus in blue. Arrowheads: intermediate cells of the stria vascularis; Arrows: melanoblast of the vestibule; CVN: Cochleo-vestibular neurons; SGN: Spiral ganglion neurons; S: saccule; U: utricle. Scale bars: 100 µm.

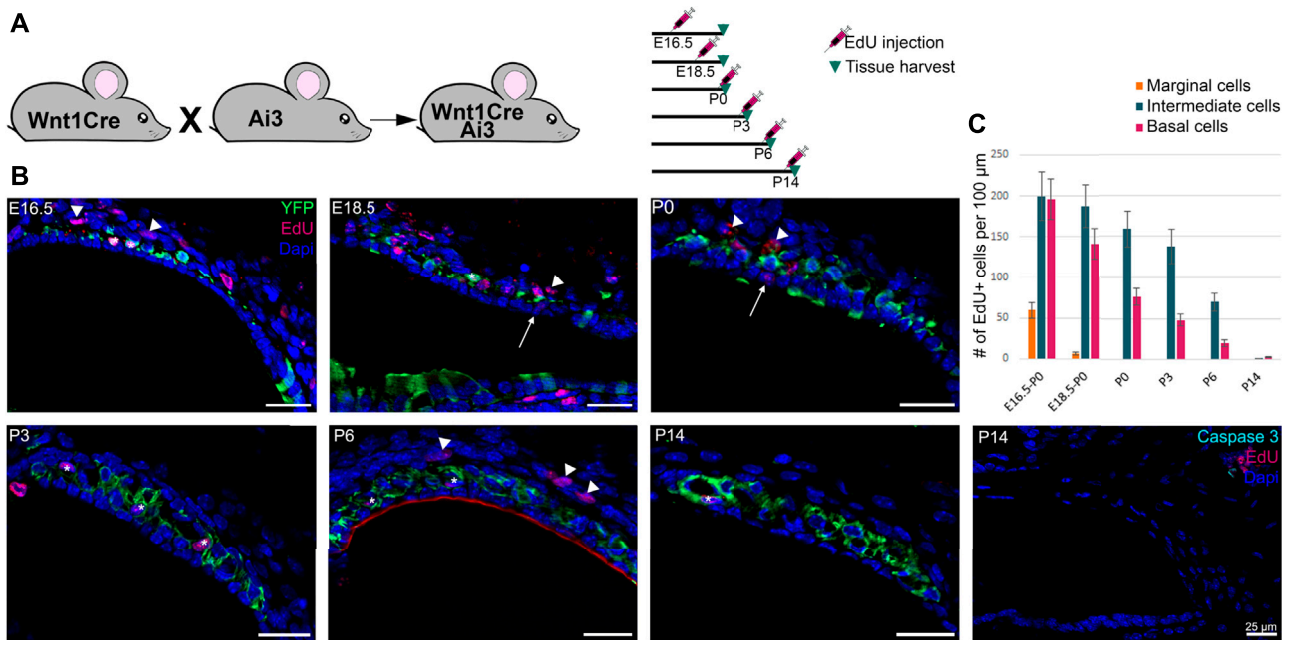

FIGURE 2 | Intermediate cells in the developing stria vascularis follow a base-to-apical gradient of ingression and undergo morphological maturation at early postnatal days. **(A)** Immunostaining of E16.5 Wnt1cre-YFP mouse with white dashed square magnified in insets. Future intermediate cells migrate (arrows) then line up on top of the cochlear duct and ingress in the lateral wall of the cochlea following a basal to apical gradient. CD44 (in red) is a cell membrane marker of melanoblast that shows the protrusion in the marginal cells layer (Arrowheads). 1: apex, 2: mid apex, 3: mid base, 4: base. **(B)** Schematic representation of the base to apex semi-ingression process. Melanoblast are represented in dark pink at the surface of the lateral wall. **(C).** Immunostaining of P0, P6 and P32 Wnt1Cre-YFP mouse with white dashed square magnified in insets. Green cells in the stria vascularis are intermediate cells labeled by Wnt1-CRE2 crossed to a EYFP reporter. KCNQ1 and Connexin 26, markers of marginal and basal cells respectively, are both in purple to delimit the intermediate cell region in the stria vascularis.

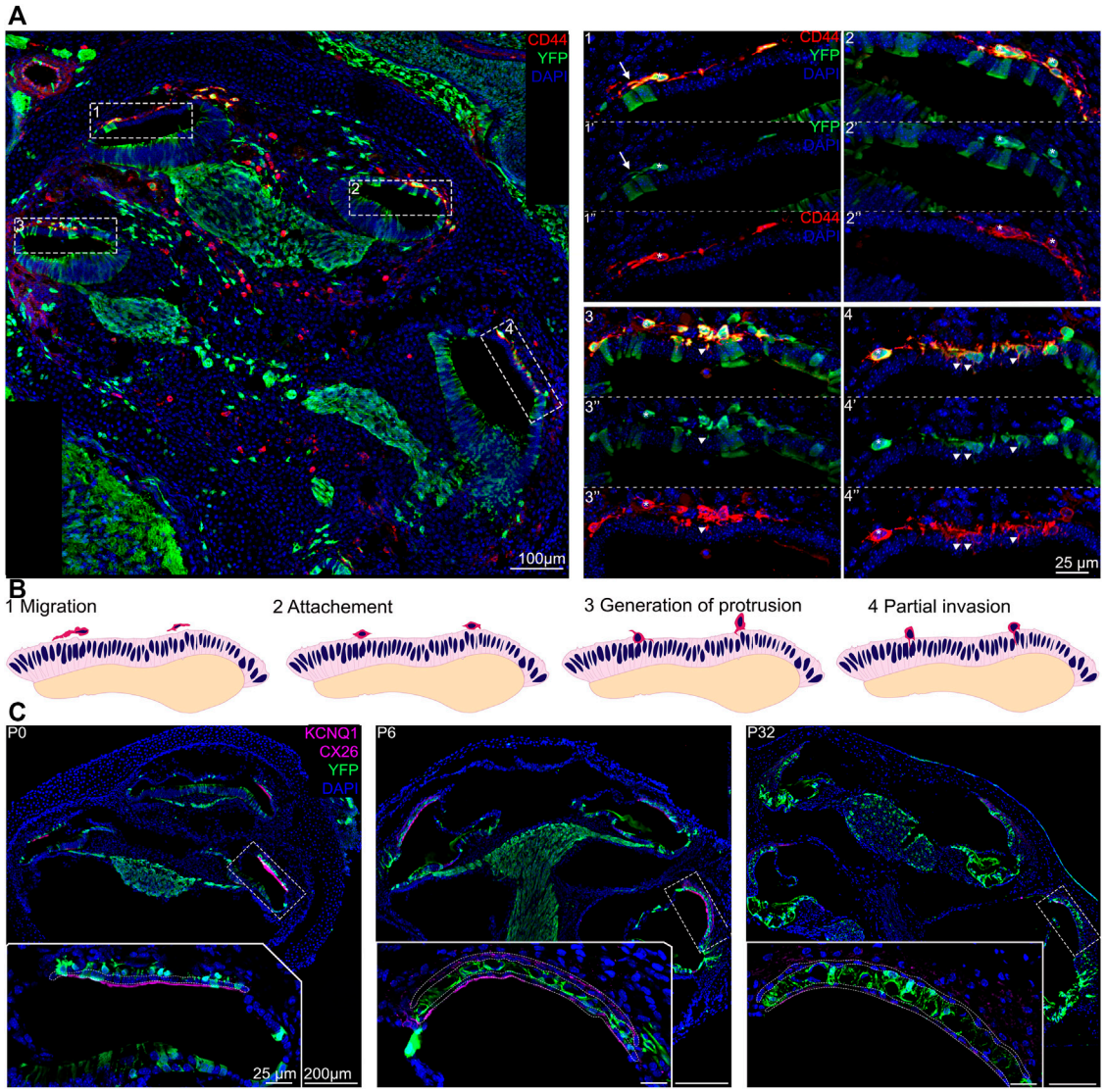

FIGURE 3 | Proliferation in the stria vascularis decreases 2 weeks after birth. **(A)** Schematic of the experimental using Edu injection at different time points during development. **(B)** Immunostaining of Wnt1Cre-YFP mice from P0 to P14 with EdU labeling (dark pink) and DAPI, a nuclear marker in blue. Some Edu positive marginal, intermediate and basal cells are shown by arrows, stars and arrowheads respectively. Anti-activated caspase 3 labeling (in turquoise) shows no significant cell death in the stria vascularis during development (right panel). **(C)** Graphic of the average proliferation in the three different layers of the inner ear from E16.5 to P14. For each stage $n = 3$.

of the intermediate cells into the stria vascularis is represented in a schematic (**Figure 2B**). As development proceeds, intermediate cells at the basal turns are already positioned between marginal and basal cells that are coalescing on the lateral wall of the cochlea (**Figure 1** E17.5, **Figures 2A–4,C**).

At P0, the future intermediate cells have completed their migration into the lateral wall of the cochlea between the marginal cell layer and the basal cells layers. At this stage, the cells have not fully differentiated and they exhibit markers of both neural crest cells and intermediate cells (Renauld et al., 2021). Neonatal intermediate cells are round in shape and individual cells are seen scattered throughout the stria between marginal and intermediate cells, from the spiral prominence to Reisner's membrane. By P6, the stria is thicker, intermediate cells begin to adopt a more columnar shape in opposition to marginal cells that become a thinner layer one cell thick. At this stage, intermediate cells begin to form close association with blood vessels that have invaded the stria from a capillary plexus in the spiral ligament (**Figure 2C and** (Ando and Takeuchi, 1998). As early as P14 the cells are fully matured, they form extensive interdigitations with both marginal and basal cells and they occupy the entire width of the stria from the outer sulcus to Reisner's membrane [**Figure 2C**; (Cable et al., 1992)].

Intermediate Cells Proliferate Until Maturation of the Stria Vascularis

During the development of the inner ear, to accompany the growth of the cochlea, the stria vascularis increases dramatically in width and length. The extension of the stria could be achieved by cell movement and growth, cell proliferation, or a combination of both. To address these possibilities, we analyzed cell proliferation in the stria starting at embryonic day E16.5 through P14 by administration of EdU, a thymidine analogue, to track newly synthesized DNA reflecting dividing cells. For embryonic stages, one pulse of EdU was administered to the pregnant female and the embryos were collected at P0. For postnatal stages, we analyzed EdU incorporation 6 h after subcutaneous administration. The design of the experiment is summarized in **Figure 3A**. We observed a rapid decline in cell proliferation in the marginal cells at late embryonic stages and no proliferation after P0. Intermediate and basal cells continue to proliferate after birth, but the rate of proliferation decreases with development and we observed little proliferation after P6 (**Figure 3B**). The quantification is shown in **Figure 3C**. Our results suggest that growth of the stria is driven by extension of intermediate cells likely due to a combination of cell movement and cell proliferation. In addition to cell proliferation, we analyzed cell death in the stria using an antibody against activated caspase-3. Although we did not see any significant cell death in any of the cell layers of the stria, occasionally we observed some caspase-3 positive cells within the fibroblasts of the spiral ligament (**Figure 3C** and Data not shown).

Dual Embryonic Origin of Intermediate Cells

Recent findings have shown that there is contribution of Schwann cell precursors on the peripheral nerves to extracutaneous melanocytes such as the melanocytes of the inner ear (Bonnamour et al., 2021; Kaucka et al., 2021). Bonnamour and colleagues used a Dhh-Cre line to genetically trace Schwann cell precursors in the inner ear and found that up to 90% of the intermediate cells of the stria vascularis were labeled by Dhh tracing. Kaucka used plp1-CreERT2 to show that the contribution of Schwann cell precursors in the inner ear melanocytes decreased after E15.5. To confirm these recent findings and address the timing of contribution of nerve-associated Schwann cell precursors to intermediate cells of the inner ear, we used genetic lineage tracing to label Schwann cell precursors together with melanoblasts markers. A Plp1-YFP mouse strain was used to label Schwann cell precursors at E12.5. Plp1 has already been studied extensively between E11.5 and E15.5 for Schwann cell lineage tracing (Adameyko et al., 2009; Adameyko et al., 2012). As early as E11.5, we observed MITF positive cells between the dermis and the otic vesicle, originating from the dorsolateral migration pathway of neural crest (arrows, **Figure 4B1**). In addition, we observed MITF positive cells in the cochleo-vestibular ganglion, suggesting that melanocytes in the inner ear can originate from the cochleovestibular nerve via Schwann cells precursors adopting a melanocytic fate (arrows, **Figure 4B2**, E11.5). At E12.5, melanoblasts originating from the dorsolateral pathway (Plp1 negative, arrow) or from Schwann cell precursors (Plp1 positive, arrowhead, asterisk) are both visible in the future lateral wall of the cochlear duct (**Figure 4B**). Interestingly, in our mix-background mice, PLP protein is still expressed in the vast majority of strial intermediate cells at postnatal day 6 (**Figure 4C**, right panel). However, some DCT positive intermediate cells are Plp1 negative (**Figure 4C**, arrow), suggesting that while the majority of intermediate cells originate from Schwann cell precursors, there are some that come from direct melanoblast migration. PLP expression could allow us to differentiate the two populations of intermediate cells in the mature stria vascularis.

Early Migratory Neural Crest Cells Give Rise to Both Glia and Melanocytes in the Inner Ear

Previous research has shown that in the trunk, avian and rodent neural crest cells behave differently with an early ventral pathway followed by a delayed dorsolateral migration of neural crest cells in the chick in contrast to a simultaneous migration in the mouse (Kuo and Erickson, 2010; Kuo and Erickson, 2011). In opposition to the trunk neural crest cells, the cephalic neural crest cells delaminate before the neural tube closure in a continuous wave and is believed to show little variation between species (Theveneau and Mayor, 2012). However, the time window of delamination of future melanocytes has been less studied in the cephalic location.

To determine whether glial cells and melanocytes in the mouse inner ear originate from distinct temporal subpopulations of neural crest, we used an inducible Wnt1-Cre (Wnt1-CreERrT2) line crossed to a YFP reporter to label early- and late-migrating populations of neural crest. Our results are summarized in **Figure 5**. We administered tamoxifen *via* oral gavage to pregnant females at E8.5, E9.5, E10.5 and E11.5. and analyzed YFP expression at P0, the experimental design is represented in **Figure 5A**.

If there was a temporal difference in the early vs. late subpopulations of migrating cephalic neural crest, as in avian trunk embryos, we would expect labeling only intermediate cells when tamoxifen was administered at E10.5 but not glial cells. Administration of tamoxifen at E8.5 recapitulates the non-inducible Wnt1-Cre2, labeling all neural crest derivatives in the inner ear (Arrowheads, **Figure 5B**). We observed a similar result when we administered tamoxifen at E9.5 although slightly fewer intermediate and glial cells were labeled when compared to tamoxifen administration at E8.5. Surprisingly, when we administered tamoxifen at E10.5, most samples presented only a few glial cells labelled and no intermediate cells or melanoblasts from the vestibule (**Figure 5B**). We speculate that this result could be due to a lower number of melanoblasts in comparison to glial cells in the cochlea. Alternatively, melanoblasts from the inner ear stop delaminating from the neural tube at an earlier stage than glial cells, or Schwann cell precursors complete their differentiation into melanocytes before E10.5. We did not observe any labeled intermediate or glial cells after giving tamoxifen at E11.5 (**Figure 5B**). The quantification of the labelled intermediate cells is represented in **Figure 5C**.

Similar to what we saw in the cochlea, in the vestibular organs we observed a decreased number of labeled cells as we increased the stage of tamoxifen administration (Arrows, **Figure 5B**).

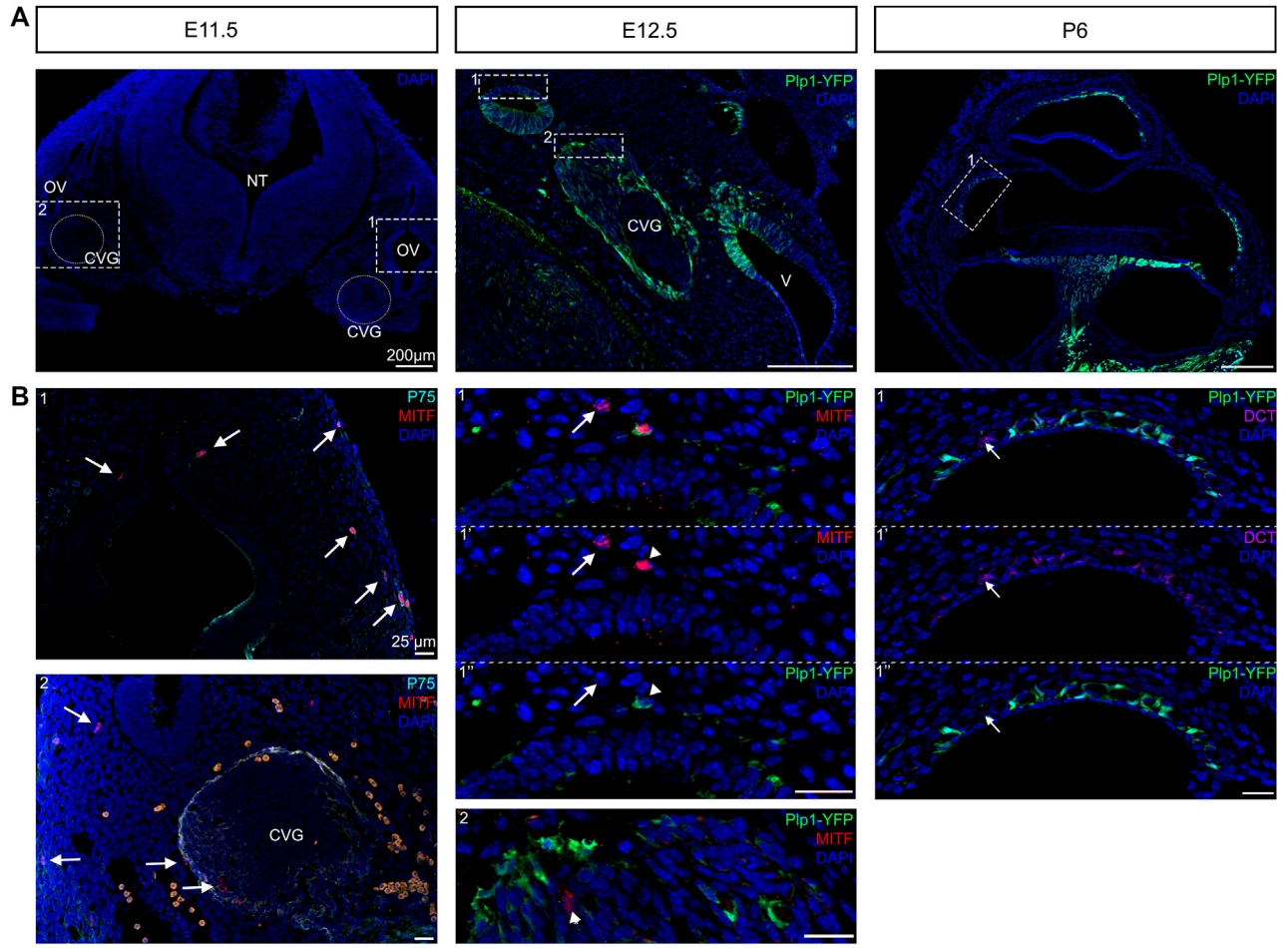

FIGURE 4 | Dual embryonic origin of intermediate cells. Immunostaining for melanoblast with MITF labelling (in red) and neural crest cells with P75 (in turquoise) shows at E11.5 the presence of melanoblast between the dermis and the otic vesicle and between the otic vesicle and the neural tube (Arrows). Lineage tracing of Schwann cell precursors using Plp1-YFP reporter line at E12.5 and P6. Immunostaining for melanoblast with the MITF antibody (red) and DAPI for nucleus (blue) show cells with both markers (arrowheads) or only melanoblast marker (arrows). Most intermediate cells express the glial cell marker PLP (green) and melanocyte markers DCT (in purple) at P6 except one cell that only express DCT (arrow). CVG: cochleaovestibular ganglion, NT: neural tube, OV: otic vesicle, V: vestibule.

DISCUSSION

Neural crest cells give rise to a wide variety of derivatives in vertebrates, including craniofacial bones, peripheral nervous system, and pigmented cells in the body. In the inner ear, the contribution of neural crest to the lateral wall of the cochlea and the glia of the spiral ganglion have been described (Kuo and Erickson, 2010; Freyer et al., 2011; Sandell et al., 2014). The cochleovestibular ganglion, which innervates the cochlea and the vestibular organs, is composed of neurons derived from the otic placode (Rosenbluth, 1962; D'Amico-Martel and Noden, 1983; Breuskin et al., 2010) and glial cells derived from the neural crest (D'Amico-Martel and Noden, 1983). Intermediate cells of the stria vascularis are neural crest derived melanocytes, described by Steel et al. (Steel and Barkway, 1989). Although these neural crest contributions in the inner ear have been known for some time, the timing of how these cells migrate and how they differentiate in their proper locations during development was not known. In addition, new data has revealed that pigmented cells in the cochlea can originate from Schwann cell precursors (Bonnamour et al., 2021; Kaucka et al., 2021). In this study we characterized the temporal migration of melanoblasts into the inner ear, their dual embryonic origin, their proliferation, morphological maturation, and the subsequent postnatal differentiation into intermediate cells.

Early Migration of Neural Crest

The neurons of the cochleovestibular ganglion delaminate from the anteroventral portion of the otic vesicle and aggregate (Altman and Bayer, 1982; Carney and Silver, 1983). As the ganglion is forming, Schwann cell precursors coalesce around the developing neurons to form the glial cells. These Schwann cell precursors are neural crest derived. It had been proposed that streams of neural crest cells migrate from the hindbrain at the level of the fourth rhombomere directly into the developing ganglion at around E10.5 and envelop the neurons of the

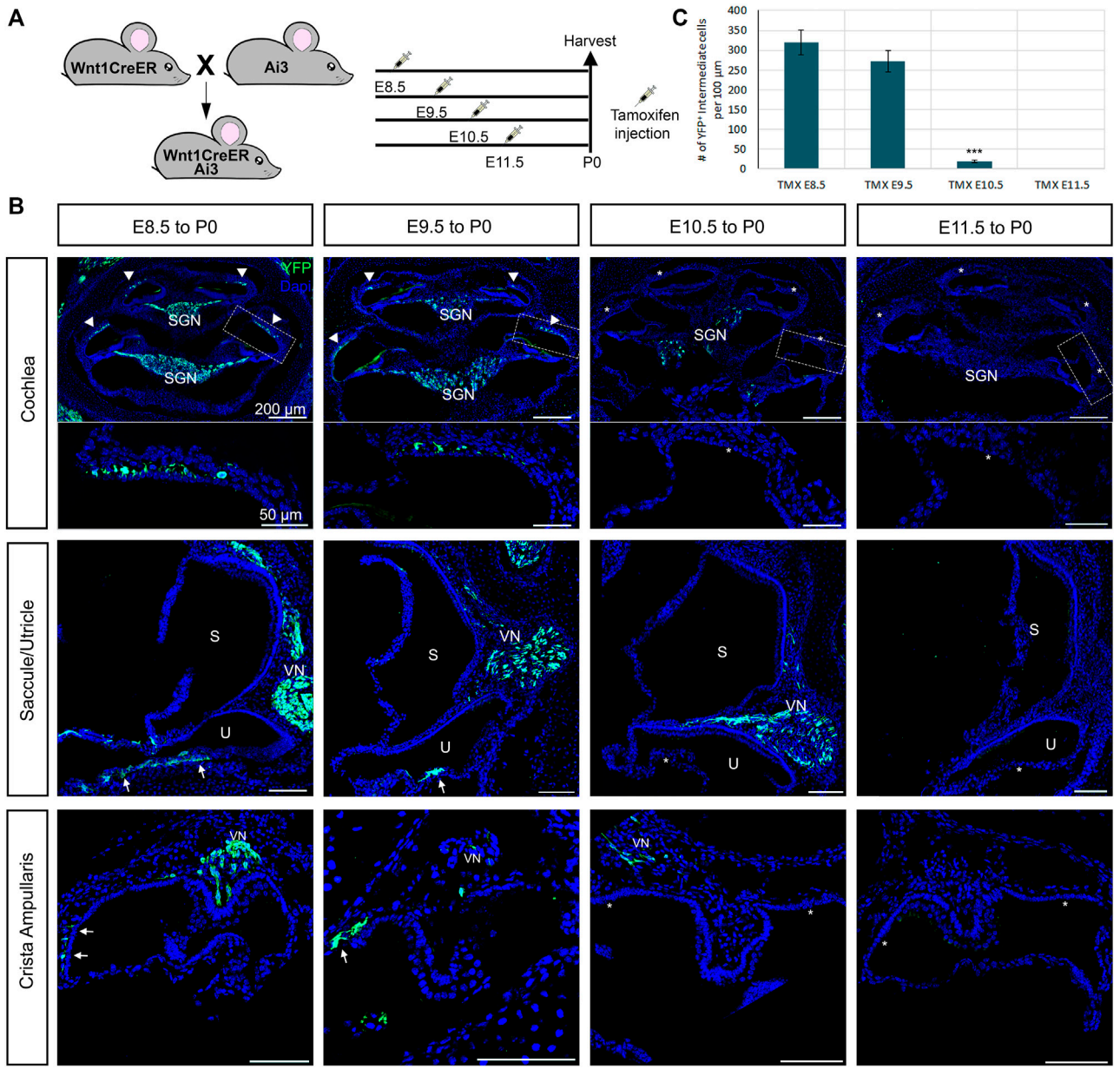

FIGURE 5 | Early migratory neural crest cells give rise to both glial cells and melanocytes cells in the inner ear. Inducible Wnt1-CreER shows no late-migrating neural crest contribution to the inner ear. **(A)** Tamoxifen was administered to pregnant females via oral gavage at the ages indicated in the experimental design and collected and analyzed at P0. **(B)** Immunostaining of Wnt1CreER-YFP mice following the experimental design at P0 with YFP (green) and DAPI for nuclear labelling. Arrows indicate the melanoblast of the vestibules, the arrowheads the intermediate cells of the stria vascularis and the stars the missing labelling in the melanoblasts and intermediate cells. **(C)** Graph shows the average number of labeled intermediate cells after administration of tamoxifen at each stage. *n* = 3. CVN: Cochleo-vestibular neurons; VN: vestibular neurons; SGN: Spiral ganglion neurons; S: saccule; U: utricle.

cochleovestibular nerve (Sandell et al., 2014). At this stage, we have already seen MITF positive cells migrating into the otic vesicle from the dorsolateral pathway, as well as MITF positive cells in the forming ganglion (**Figure 4**). MITF is an early critical transcription factor that drives melanoblast specification (Goding, 2000). MITF expression in a number of Schwann cell precursors in the ganglion is consistent with the idea of these cells adopting a melanoblast fate before migrating into the otic vesicle. Our observations are consistent with reports from Kaucka et al., who in addition to MITF positive cells migrating both from the neural crest and from the VIIIth ganglion, also described melanocytic cells migrating into the otic vesicle posteriorly from the IX and X cranial nerves (Kaucka et al., 2021). As the cochlea begins to elongate, Schwann cell precursors keep coalescing around the neurons of the VIIIth to form glia, and some differentiate into melanocytes. MITF positive cells migrate

to the roof of the cochlea in the site of the future lateral wall. By E12.5 and until E14.5 we see these cells lining up just outside of the cochlea, possibly waiting for a signal to incorporate into the stria vascularis.

Intermediate Cells Follow a Basal to Apical Gradient of Ingression Into the Lateral Wall of the Cochlea

Shibata et al. described the incorporation of neural crest cells into the lateral wall as a three-step process (Shibata et al., 2016). First, cells migrate to the location of the future stria vascularis in response to yet unknown signals. We observe this from the formation of the cochlear duct onwards. Second, the cells attach to the site where they will incorporate. At around E14.5, we see cells that are going to ingress in the lateral wall of the cochlea begin to line up just outside the site of the future stria vascularis in the cochlear duct. Third, the melanocytes incorporate into the cochlear epithelium. We observe this ingression of cells into the lateral wall beginning at around E15.5 at the base of the cochlea. The ingression seems to follow a basal to apical gradient reminiscent of the gradient of differentiation in the organ of Corti and the formation of the scala vestibuli and scala tympanii (**Figures 2A,B and** (Chen et al., 2002)). Locher et al. published a basal to apical gradient of epithelial invasion in human cochlea at W14- W16 (Locher et al., 2015). As development proceeds, cells continue to ingress in the lateral wall at the midturn of the cochlea and finally at the apex prior to birth. Interestingly, Hgf and EdnrB, are both expressed by migratory neural crest cells that will become intermediate cells. Both these genes also exhibit a basal to apical expression pattern in intermediate cells that support our observation. However, without the lineage tracing, we could not rule out the possibility that expression of these genes was turned on in a graded manner as opposed to cells ingressing following the gradient (Shibata et al., 2016; Renauld et al., 2021). These results suggest that there might be a graded signal or signals that instruct the neural crest cells when to begin ingressing into the lateral wall. There is evidence to suggest that one such signal could be hepatocyte growth factor Hgf via the receptor c-Met, whether this signaling is directly or solely responsible for the gradient of incorporation of intermediate cells into the cochlea needs further study (Shibata et al., 2016; Ohyama, 2017; Morell et al., 2020).

Intermediate Cells of the Cochlea Likely Originate From Schwann Cell Precursors

The traditional view of melanocyte formation is that melanocytes arise directly from a late-migrating population of neural crest that migrate through a dorsolateral pathway under the dermis and populates the skin. The early-migrating neural crest follow a medio ventral path of migration and form the dorsal root ganglia and eventually neurons and glia of the peripheral nervous system and the rest of the neural crest derivatives. These ideas were supported by quail-chick grafts and vital dye lineage tracing experiments in the chick embryos as well as genetic targeting experiments in the mouse (Le Douarin and Teillet, 1973; Erickson et al., 1992; Serbedzija et al., 1992; Erickson and Goins, 1995). However, recent experiments have shown that both trunk and cranial melanocytes have two distinct cellular origins: from melanoblast precursors directly derived from migrating neural crest and from nerve-associated Schwann Cell Precursors that also give rise to glial cells and are derived from the early-migrating population of neural crest (Adameyko et al., 2009; Adameyko et al., 2012; Bonnamour et al., 2021). Since then several reports have confirmed this dual origin of melanocytes. Colombo et al., found expression of Plp1, a Schwann cell precursor marker, in melanoblasts and melanocytes (Colombo et al., 2012). Similarly, single cell analysis of cochlear Plp1 positive embryonic ganglion cells found clusters expressing melanocyte markers (Tasdemir-Yilmaz et al., 2021). Finally, Kaucka et al. reported that nerve associated Schwan cell precursors contribute extracutaneous melanocytes to the heart, meninges and supraorbital locations amongst others (Kaucka et al., 2021).

Our data suggests that pigmented cells in the inner ear arise both through melanoblast precursors from neural crest migrating dorsolaterally under the dermis, and also from Schwann cell precursors associated with the cochleovestibular ganglion. As the future intermediate cells approach the cochlear duct at around E12.5 they express either markers for both glial cells and melanocytes, consistent with a Schwann cell precursor multipotent progenitor, or just melanocyte markers. At P6, most of the intermediate cells of the stria vascularis are labeled by Plp1-Cre suggesting their Schwann cell precursor origin. However, we still see intermediate cells that are Plp1 negative, which likely originated from melanoblast precursors.

Postnatal Development of Intermediate Cells

Intermediate cells of the stria vascularis begin ingressing into the lateral wall of the cochlea in a basal to apical gradient starting at around E15.5 and continue to ingress until birth (**Figure 2**). By postnatal day 0, intermediate cells occupy their final position between marginal and basal cells. At this point, the cells have begun their differentiation into melanocytes but still retain makers of multipotent neural crest (Renauld et al., 2021). Between birth and postnatal day 6, intermediate cells begin to change morphology and go from a round shape to a more elongated shape that sends protrusions that interdigitate with the other cell types of the stria forming tight junctions (Cable et al., 1992; Tachibana, 1999). By the onset of hearing, around P15, intermediate cells have fully differentiated and adopted their mature shape. They occupy the whole width of the stria, from the spiral prominence to the start of Reisner's membrane. Our data suggests that intermediate and basal cells proliferate during embryonic stages and continue to do so after birth. The proliferation declines rapidly after postnatal day 6 which can be related to the stria vascularis reaching its final volume. However, we cannot discard the possibilty that absence of labeling in posnatal stages maybe due to a decreased rate of cell proliferation in which case EdU might clear from the cells before incorporation. We did not detect significant cell death

either embryonically or in the first 2 weeks after birth (**Figure 3**). Previous studies have shown that intermediate cells resume proliferation in adult mice (Conlee et al., 1994).

Other Neural Crest Contributions to the Cochlea

Most lineage analyses have described glial cells of the VIIIth ganglion and pigmented cells of the cochlea and vestibular organs as the only neural crest derivatives in the inner ear (Mao et al., 2014; Sandell et al., 2014; Karpinski et al., 2016). A notable exception is controversial work by Freyer et al., that used not only a Wnt1-Cre driver but also a Pax3-Cre driver to label neural crest derived cells. This study showed Pax-3 labeled cells in the sensory organ of Corti (Freyer et al., 2011). A caveat of these studies is that Wnt1-Cre does not label all neural crest, and that Pax3 expression during neural tube closure is broader than just prospective neural crest, raising the possibility that other tissues might have contributed to labeling in the inner ear (reviewed in (Ritter and Martin, 2019). However, similar studies found no contribution of neural crest to the inner ear other than the glia of the VIIIth ganglion and melanocytes (Mao et al., 2014; Karpinski et al., 2016).

We have actually observed both phenotypes using the same mouse wnt1-Cre2 and Ai3 reporter lines in different studies. The present study, seems in agreement with Freyer results. We do observe EYPF positive cells present in the sensory epithelium. However, this expression does not reflect contribution of migratory neural crest. When we looked at premigratory stages (E8.5), we found expression of Wnt1-Cre2 extending beyond the dorsal neural tube and into the otic placode. We believe those positive cells originate from Wnt1 expression in the otic placode and not from neural crest cells migrating into the inner ear as shown in the **Supplementary Figure S2A**. In contrast, in a previous study when we did similar lineage tracing using Wnt1-CRE2 and reporter lines, we never observed neural crest contribution in the inner ear besides pigmented cells or glia of the VIIIth ganglion (Renauld et al., 2021).

The only difference between this study and our previous one, was the genetic background of the mice used. In our previous study, all mice had a congenic ICR background. Because here we wanted to see pigment in the melanocytes, we used a mixed background that included B6 mice in our breeding schemes. This raises the possibility that genetic background might affect Wnt1 expression. Such background differences in phenotypic expression have been previously described and it is known that genetic modifiers can alter gene expression outcomes in the ear (Kiernan et al., 2007; Kane et al., 2012).

CONCLUSION

Here, we studied the development of intermediate cells of the stria vascularis from early migration of neural crest to differentiation in the postnatal cochlea. We showed that the pigmented cells that will form intermediate cells differentiate both from migratory neural crest that adopt a dorsolateral migration pathway and from nerve-associated Schwann cell precursors. Between E12.5 and E14.5 these cells line up above the roof of the cochlea on the site of the future lateral wall. Starting at E15.5, probably in response to a signal or signals from the cochlear epithelium, these cells incorporate into the stria vascularis following a basal to apical gradient reminiscent of the differentiation of the organ of Corti. Cells in the stria proliferate as the cochlea develops and this proliferation declines rapidly after postnatal day 6.

DATA AVAILABILITY STATEMENT

The original contributions presented in the study are included in the article/**Supplementary Material**, further inquiries can be directed to the corresponding author.

ETHICS STATEMENT

The animal study was reviewed and approved by the Case Western Reserve University IACUC.

AUTHOR CONTRIBUTIONS

MB designed experiments, analyzed data and wrote the manuscript. JR designed and performed experimentss, analyzed data and wrote the manuscript VK performed experiments and analyzed data.

FUNDING

This work was funded by NIH/NIDCD 1 R01 DC015785-01to MB.

ACKNOWLEDGMENTS

The authors would like to thank William Davis for expert technical assistance.

SUPPLEMENTARY MATERIAL

The Supplementary Material for this article can be found online at: https://www.frontiersin.org/articles/10.3389/fcell.2022.867153/full#supplementary-material

Supplementary Figure S1 | Early migration of MITF+ neural crest cells MITF+ neural crest migrating both dorsally and ventrally towards the otic vesicle where they will become intermediate cells of the stria and melanoblasts of the vestiblar system, at E10.5 (MITF labeled in red, cell nucleus in blue). NT: neural tube, OV: otic vesicle.

Supplementary Figure S2 | Wnt1-Cre2 labels the otic placode in a mixed mouse background **(A)** Lineage tracing using Wnt1-Cre2 mice crossed to an EYFP reporter line was visualized by staining with the anti-GFP antibody in green and DAPI for nucleus in blue at E8.5 and P0. NT: Neural tube. Dotted line delimited the neural tube and the otic placodes. Arrows: YFP positive cells; arrowhead: positive Deiters' cell. Asterisk: positive inner hair cell. **(B)** percentage of Wnt1Cre-YFP positive cells in the organ of Corti counted on the whole mount. n = 5 from 2 different litters.

REFERENCES

Adameyko, I., Lallemend, F., Aquino, J. B., Pereira, J. A., Topilko, P., Müller, T., et al. (2009). Schwann Cell Precursors from Nerve Innervation Are a Cellular Origin of Melanocytes in Skin. *Cell* 139, 366–379. doi:10.1016/j.cell.2009.07.049

Adameyko, I., Lallemend, F., Furlan, A., Zinin, N., Aranda, S., Kitambi, S. S., et al. (2012). Sox2 and Mitf Cross-Regulatory Interactions Consolidate Progenitor and Melanocyte Lineages in the Cranial Neural Crest. *Development* 139, 397–410. doi:10.1242/dev.065581

Altman, J., and Bayer, S. A. (1982). Introduction. *Adv. Anat. Embryol. Cel Biol* 74, 1. doi:10.1007/978-3-642-68479-1_1

Ando, M., and Takeuchi, S. (1998). Postnatal Vascular Development in the Lateral wall of the Cochlear Duct of Gerbils: Quantitative Analysis by Electron Microscopy and Confocal Laser Microscopy. *Hearing Res.* 123, 148–156. doi:10.1016/s0378-5955(98)00109-9

Basch, M. L., García-Castro, M. I., and Bronner-Fraser, M. (2004). Molecular Mechanisms of Neural Crest Induction. *Birth Defects Res. C: Embryo Today Rev.* 72, 109–123. doi:10.1002/bdrc.20015

Bonnamour, G., Soret, R., and Pilon, N. (2021). Dhh -expressing Schwann Cell Precursors Contribute to Skin and Cochlear Melanocytes, but Not to Vestibular Melanocytes. *Pigment Cel Melanoma Res.* 34, 648–654. doi:10.1111/pcmr.12938

Breuskin, I., Bodson, M., Thelen, N., Thiry, M., Borgs, L., Nguyen, L., et al. (2010). Glial but Not Neuronal Development in the Cochleo-Vestibular Ganglion Requires Sox10. *J. Neurochem.* 114, 1827–1839. doi:10.1111/j.1471-4159.2010.06897.x

Cable, J., Barkway, C., and Steel, K. P. (1992). Characteristics of Stria Vascularis Melanocytes of Viable Dominantspotting () Mouse Mutants. *Hearing Res.* 64, 6–20. doi:10.1016/0378-5955(92)90164-i

Carney, P. R., and Silver, J. (1983). Studies on Cell Migration and Axon Guidance in the Developing Distal Auditory System of the Mouse. *J. Comp. Neurol.* 215, 359–369. doi:10.1002/cne.902150402

Chai, Y., Jiang, X., Ito, Y., Bringas, P., JR., Han, J., Rowitch, D. H., et al. (2000). Fate of the Mammalian Cranial Neural Crest during Tooth and Mandibular Morphogenesis. *Development* 127, 1671–1679. doi:10.1242/dev.127.8.1671

Chen, P., Johnson, J. E., Zoghbi, H. Y., and Segil, N. (2002). The Role of Math1 in Inner Ear Development: Uncoupling the Establishment of the Sensory Primordium from Hair Cell Fate Determination. *Development* 129, 2495–2505. doi:10.1242/dev.129.10.2495

Ciuman, R. R. (2009). Stria Vascularis and Vestibular Dark Cells: Characterisation of Main Structures Responsible for Inner-Ear Homeostasis, and Their Pathophysiological Relations. *J. Laryngol. Otol.* 123, 151–162. doi:10.1017/s0022215108002624

Colombo, S., Champeval, D., Rambow, F., and Larue, L. (2012). Transcriptomic Analysis of Mouse Embryonic Skin Cells Reveals Previously Unreported Genes Expressed in Melanoblasts. *J. Invest. Dermatol.* 132, 170–178. doi:10.1038/jid.2011.252

Conlee, J. W., Gerity, L. C., and Bennett, M. L. (1994). Ongoing Proliferation of Melanocytes in the Stria Vascularis of Adult guinea Pigs. *Hearing Res.* 79, 115–122. doi:10.1016/0378-5955(94)90133-3

D'Amico-Martel, A., and Noden, D. M. (1983). Contributions of Placodal and Neural Crest Cells to Avian Cranial Peripheral Ganglia. *Am. J. Anat.* 166, 445–468. doi:10.1002/aja.1001660406

Danielian, P. S., Muccino, D., Rowitch, D. H., Michael, S. K., and Mcmahon, A. P. (1998). Modification of Gene Activity in Mouse Embryos In Utero by a Tamoxifen-Inducible Form of Cre Recombinase. *Curr. Biol.* 8, 1323–S2. doi:10.1016/s0960-9822(07)00562-3

Edery, P., Attie, T., Amiel, J., Pelet, A., Eng, C., Hofstra, R. M. W., et al. (1996). Mutation of the Endothelin-3 Gene in the Waardenburg-Hirschsprung Disease (Shah-Waardenburg Syndrome). *Nat. Genet.* 12, 442–444. doi:10.1038/ng0496-442

Erickson, C. A., Duong, T. D., and Tosney, K. W. (1992). Descriptive and Experimental Analysis of the Dispersion of Neural Crest Cells along the Dorsolateral Path and Their Entry into Ectoderm in the Chick Embryo. *Dev. Biol.* 151, 251–272. doi:10.1016/0012-1606(92)90231-5

Erickson, C. A., and Goins, T. L. (1995). Avian Neural Crest Cells Can Migrate in the Dorsolateral Path Only if They Are Specified as Melanocytes. *Development* 121, 915–924. doi:10.1242/dev.121.3.915

Freyer, L., Aggarwal, V., and Morrow, B. E. (2011). Dual Embryonic Origin of the Mammalian Otic Vesicle Forming the Inner Ear. *Development* 138, 5403–5414. doi:10.1242/dev.069849

Furlan, A., and Adameyko, I. (2018). Schwann Cell Precursor: a Neural Crest Cell in Disguise? *Dev. Biol.* 444 (Suppl. 1), S25–S35. doi:10.1016/j.ydbio.2018.02.008

Goding, C. R. (2000). Mitf from Neural Crest to Melanoma: Signal Transduction and Transcription in the Melanocyte Lineage. *Genes Dev.* 14, 1712–1728. doi:10.1101/gad.14.14.1712

Hibino, H., Nin, F., Tsuzuki, C., and Kurachi, Y. (2010). How Is the Highly Positive Endocochlear Potential Formed? the Specific Architecture of the Stria Vascularis and the Roles of the Ion-Transport Apparatus. *Pflugers Arch. - Eur. J. Physiol.* 459, 521–533. doi:10.1007/s00424-009-0754-z

Hudspeth, A. J. (1989). How the Ear's Works Work. *Nature* 341, 397–404. doi:10.1038/341397a0

Kane, K. L., Longo-Guess, C. M., Gagnon, L. H., Ding, D., Salvi, R. J., and Johnson, K. R. (2012). Genetic Background Effects on Age-Related Hearing Loss Associated with Cdh23 Variants in Mice. *Hearing Res.* 283, 80–88. doi:10.1016/j.heares.2011.11.007

Karpinski, B. A., Bryan, C. A., Paronett, E. M., Baker, J. L., Fernandez, A., Horvath, A., et al. (2016). A Cellular and Molecular Mosaic Establishes Growth and Differentiation States for Cranial Sensory Neurons. *Dev. Biol.* 415, 228–241. doi:10.1016/j.ydbio.2016.03.015

Kaucka, M., Szarowska, B., Kavkova, M., Kastriti, M. E., Kameneva, P., Schmidt, I., et al. (2021). Nerve-associated Schwann Cell Precursors Contribute Extracutaneous Melanocytes to the Heart, Inner Ear, Supraorbital Locations and Brain Meninges. *Cell. Mol. Life Sci.* 78, 6033–6049. doi:10.1007/s00018-021-03885-9

Kiernan, A. E., Li, R., Hawes, N. L., Churchill, G. A., and Gridley, T. (2007). Genetic Background Modifies Inner Ear and Eye Phenotypes of Jag1 Heterozygous Mice. *Genetics* 177, 307–311. doi:10.1534/genetics.107.075960

Kuo, B. R., and Erickson, C. A. (2010). Regional Differences in Neural Crest Morphogenesis. *Cell Adhes. Migration* 4, 567–585. doi:10.4161/cam.4.4.12890

Kuo, B. R., and Erickson, C. A. (2011). Vagal Neural Crest Cell Migratory Behavior: a Transition between the Cranial and Trunk Crest. *Dev. Dyn.* 240, 2084–2100. doi:10.1002/dvdy.22715

Le Douarin, N. M., and Teillet, M. A. (1973). The Migration of Neural Crest Cells to the Wall of the Digestive Tract in Avian Embryo. *J. Embryol. Exp. Morphol.* 30 (1), 31–48.

Locher, H., De Groot, J. C. M. J., Van Iperen, L., Huisman, M. A., Frijns, J. H. M., and Chuva De Sousa Lopes, S. M. (2015). Development of the Stria Vascularis and Potassium Regulation in the Human Fetal Cochlea: Insights into Hereditary Sensorineural Hearing Loss. *Devel Neurobio* 75, 1219–1240. doi:10.1002/dneu.22279

Mao, Y., Reiprich, S., Wegner, M., and Fritzsch, B. (2014). Targeted Deletion of Sox10 by Wnt1-Cre Defects Neuronal Migration and Projection in the Mouse Inner Ear. *PLoS One* 9, e94580. doi:10.1371/journal.pone.0094580

Matsushima, Y., Shinkai, Y., Kobayashi, Y., Sakamoto, M., Kunieda, T., and Tachibana, M. (2002). A Mouse Model of Waardenburg Syndrome Type 4 with a New Spontaneous Mutation of the Endothelin-B Receptor Gene. *Mamm. Genome* 13, 30–35. doi:10.1007/s00335-001-3038-2

Morell, R. J., Olszewski, R., Tona, R., Leitess, S., Wafa, T. T., Taukulis, I., et al. (2020). Noncoding Microdeletion in Mouse Hgf Disrupts Neural Crest Migration into the Stria Vascularis, Reduces the Endocochlear Potential, and Suggests the Neuropathology for Human Nonsyndromic Deafness DFNB39. *J. Neurosci.* 40, 2976–2992. doi:10.1523/jneurosci.2278-19.2020

Morris, J. K., Maklad, A., Hansen, L. A., Feng, F., Sorensen, C., Lee, K.-F., et al. (2006). A Disorganized Innervation of the Inner Ear Persists in the Absence of ErbB2. *Brain Res.* 1091, 186–199. doi:10.1016/j.brainres.2006.02.090

Ni, C., Zhang, D., Beyer, L. A., Halsey, K. E., Fukui, H., Raphael, Y., et al. (2013). Hearing Dysfunction in heterozygousMitfMi-Wh/+ Mice, a Model for Waardenburg Syndrome Type 2 and Tietz Syndrome. *Pigment Cel Melanoma Res* 26, 78–87. doi:10.1111/pcmr.12030

Ohyama, T. (2017). There's No Place like home - HGF-C-MET Signaling and Melanocyte Migration into the Mammalian Cochlea. *Neurogenesis* 5, e1317693. doi:10.1080/23262133.2017.1317693

Renauld, J. M., Davis, W., Cai, T., Cabrera, C., and Basch, M. L. (2021). Transcriptomic Analysis and Ednrb Expression in Cochlear Intermediate Cells Reveal Developmental Differences between Inner Ear and Skin Melanocytes. *Pigment Cel Melanoma Res.* 34, 585–597. doi:10.1111/pcmr.12961

Ritter, K. E., and Martin, D. M. (2019). Neural Crest Contributions to the Ear: Implications for Congenital Hearing Disorders. *Hearing Res.* 376, 22–32. doi:10.1016/j.heares.2018.11.005

Rohacek, A. M., Bebee, T. W., Tilton, R. K., Radens, C. M., Mcdermott-Roe, C., Peart, N., et al. (2017). ESRP1 Mutations Cause Hearing Loss Due to Defects in Alternative Splicing that Disrupt Cochlear Development. *Dev. Cel* 43, 318–331. doi:10.1016/j.devcel.2017.09.026

Rosenbluth, J. (1962). The fine Structure of Acoustic Ganglia in the Rat. *J. Cel Biol* 12, 329–359. doi:10.1083/jcb.12.2.329

Sagara, T., Furukawa, H., Makishima, K., and Fujimoto, S. (1995). Differentiation of the Rat Stria Vascularis. *Hearing Res.* 83, 121–132. doi:10.1016/0378-5955(94)00195-v

Sandell, L. L., Butler Tjaden, N. E., Barlow, A. J., and Trainor, P. A. (2014). Cochleovestibular Nerve Development Is Integrated with Migratory Neural Crest Cells. *Dev. Biol.* 385, 200–210. doi:10.1016/j.ydbio.2013.11.009

Sauka-Spengler, T., and Bronner-Fraser, M. (2008). A Gene Regulatory Network Orchestrates Neural Crest Formation. *Nat. Rev. Mol. Cel Biol* 9, 557–568. doi:10.1038/nrm2428

Serbedzija, G. N., Bronner-Fraser, M., and Fraser, S. E. (1992). Vital Dye Analysis of Cranial Neural Crest Cell Migration in the Mouse Embryo. *Development* 116, 297–307. doi:10.1242/dev.116.2.297

Shibata, S., Miwa, T., Wu, H.-H., Levitt, P., and Ohyama, T. (2016). Hepatocyte Growth Factor-C-MET Signaling Mediates the Development of Nonsensory Structures of the Mammalian Cochlea and Hearing. *J. Neurosci.* 36, 8200–8209. doi:10.1523/jneurosci.4410-15.2016

Steel, K. P., and Barkway, C. (1989). Another Role for Melanocytes: Their Importance for normal Stria Vascularis Development in the Mammalian Inner Ear. *Development* 107, 453–463. doi:10.1242/dev.107.3.453

Tachibana, M. (1999). Sound Needs Sound Melanocytes to Be Heard. *Pigment Cel Res* 12, 344–354. doi:10.1111/j.1600-0749.1999.tb00518.x

Takeuchi, S., Ando, M., and Kakigi, A. (2000). Mechanism Generating Endocochlear Potential: Role Played by Intermediate Cells in Stria Vascularis. *Biophysical J.* 79, 2572–2582. doi:10.1016/s0006-3495(00)76497-6

Tasdemir-Yilmaz, O. E., Druckenbrod, N. R., Olukoya, O. O., Dong, W., Yung, A. R., Bastille, I., et al. (2021). Diversity of Developing Peripheral Glia Revealed by Single-Cell RNA Sequencing. *Dev. Cel* 56, 2516–2535. doi:10.1016/j.devcel.2021.08.005

Theveneau, E., and Mayor, R. (2012). Neural Crest Delamination and Migration: from Epithelium-To-Mesenchyme Transition to Collective Cell Migration. *Dev. Biol.* 366, 34–54. doi:10.1016/j.ydbio.2011.12.041

Trainor, P. A. (2005). Specification of Neural Crest Cell Formation and Migration in Mouse Embryos. *Semin. Cel Dev. Biol.* 16, 683–693. doi:10.1016/j.semcdb.2005.06.007

Trowe, M. O., Maier, H., Petry, M., Schweizer, M., Schuster-Gossler, K., and Kispert, A. (2011). Impaired Stria Vascularis Integrity upon Loss of E-Cadherin in Basal Cells. *Dev. Biol.* 359, 95–107. doi:10.1016/j.ydbio.2011.08.030

Yoshimura, N., Motohashi, T., Aoki, H., Tezuka, K.-i., Watanabe, N., Wakaoka, T., et al. (2013). Dual Origin of Melanocytes Defined by Sox1 Expression and Their Region-specific Distribution in Mammalian Skin. *Develop. Growth Differ.* 55, 270–281. doi:10.1111/dgd.12034

Conflict of Interest: The authors declare that the research was conducted in the absence of any commercial or financial relationships that could be construed as a potential conflict of interest.

Publisher's Note: All claims expressed in this article are solely those of the authors and do not necessarily represent those of their affiliated organizations, or those of the publisher, the editors and the reviewers. Any product that may be evaluated in this article, or claim that may be made by its manufacturer, is not guaranteed or endorsed by the publisher.

frontiers in Cell and Developmental Biology

ORIGINAL RESEARCH
published: 15 March 2022
doi: 10.3389/fcell.2022.850624

Reactivation of the Neurogenic Niche in the Adult Zebrafish Statoacoustic Ganglion Following a Mechanical Lesion

*Simone Schwarzer, Devavrat Ravindra Rekhade†, Anja Machate, Sandra Spieß, Michaela Geffarth, Diana Ezhkova and Stefan Hans**

CRTD—Center for Regenerative Therapies Dresden, Center for Molecular and Cellular Bioengineering (CMCB), Technische Universität Dresden, Dresden, Germany

OPEN ACCESS

Edited by:
Berta Alsina,
Pompeu Fabra University, Spain

Reviewed by:
Bruce B. Riley,
Texas A&M University, United States
Yingzi He,

Fernando Giraldez,
CEXS—Universidad Pompeu Fabra (UPF)—Parque de Investigación Biomédica de Barcelona (PRBB), Spain

***Correspondence:**
Stefan Hans
stefan.hans@tu-dresden.de

†Present address:
Devavrat Ravindra Rekhade, Medical Clinic 1, University Hospital Dresden, Dresden, Germany

Specialty section:
This article was submitted to Molecular and Cellular Pathology, a section of the journal Frontiers in Cell and Developmental Biology

Received: *07 January 2022*
Accepted: *03 February 2022*
Published: *15 March 2022*

Citation:
Schwarzer S, Rekhade DR, Machate A, Spieß S, Geffarth M, Ezhkova D and Hans S (2022) Reactivation of the Neurogenic Niche in the Adult Zebrafish Statoacoustic Ganglion Following a Mechanical Lesion. Front. Cell Dev. Biol. 10:850624. doi: 10.3389/fcell.2022.850624

Sensorineural hearing loss is caused by the loss of sensory hair cells and/or their innervating neurons within the inner ear and affects millions of people worldwide. In mammals, including humans, the underlying cell types are only produced during fetal stages making loss of these cells and the resulting consequences irreversible. In contrast, zebrafish produce sensory hair cells throughout life and additionally possess the remarkable capacity to regenerate them upon lesion. Recently, we showed that also inner ear neurogenesis continues to take place in the zebrafish statoacoustic ganglion (SAG) well into adulthood. The neurogenic niche displays presumptive stem cells, proliferating Neurod-positive progenitors and a high level of neurogenesis at juvenile stages. It turns dormant at adult stages with only a few proliferating presumptive stem cells, no proliferating Neurod-positive progenitors, and very low levels of newborn neurons. Whether the neurogenic niche can be reactivated and whether SAG neurons can regenerate upon damage is unknown. To study the regenerative capacity of the SAG, we established a lesion paradigm using injections into the otic capsule of the right ear. Upon lesion, the number of apoptotic cells increased, and immune cells infiltrated the SAG of the lesioned side. Importantly, the Neurod-positive progenitor cells re-entered the cell cycle displaying a peak in proliferation at 8 days post lesion before they returned to homeostatic levels at 57 days post lesion. In parallel to reactive proliferation, we observed increased neurogenesis from the Neurod-positive progenitor pool. Reactive neurogenesis started at around 4 days post lesion peaking at 8 days post lesion before the neurogenesis rate decreased again to low homeostatic levels at 57 days post lesion. Additionally, administration of the thymidine analog BrdU and, thereby, labeling proliferating cells and their progeny revealed the generation of new sensory neurons within 19 days post lesion. Taken together, we show that the neurogenic niche of the adult zebrafish SAG can indeed be reactivated to re-enter the cell cycle and to increase neurogenesis upon lesion. Studying the underlying genes and pathways in zebrafish will allow comparative studies with mammalian species and might provide valuable insights into developing cures for auditory and vestibular neuropathies.

Keywords: PNS, inner ear, neuronal stem cells, regeneration, zebrafish

INTRODUCTION

According to the World Health Organization, nearly 2.5 billion people will suffer from some degree of hearing loss in the next 2 decades, and at least one quarter will require hearing rehabilitation (https://www.who.int/news-room/fact-sheets/detail/deafness-and-hearing-loss). The vast majority of hearing impairment constitutes sensorineural hearing loss, which originates in the auditory part of the inner ear. The inner ear comprises six sensory patches containing mechanosensory hair cells that convert vestibular or auditory stimuli into electrochemical signals, as well as their innervating sensory neurons that transmit the signals to the brain *via* the eighth cranial nerve (Schwander et al., 2010). Whereas five sensory patches mediate vestibular function to perceive linear movement, gravity, and head rotation, hearing relies on a single sensory patch located in the cochlea. Damage to, or loss of, hair cells residing in the cochlea and/or their respective neurons results in sensorineural hearing loss. Unaddressed hearing loss can have severe impacts with respect to life quality and the socioeconomic status as people with untreated hearing loss are more likely to develop depression, anxieties, and feelings of inadequacy often reflected in lower household incomes (Tsakiropoulou et al., 2007). Moreover, recent epidemiological studies indicated that acquired hearing loss represents an independent risk factor for dementia and could account for approximately one-tenth of all cases (Livingston et al., 2017). Hence, unaddressed hearing loss amounts to significant economic burdens to individuals and society due to reduced productivity in the workplace as well as increased health care costs.

Despite the scale of the problem, treatment options are still largely limited, and no cell, molecular, or pharmacological therapies are currently available. To this aim, stem cell-based inner ear cell cultures derived from human embryonic stem cells as well as human-induced pluripotent stem cells provide a promising tool in the future. Stem cell-based inner ear cell cultures will be scalable and will allow generating transplantable sensory and neural progenitors *in vitro*, to replace the lost cell type *in vivo* (Chen et al., 2012; Koehler et al., 2017; Zine et al., 2021). In general, stem cell-based cell cultures use externally applied growth factors and small molecules to recapitulate the differentiation programs employed during development. In addition, direct reprogramming using transcription factor overexpression has been shown to be effective *in vitro* for the production of hair cell-like and neuron-like cells that display a transcriptomic profile resembling endogenous hair cells and neurons (Costa et al., 2015; Noda et al., 2018). However, irrespective of the methodology, robust and reproducible protocols are still missing due to the complex cellular and molecular nature of sensory and neural progenitor formation. Moreover, the cellular and molecular properties of transplantable cells to ensure functional restoration remain unclear.

A complementary approach relies on the analysis of *in vivo* models. Here, models either mimic the consequences of sensorineural hearing loss following the ablation of hair cells within the cochlea or neurons of the eighth cranial nerve or address the innate ability to replace lost cells upon damage in regeneration-competent organisms. Similar to humans, all mammalian models display no regenerative capacity. For instance, application of aminoglycosides, commonly prescribed antibiotics to treat bacterial infections, results in hair cell ablation in rats, mice, guinea pigs and Mongolian gerbils with no indication of subsequent regeneration (Astbury and Read, 1982; Forge, 1985; Taylor et al., 2008; Abbas and Rivolta, 2015). Similarly, application of the neurotoxin ouabain, an Na+/K+-ATPase inhibitor, results in the induction of cell death in most neurons of the eighth cranial nerve in mice, rats, and Mongolian gerbils with no signs of regeneration (Schmiedt et al., 2002; Lang et al., 2005; Fu et al., 2012; Wakizono et al., 2021). In contrast to mammals, all other vertebrates, such as birds, reptiles, amphibians, and fish have the remarkable intrinsic capacity to regenerate lost hair cells (Corwin and Cotanche, 1988; Ryals and Rubel, 1988; Stone and Rubel, 2000; Schuck and Smith, 2009). In particular, the zebrafish lateral line has emerged as a powerful model to study the events underlying hair cell regeneration in recent years due to its ease in applying aminoglycosides at larval stages, and single-cell RNA sequencing has recently revealed distinct stem cell populations driving this process (Stawicki et al., 2015; Lush et al., 2019). In sharp contrast, knowledge on the formation of inner ear neurons during regeneration in the regeneration-competent zebrafish is currently completely lacking. We recently showed the lifelong existence of a neurogenic niche in the eighth cranial nerve, also known as statoacoustic ganglion (SAG), in zebrafish (Schwarzer et al., 2020). We found that Neurod-positive progenitors proliferate and produce large amounts of new neurons at juvenile stages, but transition to a quiescent state at adulthood with only very rare neurogenesis. Importantly, BrdU pulse chase experiments revealed the existence of a proliferative but otherwise marker-negative cell population replenishing the Neurod-positive progenitor pool, which is never exhausted and maintained even in aged animals. Whether the neurogenic niche can adapt and increase its activity after loss of mature neurons due to injury is currently unknown. For instance, it is unclear if the events in the neurogenic niche of the SAG, which is part of the peripheral nervous system, will be similar or identical to the events in the zebrafish central nervous system. Here, low cycling or even quiescent stem cells undergo reactive proliferation upon injury yielding neural progenitors that differentiate during reactive neurogenesis to replace the damaged cells (Kroehne et al., 2011; Lenkowski and Raymond, 2014). This sequence of events is in stark contrast to the lesion response in the mammalian central nervous system, where reactive proliferation occurs upon lesion, but results in gliosis instead of the production of neural progenitors undergoing reactive neurogenesis (Adams and Gallo, 2018).

In this study, we employed a novel lesion paradigm resulting in a traumatic injury of the adult zebrafish SAG. The mechanical lesion caused an infiltration of blood and immune cells in the lesioned SAG, which persisted beyond 16 days post lesion (dpl). We found that mature SAG neurons underwent apoptosis, which was compensated by increased neurogenesis from the Neurod-

positive progenitor pool as early as 4 dpl and showed the highest neurogenesis rate at 8 dpl. Moreover, the Neurod-positive progenitors re-entered the cell cycle displaying, similar to the neurogenesis rate, a peak in proliferation at 8 days post lesion before converging to homeostatic levels at 57 days post lesion. BrdU pulse chase experiments revealed that newborn neurons developed within 14 days after proliferation of the neuronal progenitor cell. In summary, we established a mechanical lesion paradigm of the adult zebrafish SAG eliciting a strong regeneration response characterized by reactive proliferation and reactive neurogenesis. Understanding the cellular and molecular basis of neural regeneration in the adult zebrafish inner ear will reveal differences and similarities to mammalian otic neurogenesis and, thereby, identify zebrafish-specific modules of regeneration as well as mammalian-specific roadblocks.

MATERIALS AND METHODS

Ethical Statement

Fish were kept according to FELASA guidelines (Aleström et al., 2020). All animal experiments were conducted according to the guidelines and under supervision of the Regierungspräsidium Dresden (permits: TVV 79/2016, TVA 1/2017 and TVV 21/2018). All efforts were made to minimize animal suffering and the number of animals used.

Zebrafish Husbandry and Lines

Zebrafish were kept and bred according to standard procedures (Westerfield, 2000; Brand et al., 2002). Our experiments were carried out using adult zebrafish (6 months or older) from wild-type stocks with the AB genetic background and transgenic lines as the following: *TgBAC(neurod1:EGFP)nl1*, abbreviated *neurod*:GFP (Obholzer et al., 2008); *Tg(-3.5ubb:SECHsa.ANXA5-mVenus,cryaa:mCherry)*, abbreviated *ubiq*:secAnnexinV-mVenus (Morsch et al., 2015); and *Tg(elavl3:EGFP)* (Park et al., 2000). Besides date of birth and genotype, also sex and body length measured from the tip of the mouth to the basis of the caudal fin of every analyzed fish were taken.

Lesion of the Statoacoustic Ganglion *via* Injection Into the Otic Capsule

To study the regenerative capacity of the zebrafish statoacoustic ganglion, we established a lesion assay based on fluid injection into the otic capsule. Fish were anesthetized in Tricaine (Sigma) diluted in fresh fishwater. During the procedure, the anesthetized fish were placed left-sided under a stereomicroscope with dorsal to the top and rostral to the right on a tissue soaked with the Tricaine–fishwater solution laying on a petri dish. Animals were covered with a second Tricaine–fishwater-soaked tissue to keep fish moist. After creating a small hole in the triangular-shaped bone above the gills at the height of the cerebellum using a 20-gauge needle, a Hamilton syringe was carefully inserted approximately 1.2 to 1.5 mm vertically along the dorsal–ventral axis to place it above the anterior part of the SAG without rupturing it. To visualize the area of injection and prove the fluid administration to the SAG, a fluorescent dye (CellTracker™ Red CMTPX Dye, Thermo Fisher Scientific) was slowly injected into the otic capsule in a first round of experimental trials. For all other experiments, three different approaches were performed, namely, sham treatment, NaCl injection, and ouabain injection. For sham-treated animals, the Hamilton syringe was removed from the otic capsule without injecting any fluid. For NaCl and ouabain injections, 0.5–0.8 µl of fluid (0.9% NaCl solution or 100 µM ouabain, dissolved in 0.9% NaCl) was slowly injected into the otic capsule. Afterward, fish were transferred to cages with fresh fishwater for recovery. Around 60%–90% of all treated fish temporarily showed circular swimming behavior after regaining consciousness, which usually lasted for 15–30 min and only in very rare cases longer than 1 h. Minor bleedings at the injected side occurred in 50%–75% of all experimental fish.

Bromodeoxyuridine Pulse Chase Experiment

To label cells in the S-phase of the cell cycle, transgenic *neurod*:GFP zebrafish were immersed twice in 5 mM bromodeoxyuridine (BrdU) (Sigma) solution (modified after Grandel et al., 2006) for each 24 h from 2 to 3 and from 4 to 5 days post lesion with a 24-h resting period. BrdU was dissolved in E3 medium, and the pH was adjusted to pH 7.2–7.4 using freshly prepared HEPES buffer. Up to five fish were kept under oxygen supply in beakers containing 500 ml of the 5 mM BrdU solution. After the second BrdU pulse, fish were kept in the fish facility for 14 days prior to analysis.

Tissue Preparation for Immunohistochemistry

Experimental animals were sacrificed, and the skull plate was carefully removed with forceps to enable better fixation of the otic tissue underneath the brain. Samples were fixed overnight in 4% paraformaldehyde in 0.1 M phosphate buffer, pH 7.5 at 4°C, and then incubated minimum overnight in 20% sucrose/20% EDTA in 0.1 M phosphate buffer, pH 7.5 for decalcification and cryoprotection. Subsequently, samples were embedded in 7.5% gelatin/20% sucrose and stored at −80°C. Samples were cut into 12-µm-thick transverse sections and split into two series using a Thermo Scientific CryoStar NX70 Cryostat. Afterward, sectioned samples were stored at −20°C.

Modifications for CellTracker Red Dye

Samples from CellTracker red dye-injected fish were washed three times in PBS containing 0.3% Triton X-100 (PBSTx 0.3%) for 10 min. Subsequently, samples were incubated with 4,6-diamidino-2-phenylindole (DAPI 1 µg/ml, Invitrogen), diluted in PBSTx 0.3% for 30 min to counterstain the nuclei, washed again two times in PBSTx 0.3% and once in PBS before mounting them in 80% glycerol/PBS.

Immunohistochemistry

For immunohistochemistry, sections were postfixed with 100% ice-cold methanol at room temperature until all methanol was

TABLE 1 | Primary antibodies used for immunohistochemistry on sections.

Antigen	Species	Isotype	Company	Catalog code	Dilution
Bromodeoxyuridine (BrdU)	Rat	Polyclonal	Abcam	ab6326	1:500
Calretinin	Rabbit	Polyclonal	Swant Inc.	7,699/4	1:2,000
Green Fluorescent Protein (GFP)	Chicken	Polyclonal	Abcam	ab13970	1:2,000
Neural Hu Proteins C and D (HuC/D)	Mouse	IgG2b, k	Thermo Fisher Scientific	A21271	1:500–1:300
Lymphocyte Cytosolic Protein 1 (L-Plastin)	Rabbit	Polyclonal	Generated by the CRTD Antibody Facility		1:1,000
Proliferating Cell Nuclear Antigen (PCNA)	Mouse	IgG2a, k	Dako	M0879	1:500

evaporated (approximately 20–30 min). Afterward, sections were washed once with PBS and three times with PBS containing 0.3% Triton X-100 (PBSTx 0.3%). Incubation with primary antibodies in PBSTx 0.3% (see **Table 1**) was performed overnight at 4°C in a humid chamber. On the next day, sections were washed three times with PBSTx 0.3% and incubated with Alexa 488-, 555-, 633-, and 647-conjugated secondary antibodies (Thermo Fisher Scientific) in PBSTx 0.3% for 2 h at room temperature. To counterstain the nuclei, 4,6-diamidino-2-phenylindole (DAPI 1 µg/ml, Invitrogen) was added to the secondary antibody-containing solution. Sections were washed again three times with PBSTx 0.3% and once with PBS, and were mounted in 80% glycerol/PBS. Mounted samples were stored in the dark at 4°C.

Antigen Retrieval for Proliferating Cells in the Area of the Neurogenic Niche and HuC/D Staining

For simultaneous immunohistochemistry against PCNA and HuC/D, an antigen retrieval was performed prior to incubation with primary antibodies. Therefore, slides were incubated in 85°C preheated sodium citrate buffer, pH 6 (10 mM) for 15 min, followed by a 10-min cool down in the heated sodium citrate buffer at room temperature.

Modifications for Bromodeoxyuridine Staining

Since BrdU and HuC/D require different antigen retrieval methods, immunohistochemistry was performed sequentially. First, samples were stained for *neurod*:GFP and HuC/D as described above without adding DAPI while incubating with the secondary antibodies. Instead of mounting, samples were washed again with PBSTx 0.3%, and afterwards, slides were incubated for 13 min at 37°C in preheated 2 M HCl to retrieve the antigen of BrdU. Subsequently, slides were washed for 10 min in tetraborate buffer and then with PBSTx 0.3%. Slides were incubated with primary antibody against BrdU overnight at 4°C, washed with PBSTx 0.3%, incubated with all secondary antibodies plus DAPI for 2 h at room temperature, and washed again and mounted as described above.

TUNEL Assay

To analyze the presence of apoptotic cells, the ApopTag Red *In Situ* Apoptosis Detection Kit (ApopTag Chemicon S7165) was used according to the manufacturer's instructions to perform terminal deoxynucleotidyl transferase-mediated biotinylated UTP nick-end labeling (TUNEL). Since the TUNEL assay was combined with neural staining (*elavl3*:GFP or calretinin), samples were washed three times in PBSTx 0.3% after the rhodamine staining, and subsequent incubation with primary and secondary antibodies was performed as described above.

Image Acquisition

Images were taken in the light microscopy facility of the CMCB technology platform with a ZEISS Axio Imager, upright microscope with Zeiss Plan-Apochromat 10× 0.45, 20× 0.8, and 40× 0.95 Korr objectives for magnification. An Axiocam MRm (1,388 × 1,040 dexel, 6.45 × 6.45 µm)—b/w was used for detection. Sequential image acquisition was used in samples costained with multiple fluorophores. For imaging, Z-stacks were acquired to cover the full information in all three dimensions (typically, 5–25 Z-planes with an interval of 0.4–1.5 µm depending on the NA of the objective). Images were processed using ZEN blue 2012 and Fiji. Close-up images were generated from the original overview image. For overview images, a maximum projection was taken from several Z-planes, whereas only two to three Z-planes were used for the close-up images. Figures were assembled using Adobe Illustrator 2021.

Quantification and Statistical Analysis

Quantification was performed on acquired images comprising all Z-planes using the Fiji software. For analysis, the left and right SAG of each fish were taken: the untreated left SAG served as an internal control, whereas the right SAG was treated as described above. To analyze proliferation and neurogenesis upon lesion in the neurogenic niche, a square covering the neurogenic area and the surrounding cells was chosen as the region of interests (see overview images in **Figures 4** and **6**: size of square: 156.63 mm^2). From each individual, three sections of one series of the anterior SAG showing the most *neurod*:GFP/PCNA-double positive cells were chosen for quantification. In cases there are less than three sections containing *neurod*:GFP/PCNA-double positive cells in the neurogenic niche, up to three sections with the most *neurod*:GFP-positive cells were chosen. The following cell types were quantified in the region of interest: all *neurod*:GFP-positive cells, *neurod*:GFP/PCNA-double positive cells, *neurod*:GFP/HuC/D-double positive cells, and all PCNA-positive cells. All values from one fish were averaged, and the mean cell count/section was used for statistical analysis ($n = 3$ fish for all conditions and time points; exception: NaCl injected at 4 dpl). For statistical analysis,

the graph pad prism software was used to determine *p*-values with a two-way ANOVA test with a Tukey's multiple comparison test for *post-hoc* analysis. The chosen significance levels are $^{***}p \leq 0.001$, $^{**}p \leq 0.01$, $^{*}p \leq 0.05$; values above $p > 0.05$ are not considered significant. Graphs are shown as scatter plots with bars with SEM.

RESULTS

Establishment of an Injection Procedure to Label the Adult Statoacoustic Ganglion

We recently showed the presence of a lifelong but almost quiescent neurogenic niche in the adult zebrafish statoacoustic ganglion (SAG). It comprises a pool of Neurod-positive neuronal progenitor cells, which are replenished by marker-negative presumptive stem cells (Schwarzer et al., 2020). To investigate whether sensory neurons of the adult SAG can regenerate and whether the neurogenic niche is the source of these newly generated sensory neurons, we aimed to establish the first lesion paradigm of the zebrafish SAG. An established model of auditory neuropathy in mammals is the application of ouabain to the round-window membrane of the cochlea. In the Mongolian gerbil, mice, and rats, this lesion paradigm induces a rapid loss of spiral ganglion neurons while leaving the function of sensory hair cells intact (Schmiedt et al., 2002; Lang et al., 2005; Fu et al., 2012; Wakizono et al., 2021). Therefore, we decided to establish a lesion paradigm based on the application of ouabain to the sensory neurons in the adult SAG. Since fish do not possess an outer and middle ear, application of ouabain or any other solution needs to be administered by entering the inner ear enclosed within the skull. After extensively studying the anatomy and position of the SAG within the zebrafish skull, we identified a position, which allowed the insertion of a Hamilton syringe into the otic capsule without piercing the SAG or the neighboring cerebellum (**Figure 1A**). For the injection procedure, anesthetized animals were placed on their left side, and the skull was opened by puncturing the triangular-shaped area above the opercle in the area of the pterotic bone using a 20-gauge needle (**Figure 1B**, blue dotted line). Then a Hamilton syringe was inserted approximately 1.0- to 1.5-mm deep vertically along the dorsal–ventral axis into the otic capsule through the hole in the skull, without damaging the underneath-located SAG (**Figure 1B**, yellow dotted circle). To test the suitability of the potential SAG lesion paradigm, we performed injections with CellTracker Red. CellTracker Red is a stable, nontoxic dye that freely passes through cell membranes into cells, where it is transformed into a cell membrane-impermeable dye that is brightly fluorescent at a physiological pH. Ninety minutes following CellTracker Red injections, fish were sacrificed, sectioned, and colabeled with DAPI to analyze labeled structures. We find that CellTracker Red was predominantly incorporated into cells within the SAG of the injected side labeling the proximal, medial, and distal parts of the SAG (**Figure 1C**). Importantly, almost no labeling of the neighboring cerebellum was observed. However, we occasionally noticed a striking accumulation of erythrocytes, easily recognized based on their small and condensed nuclei on the injected site indicating the occurrence of a hemorrhage as a side effect of the injection procedure (**Figure 2A**, ouabain). Taken together, our injection procedure is suitable to target the SAG specifically and can be used to apply fluids into the adult zebrafish SAG.

Emergence of Apoptotic Sensory Neurons in the Adult Statoacoustic Ganglion Upon Lesion

Following the successful establishment of the injection procedure, we set out to investigate the efficacy of ouabain-induced lesions. To this aim, 0.5–0.8 µl of a 100 µM ouabain solution was slowly injected into the otic capsule of the right side. As controls, we either injected the same amount of a 0.9% NaCl solution or used sham-treated animals in which the Hamilton syringe was inserted and immediately removed without injecting any fluid. In addition, the SAG of the uninjected side of all experimental animals was used as an unlesioned, internal control. To investigate cell death of sensory neurons in the SAG upon treatment, we took two approaches addressing different biochemical hallmarks of apoptosis: 1) presence of phospholipid phosphatidylserines on the outer plasma membrane of cells and 2) the well-established TUNEL assay. In the first approach, we used the transgenic zebrafish line *ubiq*:secAnnexinV-mVenus, which ubiquitously expresses a secreted Annexin 5 fused to mVenus (Morsch et al., 2015). Annexin 5 binds phospholipid phosphatidylserines with a high affinity. Phospholipid phosphatidylserines are normally distributed asymmetrically and are only present on the inside of the cell membrane. During apoptosis, however, phospholipid phosphatidylserines are redistributed to the outer plasma membrane enabling the detection of apoptotic cells *in vitro* and *in vivo* with Annexin 5 coupled to a fluorescent protein (Morsch et al., 2015; van Genderen et al., 2006; van Ham et al., 2010). Immunohistochemistry against mVenus driven from *ubiq*: secAnnexinV-mVenus combined with the neuronal marker HuC/D detected only low mVenus levels in unlesioned control sides (**Figure 2A**). In the medial part of the SAG, comprising the neurogenic niche and the neuronal cell bodies, a few HuC/D-positive cells displayed a weak mVenus signal (**Figure 2Ab**). No mVenus was detectable in the distal part of the unlesioned SAG where the neurites of the sensory neurons innervate the sensory patch (**Figure 2Aa**). In contrast, a strong mVenus signal was present in sham-treated as well as NaCl- and ouabain-injected SAGs at 12 h post lesion (**Figure 2A**). Although the number of HuC/D and weak mVenus double-positive cells in the medial part was unchanged (**Figures 2Ad, Af, Ah**), mVenus levels in the distal part of the SAG were significantly increased in all three lesion conditions (**Figures 2Ac, Ae, Ag**). Combining immunohistochemistry with mVenus driven in *ubiq*: secAnnexinV-mVenus with an antibody staining against calretinin, which labels a subset of mature neurons including their neurites, corroborated this result (**Figure 2B**). Again, whereas no difference in mVenus expression was found in the medial part of the SAG (**Figures 2Bb, Bd**), a strong upregulation of mVenus and colocalization with calretinin was observed in the distal part of the SAG in sham-injected animals in comparison with

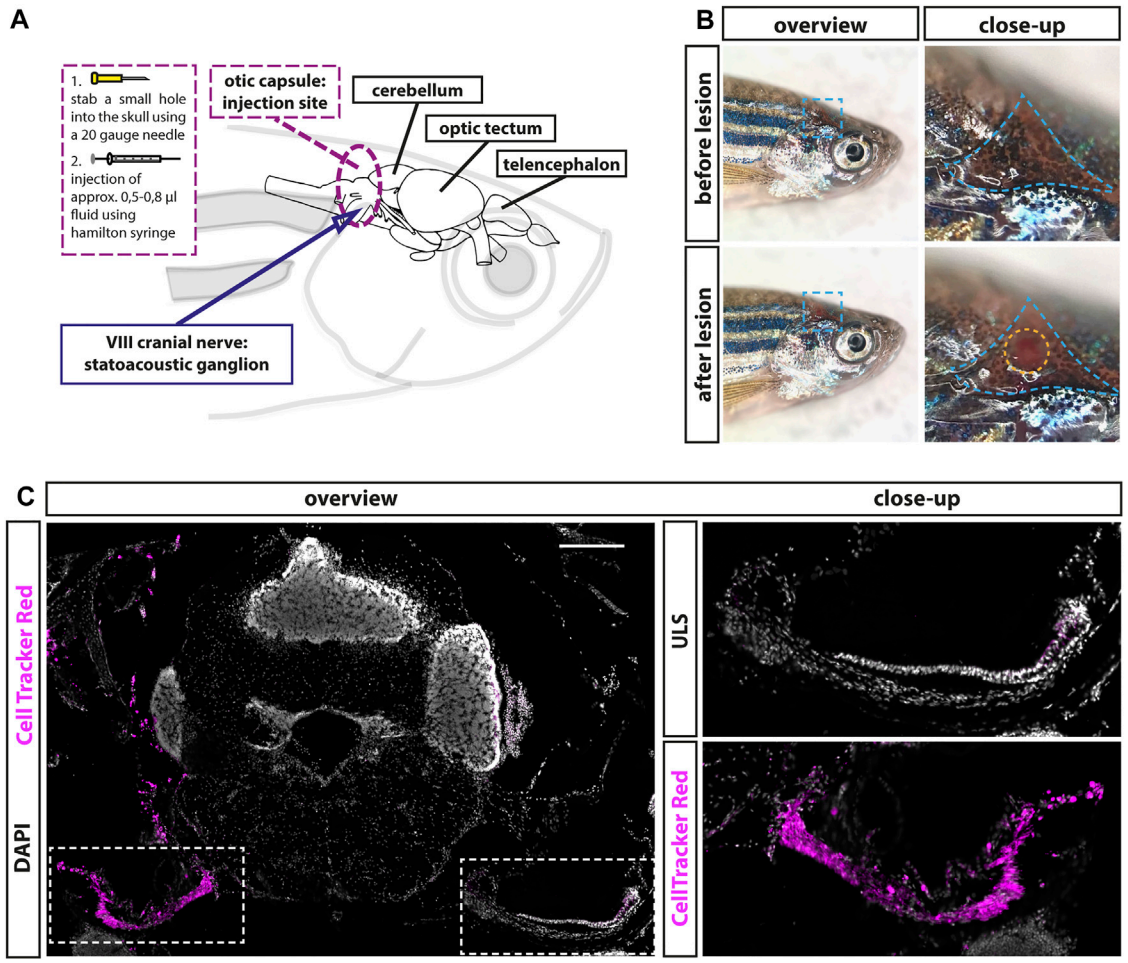

FIGURE 1 | Establishment of a lesion paradigm of the adult zebrafish statoacoustic ganglion (SAG). **(A)** Scheme of the zebrafish head with the brain inside showing the injection position in relation to the brain and the SAG. A 20-gauge needle was used to open the skull before inserting a Hamilton syringe vertically approximately 1.2- to 1.5-mm deep into the skull along the dorsal–ventral axis. Subsequently, the Hamilton syringe was either removed (sham-treated control) or 5–8 µl of either 0.9% NaCl or 100 µM ouabain solution was slowly injected. **(B)** Overview of live adult zebrafish before and after injection. Close-ups of the blue dotted boxes show the injection side within the triangular bone (dotted blue line). Lower close-up shows the hole after injection (dotted yellow circle). **(C)** Immunohistochemistry of a transverse cross section at the height of the anterior SAG following CellTracker Red injection into the right inner ear showed a strong labeling of the SAG on the injected side but no labeling of the unlesioned side (ULS). Scale bar: 200 µm.

unlesioned controls (**Figures 2Ba, Bc**). To validate the presence of apoptotic sensory neurons in contrast to mere axon degeneration, we also applied the well-established TUNEL-assay, which detects nuclear DNA fragmentation, a hallmark of apoptosis. To this aim, we employed the transgenic line *Tg(elavl3:GFP)*, which drives GFP under the promoter of the *elavl3* gene (formerly known as HuC) and, thereby, labeling all neurons in the SAG (Park et al., 2000). In addition to GFP and TUNEL, sections were costained with the neuronal marker calretinin (**Figure 2C**). In unlesioned control sides, *elavl3*:GFP/calretinin double-positive neurons were always present, but we never detected any TUNEL-positive cell within the SAG. In contrast, robust TUNEL staining was found in sham-treated as well as NaCl- and ouabain-injected SAGs at 12 h post lesion. In addition to other, unidentified TUNEL-positive cells, TUNEL/*elavl3*:GFP/calretinin triple-positive neurons could be found in the lesioned SAG irrespective of the type of lesion. Interestingly, all TUNEL/*elavl3*:GFP/calretinin-triple positive neurons were located on the dorsal side of the SAG close to the sensory patch with a greater distance to the area of the neurogenic niche on the ventral side of the SAG. Taken together, we show that insertion of a Hamilton syringe into the otic capsule induces cell death of sensory neurons in the adult SAG but observe no difference in the apoptotic response following sham treatment, and NaCl and ouabain injections.

Accumulation of Leukocytes in the Adult Statoacoustic Ganglion Persists Beyond 16 days Post Lesion

The immune system plays a crucial but beneficial role in regenerative neurogenesis after injury of the zebrafish central nervous system (Kyritsis et al., 2012). To address whether lesions

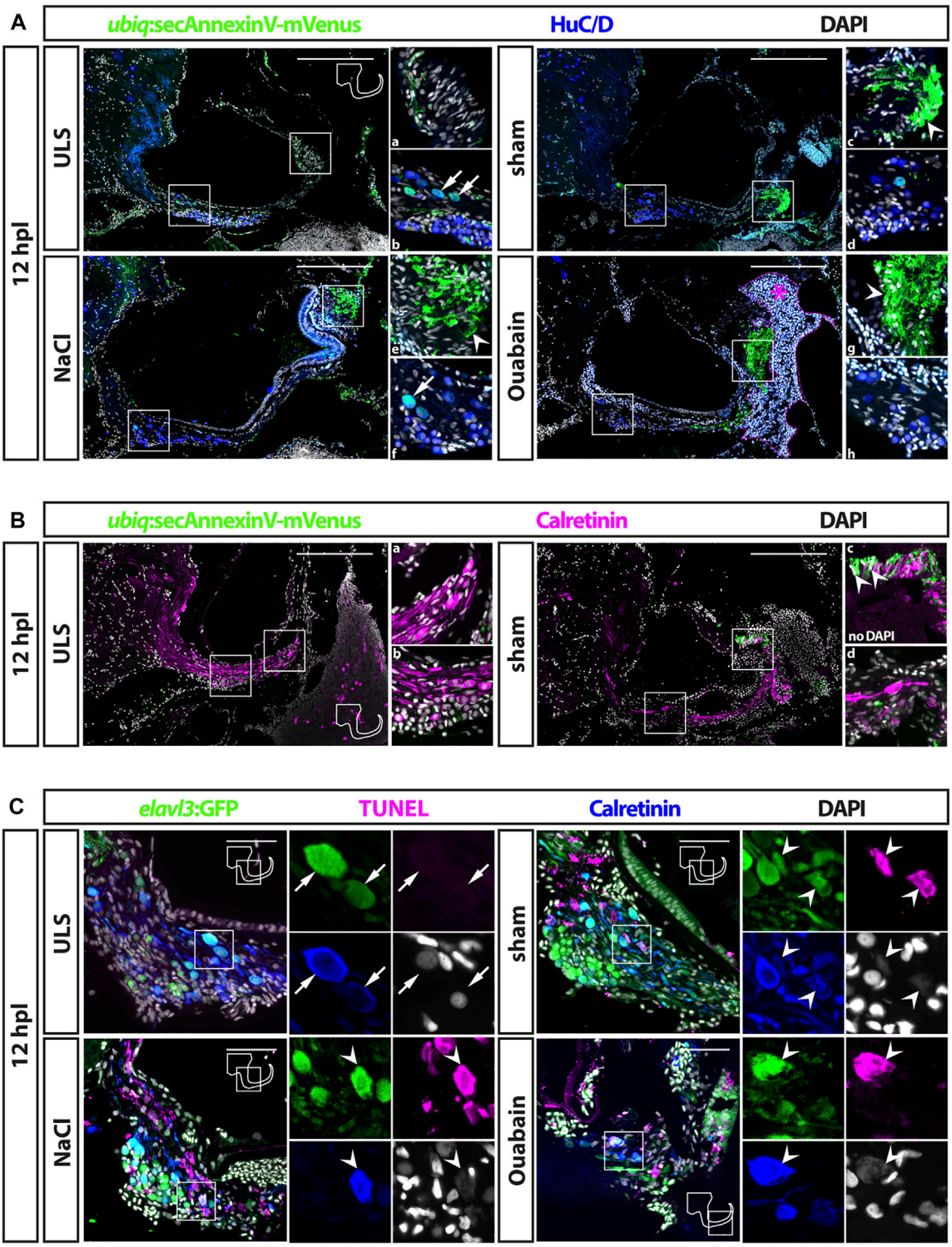

FIGURE 2 | Cell death in the adult zebrafish SAG upon lesion. **(A)** Antibody staining of the adult zebrafish SAG labeling *ubiq:*secAnnexinV-mVenus-positive cells and HuC/D-positive neurons. In contrast to unlesioned sides (ULS), a strong *ubiq:*secAnnexinV-mVenus-signal was present in the SAG following sham treatment or NaCl and Ouabain injections at 12 h post lesion (hpl). In the medial part of the SAG, which harbors the neurogenic niche and the neuronal cell bodies, only very few HuC/D-positive cells showed a weak *ubiq:*secAnnexinV-mVenus staining in all samples (arrows in b and f). In the distal part of the SAG, where the neurites of the sensory neurons innervate the sensory patch, a strong *ubiq:*secAnnexinV-mVenus staining was observed in sham-treated as well as NaCl- and ouabain-injected SAGs, but almost no signal was detected in unlesioned control sides (arrowheads in c, e, and g). Magenta dotted line and asterisk in ouabain-injected SAG indicates a massive

(*Continued*)

FIGURE 2 | hemorrhage in this injected site. **(B)** Colabeling of mVenus with calretinin revealed the presence of *ubiq:*secAnnexinV-mVenus in neurites (arrowhead in c) of sham-treated SAGs but not in unlesioned control sides. **(C)** Antibody staining labeling neurons (*elavl3*:GFP and calretinin) combined with TUNEL assay. TUNEL assay revealed presence of apoptotic neurons in the SAG of adult *elavl3*:GFP zebrafish in all three lesion types at 12 hpl, whereas no TUNEL-positive neurons were found in the unlesioned control side. Scale bars: **(A)** 200 µm; **(B)**: 50 µm.

to the SAG activate the immune system at the lesion side, we performed immunohistochemistry against the pan-leukocyte marker lymphocyte cytosolic protein 1 (L-plastin) on transgenic *neurod*:GFP zebrafish. This way, we were able to label all myelocytes (neutrophils, eosinophils, mast cells, dendritic cells, and macrophages) and lymphocytes (T cells, B cells, and natural killer cells) in relation to the *neurod*:GFP-positive neurogenic progenitor pool of the SAG at 1, 2, 4, and 16 days post lesion (**Figure 3**). Overall, we distinguished two different types of L-plastin-positive cells: 1) cells with a ramified morphology displaying a weaker L-plastin staining and 2) round cells with a strong L-plastin staining. In unlesioned control sides, we always found only a few, evenly distributed L-plastin-positive cells displaying a ramified morphology within the SAG (**Figure 3**, ULS in each time point). In addition, round cells with a strong L-plastin staining were located ventrally in close contact to the SAG at the height of the neurogenic niche labeled by *neurod*:GFP. Occasionally, also stronger accumulation of these cells was seen (e.g., **Figure 3**, ULS at 16 dpl). However, and in contrast, we observed a massive accumulation of ramified as well as round L-plastin-positive cells close to the neurogenic niche and throughout the SAG irrespective of the type of lesion at 1, 2, and 4 dpl. (**Figure 3**, sham, NaCl, and ouabain in each time point). Moreover, a massive amount of strong L-plastin-positive cells accumulated in the distal part of the SAG where the neurites of the sensory neurons innervate the sensory patch (**Figure 3**, asterisks). Overall, we found that the accumulation of leukocytes in the SAG is highly similar in sham-treated, and NaCl- or ouabain-injected SAGs. The pattern was already manifested at 1 dpl, did not change much at 2 or 4 dpl, and was even not resolved at 16 dpl, which constituted the end of our time course. Taken together, our data show that sham treatment, or NaCl or ouabain injection into to the SAG results in a massive infiltration and accumulation of immune cells in the lesioned SAG, which lasts longer than 16 dpl.

Reactive Proliferation in the Neurogenic Niche of the Adult Statoacoustic Ganglion Peaks at 8 days Post Lesion

The neurogenic niche in the SAG is highly proliferative and a source of new sensory neurons at juvenile stages but turns to a quiescent state with only very rare neurogenesis at adult stages (Schwarzer et al., 2020). Hence, it was unknown whether the neurogenic niche can be reactivated and provide neuronal cells to compensate for the loss of sensory neurons upon lesion at adult stages. To investigate the regenerative capacity, we used immunohistochemistry against the proliferation marker PCNA and GFP in transgenic *neurod*:GFP zebrafish to check for proliferating cells in the neurogenic niche in sham-treated as well as NaCl- and ouabain-injected animals at 2, 4, 8, 16, and 57 days post lesion (dpl). In contrast to our previous analysis, in which *neurod*:GFP/PCNA double-positive cells were almost always absent in the adult SAG during homeostasis (Schwarzer et al., 2020), we frequently find *neurod*:GFP/PCNA double-positive cells in sham-treated as well as NaCl- and ouabain-injected SAGs (**Figure 4**). Following injection of ouabain, *neurod*:GFP/PCNA double-positive cells were already present at 2 dpl and were also detected at 4, 8, and 16 dpl (**Figure 4**, right colomn). Similar results were obtained for sham-treated and NaCl-injected SAGs. Here, *neurod*:GFP/PCNA double-positive cells were frequently detected starting at 4 dpl and were consistently found at 8 and 16 dpl (**Figure 4**, medial columns). Importantly, *neurod*:GFP/PCNA double-positive cells were also found occasionally in some SAGs of all three lesion types even at 57 dpl, which constituted the end of our time course. This indicates that the neurogenic niche did not return completely to homeostatic levels after lesion at this time point. Surprisingly, *neurod*:GFP/PCNA double-positive cells were also present occasionally in SAGs of the unlesioned side of injected animals (**Figure 4**, left column). This finding was mostly restricted to 4, 8, and 16 dpl indicating a systemic effect of the unilateral lesion. To analyze the proliferation results in more detail, we quantified the number of all proliferating cells in the area of the neurogenic niche (PCNA-positive) as well as the number of proliferating progenitors (*neurod*:GFP/PCNA double-positive cells). Moreover, instead of combining the results of the unlesioned sides, we kept them individually obtaining the numbers of the unlesioned side for sham-treated, and NaCl- and ouabain-injected, respectively. Quantification of all PCNA-positive cells in the area of the neurogenic niche revealed that the number of proliferating cells in the unlesioned SAG for sham-treated, and NaCl- and ouabain-injected animals does not change significantly over time. It varies to an average of two to eight PCNA-positive cells per section with a slight increased number in unlesioned SAGs of ouabain-injected fish (**Figure 5A**). Compared with the respective SAGs of unlesioned sides, a significant increase in proliferating cells is observed for sham-treated SAGs at 8 dpl, NaCl-injected at 2 dpl, and ouabain-injected at 4 dpl, respectively. The number of proliferating cells decreased in all three lesion types to an average of six PCNA-positive cells per section within 57 dpl. Comparison of the number of proliferating cells of individual time points from sham-treated, or NaCl- or ouabain-injected SAGs did not reveal any significant differences with one exception. At 4 dpl, the number of PCNA-positive cells was significantly increased in ouabain-injected animals compared with sham-treated animals. Quantification of *neurod*:GFP/PCNA double-

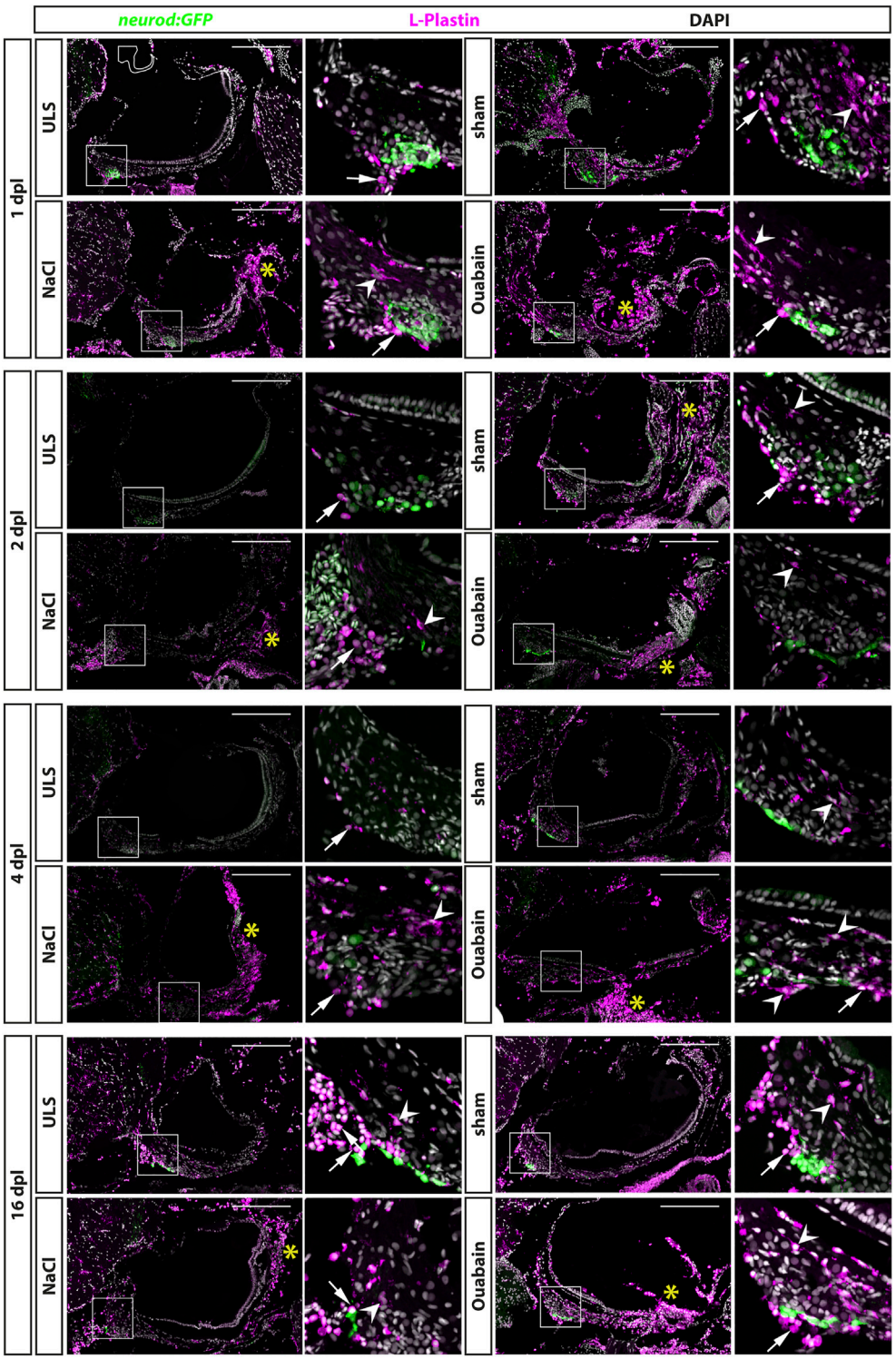

FIGURE 3 | Accumulation of leukocytes in the adult zebrafish SAG upon lesion. Antibody staining against the pan-leukocyte marker L-plastin and GFP in the SAG of transgenic *neurod*:GFP zebrafish at 1, 2, 4, and 16 days post lesion (dpl). Shown are representative images of the SAG following sham-treatment, or NaCl or ouabain injections as well as the unlesioned side (ULS) of either sham-treated, or NaCl- or ouabain-injected animal. Boxes show close-ups of the respective *neurod*:GFP-positive neurogenic niche. In the unlesioned side (ULS, upper left panel in each time point), a few ramified L-plastin-positive cells are distributed evenly throughout the entire SAG. Some round, strong L-plastin-positive cells are localized in close contact to the neurogenic niche on the ventral side of the SAG (arrows). In contrast, accumulation of ramified L-plastin-positive cells (arrowheads) in the SAG is observed close to the neurogenic niche at all time points within sham-treated, or NaCl- or ouabain-injected SAGs (upper right and lower panels in each time point). In addition, the density of L-plastin-positive cells is usually the highest at the distal part of the SAG, especially when the sensory patch is massively destroyed as, for example, seen in 1 dpl/NaCl and ouabain, 2 dpl/ouabain, and 16 dpl/ouabain, irrespective of the lesion type (yellow asterisks). Scale bars: 200 µm.

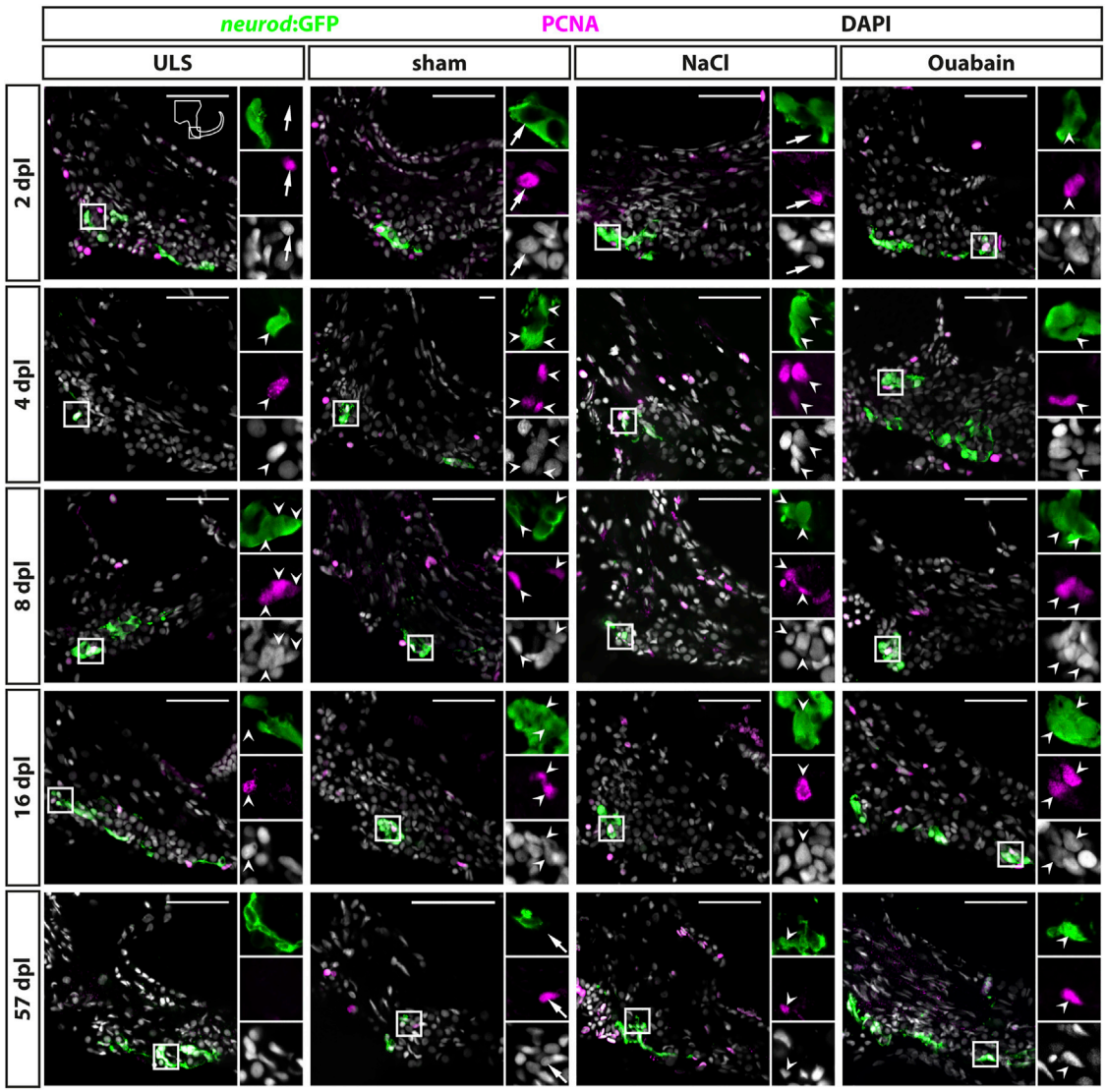

FIGURE 4 | Reactive proliferation of *neurod*:GFP-positive progenitors in the adult zebrafish SAG upon lesion. Immunohistochemistry against the proliferation marker proliferating cell nuclear antigen (PCNA) and GFP in the SAG of *neurod*:GFP transgenic animals. Shown are representative images of the neurogenic niche of the SAG following sham treatment, or NaCl or ouabain injection as well as the unlesioned side (ULS) of either sham-treated, or NaCl- or ouabain-injected animals at 2, 4, 8, 16, and 57 days post lesion (dpl). Boxes show close-ups to visualize costaining. Proliferating but marker-negative cells close to *neurod:*GFP-positive cells (arrows) were found frequently in unlesioned sides, for example, at 2 dpl and in sham-treated SAGs at 57 dpl. However, proliferating *neurod:*GFP/PCNA double-positive cells (arrowheads) were also present from 2 dpl onward in ouabain-injected animals (right column) and frequently from 4 dpl onward in sham-treated and NaCl-injected animals (medial columns). Proliferating *neurod:*GFP/PCNA double-positive cells continued to be present at 8 and 16 dpl before returning to homeostatic levels at 57 dpl when the majority of sham-treated, or NaCl- or ouabain-injected animals did not show proliferating neuronal progenitors in the lesioned SAG. In SAGs of unlesioned sides, PCNA/*neurod*:GFP double-positive cells are found occasionally, in particular, in the unlesioned sides of ouabain-injected fish at 8 dpl. Scale bar: 50 μm.

positive cells showed that reactive proliferation of neuronal progenitors in the unlesioned side of sham-treated and NaCl-injected animals is a rare event and was observed only once and twice in sham-treated and NaCl-injected animals at 8 and 2 dpl, respectively (**Figure 5B**). In contrast, one third of all analyzed animals showed low-level reactive proliferation in the neurogenic niche of the unlesioned side following ouabain injection, suggesting that a unilateral ouabain injection influences proliferation in the neurogenic niche of the unlesioned side *via* systemic cues. In the SAG of sham-treated animals, *neurod*:GFP/PCNA double-positive cells are present as early as 4 dpl. The number of proliferating progenitors peaks at 8 dpl, which represents a significant difference in comparison with the unlesioned side, before returning to lower levels at 16 and 57 dpl. Ouabain injection leads to a faster response in the neurogenic niche, where reactive proliferation is already present at 2 dpl. The number of *neurod*:GFP/PCNA double-positive cells

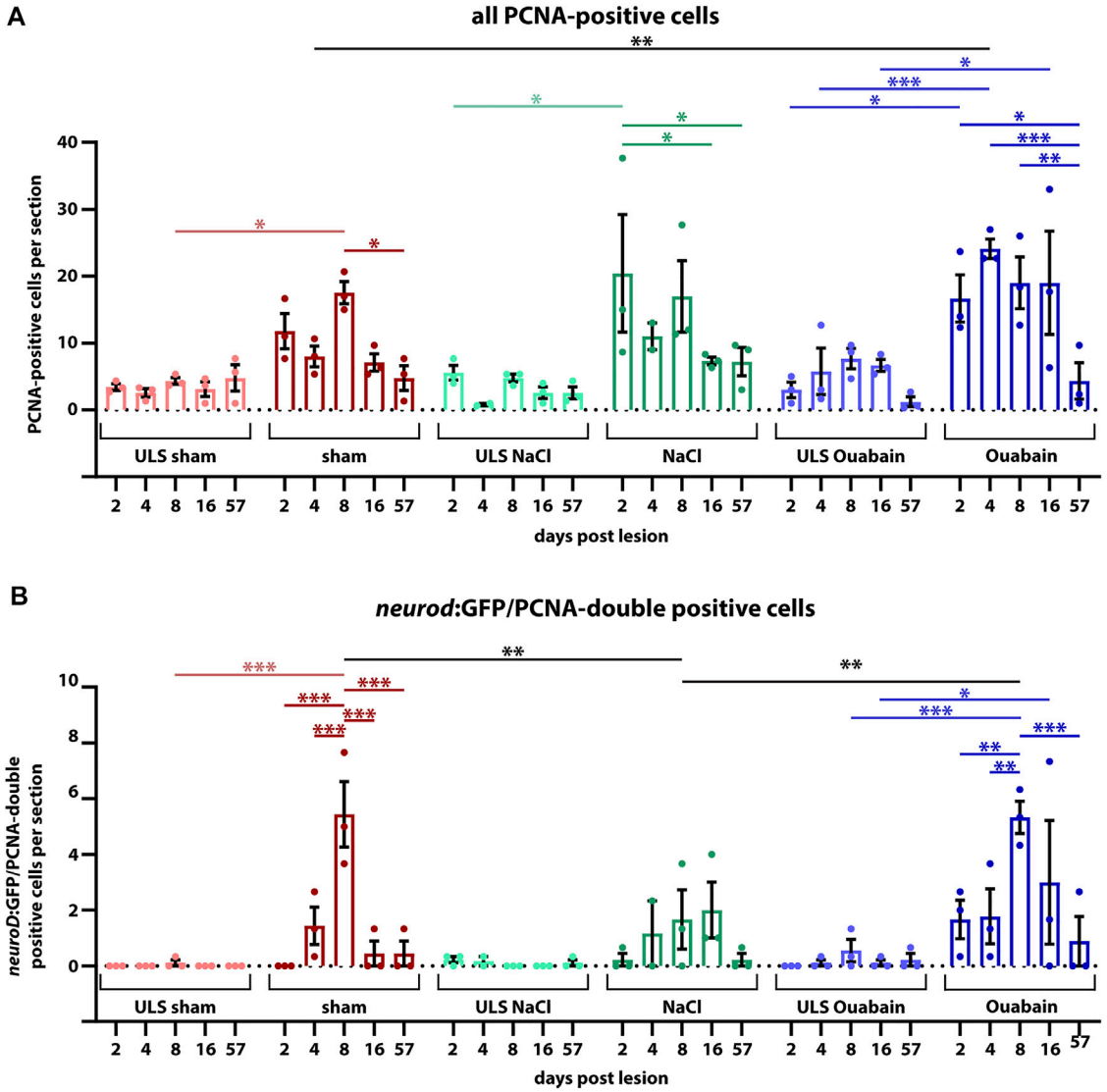

FIGURE 5 | Quantification of reactive proliferation of *neurod*:GFP-positive progenitors. **(A)** Quantification of all PCNA-positive cells. Compared with the respective SAGs of unlesioned sides (ULS sham, ULS NaCl, ULS Ouabain), the number of PCNA-positive cells per section is increased following sham treatment, or NaCl or ouabain injections in the first 8 days post lesion (dpl). An even significant increase compared with the unlesioned side is present at 2 dpl following NaCl injection, at 4 dpl following ouabain injection and at 8 dpl following sham treatment, respectively. At 57 dpl, the proliferation rate in the lesioned SAG was significantly decreased to the levels of the unlesioned side. **(B)** Quantification of *neurod*:GFP/PCNA double-positive cells. Compared with the respective SAGs of unlesioned sides, the number of *neurod*:GFP-positive cells per section that re-enter the cell cycle is increased following sham treatment, or NaCl or ouabain injections. The peak of proliferation of active cycling neuronal progenitors is observed at 8 dpl with a significantly increased number of five to six *neurod*:GFP/PCNA double-positive cells per section in sham-treated and ouabain-injected SAGs. The number of proliferating *neurod*:GFP neuronal progenitors is significantly lower in NaCl-injected SAGs compared with sham-treated and ouabain-injected SAGs at 8 dpl. However, changes in the overall proliferation rate in NaCl-injected SAGs follow a similar trend as seen in sham-treated and ouabain-injected SAGs. The number of *neurod*:GFP/PCNA double-positive cells per section has significantly decreased at 16 and 57 dpl in sham-treated and ouabain-injected SAGs, respectively, although a small number of lesioned animals still showed low numbers of *neurod*:GFP/PCNA double-positive cells in each lesion type. Notably, *neurod*:GFP/PCNA double-positive cells were infrequently also observed in the unlesioned side, in particular, in ouabain-injected animals, in which an average of 0.5–1 *neurod*:GFP/PCNA double-positive cells per section was seen. Samples size $n = 3$ (n = fish with three sections/SAG; exception: 4 dpl/NaCl: $n = 2$); data are presented as mean ± SEM. Two-way ANOVA with Tukey's multiple comparisons test; $^{***}p \leq 0.001$; $^{**}p \leq 0.01$; $^{*}p \leq 0.05$.

increases significantly over the next 6 days and peaks at 8 dpl before it decreases again. A similar profile in the number of proliferating progenitors was observed in the SAGs of NaCl-injected animals, although the overall quantified numbers of *neurod*:GFP/PCNA-proliferating cells was significantly lower at 8 dpl compared with sham-treated and ouabain-injected SAGs. In summary, we show that neuronal progenitors in the neurogenic niche of adult zebrafish SAG indeed re-enter the cell cycle upon lesion and display a peak in reactive proliferation at 8 dpl.

Reactive Neurogenesis in the Neurogenic Niche of the Adult Statoacoustic Ganglion Peaks at 8 days Post Lesion

During homeostasis, neurogenesis in the zebrafish SAG decreases significantly to very low levels at adult stages (Schwarzer et al, 2020). To investigate whether the adult SAG is capable of reactive neurogenesis upon lesion, we chose two different strategies to prove the presence of newborn neurons: 1) short-term lineage tracing using the persistence of GFP from the *neurod*:GFP transgene in the neuronal progenitors of the neurogenic niche and 2) a pulse chase experiment using bromodeoxyuridine (BrdU). For the former, we employed sham-treated or NaCl-injected or oubain-injected *neurod*:GFP transgenic zebrafish and sacrificed them for analysis at 2, 4, 8, 16, and 57 days post lesion (dpl). Using immunohistochemistry against the neuronal marker HuC/D and GFP, we analyzed the presence of HuC/D-positive neurons carrying the GFP label from the *neurod*:GFP transgene, which represent newborn neurons derived from the *neurod*:GFP-positive neuronal progenitor population. In contrast to the SAG of unlesioned sides, *neurod*:GFP/HuC/D double-positive cells were present in the lesioned SAG irrespective of the type of lesion (sham-treated, NaCl- or ouabain-injected) as early as 4 dpl (**Figure 6A**). At 8 dpl, *neurod*:GFP/HuC/D double-positive newborn neurons were frequently found in all three lesion types and occasionally in the respective SAGs of the unlesioned sides. At 57 dpl, *neurod*:GFP/HuC/D double-positive cells were rarely found in lesioned as well as in unlesioned SAGs. Quantification of *neurod*:GFP/HuC/D double-positive newborn neurons corroborated a significant increase in neurogenesis upon lesion (**Figure 6B**). At 2 dpl, the number of *neurod*:GFP/HuC/D double-positive cells per section in unlesioned and lesioned SAGs of all sham-treated, and NaCl- and ouabain-injected animals is less than 0.5, which lies within the range of the homeostatic baseline that we previously described (Schwarzer et al., 2020). However, neurogenesis rates in the SAGs of all three lesion types, but not in the respective SAGs of the unlesioned sides, exceeded the values of the homeostatic baseline already at 4 dpl. The neurogenesis rate increased even further significantly and displayed a peak of three to four *neurod*:GFP/HuC/D double-positive cells per section at 8 dpl in the lesioned SAG after sham treatment, or NaCl or ouabain injection. Interestingly, a slight increase in neurogenesis above the homeostatic baseline was also observed in the unlesioned side of sham-treated and NaCl-injected animals at 8 dpl as well as of ouabain-injected animals at 16 dpl. At 57 dpl, the number of newborn neurons returned to homeostatic levels in lesioned SAGs as well as in the respective unlesioned sides. To analyze whether newborn sensory neurons are derived from progenitors that underwent reactive proliferation, we conducted a BrdU pulse chase experiment. BrdU, a thymidine analog, is incorporated during the S-phase of the cell cycle and, thereby, marks active proliferating cells (Kiernan et al., 2005). To label a great amount of proliferating cells in sham-treated, or NaCl- or ouabain-injected *neurod*:GFP transgenic fish, we immersed lesioned animals from 2 to 3 dpl and from 4 to 5 dpl in a BrdU solution with a 24-h resting period in between (**Figure 6C**). Our previous BrdU pulse chase experiments of the adult homeostatic zebrafish SAG revealed that BrdU/*neurod*:GFP/HuC/D triple-positive newborn neurons are present at 14 days post-BrdU pulse (Schwarzer et al., 2020). Hence, experimental animals were kept for an additional 14 days, adding up to 19 dpl as the time point of analysis. Antibody staining against BrdU, HuC/D and GFP revealed that BrdU-positive cells are present in the neurogenic niche, but do not colabel with *neurod*:GFP and/or HuC/D in the unlesioned side (**Figure 6C**). In contrast, we find BrdU/*neurod*:GFP double-positive neuronal progenitors, BrdU/*neurod*:GFP/HuC/D triple-positive newborn neurons, and BrdU/HuC/D double-positive neurons in the lesioned SAG, irrespective of the type of lesion (**Figure 6C**). In summary, we show that the *neurod*:GFP-positive neuronal progenitor pool acts as a source of newborn neurons also during regeneration and that the neurogenesis rate is indeed transiently and significantly increased upon lesion. Moreover, we find that neurogenesis in the unlesioned side exceeds homeostatic levels, indicating a systemic effect caused by the unilateral lesion.

DISCUSSION

Understanding the cellular and molecular properties of sensory and neural progenitors are key to develop cell-based therapies using transplantation or reprogramming. To this aim, insights from regeneration-competent as well as regeneration-incompetent organisms complement current *in vitro* approaches. We previously showed that the neurogenic niche of the SAG in the regeneration-competent zebrafish is quiescent with only very rare neurogenesis during homeostasis (Schwarzer et al., 2020). Here, we now show that the neurogenic niche of the eighth cranial nerve in the adult zebrafish displays reactive proliferation as well as reactive neurogenesis in response to a traumatic injury. Upon a traumatic lesion using sham treatment, or NaCl or ouabain injections into the right otic capsule, mature sensory neurons are lost within hours, which is compensated by reactive proliferation of marker-negative and neuronal progenitor cells in the subsequent days and weeks (**Figure 7A**). In addition, reactive neurogenesis from the neuronal progenitor pool results in the production of newborn sensory neurons. Reactive proliferation and reactive neurogenesis continue over the next weeks until former homeostatic levels are reached. In general, we observed no fundamental differences in the three lesion types except an additional increased level of proliferation in ouabain-injected SAGs in comparison with sham-treated and NaCl-injected SAGs. Hence, we conclude that the insertion of a Hamilton syringe acts as a mechanical lesion and is already sufficient to elicit a regeneration response without any fluid injection. Similar to the regeneration of the zebrafish central nervous system, we find reactive proliferation and reactive neurogenesis, which have been described in detail for the neural retina and forebrain (Kroehne et al., 2011; Lenkowski and Raymond, 2014). Upon lesion of the zebrafish retina, quiescent Müller glia re-enter the cell cycle resulting in the production of multipotent progenitors that differentiate into all retinal cell types replacing the lost cells (Lenkowski and Raymond, 2014). Similarly, radial glia serve as neuronal stem cells in the zebrafish forebrain and show increased production of neuronal progenitors following injury (Kroehne et al., 2011). However, in contrast to the findings in the central

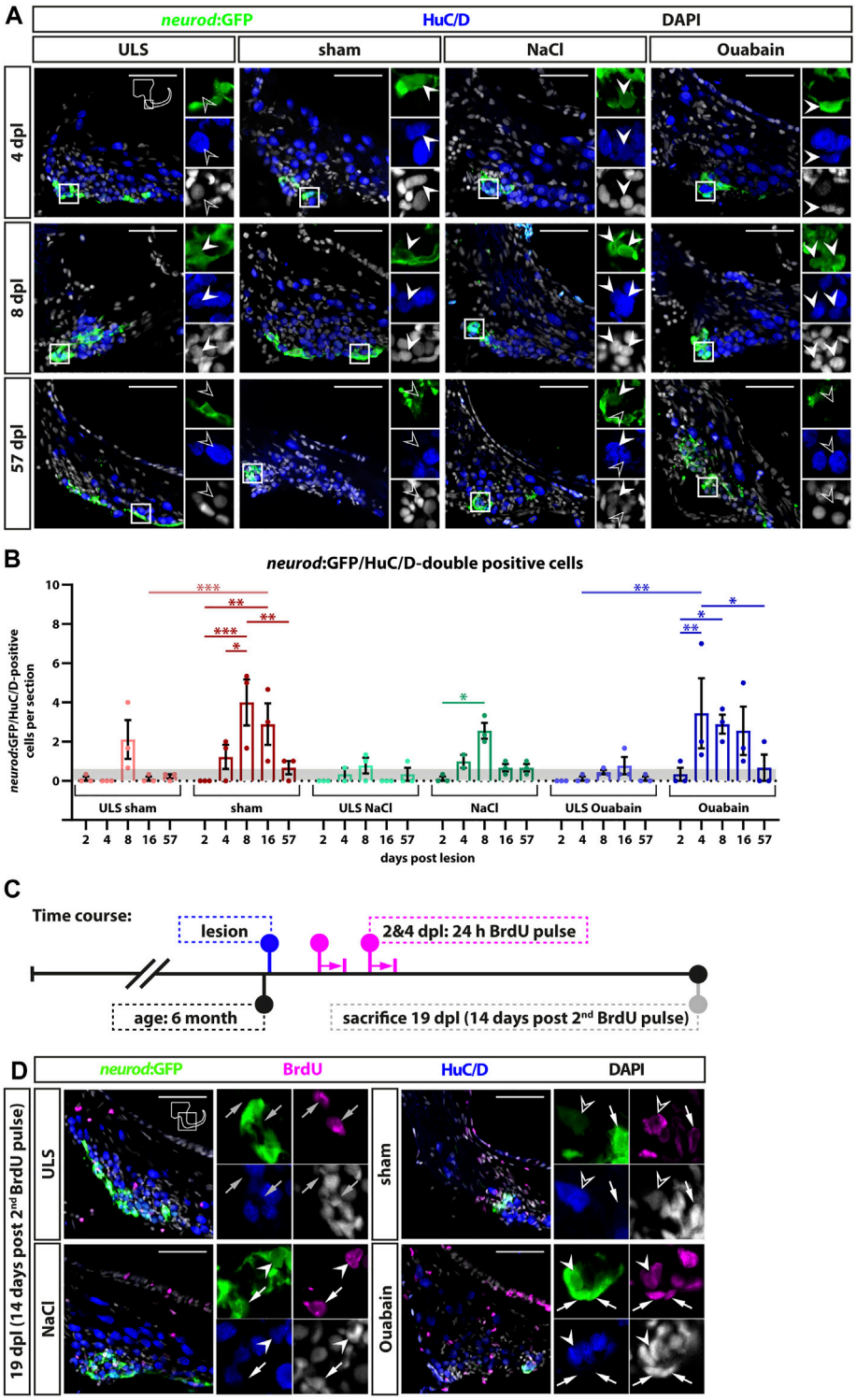

FIGURE 6 | Generation of new sensory neurons from the *neurod*:GFP-positive progenitor pool upon lesion. **(A)** Short-term lineage tracing using the persistence of GFP in the SAG of *neurod*:GFP transgenic animals. Immunohistochemistry against the neuronal marker HuC/D and GFP label newborn neurons in sham-treated, and NaCl- and ouabain-injected animals as well as the unlesioned side (ULS) of either sham-treated, or NaCl- or ouabain-injected animals at 4, 8, and 57 days post lesion (dpl). Shown are representative overviews of the neurogenic niche of the SAG as well as close-ups to visualize co-staining. At 4 dpl, several *neurod*:GFP/HuC/D double-positive cells can be found in the lesioned side independent of the type of lesion, whereas neurogenesis is almost not existing in the corresponding unlesioned side (upper row). At 8 dpl, neurogenesis is abundant in the lesioned sides and increased as well in the respective unlesioned sides in sham-treated, and NaCl- and

(*Continued*)

FIGURE 6 | ouabain-injected animals (middle row). At 57 dpl, neurogenesis returned to low levels in the lesioned and unlesioned side with only a few newborn neurons present in the SAG (lower row). **(B)** Quantification of *neurod*:GFP/HuC/D double-positive cells per section at 2, 4, 8, 16, and 57 days post lesion. The number of *neurod*:GFP/HuC/D double-positive cells per section revealed a significant increase in neurogenesis in the lesioned side in comparison with the homeostatic baseline (0.56 *neurod*:GFP/Huc/D double-positive cells per section) calculated from Schwarzer et al., 2020 (gray box). The number of newborn neurons per section peaked at 4 dpl in ouabain-injected SAGs and at 8 dpl in sham-treated as well as in NaCl-injected SAGs, respectively. At 57 dpl, neurogenesis returned to homeostatic levels in all three lesion conditions. Interestingly, neurogenesis rates in the SAGs of the respective unlesioned sides were also increased over time and slightly above the homeostatic baseline at 8 dpl in sham-treated and NaCl-injected animals as well as at 16 dpl in ouabain-injected animals. Baseline levels in neurogenesis in the respective unlesioned sides was reached again at 16 and 57 dpl, respectively. **(C)** Time course for bromodeoxyuridine (BrdU) pulse chase experiment. Six-month-old *Tg(neurod:GFP)* zebrafish were lesioned, followed by two 24-h lasting BrdU treatments at 2 and 4 days post lesion (dpl). Animals were sacrificed at 19 dpl corresponding to 14 days after the second BrdU treatment. **(D)** Antibody staining against the thymidine analog BrdU, the neuronal marker HuC/D and GFP in the SAG of sham-treated, and NaCl- and ouabain-injected *neurod*:GFP animals at 19 dpl (14 days post second BrdU pulse). In the SAG of the unlesioned side, BrdU-positive cells can be found in close proximity to *neurod*:GFP-positive cells (gray arrow). In contrast, *neurod*:GFP/BrdU double-positive progenitors (arrow), *neurod*:GFP/BrdU/HuC/D triple-positive newborn neurons (arrowhead), and BrdU/HuC/D double-positive neurons (open arrowhead) can be found in the SAG of sham-treated, and NaCl- and ouabain-injected animals. Scale bars: 50 µm. For quantification sample size $n = 3$ (n = fish with three sections/SAG; exception: 4 dpl/NaCl: $n = 2$); data are presented as mean ± SEM. Two-way ANOVA with Tukey's multiple comparisons test; $^{***}p \leq 0.001$; $^{**}p \leq 0.01$; $^{*}p \leq 0.05$.

nervous system in which reactive proliferation always precedes reactive neurogenesis, we observe, to a large extent, simultaneous reactive proliferation and reactive neurogenesis (**Figure 7B**). Hence, we hypothesize that the initial reactive neurogenesis is not dependent on previous proliferation of the neuronal progenitor but rather driven by the existing Neurod-positive progenitor pool, which is subsequently replenished by reactive proliferation of Neurod-positive progenitor cells as well as potentially by our previously postulated presumptive marker-negative stem cells. It will now be crucial to identify the nature of the presumptive stem cells and their progenitors as well as the underlying genes and pathways active during homeostasis and regeneration. To this end, single-cell RNA sequencing (scRNAseq) will represent the method of choice. The advent of high-throughput, cost-effective droplet-based scRNAseq allows the assembly of transcriptomic atlases of whole organs including the inner ear (Wu et al., 2021; Yamamoto et al., 2021). Importantly, in addition to scRNAseq data from homeostatic tissues, the transcriptional changes following trauma will be of high importance as recently pioneered by Milon and others (Milon et al., 2021). The comprehensive information gained from these datasets enables insights into the complete cellular composition of the entire tissue and the transcriptomic state of all cell populations within. Moreover, computational algorithms are available that infer a pseudotemporal ordering of cells based on comparative transcriptomic profiling, allowing to derive differentiation trajectories from stem cell or progenitor populations toward differentiated somatic cells in a given tissue or organism (Plass et al., 2018). Once established, interspecies comparisons of scRNAseq datasets from regeneration-competent as well as regeneration-incompetent organisms will identify specific modules of regeneration as well as potential mammalian-specific roadblocks. The employment of recently established conditional gene-targeting approaches, including traditional loxP-flanked alleles or more recent CRISPR/Cas9-based strategies (Hoshijima et al., 2016; Burg et al., 2018; Wu and Wang, 2020; Hans et al., 2021), will enable the rapid genetic analyses of identified pathways and provide important insights also for the currently undertaken *in vitro* approaches.

Although we show that our mechanical lesion paradigm elicits a strong regeneration response within the adult zebrafish SAG, the underlying mechanism remains unclear. The subsequent neuron loss might represent a direct and local effect on the cell cycle status of presumptive stem cells and *neurod*:GFP-positive progenitors. In this respect, it has been reported that dying retinal neurons produce tumor necrosis factor α, a secreted cytokine that is necessary and sufficient for retinal stem cells to initiate cell cycle re-entry during zebrafish retina regeneration (Nelson et al., 2013). Similarly, expression of many other mitogens from local sources has been described to induce proliferation of former quiescent stem cells during regeneration (Fuchs and Steller, 2015). Trauma to the sensory patches after insertion of the Hamilton syringe into the otic capsule, which generates an opening in the usually enclosed inner ear, might provide an additional local cue in our lesion paradigm because strong re-formation of sensory hair cells accompanies neuronal regeneration. However, in addition to local cues, systemic cues must play an important role because we observe reactive proliferation and reactive neurogenesis in the unlesioned side following a unilateral lesion, in particular, following ouabain injections. In this aspect, various systemic effects, including steroids such as estrogen or thyroid hormone, as well as peptide hormones, such as insulin or leptin, have been shown to act as mediators of complex tissue regeneration (Losner et al., 2021). With respect to leptin function, epigenetic profiling provided even evidence for regeneration-dependent enhancer elements in the regeneration-competent zebrafish that are also able to control expression in transgenic mice in a lesion-dependent context (Kang et al., 2016). Another, systemic response that elicits its effect locally constitutes the immune system. In our lesion paradigm, we observe a massive accumulation of leukocytes in the SAG upon injury, which is not resolved at 16 days post lesion, which constituted the end of our time course. In the zebrafish central nervous system, it has been shown that acute inflammation is required for the proper induction of regenerative neurogenesis from neural stem cells (Kyritsis et al., 2012; Tsarouchas et al., 2018; Silva et al., 2020). In particular, the cellular and molecular events during spinal cord regeneration have been dissected in great detail (Tsata and Wehner, 2021). Upon injury, peripheral neutrophils invade the lesion side immediately followed by macrophages, which play a pivotal role in the subsequent functional regeneration, by producing tumor necrosis factor α and controlling interleukin-1 β-mediated inflammation (Tsarouchas et al., 2018). Similarly, T-cells rapidly infiltrate the damaged spinal cord and stimulate regenerative precursor cell proliferation by

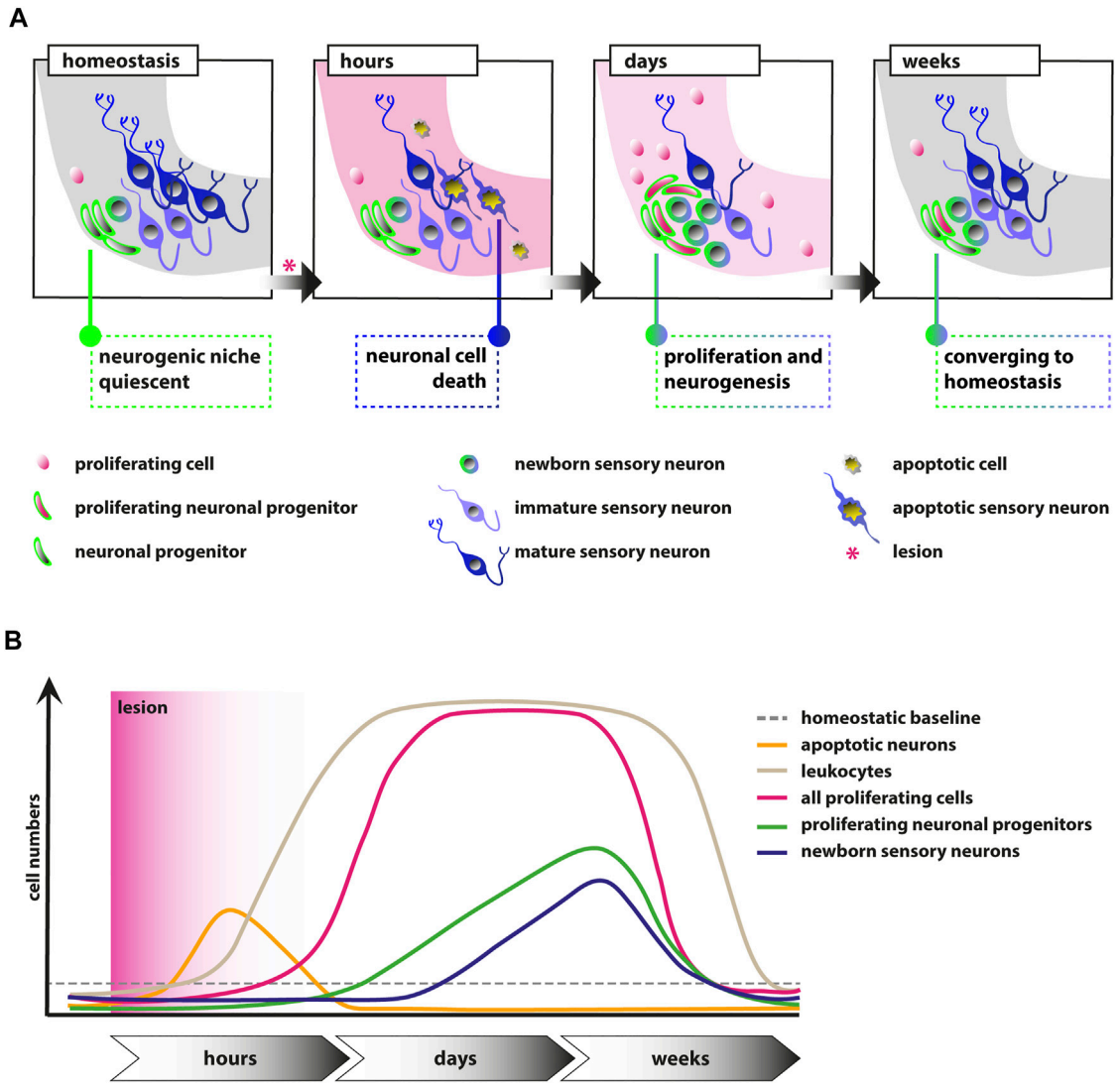

FIGURE 7 | Schematic illustrations of the events in the adult zebrafish SAG upon lesion. **(A)** Scheme depicting the cellular events within the neurogenic niche. During homeostasis, the neurogenic niche of the adult zebrafish SAG is quiescent in regard to proliferation and shows only very rare neurogenesis. Upon lesion, mature sensory neurons as well as other marker-negative cells undergo apoptosis within several hours. Within days, reactive proliferation of marker-negative and neuronal progenitor cells is observed accompanied by reactive neurogenesis from the neuronal progenitor pool. Reactive proliferation and reactive neurogenesis continue over the next weeks until previous homeostatic levels are reached. **(B)** Scheme of the temporal order of events. During homeostasis, only basal levels of proliferating marker-negative cells, proliferating neuronal progenitors, and leukocytes are present in the neurogenic niche of the SAG. In addition, only basal levels of newborn neurons derived from the neuronal progenitors and no apoptotic cells are found. Upon lesion, a strong increase in the number of apoptotic cells and, in particular, apoptotic sensory neurons is observed, which is also resolved rapidly. Also within hours, a massive accumulation of leukocytes occurs, which persists for several weeks. Within days, the number of proliferating cells increases significantly within the neurogenic niche of the SAG and remains high for a couple of weeks until it returns to lower levels. Following the general gain in proliferation, the number of proliferating neuronal progenitors is also significantly increased for approximately 2–3 weeks until it returns to baseline levels. Onset of proliferation of neuronal progenitors is accompanied by increased production of newborn neurons, which remains high for approximately 2–3 weeks until it returns to homeostatic levels.

producing proregenerative factors (Hui et al., 2017). It will be interesting to see if the very same or different mechanisms promote neuronal regeneration in the regenerating adult zebrafish SAG. In this aspect, we would expect several differences because in contrast to the central nervous system in which the number of infiltrated immune cells following injury is decreased within days (Kyritsis et al., 2012), we see persistent presence of immune cells in the lesioned SAG.

Our novel lesion paradigm shows that the neurogenic niche within the adult zebrafish SAG displays a strong regeneration response upon injury, which provides us a first entry point to address the underlying cellular and molecular events. However, to in-depthly understand the regeneration of the SAG, the establishment of various alternative lesion paradigms would be beneficial. For instance, in addition to mechanical lesions, several other injury models are available to address

regeneration of the adult retina, including intense light, application of neurotoxins, as well as pharmacogenetic approaches (Fimbel et al., 2007; Montgomery et al., 2010; Weber et al., 2013). In particular, the latter provides a conditional and unique platform for the precise ablation of cells in a tissue- or cell type-specific manner. Commonly, the nitroreductase/metronidazole system is used in which the bacterial nitroreductase expressed by a tissue- or cell type-specific transgene converts the prodrug metronidazole into a cytotoxic DNA cross-linking agent (Curado et al., 2007). Similarly, when using the human diphtheria toxin receptor/diphtheria toxin system, cells specifically expressing the human diphtheria toxin receptor undergo apoptosis after application of diphtheria toxin (Jimenez et al., 2021). Application of these alternative lesion paradigms or even their combinations will help to dissect the mechanistic underpinnings of successful SAG regeneration.

DATA AVAILABILITY STATEMENT

The original contributions presented in the study are included in the article/Supplementary Material. Further inquiries can be directed to the corresponding author.

ETHICS STATEMENT

The animal study was reviewed and approved by Regierungspräsidium Dresden, permit nos. TVV 79/2016, TVA 1/2017, and TVV 21/2018.

AUTHOR CONTRIBUTIONS

SiS and SH conceived and designed the study. SiS, DRR, AM, SaS, MG, and DE performed the experiments. SiS analyzed the data. SiS and SH wrote the original draft. All authors contributed to the manuscript revision, and read and approved the submitted version. SH acquired funding for this study.

FUNDING

Funding was provided by the Deutsche Forschungsgemeinschaft (HA 6362/1) and the TU Dresden. The funders had no role in study design, data collection and analysis, decision to publish, or preparation of the manuscript. This work was supported by the Light Microscopy Facility, a core facility of the CMCB at the Technische Universität Dresden.

ACKNOWLEDGMENTS

We thank Tjakko J. van Ham and Herma van der Linde for providing the *ubiq:*secAnnexinV-mVenus line generated from the plasmid originating from Marco Morsch. We are indebted to Judith Konantz, Marika Fischer, Silvio Kunadt, and Daniela Mögel for excellent zebrafish care. Special thanks for outstanding tissue sectioning goes to Julia Ebert, who was funded *via* the TU Dresden program "More time for science" granted to SiS. We thank Michael Brand and the members of his laboratory for the continued support and discussions as well as the helpful comments on the manuscript.

REFERENCES

Abbas, L., and Rivolta, M. N. (2015). Aminoglycoside Ototoxicity and Hair Cell Ablation in the Adult Gerbil: A Simple Model to Study Hair Cell Loss and Regeneration. *Hearing Res.* 325, 12–26. doi:10.1016/j.heares.2015.03.002

Adams, K. L., and Gallo, V. (2018). The Diversity and Disparity of the Glial Scar. *Nat. Neurosci.* 21, 9–15. doi:10.1038/s41593-017-0033-9

Aleström, P., D'Angelo, L., Midtlyng, P. J., Schorderet, D. F., Schulte-Merker, S., Sohm, F., et al. (2020). Zebrafish: Housing and Husbandry Recommendations. *Lab. Anim.* 54, 213–224. doi:10.1177/0023677219869037

Astbury, P. J., and Read, N. G. (1982). Kanamycin Induced Ototoxicity in the Laboratory Rat. *Arch. Toxicol.* 50-50, 267–278. doi:10.1007/bf00310859

Brand, M., Granato, M., and Nüsslein-Volhard, C. (2002). "Keeping and Raising Zebrafish," in *Zebrafish, A Practical Approach* (Oxford: Oxford University Press), 7–37.

Burg, L., Palmer, N., Kikhi, K., Miroshnik, E. S., Rueckert, H., Gaddy, E., et al. (2018). Conditional Mutagenesis by Oligonucleotide-Mediated Integration of loxP Sites in Zebrafish. *Plos Genet.* 14, e1007754. doi:10.1371/journal.pgen.1007754

Chen, W., Jongkamonwiwat, N., Abbas, L., Eshtan, S. J., Johnson, S. L., Kuhn, S., et al. (2012). Restoration of Auditory Evoked Responses by Human ES-Cell-Derived Otic Progenitors. *Nature* 490, 278–282. doi:10.1038/nature11415

Corwin, J. T., and Cotanche, D. A. (1988). Regeneration of Sensory Hair Cells after Acoustic Trauma. *Science* 240, 1772–1774. doi:10.1126/science.3381100

Costa, A., Sanchez-Guardado, L., Juniat, S., Gale, J. E., Daudet, N., and Henrique, D. (2015). Generation of Sensory Hair Cells by Genetic Programming with a Combination of Transcription Factors. *Development* 142, 1948–1959. doi:10.1242/dev.119149

Curado, S., Anderson, R. M., Jungblut, B., Mumm, J., Schroeter, E., and Stainier, D. Y. R. (2007). Conditional Targeted Cell Ablation in Zebrafish: A New Tool for Regeneration Studies. *Dev. Dyn.* 236, 1025–1035. doi:10.1002/dvdy.21100

Fimbel, S. M., Montgomery, J. E., Burket, C. T., and Hyde, D. R. (2007). Regeneration of Inner Retinal Neurons after Intravitreal Injection of Ouabain in Zebrafish. *J. Neurosci.* 27, 1712–1724. doi:10.1523/jneurosci.5317-06.2007

Forge, A. (1985). Outer Hair Cell Loss and Supporting Cell Expansion Following Chronic Gentamicin Treatment. *Hearing Res.* 19, 171–182. doi:10.1016/0378-5955(85)90121-2

Fu, Y., Ding, D., Jiang, H., and Salvi, R. (2012). Ouabain-Induced Cochlear Degeneration in Rat. *Neurotox Res.* 22, 158–169. doi:10.1007/s12640-012-9320-0

Fuchs, Y., and Steller, H. (2015). Live to die another way: modes of programmed cell death and the signals emanating from dying cells. *Nat. Rev. Mol. Cel Biol* 16, 329–344. doi:10.1038/nrm3999

Grandel, H., Kaslin, J., Ganz, J., Wenzel, I., and Brand, M. (2006). Neural Stem Cells and Neurogenesis in the Adult Zebrafish Brain: Origin, Proliferation Dynamics, Migration and Cell Fate. *Dev. Biol.* 295, 263–277. doi:10.1016/j.ydbio.2006.03.040

Ham, T. J., Mapes, J., Kokel, D., and Peterson, R. T. (2010). Live Imaging of Apoptotic Cells in Zebrafish. *FASEB j.* 24, 4336–4342. doi:10.1096/fj.10-161018

Hans, S., Zöller, D., Hammer, J., Stucke, J., Spieß, S., Kesavan, G., et al. (2021). Cre-Controlled CRISPR Mutagenesis Provides Fast and Easy Conditional Gene Inactivation in Zebrafish. *Nat. Commun.* 12, 1125. doi:10.1038/s41467-021-21427-6

Hoshijima, K., Jurynec, M. J., and Grunwald, D. J. (2016). Precise Editing of the Zebrafish Genome Made Simple and Efficient. *Dev. Cel.* 36, 654–667. doi:10.1016/j.devcel.2016.02.015

Hui, S. P., Sheng, D. Z., Sugimoto, K., Gonzalez-Rajal, A., Nakagawa, S., Hesselson, D., et al. (2017). Zebrafish Regulatory T Cells Mediate Organ-specific Regenerative Programs. *Dev. Cel* 43, 659–672.e655. doi:10.1016/j.devcel.2017.11.010

Jimenez, E., Slevin, C. C., Colón-Cruz, L., and Burgess, S. M., 2021. Vestibular and Auditory Hair Cell Regeneration Following Targeted Ablation of Hair Cells with Diphtheria Toxin in Zebrafish. 15 721950. doi:10.3389/fncel.2021.721950

Kang, J., Hu, J., Karra, R., Dickson, A. L., Tornini, V. A., Nachtrab, G., et al. (2016). Modulation of Tissue Repair by Regeneration Enhancer Elements. *Nature* 532, 201–206. doi:10.1038/nature17644

Kiernan, A. E., Pelling, A. L., Leung, K. K. H., Tang, A. S. P., Bell, D. M., Tease, C., et al. (2005). Sox2 Is Required for Sensory Organ Development in the Mammalian Inner Ear. *Nature* 434, 1031–1035. doi:10.1038/nature03487

Koehler, K. R., Nie, J., Longworth-Mills, E., Liu, X.-P., Lee, J., Holt, J. R., et al. (2017). Generation of Inner Ear Organoids Containing Functional Hair Cells from Human Pluripotent Stem Cells. *Nat. Biotechnol.* 35, 583–589. doi:10.1038/nbt.3840

Kroehne, V., Freudenreich, D., Hans, S., Kaslin, J., and Brand, M. (2011). Regeneration of the Adult Zebrafish Brain from Neurogenic Radial Glia-type Progenitors. *Development* 138, 4831–4841. doi:10.1242/dev.072587

Kyritsis, N., Kizil, C., Zocher, S., Kroehne, V., Kaslin, J., Freudenreich, D., et al. (2012). Acute Inflammation Initiates the Regenerative Response in the Adult Zebrafish Brain. *Science* 338, 1353–1356. doi:10.1126/science.1228773

Lang, H., Schulte, B. A., and Schmiedt, R. A. (2005). Ouabain Induces Apoptotic Cell Death in Type I Spiral Ganglion Neurons, but Not Type II Neurons. *Jaro* 6, 63–74. doi:10.1007/s10162-004-5021-6

Lenkowski, J. R., and Raymond, P. A. (2014). Müller Glia: Stem Cells for Generation and Regeneration of Retinal Neurons in Teleost Fish. *Prog. Retin. Eye Res.* 40, 94–123. doi:10.1016/j.preteyeres.2013.12.007

Livingston, G., Sommerlad, A., Orgeta, V., Costafreda, S. G., Huntley, J., Ames, D., et al. (2017). Dementia Prevention, Intervention, and Care. *The Lancet* 390, 2673–2734. doi:10.1016/s0140-6736(17)31363-6

Losner, J., Courtemanche, K., and Whited, J. L. (2021). A Cross-Species Analysis of Systemic Mediators of Repair and Complex Tissue Regeneration. *Npj Regen. Med.* 6, 21. doi:10.1038/s41536-021-00130-6

Lush, M. E., Diaz, D. C., Koenecke, N., Baek, S., Boldt, H., St Peter, M. K., et al. (2019). scRNA-Seq Reveals Distinct Stem Cell Populations that Drive Hair Cell Regeneration after Loss of Fgf and Notch Signaling. *eLife* 8, e44431. doi:10.7554/eLife.44431

Milon, B., Shulman, E. D., So, K. S., Cederroth, C. R., Lipford, E. L., Sperber, M., et al. (2021). A Cell-type-specific Atlas of the Inner Ear Transcriptional Response to Acoustic Trauma. *Cel Rep.* 36, 109758. doi:10.1016/j.celrep.2021.109758

Montgomery, J. E., Parsons, M. J., and Hyde, D. R. (2010). A Novel Model of Retinal Ablation Demonstrates that the Extent of Rod Cell Death Regulates the Origin of the Regenerated Zebrafish Rod Photoreceptors. *J. Comp. Neurol.* 518, 800–814. doi:10.1002/cne.22243

Morsch, M., Radford, R., Lee, A., Don, E., Badrock, A., Hall, T., et al. 2015. *In Vivo* characterization of Microglial Engulfment of Dying Neurons in the Zebrafish Spinal Cord. 9 321.doi:10.3389/fncel.2015.00321

Nelson, C. M., Ackerman, K. M., O'Hayer, P., Bailey, T. J., Gorsuch, R. A., and Hyde, D. R. (2013). Tumor Necrosis Factor-Alpha Is Produced by Dying Retinal Neurons and Is Required for Muller Glia Proliferation during Zebrafish Retinal Regeneration. *J. Neurosci.* 33, 6524–6539. doi:10.1523/jneurosci.3838-12.2013

Noda, T., Meas, S. J., Nogami, J., Amemiya, Y., Uchi, R., Ohkawa, Y., et al. (2018). Direct Reprogramming of Spiral Ganglion Non-neuronal Cells into Neurons: Toward Ameliorating Sensorineural Hearing Loss by Gene Therapy. *Front Cel Dev Biol* 6, 16. doi:10.3389/fcell.2018.00016

Obholzer, N., Wolfson, S., Trapani, J. G., Mo, W., Nechiporuk, A., Busch-Nentwich, E., et al. (2008). Vesicular Glutamate Transporter 3 Is Required for Synaptic Transmission in Zebrafish Hair Cells. *J. Neurosci.* 28, 2110–2118. doi:10.1523/jneurosci.5230-07.2008

Park, H.-C., Kim, C.-H., Bae, Y.-K., Yeo, S.-Y., Kim, S.-H., Hong, S.-K., et al. (2000). Analysis of Upstream Elements in the HuC Promoter Leads to the Establishment of Transgenic Zebrafish with Fluorescent Neurons. *Dev. Biol.* 227, 279–293. doi:10.1006/dbio.2000.9898

Plass, M., Solana, J., Wolf, F. A., Ayoub, S., Misios, A., Glažar, P., et al. (2018). Cell Type Atlas and Lineage Tree of a Whole Complex Animal by Single-Cell Transcriptomics. *Science* 360. doi:10.1126/science.aaq1723

Ryals, B. M., and Rubel, E. W. (1988). Hair Cell Regeneration after Acoustic Trauma in Adult *Coturnix* Quail. *Science* 240, 1774–1776. doi:10.1126/science.3381101

Schmiedt, R. A., Okamura, H.-O., Lang, H., and Schulte, B. A. (2002). Ouabain Application to the Round Window of the Gerbil Cochlea: A Model of Auditory Neuropathy and Apoptosis. *Jaro* 3, 223–233. doi:10.1007/s1016200220017

Schuck, J. B., and Smith, M. E. (2009). Cell Proliferation Follows Acoustically-Induced Hair Cell Bundle Loss in the Zebrafish Saccule. *Hearing Res.* 253, 67–76. doi:10.1016/j.heares.2009.03.008

Schwander, M., Kachar, B., and Müller, U. (2010). The Cell Biology of Hearing. *J. Cel. Biol.* 190, 9–20. doi:10.1083/jcb.201001138

Schwarzer, S., Asokan, N., Bludau, O., Chae, J., Kuscha, V., Kaslin, J., et al. (2020). Correction: Neurogenesis in the Inner Ear: the Zebrafish Statoacoustic Ganglion Provides New Neurons from a Neurod/Nestin-Positive Progenitor Pool Well into Adulthood. *Development* 147, dev176750. doi:10.1242/dev.191775

Silva, N. J., Nagashima, M., Li, J., Kakuk-Atkins, L., Ashrafzadeh, M., Hyde, D. R., et al. (2020). Inflammation and Matrix Metalloproteinase 9 (Mmp-9) Regulate Photoreceptor Regeneration in Adult Zebrafish. *Glia* 68, 1445–1465. doi:10.1002/glia.23792

Stawicki, T. M., Esterberg, R., Hailey, D. W., Raible, D. W., and Rubel, E. W., 2015. Using the Zebrafish Lateral Line to Uncover Novel Mechanisms of Action and Prevention in Drug-Induced Hair Cell Death. 9 46.doi:10.3389/fncel.2015.00046

Stone, J. S., and Rubel, E. W. (2000). Temporal, Spatial, and Morphologic Features of Hair Cell Regeneration in the Avian Basilar Papilla. *J. Comp. Neurol.* 417, 1–16. doi:10.1002/(sici)1096-9861(20000131)417:1<1::aid-cne1>3.0.co;2-e

Taylor, R. R., Nevill, G., and Forge, A. (2008). Rapid Hair Cell Loss: a Mouse Model for Cochlear Lesions. *Jaro* 9, 44–64. doi:10.1007/s10162-007-0105-8

Tsakiropoulou, E., Konstantinidis, I., Vital, I., Konstantinidou, S., and Kotsani, A. (2007). Hearing Aids: Quality of Life and Socio-Economic Aspects. *Hippokratia* 11, 183–186.

Tsarouchas, T. M., Wehner, D., Cavone, L., Munir, T., Keatinge, M., Lambertus, M., et al. (2018). Dynamic Control of Proinflammatory Cytokines Il-1β and Tnf-α by Macrophages in Zebrafish Spinal Cord Regeneration. *Nat. Commun.* 9, 4670. doi:10.1038/s41467-018-07036-w

Tsata, V., and Wehner, D. (2021). Know How to Regrow-Axon Regeneration in the Zebrafish Spinal Cord. *Cells* 10, 1404. doi:10.3390/cells10061404

van Genderen, H., Kenis, H., Lux, P., Ungeth, L., Maassen, C., Deckers, N., et al. (2006). *In Vitro* measurement of Cell Death with the Annexin A5 Affinity Assay. *Nat. Protoc.* 1, 363–367. doi:10.1038/nprot.2006.55

Wakizono, T., Nakashima, H., Yasui, T., Noda, T., Aoyagi, K., Okada, K., et al. (2021). Growth Factors with Valproic Acid Restore Injury-Impaired Hearing by Promoting Neuronal Regeneration. *JCI Insight* 6 e139171. doi:10.1172/jci.insight.139171

Weber, A., Hochmann, S., Cimalla, P., Gärtner, M., Kuscha, V., Hans, S., et al. (2013). Characterization of Light Lesion Paradigms and Optical Coherence Tomography as Tools to Study Adult Retina Regeneration in Zebrafish. *PloS one* 8, e80483. doi:10.1371/journal.pone.0080483

Westerfield, M. (2000). *The Zebrafish Book. A Guide for the Laboratory Use of Zebrafish (*Danio rerio*)*. 4th ed Eugene: Univ. of Oregon Press.

Wu, M., Xia, M., Li, W., and Li, H. (2021). Single-Cell Sequencing Applications in the Inner Ear. *Front. Cel Dev. Biol.* 9, 637779. doi:10.3389/fcell.2021.637779

Wu, Y.-C., and Wang, I.-J. (2020). Heat-shock-induced Tyrosinase Gene Ablation with CRISPR in Zebrafish. *Mol. Genet. Genomics* 295, 911–922. doi:10.1007/s00438-020-01681-x

Yamamoto, R., Ohnishi, H., Omori, K., and Yamamoto, N. (2021). In Silico analysis of Inner Ear Development Using Public Whole Embryonic Body Single-Cell RNA-Sequencing Data. *Dev. Biol.* 469, 160–171. doi:10.1016/j.ydbio.2020.10.009

Zine, A., Messat, Y., and Fritzsch, B. (2021). A Human Induced Pluripotent Stem Cell-Based Modular Platform to challenge Sensorineural Hearing Loss. *Stem Cells* 39, 697–706. doi:10.1002/stem.3346

Conflict of Interest: The authors declare that the research was conducted in the absence of any commercial or financial relationships that could be construed as a potential conflict of interest.

Publisher's Note: All claims expressed in this article are solely those of the authors and do not necessarily represent those of their affiliated organizations, or those of the publisher, the editors, and the reviewers. Any product that may be evaluated in this article, or claim that may be made by its manufacturer, is not guaranteed or endorsed by the publisher.

frontiers | Frontiers in Cell and Developmental Biology

ORIGINAL RESEARCH
published: 20 April 2022
doi: 10.3389/fcell.2022.819612

Using Light-Sheet Microscopy to Study Spontaneous Activity in the Developing Lateral-Line System

Qiuxiang Zhang and Katie S. Kindt**

Section on Sensory Cell Development and Function, National Institute on Deafness and Other Communication Disorders, National Institutes of Health, Bethesda, MD, United States

Hair cells are the sensory receptors in the auditory and vestibular systems of all vertebrates, and in the lateral-line system of aquatic vertebrates. The purpose of this work is to explore the zebrafish lateral-line system as a model to study and understand spontaneous activity *in vivo*. Our work applies genetically encoded calcium indicators along with light-sheet fluorescence microscopy to visualize spontaneous calcium activity in the developing lateral-line system. Consistent with our previous work, we show that spontaneous calcium activity is present in developing lateral-line hair cells. We now show that supporting cells that surround hair cells, and cholinergic efferent terminals that directly contact hair cells are also spontaneously active. Using two-color functional imaging we demonstrate that spontaneous activity in hair cells does not correlate with activity in either supporting cells or cholinergic terminals. We find that during lateral-line development, hair cells autonomously generate spontaneous events. Using localized calcium indicators, we show that within hair cells, spontaneous calcium activity occurs in two distinct domains—the mechanosensory bundle and the presynapse. Further, spontaneous activity in the mechanosensory bundle ultimately drives spontaneous calcium influx at the presynapse. Comprehensively, our results indicate that in developing lateral-line hair cells, autonomously generated spontaneous activity originates with spontaneous mechanosensory events.

Keywords: development, spontaneous activity, hair cell, lateral line efferents, light-sheet microscopy

OPEN ACCESS

Edited by:
Berta Alsina,
Pompeu Fabra University, Spain

Reviewed by:
Jeremy Duncan,
Western Michigan University, United States
Jonathan F. Ashmore,
University College London, United Kingdom

****Correspondence:***
Qiuxiang Zhang
qiuxianguab@gmail.com
Katie S. Kindt
katie.kindt@nih.gov

Specialty section:
This article was submitted to Molecular and Cellular Pathology, a section of the journal Frontiers in Cell and Developmental Biology

Received: *21 November 2021*
Accepted: *18 January 2022*
Published: *20 April 2022*

Citation:
Zhang Q and Kindt KS (2022) Using Light-Sheet Microscopy to Study Spontaneous Activity in the Developing Lateral-Line System. Front. Cell Dev. Biol. 10:819612. doi: 10.3389/fcell.2022.819612

INTRODUCTION

Spontaneous activity has been documented in developing sensory systems, including visual, auditory, vestibular and somatosensory systems [reviewed in: (Leighton and Lohmann, 2016)]. Spontaneous activity in sensory cells can play a role locally in synapse maturation and ion channel expression, as well as globally to pattern and refine downstream sensory circuits. For example, in the developing inner ear of mammals, spontaneous activity in sensory hair cells is thought to act locally help establish neuronal connections and globally to shape the tonotopic maps (Tritsch et al., 2007; Ceriani et al., 2019). However, in mammals, hair cells are enclosed in the bony structures of the ear—this location makes it difficult to access and record spontaneous activity *in vivo*. The purpose of this work is to explore the zebrafish lateral line as an *in vivo* model to study spontaneous activity in developing hair cells.

The lateral line is composed of superficial clusters of hair cells called neuromasts (Raible and Kruse, 2000). Unlike mammals, the lateral-line system can easily be accessed in intact zebrafish,

making, it straightforward to visualize and study developing hair cells *in vivo*. With regard to development, the lateral line forms rapidly—when larvae are 2–3 days old (2–3 days post fertilization (dpf)), the majority of the hair cells are immature. But when larvae are 5–6 days old (5–6 dpf), the majority of the hair cells are mature and the lateral-line system is functional (Kindt et al., 2012; Suli et al., 2012). This rapid developmental trajectory has made zebrafish an excellent system to study hair cell maturation. In addition to rapid development, zebrafish larvae are transparent, making it possible to visualize activity using genetically encoded calcium indicators (GECIs) (Lukasz and Kindt, 2018). The use of GECIs, along with advances in microscopy such as light-sheet fluorescence microcopy (LSFM) has increased the imaging potential of the zebrafish model (Quirin et al., 2016). LSFM uses plane illumination to rapidly image volumes with minimal photobleaching and phototoxicity. Thus, LSFM is a powerful way to image spontaneous activity in zebrafish hair cells, *in vivo*, even over extended periods of time.

In developing hair cells, two forms of spontaneous activity have been documented: 1) coordinated waves of activity among hair cells (Tritsch et al., 2007) and 2) uncoordinated, calcium action potentials that are thought to be generated autonomously (Marcotti et al., 2003; Eckrich et al., 2018). Thus far coordinated waves of activity appear to be a unique feature of the mammalian auditory system. Here, in the developing auditory epithelium, waves of calcium propagate through hair cells and the glia-like supporting cells that surround or are adjacent to hair cells. ATP signaling in supporting cells drives spontaneous activity in nearby auditory hair cells. Independent of these coordinated waves of activity, in mice and zebrafish there are also spontaneous calcium events that are not coordinated among hair cells (Eckrich et al., 2018; Hiu-Tung et al., 2019; Holman et al., 2019). In both mouse auditory hair cells, and zebrafish lateral-line hair cells, $Ca_V1.3$ calcium channels present at the hair cell presynapse are required for these events. Although the role of this uncoordinated activity is not fully understood, in the lateral line, we have shown that it can regulate presynapse size in developing hair cells (Hiu-Tung et al., 2019). Currently the origin of these uncoordinated spontaneous events in developing hair cells remains unclear.

Current evidence suggests that spontaneous activity in surrounding supporting cells is not required for uncoordinated spontaneous events in developing hair cells. In addition to surrounding supporting cells, developing hair cells in mouse and zebrafish are contacted by cholinergic efferents that descend from the brainstem (Glowatzki and Fuchs, 2000; Carpaneto Freixas et al., 2021). Furthermore, studies in mice have shown that these efferents can modulate hair cell activity during development (Glowatzki and Fuchs, 2000; Katz et al., 2004; Holman et al., 2019). Further, when the α9/α10 acetylcholine receptors required for this cholinergic modulation are disrupted, the patterns of hair cell spontaneous activity in the auditory epithelium of mice are altered (Clause et al., 2014). But whether these descending efferents are spontaneously active in hair cell systems and whether they can trigger spontaneous activity in developing hair cells is not known.

Our study applies LSFM to study spontaneous calcium activity *in vivo*, in the zebrafish lateral-line system. We show that spontaneous calcium activities are present in several cell types in the periphery of the developing lateral line: hair cells, supporting cells, as well as cholinergic efferents that innervate hair cells. Using two-color functional imaging, along with pharmacology, we find that hair cell spontaneous activity occurs independent of activity in supporting cells and cholinergic efferents. Instead, developing hair cells autonomously generate spontaneous events. By using a membrane-localized calcium indicator in hair cells, we show that spontaneous calcium activity occurs in two distinct domains: the mechanosensory bundle and the presynaptic compartment. Further, our genetic and pharmacological analyses reveal that in lateral-line hair cells, spontaneous mechanosensory activity in the mechanosensory bundle drives spontaneous calcium influx at the presynapse. Thus, mechanosensory activity is the main source of spontaneous activity in lateral-line hair cells.

METHODS

Zebrafish Husbandry and Strains

Zebrafish (Danio rerio) were raised at 28°C on a 14:10 h light/dark cycle. Larvae at 2–6 days post fertilization (dpf) were used for the experiments and were maintained in E3 embryo medium (in mM: 5 NaCl, .17 KCl, 0.33 $CaCl_2$, and 0.33 $MgSO_4$, buffered in HEPES pH 7.2) at a constant temperature of 28°C in an incubator. Because sex is not yet determined at these ages, we did not consider the animal's gender in our research. Zebrafish work performed at the National Institute of Health was approved by the Animal Use Committee under animal study protocol #1362-13. The following previously established mutant and transgenic zebrafish strains were used in this study: *Tg(myo6b:memGCaMP6s)^{idc1}* (Jiang et al., 2017), *Tg(myo6b:RGECO1)^{vo10}* (Maeda et al., 2014), *Tg(UAS:GCaMP6s)^{mpn101}* and *Tg(chat:Gal4)^{mpn202}* (Förster et al., 2017), *pcdh15a^{th263}(R306X)* (Seiler et al., 2005), and *cav1.3a/cacna1d^{tn004} (R284C)* (Sidi et al., 2004).

Vector Construction and Creation of New Transgenic Lines

We generated two additional stable transgenic fish lines for this study. Plasmid construction to create these lines was based on the tol2/gateway zebrafish kit (Kwan et al., 2007). Plasmid DNA and tol2 transposase mRNA were injected into zebrafish embryos as previously described (Kwan et al., 2007). Using this approach, in addition to the previously established transgenic lines listed above, the transgenic lines *Tg(she:GCaMP6s)^{idc17}* and *Tg(myo6b:GCaMP6s)^{idc18}* were created for and used in this study. These lines used the supporting cell-specific promoter (*she*) (Quillien et al., 2017) or hair cell-specific promoter (*myo6b*) (Obholzer et al., 2008) to express GCaMP6s in order to image spontaneous calcium activity in the cytosol.

Drug	Mode of action	Vendor	Working concentration
FFA	Gap junction blocker antagonist	Sigma-Aldrich	25 μM
MRS2500	P2yr1 selective antagonist	Tocris	1 μM
Thapsigargin	Potent inhibitor of sarco/endoplasmic reticulum Ca^{2+}-ATPases (SERCA)	Sigma-Aldrich	250 nm
α-bungarotoxin (α-Btx)	Potent inhibitor of α9 or α10 nicotinic acetylcholine receptor (nAChR)	Tocris	10 μM
Apamin	SK channel blocker	Tocris	10 μM
Isradipine	L-type Ca2+ channel CaV1.3a antagonist	Sigma-Aldrich	10 μM
BAPTA-tetrasodium salt	Disrupts hair-bundle tip links	Thermofisher	5 mM

Sample Preparation for 4D Spontaneous Calcium Imaging *In Vivo*

Larvae at 2–6 dpf were first anesthetized with 0.03% Ethyl 3-aminobenzoate methane sulfonate salt (Sigma-Aldrich, St. Louis, MO, United States) and pinned onto a Sylgard-filled recording chamber (I-2450, ASI, Eugene, OR, United States). After pinning, 125 μM α-Bungarotoxin (Tocris, Bristol, United Kingdom) was injected into the heart of intact larvae to suppress movement. Larvae were then rinsed with extracellular imaging solution (in mM: 140 NaCl, 2 KCl, 2 $CaCl_2$, 1 $MgCl_2$, and 10 HEPES, pH 7.3) and allowed to recover. To image the spontaneous calcium activity, the larvae were kept in extracellular imaging solution without applying any external stimuli.

Pharmacology

All drugs were prepared in extracellular solution with 0.1% DMSO (except no DMSO was used with BAPTA). Animals were bathed in each drug (except BAPTA) for at least 15 min prior to imaging. For BAPTA treatment, animals were incubated in BAPTA for 15 min, followed by a wash with extracellular solution. Listed in the table above are the concentrations of the drugs used in this study.

Light-Sheet System Construction

4D spontaneous calcium activity of zebrafish neuromast was imaged by a homebuilt dual-view inverted selective-plane illumination microscope (diSPIM). The microscope was built and aligned according to the previously described protocols (Kumar et al., 2014). Briefly, the bulk of the optomechanical hardware, automated stages, laser scanners, piezo elements for focus control, and control electronics were purchased from Applied Scientific Instruments (ASI, Eugene, OR, United States). Each arm of the diSPIM (SPIMA and SPIMB) consists of a water-dipping objective (Nikon CFI NIR Apo 40X Water DIC N2, Nikon, Melville, NY, United States) either emitting the laser light for excitation or collecting signals from the sample using an ORCA-Flash 4.0 sCMOS camera (Hamamatsu Photonics, Hamamatsu City, Shizuoka, Japan). Two optically pumped semiconductor laser (OBIS 488 nm LX 30 mW and OBIS 561 nm LS 80 mW, Coherent, CA, United States) were combined with a beam combiner (OBIS Galaxy, Coherent, CA, United States) and then routed to a fiber optic switch (eol 1x2 VIS, LEONI, VA, United States) for output laser wavelength selection. Two outputs from the fiber optic switch were fiber-coupled to two diSPIM head laser scanners. The open-source platform Micro-Manager (https://micro-manager.org/) (Edelstein et al., 2010) was used for hardware interfacing, data capture, and storage. A TMC vibration isolation lab table (63P-9012M, TMC, Boston, MA, United States) was used to house the light-sheet system to minimize disturbance from external movement or vibration.

DiSPIM Fast Acquisition of Volumes to Detect Spontaneous Calcium Signals

For fast, single wavelength imaging of spontaneous cytoGCaMP6s or memGCaMP6s calcium signals, one arm of the diSPIM (SPIMA) was used to acquire volumes at a rate of ~0.33 Hz (every 3 s) for 15 min. 10 (efferent) or 20 (hair cell and supporting cell) slices were acquired per volume (1 μm spacing) at 10 ms and 256 × 256 pixels per slice with 2 × 2 binning (325 nm per pixel with 2 × 2 binning). This volume encompasses the entire neuromast. Each volume was acquired in 100 (efferent) or 200 ms (hair cell or supporting cell); this acquisition speed was sufficient to measure spontaneous GCaMP6s-dependent signals near simultaneously within the volume. Further, this volumetric acquisition speed (100 or 200 ms), volumetric frame rate (every 3 s) and resolution were optimal to record spontaneous events without any significant photobleaching. No additional activity was observed with a faster acquisition speed or volumetric frame rate, or with a higher resolution. This fast, single wavelength imaging was used to acquire cytoGCaMP6s signals in either hair cells or supporting cells (**Figures 1D–E**; **Supplementary Figure S1**; **Figure 2**; **Supplementary Figures S3, S5**) or to measure cytoGCaMP6s signals in efferent terminals (**Supplementary Figures S6B, C–C′**). In addition, fast, single wavelength imaging was also used to simultaneously acquire memGCaMP6s signals in neuromast hair bundles and presynapses (**Figures 3C–C′**, **5**, **6**).

Fast, two-color imaging was performed using a similar approach. One arm of the diSPIM (SPIMA) was used to sequentially acquire volumes of green and red GECI signals at rate of ~0.2 Hz (every 5 s) for 15 min. Eight slices were acquired per volume (2 μm spacing) at 5 ms and 256 × 256 pixels per slice with 2 × 2 binning. Each volume was acquired sequentially (GCaMP6s volume followed by RGECO1 volume) with an acquisition speed of 242 ms for the 2 volumes (GCaMP6s and RGECO1). These calcium imaging parameters were optimized to minimize noise and ensure reliable correlation values. This acquisition speed and spacing was sufficient to measure

spontaneous GCaMP6s- and RGECO1-dependent signals near simultaneously within the volumes and optimal to prevent RGECO1 photobleaching. This approach was to image calcium signals in hair cells (cytoRGECO1) along with calcium signals in supporting cells (cytoGCaMP6s) or efferent terminals (cytoGCaMP6s) (**Figures 1B2–C**; **Supplementary Figure S2**; **Figures 3A1–A3′**; **Supplementary Figures S6A–A3′**). For quantitative measurements of spontaneous calcium signals, these fast, single wavelength or two-color 3D time-series were processed and used for analyses.

DiSPIM Acquisition of High-Resolution Volumes for Spatial Delineation of Morphology

To clearly delineate neighboring cells and cell-adjacent synaptic arbors in our fast acquisitions, and create 4D movies (**Supplementary Movie S1**), we acquired additional high-resolution reference image stacks. For this slower, higher resolution acquisition, volumes were acquired from each of the two views (SPIMA and SPIMB) with 166 slices (0.5 μm spacing), at 512 × 512 pixels per slice and 1 × 1 binning (162.5 nm per pixel). After high-resolution imaging, images were cropped, and the backgrounds were subtracted in ImageJ (Schneider et al., 2012). The two image stacks from SPIMA and SPIMB views were then co-registered and deconvolved jointly to obtain a single volumetric image stack with isotropic spatial resolution and an isotropic voxel spacing (0.1625 × 0.1625 × 0.1625 μm/pixel). Custom software built in C++/CUDA (Guo et al., 2020) was used to conduct image registration and deconvolution on a graphics processing unit (GPU) card. The image registration process started with transforming the image stack from SPIMB with rotation, translation, or scaling and then overlaid and compared with those from SPIMA. By minimizing a cost function via Powell's method (http://mathfaculty.fullerton.edu/mathews/n2003/PowellMethodMod.html), the best transformation matrix was obtained for registration. The images were then deconvolved jointly by an "unmatched back projector" method, which could significantly accelerate deconvolution (Guo et al., 2020). The updated code published by Min Guo and Hari Shroff can be download from GitHub at: (https://github.com/eguomin/regDeconProject; https://github.com/eguomin/diSPIMFusion; https://github.com/eguomin/microImageLib).

We also characterized the actual resolution of our diSPIM system using carboxylate-modified fluorescent beads (0.1 μm, F8803, Thermo Fisher Scientific, MA, United States), diluted 100 times before use. The full width at half-maximum (FWHM) numbers were calculated for eight beads along all axes before and after joint deconvolution (Kumar et al., 2014). Before deconvolution, the FWHM of a bead was close to 0.5 μm (lateral) and 1.5 μm (axial). After registration of the two views (SPIMA and SPIMB) and joint deconvolution, the bead FWHM was approximately isotropic with 0.32 μm ± 0.04 std (lateral) and 0.41 μm ± 0.05 std (axial) resolution.

Quantification of Spontaneous Calcium Signals

3D times-series imaged at fast acquisition were used to quantify spontaneous calcium signals. The stacks first registered by the application of the imageJ macro, Correct 3D Drift (Arganda-Carreras et al., 2006; Parslow et al., 2014). Image stacks with excessive X-Y drift or drift in Z were discarded from our analyses. After drift correction, volumes were converted into 2D time-series images by using the ImageJ Maximum Intensity Z-projection function. Volumes were Max-projected as follows, single wavelength: hair cell memGCaMP6s and cytoGCaMP6s (every 6 μm), supporting cell cytoGCaMP6s (every 4 μm), efferent cytoGCaMP6s (entire 10 μm volume), two-color: hair cell cytoRGECO (every 8 μm), supporting cell cytoGCaMP6s (every 4 μm), efferent cytoGCaMP6s (entire 16 μm volume). These projections reduced signal to noise without an overlap in signal between neighboring cells or terminals. After Max-projection another ImageJ macro, StackReg (Thevenaz et al., 1998) was used to further correct movement artifacts if necessary. If stacks could not be adequately corrected for X-Y drift they were discarded from analyses. For whole neuromast quantification, projections containing the majoring of cells or terminals were selected for analyses. For Pearson's correlation analyses, projections centered the cell or terminal of interest were used.

For quantification, a circular ROI was placed on each cell or terminal (diameter of ROI: ~5 μm hair cell base; ~2 μm hair bundle or efferent terminal; ~3 μm supporting cell soma). Using these ROIs, the fluorescent intensity value within each ROI was obtained for each time point in each cell or terminal. Next the fluorescent intensity values (ΔF) within each ROI were plotted for further processing in MATLAB R2020a (Mathworks, Natick, MA, United States). The baseline (F_0) was calculated for each timepoint using the MATLAB imerode function to create a plot of $\Delta F/F_0$ values. Using these $\Delta F/F_0$ values we quantified 1) Pearson's correlation coefficients, 2) the magnitude, frequency and duration of individual spontaneous peaks in GCaMP6s recordings and 3) the average magnitude of spontaneous signals above baseline during the recording period.

To calculate Pearson's correlation coefficient (R), Prism 8 (Graphpad, San Diego, CA, United States) was used. The correlation between two ($\Delta F/F_0$) measurements was computed at all time points during the 15 min recording period. This approach was used to correlate activity within a hair cell (hair bundle and presynapse) and between a hair cell and the innervating efferent terminal. To calculate a Pearson's correlation coefficient between a cell and its 3–4 neighboring cells, a correlation was calculated for each neighbor, and all correlations were averaged to generate one Pearson's correlation coefficient value per cell. For comparisons of

efferent terminals within a neuromast, a Pearson's correlation coefficient was calculated for all terminal pairings.

We detected peaks in our $\Delta F/F_0$ GCaMP6s traces in MATLAB using the built-in peak detection function findpeaks. After peak detection we calculated the average magnitude, frequency and duration of peaks for each ROI over the whole recording period (15 min). Then we averaged this information per neuromast to create a single value for each neuromast.

To calculate average magnitude of spontaneous GCaMP6s signals, all values of $\Delta F/F_0$ less than 10% in the recording were removed. Values below 10% were considered noise; therefore, signals above 10% $\Delta F/F_0$ were our threshold value for a true GCaMP6s signal. At the hair cell presynapse a 10% threshold was confirmed by imaging spontaneous memGCaMP6s signals in the presence of isradipine where no signals were observed (**Figure 5**). The average magnitude of spontaneous activity per cell or terminal was obtained by dividing the integral or sum of GCaMP6s signals ($\Delta F/F_0$ > 10%, our threshold value) during the whole recording period by the total frames. The average magnitude was calculated for all hair bundles, presynapses, hair cells, supporting cells and efferent terminals within a neuromast. These values were then averaged to create a single value for each neuromast.

Spatial and Temporal Visualization GCaMP6s Signals in Image Stacks

To better observe the spontaneous calcium signals temporally and spatially (**Figure 2**, **Supplementary Figure S4**), fluorescence images were scaled and represented using color maps, with red indicating an increase in calcium signal relative to the resting period (baseline). The procedure to obtain these color maps has been described previously (Lukasz and Kindt, 2018).

In **Supplementary Figure S4**, spatial and temporal changes in spontaneous activity in a single supporting cell was obtained by subtracting each image from baseline (reference image just prior to the rise signal) to represent the relative change in fluorescent signal (ΔF). Using this method, the spatial changes in ΔF (via the heat map) were visualized at multiple time points during a spontaneous event.

In **Figure 2**, the spontaneous activity in supporting cells and hair cells was represented spatially by computing the average magnitude ($\Delta F/F_0$) over the whole recording period (15 min) pixel by pixel. The $\Delta F/F_0$ values were then converted into a heat map and overlaid on a single grayscale morphological image. The accompanying cytoGCaMP6s traces in **Figure 2** were obtained by placing an ROI over the entire neuromast during the pre- and post-drug incubation time windows.

Statistical Analysis

All data were analyzed and plotted with Prism 8. Values in the text and data with error bars on graphs and in text are expressed as mean ± SEM. All experiments were performed on a minimum of three animals. From these three animals, at least four neuromasts were examined. All experiments were repeated on two independent days. These numbers were adequate to provide statistical power to avoid both Type I and Type II error. Datasets were confirmed for normality using a D'Agostino-Pearson omnibus normality test. Statistical significance between two conditions was determined by either an unpaired or paired t-test, or a Kruskal–Wallis test as appropriate. Prism 8 was used to create correlation heat maps.

RESULTS

Fast, Volumetric, *In Vivo* Imaging of Spontaneous Calcium Activity in Developing Hair Cells

Our previous work demonstrated that spontaneous presynaptic calcium activity in developing lateral-line hair cells is important for proper presynapse formation (Hiu-Tung et al., 2019), yet how presynaptic calcium influx was initiated remained unclear. To study spontaneous activity during development in more detail, we constructed a dual-view inverted selective plane illumination microscope (diSPIM) (Kumar et al., 2014). This light-sheet microscope is specialized for fast, continuous imaging of volumes over long-time windows, with minimal photodamage or bleaching. In addition, this microscope can acquire high-resolution volumes with isotropic resolution in XYZ.

We tested the capability of this fluorescence microscope to detect spontaneous calcium activities in transgenic zebrafish lines expressing the cytosolic GECIs cytoGCaMP6s or cytoRGECO1 in hair cells. Using this approach, we observed robust spontaneous calcium signals in immature hair cells (day 3; **Figures 1B1–B3, D–D′**; **Supplementary Movies S1, S2**). Consistent with our previous results where we used a membrane-localized indicator, memGCaMP6s to monitor spontaneous presynaptic calcium activity, cytoGCaMP6s signals were dramatically reduced when hair cells matured (day 6; **Figures 1D–D′**). We found that this microscope system was suitably fast for imaging the time course of these calcium signals in volumes (83 μm × 83 μm × 20 μm volumes acquired within 100 ms every 3 s) that encompass the entire neuromast organ. Despite continuous, volumetric imaging over long-time windows (15 min), we observed minimal-to-no photodamage or bleaching (**Figure 1B3**). Overall, our data indicates that the diSPIM microscope is well-suited to rapidly measure spontaneous calcium activities within entire neuromast organs.

Spontaneous Calcium Activity is Present in Zebrafish Supporting Cells

Similar to the mammalian inner ear, hair cells in the zebrafish lateral line are isolated and surrounded by supporting cells (**Figures 1A–B′**). Furthermore, studies in the developing inner ear in mice have shown that spontaneous activity in present in hair cells and supporting cells. Therefore, we tested whether zebrafish supporting cells were spontaneously active during development. To measure spontaneous calcium activity, we

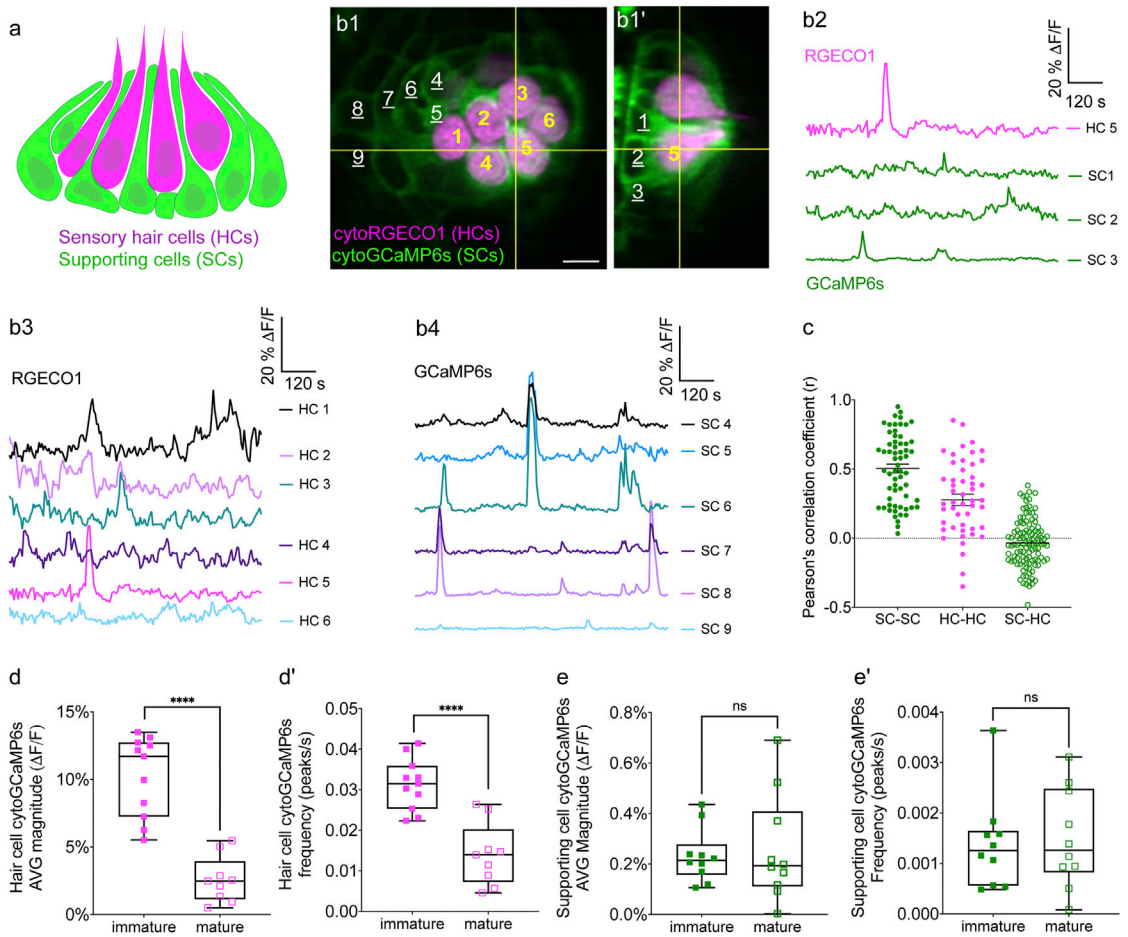

FIGURE 1 | Simultaneous imaging of spontaneous activities in hair cells and supporting cells. **(A)** Cartoon of a neuromast organ illustrating sensory hair cells (magenta) and the surrounding supporting cells (green). **(B1–B1′)** High-resolution images taken using two arms of our diSPIM system show a representative, day 3, double transgenic neuromast expressing cytoRGECO1 (hair cells, numbered in yellow) and cytoGCaMP6s (supporting cells, a subset is numbered in white, underscored). A top-down view **(B1)** and the corresponding side view of its orthogonal projection **(B1′)** clearly show the hair cells and the surrounding supporting cells at day 3. **(B2)** Temporal curves of spontaneous calcium activity in hair cell 5 (labeled in **B1–B1′**) and its three surrounding supporting cells (labeled in **B1′**) within the 15 min recording window show distinct time courses. **(B3)** Temporal curves of spontaneous calcium activity in the cluster of six hair cells (labeled in **B1**) reveals distinct response profiles. **(B4)** Temporal curves of spontaneous calcium activity in the seven supporting cells (labeled in **B1**) reveals some correlation and synchronization among neighboring supporting cells. **(C)** Comparisons of Pearson's R of spontaneous calcium activities at day 3 in neighboring supporting cells, neighboring hair cells and hair cells with its surrounding hair cells, $n = 6$ neuromasts for HC-HC or SC-SC R values and $n = 4$ neuromasts for HC-SC R values. **(D–D′)** Box plots showing quantification of the average magnitude **(D)** and frequency **(D′)** of spontaneous calcium activity in immature (day 3) and mature (day 6) hair cells. **(E–E′)** Box plots showing quantification of the average magnitude **(E)** and frequency **(E′)** of spontaneous calcium activity in supporting cells in mature (day 6) and immature (day 3) neuromasts. Each dot in **(D–E′)** represents one neuromast. An unpaired *t*-test was used in **(D–E′)**. ****$p < .0001$. Scale bar = 5 μm.

created a transgenic zebrafish line expressing the cytosolic GECI cytoGCaMP6s in supporting cells (**Figures 1B1–B1′**). Using this line, we observed that in developing neuromasts, spontaneous calcium signals were also present in supporting cells (day 3; **Figures 1B2, B4, E–E′**; **Supplementary Movie S3**).

We compared the properties of the spontaneous signals detected in supporting cells with those detected in the hair cells. For our comparison we used transgenic lines that expressed same GECI, cytoGCaMP6s in either supporting cells or hair cells (**Supplementary Figure S1**). Our analyses revealed that the average magnitude of cytoGCaMP6s signal above our baseline threshold during the 15-min recording window (average magnitude; **Supplementary Figure S1A**) was much higher in hair cells than that in supporting cells. Furthermore, there were also significantly more spontaneous calcium events occurring in the hair cells compared with supporting cells (peaks per second; **Supplementary Figure S1A′**). In addition to more spontaneous calcium events, each spontaneous calcium event lasted much longer in the hair cells compared to supporting cells (duration, Hair cells: 14.22 s ± 0.68, Supporting cells: 9.06 s ± 0.51; **Supplementary Figure S1A′′**). Despite more events with a longer time course, on average, the peak magnitudes were comparable between hair cells and supporting cells (average peak mean; **Supplementary Figure S1A′′′**). These data indicate that in the zebrafish lateral-line system, spontaneous calcium activity is present in both hair cells and supporting cells.

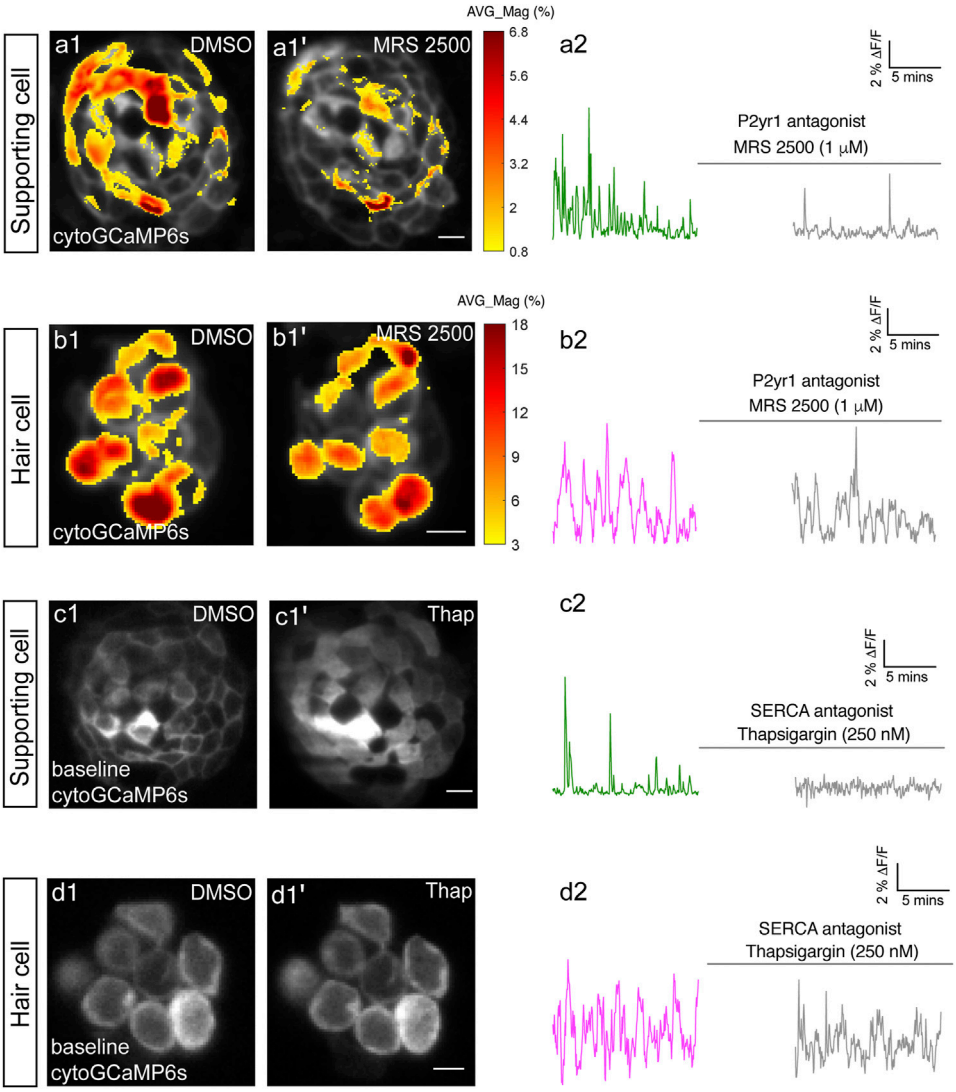

FIGURE 2 | P2yr1 signaling is required for spontaneous activity in supporting cells but not immature hair cells. The spatial patterns of the mean spontaneous calcium activities of the supporting cells **(A1–A1′)** or hair cells **(B1–B1′)** in DMSO and after 15 min of treatment with 1 μM MRS2500. Measurements were performed in immature neuromasts at day 3. The ΔF/F GCaMP6s signals were averaged over each 900 s interval (pre- and post-treatment) and then colorized according to the heat map and superimposed onto a baseline image. The corresponding temporal curves of the mean signal magnitude across the whole neuromast in supporting cells **(A2)** and in hair cells **(B2)** in DMSO and after 15 min of treatment with 1 μM MRS2500. The cytosolic baseline calcium in the supporting cells **(C1–C1′)** and hair cells **(D1–D1′)** in DMSO and after 15 min of treatment with 250 nM Thapsigargin. Measurements were performed in immature neuromasts at day 3. The corresponding temporal curves of the mean signal magnitude across the whole neuromast in supporting cells **(C2)** and in hair cells **(D2)** in DMSO and after 15 min of treatment with 250 nM Thapsigargin. Scale bar = 5 μm.

Our work indicates that spontaneous calcium signals in hair cells are restricted to development (**Figures 1D–D′**). Interestingly, we found no significant difference in spontaneous cytoGCaMP6s signals in supporting cells when we compared immature (day 3) to mature (day 6) neuromast organs (**Figures 1E–E′**). Overall, our work indicates that spontaneous activities are present in both hair cells and supporting cells in the zebrafish lateral line. Although hair cell spontaneous activity occurs primarily during development (**Figures 1D–D′**), in supporting cells, this activity is retained upon sensory system maturation.

Spontaneous Calcium Activities in Hair Cells and Supporting Cells Do Not Coincide

To understand if spontaneous calcium activities in hair cells and supporting cells are linked, we performed two-color (red and green) calcium imaging. Here we simultaneously imaged the activity in both hair cells and supporting cells, using a double-transgenic zebrafish line expressing the red cytosolic GECI cytoRGECO1 in hair cells along with the green cytosolic GECI cytoGCaMP6s in supporting cells (**Figures 1B1–B1′**). We focused our analyses on immature neuromasts (day 3) when

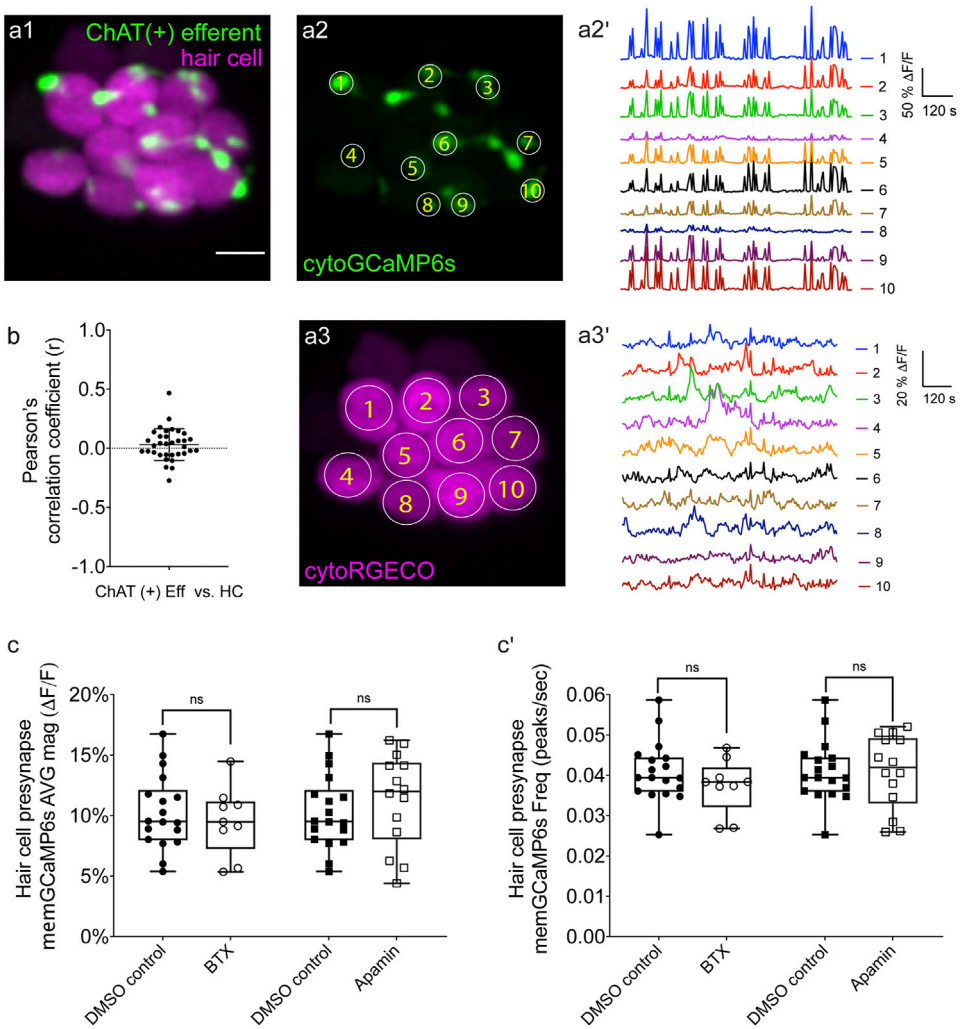

FIGURE 3 | Two-color imaging of spontaneous activities in hair cells and cholinergic efferent terminals. **(A1)** A representative Max-projection image of a double-transgenic zebrafish line expressing the red GECI cytoRGECO1 in hair cells and the green GECI cytoGCaMP6s in the cholinergic efferents terminals at day 3. **(A2)** Image depicting cholinergic efferent terminals with individual terminals contacting different hair cells in **(A1)** are labeled accordingly. **(A2′)** The corresponding temporal curves of spontaneous calcium activities of the 10 efferent terminals indicated in **(A2)**. **(A3)** Image of the individual hair cells in a1 labeled according to innervating efferent terminal. **(A3′)** The corresponding temporal curves of spontaneous calcium activities of the 10 hair cells indicated in **(A3)**. **(B)** Pearson's R values of spontaneous calcium activity between each hair cell and its contacting cholinergic efferent terminal, $n = 34$ hair cell-efferent terminal pairs from four neuromasts at day 3. Box plots showing the average magnitude **(C)** and frequency **(C′)** of spontaneous calcium activity at the hair cell presynapse in DMSO and after the treatment with 10 μM α-Btx and 10 μM apamin. Each point in **(C–C′)** represents one neuromast. All measurements were performed in immature neuromasts at day 3. A paired *t*-test was used in **(C–C′)**. Scale bar = 5 μm.

spontaneous calcium activity is robust in hair cells. Using our diSPIM microscope, along with these calcium reporters, we were able to simultaneously detect spontaneous calcium activity in all hair cells and supporting cells within whole neuromast organs (**Figures 1B,C**; **Supplementary Figure S2**; **Supplementary Movie S4**).

Next, we investigated whether there was a relationship between the spontaneous calcium activities in hair cells and the surrounding supporting cells during development (day 3). In addition to the fast-volumetric calcium imaging, diSPIM light-sheet systems can also acquire high-resolution, 3D image volumes that can be viewed in a top-down view (**Figure 1B1**) or a corresponding side view (**Figure 1B1′**) with comparable resolution (Kumar et al., 2014). These isotropic 3D volumes enabled us to spatially delineate all hair cells, as well as all surrounding supporting cells (**Figures 1B1,B1′**; **Supplementary Figures S2A1–A1′, B1–B1′, C1–C1′**). Using these isotropic volumes to delineate cells, we observed that the spontaneous calcium activities in hair cells and neighboring supporting cells (quantified from our fast-volumetric calcium imaging) did not coincide. For example, the side-view image in **Figure 1B1′** clearly highlights a hair cell (HC 5) and its three surrounding supporting cells (SC 1–3). By plotting the temporal curves of these four cells (**Figure 1B2**), we found that both hair

cells and the supporting cells were spontaneously active. But the temporal response profile in the hair cell was distinct from its surrounding supporting cells (**Supplementary Figures S2C1–C3**; Pearson's $R = 0.19$, 0.19 and −0.01). Similar results were obtained for other hair cell and supporting-cell pairings in this example (**Supplementary Figures S2A1–B3**). We extended this analysis and calculated the Pearson's correlation coefficients from cell pairings across many developing neuromasts organs (day 3) and overall found no correlation in spontaneous calcium activities between hair cells and surrounding supporting cells (**Figure 1C**, Pearson's $R = -0.04 \pm 0.02$, $n = 4$ neuromasts). In summary, analysis of our two-color functional imaging in hair cells and supporting cells revealed that there was little to no correlation in spontaneous calcium activities between immature hair cells and surrounding supporting cells.

After determining that there was no correlation in spontaneous calcium activities between hair cells and supporting cells, we examined whether there was a correlation among populations of hair cells or supporting cells within neuromast organs. Within a given neuromast, we observed that each hair cell showed distinct response profiles (example, **Figure 1B3**) and the correlation between any two neighboring hair cells was low (example, **Supplementary Figures S2D1–D2**). When we examined spontaneous calcium activity between neighboring hair cells across many developing neuromast organs, quantification revealed little to no correlation (**Figure 1C**, Pearson's $R = 0.28 \pm 0.04$, $n = 6$ neuromasts). In contrast to hair cells, by plotting temporal curves of spontaneous calcium activity from individual supporting cells, we observed clear examples of synchronized activities (examples, **Figure 1B4**; **Supplementary Figures S2D1,D3**). When examining the spontaneous calcium activity between neighboring supporting cells, quantification revealed a relatively high correlation (**Figure 1C**, Pearson's $R = 0.50 \pm 0.03$, $n = 6$ neuromasts). Numerous studies have demonstrated that supporting cells in mammals and zebrafish are electrically coupled via gap junction channels (Kikuchi et al., 2000; Zhang et al., 2018). Therefore, one possible reason for synchronized activities between supporting cells are these gap junction channels. Consistent with this idea, we found that blockage of gap junctions with flufenamic acid (FFA) significantly reduced the correlation in spontaneous calcium activity between neighboring supporting cells (control: Pearson's $R = 0.45 \pm 0.03$; 10 μM FFA: Pearson's $R = 0.08 \pm 0.02$, $n = 4$ neuromasts).

Together, our results suggest that there is no obvious temporal relationship between spontaneous calcium activities in hair cells and supporting cells. Furthermore, distinct temporal properties indicate the source or mechanism underlying these two distinct spontaneous calcium signals may also be different.

P2yr1-ER Signaling Underlies Spontaneous Calcium Activity in Supporting Cells but Not in Hair Cells

In the mammalian auditory system, work has shown that extracellular ATP acting on P2RY1 receptors triggers ER calcium release; this pathway is required for spontaneous calcium activity in supporting cells (Babola et al., 2020; Babola et al., 2021). Therefore, we used pharmacology to investigate whether P2RY1 signaling is required for initiating spontaneous calcium activity in supporting cells within the zebrafish lateral-line system.

For our analyses we measured cytoGCaMP6s signals in supporting cells in developing neuromasts. Using this approach, we found that the application of P2RY1 receptor antagonist MRS2500 significantly reduced the magnitude and frequency of spontaneous cytoGCaMP6s signals in zebrafish supporting cells (example, day 3, **Figures 2A1–A2**; **Supplementary Figures S3A–A′**). This result indicates that P2yr1 is required for spontaneous activity in zebrafish supporting cells. To determine if ER calcium was released downstream of P2ry1 in zebrafish supporting cells, we examined spontaneous calcium activity before and after inhibitors of ER calcium release. For our analysis, we used thapsigargin to block the Sarco/ER calcium ATPase (SERCA). SERCA block prevents reentry of calcium to the ER from the cytosol and ultimately depletes ER calcium stores (Courjaret et al., 2018). After application of thapsigargin, we observed that the baseline cytoGCaMP6s levels increased dramatically in supporting cells within 5 min (example, day 3, **Figures 2C1–C1′**). In addition to changes in baseline calcium, we also observed that the application of thapsigargin dramatically reduced spontaneous calcium activity in supporting cells (example, day 3, **Figure 2C2**).

To further support the idea that ER release from the cytosol acts downstream of P2yr1 receptors, we examined the spatiotemporal properties of spontaneous calcium activity in supporting cells more closely. For our analysis, we imaged supporting cells in cross-section longitudinally. We acquired cytoGCaMP6s signals in a single plane, at a faster image acquisition speed (10 fr/s; in **Figure 2** each volume was acquired in 200 ms every 3 s). We used heat maps to illustrate the spatial increase in calcium signals during a representative spontaneous event (**Supplementary Figure S4A1**). We also plotted the calcium signals at three distinct positions within the cell (**Supplementary Figures S4A2–A4**: top, middle, and bottom). Both the heat maps and plots revealed that spontaneous calcium activity in supporting cells initiates in the upper regions of the cell. These plots revealed that within 0.5 s after initiation, a calcium increase was observed throughout the entire supporting cell, with activity at the top of the cell detected ~300 ms before activity at the bottom of the cell. This apical initiation is interesting because it is the proposed location of the purinergic receptors present in supporting cells within the mammalian auditory system (Babola et al., 2021). In this scenario, the delay in calcium signal at the base of the supporting cell could be due to diffusion of calcium released from the ER at the apex of the cell.

Lastly, we also tested whether P2yr1 or SERCA block altered spontaneous calcium activity in developing hair cells. Using cytoGCaMP6s, we found that P2yr1 block with MRS2500 did not impact spontaneous calcium activity in immature hair cells (example, day 3, **Figures 2B1–B2**; **Supplementary Figures S3B–B′**). Similarly, we examined the impact of SERCA block on spontaneous calcium activity in immature hair cells. We found that neither the baseline calcium (**Figures 2D1–D1′**) nor the

spontaneous calcium signals (**Figure 2D2**) were significantly altered after thapsigargin application. These data indicate that neither P2yr1 receptor function nor ER calcium stores are critical for spontaneous calcium activity in immature hair cells.

Overall, we found that in the zebrafish lateral line, a P2yr1-ER signaling cascade is required for spontaneous calcium activity in supporting cells. While the pharmacological block of P2yr1 or ER calcium stores dramatically blocks spontaneous calcium activity in supporting cells, this same block does not alter spontaneous calcium activity in zebrafish hair cells. These pharmacological results indicate that during development, zebrafish hair cells and supporting cells use distinct mechanisms to generate spontaneous calcium signals. In addition, these results provide further evidence that in the zebrafish lateral line, spontaneous calcium activity in hair cells does not require concomitant activity in surrounding supporting cells.

Two-Color Imaging Reveals No Link Between Spontaneous Activities in Hair Cells and Efferents

If supporting cells do not trigger spontaneous calcium activity in hair cells in zebrafish, then how is this activity generated in developing hair cells? In the developing zebrafish lateral line, cholinergic efferents synapse directly onto immature hair cells (**Figure 3A1**). But whether these efferents are spontaneously active or whether they regulate the spontaneous calcium activity in immature zebrafish lateral-line hair cells is not known.

To measure calcium signals in cholinergic efferents, we used a transgenic line expressing green cytoGCaMP6s (*UAS:cytoGCaMP6s* driven by *chat:Gal4*.) used this transgenic line in combination with a transgenic line expressing red cytoRGECO1 in hair cells (**Figure 3A1**) to monitor calcium activities in these two cell types simultaneously (**Supplementary Movie S5**). Using this approach, we found that in developing neuromast organs, without any external stimuli, the efferent terminals contacting hair cells were spontaneously active (examples, day 3, **Figures 3A1–A2′**; **Supplementary Figures S6A1–A3′**). In addition, we observed that among all efferent terminals within a neuromast, spontaneous calcium activities were highly synchronized (**Supplementary Figure S6B**, Pearson's $R = 0.92 \pm 0.007$, $n = 4$ neuromasts). While the magnitude and frequency of spontaneous calcium activity in efferents terminals was robust during development (day 3), upon lateral-line maturation (day 6) the activity was reduced (**Supplementary Figures S6C–C′**). Because spontaneous calcium activities in both efferent terminals and hair cells were largely restricted to development, we reasoned that these activities could be linked. But when we compared the spontaneous calcium activity in each efferent terminal with its hair cell target, we found no correlation (**Figure 3B**; Pearson's $R = 0.03 \pm 0.02$, $n = 34$ hair cell-efferent terminal pairs). This lack of correlation indicates that cholinergic efferent neurons may not directly trigger spontaneous calcium activity in hair cells.

To further examine the role of cholinergic efferents in hair cell spontaneous activity, we took a pharmacological approach. Cholinergic efferents share a molecular mechanism that is conserved among vertebrate hair cell systems. Acetylcholine released from these efferents acts on α9 or α10 nicotinic acetylcholine receptors (nAChR), which allows calcium to enter near the hair cell presynapse. This calcium influx activates calcium-dependent potassium SK channels leading to hyperpolarization of the hair cell. To determine if this cascade of events impacts hair cell spontaneous activity, we applied α-bungarotoxin (α-Btx) and apamin, compounds that block α9 nAChRs and SK channels respectively. Recent work has shown that these compounds are effective at disrupting efferent neurotransmission onto lateral-line hair cells (Carpaneto Freixas et al., 2021). Because cholinergic signaling is thought to impact the hair cell presynapse, for our analyses we used a membrane-localized indicator memGCaMP6s which we have used previously to specifically measure spontaneous presynaptic calcium activity (Hiu-Tung et al., 2019). We found that neither α-Btx nor apamin impacted spontaneous presynaptic calcium activity in immature hair cells (day 3, **Figures 3C–C′**). Overall, our imaging revealed that both hair cells and efferents have spontaneous calcium activities during development. Further, our two-color imaging and pharmacological results support the conclusion that cholinergic efferents are not required for spontaneous calcium activity in hair cells.

Spontaneous Calcium Activity Occurs in the Mechanosensory Bundle and at the Presynapse

Our two-color calcium imaging (**Figures 1A–C**, **3A1′–A3′**) indicates that in the zebrafish lateral line, neither supporting cells nor cholinergic efferent neurons–two cell types that are spontaneously active and directly contact hair cells–trigger hair cell spontaneous calcium activity. Therefore, we hypothesized that spontaneous calcium activity in hair cells may be generated autonomously. In mature hair cells the main pathway leading to calcium influx are generated in response to sensory stimuli. In response to stimuli, mechanoelectrical transduction (MET) channels open, leading to a cationic influx in the mechanosensory hair bundle that can trigger opening of presynaptic calcium channels at the presynapse (Pickles et al., 1984). (**Figure 4A**). Therefore, one possibility is that spontaneous MET channel activity also triggers opening of presynaptic calcium channels during development.

To measure spontaneous calcium activity in mechanosensory bundles, we used a membrane-localized GECI memGCaMP6s. Previously we have used memGCaMP6s to measure evoked calcium signals in the mechanosensory bundle as well as both evoked and spontaneous calcium influx at the presynapse (Zhang et al., 2018; Hiu-Tung et al., 2019). Using memGCaMP6s, in the absence of mechanical stimuli, we observed robust, spontaneous calcium activity in apical mechanosensory bundles (**Supplementary Movie S6**). We examined spontaneous calcium activity in mechanosensory bundles in immature (day 3) and mature (day 6) hair cells. We found that similar to measurements using cytoGCaMP6s (**Figures 1D–D′**) and memGCaMP6s examining presynaptic activity (Hiu-Tung

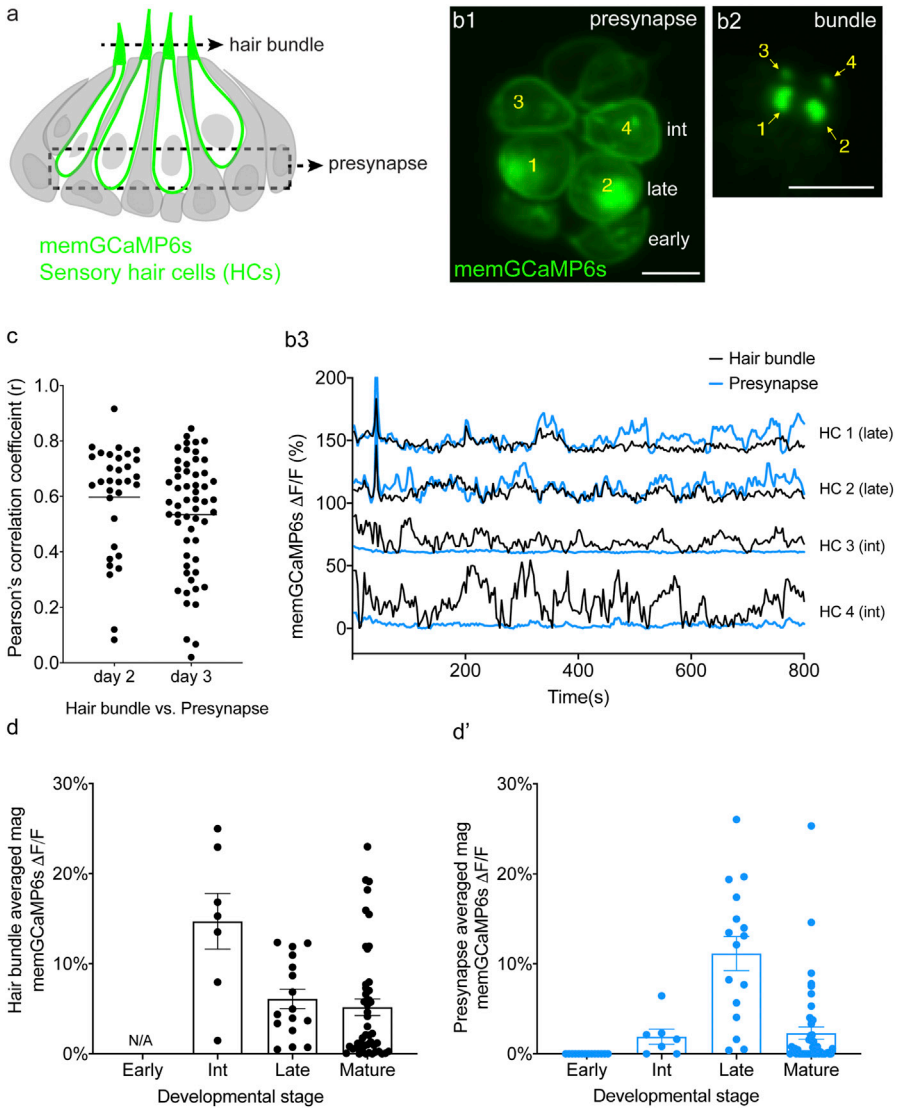

FIGURE 4 | Spontaneous calcium activity occurs in the mechanosensory bundle and at the presynapse. **(A)** Cartoon of a neuromast organ illustrating hair cells (green) expressing memGCaMP6s, surrounded by supporting cells (gray). **(B1)** Image of a representative neuromast showing the hair cell presynaptic region indicated by the dashed box in **(A)** taken from immature hair cells at day 2. Hair cells at three different developmental stages are labeled: early (no detectable hair bundle), intermediate (3, 4), and late (1, 2). **(B2)** An image of the hair bundles from the same cells as **(B1)** through the plane indicated by the dash line in **(A)**. **(B3)** Paired temporal curves of spontaneous calcium activity in hair bundles (**B2** black) and the presynaptic regions (**B1** blue) taken from the same hair cells. **(C)** Pearson's *R* values of spontaneous calcium activity between hair bundles and the presynaptic regions of the same sets of immature hair cells, $n = 32$ hair cells ($n = 6$ neuromasts), day 2 and $n = 56$ hair cells ($n = 6$ neuromasts), day 3. **(D,E)** The average magnitude of spontaneous calcium activity in hair bundles **(D)** and presynaptic region **(E)** in the same set of hair cells during the progressive stages of development: early, intermediate, late and mature. No activity can be measured in early hair bundles (N/A) as the bundles are not yet detectable. The spontaneous calcium activity in hair bundles peaks at the intermediate stage **(D)** and decreases upon maturation, while spontaneous calcium activity in the presynaptic regions peaks at the late stage **(D′)** and decreases upon maturation. Scale bar = 5 μm.

et al., 2019) (**Supplementary Figures S8B–B′**), spontaneous activity in mechanosensory bundles was largely restricted to immature hair cells (**Supplementary Figures S8A–A′**).

By acquiring top-down views of neuromasts, we were able to isolate and simultaneously measure activities in both a basal, presynaptic plane (example, **Figures 4B1–B3**) and an apical mechanosensory bundle plane (example, **Figure 4B2**) within the same hair cells. When we examined individual hair cells, in many cases, we found that the spontaneous calcium activity in each apical mechanosensory bundle and its respective presynaptic region were highly correlated (example, **Figure 4B3**, see HC 1 and HC 2). In other cases, we observed hair cells with spontaneous calcium activity in the mechanosensory bundle but not in the presynaptic region (example, **Figure 4B3**, see HC 3 and HC 4). On average, the correlation in spontaneous calcium activity at the apex and the base of individual hair cells was high in immature hair cells (**Figure 4C**, day 2, Pearson's $R = 0.60 \pm 0.035$, $n = 32$ hair cells;

day 3 Pearson's $R = 0.54 \pm 0.027$, $n = 56$ hair cells). This relatively high correlation indicates that spontaneous calcium activity at the presynaptic region may be driven by or be related to spontaneous calcium activity in the mechanosensory bundle.

Although there was an overall high correlation between spontaneous calcium activity in these two regions, we observed two distinct spontaneous activity profiles: 1) cells with synchronized spontaneous activity in the mechanosensory bundle and at the presynapse and 2) cells with spontaneous activity in the mechanosensory bundle with no accompanying activity at the presynapse. We looked more closely at individual hair cells at different stages of development to understand why there were two distinct profiles. For our analysis we examined neuromasts at day 2 when there are hair cells at different developmental stages. Previous work has demonstrated that in the lateral line, hair cell stage can be estimated by measuring the height of the tallest structure in the mechanosensory bundle, the kinocilium (Stage- hair bundle height: early- not detectable; intermediate- 1–10 μm; late- > 10 < 18 μm; mature- >18 μm. Lateral-line hair cells take roughly 20 h to complete this maturation) (Kindt et al., 2012; Dow et al., 2018). Overall, using this staging, we found that spontaneous calcium activity in both the mechanosensory bundle and the presynaptic compartment increased in strength during development and decreased upon hair cell maturation (**Figures 4D–D′**). In addition, we observed that spontaneous calcium activity in the mechanosensory bundle peaked at an earlier development stage compared to activity at the presynapse (**Figures 4D–D′**). Further, in younger hair cells, we observed spontaneous calcium activity in mechanosensory bundles but not in the presynaptic compartment (labeled as "int" in **Figure 4B1**; see HC 3 and HC 4 in **Figures 4B1–B3**). In slightly more mature hair cells, we observed spontaneous calcium activity in both the mechanosensory bundle and the presynapse (labeled as "late" in **Figure 4B1**; see HC 1 and HC2 in **Figures 4B1–B3**). At this relatively more mature stage, activity in the mechanosensory bundle and at the presynapse were highly correlated (see HC 1 and HC2 in **Figures 4B1–B3**). Thus, a differential onset in spontaneous activity (mechanosensory bundle preceding the presynapse) resulted in two distinct spontaneous activity profiles.

Overall, by measuring calcium activities at the membrane, we demonstrate for the first time that spontaneous calcium activity is present in both apical mechanosensory bundles and basal presynaptic compartments *in vivo*. At early stages of hair cell development, spontaneous calcium activity is present in mechanosensory bundles but not at the presynapse. At late stages of hair cell development spontaneous activity is present in both the mechanosensory bundle and the presynapse, and these activities are highly correlated.

$Ca_V1.3$ Channels are Required for Spontaneous Presynaptic- But Not Hair Bundle-Activity

Our memGCaMP6s-based calcium imaging indicates that spontaneous activity in immature hair cells occurs in two distinct subcellular compartments. But how these signals are initiated in lateral-line hair cells remained unclear. In the zebrafish lateral line, $Ca_V1.3$, a L-type calcium channel is required for calcium influx at the hair cell presynapse (Hiu-Tung et al., 2019). Therefore, we used both genetics and pharmacology to examine whether $Ca_V1.3$ channels are required for spontaneous calcium activity in hair cells of the lateral line.

For our analyses, we examined activity in *$ca_V1.3a$* zebrafish mutants and in wildtype animals after treatment with isradipine, a $Ca_V1.3$ channel antagonist. Both of these manipulations have been shown to block evoked presynaptic calcium influx in zebrafish hair cells (Sheets et al., 2012; Zhang et al., 2018). To measure spontaneous calcium activity, we used memGCaMP6s to detect signals in the mechanosensory bundle and at the presynapse. We found that in *$ca_V1.3a$* mutants or after acute block of $Ca_V1.3$ channels with isradipine, spontaneous calcium activity in the mechanosensory bundle was not significantly changed compared to controls (**Figures 5A–D**; **Supplementary Figures S9A–B′**). However, we found that spontaneous calcium activity occurring at the hair cell presynapse was abolished in *$ca_v1.3a$* mutants (**Figures 5E–G**; **Supplementary Figures S9C–D′**) and after isradipine treatment (**Figure 5H**; **Supplementary Figures S9C–D′**). Together these manipulations indicate that spontaneous calcium activity can occur in the mechanosensory bundle without accompanying activity at the presynapse. Furthermore, they demonstrate that while $Ca_v1.3$ channels are not required for spontaneous calcium activity in mechanosensory bundles, they are essential for spontaneous calcium activity at the presynapse.

Mechanotransduction in Hair Bundles Is Required for Spontaneous Activity at the Presynapse

Our functional calcium imaging indicates that spontaneous calcium activity at the presynapse, when present, occurs concomitantly with activity in the mechanosensory bundle (**Figure 4C**). Additionally, in mature hair cells, evoked activity opens MET channels leading to an influx of cations, including calcium, that triggers opening of $Ca_V1.3$ channels at the presynapse (Bechstedt and Howard, 2007). Therefore, we hypothesized that the spontaneous opening of MET channels in mechanosensory bundles might trigger activity at the presynapse. To test this hypothesis, we used genetics and pharmacology to determine whether MET channel function is required to trigger spontaneous calcium activity at the presynapse of immature hair cells.

For our genetic analysis, we used the zebrafish mutants lacking Protocadherin 15a (PCDH15), a core component of hair cell tip-link, a structure required to gate MET channels in mature hair cells (Seiler et al., 2005) (**Figure 6A**). For our pharmacological analysis, we applied BAPTA, an extracellular calcium chelator that breaks tip links and acutely disrupts MET channel function. We found that MET channel disruption in *pcdh15a* mutants or after BAPTA treatment significantly reduced spontaneous calcium activity in mechanosensory bundles (**Figures 6A–D**; **Supplementary Figures S10A–B′**). This indicates that in the lateral line, both evoked calcium activity in mature

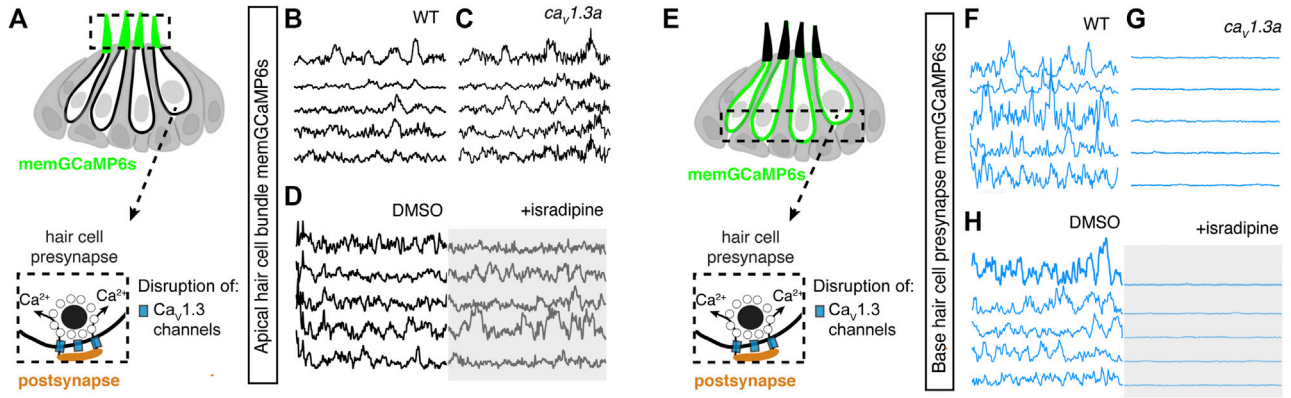

FIGURE 5 | Spontaneous calcium activity at the presynapse requires $Ca_V1.3$ channels. **(A)** Diagram illustrating the hair cells with the hair bundles highlighted by a dashed box where we measure their spontaneous calcium activity. The structure of a single ribbon synapse at the base of a hair cell is illustrated, as well as the calcium channels beneath it. **(B–D)** Representative memGCaMP6s temporal traces show that disruption of $Ca_V1.3a$ channels using *cav1.3a* mutants **(B,C)** or pharmacological block using 10 μM isradipine **(D)** does not impact spontaneous activity in apical hair bundles. **(E)** Diagram illustrating the hair cells with the presynaptic area highlighted by a dashed box where we measure the spontaneous presynaptic calcium activity. **(F–H)** Representative memGCaMP6s temporal traces show that disruption of calcium channels using *cav1.3a* mutants **(F–G)** or pharmacological block using 10 μM isradipine **(H)** completely blocked spontaneous activity at the hair cell presynapse. All measurements were performed in immature hair cells at day 3.

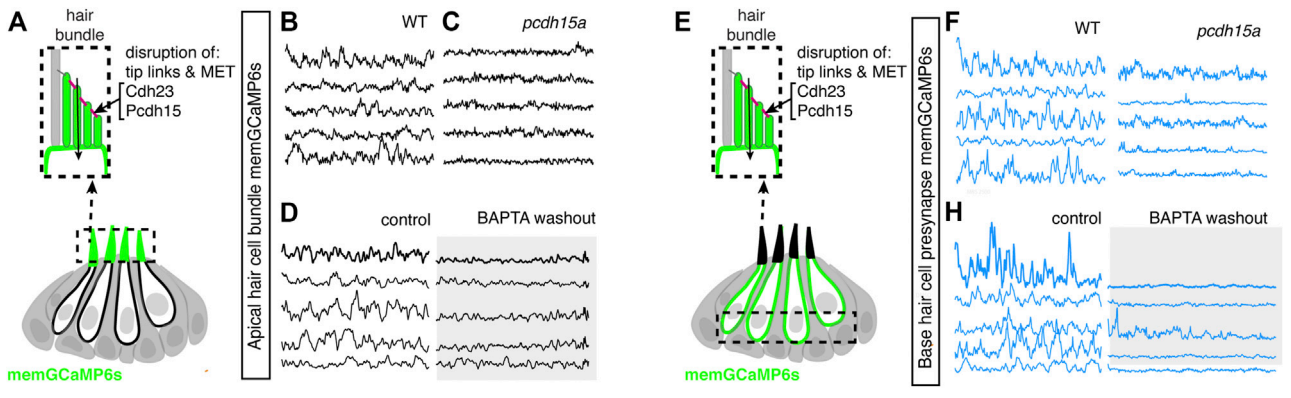

FIGURE 6 | Mechanotransduction in hair bundles is required for spontaneous activity at the presynapse. **(A)** Diagram illustrating the hair cells with the hair bundles highlighted by a dashed box where we measure their spontaneous calcium activity. The structure of the hair bundle from a single hair cell at is illustrated on top. The mechanotransduction (MET) channels are gated by tip links made up of Pcdh15a Cdh23. Pharmacological application of BAPTA, an extracellular calcium chelator, breaks tip links and acutely disrupts MET function. **(B–D)** Representative GCaMP6s temporal traces show that disruption of tip links using *pcdh15a* mutants **(B,C)** or by pharmacologically disrupting tip links using BAPTA **(D)** disrupts spontaneous activity in hair bundles. **(E)** Diagram illustrating the hair cells with the hair cell presynaptic area highlighted by a dashed box at the base of the hair cells where we measure the spontaneous presynaptic calcium activity. **(E–H)** Representative GCaMP6s temporal traces show that disruption of tip links using *pcdh15a* mutants **(F–G)** or by pharmacologically disrupting tip links using BAPTA **(H)** also disrupts spontaneous calcium activity at the presynapse. All measurements were performed in immature hair cells at day 3.

mechanosensory bundles and spontaneous calcium activity in developing mechanosensory bundles depends on MET function. Importantly, we found MET channel disruption also dramatically blocked spontaneous calcium activity at the hair cell presynapse (**Figures 6E–H**; **Supplementary Figures S9C–D′**). After our manipulations we did observe some residual spontaneous calcium activity in the mechanosensory bundle and at the presynapse, which may reflect incomplete block of MET channel function. Overall, this result indicates that spontaneous activity at the presynapse is primarily driven by the spontaneous opening of MET channels. Thus, it is spontaneous MET that generates spontaneous calcium activity at the presynapse, in order to shape synapse formation and propagate information downstream to the developing sensory system.

DISCUSSION

In this work, we show that zebrafish can be used as an *in vivo* model to study spontaneous activity in developing hair cell sensory systems. The origin and role of spontaneous activity in hair cell systems is an important area of research in sensory neuroscience. Our work uses genetics, pharmacology, GECIs

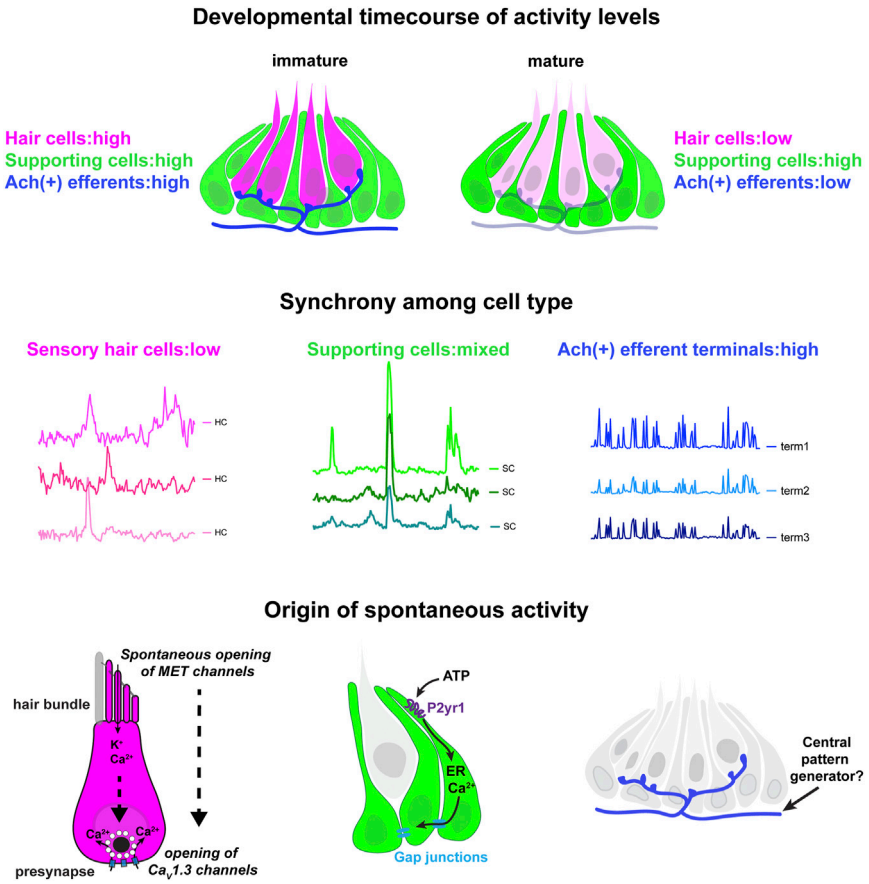

FIGURE 7 | Locations, mechanisms and developmental timecourse of spontaneous calcium activities in the lateral-line system. Top panel: we reliably detected spontaneous calcium activity in three cell types within the lateral-line system: hair cells, supporting cells and cholinergic (Ach (+)) efferent neurons. Spontaneous calcium activity in the supporting cells and cholinergic efferents is not correlated with calcium signals in hair cells. During development spontaneous calcium signals are robust in all three cell types (left side). Upon maturation, spontaneous calcium signals are decreased in hair cells and efferent neurons, but maintained in supporting cells (right side). Middle panel: Within a neuromast spontaneous calcium signals among populations of hair cells are not correlated (left side); supporting cells are moderately correlated (middle); cholinergic terminals are highly correlated (right side). Bottom panel: In developing hair cells, spontaneous opening of MET channels leads to calcium signals in mechanosensory hair bundles. This apical activity triggers opening of $Ca_V1.3$ channels at the presynapse, resulting in spontaneous presynaptic calcium signals (left side). In supporting cells, extracellular ATP acts on P2yr1 receptors. P2yr1 signaling leads to calcium release from the ER, giving rise to a spontaneous calcium signal. Spontaneous calcium signals can be propagated to neighboring supporting cells via gap junction channels (middle). Spontaneous activity in cholinergic efferents may be coupled to activity in spinal motor neurons that is present during development in order to form the central pattern generator required for locomotion (right side).

along with cutting-edge LSFM to image and characterize spontaneous calcium activity in the lateral-line system. We find that spontaneous activity is present in hair cells, supporting cells and efferent terminals–spontaneous activity in each cell type occurs with largely distinct developmental, temporal and mechanistic origins (**Figure 7**). Overall, our work demonstrates that the lateral line presents a robust model to study many facets of spontaneous activity, all within an intact sensory system.

The Origin of Spontaneous Calcium Activity in the Zebrafish Hair Cells

In our study on the zebrafish lateral line, we find that spontaneous calcium signals occur autonomously in hair cells. In support of this finding, we show that hair cell spontaneous activity is still intact when supporting cell spontaneous activity is blocked (Block P2ry1 receptors or ER calcium release, **Figure 2**; **Supplementary Figure S3**) or when the cholinergic receptors on hair cells are blocked (Block α9 nAChRs, **Figures 3C–C′**). This indicates, that in the zebrafish lateral line, neither supporting cells nor efferent neurons have a striking impact on spontaneous calcium activity in developing hair cells.

Based on our work we hypothesize that the spontaneous calcium signals we observe in lateral-line hair cells are analogous to the uncoordinated calcium signals that have been observed in the developing auditory and vestibular systems of mice (Eckrich et al., 2018; Holman et al., 2019). In mice these calcium signals have been visualized using either cytosolic GECIs or calcium dyes, or by recording calcium action potentials using electrophysiology. Our work uses both a cytosolic GECI (cytoGCaMP6s) as well as a membrane-localized GECI

(memGCaMP6s) to visualize spontaneous calcium signals in lateral-line hair cells (**Figures 1**, **4**). Importantly, using memGCaMP6s, we find that spontaneous activity within hair cells occurs in two spatially distinct domains–the mechanosensory bundle and the presynapse (**Figure 4**). Using memGCaMP6s in lateral-line hair cells, we find that $Ca_V1.3$ channels, present at the developing presynapse, are essential for spontaneous presynaptic calcium signals (**Figures 5E–H**; **Supplementary Figures S9C–D′**). Importantly, both work in mice and zebrafish indicates that during development, $Ca_V1.3$-dependent, presynaptic calcium activity is critical for proper hair cell synapse formation.

Interesting, our work found that disrupting $Ca_V1.3$ channel function did not alter spontaneous calcium activity in mechanosensory bundles. This result supports the idea that spontaneous calcium activity in mechanosensory bundles occurs upstream of activity at the presynapse. In support of this idea, we found that 1) activity in these two domains is highly correlated (**Figures 4B3–C**) 2) at the earliest stages of hair cell development spontaneous activity was present in mechanosensory bundles but not at the presynapse (**Figures 4B3, D–D′**) and 3) blocking MET channel function significantly reduced spontaneous calcium activity at the presynapse (**Figures 6E–H**; **Supplementary Figures S10C–D′**). Together our results show that in developing lateral-line hair cells, MET activity initiates autonomously generated spontaneous events. Further, this activity in hair bundles triggers presynaptic calcium influx. Work in mice has shown that MET activity in developing hair cells is important for hair cell survival, hair cell synapse maintenance, and for the proper maturation of hair cells, afferent neurons and efferent neurons (Marcotti et al., 2006; Corns et al., 2018; Sun et al., 2018). Therefore, during development, spontaneous MET function in the mechanosensory bundle likely plays many important roles.

The Origin and Role of Spontaneous Calcium Activity in the Zebrafish Supporting Cells

Together, our study in zebrafish along with work in mammals demonstrates that spontaneous calcium signals in supporting cells are a conserved feature among hair cell systems (**Figures 1B1–B1′, B4**) (Tritsch et al., 2007; Holman et al., 2019). Unlike the mouse auditory system, in the lateral line, waves of spontaneous activity in supporting cells did not propagate across neuromast organs. Interestingly, we did observe that activity between neighboring supporting cells was coupled in the lateral line (**Figures 1B4–C**; **Supplementary Figures S2D1,D3**). The level of coupling was higher in the outer most layer of supporting cells (mantle cells) compared to the more central supporting cells (**Supplementary Figures S5A–B**). In the future it will be interesting to examine spontaneous activity in these different subsets of supporting cells to understand the role of this activity.

Our findings indicate that the molecular pathway required to trigger spontaneous calcium signals in supporting cells may also be conserved between mammals and zebrafish. Our work in zebrafish indicates a P2yr1 signaling cascade leads to calcium release from the ER; this calcium release gives rise to the spontaneous calcium signals in lateral-line supporting cells (**Figures 2A1,A2,C1,C2**). This is consistent with recent work on supporting cells in the mouse auditory epithelium (Babola et al., 2020). Further, studies have shown that application of ATP evokes calcium signals in supporting cells within the auditory and vestibular epithelium–these signals also require ER calcium release (Dulon et al., 1993; Tritsch et al., 2007; Holman et al., 2019). Together these studies point towards a conserved P2-ER calcium axis that drives calcium signals in the supporting cells of hair cell epithelia. In the future, by using GECIs along with ATP sensors (Lobas et al., 2019) and two-color imaging, the zebrafish lateral line presents a useful model to study the dynamics of calcium and ATP *in vivo* during spontaneous events.

Although the molecular cascade giving rise to calcium signals in supporting cells appears largely conserved among hair cell systems, we did observe one striking difference in the lateral-line system. While spontaneous activity in supporting cells is transient in the mouse auditory and vestibular systems, it remains robust and constant in zebrafish lateral-line organs, even after the system is mature (**Figures 1E–E′**). The retention of spontaneous activity in supporting cells in the zebrafish lateral line after maturation could also be related to another difference between hair cell systems in zebrafish (and other nonmammalian vertebrates) and mammals–the ability to regenerate hair cells (Corwin and Warchol, 1991; Thomas and Raible, 2019). For example, in zebrafish, after hair cell loss, supporting cells proliferate to give rise to new hair cells–a process that happens rarely in mature hair cell systems in mammals. The retention of spontaneous calcium signals in zebrafish supporting cells may be important to trigger gene expression required for cell proliferation during regeneration. In this scenario, the retention of spontaneous activity in supporting cells could reflect a feature of their innate regenerative capacity.

The Origin and Role of Spontaneous Calcium Activity in Zebrafish Cholinergic Efferents

Our work demonstrates that cholinergic efferents in the lateral-line system are spontaneously active (**Figures 3A1–A2′**; **Supplementary Figures S6A1–A2′**). In addition, spontaneous activity in cholinergic efferents is stronger during development, indicating it may play a vital developmental role (**Supplementary Figures S6C–C′**). Numerous studies have investigated the role of cholinergic efferents in mature hair cell systems. In this context, cholinergic efferents are inhibitory, either through contacts with hair cells (outer auditory hair cells, type II vestibular hair cells, lateral-line hair cells) or afferents terminals (inner auditory hair cells, type I vestibular hair cells) (Housley and Ashmore, 1991; Lunsford et al., 2019; Poppi et al., 2020). But what role these efferents play during development is less clear. Our study suggests the activity of cholinergic efferents does not directly influence or trigger spontaneous calcium activity in immature lateral-line hair cells (**Figures 3C–C′**). It is possible that under the native conditions present within our system, the amount of acetylcholine released from the efferent fibers is not sufficient to alter hair cell calcium to a level detectable using GECIs. It is also possible that acetylcholine may act on supporting cells, other efferent

neurons, or afferents neurons in the developing lateral line. In the future it will be important examine the impact and target of cholinergic efferent neurons in the lateral line more closely, in the context of development.

In addition to studies focused on the periphery, work in mice has shown that hair cell spontaneous activity is mirrored downstream, in the central auditory pathway. Furthermore, spontaneous activity from each ear is patterned centrally, in a bilateral manner. Recent work has shown that cholinergic efferent neurons are required to ensure that spontaneous activity is patterned in a bilateral manner (Babola et al., 2021). In our work, we demonstrated that spontaneous activity is highly correlated at all efferent terminals within a neuromast. We also found that correlated activity in the cholinergic efferent (likely the same fiber) extends to multiple neuromasts along one side of the fish body (**Supplementary Figures S7A,B**). Therefore, it is possible that cholinergic efferents may regulate hair cell or afferent spontaneous activity in a manner that is bilateral (left versus right side of the fish body). In the future it will be interesting to develop methods to image activity from cholinergic efferents innervating each side of the zebrafish body. In addition, it will be interesting to determine how hair cell spontaneous activity is reflected in the brain, and whether cholinergic efferents impact the patterning of this activity more centrally.

Could cholinergic efferents pattern bilaterality? Recent work has shown in mature zebrafish larvae, during swimming cholinergic efferents are synchronously active with spinal motor neurons (Lunsford et al., 2019). Therefore, one possibility is that during development, spontaneous activity in cholinergic efferents may also reflect the activity of spinal motor neurons. During spinal cord development, the central pattern generator (CPG) is established, in order to create the oscillatory rhythms needed for locomotion (Grillner et al., 1998). As part of CPG maturation, a rhythmic alternation between the two sides of the spinal cord is established. This motor prerequisite to swimming behavior may also synchronize with spontaneous activity in cholinergic efferents of the lateral line. If the cholinergic efferents set up bilateral patterning of the lateral line, tapping into the activity of the developing spinal motor neurons and the CPG is a viable way for this to occur (**Figure 7**).

In summary our work provides a comprehensive characterization of spontaneous activity in the zebrafish lateral line. Using LSFM we demonstrate that in neuromast organs, spontaneous activity is present in hair cells, supporting cells and cholinergic efferent terminals. Within the lateral-line, each of these activities may play unique roles in sensory system function, development, maintenance, regeneration, and response to damage. Exploring the role of these spontaneous activities in these important biological contexts will make for exciting future work.

DATA AVAILABILITY STATEMENT

The raw data supporting the conclusion of this article will be made available by the authors, without undue reservation. Matlab R2020a used to process functional imaging data and the code is available upon request.

ETHICS STATEMENT

The animal study was reviewed and approved by Animal Use Committee at the National Institute of Health-approved under animal study protocol #1362-13.

AUTHOR CONTRIBUTIONS

QZ and KK conceived and planned the experiments and contributed to the interpretation of the results. QZ carried out the experiments and analyses. QZ and KK wrote the manuscript.

FUNDING

This work was supported by a National Institute on Deafness and Other Communication Disorders (NIDCD) Intramural Research Program Grant 1ZIADC000085-01 (KSK).

ACKNOWLEDGMENTS

We thank Hari Shroff, Harshad Vishwasrao, Min Guo and Jiji Chen from NIBIB for help constructing our diSPIM system. We acknowledge Alisha Beirl for helping to make the *she:GCaMP6s* and *myo6b:GCaMP6s* transgenic lines. We thank Nathan Lawson and Tatjana Piotrowski for providing the *she* promoter and Jennifer Li for sending the *chat:Gal4;UAS:GCaMP6s* transgenic line. We would also like to thank Osama Hamdi for his contribution to early Matlab analyses of spontaneous calcium activities. We thank Lavinia Sheets, Cat Weisz and Juan Angueyra for thoughtful comments on the manuscript. This work corresponds to the bioRxiv preprint doi: https://doi.org/10.1101/2021.11.23.469686.

SUPPLEMENTARY MATERIAL

The Supplementary Material for this article can be found online at: https://www.frontiersin.org/articles/10.3389/fcell.2022.819612/full#supplementary-material

REFERENCES

Arganda-Carreras, I., Sorzano, C. O., Marabini, R., Carazo, J. M., Ortiz-De-Solorzano, C., and Kybic, J. (2006). "Consistent and Elastic Registration of Histological Sections Using Vector-Spline Regularization," in *International Workshop on Computer Vision Approaches to Medical Image Analysis* (Springer), 85–95.

Babola, T. A., Kersbergen, C. J., Wang, H. C., and Bergles, D. E. (2020). Purinergic Signaling in Cochlear Supporting Cells Reduces Hair Cell Excitability by Increasing the Extracellular Space. *Elife* 9, e52160. doi:10.7554/eLife.52160

Babola, T. A., Li, S., Wang, Z., Kersbergen, C. J., Elgoyhen, A. B., Coate, T. M., et al. (2021). Purinergic Signaling Controls Spontaneous Activity in the Auditory System throughout Early Development. *J. Neurosci.* 41, 594–612. doi:10.1523/jneurosci.2178-20.2020

Bechstedt, S., and Howard, J. (2007). Models of Hair Cell Mechanotransduction. *Curr. Top. membranes* 59, 399–424. doi:10.1016/s1063-5823(06)59015-5

Carpaneto Freixas, A. E., Moglie, M. J., Castagnola, T., Salatino, L., Domene, S., Marcovich, I., et al. (2021). Unraveling the Molecular Players at the Cholinergic Efferent Synapse of the Zebrafish Lateral Line. *J. Neurosci.* 41, 47–60. doi:10.1523/jneurosci.1772-20.2020

Ceriani, F., Hendry, A., Jeng, J. Y., Johnson, S. L., Stephani, F., Olt, J., et al. (2019). Coordinated Calcium Signalling in Cochlear Sensory and Non-sensory Cells Refines Afferent Innervation of Outer Hair Cells. *EMBO J.* 38. doi:10.15252/embj.201899839

Clause, A., Kim, G., Sonntag, M., Weisz, C. J. C., Vetter, D. E., Rűbsamen, R., et al. (2014). The Precise Temporal Pattern of Prehearing Spontaneous Activity Is Necessary for Tonotopic Map Refinement. *Neuron* 82, 822–835. doi:10.1016/j.neuron.2014.04.001

Corns, L. F., Johnson, S. L., Roberts, T., Ranatunga, K. M., Hendry, A., Ceriani, F., et al. (2018). Mechanotransduction Is Required for Establishing and Maintaining Mature Inner Hair Cells and Regulating Efferent Innervation. *Nat. Commun.* 9, 4015. doi:10.1038/s41467-018-06307-w

Corwin, J. T., and Warchol, M. E. (1991). Auditory Hair Cells: Structure, Function, Development, and Regeneration. *Annu. Rev. Neurosci.* 14, 301–333. doi:10.1146/annurev.ne.14.030191.001505

Courjaret, R., Dib, M., and Machaca, K. (2018). Spatially Restricted Subcellular Ca2+ Signaling Downstream of Store-Operated Calcium Entry Encoded by a Cortical Tunneling Mechanism. *Sci. Rep.* 8, 11214. doi:10.1038/s41598-018-29562-9

Dow, E., Jacobo, A., Hossain, S., Siletti, K., and Hudspeth, A. J. (2018). Connectomics of the Zebrafish's Lateral-Line Neuromast Reveals Wiring and Miswiring in a Simple Microcircuit. *Elife* 7, e33988. doi:10.7554/eLife.33988

Dulon, D., Moataz, R., and Mollard, P. (1993). Characterization of Ca2+ Signals Generated by Extracellular Nucleotides in Supporting Cells of the Organ of Corti. *Cell Calcium* 14, 245–254. doi:10.1016/0143-4160(93)90071-d

Eckrich, T., Blum, K., Milenkovic, I., and Engel, J. (2018). Fast Ca2+ Transients of Inner Hair Cells Arise Coupled and Uncoupled to Ca2+ Waves of Inner Supporting Cells in the Developing Mouse Cochlea. *Front. Mol. Neurosci.* 11, 264. doi:10.3389/fnmol.2018.00264

Edelstein, A., Amodaj, N., Hoover, K., Vale, R., and Stuurman, N. (2010). Computer Control of Microscopes Using μManager. *Curr. Protoc. Mol. Biol.* 14. Unit14 20. doi:10.1002/0471142727.mb1420s92

Förster, D., Arnold-Ammer, I., Laurell, E., Barker, A. J., Fernandes, A. M., Finger-Baier, K., et al. (2017). Genetic Targeting and Anatomical Registration of Neuronal Populations in the Zebrafish Brain with a New Set of BAC Transgenic Tools. *Sci. Rep.* 7, 5230. doi:10.1038/s41598-017-04657-x

Glowatzki, E., and Fuchs, P. A. (2000). Cholinergic Synaptic Inhibition of Inner Hair Cells in the Neonatal Mammalian Cochlea. *Science* 288, 2366–2368. doi:10.1126/science.288.5475.2366

Grillner, S., EkebergEl Manira, Ö., El Manira, A., Lansner, A., Parker, D., Tegnér, J., et al. (1998). Intrinsic Function of a Neuronal Network - a Vertebrate central Pattern Generator. *Brain Res. Rev.* 26, 184–197. doi:10.1016/s0165-0173(98)00002-2

Guo, M., Li, Y., Su, Y., Lambert, T., Nogare, D. D., Moyle, M. W., et al. (2020). Rapid Image Deconvolution and Multiview Fusion for Optical Microscopy. *Nat. Biotechnol.* 38, 1337–1346. doi:10.1038/s41587-020-0560-x

Holman, H. A., Poppi, L. A., Frerck, M., and Rabbitt, R. D. (2019). Spontaneous and Acetylcholine Evoked Calcium Transients in the Developing Mouse Utricle. *Front. Cel. Neurosci.* 13, 186. doi:10.3389/fncel.2019.00186

Housley, G. D., and Ashmore, J. F. (1991). Direct Measurement of the Action of Acetylcholine on Isolated Outer Hair Cells of the guinea Pig Cochlea. *Proc. Biol. Sci.* 244, 161–167. doi:10.1098/rspb.1991.0065

Jiang, T., Kindt, K., and Wu, D. K. (2017). Transcription Factor Emx2 Controls Stereociliary Bundle Orientation of Sensory Hair Cells. *Elife* 6, e23661. doi:10.7554/eLife.23661

Katz, E., Elgoyhen, A. B., Gomez-Casati, M. E., Knipper, M., Vetter, D. E., Fuchs, P. A., et al. (2004). Developmental Regulation of Nicotinic Synapses on Cochlear Inner Hair Cells. *J. Neurosci.* 24, 7814–7820. doi:10.1523/jneurosci.2102-04.2004

Kikuchi, T., Kimura, R. S., Paul, D. L., Takasaka, T., and Adams, J. C. (2000). Gap junction Systems in the Mammalian Cochlea. *Brain Res. Rev.* 32, 163–166. doi:10.1016/s0165-0173(99)00076-4

Kindt, K. S., Finch, G., and Nicolson, T. (2012). Kinocilia Mediate Mechanosensitivity in Developing Zebrafish Hair Cells. *Developmental Cel.* 23, 329–341. doi:10.1016/j.devcel.2012.05.022

Kumar, A., Wu, Y., Christensen, R., Chandris, P., Gandler, W., Mccreedy, E., et al. (2014). Dual-view Plane Illumination Microscopy for Rapid and Spatially Isotropic Imaging. *Nat. Protoc.* 9, 2555–2573. doi:10.1038/nprot.2014.172

Kwan, K. M., Fujimoto, E., Grabher, C., Mangum, B. D., Hardy, M. E., Campbell, D. S., et al. (2007). The Tol2kit: A Multisite Gateway-Based Construction Kit forTol2 Transposon Transgenesis Constructs. *Dev. Dyn.* 236, 3088–3099. doi:10.1002/dvdy.21343

Leighton, A. H., and Lohmann, C. (2016). The Wiring of Developing Sensory Circuits-From Patterned Spontaneous Activity to Synaptic Plasticity Mechanisms. *Front. Neural Circuits* 10, 71. doi:10.3389/fncir.2016.00071

Lobas, M. A., Tao, R., Nagai, J., Kronschläger, M. T., Borden, P. M., Marvin, J. S., et al. (2019). A Genetically Encoded Single-Wavelength Sensor for Imaging Cytosolic and Cell Surface ATP. *Nat. Commun.* 10, 711. doi:10.1038/s41467-019-08441-5

Lukasz, D., and Kindt, K. S. (2018). *In Vivo* Calcium Imaging of Lateral-Line Hair Cells in Larval Zebrafish. *J. Vis. Exp.* 141. doi:10.3791/58794

Lunsford, E. T., Skandalis, D. A., and Liao, J. C. (2019). Efferent Modulation of Spontaneous Lateral Line Activity during and after Zebrafish Motor Commands. *J. Neurophysiol.* 122, 2438–2448. doi:10.1152/jn.00594.2019

Maeda, R., Kindt, K. S., Mo, W., Morgan, C. P., Erickson, T., Zhao, H., et al. (2014). Tip-link Protein Protocadherin 15 Interacts with Transmembrane Channel-like Proteins TMC1 and TMC2. *Proc. Natl. Acad. Sci.* 111, 12907–12912. doi:10.1073/pnas.1402152111

Marcotti, W., Erven, A., Johnson, S. L., Steel, K. P., and Kros, C. J. (2006). Tmc1is Necessary for normal Functional Maturation and Survival of Inner and Outer Hair Cells in the Mouse Cochlea. *J. Physiol.* 574, 677–698. doi:10.1113/jphysiol.2005.095661

Marcotti, W., Johnson, S. L., Rüsch, A., and Kros, C. J. (2003). Sodium and Calcium Currents Shape Action Potentials in Immature Mouse Inner Hair Cells. *J. Physiol.* 552, 743–761. doi:10.1113/jphysiol.2003.043612

Obholzer, N., Wolfson, S., Trapani, J. G., Mo, W., Nechiporuk, A., Busch-Nentwich, E., et al. (2008). Vesicular Glutamate Transporter 3 Is Required for Synaptic Transmission in Zebrafish Hair Cells. *J. Neurosci.* 28, 2110–2118. doi:10.1523/jneurosci.5230-07.2008

Parslow, A., Cardona, A., and Bryson-Richardson, R. J. (2014). Sample Drift Correction Following 4D Confocal Time-Lapse Imaging. *J. visualized experiments: JoVE*. doi:10.3791/51086

Pickles, J. O., Comis, S. D., and Osborne, M. P. (1984). Cross-links between Stereocilia in the guinea Pig Organ of Corti, and Their Possible Relation to Sensory Transduction. *Hearing Res.* 15, 103–112. doi:10.1016/0378-5955(84)90041-8

Poppi, L. A., Holt, J. C., Lim, R., and Brichta, A. M. (2020). A Review of Efferent Cholinergic Synaptic Transmission in the Vestibular Periphery and its Functional Implications. *J. Neurophysiol.* 123, 608–629. doi:10.1152/jn.00053.2019

Quillien, A., Abdalla, M., Yu, J., Ou, J., Zhu, L. J., and Lawson, N. D. (2017). Robust Identification of Developmentally Active Endothelial Enhancers in Zebrafish Using FANS-Assisted ATAC-Seq. *Cel Rep.* 20, 709–720. doi:10.1016/j.celrep.2017.06.070

Quirin, S., Vladimirov, N., Yang, C.-T., Peterka, D. S., Yuste, R., and B. Ahrens, M. (2016). Calcium Imaging of Neural Circuits with Extended Depth-Of-Field Light-Sheet Microscopy. *Opt. Lett.* 41, 855–858. doi:10.1364/ol.41.000855

Raible, D. W., and Kruse, G. J. (2000). Organization of the Lateral Line System in Embryonic Zebrafish. *J. Comp. Neurol.* 421, 189–198. doi:10.1002/(sici)1096-9861(20000529)421:2<189::aid-cne5>3.0.co;2-k

Schneider, C. A., Rasband, W. S., and Eliceiri, K. W. (2012). NIH Image to ImageJ: 25 Years of Image Analysis. *Nat. Methods* 9, 671–675. doi:10.1038/nmeth.2089

Seiler, C., Finger-Baier, K. C., Rinner, O., Makhankov, Y. V., Schwarz, H., Neuhauss, S. C. F., et al. (2005). Duplicated Genes with Split Functions: Independent Roles Ofprotocadherin15orthologues in Zebrafish Hearing and Vision. *Development* 132, 615–623. doi:10.1242/dev.01591

Sheets, L., Kindt, K. S., and Nicolson, T. (2012). Presynaptic CaV1.3 Channels Regulate Synaptic Ribbon Size and Are Required for Synaptic Maintenance in Sensory Hair Cells. *J. Neurosci.* 32, 17273–17286. doi:10.1523/jneurosci.3005-12.2012

Sidi, S., Busch-Nentwich, E., Friedrich, R., Schoenberger, U., and Nicolson, T. (2004). Gemini Encodes a Zebrafish L-type Calcium Channel that Localizes at Sensory Hair Cell Ribbon Synapses. *J. Neurosci.* 24, 4213–4223. doi:10.1523/jneurosci.0223-04.2004

Suli, A., Watson, G. M., Rubel, E. W., and Raible, D. W. (2012). Rheotaxis in Larval Zebrafish Is Mediated by Lateral Line Mechanosensory Hair Cells. *PLoS One* 7, e29727. doi:10.1371/journal.pone.0029727

Sun, S., Babola, T., Pregernig, G., So, K. S., Nguyen, M., Su, S.-S. M., et al. (2018). Hair Cell Mechanotransduction Regulates Spontaneous Activity and Spiral Ganglion Subtype Specification in the Auditory System. *Cell* 174, 1247–1263. e1215. doi:10.1016/j.cell.2018.07.008

Thevenaz, P., Ruttimann, U. E., and Unser, M. (1998). A Pyramid Approach to Subpixel Registration Based on Intensity. *IEEE Trans. Image Process.* 7, 27–41. doi:10.1109/83.650848

Thomas, E. D., and Raible, D. W. (2019). Distinct Progenitor Populations Mediate Regeneration in the Zebrafish Lateral Line. *Elife* 8. doi:10.7554/eLife.43736

Tritsch, N. X., Yi, E., Gale, J. E., Glowatzki, E., and Bergles, D. E. (2007). The Origin of Spontaneous Activity in the Developing Auditory System. *Nature* 450, 50–55. doi:10.1038/nature06233

Wong, H. C., Zhang, Q., Beirl, A. J., Petralia, R. S., Wang, Y. X., and Kindt, K. (2019). Synaptic Mitochondria Regulate Hair-Cell Synapse Size and Function. *Elife* 8, e48914. doi:10.7554/eLife.48914

Zhang, Q., Li, S., Wong, H.-T. C., He, X. J., Beirl, A., Petralia, R. S., et al. (2018). Synaptically Silent Sensory Hair Cells in Zebrafish Are Recruited after Damage. *Nat. Commun.* 9, 1388. doi:10.1038/s41467-018-03806-8

Conflict of Interest: The authors declare that the research was conducted in the absence of any commercial or financial relationships that could be construed as a potential conflict of interest.

Publisher's Note: All claims expressed in this article are solely those of the authors and do not necessarily represent those of their affiliated organizations, or those of the publisher, the editors and the reviewers. Any product that may be evaluated in this article, or claim that may be made by its manufacturer, is not guaranteed or endorsed by the publisher.

frontiers | Frontiers in Cell and Developmental Biology

REVIEW
published: 23 June 2022
doi: 10.3389/fcell.2022.884240

Cochlear Development; New Tools and Approaches

*Matthew W. Kelley**

Laboratory of Cochlear Development, National Institute on Deafness and Other Communication Disorders, National Institutes of Health, Bethesda, MD, United States

The sensory epithelium of the mammalian cochlea, the organ of Corti, is comprised of at least seven unique cell types including two functionally distinct types of mechanosensory hair cells. All of the cell types within the organ of Corti are believed to develop from a population of precursor cells referred to as prosensory cells. Results from previous studies have begun to identify the developmental processes, lineage restrictions and signaling networks that mediate the specification of many of these cell types, however, the small size of the organ and the limited number of each cell type has hampered progress. Recent technical advances, in particular relating to the ability to capture and characterize gene expression at the single cell level, have opened new avenues for understanding cellular specification in the organ of Corti. This review will cover our current understanding of cellular specification in the cochlea, discuss the most commonly used methods for single cell RNA sequencing and describe how results from a recent study using single cell sequencing provided new insights regarding cellular specification.

Keywords: hair cell, organ of corti (OC), single cell RNA sequencing, cell fate, hearing

OPEN ACCESS

Edited by:
Raj Ladher,
National Centre for Biological Sciences, India

Reviewed by:
Andy Groves,
Baylor College of Medicine, United States
Jinwoong Bok,
Yonsei University College of Medicine, South Korea
Tomoko Tateya,
Kyoto University of Advanced Science (KUAS), Japan
Brandon C. Cox,
Southern Illinois University School of Medicine, Carbondale, United States

***Correspondence:**
Matthew W. Kelley
kelleymt@nidcd.nih.gov

Specialty section:
This article was submitted to Morphogenesis and Patterning, a section of the journal Frontiers in Cell and Developmental Biology

Received: *25 February 2022*
Accepted: *19 May 2022*
Published: *23 June 2022*

Citation:
Kelley MW (2022) Cochlear Development; New Tools and Approaches. Front. Cell Dev. Biol. 10:884240. doi: 10.3389/fcell.2022.884240

INTRODUCTION

In mammals, sounds are initially perceived in the cochlea, the coiled structure that makes up the ventral portion of the inner ear (**Figure 1A**). . Structurally, the cochlear spiral contains three fluid filled chambers, the scala vestibuli, scala media and scala tympani which extend along it is long axis (**Figure 1B**). Located in the middle third of the floor of the scala media is the auditory sensory epithelium, also called the organ of Corti (OC). The OC is comprised of a band of cells that extends along the full length of the spiral (**Figure 1C**). Medial to the OC is the inner sulcus while the lateral third of the scala media floor contains the outer sulcus. In contrast with hair cell (HC) sensory epithelia in other vertebrates, and even in other parts of the mammalian inner ear, the OC is comprised of a highly rigorous mosaic of HCs and associated supporting cells (SCs) arranged in precise rows (Kelley, 2006; Groves and Fekete, 2012; Driver and Kelley, 2020). Moreover, both the HC and SC populations have become diversified to create two functionally distinct types of HCs and at least five distinct types of SCs (**Figure 1C**). Morphologically, the OC can be divided into two domains, a medial domain which is made up of inner hair cells (IHC) and surrounding inner phalangeal cells and border cells and a lateral domain typically containing three rows of outer hair cells (OHC), single rows of inner and outer pillar cells and three rows of Deiters' cells. Adjacent to the third row of Deiters' cells are the Hensen's cells (**Figure 1C**). Whether these cells should be considered part of the lateral compartment of the OC or part of the outer sulcus is unclear (Chrysostomou et al., 2020). The medial domain appears similar in overall structure and function to other HC sensory epithelia. IHCs are separated from each other by interdigitating inner phalangeal cells while the medial and lateral sides of each IHC are contacted by border cells (Munnamalai and

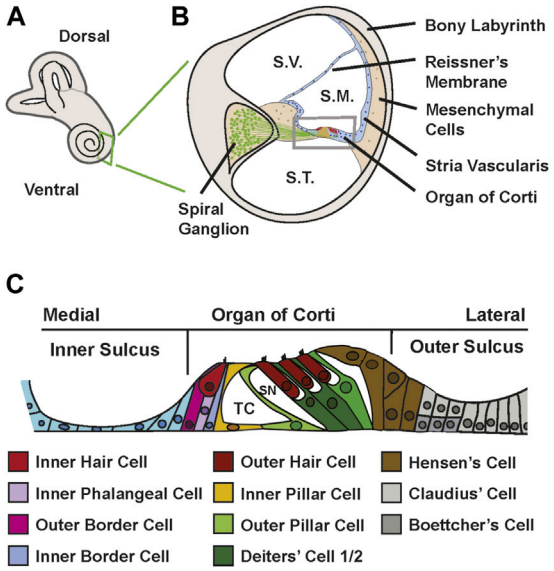

FIGURE 1 | Structure of the cochlea and organ of Corti. **(A)** Diagram of the mammalian inner ear. The coiled cochlea is located on the ventral side. **(B)** Schematic cross-section of the mature cochlea. Sound waves travel up the cochlear spiral through the scala vestibuli (S.V.), pass through the scala media (S.M.) which contains the organ of Corti, and then travel back down the spiral through the scala tympani (S.T.). The scala media is a triangular-shaped structure with three morphologically distinct arms. Reissner's membrane is a bilayered structure that separates the scala media from the scala vestibuli. The stria vascularis, which plays a key role in maintaining ionic homeostasis in the scala media, forms the majority of the lateral wall. The floor of the scala media contains the organ of Corti along with the adjacent inner and outer sulci (boxed area). HCs within the organ of Corti are innervated by neurons located in the spiral ganglion. The entire structure is encased in a capsule, the bony labyrinth. **(C)** Schematic of the floor of the scala media. Medial and lateral sides and the three divisions of the floor are indicated. The medial third of the floor is comprised of the inner sulcus, a monolayer of epithelial cells that represents the remnants of Kolliker's organ. A similar structure, the outer sulcus comprises the lateral third. In the center of the floor is the organ of Corti. The medial edge of the organ contains a single IHC surrounded by inner phalangeal cells and inner and outer border cells. Moving laterally, single inner and outer pillar cells combine to form the tunnel of Corti (TC), a fluid filled space that is presumed to contribute to structural stability. In the lateral half of the organ, three OHCs are surrounded by Deiters' cells which can be divided into $1^{st}/2^{nd}$ row and 3^{rd} row cells at P1 based on gene expression. The Deiters' cells create the spaces of Neul (SN) between the outer hair cells. . At the extreme lateral edge of the organ are Hensen's cells which probably provide structural stability to the organ.

Fekete, 2020). Both inner phalangeal cells and border cells contact IHCs along their entire basolateral surface. Functionally, IHCs act similarly to afferent neurons releasing neurotransmitter in response to mechanical stimulation (Forge and Wright, 2002). In contrast, the function of the lateral domain has been modified to act as an active amplifier of incoming stimuli (Soons et al., 2015). OHCs are electrically motile, enhancing the stimulating signal that acts to activate adjacent IHCs (Hudspeth, 2008; Santos-Sacchi, 2019). The surrounding pillar cells and Deiters' cells provide structural stability and intracellular spaces that are thought to be required for appropriate electromotility (Motallebzadeh et al., 2018; Ashmore, 2019; Santos-Sacchi, 2019). The emergence of OHCs, pillar cells and Deiters' cells correlates with the evolution of high frequency hearing, leading to the general assumption that the structural changes in the lateral part of the OC are required for the perception of high frequencies and increased sensitivity (Okoruwa et al., 2008; Jahan et al., 2018).

As outlined above, by comparison with the elongated hearing organs in birds and some reptiles, the density of HCs along the medial-to-lateral axis of the auditory organ is decreased, a trend that also correlates with increased sensitivity and frequency range (Koppl and Manley, 2019). These changes suggest that the overall size of the sensory epithelium within the mammalian cochlear duct has decreased with evolution, a process that is likely to occur during the early development of the duct. The specific benefits of a single row of mechanosensors and three or four rows of amplifiers is not fully understood, but the exceptional performance of the mammalian cochlea is evident with champion hearing species like bats and toothed whales able to perceive sounds in excess of 150,000 Hz (Bohn et al., 2006; Wang et al., 2021). Finally, an unfortunate consequence of the evolution of the OC seems to be a complete loss of regenerative ability (Brignull et al., 2009; Denans et al., 2019). HC epithelia in all other vertebrate classes are able to robustly regenerate both HCs and auditory or vestibular function (Burns and Corwin, 2013; Burns et al., 2013) and even mammalian vestibular epithelia have been shown to be capable of a limited regenerative response (Forge et al., 1993; Warchol et al., 1993; Forge et al., 1998; Golub et al., 2012). In contrast, in the OC, all ability to regenerate HCs is lost prior to the onset of hearing (Kelley et al., 1995; Shi et al., 2013; Bramhall et al., 2014; Cox et al., 2014; Li et al., 2015; Maass et al., 2015; Tao et al., 2021). Whether this change arose as a result of the evolution of the OC's diversity of cell types or precise patterning remains unclear.

Considering the diverse number of unique cell types that are required for the normal function of the OC, a better understanding of the pathways and processes that specify each type would provide valuable insights regarding cochlear development and possible strategies for regeneration. Unfortunately, because of its small size, the OC contains limited numbers of any particular cell type. A single mouse cochlea contains only approximately 1,000 IHCs while a human cochlea contains only 3 times more (Burda et al., 1988; Lim and Brichta, 2016). This limitation has significantly hindered efforts to understand the full diversity of cell types within the OC and, as important, the factors that direct cells along specific cellular lineages/fates. However, within the last 10 years, technical improvements have significantly increased the sensitivity of assays related to the capture and quantification of cellular genomic, transcriptomic and proteomic data (Cuevas-Diaz Duran et al., 2017; Butler et al., 2018; Kashima et al., 2020; Armand et al., 2021; Asada et al., 2021). As a result, it is now possible to profile development at the level of single cells. For organ systems such as the inner ear, these advances provide exciting new opportunities to significantly advance our understanding of the diversity of cells present within a specific organ and to examine how those cells are specified. This review will discuss our current understanding of the factors that specify cellular identity during development and then provide an

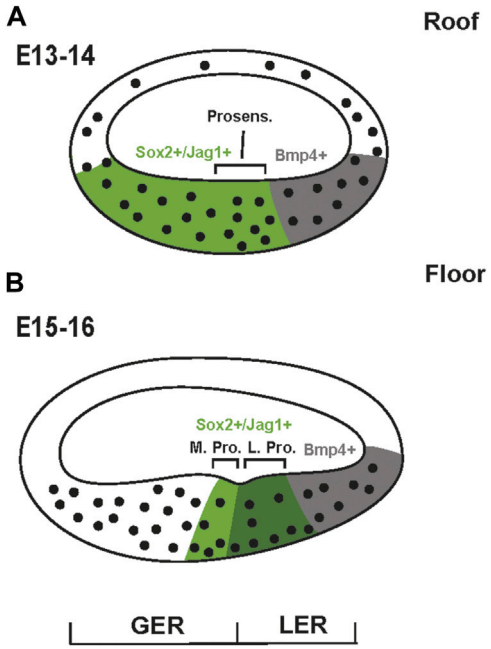

FIGURE 2 | Development of the cochlear duct. **(A)** Schematic cross-section of the mouse cochlear duct on E13 or E14. While the entire duct is comprised of morphologically undifferentiated epithelial cells, the floor is already significantly thicker than the roof. Previous results have demonstrated that the floor can already be divided into $Sox2^{+}/Jag1^{+}$ and $Bmp4^{+}$ domains. The prosensory region is located at the lateral edge of the $Sox2^{+}/Jag1^{+}$ domain. **(B)** At E15-E16 the floor of the duct has become more differentiated. A physical notch in the epithelium defines greater and lesser epithelial ridges (GER and LER) which separate the Medial and Lateral Prosensory domains (M. Pro. and L. Pro.). By this stage, expression of Sox2 and Jag1 is largely confined to the prosensory domain. The lateral domain of *Bmp4*-expression still persists.

overview of some of the most frequently used techniques for single cell transcriptional profiling. Finally, recent findings using single cell approaches to examine cellular diversity in the cochlea will be covered.

COCHLEAR DEVELOPMENT

The inner ear is derived from the otocyst which begins as a placode located adjacent to the developing hindbrain (Wu and Kelley, 2012; Basch et al., 2016a; Driver and Kelley, 2020). Beginning around embryonic day (E) 10.5 in the mouse, the developing inner ear begins to extend a ducted protrusion from its ventral side. This duct then coils as it extends ultimately giving rise to the snail-shaped cochlea (Morsli et al., 1998). By E13 the duct is ovoid in cross-section and lined with morphologically undifferentiated pseudostratified epithelial cells (Lim and Anniko, 1985) (**Figure 2A**). However, the duct is not homogeneous. The dorsal surface, generally referred to as the floor, is noticeably thicker than the corresponding roof and will ultimately give rise to the OC and the flanking inner and outer sulci while the roof will develop as Reissner's membrane and the stria vascularis (**Figure 1A**). While the cells of the duct appear largely homogeneous, molecular studies have demonstrated that at least two distinct populations of cells exist within the floor. A large population, marked by expression of the transcription factor Sox2 and the Notch ligand Jagged1 (Jag1), extends roughly two thirds of the distance from the medial edge while a smaller $Bmp4^{+}$ population covers the final third of the medial-to-lateral axis (Morrison et al., 1999; Kiernan et al., 2005b; Brooker et al., 2006; Kiernan et al., 2006; Chang et al., 2008; Dabdoub et al., 2008; Ohyama et al., 2010). Based on persistent expression of Bmp4, the lateral-most cells are believed to give rise to the cells of the outer sulcus (**Figure 1**). The cells that will give rise to the OC, referred to as prosensory cells because of their unique ability to give rise to HCs and SCs (Kelley et al., 1993), form near the middle of the duct in the lateral half of the $Sox2/Jag1^{+}$ population. As development proceeds, several changes occur nearly simultaneously within the $Sox2/Jag1^{+}$-population. First, expression of Sox2/Jag1 becomes restricted to the central region of the duct, correlating with the prosensory domain (Morrison et al., 1999; Kiernan et al., 2001; Dabdoub et al., 2008). Second, in a gradient that begins at the apex of the cochlear duct around E12.5, cells within the prosensory domain upregulate expression of the cell cycle inhibitor, Cdkn1b (formerly $p27^{kip1}$), leading to cell cycle exit and the formation of the zone of non-proliferation (ZNP) that reaches the base of the cochlea by E14.5 (Ruben, 1967; Chen and Segil, 1999; Lee et al., 2006). Concomitant with the arrival of the wave of cell cycle exit at the base, the prosensory region separates into medial and lateral domains (**Figure 2B**) (Pirvola et al., 2002; Bermingham-McDonogh et al., 2006; Huh et al., 2012; Yang et al., 2019). The specific fates of cells within each domain are consistent with the evolutionary changes that have occurred within the mammalian lineage. Fate mapping of the lateral prosensory domain, which expresses both Fibroblast Growth Factor Receptor 3 (Fgfr3) and Prospero Homolog 1 (Prox1), indicates that these cells will give rise to OHCs, pillar cells and Deiters' cells (Kolla et al., 2020). While cells within the medial domain, are believed to give rise to IHCs, inner phalangeal cells and border cells.

The factors that specify the medial and lateral domains are unknown but may be linked to the overall specification of cellular identities along the medial-to-lateral axis of the cochlear duct. As discussed, cells located at the lateral edge of the duct express a known morphogen, Bmp4, while cells throughout the duct express the Bmp4 receptors *Alk3* and *Alk6* (Ohyama et al., 2010). Deletion of these receptors leads to changes in gene expression that are consistent with increased medial phenotypes and decreased lateral phenotypes. Consistent with these results, cochlear explants treated with the Bmp receptor antagonist dorsomorphin show a decrease in the size of the $Prox1^{+}$-domain (lateral) and an apparent increase in the size of the medial domain (Munnamalai and Fekete, 2016). Similarly, treatment of cochlear explants with the Glycogen Synthase Kinase 3 (Gsk3) inhibitor CHIR99021 induces decreases in *Bmp4* expression and phosphorylation of the Bmp4 target, SMAD1, and an OC that contains multiple rows of IHCs at the expense of OHCs (Ellis et al., 2019). Fate mapping demonstrates that this

phenotype arises, at least in part, as a result of a shift in the medial-lateral boundary within the OC, suggesting that the gradient of Bmp4 plays a key role in the establishment of the medial-lateral axis. Consistent with this hypothesis, addition of Bmp4 to CHIR99021-treated explants partially rescues the phenotype. Gsk3β has been shown to modulate a number of different signaling pathways, in particular it acts as a Wnt inhibitor, meaning that treatment with CHIR99021 can act as a Wnt agonist (Doble and Woodgett, 2003; Patel and Woodgett, 2017). In fact, several Wnts have been shown to be expressed in the medial half of the cochlear duct, suggesting that Wnt may act in the specification of medial identity, possibly in a counter-gradient to Bmp4 (Shi et al., 2014; Geng et al., 2016). Consistent with this idea, treatment of cochlear explants with CHIR99021 for 24 h beginning on the equivalent of E13.5 induces a significant increase in IHCs but no decrease in OHCs (Munnamalai and Fekete, 2016). This phenotype differs from the experiments described above in terms of time of exposure and dosage but are consistent with Wnts playing a role in specification of the medial domain that is independent of the down-regulation of Bmp4 at the lateral edge of the duct. However, results from other studies suggest that the increased representation of medial OC cells following CHIR99021 treatment may not be mediated through Wnt signaling. First, application of a Wnt agonist targeting TCF transcriptional activation directly, did not replicate the phenotype observed following treatment with CHIR99021 (Ellis et al., 2019). Perhaps more compelling, while genetic deletion of *β-catenin* (a key regulator of Wnt function and the target of Gsk3β) induced a shift in the OC medial-lateral boundary, the shift was in the same direction, medially, as was observed following CHIR99021 treatment (Jansson et al., 2019). Moreover, the same study provided evidence that the phenotype is dependent on β-catenin's role in cell adhesion, rather than as an activator of Wnt signaling. So, to summarize, these results are consistent with a role for Bmp4, likely acting as a morphogen, in the specification of cellular identities along the medial-lateral axis of the cochlea. While Wnts clearly also play a role in cochlear development and patterning, whether this includes acting as a counter gradient to Bmp4 remains to be determined.

An additional signaling pathway that may play a role in medial-lateral patterning is the Notch pathway, and in particular, the Notch ligand Jag1. Notch signaling plays multiple roles in inner ear development (Kiernan, 2013; Brown and Groves, 2020; Daudet and Zak, 2020). Inductive interactions between Jag1 and Notch1 during early stages of otocyst development specify vestibular and auditory prosensory patches (Brooker et al., 2006; Kiernan et al., 2006). Also, following the onset of their differentiation, HCs upregulate expression of two Notch ligands, *Delta-like 1* (*Dll1*) and *Jagged2* (*Jag2*) which bind to and activate Notch1 in adjacent prosensory cells, inhibiting those cells from forming as HCs and forcing them towards a SC fate in a classic example of the role of Notch in mediating lateral Inhibition (Lanford et al., 1999; Kiernan et al., 2005a). However, the role of Jag1 during cochlear development is more complicated. As the OC develops, Jag1 expression is down-regulated in HCs but maintained in SCs (Lewis et al., 1998; Morrison et al., 1999), a pattern that is inconsistent with a role in lateral Inhibition. Consistent with this observation are the results of studies that have examined cochlear phenotypes in mice with ENU-induced point mutations in *Jag1*. *Slalom, Headturner* and *Ozzy* mice all carry point mutations in the extracellular domain of *Jag1* leading to missense mutations but none of these mice have cochlear phenotypes that suggest defects in lateral inhibition (Kiernan et al., 2001; Tsai et al., 2001; Vrijens et al., 2006). Instead, all three lines show a consistent phenotype of increased IHCs and decreased OHCs. In addition, atypical HCs, often located in the pillar cell region are also observed. These results are consistent with changes in patterning along the medial-lateral axis of the OC. However, considering that Jag1 is expressed in all SCs during cochlear development, a mechanism for its role in patterning remains unclear. Finally, conditional deletion of *Jag1* in the cochlea beginning on E14.5 has no obvious effect on the patterning of HCs and SCs or on the ratio of IHCs to OHCs (Chrysostomou et al., 2020). Since the medial-lateral axis is thought to be specified prior to E14.5 (Basch et al., 2016b; Ohyama et al., 2010), this result is not inconsistent with a role for Jag1 in axial patterning, but it also, unfortunately, doesn't provide any additional insights regarding the role of Notch in this process.

Terminal mitosis of the prosensory cells and specification of the medial-lateral axis is followed by cellular differentiation which begins around E14.5. But in contrast with the gradient of cell cycle exit, which extends from apex-to-base, differentiation extends in a gradient from base-to-apex (Rubel, 1978). As a result, prosensory cells located at the apex of the cochlea remain in a post-mitotic, undifferentiated state for several days in mouse and probably longer in humans (Chen et al., 2002). The biological benefits, if any, for this unconventional pattern of terminal mitosis and differentiation are unclear. While the factors the regulate the timing and pattern of cellular differentiation remain poorly understood, recent studies have demonstrated important roles for *Sonic hedgehog* (*Shh*), and two sets of interacting signaling molecules, *let-7/Lin28b* and *Activin A* (*Inhba*)/*Follistatin* (*Fst*) (Bok et al., 2013; Golden et al., 2015; Prajapati-DiNubila et al., 2019) in this process. Prior to E14, the developing spiral ganglion (**Figure 1A**) acts as a source of Shh which blocks HC differentiation in the adjacent cochlear epithelium. *Shh* is then down-regulated in a basal-to-apical gradient the parallels differentiation (Liu et al., 2010; Bok et al., 2013). Modulation of Shh signaling either *in vivo* or *in vitro* alters the timing and patterning of HC formation and also leads to hearing deficits (Driver et al., 2008). Interestingly, the basal-to-apical pattern of cellular differentiation is flipped in Shh conditional mutants, resulting in a gradient that more closely parallels the gradient of terminal mitosis (Bok et al., 2013).

In contrast with Shh, which arises outside the epithelium, developing prosensory cells express *let-7/Lin28b* and *Inhba/Fst*. *Lin28b* and *Fst*, both of which inhibit HC differentiation, are broadly expressed throughout the cochlear duct prior to E14 (Golden et al., 2015; Prajapati-DiNubila et al., 2019). Concomitant with the onset of differentiation, expression of *let-7*, a microRNA which targets cell cycle genes in addition to *Lin28b*, and *Inhba*, which codes for a secreted antagonist of

Follistatin, increases beginning in the base of the cochlea. Perturbation of either of these pathways leads to changes in the timing and patterning of HC differentiation and can also influence stemness in some SCs. Whether either of these pathways is controlled through Shh has not been determined however, evidence from the CNS suggests that Shh signaling may act to inhibit *let-7* expression (Tanno et al., 2016).

The first cells to differentiate are generally believed to be IHCs located near the base of the cochlea. Certainly, molecular markers for HCs first appear in the mid-basal IHC region (Montcouquiol and Kelley, 2003). HC differentiation then proceeds in gradients that extend primarily apically but also towards the base (Rubel, 1978). In addition, HCs differentiate in a medial-to-lateral gradient at any given position along the spiral. SCs appear to differentiate in the same pattern, although this has been harder to study, largely because SC differentiation is a longer process, extending, in the mouse, through the first two postnatal weeks (Lim and Anniko, 1985; Tucker et al., 1993; Chen et al., 2018), and because definitive markers of SC differentiation are limited. Instead, many of the genes that are expressed in SCs are also expressed in prosensory cells.

While IHCs are thought to be the first cells to differentiate, it is important to consider that inner pillar cells may actually be specified, at some level, prior to the onset of IHC development (Thelen et al., 2009). Early histological studies of cross-sections through the embryonic cochlear duct often noted a physical notch located in the general region of the future OC which creates two clusters of epithelial cells referred to as the greater (medial) and lesser (lateral) epithelial ridges (**Figure 2B**). The notch arises because the epithelium constricts from a multilayered pseudostratified epithelium down to a single cell. A study examining early development of the cochlear duct in rats provided strong evidence that this cell represents the future inner pillar cell. Moreover, by labeling for the presence of polysaccharides, which are strongly expressed in mature inner pillar cells, the authors demonstrated that this single cell contained polysaccharides before the differentiation of IHCs. So, while these cells must go through extensive developmental changes to assume the morphology of inner pillar cells, these results suggest that some level of cellular specification has occurred in pillar cells prior to the development of IHCs. However, these cells are not yet committed to an Inner pillar cell fate as Fgf8-mediated activation of Fgfr3 beginning around E15 is required to both prevent these cells from converting to a HC fate and to drive their subsequent development (Mueller et al., 2002; Jacques et al., 2007; Mansour et al., 2009; Mansour et al., 2013).

As development continues, cell-cell interactions between HCs and surrounding prosensory cells act to regulate the subsequent development and patterning of the OC. First, as discussed, HCs express Dll1 and Jag2, which activate the Notch pathway in surrounding cells to inhibit those cells from developing as HCs (Lanford et al., 1999; Kiernan et al., 2005a; Brooker et al., 2006). In addition, HCs generate largely unknown inductive signals that recruit surrounding cells to develop as SCs (Woods et al., 2004). Activation of Notch has been shown to play a role in this inductive process (Campbell et al., 2016), and, as mentioned in the previous paragraph, in the case of the developing PCs and DCs, Fgf8 secreted from IHCs is also required for normal formation.

Following the initial onset of differentiation, both HCs and surrounding SCs go through a protracted period of differentiation that, in the mouse, lasts through the first and second postnatal weeks. Over the course of this process, HCs will develop mature stereociliary bundles, mechanotransductive channels and synaptic structures while SCs will undergo significant morphological changes leading to the formation of the tunnel of Corti and the opening of the spaces of Neul (Inoshita et al., 2008). While this process appears to occur in a similar fashion along the entire length of the cochlear spiral, subtle differences related to frequency tuning are evident in the size and morphology of both HCs and SCs (Vater and Kossl, 2011; Yarin et al., 2014). Therefore, in terms of the genetic regulation of cochlear development, it seems reasonable to expect that both conserved and variable genetic signaling pathways must be activated in spatially specific patterns to drive the formation of the mature structure. The observation that some aspects of OC structure and function vary along the tonotopic axis emphasizes the need to be able to study cochlear development at the single cell level.

SINGLE CELL ANALYSES–A NEW APPROACH TO ANSWER OLD QUESTIONS

The feasibility of profiling mRNA expression at the level of single cells was initially demonstrated by Eberwine and others (Eberwine et al., 1992) who dissociated adult hippocampal neurons and then performed patch clamp recordings. At the end of each recording, cytoplasm from the cell was drawn into the patch pipette which contained a mixture of primers, nucleotides and reverse-transcriptase. Following multiple rounds of amplification, the resulting cDNA was used to screen for expression of known neuronal genes. While this study demonstrated that isolation and detection of mRNAs from single cells was possible, the approach was laborious and inefficient. In the 30 years since then, multiple advances, including the development of Illumina sequencing, the sequencing of the mouse and human genomes, and increased efficiency of generation and subsequent amplification of cDNA has improved and simplified the ability to profile mRNA expression from single cells.

A key first step in any effort to generate profiles at a single cell level is a determination of whether individual cells need to be isolated, and if so, what is the best method. Laser-capture microdissection, which offers the advantage of providing spatial information about the collected sample, uses laser light to excise a specific region(s) from a tissue section (Cheng et al., 2013; Datta et al., 2015; Bhamidipati et al., 2022). The excised region is then captured and digested to collect mRNAs. However, the fixation process often leads to degradation of mRNA leading to low efficiency. Moreover, depending on the thickness of the section and the plane of the cut, it is possible to collect mRNA from two distinct cells in a single section. More frequently, tissues are dissociated to generate isolated single cells. The ease with

which this can be accomplished varies depending on the nature of the tissue and its age. This approach generally leads to high mRNA yields and reasonable efficiency. However, these benefits come at the loss of positional information and in some circumstances an induction of stress responses which can skew the resulting transcriptomic data (Machado et al., 2021). Finally, for some tissues, such as the mature brain, the intertwining of cells and the existence of long axonal projections may make dissociation extremely difficult leading to cell damage, stress and possibly apoptosis. For these types of tissues, rather than isolating single cells, it can be more expeditious and provide higher purity to isolate single nuclei (Habib et al., 2016; Ding et al., 2020). Moreover, since one of the first steps in isolating single nuclei is cell lysis, stress responses are not initiated. However, since nuclei contain lower amounts of mRNA, results from single nuclei typically have less information in terms of gene expression and may not accurately reflect the full spectrum of mRNAs expressed in the cell. Finally, the technique pioneered by Eberwine et al., now called Patchseq, can still be applied although this approach remains labor intensive and can have low efficiency (Cadwell et al., 2016; Fuzik et al., 2016). Each of these approaches has advantages and disadvantages that often must be weighed against the nature of the tissue to be profiled as well as the specific questions to be addressed. In particular, in tissues such as the inner ear, where cellular structure and function are often directly related to position, the loss of positional information may need to be addressed. However, while beyond the scope of this review, novel methods are or will soon be available to generate comprehensive transcriptomic data while maintaining positional identity (Rodriques et al., 2019; Dar et al., 2021; Lohoff et al., 2022).

Concomitant with the consideration of how to isolate cells are the questions of how to collect those cells and what type of expression data is needed. Options for collections of cells includes physical picking of cells using pulled micropipettes, serial dilution of cells into plates containing 96, 384 or thousands of individual wells, fluorescent activated cell sorting (FACS), or microfluidic approaches that can capture single cells in individual wells or aqueous droplets. In general, there is an inverse relationship between the number of cells captured and the number of genes detected and number of sequencing reads per gene.

A final consideration is the depth of data that will be needed for a specific project. For instance, to characterize different cell types from a tissue comprised of disparate cellular phenotypes, quantifying a percentage of the genes that are expressed in each cell may be sufficient. But to explore differences in splice variants or isoform usage in a population of phenotypically similar cells, significantly deeper sequencing may be required. As will be discussed below, the approach used to amplify and label mRNAs from each cell can be customized at different points based on the specific question being asked.

Currently the two most common methods for capturing mRNAs from single cells are SMARTseq (currently on version 4) and bead-based bar coding, which also uses SMARTseq technology. Each will be discussed briefly below.

SMARTseq (Switching Mechanism at 5′ End of RNA Template) relies on the template switching (TS) activity of reverse transcriptases (RT) such as Maloney Murine Leukemia Virus (MMLV)-RT (Ramskold et al., 2012; Picelli et al., 2013; Picelli et al., 2014). Briefly, mRNAs are captured from lysed individual cells and reverse transcription is initiated using oligo-dT primers that also add a PCR primer sequence. When the RT reaches the 5′ end of each mRNA strand, several additional nucleotides, typically cytidines, are added to the cDNA strand. These extra bases hybridize with a TS-oligo containing another PCR primer and the RT then switches to the TS-oligo to form a cDNA that contains primer sites on each end. Because TS requires that the RT reach the 5' end of each mRNA, SMARTseq generates full length cDNAs. These cDNAs are then amplified using polymerase chain reaction followed by library preparation, shearing and Illumina-sequencing. The resulting data is then aligned to current genomic builds. A distinct advantage of SMARTseq approaches is the generation of full-length data and considerably higher read depth and gene detection per cell.

Bead-based bar-coding approaches are generally used in combination with approaches that seek to collect significantly greater numbers of cells, primarily using aqueous droplets to capture cells (Klein et al., 2015; Macosko et al., 2015; Zheng et al., 2017). Briefly, isolated cells and oligo-coated gel beads-in-emulsion (GEMs) are flowed in a microfluidic apparatus designed to generate droplets that contain one bead and 1 cell. Each bead is arrayed with multiple oligos that all contain the same nucleotide bar code along with an oligo-dT region for capture of mRNAs. Thousands of cells can be collected in a single run. Once the run is complete, cells are lysed and cDNAs are generated, largely as described above except that the molecular bar code is incorporated at the 3′ end of the resulting cDNAs. Following library preparation, cDNAs are sheared prior to sequencing. Since bar codes are only present at the 3′ end of each cDNA, relatively short 90-base pair reads are used to quantify gene expression based solely on 3' sequences. The presence of the barcode with each sequence allows every cDNA to be assigned to a particular cell. So, while no data on isoform usage or splice variants can be obtained, thousands of cells can be sequenced in a single run.

While the choice of which isolation and sequencing approaches to use should be made based on the biological question(s) being addressed, experience from our laboratory and others has provided some insights regarding cochlear cells. As is the case for many tissues, during embryonic development, both epithelial and mesenchymal cells are easily dissociated and, more importantly, quite robust in terms of their ability to survive following dissociation. In our experience, single cell suspensions of viable cells can be obtained from mouse cochlear cells aged P5 or less (Burns et al., 2015; Kolla et al., 2020). Therefore, at embryonic and early post-natal ages, the approach can be decided on, largely, based on the question that is being asked. For questions related to the identification of unique cell types or transcriptional profiles, a higher-volume, lower read depth approach, such as 10X captures could be used while questions related to discovery of novel mRNA transcripts or alternative splicing could also be addressed using lower-throughput approaches combined with SMART-Seq or PacBio long read sequencing.

At older ages, we have observed increasing difficulty in obtaining high numbers (> than 1,000 from a single experiment) of good quality single cells, in particular HCs. However, we have successfully isolated adult SCs following FACS enrichment (Burns et al., 2015; Hoa et al., 2020). Therefore, to obtain high numbers of both HCs and SCs from cochleae older than P5, a single nucleus approach would be preferable. Similar studies have demonstrated that this approach can be used to isolate cells from the stria vascularis (Korrapati et al., 2019; Gu et al., 2020; Taukulis et al., 2021). For lower throughput but greater depth, several laboratories have combined dissociation, visual identification and individual selection using micropipettes to collect cells of known phenotypes (Liu et al., 2014; Li et al., 2018; Ranum et al., 2019). While the numbers of cells that can be collected using this technique is limited, the potential for a more comprehensive survey of transcriptional expression along with novel alternative splicing and even epigenomic profiling (see below) is high.

Finally, as mentioned above, for many aspects of cochlear development and function, the spatial location of each cell fundamentally influences that cell's phenotype and physiology. Unfortunately, the relatively small number of cells in a single cochlea limits the ability to collect cells from a sub-region (such as a specific frequency range). Broader isolations, such as basal or apical halves of the cochlea have been successfully executed providing data on difference in developmental progression. Novel approaches in which a matrix of GEM-type beads are adhered to a glass slide, are currently in development (Rodriques et al., 2019; Marshall et al., 2022; Wang et al., 2022; Zhao et al., 2022). For this approach, the bar-code for each bead is determined initially and then a frozen tissue section is placed on top of the matrix. mRNAs are captured as described for the 10X Genomics system and following sequencing individual mRNAs can be assigned to a specific position in the initial tissue section. Current bead sizes are approximately 50 μm, which prevents single cell resolution for cochlear cells, but technological advances may decrease bead size to 5 μm in the near future.

While RNA sequencing has been the focus of most single cell studies, it is now possible to also assess the epigenetic state of a single cell using Assay for Transposase Accessible Chromatin Sequencing (ATACSeq) alone or in combination with RNAseq (Macaulay et al., 2017; Mezger et al., 2018; Satpathy et al., 2019). In addition, the development of long-read technologies in which entire cDNAs are sequenced, such as Nanopore MinIon or Pacific Biosciences Sequel platforms, have the potential to provide data on novel splice variants at the level of single cells (Lu et al., 2016; Chu et al., 2017; Midha et al., 2019). Finally, expression of a significant number of proteins can be now be assayed at the single cell level using shotgun mass spectrometry (Zhu et al., 2019).

CELLULAR DIVERSITY IN THE COCHLEAR DUCT; IMPROVED RESOLUTION USING SINGLE CELL RNASEQ

As discussed above, the cochlear duct goes through multiple rounds of cellular specification during development. Based on gene expression studies, at E14 the floor of the duct can divided into three regions from medial-to-lateral: Kolliker's organ, the prosensory domain and the Bmp4+ lesser epithelial ridge (LER) (Ohyama et al., 2010). However, a recent single cell analysis of cell types within the duct at E14 indicated a greater degree of cellular diversity (Kolla et al., 2020). Kolliker's organ was fairly homogenous at this time although two small additional clusters were observed (**Figure 3A**). One of the smaller clusters represented immature interdental cells which have already begun to generate components of the tectorial membrane and the other cluster expressed the high mobility group nucleosome-binding chromosomal protein *Hmgn2*, suggesting possible changes in transcriptional activity within these cells. Similarly, the *Bmp4*$^{+}$ LER resolved into three different clusters. All three expressed *Bmp4*, as well as the Bmp-related molecule *Follistatin* (*Fst*), but were transcriptionally distinct based on expression of other genes. The potential different roles and/or fates of these distinct groups remain to be determined.

Finally, as discussed above, the prosensory domain resolved into two separate clusters (**Figures 2A**, **3C**). Consistent with previous studies, *Fgfr1, Fgfr3, Prox1, Bmp2, Ngfr* and *Nrcam* were all restricted to what was classified as the lateral prosensory domain (von Bartheld et al., 1991; Mueller et al., 2002; Pirvola et al., 2002; Bermingham-McDonogh et al., 2006; Hwang et al., 2010; Harley et al., 2018) (**Figure 3C**). In contrast, the medial domain expressed fewer unique transcripts with *Fgf20* the most differentially expressed gene in this domain although previous studies indicated the *Fgf20* is expressed in the lateral domain as well prior to E14 (Hayashi et al., 2008; Huh et al., 2012).

By 2 days later, at E16, additional OC cell types can be identified (**Figure 2D**). Along with IHCs and OHCs, a specific population of inner pillar cells separates from other lateral prosensory cells. Deiters' cells have not differentiated sufficiently to separate from lateral prosensory cells and a population of medial prosensory cells is still present as well. However, a population of inner phalangeal cells, that clusters independently from the medial prosensory cells, is also present. Interestingly, this cluster of cells shows a greater degree of transcriptional similarity with cells in Kolliker's organ by comparison with medial prosensory cells. The most reasonable explanation for this result is that differentiated inner phalangeal cells become transcriptionally similar to cells in Kolliker's organ, in particular cells located at the lateral edge of Kolliker's organ (see below), but an alternative possibility is that some inner phalangeal cells are derived from Kolliker's organ rather than medial prosensory cells. Fate-mapping using *Fgf20*^{cre} mice, a prosensory marker, indicates that most inner phalangeal cells are derived from prosensory cells (Landin Malt et al., 2019) but functional data has demonstrated that cells from Kolliker's organ can develop as inner phalangeal cells following ablation of the native inner phalangeal cell population (Mellado Lagarde et al., 2014).

Finally, consistent with ongoing development of the cochlea, single cell analysis at P1 indicated no prosensory cells. But all of the major OC cell types, inner phalangeal cells, both types of pillar cells, Deiters' cells (in two clusters, Deiters' cell1/2 and 3), Claudius and Hensen's along with IHCs and OHCs are present (**Figure 4A**). A further analysis at P7 clustered all

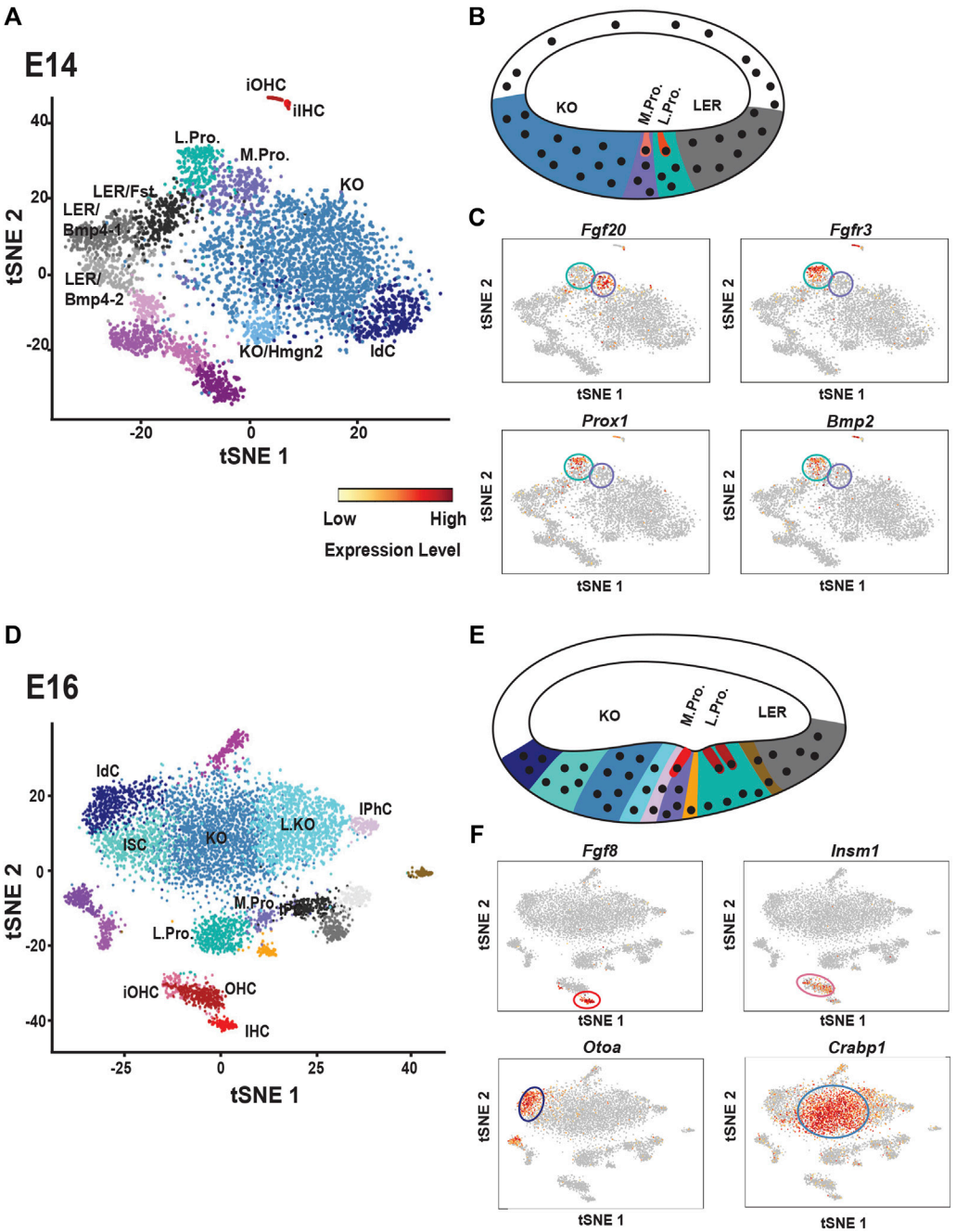

FIGURE 3 | Single cell analysis of cochlear development at E14 and E16. **(A)** t-distributed stochastic neighbor embedding (tSNE) plot of cochlear single cells collected at E14. Transcriptionally unique clusters are indicated in different colors. Clusters with transcriptional similarity, such as those determined to be located in Kolliker's organ (KO) are colored similarly. Clusters discussed in the text are labeled. See text for details. **(B)** Schematic cross-section through the base of the cochlear duct at E14. The general locations of Kolliker's organ (KO), the medial and lateral prosensory cells (M. Pro. and L. Pro.) and the lesser epithelial ridge cells (LER) which will develop as the outer sulcus, are indicated and color-coded to match cell clusters in **(A)**. Note: KO and M.Pro. together constitute the GER while LER technically includes L.Pro. as well as the region labeled LER. **(C)** Feature plots showing expression of medial (*Fgf20*) and lateral (*Fgfr3, Prox1, Bmp2*) prosensory markers in the single cell data. Medial prosensory cells are circled in purple and lateral prosensory cells are circled in Aqua. Compare each feature plot with the plot in **(A)** Scale bar indicates level of mRNA expression per cell. Abbreviations: iOHC: immature outer hair cells, OHC: outer hair cells, IHC: inner hair cells, IdC: interdental cells. **(D)** tSNE plot of cochlear single cells collected at E16. As discussed in the text, note the increased diversity of cell types within KO and the transcriptional similarity between Inner Phalangeal Cells (IPhC) and KO cells. **(E)** Schematic cross-section through the cochlear duct at E16. Immature IHCs and OHCs (shades of red) can be identified as can developing inner pillar cells (gold) and some inner phalangeal cells (pink). However, medial prosensory cells (purple) are still present as well. Cells in KO have become transcriptionally heterogenous with different cell clusters located along the medial-to-lateral axis of the duct. See text for details. **(F)** Feature plots showing expression of makers for developing IHCs (*Fgf8*) and OHCs (*Insm1*) as well as two genes, *Otoa* and *Crabp1* that are restricted to specific regions of KO cells. Abbreviations: IPC: inner pillar cells, ISC: inner sulcus cells All tSNE and feature plot images were generated using gEAR (umd.gear).

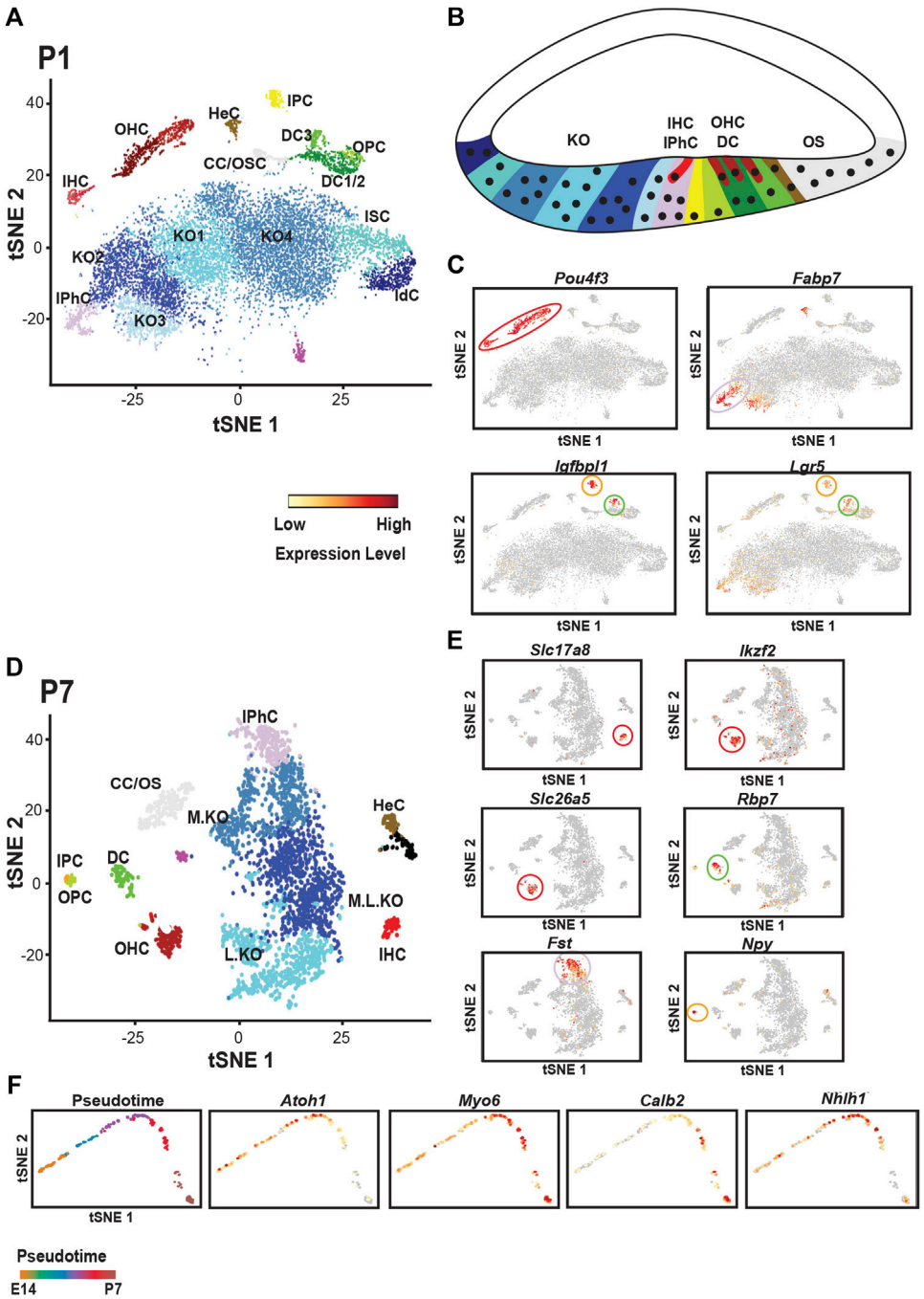

FIGURE 4 | Single cell analysis of cochlear development at P1 and P7. **(A)** tSNE plot for single cells collected from the floor of the cochlear duct at P1. All of the known cell types within the organ of Corti can be identified as can Hensen's and Claudius' cells (HeC and CC). In addition, multiple transcriptionally distinct cell types are identified in Kolliker's organ (KO1-4), Interdental cells (IdC) and Inner Sulcus cells (ISC)). **(B)** Schmatic of the cochlear duct at P1 with positions of cells from A indicated by color. The basic pattern within the organ of Corti is present although many of the supporting cells have not fully differentiated at this time point. **(C)** Feature plots illustrating expression of marker genes for hair cells (*Pou4f3*), inner phalangeal cells (*Fabp7*), and inner pillar cells/Deiters' cells (*Igfbp1* and *Lgr5*). **(D)** tSNE plot for cochlear single cells collected at P7. All of the cell types within the organ of Corti can be identified. Inner and outer pillar cells (IPC, OPC) are very similar transcriptionally, a change from P1. In addition, all three rows of Deiters' cells cluster together suggesting that the transcriptional differences between Deiters' cells in rows one and two versus three at P1 may be a result of differences in the timing of their development. In contrast with P1, the number of unique cell clusters in Kolliker's organ has decreased to three. For relative positions of different cells types in the cochlea, refer to **Figure 1B**. **(E)** Feature plots illustrating marker genes for different cell types in the organ of Corti at P7. *Slc17a8* marks IHCs while OHCs express *Ikzf2* and *Slc2615* (*Prestin*). Deiters' cells uniquely expressed the retinol binding protein *Rbp7*, inner phalangeal cells express *Fst* and inner pillar cells express *Npy*. **(F)** Pseudotime projection for developing OHCs collected from all four time points (E14, E16, P1 and P7). Color coding in upper left panel indicates relative age across the pseudotime projection from E14 to P7. All other panels show expression of specific genes across pseudotime (see scale bar in 4C). *Atoh1* is down-regulated as hair cells develop, *Myo6* and *Calb2* are up-regulated as hair cells mature and the transcription factor *Nhlh1* shows transient expression. All tSNE and feature plot images were generated using gEAR (umd.gear).

Deiters' cells together suggesting a convergence in transcriptional profiles as Detiers' cells mature (Kolla et al., 2020). However, because of the difficulty in collecting cells at P7, the overall size of the data set was smaller by comparison with early ages which may have obscured transcriptional differences between different Deiters' cell types. Overall, the results of the study by Kolla et al. (2020) provided novel in depth transcriptional profiles for each of the known cell types within the OC including new markers for several cell types. However, with the exception of the separation between Deiters' cells located in rows one and two versus row three at P1, which was already known, novel cell subtypes were not described. While this may indicate limited heterogeneity within these cell populations, several caveats should be considered. First, the numbers of cells collected for each cell type was relatively low. As will be discussed below, a much greater number of cells were collected from Kolliker's organ which revealed multiple subtypes. In addition, since all the cells from each time point were analyzed together, subtle differences in transcriptional expression could have been obscured. Additional analyses in which cells within a single cluster are isolated and reanalyzed could reveal individual differences that were masked in the analysis of the larger data set. Along the same lines, the addition of more OC cells could improve cellular resolution. Finally, as discussed, sequencing data derived using the 10x Genomics approach is limited to the 3′ end of each transcript. So, differences in splice variant or isoform usage cannot be determined. Therefore, additional studies using long-read platforms could be applied to reveal additional heterogeneity within OC cell types.

CELLULAR DIVERSITY IN KOLLIKER'S ORGAN

As discussed above, Kolliker's organ is comprised of a population of epithelial cells located between the prosensory domain and the medial edge of the cochlear duct. The organ is transient as approximately 90% of the cells within the structure will undergo apoptosis prior to the onset of hearing leading to the formation of the inner sulcus which is lined by a monolayer of cuboidal epithelial cells, the last remnants of Kolliker's organ (Knipper et al., 1999; Peeters et al., 2015). However, recent studies have demonstrated key roles for Kolliker's organ in cochlear development. In particular, cells within the organ generate the bulk of the extracellular components that will form the tectorial membrane (Goodyear and Richardson, 2018) and spontaneous activity originating in Kolliker's organ cells plays a key role in the organization of higher auditory centers (Tritsch et al., 2007; Tritsch and Bergles, 2010; Tritsch et al., 2010; Wang et al., 2015). Moreover, multiple studies have demonstrated that cells within Kolliker's organ retain a high level of prosensory potential (Zheng and Gao, 2000; Woods et al., 2004; Ahmed et al., 2012; Kelly et al., 2012). Forced expression of *Atoh1* in Kolliker's organ cells induces a HC-like phenotype and those *Atoh1*$^{+}$-cells then go on to induce surrounding cells to develop as SCs (Woods et al., 2004). As discussed, single cell analysis at E14 indicated a largely homogeneous population of Kolliker's organ cells. But a similar analysis of the cochlear duct at E16 indicated four transcriptionally unique Kolliker's organ clusters which increased to six by P1 (**Figures 3D**, **4A**). Consistent with the decreasing size of Kolliker's organ postnatally, only three clusters were present at P7 (**Figure 4D**). Interestingly, the different populations of Kolliker's organ cells appear to be largely spatially separated along the medial-to-lateral axis of the cochlear duct. Labeling of Kolliker's organ cells by *in situ* hybridization or immunolocalization indicates bands of expression of cluster-specific genes at specific locations along the medial-lateral border rather than diffuse expression throughout the organ (Okano et al., 2011; Okano and Kelley, 2013; Kolla et al., 2020). The roles of these different Kolliker's organ cell types are just beginning to be understood.

One of the more intriguing aspects of Kolliker's organ cells is the ability of some of these cells to develop as HCs or SCs under different circumstances. In addition to forced expression of Atoh1, inhibition of Sonic Hedgehog signaling leads to random patches of HCs and SCs within Kolliker's organ (Driver et al., 2008). A key factor in the sensory potential of Kolliker's organ cells appears to be expression of Sox2 and Jag1. At early time points, prior to E15, Sox2/Jag1 is expressed throughout much of Kolliker's organ, and prosensory potential is also broad. As development continues, Sox2/Jag1 expression within Kolliker's organ resolves to the two clusters located adjacent to the medial edge of the OC, as apparently, does prosensory potential. Consistent with this observation, a recent study that examined the sphere-forming potential of cells within the postnatal cochlea concluded that the bulk of the cells that can act as stem cells (as defined by forming spheres) are located in Kolliker's organ, and, specifically, adjacent to the medial edge of the OC (Kubota et al., 2021). Finally, genetic lesioning of inner phalangeal cells during the early postnatal period induces Kolliker's organ cells to move into the OC and to develop as replacement inner phalangeal cells, further demonstrating the developmental plasticity and prosensory potential in this cellular population (Mellado Lagarde et al., 2014). These results suggest an interesting evolutionary history for Kolliker's organ. While soft tissues from transitional auditory organs have not been preserved, a reasonable inference is that there has been a progressive reduction in the size of the sensory epithelium over evolutionary time (Manley, 2012; Koppl and Manley, 2019). Does Kolliker's organ represent a population of cells that were originally prosensory in nature and contributed to a larger mammalian sensory epithelium? If so, did those cells simultaneously provide the other functions noted above? Or were these new functions acquired after Kolliker's organ cells lost their prosensory function? Inhibition of hedgehog signaling leads to random patches of sensory tissue in Kolliker's organ. Is this signaling pathway one mechanism that was invoked to decrease the size of the sensory epithelium? Are there others and how would hearing be affected in a cochlea that contained significant HCs in the inner sulcus?

NEW REGULATORS OF THE DEVELOPMENT OF THE LATERAL PROSENSORY DOMAIN

Development of the lateral prosensory domain is regulated in large part through activation of Fgfr1 and then Fgfr3. But,

deletion of either gene does not lead to an OC that is completely devoid of lateral cell types (Hayashi et al., 2007; Puligilla et al., 2007; Huh et al., 2012). In fact, in the case of Fgfr3, most lateral cell types, with the exception of inner pillar cells, are present. These results suggest that other signaling pathways must also play a role in development of this domain. One way to identify other potential candidates is through an analysis of differentially expressed genes in different single cell clusters. Analysis of the lateral prosensory domain cells at E14 identified *Transforming Growth Factor B Receptor 1* (*Tgfbr1*) and *Frizzled9* (*Fzd9*), as uniquely expressed in this population (Kolla et al., 2020) (**Figure 3C**). While a hearing phenotype has not been reported in viable *Fzd9* mutant mice (Ranheim et al., 2005), inhibition of Tgfbr1 *in vitro* significantly inhibited OHC formation, but had a minimal effect on IHCs (Kolla et al., 2020). Similarly, hearing loss has been reported in individuals with Loeys-Deitz syndrome, which can be caused by mutations in *Tgfbr1* (Van Laer et al., 2014; Riise et al., 2018; Takeda et al., 2018). Additional analysis of the genes and pathways that define medial and lateral prosensory clusters should provide new insights regarding the development of both domains and the unique cell types that are derived from each population.

SPECIFICATION OF HAIR CELL PHENOTYPES

One of the more intriguing applications of single cell approaches in developmental biology is the ability to treat the information from each cell as a single developmental data/time point. For instance, differentiation of the OC occurs in a gradient that begins in the basal region of the cochlea and extends, primarily, towards the apex. Therefore, a collection of single cells from a single time point contains cells at different stages of development. Ordering these cells from least mature to most mature creates a developmental trajectory of transcriptional expression. When this was done for OHCs collected at E14, E16, P1 and P7 in the Kolla et al. (2020) study, the results indicated four phases of unique transcriptional expression. While the trajectory was not studied in full, analysis of known genes largely confirmed the general accuracy of the analysis. *Sox2* and *Isl1* are only observed in phase 1 (Radde-Gallwitz et al., 2004; Deng et al., 2014), corresponding to E12-E14, while *Atoh1*, and *Pou4f3* show onset of expression in phase 2, corresponding to E14-E16 (Erkman et al., 1996; Xiang et al., 1998; Bermingham et al., 1999; Lanford et al., 2000; Driver et al., 2013) (**Figure 4F**). *Barhl1* and *Nhlh1* are upregulated in phase 3 (Li et al., 2002; Kruger et al., 2006), corresponding to E17-E19 and then *Tmc1* and, *Calb2* appear in stage 4 (Kurima et al., 2015), corresponding to postnatal time points, suggesting that this represents the final stage of functional onset (**Figure 4F**). An analysis of additional transcription factors using DAVID (Huang et al., 2007a; Huang et al., 2007b; Sherman et al., 2007) identified candidates, including *Bach2, Irx2*, *Zbtb8b, and Bhlhe40* (Chang and Kelley, unpublished), that await confirmation and analysis.

While the single cell RNAseq results described above have identified a number of candidate genes which may be involved in the development of OHCs, several recent papers have used other methods to identify genes that play key roles in OHC formation. First, screening for expression of the transcriptional inhibitor *Insm1* in the inner ear demonstrated that this gene is transiently expressed in OHCs between E15.5 and P2 (**Figure 2B**) (Lorenzen et al., 2015). In contrast, *Insm1* is never expressed in IHCs or vestibular HCs. Deletion of *Insm1* in the inner ear leads to disruption of expression of OHC-specific genes and an upregulation of expression of IHC-specific genes in some OHCs (Wiwatpanit et al., 2018). Moreover, overall cellular patterning in the OC is also disrupted and, consistent with these defects, significant elevations in ABR and DPOAE recordings were observed in *Insm1* conditional mutants. Population RNA sequencing confirmed that *Insm1* acts to repress a subset of early IHC-specific genes, suggesting that a first step in OHC differentiation may be to suppress an IHC-phenotype. Interestingly, some IHC-specific genes were not upregulated in *Insm1* mutant HCs, suggesting that other factors may also act to suppress the IHC phenotype. Moreover, many OHCs in *Insm1* conditional mutants expressed OHC-specific genes. Whether this represents limited recombination in the conditional mutants or roles for additional co-factors, such as *NeuroD2*, which is also expressed only in OHCs, remains to be determined.

A second study published in parallel with the Insm1 work used RiboTag to profile genes that are expressed in developing OHCs during the early postnatal and adult time period (Chessum et al., 2018). Bioinformatic analysis of the resulting datasets identified the transcription factor *Ikzf2* as strongly expressed in OHCs at all time points and immunolocalization confirmed OHC-specific expression of Ikzf2 beginning at P4. Inactivation of *Ikzf2* leads to OHC degeneration and hearing loss by P30, however the initial steps in OHC differentiation, including development of resting membrane potential and mechanotransduction currents are unaffected. Electromotility is also present in *Ikzf2*$^{-/-}$ OHCs although the magnitude of membrane shortening is reduced. A comparison of gene expression in OHCs from *Ikzf2*$^{-/-}$ and wildtype littermates indicated 36 genes that were down regulated and 105 genes that were upregulated in the absence of *Ikzf2* with several of the down-regulated genes already identified as OHC-specific. Finally, viral transfection was used to force expression of Ikzf2 in IHCs. Consistent with the mutant data, IHCs that express Ikzf2 show a partial transformation towards an OHC phenotype including a down-regulation of IHC-specific genes and an up-regulation of some OHC-specific genes and the development of stereociliary bundles with OHC-like morphologies. A subsequent study used a transgenic approach to confirm that forced expression of Ikzf2, in this case along with Atoh1, induces expression of *Slc26a5* (*Prestin*) and other OHC genes in SCs that have been induced to develop as HCs (Sun et al., 2021).

While the developmental processes that generate OHCs are not completely understood, the results described above are consistent with the following process. At the prosensory (precursor) stage, expression of set of unique transcription factors, which may include Prox1, induce a change in the competence of those prosensory cells, now referred to as lateral prosensory cells. As development continues, lateral

prosensory cells are sorted into HC and SC fates, probably through a conserved Atoh1/Notch-mediated sorting process. Once a subset of the prosensory cells become committed to a HC fate, those cells activate an auditory HC differentiation program, that, if unaltered, would lead to the development of IHC-like cells. However, HCs derived from the lateral prosensory domain up-regulate expression of the repressor Insm1, along with possibly other repressors, which inhibits the IHC program. At the same time, additional transcription factors are probably required to drive these cells towards an OHC fate. While no factors have been shown to play a role in this process yet, scRNAseq results have identified some candidate genes. As development continues, other transcription factors, such as Ikzf2, are activated to drive specific aspects of OHC development. It is interesting to note that Ikzf2, while crucial for OHC development and function, does not appear to act as a master regulator for the late stages of OHC differentiation. Does this mean that another transcription factor might act up stream, activating Ikzf2 along with other factors that act in parallel? Alternatively, is Ikzf2 just one of a cascade of factors reflecting different steps in the evolution of the derived OHC phenotype? Additional experiments will clearly be required to discriminate between these possibilities.

CONCLUSION

Over the course of the last 20 years, significant progress has been made in understanding the developmental processes and genetic signaling pathways that regulate development of the organ of Corti. However, many important questions remain unanswered. In particular, the signaling networks that are required to drive precursor cells to develop as mature OC cell types have not been discovered. For HCs, transcriptional networks are being assembled, but it is still not possible to drive a naïve cell to develop as a functional IHC or OHC. For SC types, even less is known. However, the advent of single cell technologies now allows us to characterize different cell types within the ear in terms of gene expression, epigenetic state and, potentially, protein expression. Moving forward, these techniques should lead to significant insights regarding the pathways that regulate the development of all the cell types with the organ of Corti.

AUTHOR CONTRIBUTIONS

MK reviewed the literature, generated the figures and wrote the article.

FUNDING

The generation of this review was supported by the Intramural Program at NIDCD (DC000059 to MK).

ACKNOWLEDGMENTS

The author also wishes to apologize for the potential omission of any relevant studies as a result of space and length constraints. The author wishes to thank Doris Wu and Michael Hoa for reading an an earlier version of this manuscript and the reviewers for providing suggestions that significantly improved the manuscript.

REFERENCES

Ahmed, M., Xu, J., and Xu, P.-X. (2012). EYA1 and SIX1 Drive the Neuronal Developmental Program in Cooperation with the SWI/SNF Chromatin-Remodeling Complex and SOX2 in the Mammalian Inner Ear. *Development* 139, 1965–1977. doi:10.1242/dev.071670

Armand, E. J., Li, J., Xie, F., Luo, C., and Mukamel, E. A. (2021). Single-Cell Sequencing of Brain Cell Transcriptomes and Epigenomes. *Neuron* 109, 11–26. doi:10.1016/j.neuron.2020.12.010

Asada, K., Takasawa, K., Machino, H., Takahashi, S., Shinkai, N., Bolatkan, A., et al. (2021). Single-Cell Analysis Using Machine Learning Techniques and its Application to Medical Research. *Biomedicines* 9, 1513. doi:10.3390/biomedicines9111513

Ashmore, J. (2019). Outer Hair Cells and Electromotility. *Cold Spring Harb. Perspect. Med.* 9, a033522. doi:10.1101/cshperspect.a033522

Basch, M. L., Brown, R. M., 2nd, Jen, H.-I., and Groves, A. K. (2016a). Where Hearing Starts: The Development of the Mammalian Cochlea. *J. Anat.* 228, 233–254. doi:10.1111/joa.12314

Basch, M. L., Brown, R. M., 2nd, Jen, H. I., Semerci, F., Depreux, F., Edlund, R. K., et al. (2016b). Fine-tuning of Notch Signaling Sets the Boundary of the Organ of Corti and Establishes Sensory Cell Fates. *Elife* 5, e19921. doi:10.7554/eLife.19921

Bermingham, N. A., Hassan, B. A., Price, S. D., Vollrath, M. A., Ben-Arie, N., Eatock, R. A., et al. (1999). Math1: An Essential Gene for the Generation of Inner Ear Hair Cells. *Science* 284, 1837–1841. doi:10.1126/science.284.5421.1837

Bermingham-McDonogh, O., Oesterle, E. C., Stone, J. S., Hume, C. R., Huynh, H. M., and Hayashi, T. (2006). Expression of Prox1 during Mouse Cochlear Development. *J. Comp. Neurol.* 496, 172–186. doi:10.1002/cne.20944

Bhamidipati, T., Sinha, M., Sen, C. K., and Singh, K. (2022). Laser Capture Microdissection in the Spatial Analysis of Epigenetic Modifications in Skin: A Comprehensive Review. *Oxid. Med. Cell Longev.* 2022, 4127238. doi:10.1155/2022/4127238

Bohn, K. M., Moss, C. F., and Wilkinson, G. S. (2006). Correlated Evolution between Hearing Sensitivity and Social Calls in Bats. *Biol. Lett.* 2, 561–564. doi:10.1098/rsbl.2006.0501

Bok, J., Zenczak, C., Hwang, C. H., and Wu, D. K. (2013). Auditory Ganglion Source of Sonic Hedgehog Regulates Timing of Cell Cycle Exit and Differentiation of Mammalian Cochlear Hair Cells. *Proc. Natl. Acad. Sci. U.S.A.* 110, 13869–13874. doi:10.1073/pnas.1222341110

Bramhall, N. F., Shi, F., Arnold, K., Hochedlinger, K., and Edge, A. S. B. (2014). Lgr5-positive Supporting Cells Generate New Hair Cells in the Postnatal Cochlea. *Stem cell Rep.* 2, 311–322. doi:10.1016/j.stemcr.2014.01.008

Brignull, H. R., Raible, D. W., and Stone, J. S. (2009). Feathers and Fins: Non-mammalian Models for Hair Cell Regeneration. *Brain Res.* 1277, 12–23. doi:10.1016/j.brainres.2009.02.028

Brooker, R., Hozumi, K., and Lewis, J. (2006). Notch Ligands with Contrasting Functions: Jagged1 and Delta1 in the Mouse Inner Ear. *Development* 133, 1277–1286. doi:10.1242/dev.02284

Brown, R., and Groves, A. K. (2020). Hear, Hear for Notch: Control of Cell Fates in the Inner Ear by Notch Signaling. *Biomolecules* 10, 370. doi:10.3390/biom10030370

Burda, H., Ballast, L., and Bruns, V. (1988). Cochlea in Old World Mice and Rats (Muridae). *J. Morphol.* 198, 269–285. doi:10.1002/jmor.1051980303

Burns, J. C., and Corwin, J. T. (2013). A Historical to Present-Day Account of Efforts to Answer the Question: "What Puts the Brakes on Mammalian Hair Cell Regeneration?". *Hear. Res.* 297, 52–67. doi:10.1016/j.heares.2013.01.005

Burns, J. C., Collado, M. S., Oliver, E. R., and Corwin, J. T. (2013). Specializations of Intercellular Junctions are Associated with the Presence and Absence of Hair Cell Regeneration in Ears from Six Vertebrate Classes. *J. Comp. Neurol.* 521, 1430–1448. doi:10.1002/cne.23250

Burns, J. C., Kelly, M. C., Hoa, M., Morell, R. J., and Kelley, M. W. (2015). Single-cell RNA-Seq Resolves Cellular Complexity in Sensory Organs from the Neonatal Inner Ear. *Nat. Commun.* 6, 8557. doi:10.1038/ncomms9557

Butler, A., Hoffman, P., Smibert, P., Papalexi, E., and Satija, R. (2018). Integrating Single-Cell Transcriptomic Data across Different Conditions, Technologies, and Species. *Nat. Biotechnol.* 36, 411–420. doi:10.1038/nbt.4096

Cadwell, C. R., Palasantza, A., Jiang, X., Berens, P., Deng, Q., Yilmaz, M., et al. (2016). Electrophysiological, Transcriptomic and Morphologic Profiling of Single Neurons Using Patch-Seq. *Nat. Biotechnol.* 34, 199–203. doi:10.1038/nbt.3445

Campbell, D. P., Chrysostomou, E., and Doetzlhofer, A. (2016). Canonical Notch Signaling Plays an Instructive Role in Auditory Supporting Cell Development. *Sci. Rep.* 6, 19484. doi:10.1038/srep19484

Chang, W., Lin, Z., Kulessa, H., Hebert, J., Hogan, B. L. M., and Wu, D. K. (2008). Bmp4 is Essential for the Formation of the Vestibular Apparatus that Detects Angular Head Movements. *PLoS Genet.* 4, e1000050. doi:10.1371/journal.pgen.1000050

Chen, P., and Segil, N. (1999). p27(Kip1) Links Cell Proliferation to Morphogenesis in the Developing Organ of Corti. *Development* 126, 1581–1590. doi:10.1242/dev.126.8.1581

Chen, P., Johnson, J. E., Zoghbi, H. Y., and Segil, N. (2002). The Role of Math1 in Inner Ear Development: Uncoupling the Establishment of the Sensory Primordium from Hair Cell Fate Determination. *Development* 129, 2495–2505. doi:10.1242/dev.129.10.2495

Chen, S., Xie, L., Xu, K., Cao, H. Y., Wu, X., Xu, X. X., et al. (2018). Developmental Abnormalities in Supporting Cell Phalangeal Processes and Cytoskeleton in the Gjb2 Knockdown Mouse Model. *Dis. Model Mech.* 11, dmm033019. doi:10.1242/dmm.033019

Cheng, L., Zhang, S., MacLennan, G. T., Williamson, S. R., Davidson, D. D., Wang, M., et al. (2013). Laser-assisted Microdissection in Translational Research: Theory, Technical Considerations, and Future Applications. *Appl. Immunohistochem. Mol. Morphol.* 21, 31–47. doi:10.1097/pai.0b013e31824d0519

Chessum, L., Matern, M. S., Kelly, M. C., Johnson, S. L., Ogawa, Y., Milon, B., et al. (2018). Helios is a Key Transcriptional Regulator of Outer Hair Cell Maturation. *Nature* 563, 696–700. doi:10.1038/s41586-018-0728-4

Chrysostomou, E., Zhou, L., Darcy, Y. L., Graves, K. A., Doetzlhofer, A., and Cox, B. C. (2020). The Notch Ligand Jagged1 is Required for the Formation, Maintenance, and Survival of Hensen's Cells in the Mouse Cochlea. *J. Neurosci.* 40, 9401–9413. doi:10.1523/jneurosci.1192-20.2020

Chu, J., Mohamadi, H., Warren, R. L., Yang, C., and Birol, I. (2017). Innovations and Challenges in Detecting Long Read Overlaps: An Evaluation of the State-Of-The-Art. *Bioinformatics* 33, 1261–1270. doi:10.1093/bioinformatics/btw811

Cox, B. C., Chai, R., Lenoir, A., Liu, Z., Zhang, L., Nguyen, D.-H., et al. (2014). Spontaneous Hair Cell Regeneration in the Neonatal Mouse Cochlea *In Vivo*. *Development* 141, 816–829. doi:10.1242/dev.103036

Cuevas-Diaz Duran, R., Wei, H., and Wu, J. Q. (2017). Single-cell RNA-Sequencing of the Brain. *Clin. Transl. Med.* 6, 20. doi:10.1186/s40169-017-0150-9

Dabdoub, A., Puligilla, C., Jones, J. M., Fritzsch, B., Cheah, K. S. E., Pevny, L. H., et al. (2008). Sox2 Signaling in Prosensory Domain Specification and Subsequent Hair Cell Differentiation in the Developing Cochlea. *Proc. Natl. Acad. Sci. U.S.A.* 105, 18396–18401. doi:10.1073/pnas.0808175105

Dar, D., Dar, N., Cai, L., and Newman, D. K. (2021). Spatial Transcriptomics of Planktonic and Sessile Bacterial Populations at Single-Cell Resolution. *Science* 373, eabi4882. doi:10.1126/science.abi4882

Datta, S., Malhotra, L., Dickerson, R., Chaffee, S., Sen, C. K., and Roy, S. (2015). Laser Capture Microdissection: Big Data from Small Samples. *Histol. Histopathol.* 30, 1255–1269. doi:10.14670/HH-11-622

Daudet, N., and Żak, M. (2020). Notch Signalling: The Multitask Manager of Inner Ear Development and Regeneration. *Adv. Exp. Med. Biol.* 1218, 129–157. doi:10.1007/978-3-030-34436-8_8

Denans, N., Baek, S., and Piotrowski, T. (2019). Comparing Sensory Organs to Define the Path for Hair Cell Regeneration. *Annu. Rev. Cell Dev. Biol.* 35, 567–589. doi:10.1146/annurev-cellbio-100818-125503

Deng, M., Yang, H., Xie, X., Liang, G., and Gan, L. (2014). Comparative Expression Analysis of POU4F1, POU4F2 and ISL1 in Developing Mouse Cochleovestibular Ganglion Neurons. *Gene Expr. Patterns* 15, 31–37. doi:10.1016/j.gep.2014.03.001

Ding, J., Adiconis, X., Simmons, S. K., Kowalczyk, M. S., Hession, C. C., Marjanovic, N. D., et al. (2020). Systematic Comparison of Single-Cell and Single-Nucleus RNA-Sequencing Methods. *Nat. Biotechnol.* 38, 737–746. doi:10.1038/s41587-020-0465-8

Doble, B. W., and Woodgett, J. R. (2003). GSK-3: Tricks of the Trade for a Multi-Tasking Kinase. *J. Cell Sci.* 116, 1175–1186. doi:10.1242/jcs.00384

Driver, E. C., and Kelley, M. W. (2020). Development of the Cochlea. *Development* 147, dev162263. doi:10.1242/dev.162263

Driver, E. C., Pryor, S. P., Hill, P., Turner, J., Ruther, U., Biesecker, L. G., et al. (2008). Hedgehog Signaling Regulates Sensory Cell Formation and Auditory Function in Mice and Humans. *J. Neurosci.* 28, 7350–7358. doi:10.1523/jneurosci.0312-08.2008

Driver, E. C., Sillers, L., Coate, T. M., Rose, M. F., and Kelley, M. W. (2013). The Atoh1-Lineage Gives Rise to Hair Cells and Supporting Cells within the Mammalian Cochlea. *Dev. Biol.* 376, 86–98. doi:10.1016/j.ydbio.2013.01.005

Eberwine, J., Yeh, H., Miyashiro, K., Cao, Y., Nair, S., Finnell, R., et al. (1992). Analysis of Gene Expression in Single Live Neurons. *Proc. Natl. Acad. Sci. U.S.A.* 89, 3010–3014. doi:10.1073/pnas.89.7.3010

Ellis, K., Driver, E. C., Okano, T., Lemons, A., and Kelley, M. W. (2019). GSK3 Regulates Hair Cell Fate in the Developing Mammalian Cochlea. *Dev. Biol.* 453, 191. doi:10.1016/j.ydbio.2019.06.003

Erkman, L., McEvilly, R. J., Luo, L., Ryan, A. K., Hooshmand, F., O'Connell, S. M., et al. (1996). Role of Transcription Factors a Brn-3.1 and Brn-3.2 in Auditory and Visual System Development. *Nature* 381, 603–606. doi:10.1038/381603a0

Forge, A., and Wright, T. (2002). The Molecular Architecture of the Inner Ear. *Br. Med. Bull.* 63, 5–24. doi:10.1093/bmb/63.1.5

Forge, A., Li, L., Corwin, J., and Nevill, G. (1993). Ultrastructural Evidence for Hair Cell Regeneration in the Mammalian Inner Ear. *Science* 259, 1616–1619. doi:10.1126/science.8456284

Forge, A., Li, L., and Nevill, G. (1998). Hair Cell Recovery in the Vestibular Sensory Epithelia of Mature guinea Pigs. *J. Comp. Neurol.* 397, 69–88. doi:10.1002/(sici)1096-9861(19980720)397:1<69::aid-cne6>3.0.co;2-g

Fuzik, J., Zeisel, A., Máté, Z., Calvigioni, D., Yanagawa, Y., Szabó, G., et al. (2016). Integration of Electrophysiological Recordings with Single-Cell RNA-Seq Data Identifies Neuronal Subtypes. *Nat. Biotechnol.* 34, 175–183. doi:10.1038/nbt.3443

Geng, R., Noda, T., Mulvaney, J. F., Lin, V. Y. W., Edge, A. S. B., and Dabdoub, A. (2016). Comprehensive Expression of Wnt Signaling Pathway Genes during Development and Maturation of the Mouse Cochlea. *PLoS One* 11, e0148339. doi:10.1371/journal.pone.0148339

Golden, E. J., Benito-Gonzalez, A., and Doetzlhofer, A. (2015). The RNA-Binding Protein LIN28B Regulates Developmental Timing in the Mammalian Cochlea. *Proc. Natl. Acad. Sci. U. S. A.* 112, E3864–E3873. doi:10.1073/pnas.1501077112

Golub, J. S., Tong, L., Ngyuen, T. B., Hume, C. R., Palmiter, R. D., Rubel, E. W., et al. (2012). Hair Cell Replacement in Adult Mouse Utricles after Targeted Ablation of Hair Cells with Diphtheria Toxin. *J. Neurosci.* 32, 15093–15105. doi:10.1523/jneurosci.1709-12.2012

Goodyear, R. J., and Richardson, G. P. (2018). Structure, Function, and Development of the Tectorial Membrane: An Extracellular Matrix Essential for Hearing. *Curr. Top. Dev. Biol.* 130, 217–244. doi:10.1016/bs.ctdb.2018.02.006

Groves, A. K., and Fekete, D. M. (2012). Shaping Sound in Space: the Regulation of Inner Ear Patterning. *Development* 139, 245–257. doi:10.1242/dev.067074

Gu, S., Olszewski, R., Taukulis, I., Wei, Z., Martin, D., Morell, R. J., et al. (2020). Characterization of Rare Spindle and Root Cell Transcriptional Profiles in the Stria Vascularis of the Adult Mouse Cochlea. *Sci. Rep.* 10, 18100. doi:10.1038/s41598-020-75238-8

Habib, N., Li, Y., Heidenreich, M., Swiech, L., Avraham-Davidi, I., Trombetta, J. J., et al. (2016). Div-Seq: Single-Nucleus RNA-Seq Reveals Dynamics of Rare Adult Newborn Neurons. *Science* 353, 925–928. doi:10.1126/science.aad7038

Harley, R. J., Murdy, J. P., Wang, Z., Kelly, M. C., Ropp, T.-J. F., Park, S. H., et al. (2018). Neuronal Cell Adhesion Molecule (NrCAM) is Expressed by Sensory Cells in the Cochlea and is Necessary for Proper Cochlear Innervation and Sensory Domain Patterning during Development. *Dev. Dyn.* 247, 934–950. doi:10.1002/dvdy.24629

Hayashi, T., Cunningham, D., and Bermingham-McDonogh, O. (2007). Loss of Fgfr3 Leads to Excess Hair Cell Development in the Mouse Organ of Corti. *Dev. Dyn.* 236, 525–533. doi:10.1002/dvdy.21026

Hayashi, T., Ray, C. A., and Bermingham-McDonogh, O. (2008). Fgf20 is Required for Sensory Epithelial Specification in the Developing Cochlea. *J. Neurosci.* 28, 5991–5999. doi:10.1523/jneurosci.1690-08.2008

Hoa, M., Olszewski, R., Li, X., Taukulis, I., Gu, S., DeTorres, A., et al. (2020). Characterizing Adult Cochlear Supporting Cell Transcriptional Diversity Using Single-Cell RNA-Seq: Validation in the Adult Mouse and Translational Implications for the Adult Human Cochlea. *Front. Mol. Neurosci.* 13, 13. doi:10.3389/fnmol.2020.00013

Huang, D. W., Sherman, B. T., Tan, Q., Collins, J. R., Alvord, W. G., Roayaei, J., et al. (2007a). The DAVID Gene Functional Classification Tool: A Novel Biological Module-Centric Algorithm to Functionally Analyze Large Gene Lists. *Genome Biol.* 8, R183. doi:10.1186/gb-2007-8-9-r183

Huang, D. W., Sherman, B. T., Tan, Q., Kir, J., Liu, D., Bryant, D., et al. (2007b). DAVID Bioinformatics Resources: Expanded Annotation Database and Novel Algorithms to Better Extract Biology from Large Gene Lists. *Nucleic Acids Res.* 35, W169–W175. doi:10.1093/nar/gkm415

Hudspeth, A. J. (2008). Making an Effort to Listen: Mechanical Amplification in the Ear. *Neuron* 59, 530–545. doi:10.1016/j.neuron.2008.07.012

Huh, S.-H., Jones, J., Warchol, M. E., and Ornitz, D. M. (2012). Differentiation of the Lateral Compartment of the Cochlea Requires a Temporally Restricted FGF20 Signal. *PLoS Biol.* 10, e1001231. doi:10.1371/journal.pbio.1001231

Hwang, C. H., Guo, D., Harris, M. A., Howard, O., Mishina, Y., Gan, L., et al. (2010). Role of Bone Morphogenetic Proteins on Cochlear Hair Cell Formation: Analyses of Noggin and Bmp2 Mutant Mice. *Dev. Dyn.* 239, 505–513. doi:10.1002/dvdy.22200

Inoshita, A., Iizuka, T., Okamura, H.-O., Minekawa, A., Kojima, K., Furukawa, M., et al. (2008). Postnatal Development of the Organ of Corti in Dominant-Negative Gjb2 Transgenic Mice. *Neuroscience* 156, 1039–1047. doi:10.1016/j.neuroscience.2008.08.027

Jacques, B. E., Montcouquiol, M. E., Layman, E. M., Lewandoski, M., and Kelley, M. W. (2007). Fgf8 Induces Pillar Cell Fate and Regulates Cellular Patterning in the Mammalian Cochlea. *Development* 134, 3021–3029. doi:10.1242/dev.02874

Jahan, I., Elliott, K. L., and Fritzsch, B. (2018). Understanding Molecular Evolution and Development of the Organ of Corti Can Provide Clues for Hearing Restoration. *Integr. Comp. Biol.* 58, 351–365. doi:10.1093/icb/icy019

Jansson, L., Ebeid, M., Shen, J. W., Mokhtari, T. E., Quiruz, L. A., Ornitz, D. M., et al. (2019). β-Catenin is Required for Radial Cell Patterning and Identity in the Developing Mouse Cochlea. *Proc. Natl. Acad. Sci. U.S.A.* 116, 21054–21060. doi:10.1073/pnas.1910223116

Kashima, Y., Sakamoto, Y., Kaneko, K., Seki, M., Suzuki, Y., and Suzuki, A. (2020). Single-cell Sequencing Techniques from Individual to Multiomics Analyses. *Exp. Mol. Med.* 52, 1419–1427. doi:10.1038/s12276-020-00499-2

Kelley, M. W., Xu, X. M., Wagner, M. A., Warchol, M. E., and Corwin, J. T. (1993). The Developing Organ of Corti Contains Retinoic Acid and Forms Supernumerary Hair Cells in Response to Exogenous Retinoic Acid in Culture. *Development* 119, 1041–1053. doi:10.1242/dev.119.4.1041

Kelley, M., Talreja, D., and Corwin, J. (1995). Replacement of Hair Cells after Laser Microbeam Irradiation in Cultured Organs of Corti from Embryonic and Neonatal Mice. *J. Neurosci.* 15, 3013–3026. doi:10.1523/jneurosci.15-04-03013.1995

Kelley, M. W. (2006). Regulation of Cell Fate in the Sensory Epithelia of the Inner Ear. *Nat. Rev. Neurosci.* 7, 837–849. doi:10.1038/nrn1987

Kelly, M. C., Chang, Q., Pan, A., Lin, X., and Chen, P. (2012). Atoh1 Directs the Formation of Sensory Mosaics and Induces Cell Proliferation in the Postnatal Mammalian Cochlea *In Vivo*. *J. Neurosci.* 32, 6699–6710. doi:10.1523/jneurosci.5420-11.2012

Kiernan, A. E., Ahituv, N., Fuchs, H., Balling, R., Avraham, K. B., Steel, K. P., et al. (2001). The Notch Ligand Jagged1 is Required for Inner Ear Sensory Development. *Proc. Natl. Acad. Sci. U.S.A.* 98, 3873–3878. doi:10.1073/pnas.071496998

Kiernan, A. E., Cordes, R., Kopan, R., Gossler, A., and Gridley, T. (2005a). The Notch Ligands DLL1 and JAG2 Act Synergistically to Regulate Hair Cell Development in the Mammalian Inner Ear. *Development* 132, 4353–4362. doi:10.1242/dev.02002

Kiernan, A. E., Pelling, A. L., Leung, K. K. H., Tang, A. S. P., Bell, D. M., Tease, C., et al. (2005b). Sox2 is Required for Sensory Organ Development in the Mammalian Inner Ear. *Nature* 434, 1031–1035. doi:10.1038/nature03487

Kiernan, A. E., Xu, J., and Gridley, T. (2006). The Notch Ligand JAG1 is Required for Sensory Progenitor Development in the Mammalian Inner Ear. *PLoS Genet.* 2, e4. doi:10.1371/journal.pgen.0020004

Kiernan, A. E. (2013). Notch Signaling during Cell Fate Determination in the Inner Ear. *Seminars Cell Dev. Biol.* 24, 470–479. doi:10.1016/j.semcdb.2013.04.002

Klein, A. M., Mazutis, L., Akartuna, I., Tallapragada, N., Veres, A., Li, V., et al. (2015). Droplet Barcoding for Single-Cell Transcriptomics Applied to Embryonic Stem Cells. *Cell* 161, 1187–1201. doi:10.1016/j.cell.2015.04.044

Knipper, M., Gestwa, L., Ten Cate, W.-J., Lautermann, J. r., Brugger, H., Maier, H., et al. (1999). Distinct Thyroid Hormone-dependent Expression of TrKB and p75NGFR in Nonneuronal Cells during the Critical TH-dependent Period of the Cochlea. *J. Neurobiol.* 38, 338–356. doi:10.1002/(sici)1097-4695(19990215)38:3<338::aid-neu4>3.0.co;2-1

Kolla, L., Kelly, M. C., Mann, Z. F., Anaya-Rocha, A., Ellis, K., Lemons, A., et al. (2020). Characterization of the Development of the Mouse Cochlear Epithelium at the Single Cell Level. *Nat. Commun.* 11, 2389. doi:10.1038/s41467-020-16113-y

Koppl, C., and Manley, G. A. (2019). A Functional Perspective on the Evolution of the Cochlea. *Cold Spring Harb. Perspect. Med.* 9, a033241. doi:10.1101/cshperspect.a033241

Korrapati, S., Taukulis, I., Olszewski, R., Pyle, M., Gu, S., Singh, R., et al. (2019). Single Cell and Single Nucleus RNA-Seq Reveal Cellular Heterogeneity and Homeostatic Regulatory Networks in Adult Mouse Stria Vascularis. *Front. Mol. Neurosci.* 12, 316. doi:10.3389/fnmol.2019.00316

Kruger, M., Schmid, T., Krüger, S., Bober, E., and Braun, T. (2006). Functional Redundancy of NSCL-1 and NeuroD during Development of the Petrosal and Vestibulocochlear Ganglia. *Eur. J. Neurosci.* 24, 1581–1590. doi:10.1111/j.1460-9568.2006.05051.x

Kubota, M., Scheibinger, M., Jan, T. A., and Heller, S. (2021). Greater Epithelial Ridge Cells Are the Principal Organoid-Forming Progenitors of the Mouse Cochlea. *Cell Rep.* 34, 108646. doi:10.1016/j.celrep.2020.108646

Kurima, K., Ebrahim, S., Pan, B., Sedlacek, M., Sengupta, P., Millis, B. A., et al. (2015). TMC1 and TMC2 Localize at the Site of Mechanotransduction in Mammalian Inner Ear Hair Cell Stereocilia. *Cell Rep.* 12, 1606–1617. doi:10.1016/j.celrep.2015.07.058

Landin Malt, A., Dailey, Z., Holbrook-Rasmussen, J., Zheng, Y., Hogan, A., Du, Q., et al. (2019). Par3 is Essential for the Establishment of Planar Cell Polarity of Inner Ear Hair Cells. *Proc. Natl. Acad. Sci. U.S.A.* 116, 4999–5008. doi:10.1073/pnas.1816333116

Lanford, P. J., Lan, Y., Jiang, R., Lindsell, C., Weinmaster, G., Gridley, T., et al. (1999). Notch Signalling Pathway Mediates Hair Cell Development in Mammalian Cochlea. *Nat. Genet.* 21, 289–292. doi:10.1038/6804

Lanford, P. J., Shailam, R., Norton, C. R., Ridley, T., and Kelley, M. W. (2000). Expression of Math1 and HES5 in the Cochleae of Wildtype and Jag2 Mutant Mice. *J. Assoc. Res. Otolaryngol.* 1, 161–171. doi:10.1007/s101620010023

Lee, Y.-S., Liu, F., and Segil, N. (2006). A Morphogenetic Wave of p27Kip1 Transcription Directs Cell Cycle Exit during Organ of Corti Development. *Development* 133, 2817–2826. doi:10.1242/dev.02453

Lewis, A. K., Frantz, G. D., Carpenter, D. A., de Sauvage, F. J., and Gao, W.-Q. (1998). Distinct Expression Patterns of Notch Family Receptors and Ligands during Development of the Mammalian Inner Ear. *Mech. Dev.* 78, 159–163. doi:10.1016/s0925-4773(98)00165-8

Li, S., Price, S. M., Cahill, H., Ryugo, D. K., Shen, M. M., and Xiang, M. (2002). Hearing Loss Caused by Progressive Degeneration of Cochlear Hair Cells in Mice Deficient for the Barhl1 Homeobox Gene. *Development* 129, 3523–3532. doi:10.1242/dev.129.14.3523

Li, W., Wu, J., Yang, J., Sun, S., Chai, R., Chen, Z.-Y., et al. (2015). Notch Inhibition Induces Mitotically Generated Hair Cells in Mammalian Cochleae via Activating the Wnt Pathway. *Proc. Natl. Acad. Sci. U.S.A.* 112, 166–171. doi:10.1073/pnas.1415901112

Li, Y., Liu, H., Giffen, K. P., Chen, L., Beisel, K. W., and He, D. Z. Z. (2018). Transcriptomes of Cochlear Inner and Outer Hair Cells from Adult Mice. *Sci. Data* 5, 180199. doi:10.1038/sdata.2018.199

Lim, D. J., and Anniko, M. (1985). Developmental Morphology of the Mouse Inner Ear. A Scanning Electron Microscopic Observation. *Acta Otolaryngol. Suppl.* 422, 1–69. doi:10.3109/00016488509121766

Lim, R., and Brichta, A. M. (2016). Anatomical and Physiological Development of the Human Inner Ear. *Hear. Res.* 338, 9–21. doi:10.1016/j.heares.2016.02.004

Liu, Z., Owen, T., Zhang, L., and Zuo, J. (2010). Dynamic Expression Pattern of Sonic Hedgehog in Developing Cochlear Spiral Ganglion Neurons. *Dev. Dyn.* 239, 1674–1683. doi:10.1002/dvdy.22302

Liu, H., Pecka, J. L., Zhang, Q., Soukup, G. A., Beisel, K. W., and He, D. Z. Z. (2014). Characterization of Transcriptomes of Cochlear Inner and Outer Hair Cells. *J. Neurosci.* 34, 11085–11095. doi:10.1523/jneurosci.1690-14.2014

Lohoff, T., Ghazanfar, S., Missarova, A., Koulena, N., Pierson, N., Griffiths, J. A., et al. (2022). Integration of Spatial and Single-Cell Transcriptomic Data Elucidates Mouse Organogenesis. *Nat. Biotechnol.* 40, 74–85. doi:10.1038/s41587-021-01006-2

Lorenzen, S. M., Duggan, A., Osipovich, A. B., Magnuson, M. A., and García-Añoveros, J. (2015). Insm1 Promotes Neurogenic Proliferation in Delaminated Otic Progenitors. *Mech. Dev.* 138 (Pt 3), 233–245. doi:10.1016/j.mod.2015.11.001

Lu, H., Giordano, F., and Ning, Z. (2016). Oxford Nanopore MinION Sequencing and Genome Assembly. *Genomics Proteomics Bioinform.* 14, 265–279. doi:10.1016/j.gpb.2016.05.004

Maass, J. C., Gu, R., Basch, M. L., Waldhaus, J., Lopez, E. M., Xia, A., et al. (2015). Changes in the Regulation of the Notch Signaling Pathway are Temporally Correlated with Regenerative Failure in the Mouse Cochlea. *Front. Cell. Neurosci.* 9, 110. doi:10.3389/fncel.2015.00110

Macaulay, I. C., Ponting, C. P., and Voet, T. (2017). Single-Cell Multiomics: Multiple Measurements from Single Cells. *Trends Genet.* 33, 155–168. doi:10.1016/j.tig.2016.12.003

Machado, L., Relaix, F., and Mourikis, P. (2021). Stress Relief: Emerging Methods to Mitigate Dissociation-Induced Artefacts. *Trends Cell Biol.* 31, 888–897. doi:10.1016/j.tcb.2021.05.004

Macosko, E. Z., Basu, A., Satija, R., Nemesh, J., Shekhar, K., Goldman, M., et al. (2015). Highly Parallel Genome-wide Expression Profiling of Individual Cells Using Nanoliter Droplets. *Cell* 161, 1202–1214. doi:10.1016/j.cell.2015.05.002

Manley, G. A. (2012). Evolutionary Paths to Mammalian Cochleae. *J. Assoc. Res. Otolaryngol.* 13, 733–743. doi:10.1007/s10162-012-0349-9

Mansour, S. L., Twigg, S. R. F., Freeland, R. M., Wall, S. A., Li, C., and Wilkie, A. O. M. (2009). Hearing Loss in a Mouse Model of Muenke Syndrome. *Hum. Mol. Genet.* 18, 43–50. doi:10.1093/hmg/ddn311

Mansour, S. L., Li, C., and Urness, L. D. (2013). Genetic Rescue of Muenke Syndrome Model Hearing Loss Reveals Prolonged FGF-dependent Plasticity in Cochlear Supporting Cell Fates. *Genes Dev.* 27, 2320–2331. doi:10.1101/gad.228957.113

Marshall, J. L., Noel, T., Wang, Q. S., Chen, H., Murray, E., Subramanian, A., et al. (2022). High-resolution Slide-seqV2 Spatial Transcriptomics Enables Discovery of Disease-specific Cell Neighborhoods and Pathways. *iScience* 25, 104097. doi:10.1016/j.isci.2022.104097

Mellado Lagarde, M. M., Wan, G., Zhang, L., Gigliello, A. R., McInnis, J. J., Zhang, Y., et al. (2014). Spontaneous Regeneration of Cochlear Supporting Cells after Neonatal Ablation Ensures Hearing in the Adult Mouse. *Proc. Natl. Acad. Sci. U.S.A.* 111, 16919–16924. doi:10.1073/pnas.1408064111

Mezger, A., Klemm, S., Mann, I., Brower, K., Mir, A., Bostick, M., et al. (2018). High-throughput Chromatin Accessibility Profiling at Single-Cell Resolution. *Nat. Commun.* 9, 3647. doi:10.1038/s41467-018-05887-x

Midha, M. K., Wu, M., and Chiu, K.-P. (2019). Long-read Sequencing in Deciphering Human Genetics to a Greater Depth. *Hum. Genet.* 138, 1201–1215. doi:10.1007/s00439-019-02064-y

Montcouquiol, M., and Kelley, M. W. (2003). Planar and Vertical Signals Control Cellular Differentiation and Patterning in the Mammalian Cochlea. *J. Neurosci.* 23, 9469–9478. doi:10.1523/jneurosci.23-28-09469.2003

Morrison, A., Hodgetts, C., Gossler, A., Hrabé de Angelis, M., and Lewis, J. (1999). Expression of Delta1 and Serrate1 (Jagged1) in the Mouse Inner Ear. *Mech. Dev.* 84, 169–172. doi:10.1016/s0925-4773(99)00066-0

Morsli, H., Choo, D., Ryan, A., Johnson, R., and Wu, D. K. (1998). Development of the Mouse Inner Ear and Origin of its Sensory Organs. *J. Neurosci.* 18, 3327–3335. doi:10.1523/jneurosci.18-09-03327.1998

Motallebzadeh, H., Soons, J. A. M., and Puria, S. (2018). Cochlear Amplification and Tuning Depend on the Cellular Arrangement within the Organ of Corti. *Proc. Natl. Acad. Sci. U.S.A.* 115, 5762–5767. doi:10.1073/pnas.1720979115

Mueller, K. L., Jacques, B. E., and Kelley, M. W. (2002). Fibroblast Growth Factor Signaling Regulates Pillar Cell Development in the Organ of Corti. *J. Neurosci.* 22, 9368–9377. doi:10.1523/jneurosci.22-21-09368.2002

Munnamalai, V., and Fekete, D. M. (2016). Notch-Wnt-Bmp Crosstalk Regulates Radial Patterning in the Mouse Cochlea in a Spatiotemporal Manner. *Development* 143, 4003–4015. doi:10.1242/dev.139469

Munnamalai, V., and Fekete, D. M. (2020). The Acquisition of Positional Information across the Radial axis of the Cochlea. *Dev. Dyn.* 249, 281–297. doi:10.1002/dvdy.118

Ohyama, T., Basch, M. L., Mishina, Y., Lyons, K. M., Segil, N., and Groves, A. K. (2010). BMP Signaling is Necessary for Patterning the Sensory and Nonsensory Regions of the Developing Mammalian Cochlea. *J. Neurosci.* 30, 15044–15051. doi:10.1523/jneurosci.3547-10.2010

Okano, T., and Kelley, M. W. (2013). Expression of Insulin-like Growth Factor Binding Proteins during Mouse Cochlear Development. *Dev. Dyn.* 242, 1210–1221. doi:10.1002/dvdy.24005

Okano, T., Xuan, S., and Kelley, M. W. (2011). Insulin-like Growth Factor Signaling Regulates the Timing of Sensory Cell Differentiation in the Mouse Cochlea. *J. Neurosci.* 31, 18104–18118. doi:10.1523/jneurosci.3619-11.2011

Okoruwa, O. E., Weston, M. D., Sanjeevi, D. C., Millemon, A. R., Fritzsch, B., Hallworth, R., et al. (2008). Evolutionary Insights into the Unique Electromotility Motor of Mammalian Outer Hair Cells. *Evol. Dev.* 10, 300–315. doi:10.1111/j.1525-142x.2008.00239.x

Patel, P., and Woodgett, J. R. (2017). Glycogen Synthase Kinase 3: A Kinase for All Pathways? *Curr. Top. Dev. Biol.* 123, 277–302. doi:10.1016/bs.ctdb.2016.11.011

Peeters, R. P., Ng, L., Ma, M., and Forrest, D. (2015). The Timecourse of Apoptotic Cell Death during Postnatal Remodeling of the Mouse Cochlea and its Premature Onset by Triiodothyronine (T3). *Mol. Cell. Endocrinol.* 407, 1–8. doi:10.1016/j.mce.2015.02.025

Picelli, S., Björklund, Å. K., Faridani, O. R., Sagasser, S., Winberg, G., and Sandberg, R. (2013). Smart-seq2 for Sensitive Full-Length Transcriptome Profiling in Single Cells. *Nat. Methods* 10, 1096–1098. doi:10.1038/nmeth.2639

Picelli, S., Faridani, O. R., Björklund, Å. K., Winberg, G., Sagasser, S., and Sandberg, R. (2014). Full-length RNA-Seq from Single Cells Using Smart-Seq2. *Nat. Protoc.* 9, 171–181. doi:10.1038/nprot.2014.006

Pirvola, U., Ylikoski, J., Trokovic, R., Hébert, J. M., McConnell, S. K., and Partanen, J. (2002). FGFR1 is Required for the Development of the Auditory Sensory Epithelium. *Neuron* 35, 671–680. doi:10.1016/s0896-6273(02)00824-3

Prajapati-DiNubila, M., Benito-Gonzalez, A., Golden, E. J., Zhang, S., and Doetzlhofer, A. (2019). A Counter Gradient of Activin A and Follistatin Instructs the Timing of Hair Cell Differentiation in the Murine Cochlea. *Elife* 8, e47613. doi:10.7554/eLife.47613

Puligilla, C., Feng, F., Ishikawa, K., Bertuzzi, S., Dabdoub, A., Griffith, A. J., et al. (2007). Disruption of Fibroblast Growth Factor Receptor 3 Signaling Results in Defects in Cellular Differentiation, Neuronal Patterning, and Hearing Impairment. *Dev. Dyn.* 236, 1905–1917. doi:10.1002/dvdy.21192

Radde-Gallwitz, K., Pan, L., Gan, L., Lin, X., Segil, N., and Chen, P. (2004). Expression of Islet1 Marks the Sensory and Neuronal Lineages in the Mammalian Inner Ear. *J. Comp. Neurol.* 477, 412–421. doi:10.1002/cne.20257

Ramskold, D., Luo, S., Wang, Y.-C., Li, R., Deng, Q., Faridani, O. R., et al. (2012). Full-length mRNA-Seq from Single-Cell Levels of RNA and Individual Circulating Tumor Cells. *Nat. Biotechnol.* 30, 777–782. doi:10.1038/nbt.2282

Ranheim, E. A., Kwan, H. C. K., Reya, T., Wang, Y.-K., Weissman, I. L., and Francke, U. (2005). Frizzled 9 Knock-Out Mice Have Abnormal B-Cell Development. *Blood* 105, 2487–2494. doi:10.1182/blood-2004-06-2334

Ranum, P. T., Goodwin, A. T., Yoshimura, H., Kolbe, D. L., Walls, W. D., Koh, J.-Y., et al. (2019). Insights into the Biology of Hearing and Deafness Revealed by Single-Cell RNA Sequencing. *Cell Rep.* 26, 3160–3171. doi:10.1016/j.celrep.2019.02.053

Riise, N., Lindberg, B. R., Kulseth, M. A., Fredwall, S. O., Lundby, R., Estensen, M.-E., et al. (2018). Clinical Diagnosis of Larsen Syndrome, Stickler Syndrome and Loeys-Dietz Syndrome in a 19-year Old Male: A Case Report. *BMC Med. Genet.* 19, 155. doi:10.1186/s12881-018-0671-0

Rodriques, S. G., Stickels, R. R., Goeva, A., Martin, C. A., Murray, E., Vanderburg, C. R., et al. (2019). Slide-seq: A Scalable Technology for Measuring Genome-wide Expression at High Spatial Resolution. *Science* 363, 1463–1467. doi:10.1126/science.aaw1219

Rubel, E. W. (1978). "Ontogeny of Structure and Function in the Vertebrate Auditory System," In *Handbook of Sensory Physiology*. Editor M. Jacobson (New York: Springer-Verlag), 135–237. doi:10.1007/978-3-642-66880-7_5

Ruben, R. J. (1967). Development of the Inner Ear of the Mouse: a Radioautographic Study of Terminal Mitoses. *Acta Otolaryngol.* 220, 44.

Santos-Sacchi, J. (2019). The Speed Limit of Outer Hair Cell Electromechanical Activity. *HNO* 67, 159–164. doi:10.1007/s00106-019-0615-9

Satpathy, A. T., Granja, J. M., Yost, K. E., Qi, Y., Meschi, F., McDermott, G. P., et al. (2019). Massively Parallel Single-Cell Chromatin Landscapes of Human Immune Cell Development and Intratumoral T Cell Exhaustion. *Nat. Biotechnol.* 37, 925–936. doi:10.1038/s41587-019-0206-z

Sherman, B. T., Huang, D. W., Tan, Q., Guo, Y., Bour, S., Liu, D., et al. (2007). DAVID Knowledgebase: A Gene-Centered Database Integrating Heterogeneous Gene Annotation Resources to Facilitate High-Throughput Gene Functional Analysis. *BMC Bioinform.* 8, 426. doi:10.1186/1471-2105-8-426

Shi, F., Hu, L., and Edge, A. S. B. (2013). Generation of Hair Cells in Neonatal Mice by β-catenin Overexpression in Lgr5-Positive Cochlear Progenitors. *Proc. Natl. Acad. Sci. U.S.A.* 110, 13851–13856. doi:10.1073/pnas.1219952110

Shi, F., Hu, L., Jacques, B. E., Mulvaney, J. F., Dabdoub, A., and Edge, A. S. B. (2014). β-Catenin is Required for Hair-Cell Differentiation in the Cochlea. *J. Neurosci.* 34, 6470–6479. doi:10.1523/jneurosci.4305-13.2014

Soons, J. A. M., Ricci, A. J., Steele, C. R., and Puria, S. (2015). Cytoarchitecture of the Mouse Organ of Corti from Base to Apex, Determined Using *In Situ* Two-Photon Imaging. *J. Assoc. Res. Otolaryngol.* 16, 47–66. doi:10.1007/s10162-014-0497-1

Sun, S., Li, S., Luo, Z., Ren, M., He, S., Wang, G., et al. (2021). Dual Expression of Atoh1 and Ikzf2 Promotes Transformation of Adult Cochlear Supporting Cells into Outer Hair Cells. *Elife* 10, e66547. doi:10.7554/elife.66547

Takeda, N., Hara, H., Fujiwara, T., Kanaya, T., Maemura, S., and Komuro, I. (2018). TGF-β Signaling-Related Genes and Thoracic Aortic Aneurysms and Dissections. *Int. J. Mol. Sci.* 19, 2125. doi:10.3390/ijms19072125

Tanno, B., Babini, G., Leonardi, S., Giardullo, P., Stefano, I. D., Pasquali, E., et al. (2016). *Ex Vivo* miRNome Analysis in Ptch1+/− Cerebellum Granule Cells Reveals a Subset of miRNAs Involved in Radiation-Induced Medulloblastoma. *Oncotarget* 7, 68253–68269. doi:10.18632/oncotarget.11938

Tao, L., Yu, H. V., Llamas, J., Trecek, T., Wang, X., Stojanova, Z., et al. (2021). Enhancer Decommissioning Imposes an Epigenetic Barrier to Sensory Hair Cell Regeneration. *Dev. Cell* 56, 2471–2485. doi:10.1016/j.devcel.2021.07.003

Taukulis, I. A., Olszewski, R. T., Korrapati, S., Fernandez, K. A., Boger, E. T., Fitzgerald, T. S., et al. (2021). Single-Cell RNA-Seq of Cisplatin-Treated Adult Stria Vascularis Identifies Cell Type-specific Regulatory Networks and Novel Therapeutic Gene Targets. *Front. Mol. Neurosci.* 14, 718241. doi:10.3389/fnmol.2021.718241

Thelen, N., Breuskin, I., Malgrange, B., and Thiry, M. (2009). Early Identification of Inner Pillar Cells during Rat Cochlear Development. *Cell Tissue Res.* 337, 1–14. doi:10.1007/s00441-009-0810-1

Tritsch, N. X., and Bergles, D. E. (2010). Developmental Regulation of Spontaneous Activity in the Mammalian Cochlea. *J. Neurosci.* 30, 1539–1550. doi:10.1523/jneurosci.3875-09.2010

Tritsch, N. X., Yi, E., Gale, J. E., Glowatzki, E., and Bergles, D. E. (2007). The Origin of Spontaneous Activity in the Developing Auditory System. *Nature* 450, 50–55. doi:10.1038/nature06233

Tritsch, N. X., Rodríguez-Contreras, A., Crins, T. T. H., Wang, H. C., Borst, J. G. G., and Bergles, D. E. (2010). Calcium Action Potentials in Hair Cells Pattern Auditory Neuron Activity before Hearing Onset. *Nat. Neurosci.* 13, 1050–1052. doi:10.1038/nn.2604

Tsai, H., Hardisty, R. E., Rhodes, C., Kiernan, A. E., Roby, P., Tymowska-Lalanne, Z., et al. (2001). The Mouse Slalom Mutant Demonstrates a Role for Jagged1 in Neuroepithelial Patterning in the Organ of Corti. *Hum. Mol. Genet.* 10, 507–512. doi:10.1093/hmg/10.5.507

Tucker, J. B., Paton, C. C., Henderson, C. G., and Mogensen, M. M. (1993). Microtubule Rearrangement and Bending during Assembly of Large Curved Microtubule Bundles in Mouse Cochlear Epithelial Cells. *Cell Motil. Cytoskelet.* 25, 49–58. doi:10.1002/cm.970250107

Van Laer, L., Dietz, H., and Loeys, B. (2014). Loeys-Dietz Syndrome. *Adv. Exp. Med. Biol.* 802, 95–105. doi:10.1007/978-94-007-7893-1_7

Vater, M., and Kossl, M. (2011). Comparative Aspects of Cochlear Functional Organization in Mammals. *Hear. Res.* 273, 89–99. doi:10.1016/j.heares.2010.05.018

von Bartheld, C. S., Patterson, S. L., Heuer, J. G., Wheeler, E. F., Bothwell, M., and Rubel, E. W. (1991). Expression of Nerve Growth Factor (NGF) Receptors in the Developing Inner Ear of Chick and Rat. *Development* 113, 455–470. doi:10.1242/dev.113.2.455

Vrijens, K., Thys, S., De Jeu, M. T., Postnov, A. A., Pfister, M., Cox, L., et al. (2006). Ozzy, a Jag1 Vestibular Mouse Mutant, Displays Characteristics of Alagille Syndrome. *Neurobiol. Dis.* 24, 28–40. doi:10.1016/j.nbd.2006.04.016

Wang, H. C., Lin, C.-C., Cheung, R., Zhang-Hooks, Y., Agarwal, A., Ellis-Davies, G., et al. (2015). Spontaneous Activity of Cochlear Hair Cells Triggered by Fluid Secretion Mechanism in Adjacent Support Cells. *Cell* 163, 1348–1359. doi:10.1016/j.cell.2015.10.070

Wang, Z., Ma, Q., Lu, J., Cui, X., Chen, H., Wu, H., et al. (2021). Functional Parameters of Prestin Are Not Correlated with the Best Hearing Frequency. *Front. Cell Dev. Biol.* 9, 638530. doi:10.3389/fcell.2021.638530

Wang, I.-H., Murray, E., Andrews, G., Jiang, H.-C., Park, S. J., Donnard, E., et al. (2022). Spatial Transcriptomic Reconstruction of the Mouse Olfactory Glomerular Map Suggests Principles of Odor Processing. *Nat. Neurosci.* 25, 484–492. doi:10.1038/s41593-022-01030-8

Warchol, M., Lambert, P., Goldstein, B., Forge, A., and Corwin, J. (1993). Regenerative Proliferation in Inner Ear Sensory Epithelia from Adult Guinea Pigs and Humans. *Science* 259, 1619–1622. doi:10.1126/science.8456285

Wiwatpanit, T., Lorenzen, S. M., Cantú, J. A., Foo, C. Z., Hogan, A. K., Márquez, F., et al. (2018). Trans-differentiation of Outer Hair Cells into Inner Hair Cells in the Absence of INSM1. *Nature* 563, 691–695. doi:10.1038/s41586-018-0570-8

Woods, C., Montcouquiol, M., and Kelley, M. W. (2004). Math1 Regulates Development of the Sensory Epithelium in the Mammalian Cochlea. *Nat. Neurosci.* 7, 1310–1318. doi:10.1038/nn1349

Wu, D. K., and Kelley, M. W. (2012). Molecular Mechanisms of Inner Ear Development. *Cold Spring Harb. Perspect. Biol.* 4, a008409. doi:10.1101/cshperspect.a008409

Xiang, M., Gao, W. Q., Hasson, T., and Shin, J. J. (1998). Requirement for Brn-3c in Maturation and Survival, but Not in Fate Determination of Inner Ear Hair Cells. *Development* 125, 3935–3946. doi:10.1242/dev.125.20.3935

Yang, L. M., Cheah, K. S. E., Huh, S.-H., and Ornitz, D. M. (2019). Sox2 and FGF20 Interact to Regulate Organ of Corti Hair Cell and Supporting Cell Development in a Spatially-Graded Manner. *PLoS Genet.* 15, e1008254. doi:10.1371/journal.pgen.1008254

Yarin, Y. M., Lukashkin, A. N., Poznyakovskiy, A. A., Meissner, H., Fleischer, M., Baumgart, J., et al. (2014). Tonotopic Morphometry of the Lamina Reticularis of the guinea Pig Cochlea with Associated Microstructures and Related Mechanical Implications. *J. Assoc. Res. Otolaryngol.* 15, 1–11. doi:10.1007/s10162-013-0420-1

Zhao, T., Chiang, Z. D., Morriss, J. W., LaFave, L. M., Murray, E. M., Del Priore, I., et al. (2022). Spatial Genomics Enables Multi-Modal Study of Clonal Heterogeneity in Tissues. *Nature* 601, 85–91. doi:10.1038/s41586-021-04217-4

Zheng, J. L., and Gao, W.-Q. (2000). Overexpression of Math1 Induces Robust Production of Extra Hair Cells in Postnatal Rat Inner Ears. *Nat. Neurosci.* 3, 580–586. doi:10.1038/75753

Zheng, G. X., Terry, J. M., Belgrader, P., Ryvkin, P., Bent, Z. W., Wilson, R., et al. (2017). Massively Parallel Digital Transcriptional Profiling of Single Cells. *Nat. Commun.* 8, 14049. doi:10.1038/ncomms14049

Zhu, Y., Scheibinger, M., Ellwanger, D. C., Krey, J. F., Choi, D., Kelly, R. T., et al. (2019). Single-cell Proteomics Reveals Changes in Expression during Hair-Cell Development. *Elife* 8, e50777. doi:10.7554/eLife.50777

Conflict of Interest: The author declares that the research was conducted in the absence of any commercial or financial relationships that could be construed as a potential conflict of interest.

Publisher's Note: All claims expressed in this article are solely those of the authors and do not necessarily represent those of their affiliated organizations, or those of the publisher, the editors and the reviewers. Any product that may be evaluated in this article, or claim that may be made by its manufacturer, is not guaranteed or endorsed by the publisher.

frontiers | Frontiers in Cell and Developmental Biology

TYPE Original Research
PUBLISHED 26 August 2022
DOI 10.3389/fcell.2022.959624

OPEN ACCESS

EDITED BY
Berta Alsina,
Pompeu Fabra University, Spain

REVIEWED BY
Bryan Douglas Crawford,
University of New Brunswick
Fredericton, Canada
Stefan Heller,
Stanford University, United States

*CORRESPONDENCE
Tanya T. Whitfield,
t.whitfield@sheffield.ac.uk

†These authors contributed equally to this work and share first authorship

SPECIALTY SECTION
This article was submitted to Molecular and Cellular Pathology, a section of the journal Frontiers in Cell and Developmental Biology

RECEIVED 01 June 2022
ACCEPTED 12 July 2022
PUBLISHED 26 August 2022

CITATION
Jones AA, Diamantopoulou E, Baxendale S and Whitfield TT (2022), Presence of chondroitin sulphate and requirement for heparan sulphate biosynthesis in the developing zebrafish inner ear.
Front. Cell Dev. Biol. 10:959624.
doi: 10.3389/fcell.2022.959624

Presence of chondroitin sulphate and requirement for heparan sulphate biosynthesis in the developing zebrafish inner ear

Ana A. Jones †, Elvira Diamantopoulou †, Sarah Baxendale and Tanya T. Whitfield *

Development, Regeneration and Neurophysiology, School of Biosciences, and Bateson Centre, University of Sheffield, Sheffield, United Kingdom

Epithelial morphogenesis to form the semicircular canal ducts of the zebrafish inner ear depends on the production of the large glycosaminoglycan hyaluronan, which is thought to contribute to the driving force that pushes projections of epithelium into the lumen of the otic vesicle. Proteoglycans are also implicated in otic morphogenesis: several of the genes coding for proteoglycan core proteins, together with enzymes that synthesise and modify their polysaccharide chains, are expressed in the developing zebrafish inner ear. In this study, we demonstrate the highly specific localisation of chondroitin sulphate to the sites of epithelial projection outgrowth in the ear, present before any morphological deformation of the epithelium. Staining for chondroitin sulphate is also present in the otolithic membrane, whereas the otoliths are strongly positive for keratan sulphate. We show that heparan sulphate biosynthesis is critical for normal epithelial projection outgrowth, otolith growth and tethering. In the *ext2* mutant ear, which has reduced heparan sulphate levels, but continues to produce hyaluronan, epithelial projections are rudimentary, and do not grow sufficiently to meet and fuse to form the pillars of tissue that normally span the otic lumen. Staining for chondroitin sulphate and expression of *versican b*, a chondroitin sulphate proteoglycan core protein gene, persist abnormally at high levels in the unfused projections of the *ext2* mutant ear. We propose a model for wild-type epithelial projection outgrowth in which hyaluronan and proteoglycans are linked to form a hydrated gel that fills the projection core, with both classes of molecule playing essential roles in zebrafish semicircular canal morphogenesis.

KEYWORDS

extracellular matrix, heparan sulphate proteoglycan, chondroitin sulphate proteoglycan, epithelial morphogenesis, semicircular canals, otoliths, zebrafish, Ext2

1 Introduction

Morphogenesis of the vertebrate inner ear is an excellent exemplar of epithelial morphogenesis. Development of this organ system involves a series of events that shape and fold the otic epithelium, converting it from a fluid-filled vesicle into a series of interlinked sensory chambers and tubes (reviewed in Alsina and Whitfield, 2017). In the zebrafish, morphogenesis of the semicircular canal ducts is initiated when finger-like protrusions or projections of epithelium move into the lumen of the vesicle. Between days 2 and 3 of embryonic development, anterior, posterior and ventral projections fuse in a stereotyped sequence with corresponding bulges from a lateral projection. These fusion events create three new columns or pillars of tissue that span the otic lumen, defining the three semicircular canals (Waterman and Bell, 1984; Haddon and Lewis, 1996).

It has long been recognised that the extracellular matrix (ECM) plays a critical role in formation and outgrowth of the epithelial projections in the zebrafish and *Xenopus* ear. Electron microscopy studies revealed that the acellular cores of the projections are filled with "fibrillar and granular material", and that cells of the projection epithelium are rich in endoplasmic reticulum and lack a basal lamina, consistent with high levels of ECM production and secretion (Waterman and Bell, 1984; Haddon and Lewis, 1991). A major ECM component of the projection cores is the glycosaminoglycan (GAG) hyaluronan (also known as hyaluronic acid or HA) (Haddon and Lewis, 1991; Toole, 2001; Busch-Nentwich et al., 2004). Haddon and Lewis first proposed that localised synthesis and retention of this large, space-filling polymer could act as a driving force for the outgrowth of epithelial projections into the lumen of the *Xenopus* otic vesicle (Haddon and Lewis, 1991). In support of this hypothesis, localised enzymatic digestion of HA blocks projection outgrowth in both *Xenopus* (Haddon and Lewis, 1991) and zebrafish (Geng et al., 2013; Munjal et al., 2021). Moreover, reducing HA production in zebrafish, via morpholino-mediated knockdown of *dfna5* (orthologue of the human deafness autosomal dominant *DFNA5* gene) or *hyaluronan synthase* (*has3*), or genetic mutation of *UDP-glucose dehydrogenase* (*ugdh*), compromises projection outgrowth (Neuhauss et al., 1996; Walsh and Stainier, 2001; Busch-Nentwich et al., 2004; Munjal et al., 2021).

The zebrafish *ugdh* (*jekyll*) mutant otic phenotype is severe, with very small and rudimentary projections, even by 6 days post fertilisation (dpf) (Neuhauss et al., 1996). The *ugdh* gene, which is expressed in the epithelial projections of the zebrafish ear (Walsh and Stainier, 2001; Busch-Nentwich et al., 2004), is an orthologue of *sugarless* (*sgl*) in *Drosophila* (Häcker et al., 1997), and codes for the enzyme UDP-glucose 6-dehydrogenase (Ugdh). Ugdh catalyses the production of glucuronic acid, an essential building block not only of HA, but also of various proteoglycans, including heparan sulphate, chondroitin sulphate and keratan sulphate proteoglycans (HSPGs, CSPGs, KSPGs) (reviewed in Zimmer et al., 2021), suggesting that deficiencies of these molecules might also contribute to the *ugdh* mutant phenotype.

Proteoglycans are negatively charged ECM molecules consisting of sulphated GAG chains attached to a protein core, with widespread roles in animal development (reviewed in Bülow and Hobert, 2006). Chondroitin sulphate proteoglycans (CSPGs) are already implicated in zebrafish otic morphogenesis. The CSPG core protein gene *versican a* (*vcana*) is highly expressed in the epithelial projections during their growth phase, but is rapidly downregulated on fusion to form pillars (Geng et al., 2013). The zebrafish ear expresses chondroitin synthase and glycosyltransferase genes coding for enzymes involved in the polymerisation of CS chains (Li et al., 2010; Filipek-Górniok et al., 2013), together with sulfotransferase genes involved in CS modification (Habicher et al., 2015). Morpholino-mediated knockdown of *chondroitin synthase 1* (*chsy1*) leads to epithelial projection defects in the zebrafish ear (Li et al., 2010). Here, we use immunohistochemistry to show that localised deposition of CS prefigures the sites of projection outgrowth in wild-type zebrafish ears.

To test the role of heparan sulphate (HS) in zebrafish semicircular canal morphogenesis, we have examined the otic phenotype of the *exostosin 2* (*ext2/dackel*) mutant, which lacks the function of a glycosyltransferase involved in HS biosynthesis (Lee et al., 2004). Mutants have a global reduction in HS levels by 5 days post fertilisation (dpf), and form a model for the human autosomal dominant condition multiple osteochondromas (Lee et al., 2004; Clément et al., 2008; Holmborn et al., 2012). Homozygous zebrafish *ext2* mutations disrupt development of cartilage, bone and teeth (Schilling et al., 1996; Clément et al., 2008; Wiweger et al., 2012; Wiweger et al., 2014), pectoral fins (van Eeden et al., 1996), the retinotectal projection (Karlstrom et al., 1996; Trowe et al., 1996; Lee et al., 2004), and the lateral line (Venero Galanternik et al., 2015). These pleiotropic effects reflect the widespread requirement of HSPGs for the activity of various developmental signalling pathways (see, for example, Norton et al., 2005; Fischer et al., 2011; Venero Galanternik et al., 2015). Otic defects were noted in *ext2* mutants (Whitfield et al., 1996), but were not characterised in detail. We now show that *ext2* mutants have otic defects similar to those seen after disruption of HA or CS, demonstrating an essential role for HS biosynthesis in epithelial projection outgrowth and formation of the semicircular canal system. Our results indicate that the otic ECM is composed of both HA and proteoglycans, and that the loss of either class of molecule compromises the early steps of semicircular canal morphogenesis.

2 Materials and methods

2.1 Animals

Standard zebrafish husbandry methods were employed (Westerfield, 2007; Aleström et al., 2020). The wild-type strain used was AB (ZDB-GENO-960809-7), and the *ext2* mutant allele used was *dak*^{tw25e} (ZDB-ALT-980203-1459) (Haffter et al., 1996).

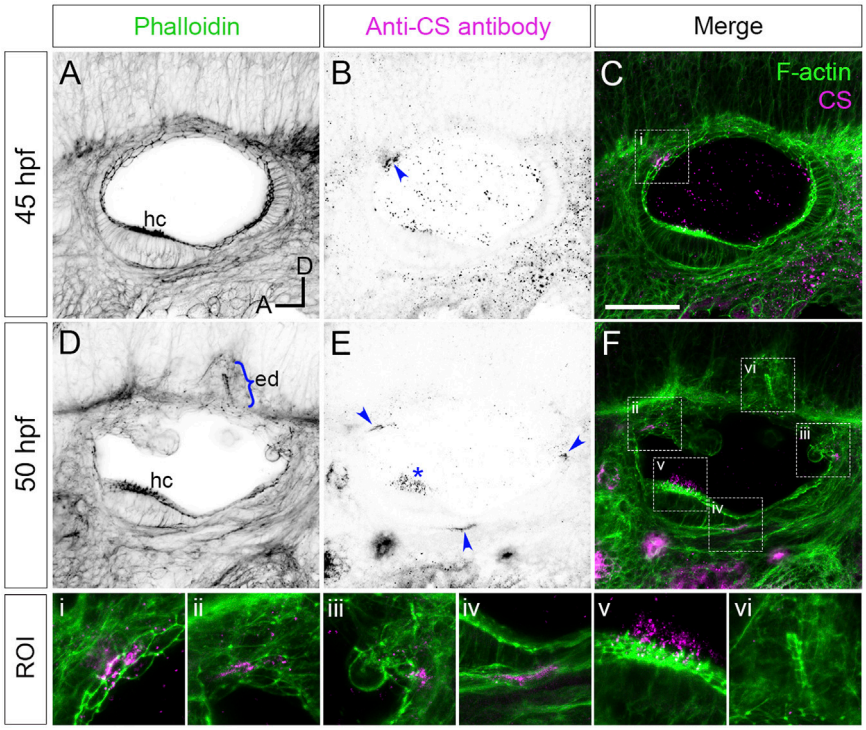

FIGURE 1
Staining for chondroitin sulphate in phenotypically wild-type zebrafish ears marks sites of epithelial projection outgrowth.
(A–F) Confocal images of Alexa-phalloidin (green) and anti-CS antibody (magenta) whole-mount stains of phenotypically wild-type ears (Section 2). Blue arrowheads mark foci of chondroitin sulphate (CS) staining associated with the emergence (evagination) of epithelial projections from the otic epithelium; blue bracket marks the invaginating endolymphatic duct (ed); blue asterisk marks staining in the otolithic membrane overlying hair cells of the anterior (utricular) macula. Boxed areas highlight regions of interest (ROI), enlarged in the bottom row of panels: **(i)**, apical focus of CS staining at 45 hpf prefiguring site of emergence of the anterior projection; **(ii,iii)**, foci of CS staining associated with the anterior and posterior projections, respectively, at 50 hpf; **(iv)**, basal focus of CS staining prefiguring site of emergence of the ventral projection; **(v)**, CS staining in the utricular otolithic membrane; **(vi)**, absence of CS stain in the endolymphatic duct. All panels are lateral views with anterior to left, and dorsal to top (orientation shown in **(A)**: A, anterior; D, dorsal). Scale bar in **(C)**, 50 µm (applies to **(A–F)**). Abbreviations: CS, chondroitin sulphate; ed, endolymphatic duct; hc, stereociliary bundles on the apices of hair cells in the anterior (utricular) macula. Additional examples and developmental stages are shown in Figure 4; Supplementary Figure S1; Supplementary Movie S1.

This allele has a T >A mutation in exon 5, introducing a STOP codon and predicting a truncation of the protein sequence at amino acid 227 (Lee et al., 2004). In all examples shown, mutant embryos were homozygous for the zygotic *dak*^{tw25e} allele. For some experiments, fish were crossed onto a *nacre* (*mitfa*$^{-/-}$; ZDB-GENO-990423-18) background, which has reduced body pigmentation, facilitating visualisation of staining patterns (Lister et al., 1999). The phenotypically wild-type sibling embryos shown in Figures 1, 4E,E', were from a cross between parents heterozygous for mutations in *tbx1*^{tm208} (ZDB-ALT-980203-1362). Embryos were raised in E3 embryo medium (5 mM NaCl, 0.17 mM KCl, 0.33 mM $CaCl_2$, 0.33 mM $MgSO_4$) (Westerfield, 2007) at 28.5°C. In some cases, to obtain the desired stage, embryos were raised at temperatures ranging from 23°C to 33°C, and staged according to the equivalent hours post fertilisation (hpf) at 28.5°C using a conversion formula (Kimmel et al., 1995). Methylene blue (0.0001%) was added to reduce fungal growth, and where necessary, 0.003% 1-phenyl 2-thiourea (PTU; 0.003%) was added to block the development of pigmentation. We use the term embryo throughout to refer to zebrafish embryos and larvae from 0 to 5 days post fertilisation (dpf).

2.2 Genotyping

The *dak*^{tw25e} mutation introduces an *Mse*I restriction site into the genomic DNA sequence, allowing the identification of mutant embryos at early stages [up to 48 h post fertilisation (hpf), before the onset of any obvious phenotype] by genotyping. Forward (5'-GGCTTCTCCACATGGACCTA-3') and reverse (5'-CCGAGGACTGGAAGAAAAAC-3') primers were used to amplify genomic DNA from individual embryos by PCR. The

amplified product (188 base pairs, bp) was digested with *Mse*I (New England Biolabs, R0525S), which cuts the mutant sequence to generate two fragments of 158 bp and 30 bp.

2.3 Immunofluorescence and phalloidin staining

Embryos were dechorionated and fixed at the desired stages in 4% paraformaldehyde for 2–4 h at room temperature (except 40 hpf embryos, which were fixed overnight at 4°C). Fixed embryos were permeabilised in PBS-Tr (phosphate-buffered saline (PBS),1% Triton X-100) for 3 × 5 min, blocked in Blocking Solution (PBS-Tr with the addition of 10% sheep or donkey serum, depending on the secondary antibody used) for 60 min, and incubated overnight at 4°C in Blocking Solution and 1% DMSO, with the addition of the relevant primary antibody at the following concentrations: anti-Chondroitin Sulphate (CS) (C8035 mouse monoclonal, Sigma-Aldrich), 1:100; anti-Keratan Sulphate (KS) (3H1 mouse anti-rat monoclonal, R. U. Margolis and R. J. Margolis, Developmental Studies Hybridoma Bank), 1:100. Embryos were washed in PBS-Tr for 3 × 5 min and 4 × 30 min, and then incubated overnight at 4°C in Blocking Solution and 1% DMSO with the addition of an Alexa-647-conjugated goat anti-mouse secondary antibody (A21235, Invitrogen; 1:200). Embryos were counterstained for F-actin by the addition of Alexa Fluor 488 Phalloidin (8878, Cell Signalling Technology, 1:100 from a 6.6 μM stock) to the secondary antibody staining step. Embryos were washed in PBS-Tr for 4 × 5 min, and stored in PBS-Tr at 4°C before mounting. Staining with the secondary antibody only gave no signal in the ear (not shown). As an additional control, embryos from the same batch were stained with primary antibodies to CS or KS in the same experiment, using the same secondary antibody. Each primary antibody gave a different and reproducible staining pattern (Supplementary Figure S1). Staining experiments were performed in duplicate, and at least two embryos were imaged for each genotype and stage.

2.4 Hyaluronic acid binding protein staining

The protocol for HABP staining was adapted from a published method (Munjal et al., 2021). Embryos were dechorionated at 57 hpf and fixed in 4% paraformaldehyde at room temperature for 2 h. Embryos were washed in PBS for 3 × 5 min, before permeabilisation with ice-cold acetone at −20°C for 7 min. Embryos were washed in PBS-Tr for 3 × 5 min and blocked in PBS-Tr containing 5% BSA for 60 min at room temperature. Embryos were incubated in blocking solution containing biotinylated Hyaluronan Binding Protein (HABP from EMD Millipore, 1:100 dilution of 0.5 μg/μL stock) at 4°C, overnight. Embryos were washed 3 × 15 min with PBS (detergent was avoided due to low binding affinity of HABP to HA). Embryos were incubated with Streptavidin Alexa Fluor 546 (Invitrogen S11225, 1:500) and counterstained for F-actin with Alexa Fluor 488 Phalloidin (8878, Cell Signalling Technology, 1:100 from a 6.6 μM stock). Embryos were washed for 3 × 15 min with PBS before mounting for imaging.

2.5 Whole-mount *in situ* hybridisation

Embryos were dechorionated and fixed in 4% paraformaldehyde overnight at 4°C. Fixed embryos were rinsed in PBS, dehydrated through a methanol series, and stored in methanol at −20°C. Whole-mount *in situ* hybridisation to the genes listed in Supplementary Table S1 was performed based on the standard protocol (Thisse and Thisse, 2008) with minor modifications. Data shown in Figure 2 are representative of two individual experiments for each gene (n = 50 embryos analysed per embryonic stage).

2.6 Microscopy and photography

For live imaging, zebrafish embryos were anaesthetised in 4% (w/v) tricaine (MS222) in E3 medium and mounted in 3% (w/v) methylcellulose in a cavity created by cutting a small window in three layers of electrical insulation tape stuck on a glass slide, and coverslipped. For immunofluorescence, fixed embryos were dissected to remove the yolk and eyes, and then mounted laterally in 1–1.5% Low Melting Point Agarose in PBS in the centre of a 35-mm Wilco glass-bottomed Petri dish. Image stacks (z-step, 1 μm) were acquired on a Nikon A1 confocal microscope with a × 40 objective using the 488 and 647 nm excitation laser lines. HABP-stained embryos were mounted in low-melting point agarose in glass capillaries and imaged using a Zeiss Z1 light-sheet microscope. Image stacks were acquired with a ×20 objective using the 488 and 561 excitation laser lines. Images were taken dorsally with the embryo rotated by 25° to obtain the best view of the acellular core of the lateral projection in the ear.

Images of live embryos and those stained using *in situ* hybridisation were acquired on an Olympus BX-51 compound microscope equipped with a C3030ZOOM camera and CELL B software, or a Micropublisher 6 camera and Ocular software. Images for the measurements shown in Figure 2; Supplementary Figure S2 were acquired on a Zeiss Axio Zoom. V16 microscope. Unless otherwise stated, embryos were oriented laterally, with anterior to the left. Single channel images are displayed in inverted grayscale. Images were processed in Fiji (Schindelin et al., 2012), and figures were assembled with Adobe Photoshop v22.5.1.

2.7 Otolith displacement ("tapping") assay

Anaesthetised *ext2* mutants (N = 8) and phenotypically wild-type siblings (N = 8) at 5 dpf were individually mounted in 4% methylcellulose in a cavity made by cutting a window

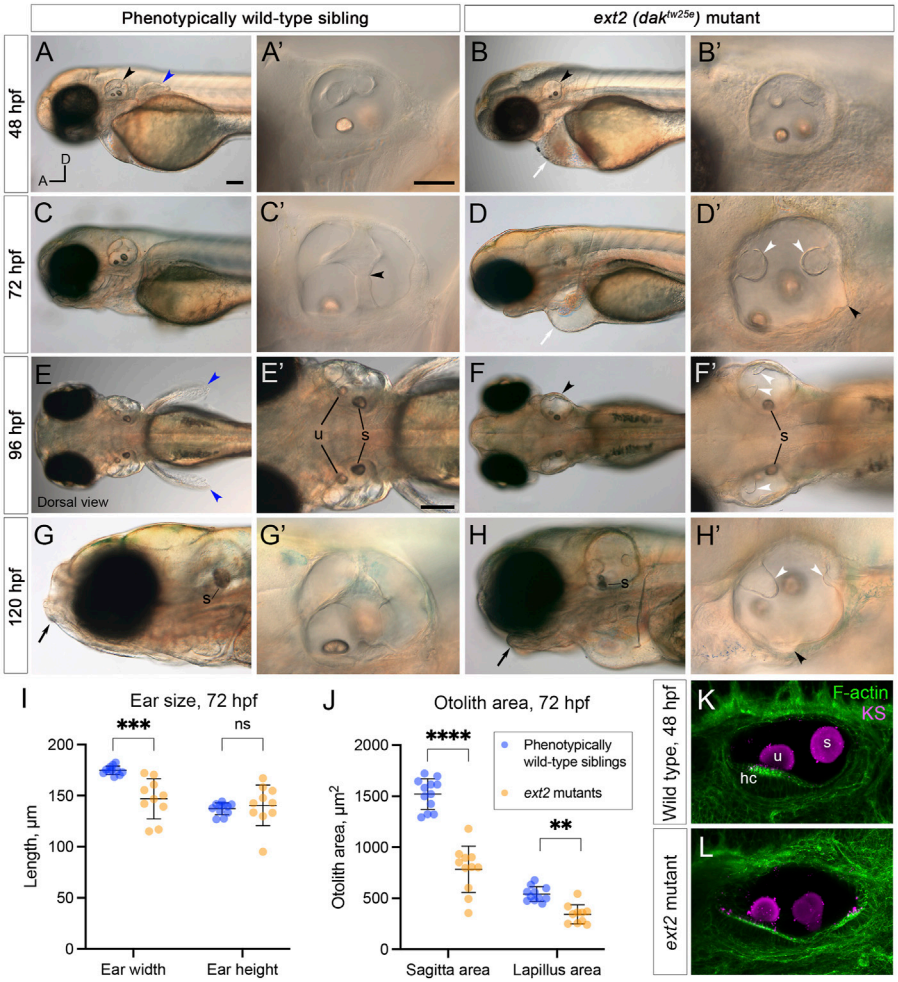

FIGURE 2
Morphological defects in the inner ear of *ext2* mutant embryos. **(A–H')** Live DIC images of phenotypically wild-type sibling and *ext2* homozygous mutant embryos at 48–120 hpf. The otic vesicle (enlarged in the second and fourth columns) is marked with a black arrowhead in **(A,B,F)**. Note the absence of the pectoral fin bud [**(A,E)**, blue arrowheads in wild type], cardiac oedema [**(B,D)**, white arrows], and abnormal jaw [**(G,H)**, black arrows] in the mutant. At 72 hpf, epithelial projections have fused and formed pillars in the wild-type ear [black arrowhead in **(C')** marks the fusion plate of the ventral pillar], whereas in the *ext2* mutant ear, the projections stayed small and often did not fuse [white arrowheads, **(D',F',H')**]. Black arrowheads in **(D')** and **(H')** mark abnormal out-pocketings of the epithelium. Scale bars: **(A)**, 100 µm [also applies to **(B,C,D,E,F,G,H)**]; **(A')**, 50 µm [also applies to **(B',C',D',G',H')**]; **(E')**, 100 µm [also applies to **(F')**]. All panels are lateral views with anterior to the left (orientation shown in **(A)**: A, anterior; D, dorsal), apart from **(E–F')** (dorsal views, anterior to the left). **(I,J)** Morphometric measurements of ear width and height **(I)**, and otolith area **(J)**, traced from micrographs at 72 hpf [N = 6 embryos, n = 12 ears of each genotype (some data points missing)]. See Supplementary Figure S2 for details. Horizontal bars show mean +/− standard deviation. Two-way ANOVA (mixed-effects model) with Šídák's correction for multiple comparisons: ns, not significant; $^{**}p$ = 0.0082; $^{***}p$ = 0.0008; $^{****}p < 0.0001$. **(K,L)** Ears at 48 hpf, stained with Alexa phalloidin (green) and an antibody to keratan sulphate (magenta). Abbreviations: hc, hair cells in the utricular macula; s, saccular otolith (sagitta); u, utricular otolith (lapillus).

in four layers of electrical insulation tape on a microscope slide, and covered with a coverslip. The slide was then gently tapped on the benchtop for 10 s. Images were taken before and after tapping. This protocol was adapted from an earlier study, where it was used to measure otolith tethering in zebrafish mutants for *otogelin* and *tecta* (Stooke-Vaughan et al., 2015).

2.8 Measurements and statistical analysis

Ear and otolith morphometric measurements were made from 2D micrographs in Fiji (Schindelin et al., 2012). Data were analysed and presented using GraphPad Prism v9.1.2. Statistical tests used are stated in the relevant figure legend.

3 Results

3.1 Foci of chondroitin sulphate staining prefigure emergence of the semicircular canal projections in wild-type ears

Versican genes, which code for the core proteins of chondroitin sulphate proteoglycans (CSPGs), are expressed in a dynamic pattern in the zebrafish ear, with maximum mRNA expression levels during projection outgrowth (Geng et al., 2013). To examine the distribution of chondroitin sulphate (CS) in the ear, we stained fixed samples with an antibody to CS. In phenotypically wild-type embryos (Section 2), anti-CS antibody staining revealed reproducible, small (10–20 μm diameter) foci that prefigure the emergence (evagination) of the lateral, anterior, posterior and ventral semicircular canal projections (Figure 1; Supplementary Movie S1; additional examples at different stages in Figure 4; Supplementary Figure S1A). For the anterior projection, staining was present at 40 hpf on the apical (lumenal) side of the epithelium (Figures 1A–C; see also Figures 4A, A'), with foci of staining present at the base of the lateral, anterior and posterior projections at 45–50 hpf (Figure 1E). For the ventral projection at 48–50 hpf, staining was present in a discrete patch or streak on the basal side of the epithelium, beneath a small group of cells that were about to evaginate to form the projection (Figure 1E; Supplementary Movie S1). By contrast, CS staining was absent from cells invaginating to form the endolymphatic duct, a short tube that extends from dorsal otic epithelium (Figures 1D,F). At later stages, after fusion of epithelial projections and bulges to form pillars, there was very little CS staining evident in the cores of the pillars or lateral projection in wild-type ears (Supplementary Movie S3; see also Figures 4E,G). Positive staining for CS also marked the otolithic membrane overlying sensory hair cells of the utricular macula (asterisks, Figure 1E, Supplementary Figure S1A–A", Supplementary Movie S3).

3.2 The ears of *ext2* mutants, which have reduced heparan sulphate biosynthesis, have epithelial projection and otolith defects.

To test the role of heparan sulphate (HS) biosynthesis in otic morphogenesis, we imaged the developing ear in live zebrafish *ext2* (*dak*^{tw25e}) homozygous mutant embryos, at developmental stages when the otic epithelium is undergoing morphogenetic deformation to form the semicircular canal system (2–5 days post fertilisation, dpf). Otic development normally progresses by the formation of epithelial projections and bulges that fuse to form pillars of tissue spanning the otic lumen (Waterman and Bell, 1984; Haddon and Lewis, 1996). At 48 h post fertilisation (hpf), the *ext2* mutant otic vesicle was rounder in shape than that of phenotypically wild-type sibling embryos (Figures 2, 4). The lateral projection formed an anterior bulge, but formation of the posterior and ventral bulges was delayed or absent (Figures 2A,F'). By 72 hpf, epithelial projections in the wild-type ear had fused to form three pillars in all cases (N = 16 embryos; n = 32 ears; Figure 2C). By contrast, in *ext2* mutants at 72 hpf, the anterior projection had fused in some ears (N = 4 embryos; n = 5/8 ears), but the posterior projection had only fused in 1/8 mutant ears examined, and the ventral projection remained very small in all ears examined (n = 8/8). Unfused projections were also present in the ear at 4 and 5 days post fertilisation (dpf) (Figures 2D',F',H'), and the ears, although smaller than normal, became swollen, visible in a dorsal view (Figure 2F,F'; further examples in Figure 6). Some mutant ears also had abnormal out-pocketings of the epithelium, not present in the wild type (black arrowheads, Figure 2D,H').

Measurements of ear size at 72 hpf indicated that the *ext2* mutant ears were narrower in the anteroposterior dimension in a lateral view ("ear width") than in the wild type, with more variation in size and shape (Figure 2I; Supplementary Figure S2). Ear height in *ext2* mutants was also more variable, but the mean value was not significantly different from the wild type (Figure 2I; Supplementary Figure S2). Two otoliths were present in the *ext2* mutant ear, but were smaller than normal at 72 hpf (Figure 2J). However, the otoliths stain strongly with an antibody to keratan sulphate, as in the wild type (Figures 2K,L; Supplementary Figure S1B–B"). Phalloidin staining confirmed that all five sensory patches (two maculae and three cristae) were present in the *ext2* mutant ear at 3–5 dpf, and contained differentiated hair cells (Figure 2K,L; additional examples in Figure 4).

The *ext2* gene is expressed maternally and ubiquitously up to 36 hpf (Lee et al., 2004); transcript levels were found to be reduced in *ext2* mutants as measured by qPCR at 5 dpf (Wiweger et al., 2014). We used *in situ* hybridisation to examine the spatial expression pattern of *ext2* beyond 36 hpf (Supplementary Figure S3). Expression of *ext2* was regionalised at 50 and 72 hpf, with highest levels in the brain and retina, spinal cord, pectoral fin and pharyngeal region, whereas expression in the somites, lens and heart was weaker or undetectable. Expression was present in both the ear and lateral line neuromasts. mRNA for *ext2* was still expressed in *ext2* mutants, but levels appeared slightly reduced throughout, including in the ear at 72 hpf (Supplementary Figure S3).

3.3 Expression of *vcanb* and *chsy1* mRNA persists abnormally in the unfused epithelial projections of the *ext2* mutant ear

We next tested the expression of *versican b* (*vcanb*) and *chondroitin synthase 1* (*chsy1*) mRNA in the wild-type and *ext2*

10.3389/fcell.2022.959624

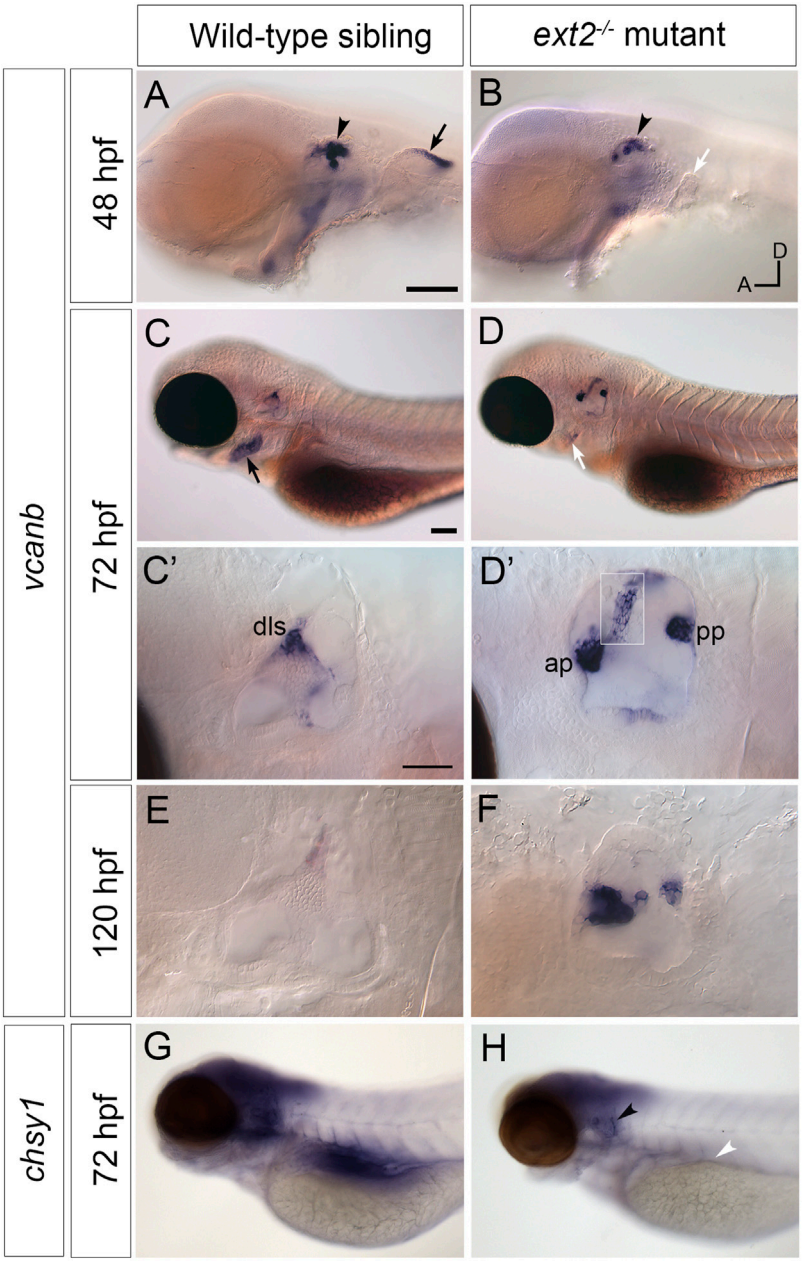

FIGURE 3
Expression of *vcanb* and *chsy1* in the *ext2* mutant ear. **(A–H)** *In situ* hybridisation to *vcanb* **(A–F)** and *chsy1* **(G,H)** mRNA in phenotypically wild-type sibling and *ext2* mutant embryos. **(A)** Expression of *vcanb* is present in the ear (black arrowhead) and pectoral fin (black arrow) in sibling embryos. **(B)** Only a rudimentary pectoral fin bud is present in the *ext2* mutant, and the associated *vcanb* staining is missing (white arrow). **(C,D)** At 72 hpf, *vcanb* expression is strongly reduced in the periderm of the second arch (future operculum) in *ext2* mutants [black arrowhead in **(C)**, white arrowhead in **(D)**]. **(C',D')** Enlargements of the ears shown in **(C,D)**, respectively. Expression of *vcanb* is now down-regulated in the pillars of the wild-type ear, remaining only in the dorsolateral septum (dls). In the *ext2* mutant, expression persists abnormally in the unfused anterior and posterior projections [ap, pp, **(D')**] and in an abnormal pillar-like structure (boxed insert of same ear taken at a different focal plane). **(E,F)** *vcanb* expression persists abnormally in the unfused projections in mutant ears until at least 120 hpf. **(G,H)** Overall levels of *chsy1* expression are slightly reduced in *ext2* mutants **(H)**; expression is missing in the viscera (white arrowhead), but persists in unfused epithelial projections in the ear (black arrowhead). All panels are lateral views with anterior to the left, dorsal to the top (orientation shown in **(B)**: A, anterior; D, dorsal). Scale bars: in **(A)**, 100 μm (also applies to **(B)**); in **(C)**, 100 μm [also applies to **(D,G,H)**]; in **(C)**, 50 μm [also applies to **(D')**].

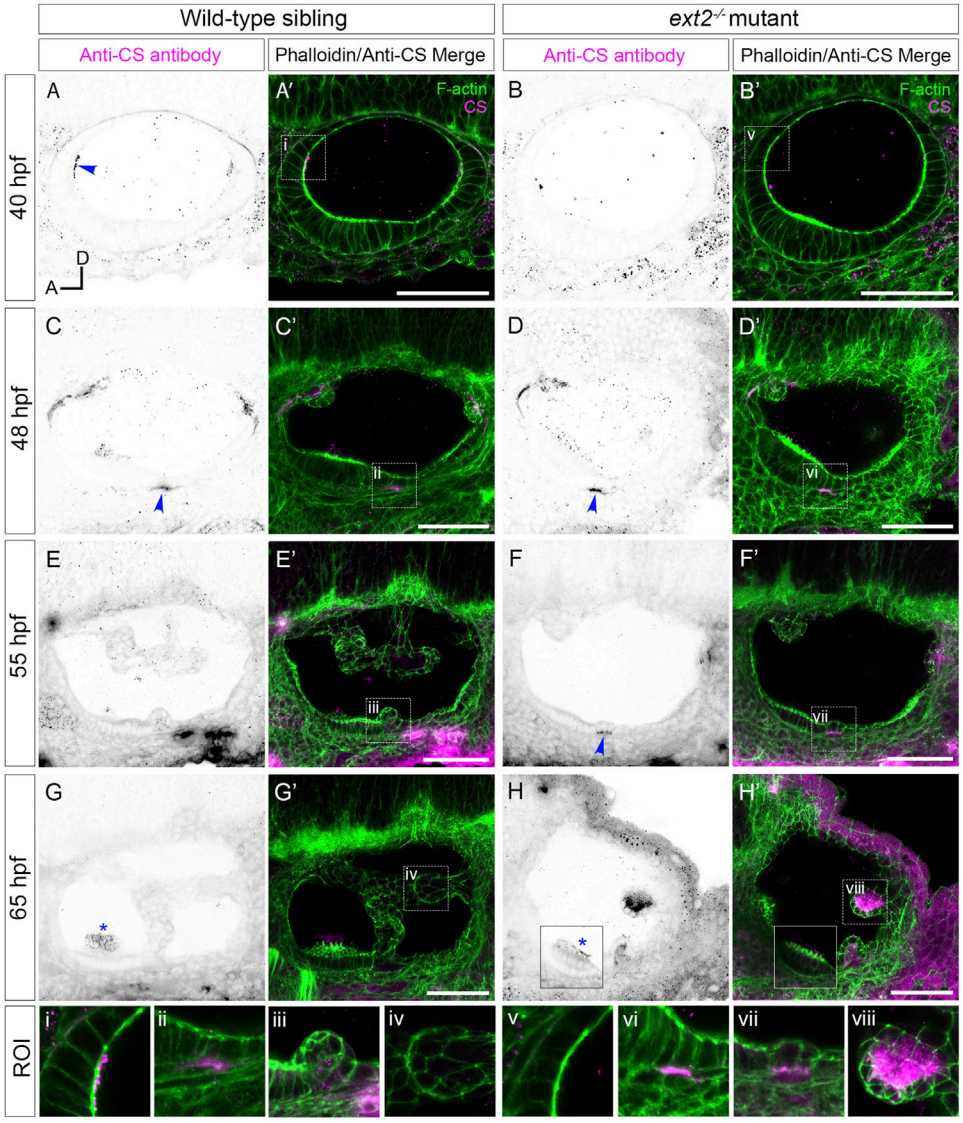

FIGURE 4
Staining for chondroitin sulphate in the *ext2* mutant ear is delayed at early stages, but accumulates abnormally in unfused epithelial projections by 65 hpf. **(A–H')** Confocal images of Alexa-phalloidin (green) and anti-CS antibody (magenta) whole-mount stains of phenotypically wild-type sibling and *ext2* mutant ears (Section 2). Blue arrowheads mark foci of chondroitin sulphate (CS) staining associated with the emergence (evagination) of epithelial projections from the otic epithelium; blue asterisks mark staining in the otolithic membrane overlying hair cells of the anterior (utricular) macula. Boxed areas highlight regions of interest (ROI), enlarged in the bottom row of panels: **(i, v)**, apical focus of CS staining at 40 hpf, absent in the *ext2* mutant, prefiguring site of emergence of the anterior projection in the wild-type ear; **(ii, vi)**, foci of CS staining associated with the ventral projection at 48 hpf; **(iii, vii)**, CS staining in the emerging ventral projection, delayed in the *ext2* mutant; **(iv, viii)** no detectable staining in the wild-type posterior projection **(iv)** contrasts with strong staining in the unfused posterior projection in the *ext2* mutant **(viii)**. The boxed area in the lower left of **(H, H')** is taken from a different focal plane in the stack to show the anterior (utricular) macula and otolithic membrane. All images are maximum intensity projections (MIPs) of between 3 and 10 selected *z*-slices, with the exception of the images at 40 hpf, which are single *z*-slices. All images are lateral views with anterior to left and dorsal to top (orientation shown in **(A)**: A, anterior; D, dorsal). Scale bars, 50 μm. Abbreviation: CS, chondroitin sulphate.

mutant ear. Expression of *vcanb* in the wild-type ear is very similar to that of *vcana* (Geng et al., 2013), with high levels of expression in the epithelial projections as they evaginate and grow out into the lumen of the ear, becoming rapidly down-regulated after fusion to form a pillar (Figures 3A,C,E). Expression remains in the dorsolateral septum of the wild-type ear at 72 hpf (Figure 3C,C'), more weakly at 5 dpf (Figure 3E). Expression in the *ext2* mutants showed some

10.3389/fcell.2022.959624

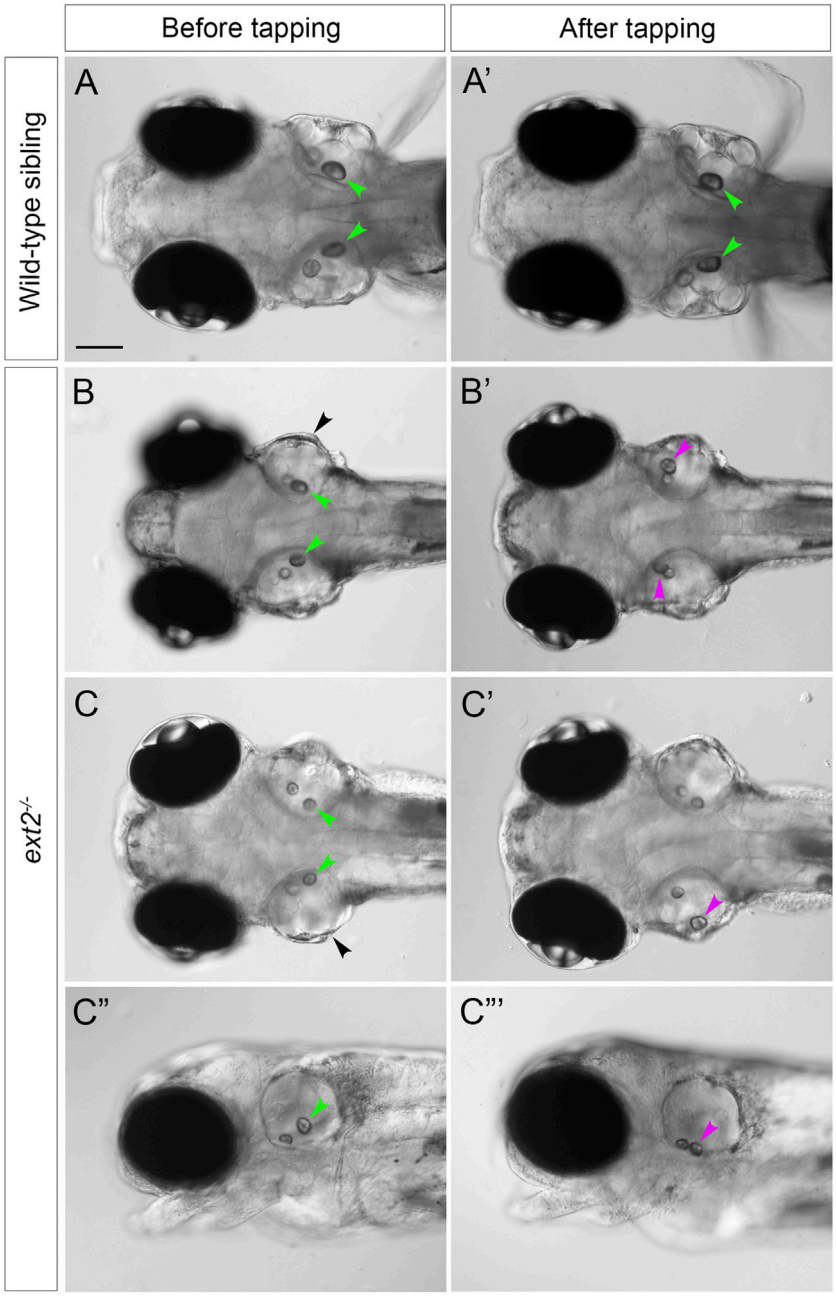

FIGURE 5
Saccular otoliths are not tethered correctly in the homozygous *ext2* mutant ear at 5 dpf. **(A–C"')** Live DIC images of embryos at 5 dpf, before (left-hand column) and after (right-hand column) tapping. In phenotypically wild-type sibling embryos **(A,A')**, saccular otoliths (green arrowheads) remain in place after tapping (in this example, one of the utricular otoliths in **(A')** has become slightly displaced). In *ext2* mutant embryos **(B–D')**, the saccular otolith in one or both ears becomes displaced (magenta arrowheads show new position after tapping). **(A–C')** are dorsal views with anterior to the left; **(C",C"')** are lateral views of the embryo shown in **(C,C')**. Note also the swollen ear morphology in the *ext2* mutants [**(B,C)**, black arrowheads]. In all panels, anterior is to the left. Scale bar in **(A)**, 100 μm (applies to all panels).

striking differences to the wild-type pattern. At 48 hpf, otic *vcanb* mRNA expression levels were lower in all *ext2* mutants tested (26/26) (Figure 3A'). However, by 72 hpf, *vcanb* expression in the unfused epithelial projections was abnormally high, and persisted until at least 5 dpf (Figure 3D,D',F). Mutants can easily be distinguished by their lack of pectoral fins, normally a strong site of *vcanb* expression at 50 hpf (Figure 3A,A'). Expression of *vcanb* in the periderm of the second arch (epidermis of the

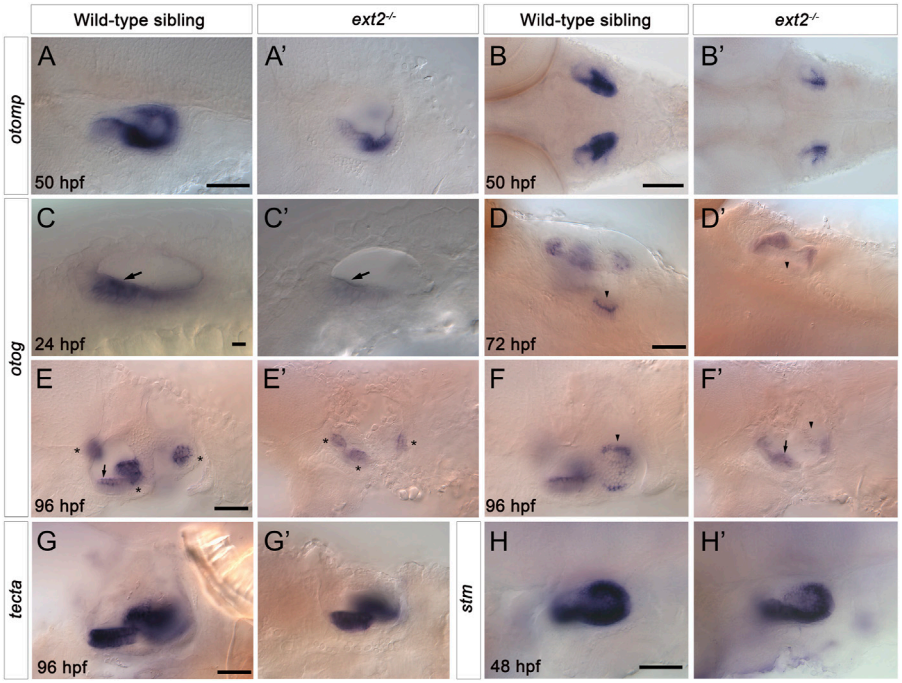

FIGURE 6
Expression of *otomp*, *otog* and *stm* is reduced in the saccular macula of the *ext2*$^{-/-}$ mutant ear. **(A–H')** *In situ* hybridisation to otolith marker genes in the ears of phenotypically wild-type sibling and *ext2* mutant embryos. **(A–B')** Levels of *otomp* expression in the *ext2* mutant ear **(A',B')** at 50 hpf were reduced compared with the wild type **(A,B)**. **(C–F')** Expression of *otog* at 24 hpf **(C,C')**, 72 hpf **(D,D')**, and 96 hpf **(E-F')** was significantly reduced in the *ext2* mutant ear. The images in **(F,F')** show a more medial focal plane of the same ears depicted in **(E,E')**, respectively. **(G,G')** Expression of *tecta* in the *ext2* mutant ear was unaltered at 96 hpf. **(H,H')** Expression of *stm* expression at 48 hpf was reduced in the posterior macula (arrowhead) of the *ext2* mutant ear. Arrowheads mark the posterior (saccular) macula; arrows mark the anterior (utricular) macula; asterisks mark the cristae. All images are lateral views with anterior to the left, apart from **(B,B',D,D')** (dorsal views with anterior to the left). In all panels, anterior is to the left. Scale bars: in **(A)**, 50 μm for **(A')**; in **(B)**, 100 μm for **(B')**; in **(C)**, 10 μm for **(C')**; in **(D)**, 50 μm for **(D')**; in **(E)**, 50 μm for **(E'–F')**; in **(G)**, 50 μm for **(G')**; in **(H)**, 50 μm for **(H')**.

developing operculum) was also considerably reduced in *ext2* mutants (Figure 3,B'). The *chsy1* transcript, known to be expressed in the outgrowing projections of the wild-type ear (Li et al., 2010), was also mildly up-regulated in the unfused projections of the *ext2* mutant ear at 72 hpf, although overall levels in the brain of *ext2* mutants were slightly lower than in the wild type (Figures 3G,H).

3.4 The pattern of chondroitin sulphate staining is altered, but hyaluronan is still present, in the *ext2* mutant ear

Overall levels of chondroitin sulphate (CS) were previously found to be normal in zebrafish *ext2* mutants at 6 dpf by reverse-phase ion-pair high-performance liquid chromatography (Holmborn et al., 2012). We used antibody staining to examine the spatial pattern of chondroitin sulphate (CS) in *ext2* mutant ears (Figure 4; Supplementary Movies S2,S4). The apical staining seen in phenotypically wild-type sibling ears at 40–45 hpf was not present in the mutant, even at later stages (Figure 4A–B'). Basal staining prefiguring projection outgrowth was delayed relative to that in the wild type, but otherwise appeared normal (Figures 4C–F'). At 48 hpf, a discrete patch of CS staining was found directly posterior to the anterior (utricular) macula in both wild-type and mutant embryos, marking the site of emergence of the ventral projection. In the example shown in Figure 4F', staining was specifically localised to the basal side of the cells that have just started to evaginate and move into the otic lumen. By 65 hpf, little CS signal remained in the acellular cores of the semicircular canal pillars in the wild-type ear (Figures 4G,G'; Supplementary Movie S3). By contrast, CS staining in the *ext2* mutant ear, like expression of *vcanb*, persisted abnormally and strongly in the unfused epithelial projections (Figures 4H, H', Supplementary Movie S4). Staining for CS indicated that an otolithic membrane was present in the *ext2* mutant, although staining at 65 hpf was reduced compared with that in the wild type, possibly indicating a thinner membrane (Figures 4G–H', blue asterisks; Supplementary Movies S3,S4).

To test whether hyaluronan (HA) is produced in the *ext2* mutant ear, we stained embryos for the expression of *ugdh*, a gene required for the production of HA, and with a biotinylated hyaluronic acid binding protein (HABP). Expression of *ugdh* was present, but reduced in levels, throughout the head of *ext2* mutant embryos, including in the ear (Supplementary Figure S4). Staining with HABP indicated that HA was still present in the cores of the unfused epithelial projections of the *ext2* mutant ear (Supplementary Figure S5).

3.5 Otoliths in the *ext2* mutant ear are not tethered correctly to the saccular macula

The posterior otolith (sagitta) frequently appeared misplaced in *ext2* mutants between 72 hpf and 5 dpf (Figures 2G,H), indicating defective tethering to its cognate sensory patch (the saccular macula). To investigate further, we performed a simple experiment to test whether the otolith could become dislodged after tapping the slide on which the fish was mounted (see Methods). Images of the ears were taken before and after tapping (Figure 5). In wild-type ears, all saccular otoliths (sagittae) remained in place after tapping (N = 8 embryos, n = 16 otoliths), whereas in 7 out of 8 *ext2* mutant embryos, one or both sagittae were displaced (Figure 5). Unlike the sagitta, the anterior otolith (lapillus) did not appear misplaced in any of the mutant embryos after tapping (N = 8 mutant embryos).

3.6 Genes involved in otolith formation and tethering show reduced expression in the *ext2* mutant ear

To test whether the otolith size and tethering defects reflect changes in the expression of genes coding for otolith matrix or otolithic membrane components, we examined the expression of selected markers using *in situ* hybridisation (Figure 6). Expression of *otolith matrix protein* (*otomp*) mRNA was significantly reduced in both the anterior and the posterior maculae in *ext2*$^{-/-}$ mutants (Figures 6A–B'). Expression of *starmaker* (*stm*) was present in both maculae in *ext2* mutants, with levels slightly reduced in the posterior (saccular) macula (Figures 6C,C'). We also analysed the expression of mRNA for *otogelin* (*otog*) and *alpha-tectorin* (*tecta*). Expression of *otog* was significantly reduced in the anterior (utricular) macula of *ext2* mutants at 24 hpf, and was absent from the posterior (saccular) macula from 72 to 120 hpf (Figures 6I–F'). Expression of *otog* in the three sensory cristae was also reduced in *ext2* mutants (Figures 6E,E'). However, expression of *tecta* mRNA appeared normal in the *ext2* mutant ear (Figures 6I–J').

4 Discussion

4.1 Presence of chondroitin sulphate marks initial sites of evagination of the otic epithelium

An unsolved question in zebrafish semicircular canal duct morphogenesis is what establishes the site of evagination of each of the epithelial projections, where a small number of cells start to move towards the lumen of the ear, involving a localised inversion of curvature of the epithelial sheet. To begin to answer this, our results identify the earliest signs of projection outgrowth: exquisitely localised patches of CS staining marking the sites where the epithelium will deform, present before any obvious morphological changes. These observations corroborate the finding that *chsy1*, which codes for the enzyme Chondroitin synthase 1, is expressed in the epithelial projections of the ear, and is required for their normal morphogenesis (Li et al., 2010). A similar transient and spatially restricted pattern of CS staining has been observed in the developing zebrafish heart, where it is required for normal atrioventricular canal formation (Peal et al., 2009). In the ear, CS staining was absent from cells forming the endolymphatic duct (ED), a tube that invaginates from dorsal otic epithelium. Unlike the evaginating epithelial projections, formation of the ED does not require any inversion of epithelial curvature. ED cells show apical constriction (Swinburne et al., 2018), and differ significantly in shape from those of the epithelial projections (Mendonca et al., 2021). Thus, the presence or absence of CS distinguishes between deformations of the epithelium with opposite orientations in the zebrafish ear; it will be interesting to see whether this is a general principle.

4.2 Growth of the epithelial projections in the zebrafish ear requires both hyaluronan and proteoglycans: proposal for a hyaluronan-proteoglycan-driven mechanism

Numerous lines of evidence support a model in which the synthesis of the non-sulphated GAG hyaluronan (HA), a giant linear polysaccharide of several million Daltons (reviewed in Toole, 2001), acts to propel the epithelial projections into the lumen of the anamniote inner ear. Local enzymatic digestion of HA, or a systemic block to HA biosynthesis, results in rudimentary epithelial projections that fail to meet and fuse (Haddon and Lewis, 1991; Busch-Nentwich et al., 2004; Geng et al., 2013; Munjal et al., 2021). However, the similar otic phenotypes in zebrafish morphants for *chsy1* (Li et al., 2010) and mutants for *ext2* (this work) demonstrate that synthesis of chondroitin sulphate (CS) and heparan sulphate (HS), respectively, are also critical for normal epithelial projection outgrowth. As HA is still present in *ext2* mutant ears, this

argues that HA alone is not sufficient for normal epithelial projection outgrowth, and that CSPGs and HSPGs are likely to play a role. In addition, ECM proteins expressed in the projections, such as the Type II collagens (Geng et al., 2013), might also contribute to projection outgrowth.

One of the remarkable aspects of semicircular canal morphogenesis in the zebrafish or *Xenopus* ear is the finger-like nature of the evaginating epithelial protrusions or projections, differing markedly from the walls of the flattened out-pocketings or pouches of the otic epithelium that form in the amniote ear (reviewed in Alsina and Whitfield, 2017). In the mouse, reciprocal signalling between otic epithelium and periotic mesenchyme, resulting in mesenchymal cell proliferation, is thought to be required to drive the epithelial walls of the pouches together to meet at a fusion plate (Salminen et al., 2000; Pirvola et al., 2004). By contrast, the epithelial projections in zebrafish are not underlain by mesenchyme as they grow into the otic lumen; instead, each projection has an acellular (matrix-filled) core. With only three or 4 cells at their tip (Waterman and Bell, 1984), these projections represent a highly anisotropic mode of growth. Haddon and Lewis recognised that HA must not only be synthesised locally but also be held in place in order to generate localised outgrowth (Haddon and Lewis, 1991). Munjal and others have extended this model, proposing that differential tissue stiffness, mediated by tensioned cell tethers, in combination with isotropic pressure from HA, acts to shape the projections (Munjal et al., 2021).

It is also possible that aggregation of proteoglycans and HA could generate a local expansion of the ECM beneath cells of the projection. HSPGs and CSPGs bind to HA via hyaluronan-proteoglycan link proteins (Haplns), generating large charged aggregates (reviewed in Toole, 2001). The Hapln genes *hapln1a* and *hapln3* are expressed in the epithelial projections of the zebrafish ear (Geng et al., 2013). Addition of proteoglycans is sufficient to cause the 'drastic swelling' of HA films *in vitro*, where linear HA chains, normally present in a random coil configuration, become stretched on incorporation of relatively small quantities of proteoglycan (Attili and Richter, 2013; Chang et al., 2016; reviewed in Richter et al., 2018). There are interesting parallels with the Hapln1a-dependent left-sided expansion of the cardiac ECM that occurs in the developing zebrafish heart prior to looping (Derrick et al., 2021). In the ear, anisotropy of the matrix in the projection cores, mediated by the stretching of HA chains driven by localised incorporation of proteoglycan, or alignment of other fibrillar components such as collagen, could help to direct projection outgrowth: this idea remains to be tested. The sulphation of HSPGs and CSPGs also confers a strong negative charge, important for hydration of the matrix. Diversity in the proteoglycan sulphation pattern, mediated by the enzymes coded for by *sulf* genes, some of which are expressed in the zebrafish ear (Gorsi et al., 2010; Meyers et al., 2013; Habicher et al., 2015), might provide further local heterogeneity in the mechanical properties of the otic ECM.

4.3 Implications for cell signalling in the developing ear

As in other species, zebrafish proteoglycans play an important role in the correct function of various signalling pathways, including Fgf, BMP and Wnt (see, for example, Norton et al., 2005; Li et al., 2010; Fischer et al., 2011; Meyers et al., 2013; Venero Galanternik et al., 2015). Although this was not the focus of our study, it is likely that disrupted signalling also contributes to the morphogenetic and patterning defects in the *ext2* mutant ear. Expression of *fgf8a* in the utricular macula appears relatively normal in the ears of *ext2*^{fw25e} mutants at 48 hpf, but the Fgf target gene *etv5b* is downregulated in various tissues, including the otic vesicle (Fischer et al., 2011). By contrast, expression of the Fgf target gene *pea3* appeared unchanged in the ear in *ext2* mutants or by treatment with SU5402 alone, but was strongly downregulated in SU5402-treated *ext2* mutants (Fischer et al., 2011). A detailed comparison of otic phenotypes will be important to reveal any similarities between the ears of *ext2* mutants and those with disrupted Fgf, BMP or Wnt signalling.

4.4 Development and tethering of otoliths in the *ext2* mutant ear

In addition to semicircular canal defects, the *ext2* mutant ear has otolith size and tethering abnormalities. Morpholino-mediated knockdown of *otomp* has been linked to slowed otolith growth (Murayama et al., 2005), and *otomp* expression is reduced in *ext2* mutant ears. Although otoliths were small in the *ext2* mutant, they stained for keratan sulphate (KS) as in the wild type. Keratan sulphate proteoglycans (KSPGs) are well-known constituents of amniote otoconia (reviewed in Lundberg et al., 2015). In the chicken, alpha-Tectorin, a major glycoprotein constitutent of the tectorial membrane, has characteristics of a "light" KSPG (Killick and Richardson, 1997), and KS on alpha-Tectorin might account for the otolithic membrane KS staining seen in the zebrafish. In zebrafish, Otogelin and alpha-Tectorin, respectively, establish and maintain otolith adhesion to the macula during otolith growth and biomineralisation (Stooke-Vaughan et al., 2015). A loss of adhesion of the sagitta (saccular otolith) in *ext2* mutants might be attributed to the lack of *otogelin* expression in the saccular macula. However, the early *ext2* mutant phenotype does not resemble that of the *otogelin* mutant, where only one otolith forms in each mutant ear (Stooke-Vaughan et al., 2015). Instead, the loss of saccular otolith tethering in the *ext2* mutant is more reminiscent of the mutant phenotype for *tecta*, where the sagittae can become dislodged between 3 dpf and 5 dpf, but the lapilli (utricular otoliths) are unaffected (Stooke-Vaughan et al., 2015). *Tecta* mRNA is expressed normally in the *ext2* mutant ear, and so it is not possible to attribute the otolith tethering defect to a loss of alpha-Tectorin. However, the *ext2* mutant phenotype suggests that one or more HSPGs are required for formation of a normal otolithic membrane and for normal

otolith tethering. Given the capacity of HS to interact with a large number of proteins (Vallet et al., 2022), HS-protein binding is likely to contribute to otolith tethering in the zebrafish ear.

5 Conclusion

In summary, our data show that the temporally- and spatially-restricted presence of CS marks the sites of epithelial projection outgrowth in the zebrafish ear. In addition, otic defects in the *ext2* mutant demonstrate that HS biosynthesis is essential for the evagination and growth of the epithelial projections, and for otolith tethering. These findings suggest that CSPGs and HSPGs, as well as HA, play important roles in semicircular canal duct morphogenesis, and are likely to impact both the mechanical and signalling properties of the otic epithelium.

Data availability statement

The original contributions presented in the study are included in the article/Supplementary Material; further inquiries can be directed to the corresponding author.

Ethics statement

Zebrafish were maintained according to recommended guidelines (Aleström et al., 2020). All animal work was reviewed and approved by the University of Sheffield Animal Welfare and Ethical Review Body (AWERB), and performed under licence from the UK Home Office (P66320E4E).

Author contributions

Data collection, curation, and analysis: AJ, SB, ED, and TW. Project administration and supervision: SB, TW. Funding acquisition: SB, TW. Writing: TW, with input from all other authors.

Funding

This work was funded by the Biotechnology and Biological Sciences Research Council (BBSRC: BB/J003050 to TW, BB/M01021X/1 and BB/S007008/1 to TW and SB). AJ was funded by a Doctoral Training Award from the Biotechnology and Biological Sciences Research Council BBSRC White Rose Doctoral Training Partnership in Mechanistic Biology (BB/M011151/1). ED was funded by a PhD studentship from the University of Sheffield (314420). Imaging was carried out in the Wolfson Light Microscopy Facility, supported by a BBSRC ALERT14 award to TW and SB for light-sheet microscopy (BB/M012522/1). The Sheffield zebrafish aquarium facilities were supported by the Medical Research Council (MRC: G0700091). The funders had no role in study design, data collection and analysis, decision to publish, or preparation of the manuscript.

Acknowledgments

We thank Henry Roehl for providing the *dak*^{tw25e} zebrafish mutant line and the *ext2* cDNA, for sharing reagents, and for advice on expression patterns. We thank the Sheffield Aquarium Team for expert care of the fish, Nick van Hateren for help with imaging, and Sarah Burbridge and Mar Marzo for technical assistance.

Conflict of interest

The authors declare that the research was conducted in the absence of any commercial or financial relationships that could be construed as a potential conflict of interest.

Publisher's note

Supplementary material

The Supplementary Material for this article can be found online at: https://www.frontiersin.org/articles/10.3389/fcell.2022.959624/full#supplementary-material

References

Aleström, P., D'Angelo, L., Midtlyng, P. J., Schorderet, D. F., Schulte-Merker, S., Sohm, F., et al. (2020). Zebrafish: Housing and husbandry recommendations. *Lab. Anim.* 54, 213–224. doi:10.1177/0023677219869037

Alsina, B., and Whitfield, T. T. (2017). Sculpting the labyrinth: Morphogenesis of the developing inner ear. *Semin. Cell Dev. Biol.* 65, 47–59. doi:10.1016/j.semcdb.2016.09.015

Attili, S., and Richter, R. P. (2013). Self-assembly and elasticity of hierarchical proteoglycan-hyaluronan brushes. *Soft Matter* 9, 10473. doi:10.1039/c3sm51213d

Bülow, H. E., and Hobert, O. (2006). The molecular diversity of glycosaminoglycans shapes animal development. *Annu. Rev. Cell Dev. Biol.* 22, 375–407. doi:10.1146/annurev.cellbio.22.010605.093433

Busch-Nentwich, E., Söllner, C., Roehl, H., and Nicolson, T. (2004). The deafness gene dfna5 is crucial for ugdh expression and HA production in the developing ear in zebrafish. *Development* 131, 943–951. doi:10.1242/dev.00961

Chang, P. S., McLane, L. T., Fogg, R., Scrimgeour, J., Temenoff, J. S., Granqvist, A., et al. (2016). Cell surface access is modulated by tethered bottlebrush proteoglycans. *Biophys. J.* 110, 2739–2750. doi:10.1016/j.bpj.2016.05.027

Clément, A., Wiweger, M., von der Hardt, S., Rusch, M. A., Selleck, S. B., Chien, C.-B., et al. (2008). Regulation of Zebrafish Skeletogenesis by ext2/dackel and papst1/pinscher. *PLoS Genet.* 4, e1000136. doi:10.1371/journal.pgen.1000136

Derrick, C. J., Sánchez-Posada, J., Hussein, F., Tessadori, F., Pollitt, E. J. G., Savage, A. M., et al. (2021). Asymmetric Hapln1a drives regionalized cardiac ECM expansion and promotes heart morphogenesis in zebrafish development. *Cardiovasc. Res.*, 1–15. doi:10.1101/838128

Filipek-Górniok, B., Holmborn, K., Haitina, T., Habicher, J., Oliveira, M. B., Hellgren, C., et al. (2013). Expression of chondroitin/dermatan sulfate glycosyltransferases during early zebrafish development. *Dev. Dyn.* 242, 964–975. doi:10.1002/dvdy.23981

Fischer, S., Filipek-Gorniok, B., and Ledin, J. (2011). *Zebrafish Ext2 is necessary for Fgf and Wnt signaling, but not for Hh signaling.*

Geng, F.-S., Abbas, L., Baxendale, S., Holdsworth, C. J., Swanson, A. G., Slanchev, K., et al. (2013). Semicircular canal morphogenesis in the zebrafish inner ear requires the function of *gpr126* (*lauscher*), an adhesion class G protein-coupled receptor gene. *Development* 140, 4362–4374. doi:10.1242/dev.098061

Gorsi, B., Whelan, S., and Stringer, S. E. (2010). *Dynamic expression patterns of 6-O endosulfatases during zebrafish development suggest a subfunctionalisation event for sulf2*, 3312–3323.

Habicher, J., Haitina, T., Eriksson, I., Holmborn, K., Dierker, T., Ahlberg, P. E., et al. (2015). Chondroitin/dermatan sulfate modification enzymes in zebrafish development. *PLoS One* 10, e0121957. doi:10.1371/journal.pone.0121957

Häcker, U., Lin, X., Perrimon, N., and Hacker, U. (1997). The Drosophila sugarless gene modulates Wingless signaling and encodes an enzyme involved in polysaccharide biosynthesis. *Development* 124, 3565–3573. doi:10.1242/dev.124.18.3565

Haddon, C., and Lewis, J. (1996). Early ear development in the embryo of the zebrafish, *Danio rerio*. *J. Comp. Neurol.* 365, 113–128. doi:10.1002/(SICI)1096-9861(19960129)365:1<113::AID-CNE9>3.0.CO;2-6

Haddon, C. M., and Lewis, J. H. (1991). Hyaluronan as a propellant for epithelial movement: The development of semicircular canals in the inner ear of *Xenopus*. *Development* 112, 541–550. doi:10.1242/dev.112.2.541

Haffter, P., Granato, M., Brand, M., Mullins, M. C., Hammerschmidt, M., Kane, D. A., et al. (1996). The identification of genes with unique and essential functions in the development of the zebrafish, *Danio rerio*. *Development* 123, 1–36. doi:10.1242/dev.123.1.1

Holmborn, K., Habicher, J., Kasza, Z., Eriksson, A. S., Filipek-Gorniok, B., Gopal, S., et al. (2012). On the roles and regulation of chondroitin sulfate and heparan sulfate in zebrafish pharyngeal cartilage morphogenesis. *J. Biol. Chem.* 287, 33905–33916. doi:10.1074/jbc.M112.401646

Kang, J. S., Oohashi, T., Kawakami, Y., Bekku, Y., Izpisúa Belmonte, J. C., Ninomiya, Y., et al. (2004). Characterization of *dermacan*, a novel zebrafish lectican gene, expressed in dermal bones. *Mech. Dev.* 121, 301–312. doi:10.1016/j.mod.2004.01.007

Karlstrom, R. O., Trowe, T., Klostermann, S., Baier, H., Brand, M., Crawford, A. D., et al. (1996). Zebrafish mutations affecting retinotectal axon pathfinding. *Development* 123, 427–438. doi:10.1242/dev.123.1.427

Killick, R., and Richardson, G. P. (1997). Antibodies to the sulphated, high molecular mass mouse tectorin stain hair bundles and the olfactory mucus layer. *Hear. Res.* 103, 131–141. doi:10.1016/s0378-5955(96)00174-8

Kimmel, C. B., Ballard, W. W., Kimmel, S. R., Ullmann, B., and Schilling, T. F. (1995). Stages of embryonic development of the zebrafish. *Dev. Dyn.* 203, 253–310. doi:10.1002/aja.1002030302

Lee, J. S., von der Hardt, S., Rusch, M. A., Stringer, S. E., Stickney, H. L., Talbot, W. S., et al. (2004). Axon sorting in the optic tract requires HSPG synthesis by *ext2* (*dackel*) and *extl3* (*boxer*). *Neuron* 44, 947–960. doi:10.1016/j.neuron.2004.11.029

Li, Y., Laue, K., Temtamy, S., Aglan, M., Kotan, L. D., Yigit, G., et al. (2010). Temtamy preaxial brachydactyly syndrome is caused by loss-of-function mutations in chondroitin synthase 1, a potential target of BMP signaling. *Am. J. Hum. Genet.* 87, 757–767. doi:10.1016/j.ajhg.2010.10.003

Lister, J. A., Robertson, C. P., Lepage, T., Johnson, S. L., and Raible, D. W. (1999). *Nacre* encodes a zebrafish microphthalmia-related protein that regulates neural-crest-derived pigment cell fate. *Development* 126, 3757–3767. doi:10.1242/dev.126.17.3757

Lundberg, Y. W., Xu, Y., Thiessen, K. D., and Kramer, K. L. (2015). *Mechanisms of otoconia and otolith development*, 239–253.

Mendonca, T., Jones, A. A., Pozo, J. M., Baxendale, S., Whitfield, T. T., Frangi, A. F., et al. (2021). Origami: Single-cell 3D shape dynamics oriented along the apico-basal axis of folding epithelia from fluorescence microscopy data. *PLoS Comput. Biol.* 17, e1009063. doi:10.1371/journal.pcbi.1009063

Meyers, J. R., Planamento, J., Ebrom, P., Krulewitz, N., Wade, E., Pownall, E., et al. (2013). Sulf1 modulates BMP signaling and is required for somite morphogenesis and development of the horizontal myoseptum. *Dev. Biol.* 378, 107–121. doi:10.1016/j.ydbio.2013.04.002

Munjal, A., Hannezo, E., Tsai, T. Y., Mitchison, T. J., and Megason, S. G. (2021). Extracellular hyaluronate pressure shaped by cellular tethers drives tissue morphogenesis. *Cell* 184, 6313–6325.e18. doi:10.1016/j.cell.2021.11.025.e18

Murayama, E., Herbomel, P., Kawakami, A., Takeda, H., and Nagasawa, H. (2005). Otolith matrix proteins OMP-1 and Otolin-1 are necessary for normal otolith growth and their correct anchoring onto the sensory maculae. *Mech. Dev.* 122, 791–803. doi:10.1016/j.mod.2005.03.002

Neuhauss, S. C. F., Solnica-Krezel, L., Schier, A. F., Zwartkruis, F., Stemple, D. L., Malicki, J., et al. (1996). Mutations affecting craniofacial development in zebrafish. *Development* 123, 357–367. doi:10.1242/dev.123.1.357

Norton, W. H. J., Ledin, J., Grandel, H., and Neumann, C. J. (2005). HSPG synthesis by zebrafish Ext2 and Extl3 is required for Fgf10 signalling during limb development. *Development* 8, 4963–4973. doi:10.1242/dev.02084

Peal, D. S., Burns, C. G., Macrae, C. A., and Milan, D. (2009). Chondroitin sulfate expression is required for cardiac atrioventricular canal formation. *Dev. Dyn.* 238, 3103–3110. doi:10.1002/dvdy.22154

Pirvola, U., Zhang, X., Mantela, J., Ornitz, D. M., and Ylikoski, J. (2004). Fgf9 signaling regulates inner ear morphogenesis through epithelial-mesenchymal interactions. *Dev. Biol.* 273, 350–360. doi:10.1016/j.ydbio.2004.06.010

Richter, R. P., Baranova, N. S., Day, A. J., and Kwok, J. C. (2018). Glycosaminoglycans in extracellular matrix organisation: Are concepts from soft matter physics key to understanding the formation of perineuronal nets? *Curr. Opin. Struct. Biol.* 50, 65–74. doi:10.1016/j.sbi.2017.12.002

Salminen, M., Meyer, B. I., Bober, E., and Gruss, P. (2000). Netrin 1 is required for semicircular canal formation in the mouse inner ear. *Development* 127, 13–22. doi:10.1242/dev.127.1.13

Schilling, T. F., Piotrowski, T., Grandel, H., Brand, M., Heisenberg, C.-P., Jiang, Y.-J., et al. (1996). Jaw and branchial arch mutants in zebrafish I: Branchial arches. *Development* 123, 329–344. doi:10.1242/dev.123.1.329

Schindelin, J., Arganda-Carreras, I., Frise, E., Kaynig, V., Longair, M., Pietzsch, T., et al. (2012). Fiji: An open-source platform for biological-image analysis. *Nat. Methods* 9, 676–682. doi:10.1038/nmeth.2019

Söllner, C., Burghammer, M., Busch-Nentwich, E., Berger, J., Schwarz, H., Riekel, C., et al. (2003). Control of crystal size and lattice formation by Starmaker in otolith biomineralization. *Science* 302, 282–286. doi:10.1126/science.1088443

Stooke-Vaughan, G. A., Obholzer, N. D., Baxendale, S., Megason, S. G., and Whitfield, T. T. (2015). Otolith tethering in the zebrafish otic vesicle requires Otogelin and alpha-Tectorin. *Development* 142, 1137–1145. doi:10.1242/dev.116632

Swinburne, I. A., Mosaliganti, K. R., Upadhyayula, S., Liu, T. L., Hildebrand, D. G. C., Tsai, T. Y. C., et al. (2018). Lamellar projections in the endolymphatic sac act as a relief valve to regulate inner ear pressure. *Elife* 7, e37131. doi:10.7554/eLife.37131

Thisse, C., and Thisse, B. (2008). High-resolution *in situ* hybridization to whole-mount zebrafish embryos. *Nat. Protoc.* 3, 59–69. doi:10.1038/nprot.2007.514

Toole, B. P. (2001). Hyaluronan in morphogenesis. *Semin. Cell Dev. Biol.* 12, 79–87. doi:10.1006/scdb.2000.0244

Trowe, T., Klostermann, S., Baier, H., Granato, M., Crawford, A. D., Grunewald, B., et al. (1996). Mutations disrupting the ordering and topographic mapping of axons in the retinotectal projection of the zebrafish, *Danio rerio*. *Development* 123, 439–450. doi:10.1242/dev.123.1.439

Vallet, S. D., Berthollier, C., and Ricard-Blum, S. (2022). The glycosaminoglycan interactome 2.0. *Am J Physiol Cell Physiol.* 322, C1271–C1278. doi:10.1152/ajpcell.00095.2022

van Eeden, F. J. M., Granato, M., Schach, U., Brand, M., Furutani-Seiki, M., Haffter, P., et al. (1996). Genetic analysis of fin formation in the zebrafish , *Danio rerio*. *Development* 123, 255–262. doi:10.1242/dev.123.1.255

Venero Galanternik, M., Kramer, K. L., and Piotrowski, T. (2015). Heparan sulfate proteoglycans regulate fgf signaling and cell polarity during collective cell migration. *Cell Rep.* 10, 414–428. doi:10.1016/j.celrep.2014.12.043

Walsh, E. C., and Stainier, D. Y. R. (2001). UDP-glucose dehydrogenase required for cardiac valve formation in zebrafish. *Science.* 293, 1670–1673. doi:10.1126/science.293.5535.1670

Waterman, R. E., and Bell, D. H. (1984). Epithelial fusion during early semicircular canal formation in the embryonic zebrafish, *Brachydanio rerio*. *Anat. Rec.* 210, 101–114. doi:10.1002/ar.1092100113

Westerfield, M. (2007). *The zebrafish book: A guide for the laboratory use of zebrafish (*Danio rerio*)*. Eugene: University of Oregon Press.

Whitfield, T. T., Granato, M., van Eeden, F. J. M., Schach, U., Brand, M., Furutani-Seiki, M., et al. (1996). Mutations affecting development of the zebrafish inner ear and lateral line. *Development* 123, 241–254. doi:10.1242/dev.123.1.241

Wiweger, M. I., De Andrea, C. E., Scheepstra, K. W. F., Zhao, Z., and Hogendoorn, P. C. W. (2014). Possible effects of EXT2 on mesenchymal differentiation - lessons from the zebrafish. *Orphanet J. Rare Dis.* 9, 35. doi:10.1186/1750-1172-9-35

Wiweger, M. I., Zhao, Z., van Merkesteyn, R. J., Roehl, H. H., and Hogendoorn, P. C. (2012). HSPG-deficient zebrafish uncovers dental aspect of multiple osteochondromas. *PLoS One* 7, e29734. doi:10.1371/journal.pone.0029734

Zimmer, B. M., Barycki, J. J., and Simpson, M. A. (2021). Integration of sugar metabolism and proteoglycan synthesis by UDP-glucose dehydrogenase. *J. Histochem. Cytochem.* 69, 13–23. doi:10.1369/0022155420947500

Advantages of publishing in Frontiers

OPEN ACCESS
Articles are free to read for greatest visibility and readership

FAST PUBLICATION
Around 90 days from submission to decision

HIGH QUALITY PEER-REVIEW
Rigorous, collaborative, and constructive peer-review

TRANSPARENT PEER-REVIEW
Editors and reviewers acknowledged by name on published articles

Frontiers
Avenue du Tribunal-Fédéral 34
1005 Lausanne | Switzerland

Visit us: www.frontiersin.org
Contact us: frontiersin.org/about/contact

REPRODUCIBILITY OF RESEARCH
Support open data and methods to enhance research reproducibility

DIGITAL PUBLISHING
Articles designed for optimal readership across devices

FOLLOW US
@frontiersin

IMPACT METRICS
Advanced article metrics track visibility across digital media

EXTENSIVE PROMOTION
Marketing and promotion of impactful research

LOOP RESEARCH NETWORK
Our network increases your article's readership